

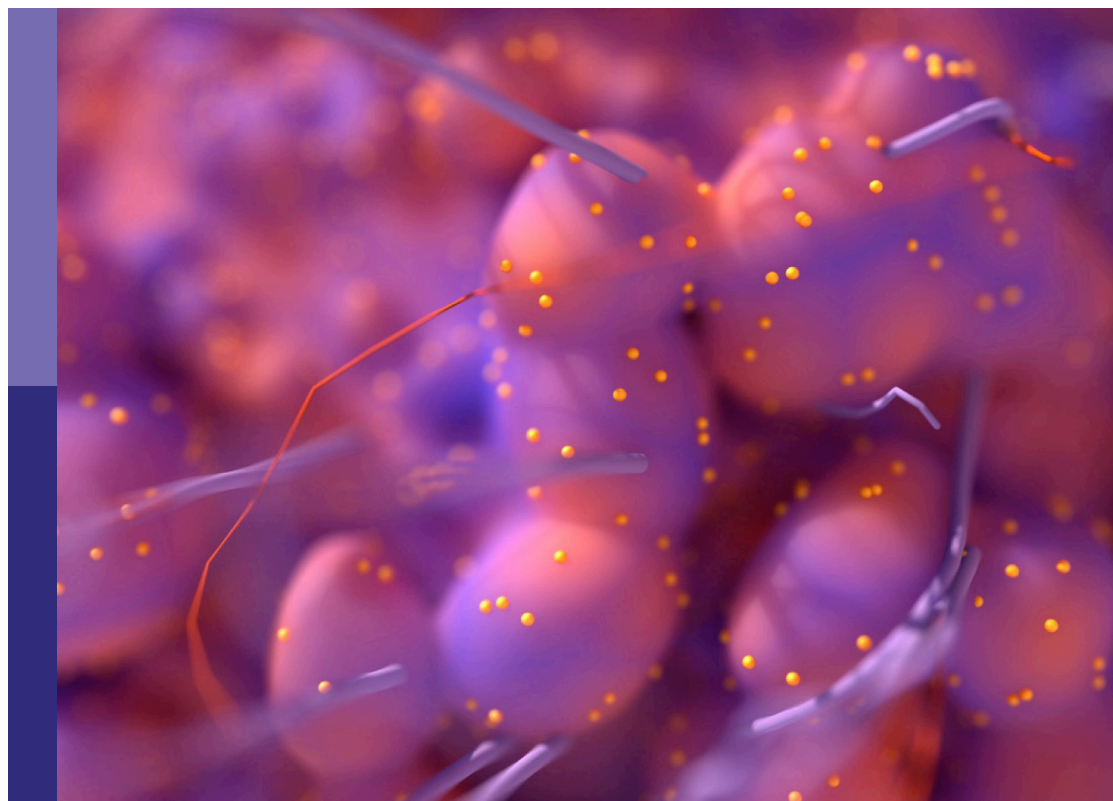
Out-of-field second primary cancer induction: Radiation-biology, epidemiology, dosimetry and modelling

Edited by

Beatriz Sanchez-Nieto, Alexandru Dasu, Francisco Sanchez-Doblado, Liliana Stolarczyk and Wayne D. Newhauser

Published in

Frontiers in Oncology



FRONTIERS EBOOK COPYRIGHT STATEMENT

The copyright in the text of individual articles in this ebook is the property of their respective authors or their respective institutions or funders. The copyright in graphics and images within each article may be subject to copyright of other parties. In both cases this is subject to a license granted to Frontiers.

The compilation of articles constituting this ebook is the property of Frontiers.

Each article within this ebook, and the ebook itself, are published under the most recent version of the Creative Commons CC-BY licence. The version current at the date of publication of this ebook is CC-BY 4.0. If the CC-BY licence is updated, the licence granted by Frontiers is automatically updated to the new version.

When exercising any right under the CC-BY licence, Frontiers must be attributed as the original publisher of the article or ebook, as applicable.

Authors have the responsibility of ensuring that any graphics or other materials which are the property of others may be included in the CC-BY licence, but this should be checked before relying on the CC-BY licence to reproduce those materials. Any copyright notices relating to those materials must be complied with.

Copyright and source acknowledgement notices may not be removed and must be displayed in any copy, derivative work or partial copy which includes the elements in question.

All copyright, and all rights therein, are protected by national and international copyright laws. The above represents a summary only. For further information please read Frontiers' Conditions for Website Use and Copyright Statement, and the applicable CC-BY licence.

ISSN 1664-8714
ISBN 978-2-83251-093-3
DOI 10.3389/978-2-83251-093-3

About Frontiers

Frontiers is more than just an open access publisher of scholarly articles: it is a pioneering approach to the world of academia, radically improving the way scholarly research is managed. The grand vision of Frontiers is a world where all people have an equal opportunity to seek, share and generate knowledge. Frontiers provides immediate and permanent online open access to all its publications, but this alone is not enough to realize our grand goals.

Frontiers journal series

The Frontiers journal series is a multi-tier and interdisciplinary set of open-access, online journals, promising a paradigm shift from the current review, selection and dissemination processes in academic publishing. All Frontiers journals are driven by researchers for researchers; therefore, they constitute a service to the scholarly community. At the same time, the *Frontiers journal series* operates on a revolutionary invention, the tiered publishing system, initially addressing specific communities of scholars, and gradually climbing up to broader public understanding, thus serving the interests of the lay society, too.

Dedication to quality

Each Frontiers article is a landmark of the highest quality, thanks to genuinely collaborative interactions between authors and review editors, who include some of the world's best academicians. Research must be certified by peers before entering a stream of knowledge that may eventually reach the public - and shape society; therefore, Frontiers only applies the most rigorous and unbiased reviews. Frontiers revolutionizes research publishing by freely delivering the most outstanding research, evaluated with no bias from both the academic and social point of view. By applying the most advanced information technologies, Frontiers is catapulting scholarly publishing into a new generation.

What are Frontiers Research Topics?

Frontiers Research Topics are very popular trademarks of the *Frontiers journals series*: they are collections of at least ten articles, all centered on a particular subject. With their unique mix of varied contributions from Original Research to Review Articles, Frontiers Research Topics unify the most influential researchers, the latest key findings and historical advances in a hot research area.

Find out more on how to host your own Frontiers Research Topic or contribute to one as an author by contacting the Frontiers editorial office: frontiersin.org/about/contact

Out-of-field second primary cancer induction: Radiation-biology, epidemiology, dosimetry and modelling

Topic editors

Beatriz Sanchez-Nieto — Pontifical Catholic University of Chile, Chile

Alexandru Dasu — Skandion Clinic, Sweden

Francisco Sanchez-Doblado — Sevilla University, Spain

Liliana Stolarczyk — Aarhus University Hospital, Denmark

Wayne D. Newhauser — Louisiana State University, United States

Citation

Sanchez-Nieto, B., Dasu, A., Sanchez-Doblado, F., Stolarczyk, L., Newhauser, W. D., eds. (2023). *Out-of-field second primary cancer induction: Radiation-biology, epidemiology, dosimetry and modelling*. Lausanne: Frontiers Media SA.
doi: 10.3389/978-2-83251-093-3

Table of contents

- 05 **Editorial: Out-of-field second primary cancer induction: Dosimetry and modelling**
Beatriz Sánchez-Nieto, Liliana Stolarczyk, Alexandru Dasu, Wayne D. Newhauser and Francisco Sánchez-Doblado
- 08 **Peripheral Organ Equivalent Dose Estimation Procedure in Proton Therapy**
Carles Domingo, Juan Ignacio Lagares, Maite Romero-Expósito, Beatriz Sánchez-Nieto, Jaime J. Nieto-Camero, Jose Antonio Terrón, Leticia Irazola, Alexandru Dasu and Francisco Sánchez-Doblado
- 22 **Determining Out-of-Field Doses and Second Cancer Risk From Proton Therapy in Young Patients—An Overview**
Maite Romero-Expósito, Iuliana Toma-Dasu and Alexandru Dasu
- 37 **Validation of a Monte Carlo Framework for Out-of-Field Dose Calculations in Proton Therapy**
Marijke De Saint-Hubert, Nico Verbeek, Christian Bäumer, Johannes Esser, Jörg Wulff, Racell Nabha, Olivier Van Hoey, Jérémie Dabin, Florian Stuckmann, Fabiano Vasi, Stephan Radonic, Guillaume Boissonnat, Uwe Schneider, Miguel Rodriguez, Beate Timmermann, Isabelle Thierry-Chef and Lorenzo Brualla
- 52 **Experimental Validation of an Analytical Program and a Monte Carlo Simulation for the Computation of the Far Out-of-Field Dose in External Beam Photon Therapy Applied to Pediatric Patients**
Marijke De Saint-Hubert, Finja Suesselbeck, Fabiano Vasi, Florian Stuckmann, Miguel Rodriguez, Jérémie Dabin, Beate Timmermann, Isabelle Thierry-Chef, Uwe Schneider and Lorenzo Brualla
- 64 **Neutron Radiation Dose Measurements in a Scanning Proton Therapy Room: Can Parents Remain Near Their Children During Treatment?**
Vladimir Mares, Jad Farah, Marijke De Saint-Hubert, Szymon Domański, Carles Domingo, Martin Dommert, Magdalena Kłodowska, Katarzyna Krzempek, Michał Kuć, Immaculada Martínez-Rovira, Edyta Michaś, Natalia Mojżeszek, Łukasz Murawski, Ondrej Ploc, Maite Romero-Expósito, Marco Tisi, François Trompier, Olivier Van Hoey, Laurent Van Ryckeghem, Marek Wielunski, Roger M. Harrison, Liliana Stolarczyk and Paweł Olko
- 77 **Out-of-Field Doses Produced by a Proton Scanning Beam Inside Pediatric Anthropomorphic Phantoms and Their Comparison With Different Photon Modalities**
Željka Knežević, Liliana Stolarczyk, Iva Ambrožová, Miguel Á. Caballero-Pacheco, Marie Davidková, Marijke De Saint-Hubert, Carles Domingo, Kinga Jeleń, Renata Kopeć, Dawid Krzempek, Marija Majer, Saveta Miljanić, Natalia Mojżeszek, Maite Romero-Expósito, Immaculada Martínez-Rovira, Roger M. Harrison and Paweł Olko

- 91 **Comparison of Breast Cancer Radiotherapy Techniques Regarding Secondary Cancer Risk and Normal Tissue Complication Probability – Modelling and Measurements Using a 3D-Printed Phantom**
Marc Vogel, Jonas Gade, Bernd Timm, Michaela Schürmann, Hendrik Auerbach, Frank Nüsken, Christian Rübe, Patrick Melchior and Yvonne Dzierma
- 114 **Range-shifter effects on the stray field in proton therapy measured with the variance–covariance method**
Linda Eliasson, Jan Lillhök, Torbjörn Bäck, Robert Billnert-Maróti, Alexandru Dasu and Malgorzata Liszka
- 128 **Comparison of 3DCRT and IMRT out-of-field doses in pediatric patients using Monte Carlo simulations with treatment planning system calculations and measurements**
Ana Cravo Sá, Andreia Barateiro, Bryan P. Bednarz, Pedro Almeida, Pedro Vaz and Tiago Madaleno
- 142 **Simulation and experimental verification of ambient neutron doses in a pencil beam scanning proton therapy room as a function of treatment plan parameters**
Olivier Van Hoey, Liliana Stolarczyk, Jan Lillhök, Linda Eliasson, Natalia Mojzeszek, Malgorzata Liszka, Ali Alkhiat, Vladimir Mares, François Trompier, Sebastian Trinkl, Immaculada Martínez-Rovira, Maite Romero-Expósito, Carles Domingo, Ondrej Ploc, Roger Harrison and Pawel Olko
- 164 **A simple analytical model for a fast 3D assessment of peripheral photon dose during coplanar isocentric photon radiotherapy**
Beatriz Sánchez-Nieto, Ignacio N. López-Martínez, José Luis Rodríguez-Mongua and Ignacio Espinoza



OPEN ACCESS

EDITED AND REVIEWED BY
Timothy James Kinsella,
Brown University, United States

*CORRESPONDENCE

Beatriz Sánchez-Nieto
bsanchezn@uc.cl

SPECIALTY SECTION

This article was submitted to
Radiation Oncology,
a section of the journal
Frontiers in Oncology

RECEIVED 22 October 2022

ACCEPTED 28 October 2022

PUBLISHED 05 December 2022

CITATION

Sánchez-Nieto B, Stolarczyk L,
Dasu A, Newhauser WD and
Sánchez-Doblado F (2022) Editorial:
Out-of-field second primary cancer
induction: Dosimetry and modelling.
Front. Oncol. 12:1076792.
doi: 10.3389/fonc.2022.1076792

COPYRIGHT

© 2022 Sánchez-Nieto, Stolarczyk,
Dasu, Newhauser and Sánchez-
Doblado. This is an open-access article
distributed under the terms of the
Creative Commons Attribution License
(CC BY). The use, distribution or
reproduction in other forums is
permitted, provided the original
author(s) and the copyright owner(s)
are credited and that the original
publication in this journal is cited, in
accordance with accepted academic
practice. No use, distribution or
reproduction is permitted which does
not comply with these terms.

Editorial: Out-of-field second primary cancer induction: Dosimetry and modelling

Beatriz Sánchez-Nieto^{1*}, Liliana Stolarczyk^{2,3},
Alexandru Dasu^{4,5}, Wayne D. Newhauser⁶
and Francisco Sánchez-Doblado⁷

¹Institute of Physics, Faculty of Physics, Pontifical Catholic University of Chile, Santiago, Chile,

²Danish Center for Particle Therapy, Aarhus University Hospital, Aarhus, Denmark, ³The Henryk Niewodniczański Institute of Nuclear Physics, Polish Academy of Sciences, Krakow, Poland,

⁴Medical Radiation Sciences, Department of Immunology, Genetics and Pathology, Uppsala University, Uppsala, Sweden, ⁵The Skandion Clinic, Uppsala, Sweden, ⁶Department of Physics and Astronomy, Louisiana State University, Baton Rouge, LA, United States, ⁷Faculty of Medicine, University of Seville, Seville, Spain

KEYWORDS

peripheral dose, out-of-field dose, photon radiotherapy, proton radiotherapy, radiation induced cancer, second cancer

Editorial on the Research Topic

Out-of-field second primary cancer induction: Dosimetry and modelling

Second primary cancer induction is a growing concern, particularly for the younger cancer patient population with a longer life expectancy, as demonstrated by the increasing number of publications on the topic. Still, there is much work to do (1), such as assessing problems associated with the dosimetry under no reference conditions (particularly in proton treatments) or the presence of mixed-fields. Additionally, due to the poor performance of commercial treatment planning systems (TPS) in stray dose calculations for photon (2) and proton radiotherapy (RT), the development and implementation of computational tools are needed for out-of-field dose estimation in a systematic way. Thus, dosimetric information might be part of databases for cancer patients treated with modern RT techniques together with detrimental outcomes such as second primary cancers. The latter will improve existing risk models, which should also be considered during RT plan optimization.

This issue focuses mainly on the dosimetric and modeling aspects of the out-of-field radiation generated during photon (Sa et al., Saint-Hubert et al., Sánchez-Nieto et al., Vogel et al.), proton (Eliasson et al., Carles Domingo et al., Hoey et al., Mares et al. and Saint-Hubert et al.) therapies as well as a comparison between the second therapies (Knežević et al.). A review (Romero-Expósito et al.) of the current status of the problems encountered when determining out-of-field doses in proton therapy in young patients is also part of this issue.

Sa et al. study out-of-field doses during photon RT of a brain tumor in a pediatric phantom using TLD measurements and Monte Carlo (MC) simulations for three-

dimensional conformal radiotherapy (3DCRT), and intensity modulated radiotherapy (IMRT). Similarly, [Vogel et al.](#) present a planning exercise on breast irradiation comparing the two mentioned techniques with the addition of either sequential or simultaneous integrated external RT or interstitial multicatheter brachytherapy. The results from both papers show that in terms of peripheral doses, the 3DCRT, combined with an interstitial multicatheter brachytherapy boost, is the most suitable technique. However, it is essential to highlight the apparent advantages of IMRT (e.g., better target conformity and thus lower NTCP) when considering a more comprehensive biological index performance (3).

Two studies delve into developing computational tools for stray dose calculation in photon RT. [Saint-Hubert et al.](#), present the experimental validation of Hauri's model (4) and a fast Monte Carlo algorithm, both coded as a script running in the Eclipse Treatment Planning System (TPS) (v. 15.6). Discrepancies between the analytical model and MC were in general smaller than 40% and 20%, respectively. [Sánchez-Nieto et al.](#) propose a relatively simple analytical model which, from minimum information of the associated RT plan, calculates the DVH of out-of-field organs through a graphical user interface (termed Periphocal 3D). The model was trained using 3D dose volume data calculated by MC simulations and allows peripheral dose calculation for isocentric 3DCRT, IMRT, or VMAT with an uncertainty of $\pm 23\%$. Comparison of the model with TLD measurements inside an anthropomorphic phantom for a VMAT treatment and with a previously published physics-based analytical model (5) showed agreement within the model's uncertainties. These two implementations of out-of-field dose computational tools ease the theoretical second cancer risk assessment, proper analysis of data derived from epidemiological reports, and treatment plan optimization, considering second primary cancer probabilities as an objective function.

The second part of this issue deals with out-of-field doses from proton irradiation. Compared to conventional photon therapy, proton therapy (PT) has the potential to reduce exposure and radiation risks outside the target volume. Nevertheless, there is still a concern that stray radiation can increase secondary cancer risks (particularly in young patients who are more radiosensitive). As mentioned in the review ([Romero-Expósito et al.](#)), most of the published research has been conducted for passive scattering installations, while studies on the more recent scanning proton beams dominate this issue. [Hoey et al.](#), [Mares et al.](#) and [Eliasson et al.](#) analyze the complex dependences of patient and proton field size, range, modulation width, or the use of a range shifter on the peripheral dose. [Hoey et al.](#) present a general MC model as the first step toward a tool for predicting out-of-field neutron doses in scanning proton therapy facilities. Simulations with the verified model enabled a detailed study of the neutron ambient dose equivalent $H^*(10)$ variation with plan parameters. They concluded that it is not enough to normalize the out-of-field neutron doses only to the

target dose, as done in most of the published papers, but that it is essential to provide additional properties of the treatment plan, such as range, modulation, and field size. [Mares et al.](#) show the impact of the (pediatric) patient size on $H^*(10)$ with a focus on the possibility that parents or other comforters can remain inside the treatment room during scanning PT (which may be beneficial when it is not possible to treat children under anesthesia). However, it is acknowledged that further work considering other factors such as field size, range, modulation width, or the presence and position of the range shifter is required before general recommendations can be given. In [Eliasson et al.](#), the influence of beam energy, detector and range-shifter positions on the absorbed dose, LET, and dose equivalent was investigated using MC simulations and experimental measurements with microdosimetric tissue-equivalent proportional counters (TEPCs). They showed that the proton contribution scattered directly from the range shifter dominates in some situations, and although the LET of the radiation is decreased, $H^*(10)$ is increased by a factor of up to 3.

The complex and different dependencies of proton technique, patient size, and treatment parameters on the stray dose distribution may make non-trivial the development of methodologies for the estimation of out-of-field dose equivalent. This is the aim of the works by [Saint-Hubert et al.](#) and [Domingo et al.](#) The first study presents the evaluation of the accuracy of a computational method (based on the TOPAS framework) compared to experimental measurements. The development of such an MC framework could lead to tools for dose optimization in pediatric PT. A different approach is followed by [Domingo et al.](#) who propose a reproducible methodology for head and abdomen PT treatments (based on measurements of photon and neutron fluences using passive dosimeters inside an anthropomorphic phantom and complemented by the MC generation of the neutron spectra at the same points) that allows calculation of the dose equivalent to out-of-field organs in passive facilities.

As a finishing touch, the work by [Knežević et al.](#) analyzes and compares out-of-field neutron and non-neutron organ doses inside 5- and 10-year-old pediatric anthropomorphic phantoms from PT for a brain tumor. Out-of-field doses measured using intensity-modulated proton therapy (IMPT) were compared with IMRT, 3DCRT, and Gamma Knife radiosurgery. The total organ dose equivalent expressed as the sum of neutron and non-neutron components in IMPT was found to be significantly lower (2-3 orders of magnitude) compared with photon RT techniques for the same target dose.

Author contributions

BS-N drafted the editorial, and AD, FS-D, LS, and WN contributed by summarizing the published manuscripts for which they acted as editors, revised the draft, and make

suggestions for the final text. All authors contributed to the article and approved the submitted version.

Conflict of interest

The authors declare that the research was conducted in the absence of any commercial or financial relationships that could be construed as a potential conflict of interest.

Publisher's note

All claims expressed in this article are solely those of the authors and do not necessarily represent those of their affiliated organizations, or those of the publisher, the editors and the reviewers. Any product that may be evaluated in this article, or claim that may be made by its manufacturer, is not guaranteed or endorsed by the publisher.

References

1. Mazonakis M, Damilakis J. Out-of-Field organ doses and associated risk of cancer development following radiation therapy with photons. *Physica Med* (2021) 90(October):73–82. doi: 10.1016/j.ejmp.2021.09.005
2. Sánchez-Nieto B, Medina-Ascanio KN, Rodríguez-Mongua JL, Doerner E, Espinoza I. Study of out-of-Field dose in photon radiotherapy: A commercial treatment planning system versus measurements and Monte Carlo simulations. *Med Phys* (2020) 47(9):4616–25. doi: 10.1002/mp.14356
3. Sánchez-Nieto B, Romero-Expósito M, Terrón JA, Irazola L, García Hernández MT, Mateos JC, et al. External photon radiation treatment for prostate cancer: Uncomplicated and cancer-free control probability assessment of 36 plans. *Physica Med* (2019) 66: 88–96 doi: 10.1016/j.ejmp.2019.09.076
4. Hauri P, Hälg RA, Besserer Jürgen, Schneider. U. A general model for stray dose calculation of static and intensity-modulated photon radiation. *Med Phys* (2016) 43(4):1955–685. doi: 10.1118/1.4944421
5. Schneider CW, Newhauser WD, Wilson LJ, KapschRP. A physics-based analytical model of absorbed dose from primary, leakage, and scattered photons from megavoltage radiotherapy with MLCs. *Phys Med Biol* 64 (2019) 185017 (21pp).



Peripheral Organ Equivalent Dose Estimation Procedure in Proton Therapy

Carles Domingo^{1†}, Juan Ignacio Lagares^{2†}, Maite Romero-Expósito³, Beatriz Sánchez-Nieto⁴, Jaime J. Nieto-Camero⁵, Jose Antonio Terrón⁶, Leticia Irazola⁷, Alexandru Dasu^{3,8} and Francisco Sánchez-Doblado^{9*}

OPEN ACCESS

Edited by:

Dinesh Thotala,
Washington University in St. Louis,
United States

Reviewed by:

Pedro Vaz,
Universidade de Lisboa, Portugal
James Chow,
University of Toronto, Canada
Facundo Ballester,
University of Valencia, Spain

*Correspondence:

Francisco Sánchez-Doblado
paco@us.es

[†]These authors share first authorship

Specialty section:

This article was submitted to
Radiation Oncology,
a section of the journal
Frontiers in Oncology

Received: 23 February 2022

Accepted: 19 April 2022

Published: 25 May 2022

Citation:

Domingo C, Lagares JJ, Romero-Expósito M, Sánchez-Nieto B, Nieto-Camero JJ, Terrón JA, Irazola L, Dasu A and Sánchez-Doblado F (2022) Peripheral Organ Equivalent Dose Estimation Procedure in Proton Therapy. *Front. Oncol.* 12:882476. doi: 10.3389/fonc.2022.882476

¹ Departament de Física, Universitat Autònoma de Barcelona, Bellaterra, Spain, ² Unidad de Aplicaciones Médicas, Departamento de Tecnología, Centro de Investigaciones Energéticas Medioambientales y Tecnológicas (CIEMAT), Madrid, Spain, ³ The Skandion Clinic, Uppsala, Sweden, ⁴ Instituto de Física, Pontificia Universidad Católica de Chile, Santiago, Chile, ⁵ Medical Radiation Group, iThemba Labs, Faure, South Africa, ⁶ Servicio de Radiofísica, Hospital Universitario Virgen Macarena, Sevilla, Spain, ⁷ Servicio de Radiofísica y Protección Radiológica, Clínica Universidad de Navarra, Pamplona, Spain, ⁸ Medical Radiation Sciences, Department of Immunology, Genetics and Pathology, Uppsala University, Uppsala, Sweden, ⁹ Dpto Fisiología Médica y Biofísica, Universidad de Sevilla, Sevilla, Spain

The aim of this work is to present a reproducible methodology for the evaluation of total equivalent doses in organs during proton therapy facilities. The methodology is based on measuring the dose equivalent in representative locations inside an anthropomorphic phantom where photon and neutron dosimeters were inserted. The Monte Carlo simulation was needed for obtaining neutron energy distribution inside the phantom. The methodology was implemented for a head irradiation case in the passive proton beam of iThemba Labs (South Africa). Thermoluminescent dosimeter (TLD)-600 and TLD-700 pairs were used as dosimeters inside the phantom and GEANT code for simulations. In addition, Bonner sphere spectrometry was performed inside the treatment room to obtain the neutron spectra, some relevant neutron dosimetric quantities per treatment Gy, and a percentual distribution of neutron fluence and ambient dose equivalent in four energy groups, at two locations. The neutron spectrum at one of those locations was also simulated so that a reasonable agreement between simulation and measurement allowed a validation of the simulation. Results showed that the total out-of-field dose equivalent inside the phantom ranged from 1.4 to 0.28 mSv/Gy, mainly due to the neutron contribution and with a small contribution from photons, 10% on average. The order of magnitude of the equivalent dose in organs was similar, displaying a slow reduction in values as the organ is farther from the target volume. These values were in agreement with those found by other authors in other passive beam facilities under similar irradiation and measurement conditions.

Keywords: peripheral organ dose, proton therapy, neutron spectrometry, secondary cancer risk, neutron and photon dose

1 INTRODUCTION

Worldwide, an estimated 19.3 million new cancer cases were diagnosed in 2020 (1). Many of these cancers can be cured if detected early and treated efficiently. Noteworthy, more than 50% of the diagnosed patients undergo radiotherapy (RT), alone or in combination with chemotherapy or surgery, at some stage of the treatment. Photon RT techniques are the most common, and they have progressed very efficiently, from the geometrical conformation of fields to modulated intensity and RapidArc treatments, so that their therapeutic potential has increased. Nonetheless, this benefit has been accompanied by a growing concern about the risk of second radiation-induced tumors. It has been long known that patients treated with ionizing radiation carry a risk of developing a second cancer in their lifetimes, but the renewed concern comes from the substantial improvements in cancer survival, longer than the latency time of second cancers, together with the potential increase of out-of-field doses to healthy tissues distant from the target volume, which might be more significant for the intensity-modulated techniques (2, 3).

Compared with photon RT, proton therapy has the benefit of achieving up to 60% reduction of the radiation dose delivered to the healthy tissues around the tumor (3–5) while delivering a higher dose to the tumor itself. Therefore, proton therapy appeared as a safer and more effective therapy for some anatomic sites and tumors than photon therapy. The rationale is that, due to the Bragg peak, proton therapy provides a lower radiation dose to the non-target tissue while a high dose is delivered to a very specific area. These results are based on the physics fact that the proton range in tissue is finite while photon absorption follows an exponential decay function, and hence, some doses are received for the full-beam path in the body. However, the absorbed dose is not everything; it is necessary to consider the relative biological effectiveness (RBE) of the different out-of-field particles. Precisely, the higher RBE of neutrons compared to photons, the larger the biological impact of the former. In photon RT, the main contribution to out-of-field doses comes from stray photons, with a smaller contribution from neutrons when high energies are used for irradiation. On the contrary, neutrons are the main contributors to out-of-field doses in proton therapy. Despite this, overall proton therapy generally offers a substantial benefit in the non-target dose, as the out-of-field equivalent dose resulting from proton therapy is typically smaller than that resulting from photon RT (6). Consequently, it has been claimed that the second cancer risk associated with proton therapy is lower than that expected in photon therapy (7). This advantage is more obvious for low-energy proton treatments and scanning beam therapy (6), being one of the arguments toward the current tendency to the clinical use of scanning vs. passive proton beam equipment. However, tens of thousands of patients were already (and are currently) treated with passive scattering beams, which cannot be disregarded as they are an invaluable data source in terms of longer clinical follow-up for epidemiological studies (8).

Neutron dosimetry is very challenging, particularly the estimation of the neutron equivalent dose to organs in patients

under proton therapy. Finding a methodology for this issue would optimize future proton treatments and bring out epidemiology studies to develop more accurate cancer risk prediction models (9).

The goal of this work was to establish a methodology for evaluating the peripheral neutron and photon equivalent dose to organs at risk, valid for any situation in proton therapy. The authors have experience in determining peripheral neutron and photon equivalent doses in organs for photon RT (10–17). The steps already followed for the implementation of the procedure in photon RT were applied in this work to proton therapy. Firstly, neutron spectra measurements were made at specific points inside the treatment room using an extended-range Bonner sphere spectrometer (ERBSS). A Monte Carlo (MC) simulation of the neutron field in the treatment room and inside an anthropo-geometrical phantom was performed and validated with the ERBSS measurements. Secondly, measurements inside the phantom using photon and neutron dosimeters were performed with calibrated passive dosimeters. The above data allowed the calculation of the equivalent dose in the patient's organs, which is the relevant quantity for estimating a second cancer risk. Measurements and simulations were performed for the iThemba proton therapy facility (Cape Town, South Africa).

2 MATERIAL AND METHODS

2.1 Irradiations

The adult female anthropomorphic phantom (NORMA) (Figure 1) (11) was used for irradiations and was modeled for simulations. This phantom was manufactured in polyethylene, except for the low-density wood that was used for simulating lung tissue. This material composition was previously validated as adequate for mimicking neutron interaction with human tissue (17). Sixteen customized detector holes (see Figure 1 and Table 1) were distributed inside NORMA, at different positions and depths, so that the detectors placed in them could be used to determine the equivalent dose in relevant organs.

The iThemba proton therapy facility uses a 200 MeV fixed horizontal beam line with collimator arrangements and energy degraders to properly define the irradiated volume (8). In our case, two types of static field treatments were considered:

- In the pelvic region, with an irradiated cylindrical volume 3 cm in diameter and 3 cm height centered at the pelvis mid-point, identified as point#11 in the NORMA phantom (11). Neutron spectrometry, as described in Section *Bonner Sphere Spectrometry* was performed in two positions inside the treatment room during this irradiation with the aim of validating the MC simulation.
- In the head region, reproducing a brain treatment, in an irradiated volume equal to that of the case (1), centered at the head mid-point, identified as point#2 in the NORMA phantom (11). During this irradiation, the pairs of TLD-600 and TLD-700 were located inside the phantom holes (see Section *Thermoluminescent Dosimeters*).

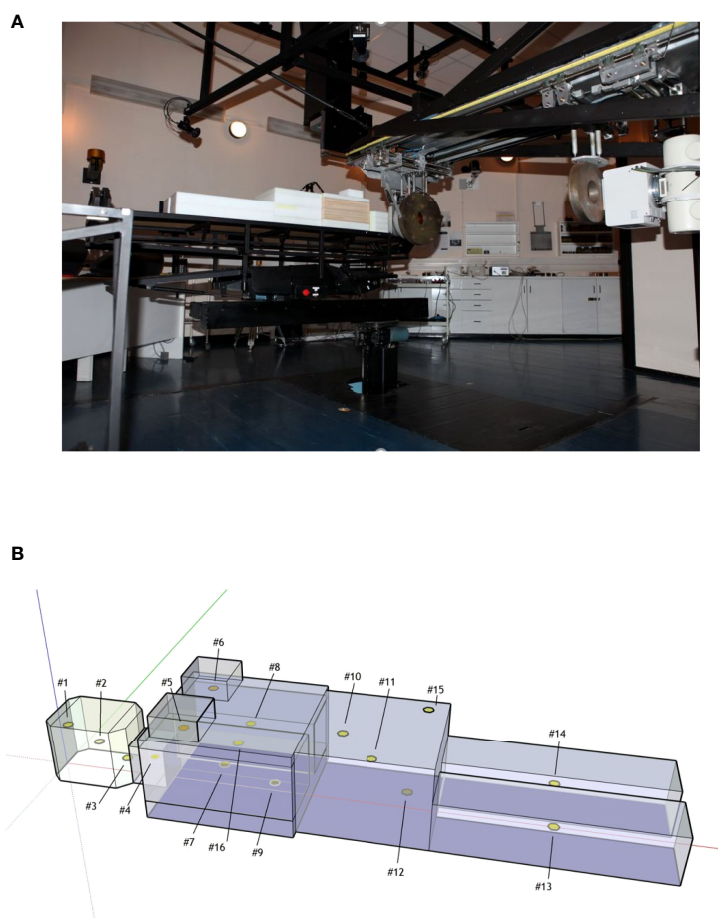


FIGURE 1 | (A) NORMA phantom during the head irradiation in the iThemba facility. **(B)** Sketch of NORMA phantom and detector positions.

TABLE 1 | Points in NORMA phantom.

Point	Location	Distance to iso* in CC direction (cm)
1	Head up	9
2	Head medium	0
3	Head down	8
4	Neck	17
5	Right breast	31
6	Left breast	31
7	Right thorax lung	42
8	Left thorax lung	42
9	Thorax spine	52
10	Pelvis up	71
11	Pelvis medium	79
12	Pelvis down	89
13	Right leg	127
14	Left leg	127
15	Skin	92
16	Mediastine	42

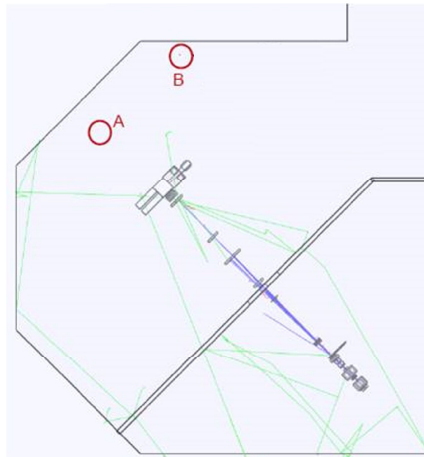
*In the head treatment. CC, craneo-caudal.

2.2 Bonner Sphere Spectrometry

The active ERBSS from Universitat Autònoma de Barcelona (18) was used for the measurements of neutron spectra inside the

treatment room. A proportional ^3He counter (EURYSYS model 05NH1) was placed in the center of the moderating spheres. A set of 9 polyethylene spheres, with diameters 2.5, 3, 4.2, 5, 6, 7, 8, 10, and 12 in., was used. The 7 in. sphere was used, in addition, to host a 1 in. thick Cu inset and another 1 in. thick Pb inset to make it sensitive to high-energy (>20 MeV) neutrons. A discriminator level conveniently set in the counter electronics is employed for neutron-gamma separation. Measurements were performed at two points in the irradiation room, marked with A and B in **Figure 2A**, during the irradiation of the pelvic region of NORMA. Point A is located downstream in the beam direction, 2.33 m after the isocenter. As high-energy neutrons are mainly produced in the forward direction, the detectors placed at point A are able to detect high-energy neutrons coming from beam passive elements and a phantom. This position has been extensively evaluated in spot-scanning proton beams, such as the study of Mares et al. (2016) (19). Point B is 3.4 m away from the isocenter, in a direction $\sim 60^\circ$ with respect to the beam line, downstream and to the right side. Point B was selected close to the wall in a position where any other neutron monitor, such as a Berthold or a Tissue-Equivalent Proportional Counter (TEPC), could be located without interfering with the clinical routine. The

A



B

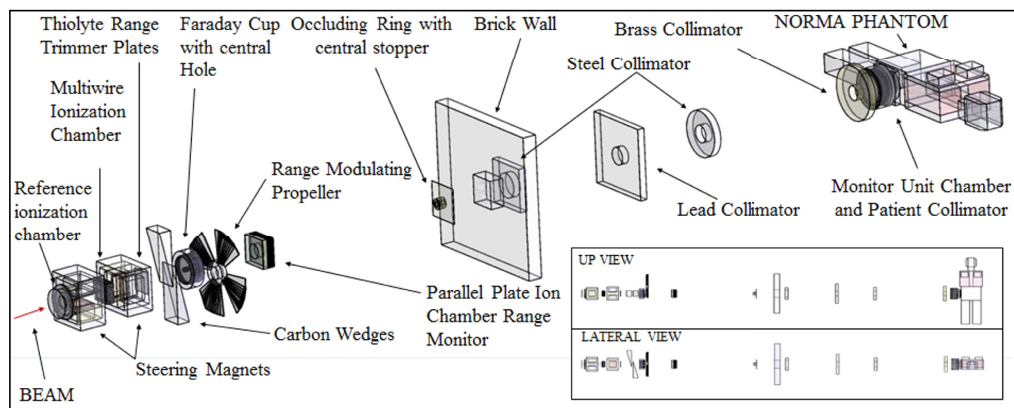


FIGURE 2 | (A) Sketch of the treatment room with the points selected for BSS experimental measurements and MC simulations. Point A is located in the beam direction, downstream 2.33 m after the isocenter. Point B is 3.4 m away from the isocenter $\sim 60^\circ$ with respect to the beam line, downstream and to the right side. **(B)** Beam elements simulated in MC together with the NORMA phantom inside the treatment room. Room walls are not shown for clarity.

knowledge of the neutron spectra for this kind of neutron monitors could be useful. No protons that could entangle the measurements are expected to reach points A and B. In fact, point A is behind NORMA, which is sufficiently thick to stop the primary proton beam, and point B is out of the primary beam direction. The necessary unfolding procedure for obtaining neutron spectra from Bonner sphere measurements was performed using the Frascati Unfolding Interactive Tool (FRUIT) unfolding code (20). When used in the *parametric mode*, Frascati Unfolding Interactive Tool (FRUIT) does not need a specified guess spectrum; it models the neutron spectrum using a reduced (≤ 7) set of meaningful physical parameters that depend on the type of radiation environment under study. The accepted solution is the spectrum obtained from the specific parameter array that fulfills better the unfolding convergence criteria. FRUIT can also be used in *numeric mode*, by perturbing an initial default *guess* spectrum according to the special gradient method (SGM). The *guess* spectrum is often obtained from computer simulation, but there are situations where the simulation results for a given energy range may be inaccurate

or display significant uncertainties because of poor statistics, which may require considerable computing time. In such cases, it is particularly suitable to combine simulation results in the energy region where they are robust enough, with the spectrum obtained from FRUIT in the parametric mode in the region where simulation results may be poor. In both *parametric* and *numeric* modes, once a solution is accepted, uncertainties at each individual energy bin of the resulting fluence spectrum are evaluated from a variability analysis, either of the spectrum parameters (in parametric mode) or of a set of spectra obtained by randomly perturbing the solution (in numerical mode). These uncertainties are strongly energy and problem dependent. In this work, each spectrum obtained by *parametric mode* was used as the *guess* spectrum for a subsequent *numeric* unfolding to refine the solution. In such a way, the experimental results obtained from the unfolding process do not depend on the MC simulation, as would be the case if unfolding was performed starting from a simulated spectrum. The MC codes for neutron transport are known to be accurate up to 20 MeV, where the relevant cross sections are well known and evaluated

from experimental results, but they provide model-dependent results above this energy. Cross sections up to 150 MeV are available only for the interaction of neutrons with only a few nuclear species, and physical models must be used otherwise (always above 150 MeV). The decision of using the described *parametric + numeric* approach was taken after the results of test runs using the MC spectrum as a guess either did not fulfill the convergence criterion or gave unphysical trends in the resulting spectra. The relevant dosimetric quantities and fractions of fluence and ambient dose equivalent for specified energy intervals, as well as their distributions, were obtained from the unfolding procedure and uncertainty analysis.

The global uncertainties of the total fluence and ambient-dose equivalent are normally within the range of 3%–6% and 4%–7%, respectively (18, 21).

2.3 Thermoluminescent Dosimeters

Standard 6 LiF/7 LiF pairs of dosimeters TLD-600/TLD-700 ($3 \times 3 \times 0.9 \text{ mm}^3$ chips) were used as an independent system to assess the thermal neutron fluences in the selected points inside the phantom. The sensitivity of both TLDs for photons can be considered the same because the chemical composition governs them, so either of them can be used for direct estimation of the photon-absorbed dose (22). In this work, absorbed doses were directly estimated from TLD-700. TLD-600 and TLD-700 had been previously calibrated using a ^{137}Cs source at the Metrology Laboratory for Ionizing Radiation of the CIEMAT (see values below).

Neutron thermal fluences were obtained using the differences between TLD-600 and TLD-700 results for each measured point in NORMA (R) and the calibration factors as follows:

$$\Phi_{th} = f_{600/700}^n \left[R_{600} - \frac{f_{700}^\gamma}{f_{600}^\gamma} R_{700} \right] \quad (1)$$

where the calibration factors used were $f_{600/700}^n = 488 \text{ n cm}^{-2}$ (6%) for neutrons and $f_{700}^\gamma = 1.86 \times 10^{-4} \text{ mGy au}^{-1}$ (4%) and $f_{600}^\gamma = 1.99 \times 10^{-4} \text{ mGy au}^{-1}$ (5%) for gammas (11).

Neutron calibration was carried out at Physikalisch-Technische Bundesanstalt in scattered neutron reference radiation fields produced by a bare ^{252}Cf and a D_2O -moderated ^{252}Cf neutron source (23).

TLD readouts were carried out using a Harshaw reader, model 4000, with linear heating from room temperature up to 280°C at a heating rate of 3°C s^{-1} . A pre-irradiation thermal treatment of 1 h at 400°C , followed by a reproducible cooling down to room temperature, was constantly employed before reusing the detectors. The temperature and duration of the heating and cooling stages were adequately controlled.

The uncertainties of TLD results were derived from the standard uncertainties of calibration factors.

2.4 Monte Carlo Simulation

Computer simulations were carried out using the GAMOS (v 6.2)/GEANT 4 package (v 10.6) (24, 25) following a “full Monte Carlo” approach, that is, in a single run simulating the 201.36 MeV primary proton beam impinging in all elements present in

the line (shutters, diaphragms, energy degraders, filters) close to the irradiation room, as well as the room walls and the presence of the anthropomorphic phantom (see **Figure 2B**). Calculations were done using two high-performance computer clusters at CIEMAT.

The aim of the simulation was to evaluate the neutron energy distribution inside the treatment room and the neutron spectra inside the NORMA phantom. To do this, a spherical detector (1 cm radius) was defined in each position and the neutron track length over the sphere volume was scored for each energy bin. In order to obtain the most realistic neutron spectra, the most up-to-date accurate geometry and material composition were considered. The Geant4 physics list used was QGSP_BIC_All_HP, recommended for proton and neutron transport under 200 MeV (26). The number of source protons was 1.9×10^9 and 2.1856×10^{10} for the simulation inside the treatment room and the phantom, respectively.

A standard uncertainty from simulation has a statistical component associated to the number of source particles. However, simulations in this energy range rely on nuclear models and different results can be obtained when using different models or even codes (27). This variability could be used as a measure of the accuracy of simulations, and, based on results from De-Saint Hubert et al. (27), we estimate a value of 20% to combine to statistical uncertainty.

The ERBSS results from irradiation during the pelvic treatment, obtained independently from the MC simulation, served as the validation of the MC model.

2.5 Evaluation of Total Equivalent Dose in Organs

The total equivalent dose in organs was obtained as the average of the total dose equivalent in the representative points inside the phantom, using the assignment in **Table 2**. This section describes the methodology followed for evaluating the dose equivalent in each point.

The total dose equivalent is calculated from the addition of the photon and neutron dose equivalent ($H_\gamma + H_n$). The photon contribution is directly calculated from the absorbed dose measured with the TLD-700 (taking into account that $w_R=1$). The neutron dose equivalent can be derived using the following equation, as discussed in Romero-Expósito et al. (28):

TABLE 2 | Point assignment for organ definition (11).

Organ	NORMA points
Thyroid	4
Esophagus	4, 9, 16
Lung	7, 8
Breast	5, 6, 15
Stomach	9, 11, 16
Liver	9, 10, 11, 16
Colon	11, 12
Urinary bladder	10
Ovary	11, 12
Prostate	11, 12
Uterus	11, 12

$$H_n = \Phi \int_E Q(E) \cdot k(E) \cdot \frac{d\phi_i(E)}{dE} \cdot dE \quad (2)$$

where Φ is the total neutron fluence, $Q(E)$ is neutron quality factor as a function of energy, $k(E)$ is the kerma factor for soft tissue [defined by the International Commission on Radiation Units and Measurements (ICRU)] as a function of energy (obtained from Siebert and Schuhmacher (29) for neutrons up to 20 MeV and in the work of Chadwick et al. (30) up to 150 MeV), and $(d\phi_i(E))/dE$, the energy spectrum of the unit neutron fluence at point i . This expression is based on the kerma approximation for the calculation of the absorbed dose, which is subsequently converted to dose equivalent by means of the quality factor $Q(E)$.

In practice, to calculate H_n at each point inside the phantom from equation (2), MC simulations are used in this work to determine the neutron energy spectrum $(d\phi_i(E))/dE$ at the relevant point. $Q(E) \cdot k(E)$ were taken from references (29) and (30). Finally, the total neutron fluence at the point (Φ) was calculated from the fluence measured using the thermoluminescence dosimeters. Then, at each point, the total neutron fluence equals the ratio of the thermal fluence Φ_{th} (measured by TLD-600/700 pairs) to the fraction of thermal neutrons p_{th} (obtained from the normalized simulated spectrum), as written in Equation 3:

$$\Phi = \frac{\Phi_{th}}{p_{th}} \quad (3)$$

Standard uncertainty in dose equivalent was obtained combining the experimental uncertainty of TLD results together with MC uncertainty. As equivalent dose in the organ is obtained as an average of the dose equivalent in several points, the uncertainty was derived as a propagation of uncertainty in each point.

3 RESULTS

3.1 Neutron Field Inside the Treatment Room

The simulated neutron unit spectrum at point B is represented in **Figure 3** together with those obtained from unfolding with FRUIT the Bonner sphere measurements at points A and B. All spectra show in general similar trends, with prominent thermal ($E < 0.4$ eV) and fast (evaporation – $0.1 \text{ MeV} < E < 20 \text{ MeV}$) peaks and a smaller contribution of high-energy neutrons ($20 \text{ MeV} < E < 200 \text{ MeV}$). The simulated spectrum displays a kind of double-peak structure in the evaporation region, approximately 1 MeV, which does not appear in the unfolded spectra. The origin of this discrepancy is that the energy binning of the simulation is fine enough to somehow preserve the resonances of the interaction cross sections of neutrons with heavy elements, while the energy resolution of Bonner sphere spectrometry is not enough to display this fine structure. In fact, Bonner sphere spectrometry has the advantage of being able to cover a huge energy interval (11 orders of magnitude) but with limited energy resolution. The evaporation peak for the simulated spectrum is widened toward the lower energies (0.1 MeV), but the fluence fractions corresponding to this peak are similar in all cases, as discussed later (**Table 3**). We consider that there is good agreement between simulated and unfolded spectrum in point B, especially from 0.1 MeV onwards, which is the relevant part in terms of the dose (see below) and because the total fraction of fluence above 0.1 MeV is similar for all spectra.

The fact that the spectra in the two points are similar (see also fluence fractions in **Table 3**) is a consequence of the particular geometric characteristics of the beam line, beam elements, and

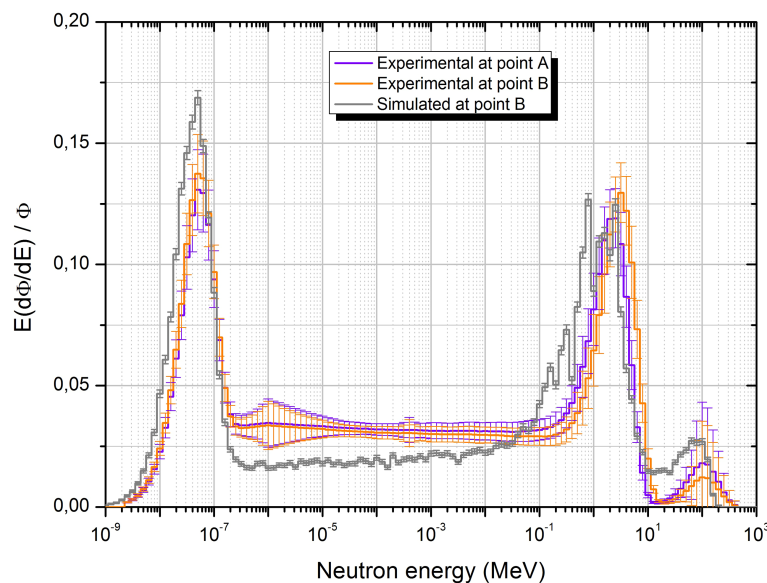


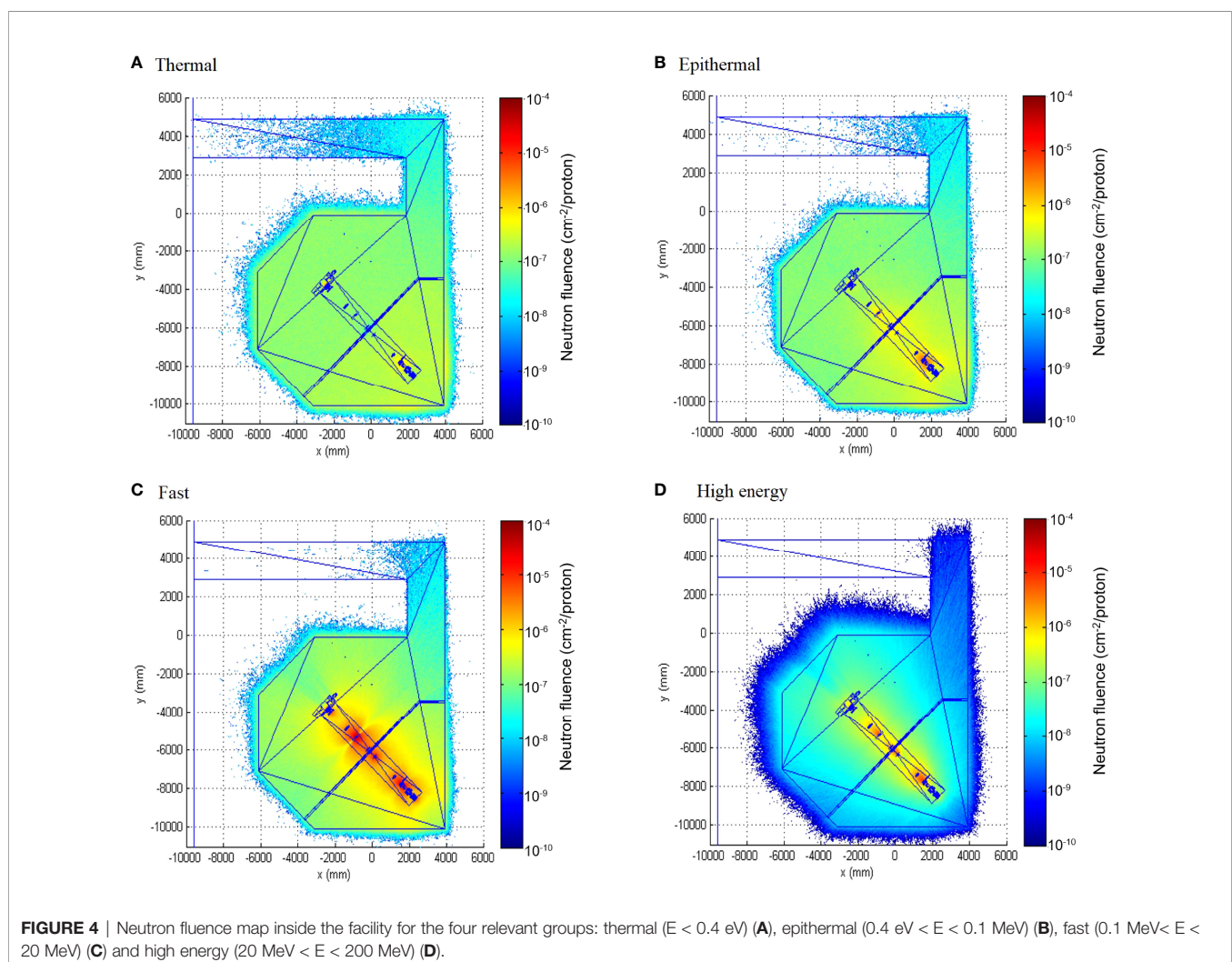
FIGURE 3 | Neutron unit spectra obtained from unfolding with FRUIT at points A and B together with the simulation spectrum at point B.

TABLE 3 | Neutron fluence, ambient dose equivalent, fluence-averaged energy, dose equivalent-averaged energy, and average fluence to ambient dose equivalent conversion coefficient per unit proton dose imparted at the points of measurement inside the treatment room, as well as fluence and dose equivalent fractions for the different energy ranges from experimental determination and simulation.

	Point A experimental	Point B experimental	Point B simulation
Φ (cm ⁻² Gy ⁻¹)	$(1.489 \pm 0.055) \times 10^6$	$(1.577 \pm 0.063) \times 10^6$	
H* (10) (μSv Gy ⁻¹)	184 ± 12	203 ± 13	
E _Φ (MeV)	3.90	3.10	
E _{H*} (MeV)	9.66	7.70	
h* (10) (pSv-cm ²)	123.7 ± 6.8	129.8 ± 6.6	
Fluence fractions			
E ≤ 0.4 eV	30.9%	31.8%	36.1%
0.4 eV < E < 100 keV	37.1%	35.5%	24.2%
100 keV ≤ E ≤ 20 MeV	29.1%	30.6%	35.5%
E > 20 MeV	2.9%	2.0%	4.2%
H* (10) fractions			
E ≤ 0.4 eV	3.0%	2.9%	2.8%
0.4 eV < E < 100 keV	4.1%	3.8%	2.6%
100 keV ≤ E ≤ 20 MeV	85.3%	88.4%	83.9%
E > 20 MeV	7.6%	4.9%	10.7%

irradiation room. In fact, all beam elements relevant for fast and high-energy neutron production are located quite far away from the treatment place, outside the irradiation room and without shielding, so that even the forward-scattered neutrons almost

uniformly cover the irradiation room. This behavior is clearly represented in **Figure 4**, where the spatial distribution of neutron fluence simulated in the four relevant energy groups is displayed. From this figure, we can conclude that high-energy neutrons,



originated almost exclusively in the beam elements, are highly directional (even outside the irradiation room), while thermal neutrons almost uniformly fill the irradiation room volume. The behavior for fast and epithermal neutrons ($0.4 \text{ eV} < E < 0.1 \text{ MeV}$) is halfway the others, with a significant amount of fast neutrons but a smaller amount of epithermal neutrons, also being produced in the beam elements and decreasing their directionality for smaller energies. The fact that the epithermal component is higher in the unfolded spectra than in the simulated one is explained by the impossibility to introduce in the simulation the detailed geometry and composition of all elements, structures, instruments, and other stuff present in the irradiation room and around the beam line, which contribute to the thermalization of neutrons.

Neutron fluence (Φ), ambient dose equivalent ($H^*(10)$), fluence-averaged energy (E_Φ), dose equivalent-averaged energy (E_H^*), and average fluence to ambient dose-equivalent conversion coefficient ($h^*(10)$) at points A and B per unit proton dose imparted are presented in **Table 3**. While neutron fluence is of the order of $10^6 \text{ cm}^{-2}/\text{Gy}$, $H^*(10)$ is of the order of 0.2 mSv/Gy in the region away from the patient. A slightly higher amount of neutrons at the patient position would be expected given that it is closer to the beam elements. The fractions of fluence and ambient dose equivalent for the thermal, epithermal, fast, and high-energy components of the neutron field are also displayed in the table. Note that the most important contribution to the dose is that from the evaporation region due to the strong energy dependence of the fluence-to-dose-equivalent conversion coefficients. It is worth noting that, even if the visual aspect of the simulated and the unfolded spectra at point B is not the same, the fractional contribution to the fluence and ambient dose equivalent of neutrons in the different energy intervals considered differ only in a few percentage points. In fact, the biggest discrepancy (approximately 11% difference), from 24.2% of the total fluence in the simulated spectrum to 35.5% of the total fluence in the experimental one, is found in the contribution to epithermal ($0.4 \text{ eV} < E < 100 \text{ keV}$) fluence. Discrepancies are 4.3% of the total fluence in the thermal ($E \leq 0.4 \text{ eV}$) component, 5.1% in the fast ($100 \text{ keV} \leq E \leq 20 \text{ MeV}$) component, and 2.2% in the high-energy ($E > 20 \text{ MeV}$) component. The contribution to the total ambient dose equivalent of the thermal and epithermal components is small, and the total contribution to the dose of the fast + high-energy components (those that are relevant because the fluence-to-dose-equivalent conversion coefficients) represents 94.6% for the simulated spectrum and 93.3% for the experimental one.

The FRUIT-unfolding process (20) leads to uncertainties of approximately 3% in fluence determination and 7% in $H^*(10)$ determination. The sources of this uncertainty, given at the standard level ($k = 1$), are as follows:

- Counting statistics in the detectors at the center of the Bonner spheres (type A): approximately 1% in this experiment
- The uncertainty of the sphere's response matrix, obtained from simulation and experimental validation (type B): 3% average.

In addition, uncertainties at each individual energy bin of the resulting fluence spectrum are obtained from a variability analysis, either of the spectrum parameters (in parametric mode) or of all spectra that fulfill the convergence criteria during unfolding (in numerical mode). These uncertainties are strongly energy and problem dependent. In our case, they range from 7% in the epithermal to fast region to over 100% in the high-energy region, as seen in **Figure 3**. Uncertainty bars at the experimental spectra in **Figure 3** include all these uncertainty sources, but only statistical simulation uncertainties are displayed in the simulated spectrum. The systematic uncertainty related to the physics models used inside the MC code could rise up to 20%, as discussed by De-Saint Hubert et al. (28), especially in the high-energy region.

3.2 Neutron Field Inside the Phantom

Figure 5 shows the neutron spectra inside the 16 points in NORMA phantom. Statistical uncertainties from the MC simulation were 8% on average. There are several differences with spectra inside the room. The most prominent one is the important reduction in the fast neutron peak. This fluence attenuates as neutrons go through the tissue and, consistently, the fast neutron fraction becomes lower, from approximately 30% in the room to 16% on average in the phantom (see fluence fractions in **Table 4**). This fast neutron attenuation leads to an increase of the thermal neutron peak. In terms of fluence fractions, from approximately 31% in the room to 56% on average inside the phantom. In **Figure 5B**, the points with a higher fast peak are those corresponding to lung tissue, which have lower density and, therefore, less attenuation.

Table 4 also presents the results of the photon dose equivalent and neutron thermal fluence measured with TLD dosimeters. While photon doses range between 0.121 and 0.0342 mSv/Gy , neutron thermal neutron fluences range from 9.47×10^6 to $1.32 \times 10^6 \text{ cm}^{-2}/\text{Gy}$. The general trend of both quantities is to decrease as the distance to the isocenter increases, with fluctuations associated to the depth of the point in the phantom.

Neutron dose equivalents were calculated from data in **Table 4** using equations 2 and 3. These values range from 1.22 to 0.237 mSv/Gy . Uncertainties of these values were 31% on average, and were composed of

- Statistical uncertainty of the MC simulation: 8% (type A)
- Experimental uncertainty of the TLD measurements: 15% on average, position dependent (type A)
- Systematic uncertainty related to the physics models used inside the MC code, as discussed by De-Saint Hubert et al. (28): 20% (type B).

All uncertainties were calculated at the standard ($k = 1$) level.

Figure 6 shows the photon, neutron, and total dose equivalent as a function of the distance to the isocenter in the craneo-caudal direction. As can be clearly noticed in the figure, the contribution of photons in this irradiation is very low. Photons represent on average 10% of the total dose. From these values, using the assignment in **Table 2**, the equivalent dose in organs was calculated. Values are presented in **Figure 7**.

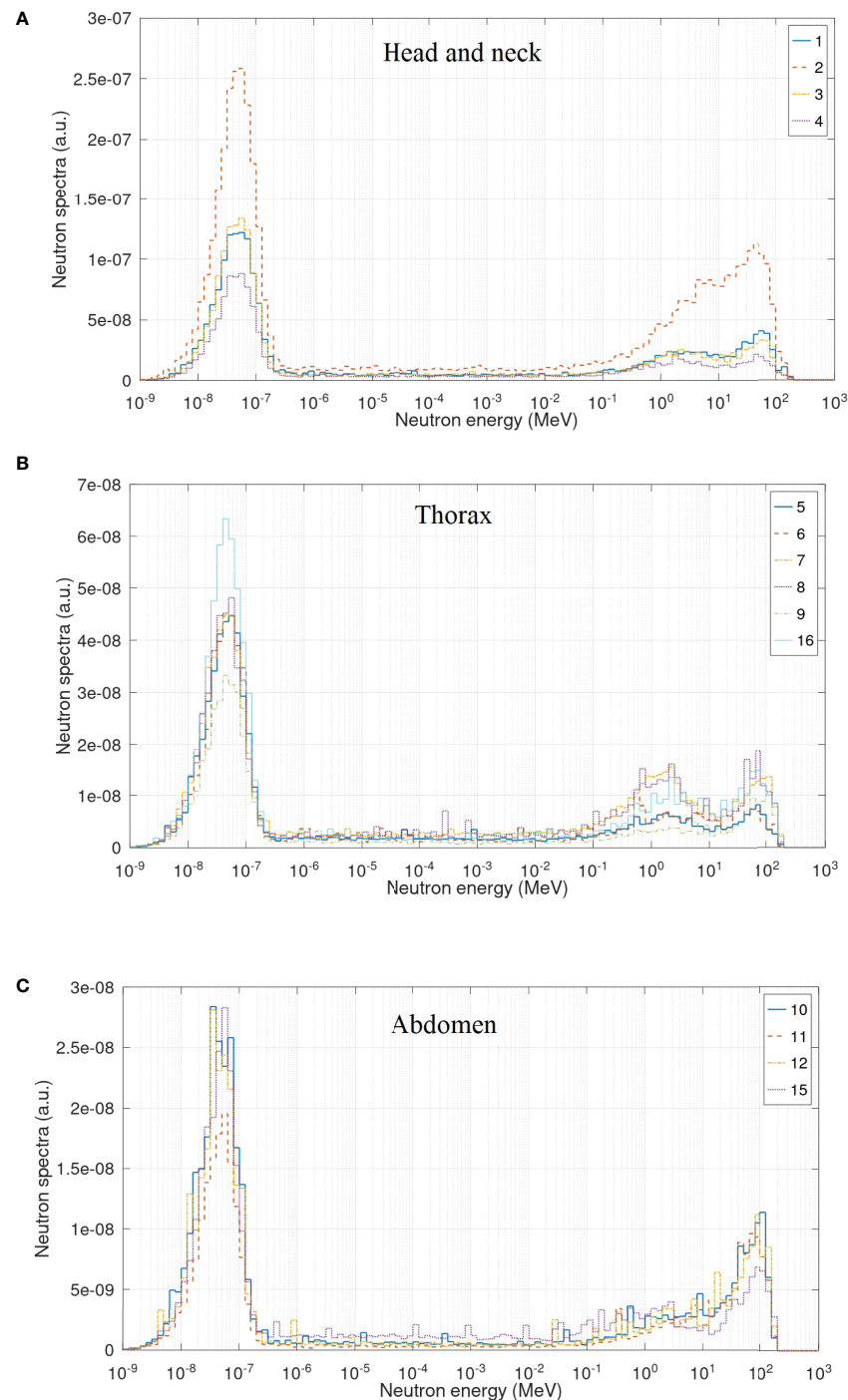


FIGURE 5 | Neutron spectra inside the NORMA phantom in the head and neck (A), thorax (B), and abdomen (C) region.

Equivalent doses keep the same trend of reducing when going farther from the target. For thyroid, the closest organ to the target, the equivalent dose is 1.32 mSv/Gy. In abdomen, for example, the stomach has an equivalent dose of 0.661 mSv/Gy, and in the pelvic area, ovaries present 0.331 mSv/Gy. The uncertainties of equivalent dose range from 16% to 30%.

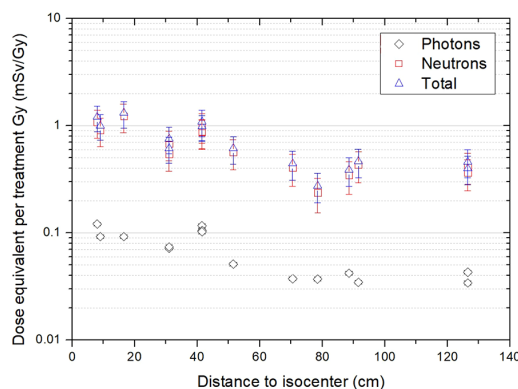
4 DISCUSSION

This work presents a methodology for the evaluation of total equivalent doses in organs based on measurements complemented by the MC simulation. Simulation is essential for neutron dosimetry as the biological effect of neutrons

TABLE 4 | Quantities evaluated in the points inside the phantom.

Point	MC neutron fluence fractions				TLD results	
	Thermal (%)	Epithermal (%)	Fast (%)	High energy (%)	Thermal neutron fluence per treatment gray ($\times 10^6 \text{ cm}^{-2} \text{ Gy}^{-1}$)	Photon dose equivalent per treatment gray ($\times 10^{-2} \text{ mSv/Gy}$)
1	54	14	18	14	6.29 ± 0.38	9.23 ± 0.37
2	48	12	22	19	*	*
3	57	14	17	12	8.27 ± 0.50	12.09 ± 0.48
4	56	15	18	11	9.47 ± 0.57	9.23 ± 0.37
5	61	16	14	9	5.34 ± 0.32	7.19 ± 0.29
6	58	16	16	9	6.05 ± 0.36	7.40 ± 0.30
7	47	17	23	13	5.53 ± 0.33	11.64 ± 0.47
8	47	18	22	14	5.61 ± 0.34	10.52 ± 0.42
9	58	15	12	15	4.67 ± 0.28	5.12 ± 0.20
10	59	9	12	20	2.82 ± 0.17	3.73 ± 0.15
11	54	7	14	25	1.320 ± 0.079	3.71 ± 0.15
12	58	9	12	21	2.32 ± 0.14	4.21 ± 0.17
13	61	10	13	15	2.86 ± 0.17	3.42 ± 0.14
14	60	10	14	16	3.19 ± 0.19	4.30 ± 0.17
15	55	18	14	13	3.71 ± 0.22	3.46 ± 0.14
16	57	13	17	13	7.30 ± 0.44	10.22 ± 0.41

*No TLD was inserted in the isocenter of the treatment.

**FIGURE 6** | Photon, neutron, and total dose equivalent per treatment Gy as a function of the distance to the isocenter.

depends on their energy and, currently, simulation is the only way to evaluate the wide range of neutron energies inside a patient. However, simulations, in turn, must be validated against measurements. In our case, ERBSS was used to determine, with a procedure completely independent from simulation, the neutron energy distribution at two points in the treatment room. The fluence and ambient dose equivalent per treatment Gy, as well as percent contribution to the fluence and ambient dose equivalent of neutrons in four energy groups, were also obtained from ERBSS measurements. Finally, the ERBSS results were used to validate the simulation results in one of the points. Although simulated and experimental spectra are not identical, probably due both to the constraints of the parametric unfolding process used and to not being able to simulate all elements affecting neutron production, their general trend, and the fractional contributions to fluence and the ambient dose

equivalent agree within a few percentage points, as can be seen in **Table 3**. The biggest discrepancy (approximately 11% difference) is found in the contribution to epithermal ($0.4 \text{ eV} < E < 100 \text{ keV}$) fluence, which gives approximately 35% of the total experimental fluence and approximately 24% of the simulated one. This is consistent with incomplete simulation of elements contributing to the energy degradation of neutrons. Nevertheless, given the strong energy dependence of the fluence to the ambient dose equivalent conversion coefficient h^* (10), the contribution of this epithermal component to the ambient dose equivalent H^* (10) is very small. Once MC simulations are validated, the neutron spectra inside the patient can be calculated and subsequently used for dose equivalent determination using Equation 2. The approach followed in this work was to evaluate the total neutron fluence appearing at the equation using an independent neutron dosimeter. With sufficient knowledge of the

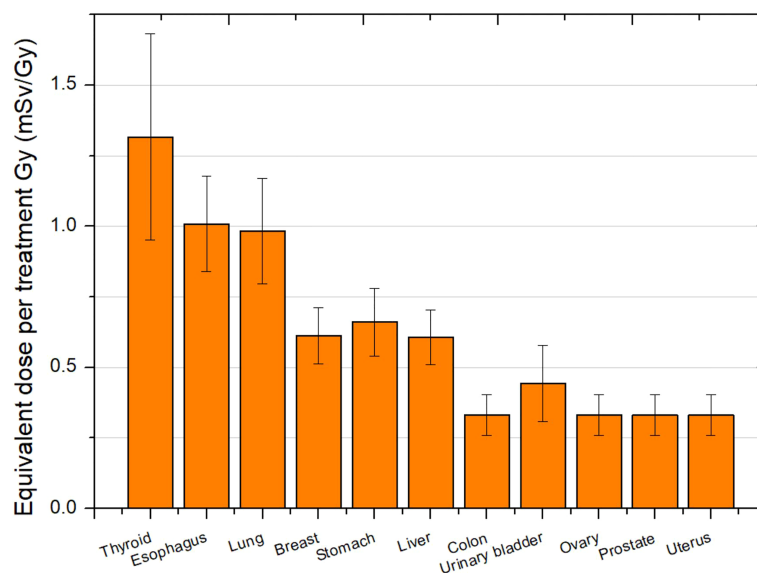


FIGURE 7 | Total equivalent dose in organs per treatment Gy for a head treatment.

accelerator parameters, it is also possible to evaluate this fluence merely from simulation, in which case an additional validation for the fluence value would be needed. Regardless of the circumstances, the methodology can be reproduced using any other phantom in any other facility.

Regarding our particular results, the spectra measured inside the treatment room are similar to those reported by Howell et al. (31) for neutrons with energies higher than a few eV in the passive scattering system Mevion 250, that is, a high contribution of evaporation neutrons and a lower peak of high-energy neutrons. The contribution of thermal neutrons is related to the treatment room volume and, therefore, is highly facility dependent. Results from Howell et al. (31) show a smaller proportion of thermal neutrons than ours, for instance. Nevertheless, their contribution to the ambient dose equivalent is very low, and then, the room size does not represent an important parameter to take into account when analyzing the neutron production. The most relevant parameters are the proton energy, target volume (trough field size and Spread-Out

Bragg Peak (SOBP) width), and the distance to neutron source. The latter is not simple to define in passive facilities, as several beam elements contribute to neutron production (32). However, the isocenter is usually considered as a reference for the position inside the room. In the case of Howell et al. (31), they reported an $H^*(10)$ value 3.90 mSv/Gy at 50 cm from the isocenter. This value is approximately 17 times larger than ours, which can be explained by their higher proton energy (250 MeV), the bigger target volume (a whole brain treatment), and the smaller distance from the point of measurement to the patient location (isocenter). Our results show a better agreement with Zheng et al. (33) and Han et al. (34) (see values in **Table 5**), where the energy and the distances to the isocenter were similar to ours. We could conclude that away from the patient (more than 2 m from the isocenter) $H^*(10)$ is of the order of 0.1 mSv/Gy. The dose range obtained for these passive scanning facilities differs from that obtained in scanned beam facilities, where the ambient dose equivalent is of the order of μ Sv/Gy in the area away from the patient (19).

TABLE 5 | Comparison of $H^*(10)$ with other works.

Reference	Method	Proton energy (MeV)	Beam characteristics	Distance to isocenter (cm)	Angle with beam axis (°)	$H^*(10)$ mSv/Gy
Zheng et al. (28)	MC	250	Unmodulated, 10×10 cm ² aperture	200	0	0.18
Howell et al. (26)	ERBSS	250	17 cm range, 16 cm modulation, 13 cm diameter aperture	50	90	3.9
Han et al. (29)	WENDI-II	218	21 cm range, 5 cm modulation, 8 cm diameter aperture	200	0	0.313
Our work	ERBSS	200	10.5 cm range, 3 cm modulation, 3 cm diameter aperture	283	45	0.203
				233	0	0.209
				340	60	0.235

Ambient dose equivalent is given the symbol $H^*(10)$.

A noteworthy aspect of our results is that we obtained similar values of $H^*(10)$ in both measurement positions, showing a quite-uniform exposure to external neutrons around the patient location. Point A showed a lower value, due to a slight attenuation in the phantom, which can be noticed in **Figures 4C, D**. This result is a geometry effect also showed by Moyer et al. (32). Their MC simulation allowed to conclude that only a small fraction of the neutrons generated in the scatters of the beamline reaches the patient. Most of the neutrons that do reach the patient are generated in the precollimators, the patient-specific aperture, and within the patient themselves. In addition, Howell et al. (31) tested the same treatment with no phantom and with different phantom materials (water, soft tissue, and plastic water). They found a nearly negligible difference in the fluence for the different phantom scenarios; the differences between no phantom at the isocenter and either water or soft tissue phantom were <2%. This indicates that at 50 cm from the isocenter (approximately 25 cm from the proximal surface of the phantom) for the considered fields, there was essentially no contribution from the neutrons produced inside the patient. That is, internal neutrons made a low-to-negligible contribution to the neutron dose equivalent in passive beam lines. Their effect is relevant in closest region around the target volume.

The low contribution of internal neutrons in passive beam lines explains the slow decay of the neutron dose equivalent inside the phantom as the distance to the isocenter increases. Our results showed a reduction from 1.22 mSv/Gy at 17 cm to 0.346 mSv/Gy at 89 cm from the isocenter. Taking into account that the locations inside NORMA are at different depths and the effect of lung tissue at middle distances, our values may not be completely representative of the trend with distance but are consistent with those reported in Hägl et al. (35). In that work, the neutron dose equivalent was measured inside the Alderson–Rando phantom in a double-scattering beamline using CR-39 detectors located along the medial patient axis during a prostate treatment. The neutron dose equivalent was 1 and 0.1 mSv/Gy at approximately 12 and 78 cm, respectively. By contrast, in the scanned beam, the dose-equivalent reduction can be of almost two orders of magnitude from positions close to the isocenter (1 mSv/Gy) to positions up to 20 cm from the isocenter (0.01 mSv/Gy) (36).

Finally, our equivalent doses in an organ can be compared to those reported by Farah et al. (37). In that work, a standard intracranial treatment with a 178 MeV proton beam was simulated with Monte Carlo N-Particle eXtended (MCNPX) code in a computational phantom. For the thyroid, the closest organ to target, they found an equivalent dose of 1.5 mSv/Gy, while in our case, it was 1.32 mSv/Gy. These values are compatible within our uncertainties, although a higher value would be expected in our case as we considered a higher proton energy. However, the small volume of our target could be a reason of obtaining a lower value. For the rest of organs, as

expected because of the proton energy, we found systematically higher doses. For example, while Farah et al. (37) reported an equivalent dose of 0.63, 0.39, and 0.43 mSv/Gy in the lung, stomach, and liver, respectively, our results were 1.01, 0.661, and 0.606 mSv/Gy for the same organs. It must be taken into account that one important limitation of our work is that organs were defined using a few points in the NORMA phantom. However, the comparison with Farah et al. (37) show that the reported values are reliable within their uncertainties. An improvement would imply to modify the phantom, drilling a higher number of holes for placing the detectors, to perform a simulation at all these points, which would be more representative of the organs of interest, and to be able to perform measurements in a bigger number of points, more representative of the organs of interest. In this way, the methodology presented could be reproduced, and the use of a soft tissue phantom with a high amount of detector holes could lead to more accurate estimations.

Results could allow to conclude that the equivalent dose in organs could be of the order of 0.1 or 1 mSv/Gy in passive facilities. It is worth noticing that these values represent both neutron and photon contributions. However, photons represent only 10% of the value, and therefore, neutrons require major attention in passive facilities.

DATA AVAILABILITY STATEMENT

The raw data supporting the conclusions of this article will be made available by the authors, without undue reservation.

AUTHOR CONTRIBUTIONS

FS-D: Leader of the project, expert in medical physics, participated in the design and realization of the experiments. CD: Expert in neutron dosimetry and responsible for the experimental neutron spectrometry. JL: Expert in Monte Carlo and responsible for the simulation. MR-E: Expert in neutron dosimetry and out-of-field dosimetry in radiotherapy, participated in the design and realization of the experiments and data analysis, and wrote the first draft of the manuscript. BS-N: Expert in medical physics, radiobiology, and peripheral dose in radiotherapy, participated in the design and data analysis, in particular, in the evaluation of the organ dose from measurements in the phantom. JN-C: Local member, participated in the design and realization of the experiments. JT: Expert in medical physics and dosimetry, participated in the experiments. LI: Expert in medical physics and dosimetry, participated in data analysis. AD: Expert in medical physics and out-of-field dose in radiotherapy, participated in the coordination and improvement of the manuscript. All authors contributed to the article and approved the submitted version.

FUNDING

This work has been partially carried out on the ACME cluster, which is owned by CIEMAT and funded by the Spanish Ministry of Economy and Competitiveness project CODEC2 (TIN2015-

63562-R) with FEDER funds as well as supported by the CYTED-co-founded RICAP Network (517RT0529). MR-E acknowledges funding from Euratom's research and innovation programme 2019-20 under grant agreement no. 945196. BS-N acknowledges project Fondecyt N1181133.

REFERENCES

- Sung H, Ferlay J, Siegel RL, Laversanne M, Soerjomataram I, Jemal A, et al. Global Cancer Statistics 2020: GLOBOCAN Estimates of Incidence and Mortality Worldwide for 36 Cancers in 185 Countries. *CA Cancer J Clin* (2021) 71(3):209–49. doi: 10.3322/caac.21660
- Sánchez-Nieto B, Romero-Expósito M, Terrón JA, Irazola L, García Hernández MT, Mateos JC, et al. External Photon Radiation Treatment for Prostate Cancer: Uncomplicated and Cancer-Free Control Probability Assessment of 36 Plans. *Phys Med* (2019) 66:88–96. doi: 10.1016/j.ejmp.2019.09.076
- Palm Å, Johansson KA. A Review of the Impact of Photon and Proton External Beam Radiotherapy Treatment Modalities on the Dose Distribution in Field and Out-of-Field; Implications for the Long-Term Morbidity of Cancer Survivors. *Acta Oncol* (2007) 46(4):462–73. doi: 10.1080/02841860701218626
- Cancer.Net. *Proton Therapy* (2022). Available at: <https://www.cancer.net/navigating-cancer-care/how-cancer-treated/radiation-therapy/proton-therapy> (Accessed February 15, 2022).
- Eaton BR, MacDonald SM, Yock TI, Tarbell NJ. Secondary Malignancy Risk Following Proton Radiation Therapy. *Front Oncol* (2015) 5:261. doi: 10.3389/fonc.2015.00261
- Kry SF, Bednarz B, Howell RM, Dauer L, Followill D, Klein E, et al. AAPM TG 158: Measurement and Calculation of Doses Outside the Treated Volume From External-Beam Radiation Therapy. *Med Phys* (2017) 44(10):e391–429. doi: 10.1002/mp.12462
- König L, Haering P, Lang C, Splinter M, von Nettelblatt B, Weykamp F, et al. Secondary Malignancy Risk Following Proton vs. X-Ray Treatment of Mediastinal Malignant Lymphoma: A Comparative Modeling Study of Thoracic Organ-Specific Cancer Risk. *Front Oncol* (2020) 10:989. doi: 10.3389/fonc.2020.00989
- Vernimmen FJ, Fredericks S, Wallace ND, Fitzgerald AP. Long-Term Follow-Up of Patients Treated at a Single Institution Using a Passively Scattered Proton Beam; Observations Around the Occurrence of Second Malignancies. *Int J Radiat Oncol Biol Phys* (2019) 103(3):680–85. doi: 10.1016/j.ijrobp.2018.10.022
- Ottolenghi A, Baiocco G, Smyth V, Trott K. The ANDANTE Project: A Multidisciplinary Approach to Neutron RBE. *Radiat Prot Dosimet* (2015) 166(1–4):311–5. doi: 10.1093/rpd/ncv158
- Sánchez-Nieto B, El-far R, Irazola L, Expósito MR, Lagares JI, Mateo JC, et al. Analytical Model for Photon Peripheral Dose Estimation in Radiotherapy Treatments. *BioMed Phys Eng Express* (2015) 1(4):045205. doi: 10.1088/2057-1976/1/4/045205
- Sánchez-Doblado F, Domingo C, Gómez F, Sánchez-Nieto B, Muñiz JL, García-Fusté MJ, et al. Estimation of Neutron-Equivalent Dose in Organs of Patients Undergoing Radiotherapy by the Use of a Novel Online Digital Detector. *Phys Med Biol* (2012) 57(19):6167–91. doi: 10.1088/0031-9155/57/19/6167
- Irazola L, Terrón JA, Bedogni R, Pola A, Lorenzoli M, Sánchez-Nieto B, et al. Improving the Neutron-to-Photon Discrimination Capability of Detectors Used for Neutron Dosimetry in High Energy Photon Beam Radiotherapy. *Appl Radiat Isot* (2016) 115:49–54. doi: 10.1016/j.apradiso.2016.06.009
- Irazola L, Terrón JA, Sánchez-Nieto B, Bedogni R, Sánchez-Doblado F. Peripheral Equivalent Neutron Dose Model Implementation for Radiotherapy Patients. *Phys Med* (2017) 42:345–52. doi: 10.1016/j.ejmp.2017.03.018
- Romero-Expósito M, Sánchez-Nieto B, Terrón JA, Lopes MC, Ferreira BC, Grishchuk D, et al. Commissioning the Neutron Production of a Linac: Development of a Simple Tool for Second Cancer Risk Estimation. *Med Phys* (2015) 42(1):276. doi: 10.1118/1.4903525
- Expósito MR, Sánchez-Nieto B, Terrón JA, Domingo C, Gómez F, Sánchez-Doblado F. Neutron Contamination in Radiotherapy: Estimation of Second Cancers Based on Measurements in 1377 Patients. *Radiother Oncol* (2013) 107(2):234–41. doi: 10.1016/j.radonc.2013.03.011
- Irazola L, Lorenzoli M, Bedogni R, Pola A, Terrón JA, Sanchez-Nieto B, et al. A New Online Detector for Estimation of Peripheral Neutron Equivalent Dose in Organ. *Med Phys* (2014) 41:112105. doi: 10.1118/1.4898591
- González-Soto X, Expósito MR, Sánchez-Nieto B, Amgarou K, Lagares JI, Gómez F, et al. Neutron Spectra Inside an Adult and Children Anthropomorphic Phantoms in High Energy Radiotherapy. *IFMBE Proc* (2013) 39, 1145–48.
- Amgarou K, Bedogni R, Domingo C, Esposito A, Gentile A, Carinci G, et al. Measurement of the Neutron Fields Produced by a 62 MeV Proton Beam on a PMMA Phantom Using Extended Range Bonner Sphere Spectrometers. *Nucl Instrum Methods Phys Res Sect A Accel Spectromet Detect Assoc Equip* (2011) 654:399–405. doi: 10.1016/j.nima.2011.07.027
- Mares V, Romero-Expósito M, Farah J, Trinkl S, Domingo C, Dommert M, et al. A Comprehensive Spectrometry Study of a Stray Neutron Radiation Field in Scanning Proton Therapy. *Phys Med Biol* (2016) 61:4127–40. doi: 10.1088/0031-9155/61/11/4127
- Bedogni R, Domingo C, Esposito A, Fernández F. FRUIT: An Operational Tool for Multisphere Neutron Spectrometry in Workplaces. *Nucl Instrument Methods Phys Res Sect A Accel Spectromet Detect Assoc Equip* (2007) 580:1301–9. doi: 10.1016/j.nima.2007.07.033
- Bedogni R, Domingo C, Amgarou K, de-San-Pedro M, Esposito A, Gentile A, et al. Spectrometry of 50 and 100 MeV Quasi Monochromatic Neutron Fields With Extended Range Bonner Spheres. *Nucl Instrum Methods Phys Res A* (2014) 746:59–63. doi: 10.1016/j.nima.2014.02.009
- Cavaliere TA, Paiva F, Fonseca G, Dalledone Siqueira PT, Yoriyaz H. *Thermoluminescent Analyses of Mean Photon Energy of a Field*. Vienna: ISSSD (2014). Available at: https://inis.iaea.org/collection/NCLCollectionStore/_Public/45/099/45099960.pdf.
- Kluge H, Alevra AV, Jetzke S, Knauf K, Matzke M, Weise K, et al. Scattered Neutron Reference Fields Produced by Radionuclide Sources. *Radiat Prot Dosim* (1997) 70:327–30. doi: 10.1093/oxfordjournals.rpd.a031968
- Arce P, Lagares JI, Harkness L, Pérez-Astudillo D, Cañadas M, Rato P, et al. Gamos: A Framework to do Geant4 Simulations in Different Physics Fields With an User-Friendly Interface. *Nucl Instrum Meth Phys Res Sect A Accel Spectromet Detect Assoc Equip* (2014) 735:304–13. doi: 10.1016/j.nima.2013.09.036
- Agostinelli S, Allison J, Amako K, Apostolakis J, Araujo H, Arce P, et al. Geant4: A Simulation Tool Kit. *Nucl Instrum Methods A* (2003) 506:250–303. doi: 10.1016/S0168-9002(03)01368-8
- Geant4 Physics Reference Manual (2022). Available at: <https://geant4-userdoc.web.cern.ch/UsersGuides/PhysicsReferenceManual/html/index.html> (Accessed February 15, 2022).
- De Saint-Hubert M, Farah J, Klodowska M, Romero-Expósito MT, Tyminska K, Mares V, et al. The Influence of Nuclear Models and Monte Carlo Radiation Transport Codes on Stray Neutron Dose Estimations in Proton Therapy. *Rad Meas* (2022) 150:106693. doi: 10.1016/j.radmeas.2021.106693
- Romero-Expósito M, Domingo C, Sánchez-Doblado F, Ortega-Gelabert O, Gallego S. Experimental Evaluation of Neutron Dose in Radiotherapy Patients: Which Dose? *Med Phys* (2016) 43:360. doi: 10.1118/1.4938578
- Siebert, Schuhmacher H. Quality Factors, Ambient and Personal Dose Equivalent for Neutrons Based on the New ICRU Stopping Power Data for Protons and Alpha Particles. *Radiat Prot Dosim* (1995) 58:177–83. doi: 10.1093/oxfordjournals.rpd.a082612
- Chadwick MB, Barschall HH, Caswell RS, DeLuca PM, Hale GM, Jones DT, et al. A Consistent Set of Neutron Kerma Coefficients From Thermal to 150 MeV for Biologically Important Materials. *Med Phys* (1999) 26:974–91. doi: 10.1118/1.598601
- Howell RM, Burgett EA, Isaacs D, Price Hedrick SG, Reilly MP, Rankine LJ, et al. Measured Neutron Spectra and Dose Equivalents From a Mevion Single-Room, Passively Scattered Proton System Used for Craniospinal Irradiation.

- Int J Radiat Oncol Biol Phys* (2016) 95(1):249–57. doi: 10.1016/j.ijrobp.2015.12.356
32. Moyers MF, Benton ER, Ghebremedhin A, Coutrakon G. Leakage and Scatter Radiation From a Double Scattering Based Proton Beamline. *Med Phys* (2008) 35(1):128–44. doi: 10.1118/1.2805086
 33. Zheng Y, Newhauser W, Klein E, Low D. Monte Carlo Simulation of the Neutron Spectral Fluence and Dose Equivalent for Use in Shielding a Proton Therapy Vault. *Phys Med Biol* (2009) 54(22):6943–57. doi: 10.1088/0031-9155/54/22/013
 34. Han SE, Cho G, Lee SB. An Assessment of the Secondary Neutron Dose in the Passive Scattering Proton Beam Facility of the National Cancer Center. *Nucl Eng Tech* (2017) 49:801–09. doi: 10.1016/j.net.2016.12.003
 35. Hälgl RA, Besserer J, Boschung M, Mayer S, Lomax AJ, Schneider U. Measurements of the Neutron Dose Equivalent for Various Radiation Qualities, Treatment Machines and Delivery Techniques in Radiation Therapy. *Phys Med Biol* (2014) 59:2457–68. doi: 10.1088/0031-9155/59/10/2457
 36. Knežević Ž, Ambrozova I, Domingo C, De Saint-Hubert M, Majer M, Martínez-Rovira I, et al. Comparison of Response of Passive Dosimetry Systems in Scanning Proton Radiotherapy—a Study Using Paediatric Anthropomorphic Phantoms. *Rad Prot Dosim* (2018) 180:256–60. doi: 10.1093/rpd/ncx254
 37. Farah J, Martinetti F, Sayah R, Lacoste V, Donadille L, Trompier F, et al. Monte Carlo Modeling of Proton Therapy Installations: A Global Experimental Method to Validate Secondary Neutron Dose Calculations. *Phys Med Biol* (2014) 59:2747–65. doi: 10.1088/0031-9155/59/11/2747

Conflict of Interest: The authors declare that the research was conducted in the absence of any commercial or financial relationships that could be construed as a potential conflict of interest.

Publisher's Note: All claims expressed in this article are solely those of the authors and do not necessarily represent those of their affiliated organizations, or those of the publisher, the editors and the reviewers. Any product that may be evaluated in this article, or claim that may be made by its manufacturer, is not guaranteed or endorsed by the publisher.

Copyright © 2022 Domingo, Lagares, Romero-Expósito, Sánchez-Nieto, Nieto-Camero, Terrón, Irazola, Dasu and Sánchez-Doblado. This is an open-access article distributed under the terms of the Creative Commons Attribution License (CC BY). The use, distribution or reproduction in other forums is permitted, provided the original author(s) and the copyright owner(s) are credited and that the original publication in this journal is cited, in accordance with accepted academic practice. No use, distribution or reproduction is permitted which does not comply with these terms.



Determining Out-of-Field Doses and Second Cancer Risk From Proton Therapy in Young Patients—An Overview

Maite Romero-Expósito^{1,2*}, Iuliana Toma-Dasu^{2,3} and Alexandru Dasu^{1,4}

¹ The Skandion Clinic, Uppsala, Sweden, ² Oncology Pathology Department, Karolinska Institutet, Stockholm, Sweden, ³ Medical Radiation Physics, Stockholm University, Stockholm, Sweden, ⁴ Medical Radiation Sciences, Department of Immunology, Genetics and Pathology, Uppsala University, Uppsala, Sweden

OPEN ACCESS

Edited by:

Susanne Rogers,
Aarau Cantonal Hospital, Switzerland

Reviewed by:

Silvia Molinelli,
National Center of Oncological
Hadrontherapy, Italy
Christian Bäumer,
West German Proton Therapy Centre
Essen (WPE), Germany

*Correspondence:

Maite Romero-Expósito
maite.romero@skandion.se

Specialty section:

This article was submitted to
Radiation Oncology,
a section of the journal
Frontiers in Oncology

Received: 08 March 2022

Accepted: 02 May 2022

Published: 31 May 2022

Citation:

Romero-Expósito M, Toma-Dasu I
and Dasu A (2022) Determining
Out-of-Field Doses and Second
Cancer Risk From Proton Therapy
in Young Patients—An Overview.
Front. Oncol. 12:892078.
doi: 10.3389/fonc.2022.892078

Proton therapy has the potential to provide survival and tumor control outcomes comparable and frequently superior to photon therapy. This has led to a significant concern in the medical physics community on the risk for the induction of second cancers in all patients and especially in younger patients, as they are considered more radiosensitive than adults and have an even longer expected lifetime after treatment. Thus, our purpose is to present an overview of the research carried out on the evaluation of out-of-field doses linked to second cancer induction and the prediction of this risk. Most investigations consisted of Monte Carlo simulations in passive beam facilities for clinical scenarios. These works established that equivalent doses in organs could be up to 200 mSv or 900 mSv for a brain or a craniospinal treatment, respectively. The major contribution to this dose comes from the secondary neutrons produced in the beam line elements. Few works focused on scanned-beam facilities, but available data show that, for these facilities, equivalent doses could be between 2 and 50 times lower. Patient age is a relevant factor in the dose level, especially for younger patients (by means of the size of the body) and, in addition, in the predicted risk by models (due to the age dependence of the radiosensitivity). For risks, the sex of the patient also plays an important role, as female patients show higher sensitivity to radiation. Thus, predicted risks of craniospinal irradiation can range from 8% for a 15-year-old male patient to 58% for a 2-year-old female patient, using a risk model from a radiological protection field. These values must be taken with caution due to uncertainties in risk models, and then dosimetric evaluation of stray radiation becomes mandatory in order to complement epidemiological studies and be able to model appropriate dose–response functions for this dose range. In this sense, analytical models represent a useful tool and some models have been implemented to be used for young patients. Research carried out so far confirmed that proton beam therapy reduces the out-of-field doses and second cancer risk. However, further investigations may be required in scanned-beam delivery systems.

Keywords: proton therapy, pediatric patient, out-of-field dose, second cancer risk, brain and other nervous system cancer

INTRODUCTION

Concern about second cancer in patients who survived a primary malignancy has increased steadily over the past decades. Multiple epidemiological studies have focused on evaluating the risk of these second malignancies (1). The absolute risk of radiation-induced second cancer rates has been estimated to be in the order of 1% (2). Better estimates of this risk are made by studies with longer follow-up, which, in turn, implies that patients were treated with older technologies different from the current highly conformal therapies. Therefore, there is an intrinsic uncertainty about the actual risk. However, although risks were low, the high and growing number of patients affected must be considered. While the World Health Organization predicted in 2003 approximately 15 million new cancer patients by the year 2020 (3), the final value was 19.3 million (4). In addition, the Surveillance, Epidemiology, and End Results (SEER) Program registries show a 5-year relative survival of 67.2% (5). All these patients will be exposed to radiation from imaging procedures on a routine basis (6), and at least 50% will receive a radiotherapy (RT) treatment. Thus, second cancer risks should be considered although the benefit of the treatment is clearly confirmed.

From the point of view of medical physicists, the main contribution to this topic is to perform accurate estimates of the doses received by the patient. Determination of the dose delivered to the treatment target and closest organs [the so-called organs at risks (OARs)] is rather accurately carried out during planning by the treatment planning system (TPS). However, TPS can be trusted for doses above 5% of the prescription dose (7). Below this level and for the rest of the patient, the out-of-field dose is defined and has been the focus of many studies concerned with the second cancer induction.

Out-of-field dose or stray dose is due to all secondary particles produced by the interaction of the treatment beam with the elements of the delivery system and the patient. In the case of photon RT, the secondary particles are photons and neutrons (the latter when the linac operates at high energy, > 10 MV). In the case of particle therapy, in addition to photons and neutrons, other nuclear fragments can be produced in interactions. The contribution of each type of particle is different among the techniques. Xu et al. (1) published a comprehensive review on studies of out-of-field doses in external-beam radiation treatments, including both photon and particle therapies. By 2017, the American Association of Physicists in Medicine (AAPM) published a Task Group Report (No. 158) on the measurement and calculation of out-of-field doses (8). This code of practice, apart from updating the studies, discusses both the uses of dosimeters and phantoms in experimental evaluations and the calculation techniques. Special attention was paid on how to report doses, and some recommendations for practice were included as well. More recent overviews can be found in Mazonakis and Damilakis (9), which focused on photon RT, and in Hägl and Schneider (10), describing the state of art in the evaluation of neutron stray doses in proton beam therapy (PBT).

Out-of-field doses and second cancers lead to a greater concern in the case of young patients (≤ 21 years of age). First, children are more

radiosensitive than adults (11), and secondly, after a successful treatment, their expected lifetime will be longer. Consequently, these factors are likely to lead to a higher risk of secondary cancer. However, this risk has to be regarded from the perspective of the treatment objective and should not prevent a patient from receiving RT.

The physical properties of PBT provide superior dose distributions compared to photons; this fact is especially relevant in pediatric RT (12). From 2004 to 2012, the proportion of children receiving PBT was significantly increasing over time from <1% to 15% (13). In USA, the National Cancer Institute estimated, by mid-2021, 10,500 new cases of cancer among children from birth to 14 years for the whole year (14). Cancer incidence rates reported by the Childhood Cancer Data Initiative were 196 and 185 per 1,000,000 for male and female patients, respectively (15). Among all the cancer sites, the most common after leukemia are cancers of the brain and the central nervous system (CNS). These cancers represent 16.4% of all new childhood cancer cases with a 5-year relative survival of 74.9%. PBT for the treatment of pediatric cancers of the CNS has been found to provide survival and tumor control outcomes comparable and frequently superior to photon therapy. Furthermore, the use of protons was shown to decrease the incidence of severe acute and late toxicities, including reduced severity of endocrine, neurological, cognitive, and quality-of-life deficits (16). At many facilities, pediatric patients represent a substantial portion of those receiving proton treatment, and CNS tumors comprise a large proportion of this group (13). An international survey carried out to evaluate the patterns of PBT in 2016 showed that 48% of pediatric patients (from a total 1,860 patients) were treated for CNS tumors, with medulloblastoma, ependymoma, low-grade glioma, and craniopharyngioma being the most frequent tumor types (17). An additional 14% of patients were treated for other head and neck tumors. Overall, 34% of patients were treated with passive scattering, 15% with uniform scanning beam, and 51% with pencil beam scanning. Data from the Pediatric Proton Consortium Registry with a total of 1,854 children enrolled by September of 2017 showed that majority of children received curative craniospinal irradiation (CSI) (17%) or involved field RT (58%) using mainly passive scattering (68%) vs. pencil-beam scanning (32%) proton therapy (18). More children with non-CNS tumors received pencil-beam scanning (39%) compared with CNS (28%). A more recent epidemiological study showed that the vast majority of pediatric patients worldwide have been treated using a passive modulation proton technique to date (19). This single-institution retrospective study of pediatric patients treated with double-scattered proton therapy for benign and malignant solid tumors found a risk of developing a second solid tumor of 1.7% if irradiated at age ≤ 5 years versus 0.1% if older ($p < 0.0005$). One limitation of the study is related to the latency of second tumors. The median follow-up was 3.3 years, and some tumors present higher latencies. In a work from the Childhood Cancer Survivor Study (CCSS) where the median follow-up was of 22.7 years after diagnosis, the analysis showed a 30-year cumulative incidence of 7.9% (20). More significantly, as childhood cancer survivors progress through adulthood, the risk of subsequent neoplasms increases.

In this context, the purpose of this manuscript is to offer an overview of the determination of out-of-field doses and the

prediction of second cancer risk so far for young patients receiving PBT. Publications were considered when published from 2008 onward [from the publication of the review of Xu et al. (1)].

It is worth pointing out the importance of including the exposures during imaging procedures for the comprehensive study of the patient doses in relation to the probability of second cancer induction (6). The recent work of Marcu et al. (21) offers a systematic review on epidemiological studies covering cumulative doses and cancer risks in children and young adults' examinations.

SECONDARY PARTICLE PRODUCTION AND DELIVERY TECHNIQUE

Secondary particles in proton therapy are produced in nuclear inelastic interactions between the projectile and target nuclei both in the beamline components and in the patient. The process can be described by the abrasion–ablation or cascade–evaporation model (22). In short, protons, neutrons, and light fragments are emitted (with energies that may exceed even a hundred MeV) mostly in the forward direction (proton beam direction) while the residual nucleus is left in an equilibrium state, with a certain excitation energy (23). The remaining nucleus follows a de-excitation process leading to lower-energy secondaries, emitted more or less isotropically. After this emission, the final excitation energy is released by γ -rays. Neutrons and photons, as long-range secondary particles, can affect tissues far away from the target. This component has been concisely referred to as the aura of dose distribution (24).

The contribution and the main sources of these secondary particles are directly related to the beam delivery system. To cover all the tumor volume, the narrow pristine Bragg peak must be extended to form the so-called spread-out-Bragg-peak (SOBP). This can be done either by passive modulation of the primary beam, or by scanning the tumor volume with a millimeter-wide beam magnetically deflected (22). In passive scattering PBT (PS-PBT) the proton beam goes through and interacts with several elements such as the range modulation wheel (RMW), scatter foils, collimators, range compensators, or patient-specific apertures before reaching the patient (25). All these elements become a source of secondary neutrons, often referred to as external neutrons or spray (24), that can reach the patient. Monte Carlo (MC) simulations have shown that most of the neutrons that do reach the patient are generated in the precollimators, and the patient-specific aperture (26). In the proton pencil beam scanning PBT (PBS-PBT) technique, magnets steer a small pencil beam of protons to specific positions within a tumor target without the need for apertures or compensators (27). Unless a range shifter (RS) is used at the nozzle exit, a negligible amount of material is in the beam path and, therefore, external neutrons are hardly produced (22). Additional to the external neutrons, there are nuclear interactions between the proton beam and the patient tissue. Neutrons generated in these reactions, the so-called internal

neutrons, are unavoidable. In short, it is considered that external neutrons are the main contributors to stray dose in patients in PS-PBT, while internal neutrons are in PBS-PBT (28).

As previously mentioned, de-excitation γ -rays are also produced by the nuclear reactions. However, the high relative biological effectiveness (RBE) of neutron in comparison to photons is responsible for the major focus on neutrons.

OUT-OF-FIELD DOSES IN YOUNG PATIENTS' TREATMENTS

The majority of studies dealing with stray radiation have been carried out by MC simulations. Some advantages of the simulations are the possibility to perform systematic studies showing the effects of changing several irradiation parameters and to evaluate separately internal and external neutron contribution in PS-PBT. As stated by ICRP, the equivalent dose in an organ is the recommended quantity for subsequent risk estimates for specific individuals (29). Then, several works reported their results using this quantity. However, some authors preferred to report absorbed dose to avoid increasing uncertainties due to the use of the radiation weighting factors (w_R). Another relevant aspect is that when reporting results, absorbed or equivalent doses are normalized by the prescription dose, which can be expressed in terms of physical proton dose in Gy or in terms of therapeutic dose in Gy (RBE). Then, it is important to specify which one is used to enable comparisons, becoming mandatory if the comparison is with photon treatments. However, the review process showed that all works used Sv/Gy to report their results, although they referred to Sv/Gy (RBE) (usually in the text, expressions like “Equivalent dose per therapeutic dose” were included). Despite this, in the present work, the unit Sv/Gy (RBE) will be preferably used. Results were corrected by $RBE = 1.1$ for those works reporting results in terms of the physical dose. Hereafter, the following sections cover the overview of works focused on brain irradiation and craniospinal irradiation (CSI).

Out-of-Field Doses in Brain Irradiations

Bonfrate et al. (30) performed the most comprehensive study on the influence of several treatment parameters on neutron production. The work modeled a passive double scattering beam line used for treating a 10-year-old female phantom in the brain. Each dependency study is summarized below.

First, the selection of beam incidence can modify the level of the doses. They compared an anterior–superior (SUP) incidence (patient oriented parallel to beam axis) and lateral (LAT) incidence (patient oriented perpendicular to beam axis). Neutron absorbed doses in thyroid and bladder were 123 μ Gy/Gy (RBE) and 22 μ Gy/Gy (RBE), respectively, in the SUP field, while for the LAT field, they were 321 μ Gy/Gy (RBE) and 76 μ Gy/Gy (RBE), respectively. On the one hand, these results showed that organ doses decrease as the distance to the target increases. On the other hand, lateral incidences produce higher doses as organs are at shorter distances from the patient

collimator, which is the beam element with a major neutron contribution to organ doses [approximately 70% according to Matsumoto et al. (31)]. In addition, in the superior incidence, the head and neck and thoracic regions become a neutron shield for the rest of the body.

Neutron absorbed doses increase as proton energy and width modulation increase. For example, an averaged factor of 2.5 was found between absorbed doses when the proton energy changed from 162 to 219 MeV. The increase with wider modulation is a bit more complex because it presents a saturation effect. When modulation width was changed from 1 cm to 3 cm, doses increase by 38% on average, but from 3 to 5.6 cm, the change was almost negligible. This behavior was also seen in ambient dose equivalent measured in the treatment room (32). As modulation width increases, a larger proton fluence is needed to deliver the same dose to the target, but beyond certain widths, the required increase in fluence becomes too small to affect the neutron production rate. The relevant consequence of the energy and modulation effect is that larger treatment volumes that are deeper in the patient will cause significantly higher neutron equivalent doses (33).

Target volume is also related to the field size fixed by the collimator aperture. However, internal and external neutrons have opposite effects. Meanwhile, increasing the diameter of collimator leads to a lower production of external neutrons as less material blocks the proton beam, the production of internal neutron increases as more protons interact with the patient. Zacharatou-Jarlskog et al. (33) performed simulations distinguishing internal and external neutrons in PS-PBT. They found that while for small fields the contribution of external neutrons could be more than 99%, it could be reduced to 60% for larger fields. In addition, due to the distance effect previously mentioned, internal neutrons have a significant contribution for organs near the target volume and a low contribution for organs located far from it (30). The complex inter-relationships hamper the derivation of a general trend. In fact, Zacharatou-Jarlskog et al. (33) disagreed with simulations of Bonfrate et al. (30). While the former obtained equivalent doses lower with larger fields, the latter found higher absorbed doses for larger collimator aperture in the SUP field. Furthermore, in the LAT incidence, absorbed doses only increased in head and neck organs and decreased in thoracic and pelvic organs. The disagreement with Zacharatou-Jarlskog et al. (33), where lateral fields were considered, can be justified by the differences in the particular configuration of the beam line in the passive facilities modeled.

Collimator and compensator thickness changes had a similar impact on absorbed dose and the incidence dependence (30). For example, for the SUP field, neutron absorbed doses tend to decrease when increasing thickness, about 13% for a change from 5 to 8.5 cm. Again, for the LAT field, organ doses presented a similar reduction but only for organs between the target and the heart. The rest of the organs were almost insensitive to the variation of collimator thickness. Finally, increasing the air gap size from 1 cm to 12 cm led to neutron absorbed doses decreasing on average by 19%, 12%, and 5% for organs located in the head and neck, thoracic, and pelvic regions, respectively.

Certainly, the most relevant effect to study for young patients is the one related to the age of the patient or, in other words, the

size of the patient. Both Zacharatou-Jarlskog et al. (33) and Sayah et al. (34) performed simulations of brain irradiation in PS-PBT in several hybrid phantoms covering representative ages for male and female patients. Phantoms used were those developed by the University of Florida (35). It is important to note that these models are being considered by ICRP to be used as pediatric reference computational phantoms as they take into account not only changes in the geometry as a function of age but also changes in the organ-specific material composition as a function of age (34). The general trend was that secondary neutron dose received by an organ decreases as the phantom's age increases; this is a consequence of the reduction in dose as the organ is farther from the target volume. An older patient has a larger size and then distances between organs are also larger. Sayah et al. (34) evaluated brain treatment using 5 field incidences (including LAT, SUP, and oblique incidences) and using the same target volume. They also reported higher doses for lateral incidences, and the antero-superior incidence delivered the lowest doses. They found, for instance, that the neutron equivalent dose in salivary glands for 1-year phantom was 1.2 times higher than for adults. This factor reached a value of 2.7 and 3.2 for bladder and uterus/prostate. As expected, differences between the child and the adult increased as the organ was farther from the target. Sayah et al. (34) also evaluated the contribution of secondary photons for the 5-year-old phantom. Their results reported a contribution between 4% and 16% of the total equivalent dose. This low contribution justifies that most works focused on neutron contamination in PS-PBT.

Figures 1–3 depict the neutron equivalent doses in several organs evaluated by the different works already discussed. From these data, it is possible to extract the ranges of neutron equivalent doses that a child could receive as a consequence of the brain treatment. In **Figure 1**, the effect of patient age can be noticed. For the thyroid, a close organ to the target, equivalent doses are similar among the phantoms, with an average of 1.69 mSv/Gy (RBE). In the rest of the organs, older patients do present lower doses. Equivalent dose in lungs ranges from 1.37 mSv/Gy (RBE) in the 1-year-old phantom to 0.83 mSv/Gy (RBE) in the 15-year-old phantom. In the abdomen, for instance, liver equivalent doses range from 0.93 mSv/Gy (RBE) to 0.49 mSv/Gy (RBE) for the 1-year-old and 15-year-old phantoms, respectively. Equivalent doses are below 0.5 mSv/Gy (RBE) in bladder for all phantoms. Equivalent doses in breasts have higher doses for all the phantoms [between 3.16 and 1.75 mSv/Gy (RBE)]. This is a consequence of the shallow depth of the tissue, which makes it more exposed to external neutrons. Consistently, male phantoms had a higher equivalent dose in comparison with female phantoms.

Figure 2 compares equivalent doses for two different PS-PBT facilities. The phantoms considered were both 5 years old and with a similar target volume. Although simulation was done for a male phantom in Matsumoto et al. (31) while Sayah et al. (34) irradiated a female phantom, differences in sizes and organ configuration could be considered negligible for 5 years. Matsumoto et al. (31) found doses 3 times higher on average, except for breast, which can be explained by the fact that they used just one lateral incidence in comparison with the 5

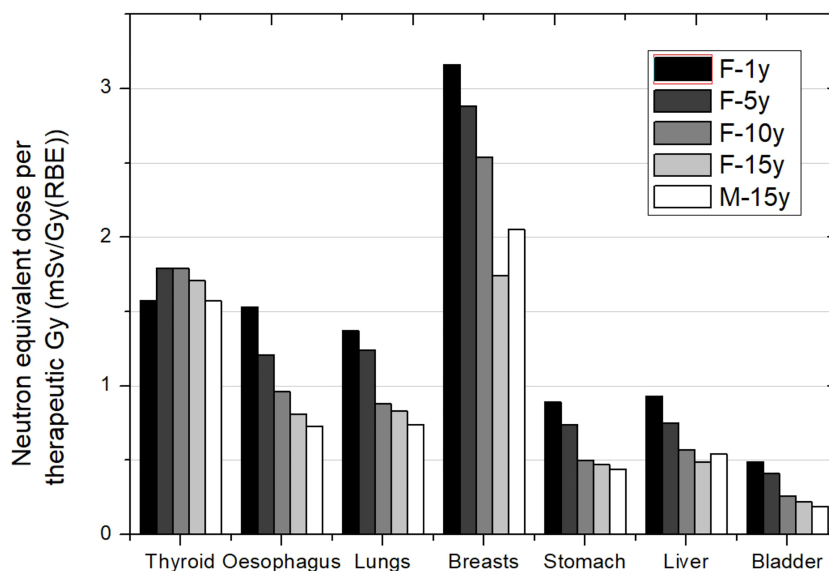


FIGURE 1 | Neutron equivalent doses per therapeutic Gy in selected organs for a brain treatment in the same passive scattering proton beam facility and several patient ages. In the legend, the sex (F, female; M, male) and age of the patient (#y = number of years) are specified. Data extracted from Sayah et al. (34).

incidences of the treatment in Sayah et al. (34). Matsumoto et al. (31) reported that previous measurements in the facility had shown higher ambient dose equivalent in the room in comparison to other facilities. In any case, all these facts agree with higher doses. The contradictory result in breast could be a consequence of reporting the dose as an average over both breasts considered as an organ. For one lateral incidence, the

closest breast to the nozzle will be significantly more exposed than the contralateral breast, while with 5 field incidences, both breasts are more homogeneously exposed.

Figure 3 shows results from Zacharatou-Jarlskog et al. (33) for the same facility and the same phantom. Treatment 1 (T1) had a target volume approximately 5 times larger than treatment 2 (T2) where one expected lower doses for the latter. However, except for

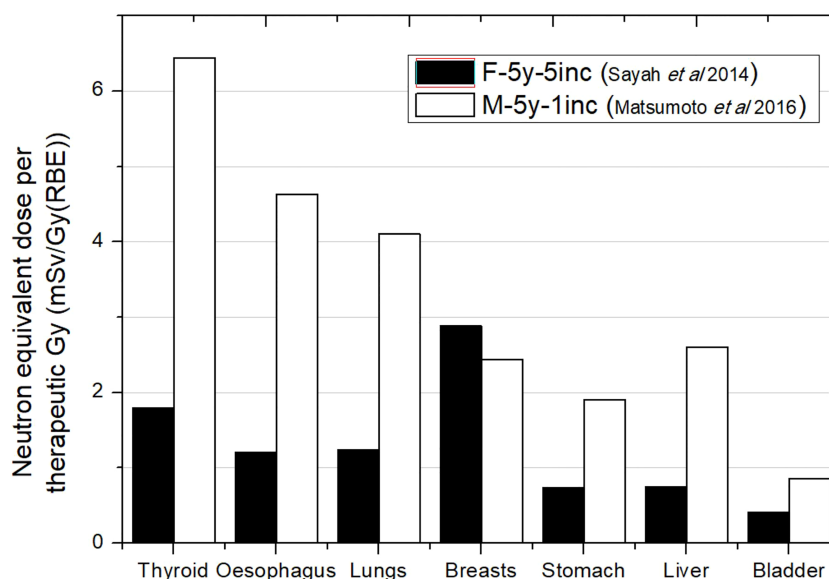


FIGURE 2 | Neutron equivalent doses per therapeutic Gy in selected organs for a brain treatment in two different passive scattering proton beam facilities. Data extracted from Matsumoto et al. (31) and Sayah et al. (34) for the same age phantom (5 years) but different target volumes and number of incidences: 83 cm³ in Matsumoto et al. (31) and 92 cm³ in Sayah et al. (34). In the legend, the sex (F, female; M, male), age of the patient (#y = number of years), and number of incidences (#inc = number of incidences) are specified.

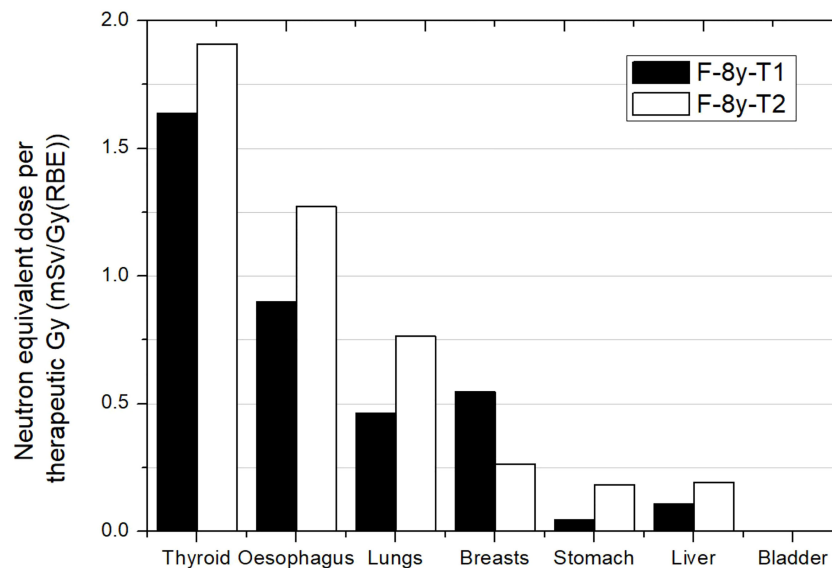


FIGURE 3 | Neutron equivalent doses per therapeutic Gy in selected organs for 2 different brain treatments in the same passive scattering proton beam facility. T1 corresponds to an irradiation with a lateral incidence and a target volume of 514 cm³. T2 corresponds to an irradiation with an oblique-inferior incidence and a target volume of 306 cm³. Equivalent doses in bladder were too low for the plot scale. Data extracted from Zacharatou-Jarlskog et al. (33).

breasts, results showed an opposite behavior. While T1 consists of a lateral field with a proton energy of 164 MeV, T2 consists of an oblique-inferior field of 180 MeV protons. It can be inferred from this result that the proton energy is the dominant parameter for neutron equivalent dose, which can even offset the effect of beam incidence and target volume. The behavior in breast is also related to beam incidence and breast position in phantom. For this irradiation, neutron equivalent doses in thyroid were 1.6 and 1.9 mSv/Gy (RBE) for treatment 1 and treatment 2, respectively. These values were similar to those reported by Sayah et al. (34), even in esophagus. For the other organs, a combination of incidence and specific configuration of beam lines could explain the differences.

Based on the works reviewed, we could establish that in PS-PBT facilities, a brain treatment could represent a neutron equivalent dose between 1.6 and 6.4 mSv/Gy (RBE) in thyroid, 4.1 and 0.51 mSv/Gy (RBE) in lungs, 2.6 and 0.12 mSv/Gy (RBE) in stomach, and below 0.1 mSv/Gy (RBE) in bladder. Assuming a prescription of 54 Gy (RBE) (30, 34, 36), total equivalent doses associated to the whole brain treatment would be approximately 216 mSv, 126 mSv, 73 mSv, and below 5.4 mSv for the thyroid, lungs, stomach and bladder, respectively.

Relatively scarcer works can be found for PBS-PBT facilities. In these facilities, while not using a significant number of absorbers in the beam line, the external neutron contribution from the treatment head becomes negligible (37). Ardenfors et al. (36) compared by MC simulation total absorbed doses in an adult and a 5-year-old patient irradiated by a pencil beam scanning system. They also considered a SUP and a LAT field. For this delivery system, neutron doses are essentially due to internal neutrons and therefore, the impact of field parameters could be different from those described in a passive facility. In fact, LAT field led to lower absorbed doses than with the SUP

field, except in one of the eyes. Equivalent dose was reported in thyroid and bladder for the SUP field. The results were 62 μ Sv/Gy (RBE) and 2 μ Sv/Gy (RBE), respectively. These values represent approximately 39- and 50-times lower doses regarding PS-PBT.

Experimental studies in scanned-beam facilities have been done by EURADOS Working Group 9 (38, 39). In their campaigns, a 5-year-old and a 10-year-old anthropomorphic phantom were irradiated with 2 incidences (LAT and oblique) and several types of dosimeters located inside. They were able to evaluate the contribution of photons and neutrons. Knežević et al. (38) reported photon absorbed doses in organs and neutron dose equivalent as a function of distance to target center (only in the 5-year-old phantom). For example, in thyroid, they measured approximately 48 and 25 μ Gy/Gy (RBE) for the 5- and 10-year-old phantoms, respectively. In general, results in the younger phantom were approximately 2 times higher. For this phantom, photon doses ranged from 47 to 0.1 μ Sv/Gy (RBE) from 12 to 50 cm. In comparison, neutron dose equivalent ranged from approximately 200 μ Sv/Gy (RBE) to 3 μ Sv/Gy (RBE) from 12 to 36 cm. The results imply that neutron stray dose is still more relevant than photon dose in PBS-PBT.

Figure 4 shows the comparison between Ardenfors et al.'s (36) total absorbed doses and photon absorbed doses in Knežević et al. (38). As can be noticed, results are not compatible in thyroid, taking into account that Ardenfors et al. (36) results included both photons and neutrons. Some explanation can be found in the different target volume and the proton energy range of treatments in both works. While, in Knežević et al. (38), the target has a volume of 65 cm³ and proton energies range from 70 to 140 MeV, in Ardenfors et al. (36), these parameters were 24 cm³ and 80–110 MeV in the lateral field and 92–124 MeV in the superior field. Therefore, higher values were expected in

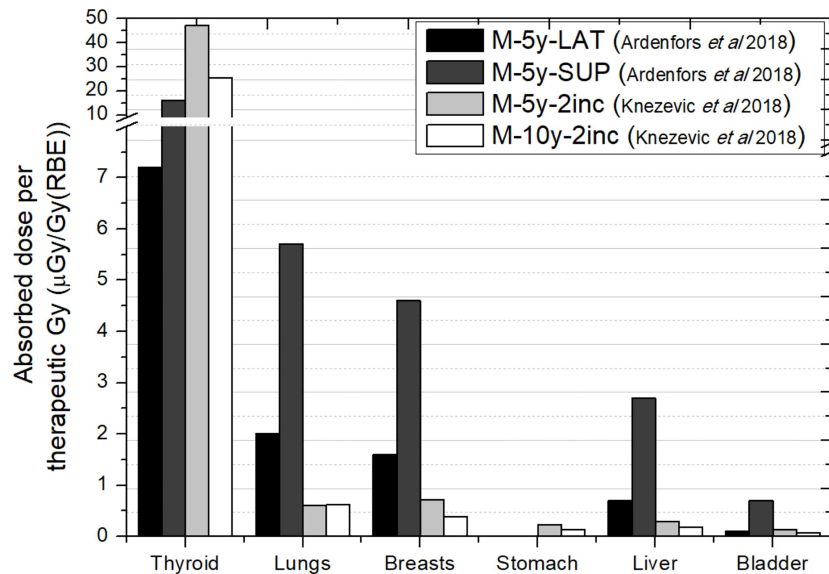


FIGURE 4 | Absorbed doses per therapeutic Gy in selected organs for a brain treatment in two different proton pencil beam scanning facilities. Data extracted from Ardenfors et al. (36) (total absorbed dose) and Knežević et al. (38) (photon absorbed dose). In the legend, the sex (F, female; M, male), age of the patient (#y=number of years) and number of incidences (#inc = number of incidences) are specified. LAT, Lateral field; SUP, Anterior-superior field.

Knežević et al. (38), although there must be other facts behind the observed inconsistency. For the remaining organs, results in Ardenfors et al. (36) were on average 5 times higher than in Knežević et al. (38). Given the result in thyroid, it is not possible to assign this difference only to neutron contribution.

In Wochnik et al. (39), the irradiation was repeated maintaining the target volume but shallowly located due to the use of an RS or a 3D printed beam compensator (BC). The introduction of these elements in the proton beam becomes a source of external neutrons and, therefore, a behavior in between PS-PBT and PBS-PBT would be expected. In this campaign, they reported both photon and neutron equivalent doses in selected organs for the 10-year-old phantom. They found, in general, a worse scenario with the RS despite of being farther from the patient. For this worst case, total equivalent doses ranged from 1.5 mSv/Gy (RBE) in thyroid to 39 μSv/Gy (RBE) in the bladder. Interestingly, equivalent dose in thyroid becomes similar to the values reported in passive scattering facilities. However, there is a faster reduction as the distance to target increases.

More studies for PBS-PBT would therefore be needed in order to be able to establish a range of equivalent doses received by the young patients.

Out-of-Field Doses in Craniospinal Irradiation

In brain treatments, the beam points to the superior edge of the patient, and CSI covers the brain and the whole spinal cord. Therefore, the target presents a significant increase in terms of volume. In addition, as the spinal fields cover almost the whole trunk of the patient, organ distance to target will be lower than in the brain irradiation. Another important difference is that an

almost whole-body CT scan of the patient is available and, therefore, can be included in simulations instead of using a voxel phantom. This is the case for the studies discussed in this section and, in addition, unless otherwise indicated, all modeled passive facilities.

Behaviors discussed in the previous section in relation to the influence of field parameters, such as beam incidence, range, modulation, or field size, are expected to occur in this case. For example, Athar and Paganetti (37) performed a simple estimation of the neutron equivalent doses expected for spinal fields in a passive facility. The aim was to compare the same fields used by Zacharatou-Jarlskog et al. (33) but with the proton beam directed posterior to the lumbar spine. **Figure 5** shows the neutron equivalent doses in several organs for the 6 fields considered (see details in the figure caption). As expected, organs in the trunk have now higher doses than in the head and neck region. Another expected behavior, discussed in the previous section, is that equivalent doses for the fields with smaller range and modulation width (T1, T2, and T3) are substantially lower than doses in the other fields (T4, T5, and T6). Their results showed that the maximum dose was 4.5 mSv/Gy (RBE).

Contributions from Taddei and collaborators (40–42) and Zhang et al. (43) did consider realistic CSI treatments. Usually, this treatment consists of a first plan covering the brain and the spinal cord with an additional boost in the brain. Each irradiation has its own prescription dose, and then the comparison of the whole plan in terms on equivalent dose per therapeutic Gy becomes difficult. Therefore, the analysis will focus on the treatments without the boost. Some works even did not simulate the boost fields assuming that the boost volume is

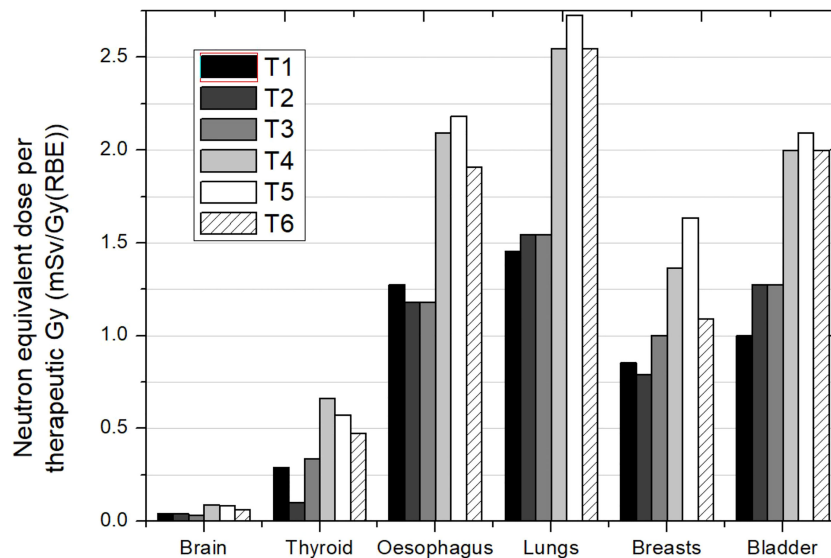


FIGURE 5 | Neutron equivalent doses per therapeutic Gy in selected organs for the 6 different spinal fields in the same passive scattering proton beam facility. T1 (aperture diameter = 3 cm), T2 (aperture diameter = 6 cm), and T3 (aperture diameter = 9 cm) had a range and a modulation width of 10 and 5 cm, respectively. T4 (aperture diameter = 3 cm), T5 (aperture diameter = 6 cm) and T6 (aperture diameter = 9 cm) had a range and a modulation width of 15 and 10 cm, respectively. Data extracted from Athar and Paganetti (37).

small and located far away from the organs, and boost fields may contribute very little to the equivalent dose (42). Zhang et al. (43) also presented the dose distribution of stray neutrons overlapping the CT of the patient, showing how neutrons penetrate the whole body.

Taddei et al. (40) showed the different contribution of the incidences used for covering the target. In the case of a 10-year-old male patient, for a lower-posterior-anterior (LPA) field, the stomach, liver, and colon received the highest equivalent doses, approximately 8 mSv/Gy (RBE) each. For the upper-posterior-anterior (UPA) field, the esophagus, thyroid, and lungs received the highest equivalent doses, in the interval of 11 to 14 mSv/Gy (RBE). For cranial fields, bone surface and thyroid received the highest equivalent doses, each over 10 mSv/Gy (RBE). **Figure 6** shows equivalent doses in several organs for this case. The behavior of organ doses is related to the distance to the corresponding target. Taking as reference the organ order in the *x*-axis in the plot, we can see how equivalent dose decreases as moving to the right for the cranial fields. Meanwhile, the field directed to the upper part of the spinal cord leads to higher doses in the organs located in the thorax. Breasts present significantly lower doses than the others (thyroid, esophagus, and lungs), which can be easily explained by the opposite position in the body regarding the beam entrance. This means that caution is required when referring to distance, as distance in cranio-caudal direction, which can be representative in the majority of irradiations, for instance in brain, is no longer suitable in CSI.

Figure 7 shows the neutron equivalent dose for the whole treatment without the boost. Data were obtained for different patient ages. The first most striking aspect is that, in general, lower doses were found for the youngest patient. The effect of

patient age in brain treatments is a consequence of the lower distances in younger patients. However, the large target in CSI makes distances in general similar between the children. Only for bladder can the age effect be slightly observed. All irradiations considered the same pattern of 4 beam incidences and, therefore, equivalent dose deviations may be attributable to differences in specific parameters of the incidence due to particular patient geometry. Based on the values reported, neutron equivalent doses range from 16 to 37 mSv/Gy (RBE) in thyroid, 14 to 27 mSv/Gy (RBE) in lungs, 12 to 18 mSv/Gy (RBE) in stomach, and 5.1 to 8.4 mSv/Gy (RBE) in bladder. These values represent an increase of one order of magnitude in comparison to brain irradiation illustrating the effect of the larger irradiated volume for CSI cases.

The worst scenario in **Figure 7** was for a 10-year-old male patient. If we add the contribution of boost fields (consisting in a left posterior oblique and a left lateral fields), we can evaluate total equivalent doses due to the whole treatment using the prescribed doses to the targets [23.4 Gy (RBE) in primary plan and 30.6 Gy (RBE) in the boost]. The results are that equivalent doses in CSI could reach values of 884 mSv, 715 mSv, 504 mSv, and 176 mSv in thyroid, lungs, stomach, and bladder, respectively.

These doses could be reduced with few modifications in the dimensions or material of some elements in the beam line as shown by Taddei et al. (41). They proposed increasing the thickness (from 4 to 8 cm) and changing the material (from brass to tungsten) of the field-defining collimator to improve the shielding in the nozzle. Additionally, a pair of jaws made of tungsten alloy were introduced in the nozzle to minimize the edge-scatter effects. This modification led to a percentage of reduction in equivalent dose from 33% to 59% in spinal fields and from 10% to 26% for the cranial fields.

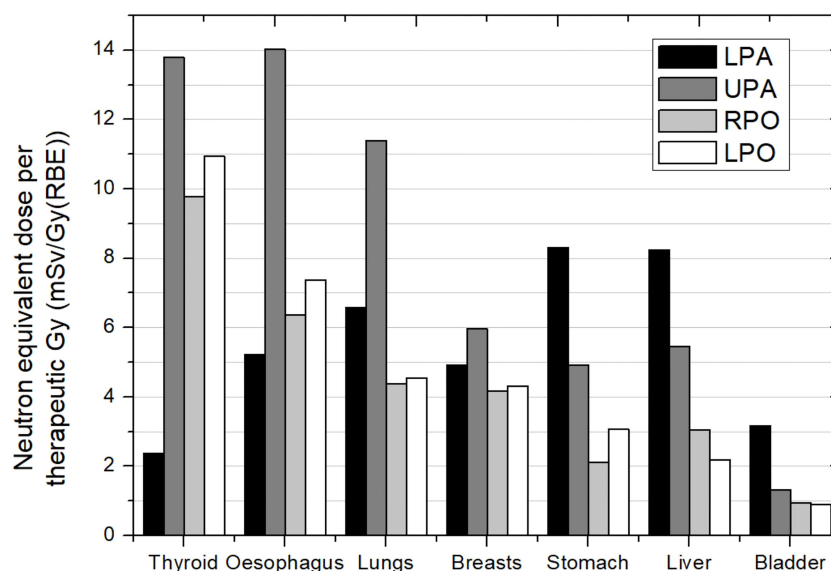


FIGURE 6 | Neutron equivalent doses per therapeutic Gy in selected organs for the different incidences in CSI. Spinal fields: LPA, lower posterior anterior; UPA, upper posterior anterior. Cranial fields: RPO, right posterior oblique and LPO, left posterior oblique. Data extracted from Taddei et al. (40).

Newhauser et al. (44) dealt with CSI in PBS-PBT. In fact, they compared the neutron equivalent doses in passive and scanned-beam facilities. Results from this work were not included in the previous discussion as they used results in adults to estimate the dose in a 3-year-old patient. Although the age of patient may not be so relevant as in brain irradiation, their assumption may bias the reported dose ranges. However, the comparison between passive and scanned-beam delivery system appears reasonable,

especially when there is a lack of studies in scanned-beam facilities. Their results showed that the equivalent dose was on average two times lower in PBS-PBT.

The work of Majer et al. (45) was the only experimental work and considered a PBS-PBT facility. They evaluated photon and neutron equivalent doses in selected positions inside a 10-year-old anthropomorphic phantom. The treatment consisted of two lateral fields for brain irradiation and three posterior anterior

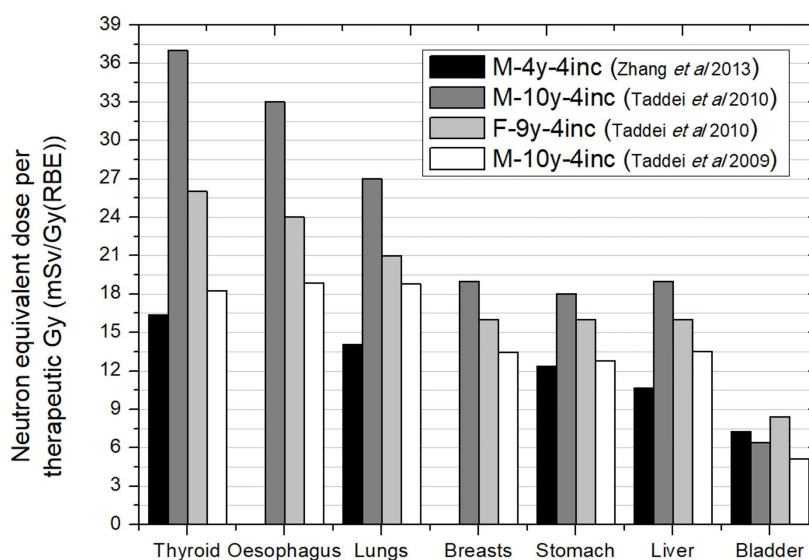


FIGURE 7 | Neutron equivalent doses per therapeutic Gy in selected organs for CSI without boost for different passive scattering proton beam facility facilities. Data extracted from Taddei et al. (2009), (2010) (40, 42) and Zhang et al. (43). In the legend, the sex (F, female; M, male), age of the patient (# = number of years) and number of incidences (#inc = number of incidences) are specified.

fields for spinal cord irradiation, all using an RS. Results for some organs are depicted in **Figure 8**. First, it can be noticed that a general trend cannot be derived when comparing photon and neutron contributions. While thyroid, lungs, and liver show higher photon equivalent doses, breasts, stomach, and bladder show lower photon doses. If we compare the neutron equivalent doses with data in **Figure 7** for PS-PBT, the most noteworthy result is that lungs and breasts are in the same range [approximately 20 mSv/Gy (RBE)]. This effect was also seen in brain irradiation when using the RS. However, neutron equivalent doses in other organs are lower in the pencil beam facility, by a factor between 5 and 10, higher than the factor 2 reported by Newhauser et al. (42). For example, the equivalent dose in thyroid was 2.7 mSv/Gy (RBE), while in PS-PBT, values can be up to 37 mSv/Gy (RBE).

SECOND CANCER RISK ESTIMATES

The estimation of second cancer risk is in general subject to considerable uncertainty and often affected by the choice of model (46). As a consequence, absolute values of risks should be taken with caution, although relative comparisons can be regarded as more reliable, for example, using the ratio of risk values as a figure of merit (43). Lifetime attributable risk (LAR), i.e., the risk for the rest of life since treatment, is the usual endpoint for evaluating the probability of acquiring a second cancer due to the RT exposure. LAR for organs of interest is calculated using an appropriate model and then summed to obtain a global value.

Estimations of risks associated to neutrons were made by Zacharatou-Jarlskog and Paganetti (47). They simulated a

passive scattered facility where voxel phantoms of different age were irradiated for a brain treatment. Using the formalism of BEIR-VII report (11), LAR was estimated assuming a treatment of 77 Gy (RBE). For calculation of LAR, a latency period and an expected maximum age attained must be considered. The BEIR report assumes a latency period of 5 years and a maximum age of 100 years. Phantoms covered ages from 9 months to 14 years and both sexes. Main results were significantly higher LAR values for female patients (about a factor of 2.5) and a fast decrease with age of exposure, especially at young ages. The fact that female patients present a higher risk is a direct consequence of the higher risk coefficients in the report (11), in accordance with epidemiological studies (48). The target volume also affected the risk, which became higher as the volume increases. As in their previous estimation of contribution of internal and external neutron to equivalent doses, they also established the contribution of each type of neutron to the risk. As expected, a similar trend was found: being the main component, the neutrons produced in the treatment nozzle between 82% and 98% of the total risk, depending on the beam parameters. Regarding the contribution of the different organs to total LAR, in male patients, solid cancers in lung and thyroid, together with leukemia, were of higher concern. For female patients, breast cancer is also included and even showing potentially the greatest concern. We have selected results from the treatment leading to the highest LAR for comparison with other works. **Tables 1, 2** collect the LAR for the most radiosensitive organs and the total LAR for several of works discussed in the present section.

Athar and Paganetti (37) completed the previous work with results in spinal irradiations for a prescription of 77 Gy (RBE) as well. They found similar behaviors in terms of age dependence or target volume. For instance, LAR in younger patients was almost

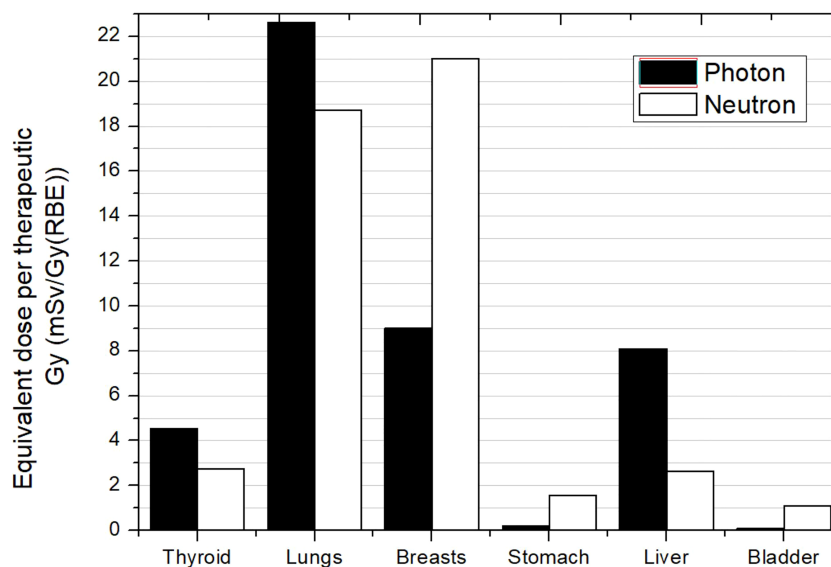


FIGURE 8 | Photon and neutron equivalent doses per therapeutic Gy in selected organs for CSI in a proton pencil beam scanning facility for a 10-year-old anthropomorphic phantom. All fields included a range shifter. Data extracted from Majer et al. (45).

twice that for older patients. Spinal irradiation also led to a higher risk in lung and breast and, in addition, rectum for female patients and esophagus and rectum for male patients. In Athar and Paganetti (50), the prescription dose was reduced to 54 Gy (RBE) for similar brain and spinal irradiations. However, complete results were not provided for patients of the same sex and age, and therefore, a comprehensive comparison in terms of prescription dose cannot be done. It was only possible to compare LAR in the lung and breast for the 8-year-old female patient. Results were very similar, but it is not possible to ensure that the same treatment is compared and therefore any further conclusion cannot be easily drawn.

Total LAR is affected by the organs considered in the sum. Normally, if the most radiosensitive organs are considered, comparisons between LAR are still appropriate. However, the inclusion of skin or the remainder will significantly increase the total risk (51) and must be considered for meaningful comparisons. This is the case for Taddei et al. (42), for CSI irradiation, assuming a treatment with a prescribed dose of 23.4 Gy (RBE) and a brain boost of 30.5 Gy (RBE), LAR values were 14.8% for a 9-year-old girl and 8.5% for a 10-year-old boy. LAR is reduced to 9.4% and 4.0% for the girl and the boy, respectively, when skin and the remainder are not considered. Their results agree with the fact that female patients have higher risks in general. For the CSI, the thyroid, lung, and breast were also major contributors to total risk.

Zhang et al. (43) evaluated the total dose received by the organs (not only due to secondary neutrons) to calculate LAR for CSI. Following also the BEIR report, they predicted a risk of 24.6% for an 8-year-old patient with a prescription dose of 23.4 Gy (RBE). If only stray neutrons had been considered, this risk would be reduced to 4.6%. Zhang et al. (43) considered the remainder for the total LAR but not the skin. If we subtract only the contribution of the skin to the value reported by Taddei et al. (42), we get a value of 6.2%, which agrees with the 4.6% reported by Zhang et al. (43). Nevertheless, the most important conclusion that can be extracted from the risk due to neutrons in comparison with total risk is that the contribution of neutron exposure comprises a much smaller proportion of the total risk (44).

The same methodology was followed in a retrospective study of 17 patients selected to be representative of a general

population of children receiving CSI (52). The maximum and minimum values obtained for male and female patients are included in **Tables 1, 2**. The LAR reported was up to 58% and 30% for a 2-year-old female and a 4-year-old male patient, respectively. Lungs were the organs with at significant higher risk in comparison with the others.

The BEIR report assumes the linear no-threshold model for risk estimates, which is appropriate for radiation protection purposes and for the low-dose region in RT (<4 Gy) (49). Stray neutron equivalent doses are maintained in the low-dose range; however, care must be taken when considering the region closer to the target, the so-called medium-dose region. For this range of doses, an appropriate risk model should incorporate the induction of DNA mutations, cell survival, cell repair, and repopulation, which occur during fractionated exposures as applied in RT. The model of Schneider based on the concept of organ equivalent dose (OED) and considering fractionation effects has been used as an alternative for risk estimation (53, 54). For example, Geng et al. (55) used the Schneider model for risk estimates in the brain tissue outside the target, resulting in a LAR approximately 0.5% and 3.2% for a 14-year-old male and a 4-year-old female patient, respectively. For the rest of the organs, the BEIR model was used for LAR calculation (some values are represented in **Tables 1, 2**). If we sum the LAR in the non-target brain to the LAR in the rest of the organs, the total risk would be 0.73% and 4.5%, respectively. These figures are consistent with the behavior observed in the sense that a higher value is obtained for the younger and female patient. A limitation of these values is that they did not consider the lung, which has shown to have a high risk. Therefore, this risk estimate should be increased. Unfortunately, as they considered a brain treatment, it is not possible to directly compare their results with those from Zhang and colleagues (52).

Few works evaluated the risk for PBS-PBT (46, 50, 55). Their results showed an expected reduction in risk as a consequence of the reduction in stray radiation. For example, in Athar and Paganetti (50), total risks associated with stray neutrons were, on average, 10 times higher in passive beam in comparison to scanned beam. The average factor was approximately 4.7 when evaluating the whole stray radiation in the patient (55). In addition, Geng et al. (55) compared the effect of adding a

TABLE 1 | LAR in thyroid and lung together with the total LAR for several irradiations in male patients at different ages.

Reference	Treatment	Patient age (years)	Therapeutic dose [Gy (RBE)]	LAR (%)		
				Total	Thyroid	Lung
Zacharatou-Jarlskog and Paganetti (44)	Brain	11	77	0.80	0.19	0.26
Geng et al. (49)	Brain	14	52.2	0.73	0.040	
Athar and Paganetti (46)	Brain	14	54	0.77	0.15	0.14
Zacharatou-Jarlskog and Paganetti (44)	Brain	14	77	0.55	0.15	0.15
Athar and Paganetti (35)	Spine	8	77	1.6	0.024	0.28
Athar and Paganetti (46)	Spine	14	54	1.4	0.020	0.33
Zhang et al. (41)	CSI	4	23.4	25		
Zhang et al. (48)	CSI	4	23.4	30	1	14
Taddei et al. (40)	CSI	10	54*	8.5	0.44	1.6
Zhang et al. (48)	CSI	15	23.4	8	0.2	4.0

*Including boost.

TABLE 2 | LAR in thyroid, lung, and breast together with the total LAR for several irradiations in female patients at different ages.

Reference	Treatment	Patient age (years)	Therapeutic dose [Gy (RBE)]	LAR (%)			
				Total	Thyroid	Lung	Breast
Geng et al. (49)	Brain	4	54	4.5	0.5405		0.519
Zacharatou-Jarlskog and Paganetti (44)	Brain	4	77	5.5	2.2	2.4	5
Athar and Paganetti (46)	Brain	8	54	3.9	1.39	0.39	0.78
Athar and Paganetti (46)	Brain	8	54	0.35	0.18	0.04	0.04
Zacharatou-Jarlskog and Paganetti (44)	Brain	8	77	3	1.5	0.8	1.6
Athar and Paganetti (46)	Spine	8	54	4.2	0.18	1.16	0.68
Athar and Paganetti (46)	Spine	8	54	0.65	0.04	0.16	0.13
Athar and Paganetti (35)	Spine	11	77	3.2	0.221	1.05	0.708
Zhang et al. (48)	CSI	2	23.4	58	4	36	4
Taddei et al. (40)	CSI	9	54*	14.8	1.7	2.79	2.98
Zhang et al. (48)	CSI	16	23.4	11	1	5	2

*Including boost.

patient-specific aperture. Their results showed that the risk increased, on average, by approximately 10% when adding the aperture. Moreover, there was a trend of increasing risk in organs as the distance from the target increases.

COMPARISON WITH PHOTON IRRADIATION

Athar et al. (56) compared the results from Zacharatou-Jarlskog et al. (33) and Athar and Paganetti (37) for brain and CSI treatments to a 6 MV IMRT plan. They found similarities in the behavior of patient scatter and treatment head contribution when increasing the target volume in both modalities. However, while, for proton therapy, the secondary doses decrease with increasing distance to the field edge, IMRT fields show a rise in the absorbed photon doses at large distances due to accelerator head leakage. Consequently, close to the field, organs receive higher secondary neutron equivalent doses from PS-PBT relative to the scattered photon or leakage photon dose in IMRT. Conversely, organs located at larger distances from the field edge receive higher doses in IMRT than those in PS-PBT. They concluded that out-of-field doses from proton treatments seemed to be comparable to scattered doses received from 6 MV IMRT fields. As protons offer a distinct advantage in-field, proton therapy would represent a better option for children. However, as discussed in the previous section, these evaluated irradiations did not represent realistic treatments, at least for spinal fields. Therefore, disagreement could be expected with other works. In fact, Zhang et al. (43) also compared the CSI proton plan with a 6 MV IMRT. They found that for each organ, the equivalent dose was at least 1.5 times higher for photon therapy than for proton therapy. In fact, differences increased in thyroid, bladder, and colon, being a factor up to 28, 18, and 15, respectively. Majer et al. (45) compared a PBS-PBT CSI with 3D conformal RT and VMAT treatments. As photon treatments were planned with energies lower than 10 MeV, the contributions of neutrons could be neglected, and stray photons are the only contributors to out-of-field doses. Their results showed that, in general, total out-of-field equivalent dose

is approximately 1 or 2 orders of magnitude lower for PBS-PBT compared to photon techniques. For lungs and breasts, 3D-CRT and PBS-PBT were comparable.

Comparison between proton and photon treatment can also be found in terms of risk. Athar and Paganetti (50) showed that PS-PBT offers an advantage for organs distant to the target, while closer to the field, the risk due to scattered dose in IMRT seems to be lower. These results were in agreement with those found for equivalent doses. However, comparison of total risk does lead to reduced values in proton therapy. Zhang et al. (52) showed that the CSI using a passive proton beam could reduce the predicted risk by 6 times. Brodin et al. (46) compared the risk in 3D conformal RT, rotational IMRT, and spot-scanned intensity-modulated proton therapy techniques for 10 patients receiving CSI for medulloblastoma. Their results showed that the scanned-beam proton therapy could reduce the risk by a factor of 7 in comparison to the photon techniques.

ANALYTICAL MODELS

As described in previous sections, there are more MC studies in comparison to experimental ones. Some authors have referred to MC simulation as the gold standard. However, one of the disadvantages of simulation is the required time for calculations. Acute models of the geometry may require the use of computational clusters, and even the most simplified model could need several hours in a normal computer. This is the reason for the development over the last decade of several analytical models that allow a comparably quicker way for out-of-field dose calculation. These models enable both *a priori* and *a posteriori* estimations of dose. The former is useful in order to include the out-of-field information in the evaluation of a treatment. The latter is required for dose reconstruction in patient cohorts for epidemiological studies. A relevant contribution to this topic has been performed by Newhauser and co-workers mainly from Texas MD Anderson Cancer Center and Louisiana State University for PS-PBT, based on a detailed MC simulation of the nozzle, the cyclotron, and the treatment bunker (including wall, ceiling, and floor) (28). For brevity, some authors have referred to all this contribution as the

LSU-MDA model. In a recent review, Newhauser et al. (28) performed a revision of these works and other available analytical models for photon and proton therapy. Since then, new extensions of the LSU-MDA model have been performed and tested in children. Gallagher and Taddei (57) adjusted the model to a clinical setting considering field parameters such as aperture size, range modulation, air gap between the treatment unit and patient, and radiation weighting factor. The model was applied to intracranial treatments and tested in two pediatric patients. The adjustment led to neutron dose equivalent estimates within a factor of 2 with the MC result. The Barandan et al. (58) model calculated in- and out-of-field neutron spectra and dose equivalent for pediatric CSI using a passive scattered proton beam, a Mevion S250 system. A double-Gaussian model of equivalent dose per proton absorbed dose using a fitted empirical parameter that apportions the relative dose contributions from high-energy and fast neutrons under reference conditions. Correction parameters related to brass aperture opening, modulation width, and thickness of the range compensator were incorporated. These models mainly consider the external neutrons that are the relevant in PS-PBT. However, PBS-PBT therapy has become the most common treatment in the last few years. Thus, one of the contributions of ANDANTE project (59) was a full parameterization of neutron absorbed dose, dose equivalent, energy quality factors, and RBE by Schneider and collaborators (60, 61). The parameterization was initially done for the Gantry 1 at the Paul Scherrer Institute (PSI), but it can be adapted to any other PBS-PBT facility. Neutron dose was modeled relative to the central axis dose, and three physical processes were considered for its description: dose build-up, inverse-square law, and exponential attenuation in a water phantom. They computed dose equivalent kernels as a function of water equivalent range and radial distance from the central axis of a single pencil beam for the nominal energies used at PSI. Depending on the specific plan, the appropriate kernel is applied at the position of each individual applied proton pencil beam of the field. The model was tested for two pediatric patients treated in PSI, one ependymoma and a cranio-spinal irradiation. The root mean square error between MC simulation and the model was up to 19% and 20% for absorbed dose and dose equivalent, respectively (61). Yeom et al. (62) also introduced a dose calculation method for reconstruction of the out-of-field neutron dose of pediatric patients based on a set of dose voxel kernels generated by MC simulation of proton pencil beams onto a water phantom with a size covering the body size of most pediatric patients. For each beam of a real plan, the dose kernel is matched with the CT of the patient to fix the first voxel irradiated and then rotated according to the direction of the proton beam. The total neutron dose is obtained accumulating the dose map for each beam. The model was tested with intracranial irradiation and CSI cases showing relative differences for most organs less than 30%. The authors highlighted the good performance regarding time, 30 min for the plan with the highest number of proton beams (7725), and regardless of the limitations, for example, the use of water instead of patient tissue with its heterogeneities, consider the model a useful tool for retrospective dose calculations to support epidemiological studies and for implementation into clinical TPS. Finally, an empirical model using a double-Gaussian function that

related the voxel's internal neutron equivalent dose per proton dose as a function of the shortest distance to field edge was developed by Gallagher and Taddei (63). The model was trained and tested using two intracranial pediatric treatments previously simulated. Their results showed that the applicable region of the model is from 3 to 49 cm, being more accurate from 3 to 10 cm, and differences with MC simulations are between 7% and 13%. For higher distances, the model overestimates dose equivalent by a factor between 2 and 3.

CONCLUSIONS

An overview of the studies carried out to evaluate out-of-field doses and second cancer risk in young patients in proton beam therapy has been presented. The most widespread treatments are brain irradiation and CSI. As majority of works focused on passive scattering proton therapy, there is room for research in scanned-beam facilities, and, in general, from an experimental point of view, given that scarce works performed measurements. Based on the overview, neutron equivalent doses can be in the range of up to 1 mSv/Gy (RBE) in brain irradiation and 10 mSv/Gy (RBE) in CSI for PS-PBT. Photon contribution is approximately 10% of these values. For PBS-PBT, lack of data only allows to estimate that neutron equivalent doses decrease by a factor between 2 and 50 compared to passive scattering ones. Predicted risks of second cancer are higher in CSI in comparison to brain treatment, and absolute values are highly dependent on the age and sex of the patient. A wide range of values has been reported from lower than 0.35% up to 58%. These absolute numbers must be taken with caution due to uncertainties in risk models, but they can also be used for comparison between treatment techniques. Results discussed confirmed that proton beam therapy, especially PBS-PBT, leads to lower second cancer risks. Finally, there are some available analytical models for young patients, which can be useful to estimate out-of-field doses for evaluation of plans or to reconstruct dose for epidemiological studies. Differences with MC simulations showed that the estimations could be from 7% up to 50%, depending on the model and region in the patient. Therefore, improvement could be achieved in further investigations.

AUTHOR CONTRIBUTIONS

MR-E and AD contributed to conception and design of the study. MR-E collected the data, performed the analysis, and wrote the first draft of the manuscript. All authors contributed to manuscript revision, read, and approved the submitted version.

FUNDING

This project has received funding from Euratom's research and innovation programme 2019-20 under grant agreement no. 945196.

REFERENCES

- Xu X, Bednarz B, Paganetti H. A Review of Dosimetry Studies on External-Beam Radiation Treatment With Respect to Second Cancer Induction. *Phys Med Biol* (2008) 53:R193–241. doi: 10.1088/0031-9155/53/13/R01
- Trott KR. Special Radiobiological Features of Second Cancer Risk After Particle Radiotherapy. *Phys Med* (2017) 42:221–7. doi: 10.1016/j.ejmp.2017.05.002
- Frankish H. 15 Million New Cancer Cases Per Year by 2020, Says WHO. *Lancet* (2003) 1278. doi: 10.1016/S0140-6736(03)13038-3
- Sung H, Ferlay J, Siegel R, Laversanne M, Soerjomataram I, Jemal A, et al. Global Cancer Statistics 2020: GLOBOCAN Estimates of Incidence and Mortality Worldwide for 36 Cancers in 185 Countries. *CA: A Cancer J Clin* (2021) 71:209–49. doi: 10.3322/caac.21660
- National Cancer Institute. *Cancer Stat Facts: Cancer of Any Site* (2022). Available at: <https://seer.cancer.gov/statfacts/html/all.html> (Accessed February 24, 2022).
- Hälg RA, Besserer J, Schneider U. Systematic Measurements of Whole-Body Imaging Dose Distributions in Image-Guided Radiation Therapy. *Med Phys* (2012) 39:7650–61. doi: 10.1118/1.4758065
- Howell R, Scarboro S, Kry S, Yaldo D. Accuracy of Out-of-Field Dose Calculations by a Commercial Treatment Planning System. *Phys Med Biol* (2010) 55:6999–7008. doi: 10.1088/0031-9155/55/23/S03
- Kry SF, Bednarz B, Howell RM, Dauer L, Followill D, Klein E, et al. AAPM TG 158: Measurement and Calculation of Doses Outside the Treated Volume From External-Beam Radiation Therapy. *Med Phys* (2017) 44:e391–429. doi: 10.1002/mp.12462
- Mazonakis M, Damilakis J. Out-Of-Field Organ Doses and Associated Risk of Cancer Development Following Radiation Therapy With Photons. *Phys Med* (2021) 90:73–82. doi: 10.1016/j.ejmp.2021.09.005
- Hälg R, Schneider U. Neutron Dose and its Measurement in Proton Therapy-Current State of Knowledge. *Brit J Radiol* (2020) 93:20190412. doi: 10.1259/bjr.20190412
- NRC. *Health Risks From Exposure to Low Levels of Ionizing Radiation: BEIR VII—Phase 2*. Washington, DC: National Academies (2006).
- Merchant T. Proton Beam Therapy in Pediatric Oncology. *Cancer J* (2009) 15:298–305. doi: 10.1097/PPO.0b013e3181b6d4b7
- Odei B, Frandsen J, Boothe D, Ermoian R, Poppe M. Patterns of Care in Proton Radiation Therapy for Pediatric Central Nervous System Malignancies. *Int J Radiat Oncol Biol Phys* (2017) 97:60–3. doi: 10.1016/j.ijrobp.2016.09.011
- National Cancer Institute. *Childhood Cancers* (2022). Available at: <https://www.cancer.gov/types/childhood-cancers> (Accessed February 24, 2022).
- National Cancer Institute. *NCCR*Explorer: An Interactive Website for NCCR Cancer Statistics*. Available at: <https://NCCRExplorer.ccdi.cancer.gov/> (Accessed February 24, 2022).
- Huynh M, Marcu L, Giles E, Short M, Matthews D, Bezak E. Are Further Studies Needed to Justify the Use of Proton Therapy for Paediatric Cancers of the Central Nervous System? A Review of Current Evidence. *Radiother Oncol* (2019) 133:140–8. doi: 10.1016/j.radonc.2019.01.009
- Journy N, Indelicato D, Withrow D, Akimoto T, Alapetite C, Araya M, et al. Patterns of Proton Therapy Use in Pediatric Cancer Management in 2016: An International Survey. *Radiother Oncol* (2019) 132:155–61. doi: 10.1016/j.radonc.2018.10.022
- Hess C, Indelicato D, Paulino A, Hartsell W, Hill-Kayser C, Perkins S, et al. An Update From the Pediatric Proton Consortium Registry. *Front Oncol* (2018) 8:165. doi: 10.3389/fonc.2018.00165
- Indelicato D, Bates J, Mailhot Vega R, Rotondo R, Hoppe B, Morris C, et al. Second Tumor Risk in Children Treated With Proton Therapy. *Pediatr Blood Cancer* (2021) 68:e28941. doi: 10.1002/pbc.28941
- Friedman D, Whittin J, Leisenring W, Mertens S, Hammond S, Stovall M, et al. Subsequent Neoplasms in 5-Year Survivors of Childhood Cancer: The Childhood Cancer Survivor Study. *J Natl Cancer Inst* (2010) 102:1083–95. doi: 10.1093/jnci/djq238
- Marcu L, Chau M, Bezak E. How Much Is Too Much? Systematic Review of Cumulative Doses From Radiological Imaging and the Risk of Cancer in Children and Young Adults. *Crit Rev Oncol Hematol* (2021) 160:103292. doi: 10.1016/j.critrevonc.2021.103292
- Durante M, Paganetti H. Nuclear Physics in Particle Therapy: A Review. *Rep Prog Phys* (2016) 79:096702. doi: 10.1088/0034-4885/79/9/096702
- Kraan AC. Range Verification Methods in Particle Therapy: Underlying Physics and Monte Carlo Modeling. *Front Oncol* (2015) 5:150. doi: 10.3389/fonc.2015.00150
- Gottschalk B, Cascio EW, Daartz J, Wagner MS. On the Nuclear Halo of a Proton Pencil Beam Stopping in Water. *Phys Med Biol* (2015) 60:5627. doi: 10.1088/0031-9155/60/14/5627
- Pérez-Andújar A, Newhauser W, Deluca P. Neutron Production From Beam-Modifying Devices in a Modern Double Scattering Proton Therapy Beam Delivery System. *Phys Med Biol* (2009) 54:993–1008. doi: 10.1088/0031-9155/54/4/012
- Moyers M, Benton E, Ghebremedhin A, Coutrakon G. Leakage and Scatter Radiation From a Double Scattering Based Proton Beamline. *Med Phys* (2008) 35:128–44. doi: 10.1118/1.2805086
- Leroy R. *Hadron Therapy in Children - an Update of the Scientific Evidence for 15 Paediatric Cancers*. Brussels: Belgian Health Care Knowledge Centre (2015).
- Newhauser W, Schneider C, Wilson L, Shrestha S, Donahue W. A Review of Analytical Models of Stray Radiation Exposures From Photon- and Proton-Beam Radiotherapies. *Rad Prot Dosim* (2018) 180:245–51. doi: 10.1093/rpd/ncx245
- ICRP. *The 2007 Recommendations of the International Commission on Radiological Protection*. Publication 103. Ann. ICRP. Netherlands: Elsevier (2007).
- Bonfrate A, Farah J, De Marzi L, Delacroix S, Hérault J, Sayah R, et al. Influence of Beam Incidence and Irradiation Parameters on Stray Neutron Doses to Healthy Organs of Pediatric Patients Treated for an Intracranial Tumor With Passive Scattering Proton Therapy. *Phys Med* (2016) 32:590–9. doi: 10.1016/j.ejmp.2016.03.009
- Matsumoto S, Koba Y, Kohno R, Lee C, Bolch W, Kai M. Secondary Neutron Doses to Pediatric Patients During Intracranial Proton Therapy: Monte Carlo Simulation of the Neutron Energy Spectrum and its Organ Doses. *Health Phys* (2016) 110:380–6. doi: 10.1097/HP.0000000000000461
- Mojszeszek N, Farah J, Kłodowska M, Ploc O, Stolarczyk L, Waligórski M, et al. Measurement of Stray Neutron Doses Inside the Treatment Room From a Proton Pencil Beam Scanning System. *Phys Med* (2017) 34:80–4. doi: 10.1016/j.ejmp.2017.01.013
- Zacharatou-Jarlskog C, Lee C, Bolch W, Xu X, Paganetti H. Assessment of Organ-Specific Neutron Equivalent Doses in Proton Therapy Using Computational Whole-Body Age-Dependent Voxel Phantoms. *Phys Med Biol* (2008) 53:693–717. doi: 10.1088/0031-9155/53/3/012
- Sayah R, Farah J, Donadille L, Hérault J, Delacroix S, De Marzi L, et al. Secondary Neutron Doses Received by Paediatric Patients During Intracranial Proton Therapy Treatments. *J Radiol Prot* (2014) 34:279–86. doi: 10.1088/0952-4746/34/2/279
- Lee C, Lodwick D, Hurtado J, Pafundi D, Williams J, Bolch W. The UF Family of Reference Hybrid Phantoms for Computational Radiation Dosimetry. *Phys Med Biol* (2010) 55:339–63. doi: 10.1088/0031-9155/55/2/002
- Ardenfors O, Gudowska I, Flejmer A, Dasu A. Impact of Irradiation Setup in Proton Spot Scanning Brain Therapy on Organ Doses From Secondary Radiation. *Radiat Prot Dosim* (2018) 180:261–6. doi: 10.1093/rpd/ncy013
- Athar B, Paganetti H. Neutron Equivalent Doses and Associated Lifetime Cancer Incidence Risks for Head & Neck and Spinal Proton Therapy. *Phys Med Biol* (2009) 54:4907–26. doi: 10.1088/0031-9155/54/16/005
- Knežević Z, Ambrozova I, Domingo C, De Saint-Hubert M, Majer M, Martínez-Rovira I, et al. Comparison of Response of Passive Dosimetry Systems in Scanning Proton Radiotherapy-A Study Using Paediatric Anthropomorphic Phantoms. *Radiat Prot Dosim* (2018) 180:256–60. doi: 10.1093/rpd/ncx254
- Wochnik A, Stolarczyk L, Ambrožová I, Davidková M, De Saint-Hubert M, Domanski S, et al. Out-Of-Field Doses for Scanning Proton Radiotherapy of Shallowly Located Paediatric Tumours—A Comparison of Range Shifter and 3D Printed Compensator. *Phys Med Biol* (2021) 66:035012. doi: 10.1088/1361-6560/abcb1f
- Taddei P, Mirkovic D, Fontenot J, Giebler A, Zheng Y, Kornguth D, et al. Stray Radiation Dose and Second Cancer Risk for a Pediatric Patient Receiving Craniospinal Irradiation With Proton Beams. *Phys Med Biol* (2009) 54:2259–75. doi: 10.1088/0031-9155/54/8/001

41. Taddei P, Mirkovic D, Fontenot J, Giebler A, Zheng Y, Titt U, et al. Reducing Stray Radiation Dose for a Pediatric Patient Receiving Proton Craniospinal Irradiation. *Nuc Tech* (2009) 168:108–12. doi: 10.1318/NT09-A9108
42. Taddei P, Mahajan A, Mirkovic D, Zhang R, Giebler A, Kornguth D, et al. Predicted Risks of Second Malignant Neoplasm Incidence and Mortality Due to Secondary Neutrons in a Girl and Boy Receiving Proton Craniospinal Irradiation. *Phys Med Biol* (2010) 55:7067–80. doi: 10.1088/0031-9155/55/23/S08
43. Zhang R, Howell R, Giebler A, Taddei P, Mahajan A, Newhauser W. Comparison of Risk of Radiogenic Second Cancer Following Photon and Proton Craniospinal Irradiation for a Pediatric Medulloblastoma Patient. *Phys Med Biol* (2013) 58:807–23. doi: 10.1088/0031-9155/58/4/807
44. Newhauser W, Fontenot J, Mahajan A, Kornguth D, Stovall M, Zheng Y, et al. The Risk of Developing a Second Cancer After Receiving Craniospinal Proton Irradiation. *Phys Med Biol* (2009) 54:2277–91. doi: 10.1088/0031-9155/54/8/002
45. Majer M, Ambrožová I, Davidková M, De Saint-Hubert M, Kasabašić M, Knežević Ž, et al. Out-Of-Field Doses in Pediatric Craniospinal Irradiations With 3D-CRT, VMAT, and Scanning Proton Radiotherapy: A Phantom Study. *Med Phys* (2022) 49:2672–83. doi: 10.1002/mp.15493
46. Brodin N, Rosenschöld P, Aznar M, Kiil-Berthelsen A, Vogelius I, Nilsson P, et al. Radiobiological Risk Estimates of Adverse Events and Secondary Cancer for Proton and Photon Radiation Therapy of Pediatric Medulloblastoma. *Acta Oncol* (2011) 50:806–16. doi: 10.3109/0284186X.2011.582514
47. Zacharatou-Jarlskog C, Paganetti H. Risk of Developing Second Cancer From Neutron Dose in Proton Therapy as Function of Field Characteristics, Organ, and Patient Age. *Int J Radiat Oncol Biol Phys* (2008) 72:228–35. doi: 10.1016/j.ijrobp.2008.04.069
48. Armstrong G, Sklar C, Hudson M, Robison L. Long-Term Health Status Among Survivors of Childhood Cancer: Does Sex Matter? *J Clin Oncol* (2007) 25:4477–89. doi: 10.1200/JCO.2007.11.2003
49. Sánchez-Nieto B, Romero-Expósito M, Terrón J, Sánchez-Doblado F. Uncomplicated and Cancer-Free Control Probability (UCFCP): A New Integral Approach to Treatment Plan Optimization in Photon Radiation Therapy. *Phys Med* (2017) 42:277–84. doi: 10.1016/j.ejmp.2017.03.025
50. Athar B, Paganetti H. Comparison of Second Cancer Risk Due to Out-of-Field Doses From 6-MV IMRT and Proton Therapy Based on 6 Pediatric Patient Treatment Plans. *Radiother Oncol* (2011) 98:87–92. doi: 10.1016/j.radonc.2010.11.003
51. Romero-Expósito M, Sánchez-Nieto B, Terrón JA, Lopes MC, Ferreira BC, Grishchuk D. Commissioning the Neutron Production of a Linac: Development of a Simple Tool for Second Cancer Risk Estimation. *Med Phys* (2015) 42:276–81. doi: 10.1118/1.4903525
52. Zhang R, Howell R, Taddei P, Giebler A, Mahajan A, Newhauser W. A Comparative Study on the Risks of Radiogenic Second Cancers and Cardiac Mortality in a Set of Pediatric Medulloblastoma Patients Treated With Photon or Proton Craniospinal Irradiation. *Radiother Oncol* (2014) 113:84–8. doi: 10.1016/j.radonc.2014.07.003
53. Schneider U, Zwahlen D, Ross D, Kaser-Hotz B. Estimation of Radiation-Induced Cancer From Three-Dimensional Dose Distributions: Concept of Organ Equivalent Dose. *Int J Rad Oncol Biol Phys* (2005) 61:1510–5. doi: 10.1016/j.ijrobp.2004.12.040
54. Schneider U, Sumila M, Robotka J. Site-Specific Dose-Response Relationships for Cancer Induction From the Combined Japanese A-Bomb and Hodgkin Cohorts for Doses Relevant to Radiotherapy. *Theor Biol Med Model* (2011) 8:27. doi: 10.1186/1742-4682-8-27
55. Geng C, Moteabbed M, Xie Y, Schuemann J, Yock T, Paganetti H. Assessing the Radiation-Induced Second Cancer Risk in Proton Therapy for Pediatric Brain Tumors: The Impact of Employing a Patient-Specific Aperture in Pencil Beam Scanning. *Phys Med Biol* (2016) 61:12–22. doi: 10.1088/0031-9155/61/1/12
56. Athar B, Bednarz B, Seco J, Hancox C, Paganetti H. Comparison of Out-of-Field Photon Doses in 6 MV IMRT and Neutron Doses in Proton Therapy for Adult and Pediatric Patients. *Phys Med Biol* (2010) 55:2879–91. doi: 10.1088/0031-9155/55/10/006
57. Gallagher K, Taddei P. Independent Application of an Analytical Model for Secondary Neutron Equivalent Dose Produced in a Passive-Scattering Proton Therapy Treatment Unit. *Phys Med Biol* (2018) 63:15NT04. doi: 10.1088/1361-6560/aad1bc
58. Baradaran-Ghahfarokhi M, Reynoso F, Sun B, Darafsheh A, Prusator M, Mutic S, et al. A Monte Carlo-Based Analytic Model of Neutron Dose Equivalent for a Mevion Gantry-Mounted Passively Scattered Proton System for Craniospinal Irradiation. *Med Phys* (2020) 47:4509–21. doi: 10.1002/mp.14299
59. Ottolenghi A, Baiocco G, Smyth V, Trott K. Andante Consortium. The Andante Project: A Multidisciplinary Approach to Neutron RBE. *Radiat Prot Dosim* (2015) 166:311–5. doi: 10.1093/rpd/ncv158
60. Schneider U, Hälgl RA, Baiocco G, Lomax T. Neutrons in Proton Pencil Beam Scanning: Parameterization of Energy, Quality Factors and RBE. *Phys Med Biol* (2016) 61:6231. doi: 10.1088/0031-9155/61/16/6231
61. Schneider U, Hälgl RA, Lomax T. Neutrons in Active Proton Therapy: Parameterization of Dose and Dose Equivalent. *Z Med Phys* (2017) 27:113–23. doi: 10.1016/j.zemedi.2016.07.001
62. Yeom YS, Griffin K, Mille M, Jung JW, Lee C, Lee C. A Dose Voxel Kernel Method for Rapid Reconstruction of Out-of-Field Neutron Dose of Patients in Pencil Beam Scanning (PBS) Proton Therapy. *Phys Med Biol* (2020) 65:175015. doi: 10.1088/1361-6560/abaa5f
63. Gallagher K, Taddei P. Analytical Model to Estimate Equivalent Dose From Internal Neutrons in Proton Therapy of Children With Intracranial Tumors. *Rad Prot Dosim* (2019) 183:460–8. doi: 10.1093/rpd/ncy166

Conflict of Interest: The authors declare that the research was conducted in the absence of any commercial or financial relationships that could be construed as a potential conflict of interest.

Publisher's Note: All claims expressed in this article are solely those of the authors and do not necessarily represent those of their affiliated organizations, or those of the publisher, the editors and the reviewers. Any product that may be evaluated in this article, or claim that may be made by its manufacturer, is not guaranteed or endorsed by the publisher.

Copyright © 2022 Romero-Expósito, Toma-Dasu and Dasu. This is an open-access article distributed under the terms of the Creative Commons Attribution License (CC BY). The use, distribution or reproduction in other forums is permitted, provided the original author(s) and the copyright owner(s) are credited and that the original publication in this journal is cited, in accordance with accepted academic practice. No use, distribution or reproduction is permitted which does not comply with these terms.



Validation of a Monte Carlo Framework for Out-of-Field Dose Calculations in Proton Therapy

Marijke De Saint-Hubert^{1†}, Nico Verbeek^{2,3,4†}, Christian Bäumer^{2,3,5,6}, Johannes Esser^{2,3,7}, Jörg Wulff^{2,3}, Racell Nabha¹, Olivier Van Hoey¹, Jérémie Dabin¹, Florian Stuckmann^{2,7,8}, Fabiano Vasi⁹, Stephan Radonic⁹, Guillaume Boissonnat¹⁰, Uwe Schneider⁹, Miguel Rodriguez^{11,12}, Beate Timmermann^{2,3,4,5,13}, Isabelle Thierry-Chef^{14,15,16} and Lorenzo Brualla^{2,3,4*}

OPEN ACCESS

Edited by:

Beatriz Sanchez-Nieto,
Pontifical Catholic University of Chile,
Chile

Reviewed by:

Silva Bortolussi,
University of Pavia, Italy
Francesco Tommasino,
University of Trento, Italy

*Correspondence:

Lorenzo Brualla
Lorenzo.Brualla@uni-due.de

[†]These authors have contributed
equally to this work and share
first authorship

Specialty section:

This article was submitted to
Radiation Oncology,
a section of the journal
Frontiers in Oncology

Received: 23 February 2022

Accepted: 04 May 2022

Published: 08 June 2022

Citation:

De Saint-Hubert M, Verbeek N, Bäumer C, Esser J, Wulff J, Nabha R, Van Hoey O, Dabin J, Stuckmann F, Vasi F, Radonic S, Boissonnat G, Schneider U, Rodriguez M, Timmermann B, Thierry-Chef I and Brualla L (2022) Validation of a Monte Carlo Framework for Out-of-Field Dose Calculations in Proton Therapy. *Front. Oncol.* 12:882489. doi: 10.3389/fonc.2022.882489

¹ Research in Dosimetric Applications, Belgian Nuclear Research Center (SCK CEN), Mol, Belgium, ² West German Proton Therapy Centre Essen WPE, Essen, Germany, ³ West German Cancer Center (WTZ), Essen, Germany, ⁴ Faculty of Medicine, University of Duisburg-Essen, Essen, Germany, ⁵ Radiation Oncology and Imaging, German Cancer Consortium DKTK, Heidelberg, Germany, ⁶ Department of Physics, TU Dortmund University, Dortmund, Germany, ⁷ Faculty of Mathematics and Science Institute of Physics and Medical Physics, Heinrich-Heine University, Düsseldorf, Germany, ⁸ Klinikum Fulda GAG, Universitätsmedizin Marburg, Fulda, Zurich, Germany, ⁹ Physik Institut, Universität Zürich, Zürich, Switzerland, ¹⁰ CEA, Université Paris-Saclay, Palaiseau, France, ¹¹ Hospital Paitilla, Panama City, Panama, ¹² Instituto de Investigaciones Científicas y de Alta Tecnología INDICASAT-AIP, Panama City, Panama, ¹³ Department of Particle Therapy, University Hospital Essen, Essen, Germany, ¹⁴ Radiation Programme, Barcelona Institute for Global Health (ISGlobal), Barcelona, Spain, ¹⁵ University Pompeu Fabra, Barcelona, Spain, ¹⁶ CIBER Epidemiología y Salud Pública, Madrid, Spain

Proton therapy enables to deliver highly conformed dose distributions owing to the characteristic Bragg peak and the finite range of protons. However, during proton therapy, secondary neutrons are created, which can travel long distances and deposit dose in out-of-field volumes. This out-of-field absorbed dose needs to be considered for radiation-induced secondary cancers, which are particularly relevant in the case of pediatric treatments. Unfortunately, no method exists in clinics for the computation of the out-of-field dose distributions in proton therapy. To help overcome this limitation, a computational tool has been developed based on the Monte Carlo code TOPAS. The purpose of this work is to evaluate the accuracy of this tool in comparison to experimental data obtained from an anthropomorphic phantom irradiation. An anthropomorphic phantom of a 5-year-old child (ATOM, CIRS) was irradiated for a brain tumor treatment in an IBA Proteus Plus facility using a pencil beam dedicated nozzle. The treatment consisted of three pencil beam scanning fields employing a lucite range shifter. Proton energies ranged from 100 to 165 MeV. A median dose of 50.4 Gy(RBE) with 1.8 Gy(RBE) per fraction was prescribed to the initial planning target volume (PTV), which was located in the cerebellum. Thermoluminescent detectors (TLDs), namely, Li-7-enriched LiF : Mg, Ti (MTS-7) type, were used to detect gamma radiation, which is produced by nuclear reactions, and secondary as well as recoil protons created out-of-field by secondary neutrons. Li-6-enriched LiF : Mg,Cu,P (MCP-6) was combined with Li-7-enriched MCP-7 to measure thermal neutrons. TLDs were calibrated in Co-60 and reported on absorbed dose in water per target dose ($\mu\text{Gy/Gy}$) as well as thermal neutron dose equivalent per

target dose ($\mu\text{Sv}/\text{Gy}$). Additionally, bubble detectors for personal neutron dosimetry (BD-PND) were used for measuring neutrons (>50 keV), which were calibrated in a Cf-252 neutron beam to report on neutron dose equivalent dose data. The Monte Carlo code TOPAS (version 3.6) was run using a phase-space file containing 10^{10} histories reaching an average standard statistical uncertainty of less than 0.2% (coverage factor $k = 1$) on all voxels scoring more than 50% of the maximum dose. The primary beam was modeled following a Fermi–Eyges description of the spot envelope fitted to measurements. For the Monte Carlo simulation, the chemical composition of the tissues represented in ATOM was employed. The dose was tallied as dose-to-water, and data were normalized to the target dose (physical dose) to report on absorbed doses per target dose (mSv/Gy) or neutron dose equivalent per target dose ($\mu\text{Sv}/\text{Gy}$), while also an estimate of the total organ dose was provided for a target dose of 50.4 Gy(RBE). Out-of-field doses showed absorbed doses that were 5 to 6 orders of magnitude lower than the target dose. The discrepancy between TLD data and the corresponding scored values in the Monte Carlo calculations involving proton and gamma contributions was on average 18%. The comparison between the neutron equivalent doses between the Monte Carlo simulation and the measured neutron doses was on average 8%. Organ dose calculations revealed the highest dose for the thyroid, which was 120 mSv, while other organ doses ranged from 18 mSv in the lungs to 0.6 mSv in the testes. The proposed computational method for routine calculation of the out-of-the-field dose in proton therapy produces results that are compatible with the experimental data and allow to calculate out-of-field organ doses during proton therapy.

Keywords: proton therapy, anthropomorphic pediatric phantom, Monte Carlo simulation, out-of-field dosimetry, TLD, bubble detector

1 INTRODUCTION

Proton therapy (PT) enables to deliver highly conformed dose distributions owing to the characteristic Bragg peak and the finite range of protons. Nevertheless, PT is unavoidably accompanied by the production of secondary high-energy neutrons in the patient and structural materials of the beamline (1). Neutrons are of particular concern, as they are capable of traveling large distances to deposit out-of-field doses in organs located far from the primary treatment field and with a relatively high biological effectiveness (2). Furthermore, non-elastic nuclear reactions will also produce secondary protons, heavier ions, and gammas. As a result, the out-of-field radiation field in PT comprises a mixed field of radiation (including photons, neutrons, protons, and other charged particles) all with different potentials to induce biological damage. Moreover, the out-of-field radiation field, and hence the secondary dose delivered to healthy tissues, largely varies with position (close to field versus far) and depends on specific treatment parameters such as patient size and positioning, beam angles, proton energies, field size, modulation width, presence of range shifters (RSs), and the use of apertures.

The development of a validated Monte Carlo (MC) framework forms an important aspect in the assessment and characterization of out-of-field doses in PT. Nevertheless, the use of general-purpose MC simulations in out-of-field dosimetry is

often restricted to detector calibration, and it has highlighted important differences between MC codes and models (3). Moreover, the coupling of MC to advanced measurement and proper benchmarking of the MC codes and models are still unknown today. Once validated, MC simulations will allow to fully describe the out-of-field radiation field and foster accurate calculations of appropriate dosimetric quantities needed for the assessment of radiation damage and risks.

Out-of-field dosimetry is especially important for the radiation protection of children who might develop radiation-induced second primary tumors during their lifetime. Nowadays, the challenge for clinicians is to increase the survival rate while treating with fewer secondary effects. There is a critical need to understand the long-term health and quality of life (QoL) challenges in these populations and to assess the potential health effects of the treatment modalities to improve the survival and health of the patients.

Some medical physicists are cautious that the existing knowledge and understanding of the out-of-field doses and associated risk of inducing secondary malignant neoplasms (SMNs) is not sufficiently mature to justify the use of modern techniques, such as PT, for treating children or pregnant women (4). Therefore, a full characterization of the out-of-field doses, particularly at the PT field edge, requires special attention for the radiation protection and prevention of SMNs (5).

This study aims to set up and optimize a computational MC framework for out-of-field dosimetry in PT, through validation measurements with advanced dosimetry techniques. The study herein presented has been conducted in the framework of a European Horizon 2020 project, HARMONIC, which is addressed at improving the knowledge of the health effects of medical exposure during childhood. A central task within HARMONIC is to set up a cohort of pediatric patients treated with modern radiotherapy, including the computation of whole-body doses. Ultimately, the goal is to estimate the risk of late health effects (including the risk of second primary cancers) after pediatric radiotherapy exposures, which relies on organ dose estimation obtained from validated tools.

2 MATERIAL AND METHODS

2.1 Experimental Setup

For this study, an anthropomorphic phantom (ATOM, Computerized Imaging Reference Systems (CIRS), Inc., Norfolk, VA, USA) representing a 5-year-old child (type 705D) was used. The phantom consists of tissue equivalent (TE) materials, and 180 dosimeters can be inserted in different organ positions. For the insertion of bubble detectors, six tissue slabs were replaced by polymethyl methacrylate (PMMA) slabs manufactured at SCK CEN with dedicated inserts for this type of detector (see **Figure 1**).

Aiming to simulate a realistic proton treatment of a brain tumor, a clinically applied treatment plan was transferred to the conditions of the experiment. The corresponding patient should feature a cranial size and shape with a reasonable resemblance to the corresponding features of the anthropomorphic phantom. A 7-year-old female patient was selected with a diffuse midline glioma (WHO grade IV). The patient received combined radiotherapy and chemotherapy after R3 resection. A median dose of 50.4 Gy(RBE) with 1.8 Gy(RBE) per fraction was prescribed to the initial planning target volume (PTV), which

was located in the cerebellum and had a volume of 195.2 cm³. The treatment plan consisted of two ipsilateral oblique fields and a contralateral oblique field. The proton fields were delivered in a gantry room in pencil beam scanning (PBS) delivery mode employing a lucite RS with a physical thickness of 4.44 cm and a water-equivalent thickness of 5.14 cm. The concerned patient was enrolled in the prospective registry study “KiProReg” (German Clinical Trials Register: DRKS-ID: DRKS00005363) after consent from her legal guardians was obtained. This study was approved by the local ethics committee.

The treatment planning of the phantom case was conducted in the treatment planning system (TPS) RayStation (version 7, RaySearch Laboratories, Stockholm, Sweden). The X-ray CT image set was contoured in the following way: the boundaries between dissimilar TE material types were delineated; then the mass density of the volumes of the individual TE materials was overwritten with the values from the datasheet of the phantom. Furthermore, the volumes containing the thermoluminescent detector (TLD) inserts were contoured. A deformable image registration (6) was established between the clinical CT and the anthropomorphic phantom. Then the contours of the target volume and organs at risk (OARs) were mapped to the CT of the phantom. After that, the contour of the PTV was fine-tuned by alignment to the boundaries between brain substitute tissue and bone substitute tissue. The proton kinetic energies of the fields ranged from 100 to 165 MeV. The air gap between the RS and phantom surface was on average 11.0 cm regarding the minimum distance and an average of 14.6 cm regarding the distance on the central axis. The dose distribution was calculated with the MC-based dose engine (version 4.1) of RayStation. The objectives of the spot fluence optimization were similar to those of the clinical plan concerning, i.e., the right cochlea, the brainstem, and the PTV.

The delivered dose in the experiments was adjusted to the sensitivity and location of the corresponding detectors. The phantom irradiation plans for TLD measurements applied 100.8 Gy(RBE) to the PTV in a single fraction. For bubble

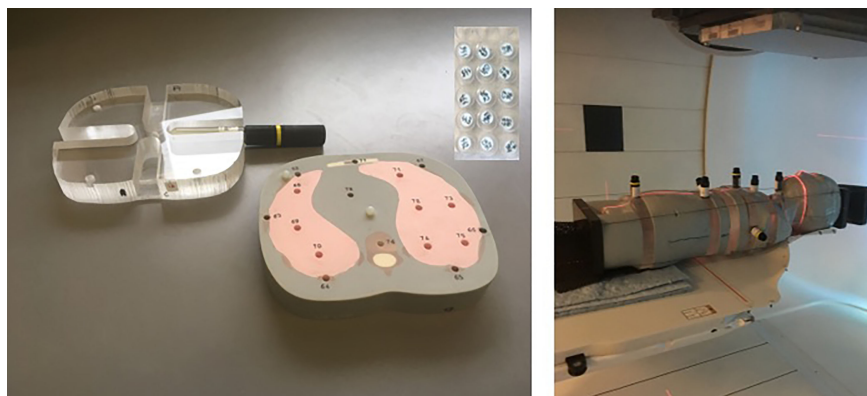


FIGURE 1 | Pictures of the experimental setup. On the left are the slabs of the anthropomorphic phantom for insertion of TLDs including one of the designed PMMA slabs for BD-PNDs. On the right is the mounted 5-year-old anthropomorphic phantom (loaded with BD-PNDs) positioned in the gantry room for PT pencil beam scanning. TLDs, thermoluminescent detectors; PMMA, polymethyl methacrylate; BD-PNDs, bubble detectors for personal neutron dosimetry; PT, proton therapy.

detectors, the delivered dose to the PTV ranged between 0.5 Gy (RBE) for close-to-field measurements and 6 Gy(RBE) for far out-of-field positions. Large changes in the dose level by modification of the overall number of monitor units (MU) are impossible in PBS because the allowed MU per beamlet ("spot") is subject to machine limitations. Thus, dedicated optimizations of the spot fluence were conducted per targeted dose level. This also included an adaptation of the spot spacing. As a result, the shape of the corresponding dose distributions was not exactly identical. This concerns, however, only the high dose region, which was not the subject of the current study.

The experiments were conducted in the West German Proton Therapy Centre Essen (WPE), which is based on the ProteusPlus proton machine (IBA PT, Louvain-La-Neuve, Belgium). Protons were accelerated in an isochronous cyclotron and subsequently slowed down in the energy selection system to adapt to the required range in the phantom. The protons were guided to a gantry-mounted, evacuated nozzle, which operated in a spot-by-spot type PBS delivery mode. The RS was mounted in a snout holder, which could be moved along the central beam axis with a linear translation stage. The cranial part of the phantom was put on a BoS Headframe (Qfix, Avondale, PA, USA), which in turn was attached to a short Patlog table (IBA PT, Schwarzenbruck, Germany). The phantom was aligned prior to the mock treatment with the lasers of the positioning system. The uncertainty was about ± 2 mm. Although it could have been reduced with the X-ray-based verification system, this was not done to avoid a contribution of X-rays to the detector signal.

2.2 Dosimetry Systems

2.2.1 Thermoluminescent Detectors

TLDs, produced by IFJ-PAN (Krakow, Poland), are small cylindrical chips with a diameter of 4.5 mm and a height of 0.9 mm. Detectors of Li-7-enriched LiF : Mg, Ti (MTS-7) type were used. During PBS therapy, MTS-7 mainly detects gamma radiation, which is produced by nuclear reactions, and primary or secondary as well as recoil protons created out-of-field by neutrons. MTS-7 sensitivity to neutrons is very limited. However, Li-6-enriched LiF : Mg,Cu,P (MCP-6) detectors are very sensitive to thermal neutrons due to their high ${}^6\text{Li}(n,\alpha){}^3\text{H}$ cross section for thermal neutrons. MCP-6 was used in combination with Li-7-enriched MCP-7 to quantify thermal neutrons.

TLD detectors were read in a Thermo Scientific Harshaw 5500 reader following a preheat for 30 min at 120°C to avoid the effects of signal fading and low-temperature anomalies in the glow curves (Parisi 2018). A heating rate of 10°C/s was used to heat up TLDs up to 340°C for MTS type and up to 255°C for MCP type.

TLDs were calibrated with a Co-60 source in terms of kerma "free in air" (K_{air}), which was then converted to absorbed dose to water (D_{W}) using conversion factor $D_{\text{W}}/K_{\text{air}} = 1.12$ determined by the ratio of the mass energy absorption coefficient for water to air for the energy of Co-60 (7). MTS-7 data were expressed in absorbed dose in water per target dose (physical) [$\mu\text{Gy}/\text{Gy}$]. To quantify the thermal neutron dose, the data from MCP-7 were subtracted from MCP-6. Next, we applied K_{air} to neutron dose equivalent conversion coefficients for thermal neutrons ($1.24 \times$

10^{-02} mSv/mGy), as described in (8). However, it should be noted that this conversion coefficient has been reported to have an uncertainty of up to a factor 2, which is related to the uncertainties on energy and angular distribution of neutrons as well as on the light collection of the TLD reader (8). Finally, data were expressed as thermal neutron dose equivalent data (μSv), which were normalized to the physical target dose (Gy) and expressed as [$\mu\text{Sv}/\text{Gy}$]. The estimated uncertainty was 100% (8).

Uncertainties on the out-of-field absorbed dose were assessed considering dosimeter reproducibility (1.8%), batch reproducibility (1.9%), Co-60 calibration uncertainty (2.4%) (9), and background uncertainties, which were dependent on the measured dose and reached up to 11% (coverage factor $k = 1$) for the farthest positions. For the energy response of MTS-7 detectors, the energy dependence for both photons (10) and protons (11) was considered. For the energy dependence of photons, a characteristic spectrum was used in the study of (12). Photon energies ranged between 30 keV and 10 MeV. Assuming a flat energy dependence above 1 MeV (10, 13), the calculated uncertainty was below 1% ($k = 1$). For the proton energy dependence, a uniform distribution over the proton energies was assumed for energies up to the maximum proton energy used in this study (165 MeV). This resulted in an uncertainty on the proton energy response of 5% ($k = 1$).

2.2.2 Bubble Detectors

Bubble detectors for personal neutron dosimetry (BD-PNDs) (Bubble Technology Industries, BTI, Chalk River, ON, Canada) were used to measure neutrons of energies above 50 keV. These cylindrical detectors are 15 cm in length and 2 cm in diameter, but the sensitive part, where bubbles are created, is only 7 cm in length and 1.6 cm in diameter (see **Figure 1**). BD-PNDs were calibrated with a Cf-252 source to obtain neutron dose equivalent by applying fluence-to-dose equivalent conversion factors derived from kerma factors $k(E)$ and a quality factor as a function of neutron energy ($Q(E)$) for ICRU tissue, as described previously (14). The final data were expressed in neutron dose equivalent per target dose (physical) [$\mu\text{Sv}/\text{Gy}$]. Uncertainties of BD-PNDs are estimated to be on average 20% ($k = 1$).

2.3 Monte Carlo Framework

The well-established Geant4 (15–17) wrap-up MC code TOPAS v3.6 (Geant4) (18), in conjunction with the Matlab (The Mathworks, Inc., Natick, MA, USA)-based matRad v2.10.1 (19) project to create a DICOM-based dose verification system, was used to simulate the out-of-field absorbed dose distribution. For this purpose, matRad was extended by including the possibility to process DICOM RTIon files. With this feature, it was then possible to create the TOPAS input files with the treatment room-specific radiation parameters employing matRad as the TOPAS syntax parser. The simulations for the determination of the neutron equivalent dose at a point and the proton and gamma out-of-field dose could then be conducted.

2.3.1 Beam Model

To simulate the anthropomorphic phantom irradiation, it was necessary to run TOPAS simulations that reproduce the

commissioned beam. Mean energy and spread have been adjusted to reproduce the measured depth dose curves following the methods of (20, 21), and (22) in 5 MeV steps from the lowest energy available (that is, 100.0 MeV) up to the highest energy available (that is, 226.7 MeV). The commissioned beam data for the corresponding reference values were yielded by measurements with the plane parallel Bragg peak chamber (PTW, Freiburg, Germany) (23). Simulated and measured depth doses agreed within ± 0.01 cm at R_{80} . In addition, the Fermi-Eyges parameters from the beam model implemented in RayStation were used to fully characterize the proton pencil beam.

Furthermore, an MU/ion calibration was performed to determine the number of protons in TOPAS corresponding to the respective MUs. For this purpose, reference fields, consisting of 1,681 spots with 0.25-cm spacing arranged in a symmetrical square around the isocenter, were simulated with 5×10^5 protons per spot for the 27 different energies that make up the beam parameter database. The protons started 50 cm upstream of the isocenter at the nozzle exit of the treatment head. The Fermi-Eyges parameters were back-projected in vacuum to the nozzle exit (24–26). The method of (27) was applied to obtain the spot positions of the protons, taking into account the deflection of the protons at the two foci from the scanning magnets of the pencil beam dedicated nozzle. Downstream, a water tank with a volume of $50 \times 50 \times 50$ cm³ was created. The isocenter was at 3-cm depth of the water tank. Simulation conditions thereby correspond to the conditions for beam-monitor calibration at the WPE, generally following reference dosimetry according to TRS 398 and DIN 6801-1 (28, 29). In the simulations, a cylindrical tally with a diameter of 1 cm and a thickness of 0.5 cm was then placed at the isocenter. The following physics models were employed (30): *g4em-standard_opt4*, *g4h-phy_QGSP_BIC_HP*, *g4decay*, *g4ion-binarycascade*, *g4h-elastic_HP*, and *g4stopping*. In accordance with (31), the mean excitation energy of G4 water was set to 78 eV. The density was set to 1 g/cm³. The overall allowed maximum step size for the condensed history algorithm in TOPAS was set to 0.1 cm. The production cut for all secondary particles was set to 0.05 cm. No variance-reduction techniques were employed. These simulations reached a standard statistical uncertainty of less than 0.6%.

The MU/ion calibration was then performed employing the simulation result of the tally in dose [Gy/MU] and using the dose meter set in [Gy(RBE)/MU]. The calibration yielded was then added to the beam parameter database so that the treatment room-specific machine parameter file included 27 mean energies, energy spreads, Fermi-Eyges parameters, and the number of protons per single MU.

2.3.2 RT Integration in TOPAS

The matRad code was extended to read DICOM RTIon files including both RT Plan and RT Struct. The RS used was considered in the matRad configuration files with the 4.44-cm-thick material lucite comprising a mean excitation energy of 74.0 eV, a density of 1.19 g/cm³, and material composition of 8.05% H, 59.98% C, and 31.96% O, corresponding to the material definition as included in the PSTAR database given by the

National Institute of Standards and Technology (NIST). Since RayStation specifies spot positions at the isocenter, these were back-calculated analogously to the procedure for MU/ion calibration. Based on the machine parameter file, the required beam data were linearly interpolated starting from the energies given by the RayStation RT Plan file for the individual energy layers. The DICOM CT images were incorporated into TOPAS using the *TSImageCube* function. The device and scan protocol-specific density corrections were applied, as well as the full Schneider model comprising 25 different stoichiometric tissues (32). The grid size of the inserted CT was in accordance with the one employed in RayStation, that is, $0.2 \times 0.2 \times 0.2$ cm³.

The matRad and TOPAS build was validated with a simulation in which the absorbed dose to water was tallied and compared with the RayStation simulation by means of a 3D gamma test. The 10^9 simulated histories were distributed based on the respective MU weights per spot. The simulations were run on four Intel® Xeon® CPU E5-2670 v3 @ 2.30GHz (48 cores) with 64.0 GB RAM each. The three applied fields were divided into four runs each so that a total of 12 individual simulations were necessary to obtain the full dose distribution. The number of histories relative to the distribution of MUs for each spot was sufficient to avoid undersampling by more than 0.01%. The results from the simulations were then obtained by summing the individual runs of the respective fields. Since the number of histories corresponding to the median dose of 50.4 Gy(RBE) is known, it can be multiplied by the appropriate factor to obtain a comparable dose within the matRad-based analysis of the results.

2.3.3 Out-of-Field Dose Calculations

According to (33) and (34), for the simulation of the neutron equivalent dose at a point and the gamma dose, respectively, the geometry of the treatment room and the gantry pit must be implemented in the MC code in order to obtain a comprehensive neutron spectrum including thermal neutrons and a gamma dose to water as accurately as possible. A fully rotating gantry around the isocenter of the treatment room was modeled in TOPAS. The geometrical models of the scanning and bending magnets, as well as of the counterweight, were simplified. The geometry also included a rotating table, a maze, a rolling floor, and a gantry pit including all walls, ceilings, and floor with the corresponding materials of the treatment room and gantry pit. The simulation environment thus had a volume of $20.0 \times 7.0 \times 20.0$ m³. The world material in these simulations was altered from vacuum to air to account for ionization occurring in the air relevant for thermal neutrons and gammas. The physical properties of air were modeled according to (31). However, to ensure that the initial protons hit the upstream side of the RS as accurately as possible with respect to the Fermi-Eyges parameters, the initial proton transport started in a vacuum box with the lateral dimensions of the RS, and a longitudinal extension of 50 cm upstream of the isocenter to the upstream side of the RS. The additional energy loss due to air scattering downstream the RS, up to the surface of the anthropomorphic phantom, was accounted for *via* a slight increase in the mean energy of each spot. This increase was calculated by an interpolation employing the data provided in the PSTAR database for the continuous

slowing down approximation in air based on a logarithmic cubic spline fit and the predicted track length of the protons. The influence of the additional air scattering on the energy spread is negligible, as well as the number of initial protons absorbed in air subsequent to the interaction in the RS.

The out-of-field dose simulations used 10^{10} primary protons. The simulation parameters were set analogously to those described above for the MU/ion calibration. The gamma and proton dose to water, as well as the neutron dose equivalent at a point, were tallied. To determine the neutron dose equivalent at a point, fluence-to-dose conversion factors within the TOPAS *AmbientDoseEquivalent* scorer were employed based on a logarithmic energy binning. The built-in conversion factors were adopted to the appropriate fluence-to-neutron dose equivalent conversion factors as described in the study from (14) by using tissue kerma factors $k(E)$ and quality factors as a function of neutron energy ($Q(E)$). In addition, simulations under identical conditions were performed in which only the dose to water of secondary protons was scored to elaborate on the effect of high-energy protons close to the irradiation field.

The spatial grid size in the TOPAS simulations was chosen analogously to the grid size in the RayStation simulations, namely, $0.2 \times 0.2 \times 0.2 \text{ cm}^3$. The doses for the neutron dose equivalent at a point, as well as the gamma and proton dose to water, were obtained from reading out the RTStructs of the contoured TLD positions *via* averaging of the voxels comprising the respective areas.

2.4 Calculation of Total Dose Equivalent and Organ Doses

Following validation of the MC framework, TOPAS simulations were used to calculate the total dose equivalent. The contribution of the following particles was considered for the out-of-field

dose, and their contributions were added to obtain the total dose equivalent:

1. Primary protons and assuming a generic RBE of 1.1.
2. Secondary gammas considering an RBE=1.
3. Neutrons as calculated according to the method described in Section 2.3.3.

Finally, organ doses were calculated relying on the specific locations of TLD inserts in the CIRS phantom, which correspond to certain organs to allow for organ dosimetry. In a total of 28 organ doses per target, the dose was calculated as well as the total dose to the child's organs considering a total target dose of 45.8 Gy (physical dose), i.e., 50.4 Gy(RBE).

3 RESULTS

3.1 Measured Out-of-Field Doses

3.1.1 MTS-7 Thermoluminescent Detectors

Absorbed dose in water per target dose, as measured with MTS-7 detectors, revealed doses ranging from $2,842 \pm 181$ to $7.9 \pm 0.5 \mu\text{Gy}/\text{Gy}$ at respectively 7.8 and 50 cm from the isocenter (see **Figure 2**). Compared to the target dose, the out-of-field dose was more than 2 orders of magnitude lower close to the field and decreased to 5 orders of magnitude lower doses beyond 35 cm out-of-field. MTS-7 results report on the absorbed dose in water from non-neutron contributions, which are dominated by protons and also gammas that contribute to their signal. Close to the field, one can expect a larger contribution of primary protons, while further away from the field, these primary protons will not be measured, as recoil protons will dominate the field.

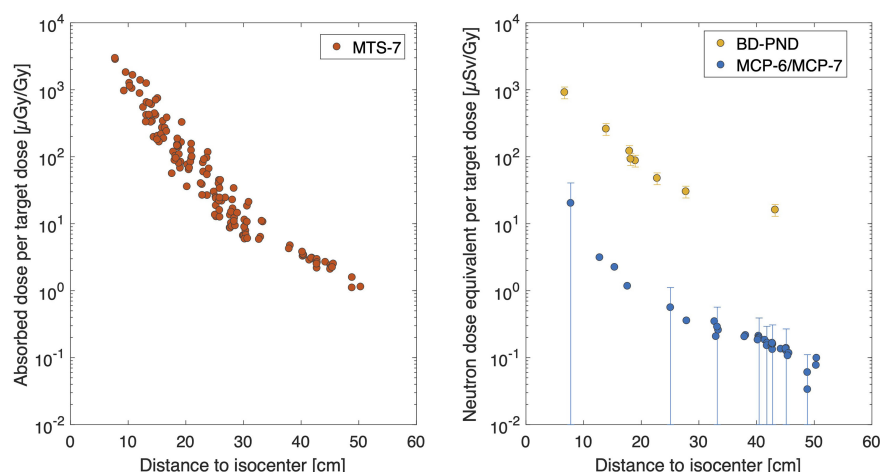


FIGURE 2 | Overview of experimental data. The absorbed dose in water per target dose [$\mu\text{Gy}/\text{Gy}$] is plotted as a function of distance for MTS-7 (left figure). The uncertainty bars in this figure are not displayed since they are smaller than the symbol size. In the right figure, the neutron dose equivalent data are plotted as a function of distance for BD-PND and MCP-6 in combination with MCP-7. Uncertainty bars ($k = 1$) are plotted for all BD-PNDs and for MCP-6/MCP-7 for every 5th data point to maintain readability of the plot. Notice that the abscissas and ordinates axes of both figures are the same for comparison purposes.

3.1.2 MCP-6 and MCP-7 Thermoluminescent Detectors

Thermal neutron dose was obtained by subtracting MCP-7 from MCP-6 detectors. The neutron dose equivalent per target dose ranged between 20.3 and 0.08 $\mu\text{Sv}/\text{Gy}$ for 7.7 to 50 cm from the isocenter, respectively (see **Figure 2**). It should be noted that the uncertainty ($k = 1$) on the calibration factor is 100%, which is due to a number of different contributions as described in (8). These data can also be expressed in gamma equivalent neutron doses (not plotted), as it is sometimes referred to by other groups to quantify the thermal neutron dose in terms of gamma dose equivalent. This easy approach is obtained by MCP-6 minus MPC-7 doses as calibrated in Co-60 dose in water (D_W). Hence, gamma equivalent neutron doses in this study ranged between 1846.0 and 6.9 $\mu\text{Gy}/\text{Gy}$.

3.1.3 Bubble Detector for Personal Neutron Dosimetry

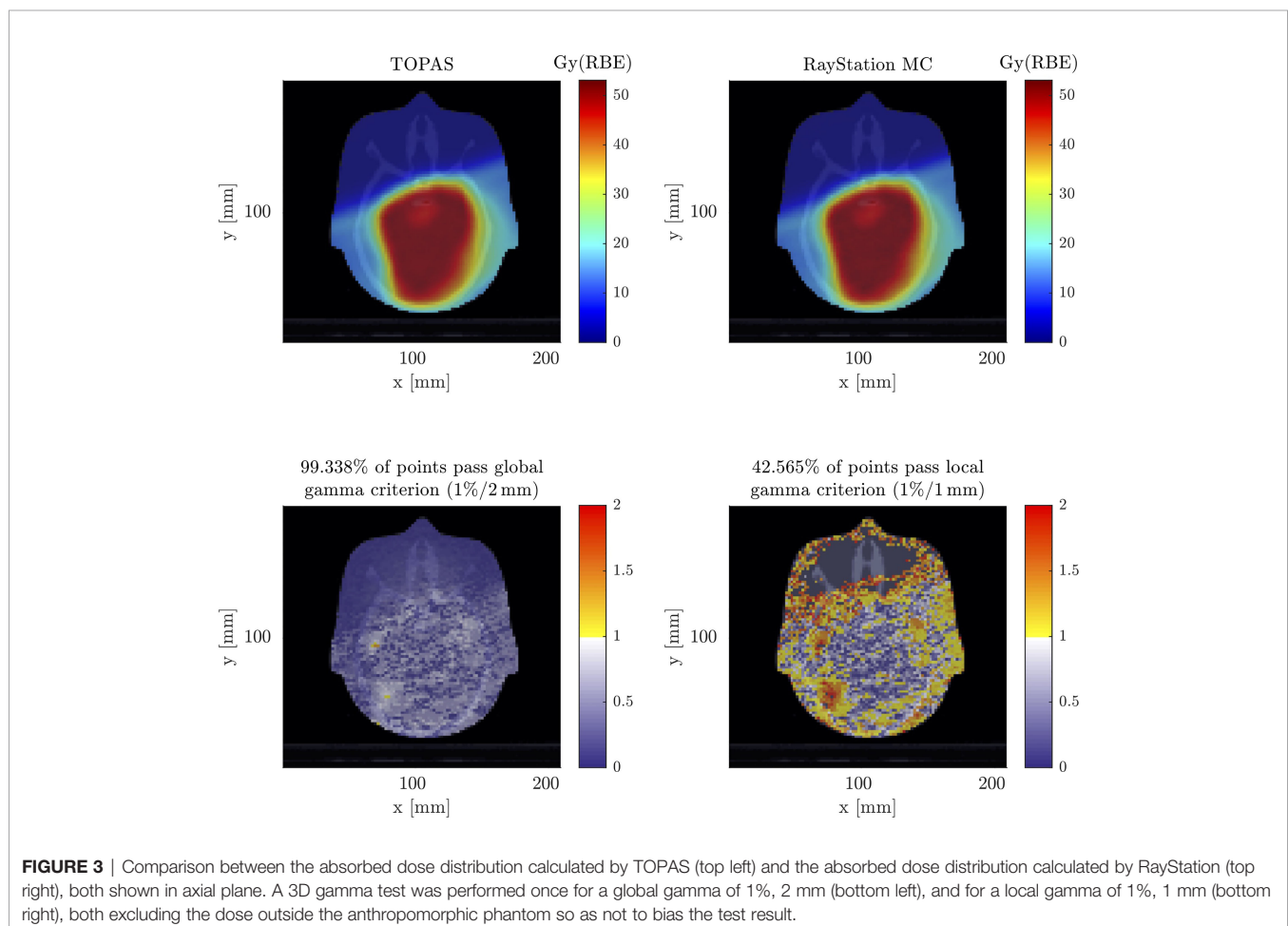
Finally, it was possible to obtain the neutron dose equivalent (neutron energies greater than 50 keV) in 6 different positions. Bubble detector data doses were between 915 ± 183 and 16 ± 3 $\mu\text{Sv}/\text{Gy}$ for respectively 6.7 cm and 43 cm from the isocenter (see **Figure 2**). When comparing these results with the data obtained

by MCP-6 in combination with MCP-7, as described in Section 3.1.2, it was noted that the thermal neutron dose equivalent data were much lower compared to the neutron dose equivalent measured by BD-PNDs (neutron energies greater than 50 keV). More specifically, the thermal neutron dose contribution to the total neutron dose was only 2.5% close to the field and decreased to 0.9% at 50 cm.

3.2 TOPAS Simulations

3.2.1 Target Dose Distribution

Figure 3 shows the result of the simulated absolute absorbed dose distribution from TOPAS. The dose to water was scored in order to compare to the RayStation results employing a 3D gamma test. On the lower left side in **Figure 3**, it can be seen that for a global 3D gamma test with passing criteria of 1%, 2 mm produces a gamma pass rate of 99.338%. This makes it evident that the implementation of the verification system was successful. To ensure that the differences between the overwritten materials of the anthropomorphic phantom in RayStation and the Schneider model did not cause discrepancies, the R_{80} range of each simulated irradiation field from TOPAS was analyzed with the corresponding R_{80} ranges of the fields from RayStation, where discrepancies were smaller than ± 0.02 cm.



On the lower right side in **Figure 3**, it can be seen that in a local 3D gamma test with 1%, 1 mm, the obtained gamma pass rate was 42.565%. It is recognized that most of the deviations occur outside the prescription range in this sensitive gamma test.

3.2.2 Out-of-Field Dose Simulations

In the top part of **Figure 4**, results demonstrate absorbed doses from different contributors including protons, all protons as well as secondary protons and gammas. Results show that the proton dose was approximately 2 mGy/Gy close to the field and drops to 1 μ Gy/Gy, at the very end of the phantom. Looking into the secondary protons, they match the total proton dose from 30 cm and higher, which points toward the fact that at only beyond 30 cm, primary protons will not contribute to the out-of-field doses. Secondary protons can be generated from the primary beam (which will be absorbed close to the field), but most likely they are created by neutrons as recoil protons. The gamma-induced dose was always lower than the proton dose and ranged on average between 1% and 54% of the proton dose close to the field and far out-of-field (50 cm), respectively. On the contrary, when neglecting the primary protons and only considering secondary protons, the gamma dose was on average 30% and 70% close to the field and far out-of-field, respectively. It should be noted that the uncertainty bars become wider the further the dose has been simulated out-of-field. This is related to the decreased particles in these regions hitting the small TLD volumes. To avoid biasing the data, no variance reduction techniques have been applied in the simulations.

Neutron dose equivalent considering all neutrons and only thermal neutrons are shown in the right plot in **Figure 4**. Data demonstrate a neutron dose equivalent of 528 ± 41 μ Sv/Gy at a 7.8-cm distance, which decreases to 11.2 μ Sv/Gy at 50 cm from the isocenter. Clearly, the contribution from thermal neutrons to the total is very small and remained below 1%. Assuming the

secondary proton production is mainly from recoil protons generated from neutrons, we also calculated the average quality factor from these data. We divided the calculated neutron dose equivalent data by the absorbed dose quantity from secondary protons and derived an average Q-factor of approximately 10, which did not vary significantly between locations out-of-field and is in line with literature data. Finally, the left plot in **Figure 4** also shows the total dose equivalent per target dose, which considers the contribution of the primary protons close to the field edge. At larger distances, it is clear that the total dose equivalent is dominated by the neutron dose, as the gamma dose does not contribute significantly to the dose equivalent (1%–6%).

3.3 Comparison of Out-of-Field Doses

In **Figure 5**, a comparison between the dose obtained from the MTS-7 detectors and TOPAS, from both protons and gamma contributions, revealed a good agreement. On average, the TOPAS doses, including proton and photon contributions, were 18% lower compared to those from the MTS-7 detectors with a slightly better agreement at larger distances. Nevertheless, the last 3 data points reveal a lower experimental dose compared to the TOPAS dose, which was within uncertainties, due to the larger uncertainties of the calculations at these positions as well as the higher uncertainties of the measurement points, as measured doses are closer to the background, and background uncertainties are 11%. In the right plot of **Figure 5**, the comparison between the experimental data obtained with BD-PNDs and simulated neutron dose equivalent data shows a good agreement close to the field and far from the field. Nevertheless, at 23 and 28 cm, the measured data were 50% lower compared to the simulated ones. One should keep in mind the use of PMMA slabs for the insertion of bubble detectors, which may have an impact on the out-of-field doses, particularly in regions where

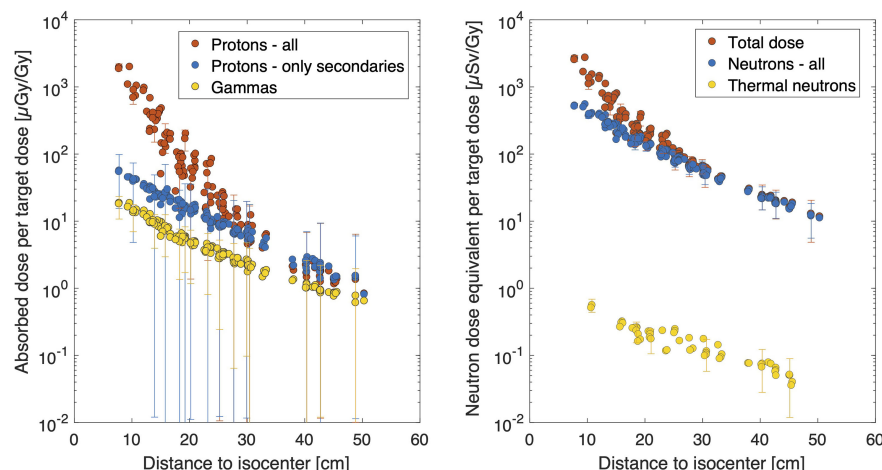


FIGURE 4 | Overview of TOPAS results. Absorbed dose in water per target dose [μ Gy/Gy] is calculated for all protons, only secondary protons and gammas (left figure). Neutron dose equivalent data are plotted as a function of distance for all neutron energies considered, and when only considering the thermal neutrons (right figure). Uncertainty bars ($k = 1$) are plotted only once every 10th data point to maintain readability of the plot.

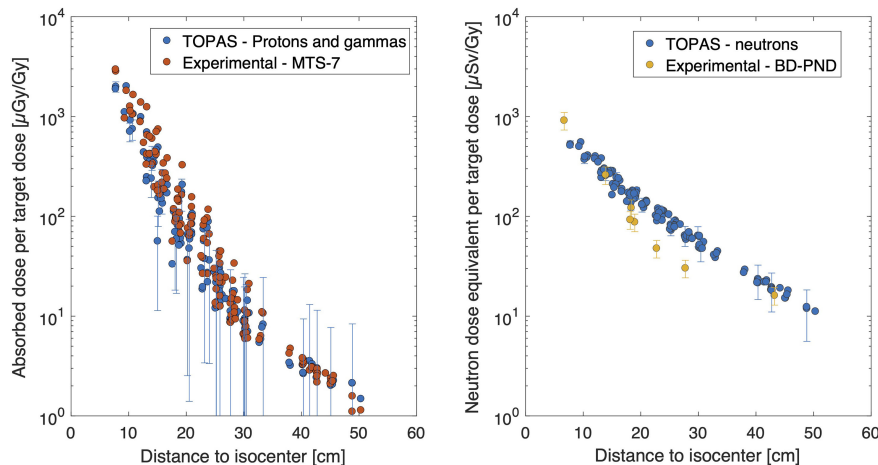


FIGURE 5 | Comparison between experimental data and TOPAS. On the left, the absorbed dose in water per target dose [μGy/Gy] is plotted for MTS-7 measurements and TOPAS simulations summing proton and gamma doses. On the right, neutron dose equivalent data are plotted for BD-PND and TOPAS simulations of neutron doses. BD-PND, bubble detector for personal neutron dosimetry.

the density of the phantom material should be lower such as the lung region. Moreover, bubble detectors have an uncertainty of 20% ($k = 1$), which does not include the uncertainty related to their energy response, as this is not known for energies above 20 MeV.

The measured thermal neutron doses are plotted in **Figure 6** together with the MC calculated thermal neutron doses. The experimental doses are higher than the simulated data. The difference is the largest close to the field where a 15-fold higher dose was measured, while out-of-field, the experimental data were a factor of 2 higher but within uncertainties.

3.4 Organ Dose Calculations

Dose calculations were grouped per organ in **Figure 7**, using a total target dose of 45.8 Gy (50.4 Gy(RBE)). The average thyroid dose per target dose was found to be 2,673 μSv/Gy corresponding to a total dose of 120 mSv. For organs in the chest region such as the lungs and thymus, average organ doses of 18 and 32 mSv were calculated for the total target dose, respectively. The breast dose was 17 mSv, while the heart dose was 8.3 mSv. For the liver and stomach, the obtained average doses were 4.1 and 3.4 mSv, respectively. Gonad doses were 1.1 and 0.6 mSv for the ovaries and testes, respectively.

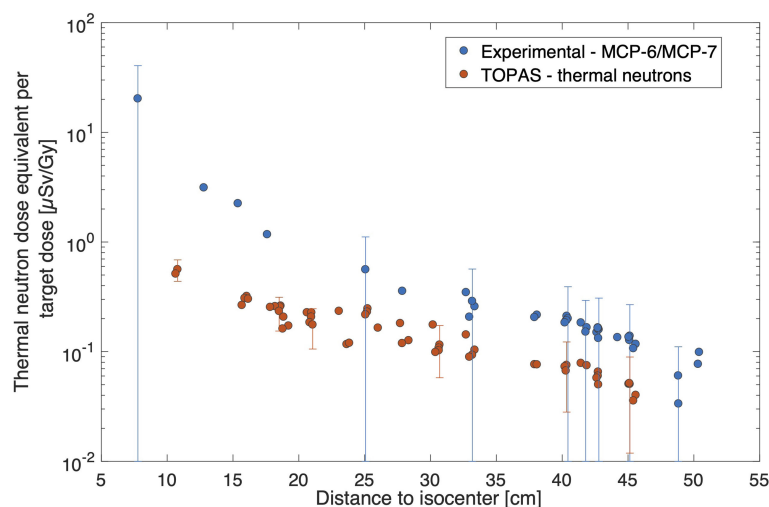


FIGURE 6 | Comparison of thermal neutron doses per target dose [μSv/Gy] for experimental data from MCP-6/MCP-7 data and TOPAS simulations. Uncertainty bars ($k = 1$) are plotted once every five points for clarity reasons.

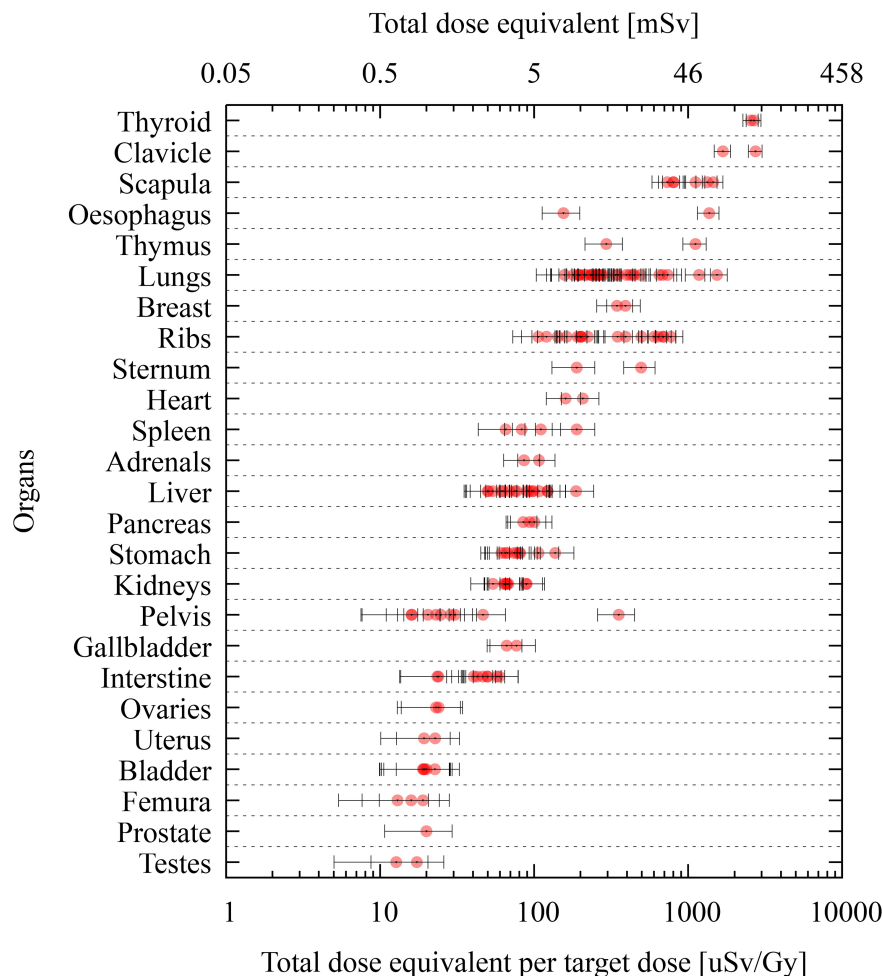


FIGURE 7 | Organ dose calculations produced by TOPAS at various TLD positions of the phantom. Data are grouped per organ, and the dose is reported as total dose equivalent per target dose [$\mu\text{Sv}/\text{Gy}$] in lower abscissas and total dose equivalent for a target dose of 45.8 Gy in the upper abscissas. Uncertainty bars ($k = 1$) are given for each position.

4 DISCUSSION

TOPAS was chosen in this study, as it is capable of calculating the dose distribution, including the aura consisting of neutrons and gammas (25, 35). Moreover, it was shown that TOPAS is able to simulate multiple Coulomb scattering in the lucite RS used in the present work with sufficient accuracy (26). As a first verification step of the MC framework, the in-field dose distribution was compared to RayStation, showing an excellent agreement in the 3D global gamma test as shown in **Figure 3**. However, the more sensitive local 3D gamma test revealed discrepancies outside the volume, which, as described in the work of (25), are due to the fact that RayStation simplifies the transport of secondary particles except for protons. For this reason, TOPAS was used to determine the out-of-field doses. Detailed modeling of the beam was performed, as well as detailed modeling of the geometry of the treatment room, including the gantry pit, to account for all possible sources of secondary

particles resulting from interactions between particles scattered and generated in the phantom, as well as the environment (33, 34).

A good agreement was observed between TLD measurements, MTS-7 type measuring the non-neutron component of the mixed radiation field, and TOPAS simulations tallying the proton and gamma component. A slight overestimation by MTS-7 detectors was however observed, which could be due to the slightly increased response of MTS detectors for protons (11). We assigned an uncertainty to this potential error of 5% ($k = 1$) in TLD data. Nevertheless, we did not use the spectra as input and assumed a uniform distribution of proton energies, which could be off for certain locations in the field, particularly when protons reach the end of their range. Nevertheless, we did not correct MTS-7 data for non-linearity in the energy response for protons and photons. Even though this can be considered a limitation, we do believe that the impact will be very small, and we considered it in the uncertainty of the detector data.

Moreover, the mentioned 12% overresponse of LiF-based TLDs for out-of-field measurements in photon beams does not apply to PT, as out-of-field spectra are much softer than in proton beams (36, 37). Furthermore, it should be noted that in the three outmost TLD positions, there is an underestimation of the dose with TLDs, which is most likely due to the very low doses measured in these positions and uncertainties associated with the background signal (11%).

Another reason for the slight overestimation of TLDs could be the contribution from heavy charged particles or fragments created by secondary neutrons in the phantom itself. This was not considered in the simulation due to the very low statistics of such particles but could have resulted in a signal in MTS-7 detectors. Still, heavy charged particles generated outside the TLD volume and created in the CIRS phantom could contribute, but due to their short range, the likelihood of reaching the TLD detector is small. Moreover, the sensitivity of TLD detectors for heavy charged particles is low, as the TL efficiency depends largely on the ionization density, as studied experimentally and using microdosimetric models (11, 38).

The use of Li-6-enriched LiF : Mg,Cu,P (MCP-6) detectors allowed us to assess the thermal neutron's contribution due to the high ${}^6\text{Li}(n, \alpha){}^3\text{H}$ cross section for thermal neutrons. However, it should be noted that the quantification of thermal neutrons and the use of appropriate conversion factors are subject to large uncertainties as previously described (8). The method assumes that the dose is deposited only by thermal neutrons, and neutrons are isotropic. Moreover, corrections are applied for superficial dose deposition in TLDs and, therefore, a decreased light attenuation. No information about the energy spectrum and angular distribution was obtained, and therefore, the calculated conversion factor has a large uncertainty (100%). In the current study, the experimental results are always higher as compared to the simulated data, which were the highest close to the field where a 15-fold higher dose was measured. This large discrepancy can be explained not only by the large measurement uncertainty but also by uncertainties in the TOPAS simulations related to the detailed modeling of beam, gantry, bed, walls, and other room components. As thermal neutrons are created by neutrons slowing down during collisions, it is very challenging to model these accurately. However, when moving out-of-field, the experimental data were a factor of 2 higher than simulated data, which could be explained by the more isotropic nature of the thermal neutrons when moving further away from the isocenter. Still, it was observed that the contribution of thermal neutrons to the total neutron dose equivalent is very small (within 1%). Similar findings, with thermal neutron doses contributing <1% to the total neutron dose equivalent, have also been observed in (39).

In general, the agreement between the measured and simulated neutron doses was good, despite the large uncertainties of the measurements performed with bubble detectors (20%, $k = 1$). Moreover, this uncertainty did not consider potential dependence on their response as a function of neutron energies. In fact, their response is well characterized until 20 MeV, above which response is not fully described. Nevertheless, previous data using BD-PNDs in PT have shown good agreement with H_p (10) reference

measurements (39). Still, an underestimation was measured in some positions, which could be assigned to the use of PMMA slabs instead of the anthropomorphic materials containing tissue materials. The discrepancy is the largest, and up to 50% lower for measured data compared to simulated data, in the area where there is lung material. As the TOPAS model was based on the phantom's CT and did not model the PMMA slabs and the exact material densities during measurements, this could be the cause of the discrepancy. Although this could be considered a limitation of the study, the dose data, namely, tissue dose, as determined in the TOPAS simulations are highly relevant for translation to the clinic and epidemiology. Another reason for the discrepancy could come from the uncertainty in neutron dose simulations due to missing cross-section data above 20 MeV for which many codes need to rely on the use of nuclear models. Several models are available; however, it is still open which models are more suitable. The choice of the binary intra-nuclear cascade (BIC) model in GEANT4 within this study was based on previous data demonstrating a good agreement with experiments (25, 34, 40).

Once validated, the MC simulation framework allowed to calculate the total dose, which was assessed as the dose quantity *dose equivalent*, considering the biological effectiveness of the radiation, which is dependent on the radiation type and energy. In previous studies, usually, the total dose in out-of-field positions is calculated considering only the neutron and gamma dose, for example, in (12, 14). Our study, however, demonstrates that closer than 30 cm from the isocenter, the contribution from primary protons is significant. We therefore added this contribution by applying a generic RBE of 1.1 for protons. We did not calculate the proton's energy, and we do recognize that this calculation may be a simplification, as the RBE will depend on the proton's linear energy transfer (LET). Still, the RBE-LET relationship is under investigation and would require more extensive calculations of (micro)dosimetric quantities, which we considered out of the scope of this paper.

Unfortunately, the calculation of the total dose equivalent was not possible from the experimental detectors, as TLDs will measure, apart from the gamma dose, both the primary and secondary protons. When summing these to the neutron doses from BD-PNDs, this will lead to an overestimation due to the double counting of recoil protons. Research is ongoing on how to combine different detector systems, with various response functions, to overcome the challenges of mixed radiation fields and to allow for an accurate experimental measurement of the total dose equivalent in the future. Similar issues are encountered for dosimetry in space where also complex mixed radiation fields consisting of neutrons, photons, protons, and heavier ions exist (41). In space, often silicon telescopes and other spectroscopic devices are used in order to be able to separate the different radiation field components and to obtain an estimation of the total dose equivalent. However, such detectors are too bulky to be used in phantom measurements in PT.

Previous works mainly evaluated out-of-field doses in PT through experimental measurements in water phantoms (1) or anthropomorphic phantoms (42–44). Only few studies have modeled the PT beam in detail to allow MC calculations of out-

of-field doses in PT (45–47). Studies connecting MC and experimental data in PT are mostly limited to measurements with ambient monitors or Bonner sphere systems in the room (33, 34, 48). Such studies are lacking in phantom measurements, which are of utmost importance for patient care. Our study provides a first step in the development of an MC framework that allows us to fully characterize the out-of-field radiation field and eventually could lead to tools for dose and risk optimization in children.

It is important to make the framework less computationally demanding, as now a very detailed beam model is used. In the same way as it was done in the study from (34), it will be important to identify the origin of the secondary radiation in the beamline component and to allow simplification of the beam model. Therefore, in the next developments, it must be considered which components of the simulation the complexity can be reduced without changing the simulation results to such an extent that it no longer coincides with the present result within the standard statistical uncertainty. For this purpose, a traceable approach is to determine which part of the treatment room has the largest share in the secondary particle generation or scattering. In this way, the dimensions of the room can presumably be reduced, which is synonymous with a reduction in the simulation time. Likewise, the origin of the secondary radiation depending on the direction of flight and momentum of the protons escaping the nozzle, as well as the scattering in the body and phantom, needs to be analyzed with the scope of simplifying the applied irradiation field, which in turn reduces the effort required to generate the phase space files and ultimately eliminates the time-consuming step function feature with the equally time-consuming phase space sampling of each spot.

The closest comparison of our experimental data to literature could be made to two studies performed within EURADOS WG9 (42, 43), measuring out-of-field doses during PT in the same anthropomorphic 5-year-old phantom treated for a brain tumor (6-cm diameter). One study described the response of passive detector systems in PT out-of-field dosimetry (42), where no RS (no RS) was used, while another study verified the impact of using an RS or 3D-printed beam compensator (BC) on the out-of-field doses (43). At 12 cm, the neutron dose equivalent data were 120 $\mu\text{Sv/Gy}$ (no RS) in the study from (42) versus 130 $\mu\text{Sv/Gy}$ (BC) and 180 $\mu\text{Sv/Gy}$ (RS) in the study from (43). Our data reported a dose of 260 $\mu\text{Sv/Gy}$, which could be due to the larger volume in the current study (195.2 cm^3) compared to the previous studies (65 cm^3) (42, 43). Interestingly, these studies also compared data to photon plans for the same phantom, tumor size, and location, revealing that intensity-modulated radiation therapy (IMRT) and 3D conformal radiation therapy (3D-CRT) (49) are at least one order of magnitude higher than PT at 30 cm. As part of another paper within this special issue, the same case was treated with IMRT and volumetric modulated arc therapy (VMAT), and we noted a reduction in out-of-field dose of a factor of approximately 5, close to the field for both IMRT and VMAT, while at 30 cm, the difference was a factor of 35 and 20 lower for PT as compared to IMRT and VMAT, respectively.

We reported on organ doses for a target dose of 50.4 Gy(RBE) by multiplying the normalized doses with the physical target

dose (45.8 Gy). Nevertheless, in the clinical treatment course, a second beam set delivered 3.6 Gy(RBE) in two fractions to a PTV, which was cut at the inferior side to protect the spinal cord. The corresponding reduction in the volume of the modified PTV amounted to 2.6%. Thus, the out-of-field contributions of the second beam set can be approximated by the corresponding values of the initial beam set.

Looking into the organ doses, the thyroid dose was the highest, yielding 120 mSv, while other organ doses ranged between 18 mSv for the lungs and 0.6 mSv for the testes. According to BEIR VII (50), the lifetime attributable risk (LAR) for cancer incidence and for an exposure at 5 years old is most elevated for the breast, lungs, and thyroid with LAR values of 914, 608, and 419/10⁵/0.1 Gy for women, respectively, while for men, the values were 261 and 76/10⁵/0.1 Gy for the lung and thyroid, respectively. Applying these risk factors to our data, we estimated a risk for secondary thyroid cancer of 0.6% for women and 0.1% for men. The risk for breast cancer was 0.2%. However, we should be aware that these risk models are mainly for low doses and low dose rates, and they cannot easily be extrapolated to radiotherapy where the dose is fractionated and organ dose is heterogeneous. These estimations should be considered with even more caution in the context of PT, as the effects of high-LET particles (i.e., protons and heavier ions) are outside the scope of the BEIR VII report.

Knowledge about potential long-term sequelae of treatment modalities needs precise data on the oncologic treatment, related to not only radiotherapies, such as the dose-volume histogram for every OAR (in the field and out of the field), but also the cumulative dose of every drug of chemotherapy (including new molecules and corticosteroids) and precise information on surgeries. This information needs to be complemented with a long period of follow-up.

The HARMONIC project was set up to provide direct evidence of the late health effects of low, moderate, and high radiation doses from modern radiotherapy techniques using protons or photons. Following up pediatric patients treated with PT will strengthen the epidemiological basis for assessing radiation risk in pediatric patients and will provide complementary information to the contribution from the large historical childhood survivor cohorts treated prior to 2000, which did not include new treatment modalities (51). The HARMONIC project therefore builds the infrastructure and instruments to evaluate the potential health, QoL, and social impacts of medical exposures to ionizing radiation in children, with potential for advanced patient-specific dose reconstruction, as presented here, and mechanistic investigations. It aims at providing evidence on the magnitude of possible cancer and non-cancer effects (including neurovascular, cardiovascular, and endocrine system effects), which may arise following cancer treatment with modern techniques, including PT in pediatrics.

5 CONCLUSION

As the role of proton beam therapy is continuously increasing, particularly when very young children are concerned, the

understanding of out-of-field doses and their impact on secondary cancer induction is essential. Since the HARMONIC project aims to investigate the incidence of secondary cancer, a reliable calculation of the out-of-field dose is of crucial importance. In this framework, the development of a validated MC system forms an important aspect in the assessment and characterization of out-of-field doses in PT. Once validated, MC simulations allow to fully describe the out-of-field radiation, permitting calculations of appropriate dosimetric quantities needed for the assessment of radiation damage and risks. In this study, the coupling of MC to advanced measurements with different detector types enabled the performance of a proper benchmarking of a widely used MC code, for use in out-of-field dosimetry.

The proposed computational method for calculation of the out-of-the-field dose in PT produces results that are compatible with the experimental data. The validated framework allowed a detailed characterization of the radiation field and the calculation of out-of-field organ doses during PT. The development of such an MC framework could lead to tools for dose and risk optimization in children.

DATA AVAILABILITY STATEMENT

The raw data supporting the conclusions of this article will be made available by the authors, without undue reservation.

AUTHOR CONTRIBUTIONS

MDS-H: experimental design, experimental setup, data analysis, and writing. NV: Monte Carlo simulation design, setup and execution, experimental setup, data analysis, and writing. CB:

treatment planning, experimental setup, and editing. JE: Monte Carlo geometry coding. JW: preparation of Monte Carlo configuration files and data analysis. RN: experimental setup. OVH: experimental analysis. JD: Monte Carlo simulations. FS: Monte Carlo data analysis and experimental setup. FV: simulation validation, data analysis, and writing—review. SR: analytical model and writing—review. GB: experimental setup writing—review. US: simulation validation and writing—review. MR: Monte Carlo data analysis. BT: clinical analysis, writing—review, and methodology. IT-C: epidemiological review, writing—review, and methodology. LB: conceptualization, supervision, writing, and writing—review. All authors contributed to the article and approved the submitted version.

FUNDING

The presented research has been funded by the HARMONIC project. The HARMONIC project (Health effects of cArdiac fluoRoscopy and MOderN radIotherapy in paediatricCs) has received funding from the Euratom research and training program 2014-2018 under grant agreement No 847707. MR acknowledges funding from the Sistema Nacional de Investigación de Panamá. IT-C acknowledges support from the Spanish Ministry of Science and Innovation and State Research Agency through the “Centro de Excelencia Severo Ochoa 2019-2023” Program (CEX2018-000806-S) and support from the Generalitat de Catalunya through the CERCA Program.

ACKNOWLEDGMENTS

The authors are thankful to Niklas Wahl from the matRad project.

REFERENCES

- Stolarczyk L, Trinkl S, Romero-Expósito M, Mojżeszek N, Ambrozova I, Domingo C, et al. Dose Distribution of Secondary Radiation in a Water Phantom for a Proton Pencil Beam—EURADOS WG9 Intercomparison Exercise. *Phys Med Biol* (2018) 63:085017. doi: 10.1088/1361-6560/aab469
- Ottolenghi A, Baiocco G, Smyth V, Trott K, Consortium A. The Andante Project: A Multidisciplinary Approach to Neutron Rbe. *Radiat Prot Dosim* (2015) 166:311–5. doi: 10.1093/rpd/ncv158
- De Saint-Hubert M, Farah J, Klodowska M, Romero-Expósito MT, Tyminska K, Mares V, et al. The Influence of Nuclear Models and Monte Carlo Radiation Transport Codes on Stray Neutron Dose Estimations in Proton Therapy. *Radiat Meas* (2022) 150. doi: 10.1016/j.radmeas.2021.106693
- Newhauser WD, Durante M. Assessing the Risk of Second Malignancies After Modern Radiotherapy. *Nat Rev Cancer* (2011) 11:438–48. doi: 10.1038/nrc3069
- Harrison RM, Ainsbury E, Alves J, Bottollier-Depois JF, Breustedt B, Caresana M, et al. EURADOS Strategic Research Agenda 2020: Vision for the Dosimetry of Ionising Radiation. *Radiat Prot Dosim* (2021) 194:42–56. doi: 10.1093/rpd/ncab063
- Westrand O, Svensson S. The ANACONDA Algorithm for Deformable Image Registration in Radiotherapy. *Med Phys* (2015) 42:40–53. doi: 10.1118/1.4894702
- Hubbell JH. *SMS. NIST Standard Reference Database*, Vol. 126. (2004).
- Van Hoey O, Parisi A. Development and Validation of a Model for Assessing Neutron Fluence With Lithium Fluoride Thermoluminescent Detectors. *Radiat Phys Chem* (2021) 188:109688. doi: 10.1016/j.radphyschem.2021.109688
- De Saint-Hubert M, De Angelis C, Knežević Z, Michalec B, Reniers B, Pyszka E, et al. Characterization of Passive Dosimeters in Proton Pencil Beam Scanning - A EURADOS Intercomparison for Mailed Dosimetry Audits in Proton Therapy Centres. *Phys Med* (2021) 82:134–43. doi: 10.1016/j.ejmp.2021.01.073
- Parisi A, Dabin J, Schoonjans W, Van Hoey O, Mégret P, Vanhavere F. Photon Energy Response of LiF : Mg,Ti (MTS) and LiF : Mg,Cu,P (MCP) Thermoluminescent Detectors: Experimental Measurements and Microdosimetric Modeling. *Radiat Phys Chem* (2019) 163:67–73. doi: 10.1016/j.radphyschem.2019.05.021
- Parisi A, Van Hoey O, Vanhavere F. Microdosimetric Modeling of the Relative Luminescence Efficiency of LiF : Mg,Ti (MTS) Detectors Exposed to Charged Particles. *Radiat Prot Dosim* (2018) 180:192–5. doi: 10.1093/rpd/ncx188
- Jia SB, Hadizadeh MH, Mowlavi AA, Loushab ME. Evaluation of Energy Deposition and Secondary Particle Production in Proton Therapy of Brain Using a Slab Head Phantom. *Rep Pract Oncol Radiother* (2014) 19:376–84. doi: 10.1016/j.rpor.2014.04.008
- Bruggmoser G, Saum R, Saum F, Gainey M, Pychlau C, Kapsch RP, et al. Correction Factors kE and kQ for LiF-TLDs for Dosimetry in Megavoltage Electron and Photon Beams. *Z Med Phys* (2015) 25:186–91. doi: 10.1016/j.zemedi.2014.03.010
- Romero-Expósito M, Domingo C, Sánchez-Doblado F, Ortega-Gelabert O, Gallego S. Experimental Evaluation of Neutron Dose in Radiotherapy Patients: Which Dose? *Med Phys* (2016) 43:360–7. doi: 10.1118/1.4938578

15. Agostinelli S, Allison J, Amako K, Apostolakis J, Araujo H, Arce P, et al. Geant4—a Simulation Toolkit. *Nucl Instrum Meth A* (2003) 506:250–303. doi: 10.1016/S0168-9002(03)01368-8
16. Allison J, Amako K, Apostolakis J, Araujo H, Arce Dubois P, Asai M, et al. Geant4 Developments and Applications. *IEEE T Nucl Sci* (2006) 53:270–8. doi: 10.1109/TNS.2006.869826
17. Allison J, Amako K, Apostolakis J, Arce P, Asai M, Aso T, et al. Recent Developments in Geant4. *Nucl Instrum Meth A* (2016) 835:186–225. doi: 10.1016/j.nima.2016.06.125
18. Perl J, Shin J, Schumann J, Faddegon B, Paganetti H. TOPAS: An Innovative Proton Monte Carlo Platform for Research and Clinical Applications. *Med Phys* (2012) 39:6818–37. doi: 10.1118/1.4758060
19. Wieser H, Cisternas E, Wahl N, Ulrich S, Stadler A, Mescher H, et al. Development of the Open-Source Dose Calculation and Optimization Toolkit Matrad. *Med Phys* (2017) 44:2556–68. doi: 10.1002/mp.12251
20. Bortfeld T, Bray T. An Analytical Approximation of the Bragg Curve for Therapeutic Proton Beams. *Med Phys* (1997) 4:2024–33. doi: 10.1118/1.598116
21. Clasié B, Depauw N, Fransen M, Gomà C, Panahandeh HR, Seco J, et al. Golden Beam Data for Proton Pencil-Beam Scanning. *Phys Med Biol* (2012) 57:1147–58. doi: 10.1088/0031-9155/57/5/1147
22. Grassberger C, Lomax A, Paganetti H. Characterizing a Proton Beam Scanning System for Monte Carlo Dose Calculation in Patients. *Phys Med Biol* (2015) 60:633–45. doi: 10.1088/0031-9155/60/2/633
23. Bäumer C, Koska B, Lambert J, Timmermann B, Mertens T, Takoukam Talla P. Evaluation of Detectors for Acquisition of Pristine Depth-Dose Curves in Pencil Beam Scanning. *Med Phys* (2015) 16:151–63. doi: 10.1120/jacmp.v16i6.5577
24. Gottschalk B. Techniques of Proton Radiotherapy: Transport Theory. *arXiv* (2012) 1204:4470.
25. Verbeek N, Wulff J, Bäumer C, Smyczek S, Timmermann B, Brualla L. Single Pencil Beam Benchmark of a Module for Monte Carlo Simulation of Proton Transport in the PENELOPE Code. *Med Phys* (2021) 48:456–76. doi: 10.1002/mp.14598
26. Verbeek N, Wulff J, Janson M, Bäumer C, Zahid S, Timmermann B, et al. Experiments and Monte Carlo Simulations on Multiple Coulomb Scattering of Protons. *Med Phys* (2021) 48:3186–99. doi: 10.1002/mp.14860
27. Kimstrand P, Traneus E, Ahnesjö A, Grusell E, Glimelius B, Tilly N. A Beam Source Model for Scanned Proton Beams. *Phys Med Biol* (2007) 52:3151–68. doi: 10.1088/0031-9155/52/11/015
28. Andreo P, Burns D, Hohlfield K, Huq M, Kanai T, Laitano F, et al. Absorbed Dose Determination in External Beam Radiotherapy: An International Code of Practice for Dosimetry Based on Standards of Absorbed Dose to Water. *IAEA Tech Rep Ser* (2006) pp 140–141.
29. DIN-Normenausschuss Radiologie (NAR). *Procedures of Dosimetry With Probe-Type Detectors for Proton and Ion Radiation - Part 1: Ionization Chambers. DIN 6801-1*. (2019).
30. Jarlskog C, Paganetti H. Physics Settings for Using the Geant4Toolkit in Proton Therapy. *IEEE Trans Nucl Sci* (2008) 55:1018–25. doi: 10.1109/TNS.2008.922816
31. ICRU Report 90. Key Data for Ionizing-Radiation Dosimetry: Measurement Standards and Applications. In: *Reports of the International Commission on Radiation Units and Measurements*.
32. Schneider U, Pedroni E, Lomax A. The Calibration of CT Hounsfield Units for Radiotherapy Treatment Planning. *Phys Med Biol* (1996) 41:111–24. doi: 10.1088/0031-9155/41/1/009
33. Trinkl S, Mares V, Englbrecht FS, Wilkens JJ, Wielunski M, Parodi K, et al. Systematic Out-of-Field Secondary Neutron Spectrometry and Dosimetry in Pencil Beam Scanning Proton Therapy. *Med Phys* (2017) 44:1912–20. doi: 10.1002/mp.12206
34. Englbrecht FS, Trinkl S, Mares V, Ruhm W, Wielunski M, Wilkens JJ, et al. A Comprehensive Monte Carlo Study of Out-of-Field Secondary Neutron Spectra in a Scanned-Beam Proton Therapy Gantry Room. *Z Med Phys* (2021) 31:215–28. doi: 10.1016/j.zemedi.2021.01.001
35. Gottschalk B, Cascio E, Daartz J, Wagner M. On the Nuclear Halo of a Proton Pencil Beam Stopping in Water. *Phys Med Biol* (2015) 60:5627–54. doi: 10.1088/0031-9155/60/14/5627
36. Scarboro SB, Followill DS, Howell RM, Kry SF. Variations in Photon Energy Spectra of a 6 MV Beam and Their Impact on TLD Response. *Med Phys* (2011) 38:2619–28. doi: 10.1118/1.3575419
37. Kry SF, Bednarz B, Howell RM, Dauer L, Followill D, Klein E, et al. AAPM TG 158: Measurement and Calculation of Doses Outside the Treated Volume From External-Beam Radiation Therapy. *Med Phys* (2017) 44:e391–429. doi: 10.1002/mp.12462
38. Berger T, Hajek M. TL-Efficiency—Overview and Experimental Results Over the Years. *Radiat Meas* (2008) 43:146–56. doi: 10.1016/j.radmeas.2007.10.029
39. De Saint-Hubert M, Saldarriaga Vargas C, Van Hoey O, Schoonjans W, De Smet V, Mathot G, et al. Secondary Neutron Doses in a Proton Therapy Centre. *Radiat Prot Dosim* (2016) 170:336–41. doi: 10.1093/rpd/ncv458
40. Arce P, Bolst D, Bordage MC, Brown JMC, Cirrone P, Cortés-Giraldo MA, et al. Report on G4-Med, a Geant4 Benchmarking System for Medical Physics Applications Developed by the Geant4 Medical Simulation Benchmarking Group. *Med Phys* (2021) 48:19–56. doi: 10.1002/mp.14226
41. Benton E, Benton E. Space Radiation Dosimetry in Low-Earth Orbit and Beyond. *Nucl Instrum Meth B* (2001) 184:255–94. doi: 10.1016/S0168-583X(01)00748-0
42. Knežević Z, Ambrozova I, Domingo C, De Saint-Hubert M, Majer M, Martínez-Rovira I, et al. Comparison of Response of Passive Dosimetry Systems in Scanning Proton Radiotherapy—a Study Using Paediatric Anthropomorphic Phantoms. *Radiat Prot Dosim* (2018) 180:256–60. doi: 10.1093/rpd/ncx254
43. Wochnik A, Stolarczyk L, Ambrožová I, Davidková M, De Saint-Hubert M, Domanski S, et al. Out-Of-Field Doses for Scanning Proton Radiotherapy of Shallowly Located Paediatric Tumours—a Comparison of Range Shifter and 3D Printed Compensator. *Phys Med Biol* (2021) 66:035012. doi: 10.1088/1361-6560/abc1bf
44. Hälgl RA, Besserer J, Boschung M, Mayer S, Lomax AJ, Schneider U. Measurements of the Neutron Dose Equivalent for Various Radiation Qualities, Treatment Machines and Delivery Techniques in Radiation Therapy. *Phys Med Biol* (2014) 59:2457–68. doi: 10.1088/0031-9155/59/10/2457
45. Taddei PJ, Mirkovic D, Fontenot JD, Giebler A, Zheng Y, Kornguth D, et al. Stray Radiation Dose and Second Cancer Risk for a Pediatric Patient Receiving Craniospinal Irradiation With Proton Beams. *Phys Med Biol* (2009) 54:2259–75. doi: 10.1088/0031-9155/54/8/001
46. Geng C, Moteabbed M, Seco J, Gao Y, George Xu X, Ramos-Méndez J, et al. Dose Assessment for the Fetus Considering Scattered and Secondary Radiation From Photon and Proton Therapy When Treating a Brain Tumor of the Mother. *Phys Med Biol* (2015) 61:683–95. doi: 10.1088/0031-9155/61/2/683
47. De Saint-Hubert M, Tyminska K, Stolarczyk L, Brkić H. Fetus Dose Calculation During Proton Therapy of Pregnant Phantoms Using Mcnp6.2 Codes. *Radiat Meas* (2021) 149. doi: 10.1016/j.radmeas.2021.106665
48. Leite AMM, Ronga MG, Giorgi M, Ristic Y, Perrot Y, Tromprier F, et al. Secondary Neutron Dose Contribution From Pencil Beam Scanning, Scattered and Spatially Fractionated Proton Therapy. *Phys Med Biol* (2021) 66:225010. doi: 10.1088/1361-6560/ac3209
49. Majer M, Stolarczyk L, De Saint-Hubert M, Kabat D, Knežević Z, Miljanic S, et al. Out-Of-Field Dose Measurements for 3d Conformal and Intensity Modulated Radiotherapy of a Paediatric Brain Tumour. *Radiat Prot Dosim* (2017) 176:331–40. doi: 10.1093/rpd/ncx015
50. National Research Council. *Health Risks From Exposure to Low Levels of Ionizing Radiation: BEIR VII Phase 2*. Washington, DC: The National Academies Press (2006). doi: 10.17226/11340
51. Winther JF, Kenborg L, Byrne J, Hjorth L, Kaatsch P, Kremer LCM, et al. Childhood Cancer Survivor Cohorts in Europe. *Acta Oncol* (2015) 54:655–68. doi: 10.3109/0284186X.2015.1008648

Conflict of Interest: The authors declare that the research was conducted in the absence of any commercial or financial relationships that could be construed as a potential conflict of interest.

Publisher's Note: All claims expressed in this article are solely those of the authors and do not necessarily represent those of their affiliated organizations, or those of

the publisher, the editors and the reviewers. Any product that may be evaluated in this article, or claim that may be made by its manufacturer, is not guaranteed or endorsed by the publisher.

Copyright © 2022 De Saint-Hubert, Verbeek, Bäumer, Esser, Wulff, Nabha, Van Hoey, Dabin, Stuckmann, Vasi, Radonic, Boissonnat, Schneider, Rodriguez,

Timmermann, Thierry-Chef and Brualla. This is an open-access article distributed under the terms of the Creative Commons Attribution License (CC BY). The use, distribution or reproduction in other forums is permitted, provided the original author(s) and the copyright owner(s) are credited and that the original publication in this journal is cited, in accordance with accepted academic practice. No use, distribution or reproduction is permitted which does not comply with these terms.



Experimental Validation of an Analytical Program and a Monte Carlo Simulation for the Computation of the Far Out-of-Field Dose in External Beam Photon Therapy Applied to Pediatric Patients

OPEN ACCESS

Edited by:

Beatriz Sanchez-Nieto,
Pontifical Catholic University of
Chile, Chile

Reviewed by:

Vanessa Panettieri,
The Alfred Hospital, Australia
Raquel Bar-Deroma,
Rambam Health Care Campus, Israel
Loredana G Marcu,
University of Oradea, Romania

*Correspondence:

Lorenzo Brualla
Lorenzo.Brualla@uni-due.de

[†]These authors have contributed
equally to this work and share
first authorship

Specialty section:

This article was submitted to
Radiation Oncology,
a section of the journal
Frontiers in Oncology

Received: 23 February 2022

Accepted: 06 June 2022

Published: 07 July 2022

Citation:

De Saint-Hubert M, Suesselbeck F,
Vasi F, Stuckmann F, Rodriguez M,
Dabin J, Timmermann B,
Thierry-Chef I, Schneider U
and Brualla L (2022) Experimental
Validation of an Analytical Program
and a Monte Carlo Simulation for the
Computation of the Far Out-of-Field
Dose in External Beam Photon
Therapy Applied to Pediatric Patients.
Front. Oncol. 12:882506.
doi: 10.3389/fonc.2022.882506

Marijke De Saint-Hubert^{1†}, Finja Suesselbeck^{2,3†}, Fabiano Vasi^{4†}, Florian Stuckmann^{5,2},
Miguel Rodriguez^{6,7}, Jérémie Dabin¹, Beate Timmermann^{2,8,9,10,11},
Isabelle Thierry-Chef^{12,13,14}, Uwe Schneider⁴ and Lorenzo Brualla^{2,8,9*}

¹ Research in Dosimetric Applications, Belgian Nuclear Research Center (SCK CEN), Mol, Belgium, ² Westdeutsches Protonentherapiezentrum Essen (WPE), Essen, Germany, ³ Faculty of Mathematics and Science Institute of Physics and Medical Physics, Heinrich-Heine University, Düsseldorf, Germany, ⁴ Physik Institut, Universität Zürich, Zürich, Switzerland, ⁵ Klinikum Fulda GAG, Universitätsmedizin Marburg, Fulda, Germany, ⁶ Hospital Paitilla, Panama City, Panama, ⁷ Instituto de Investigaciones Científicas y de Alta Tecnología INDICASAT-AIP, Panama City, Panama, ⁸ Medizinische Fakultät, Universität Duisburg-Essen, Essen, Germany, ⁹ West German Cancer Center (WTZ), Essen, Germany, ¹⁰ Department of Particle Therapy, University Hospital Essen, Essen, Germany, ¹¹ Radiation Oncology and Imaging, German Cancer Consortium DKTK, Heidelberg, Germany, ¹² Radiation Programme, Barcelona Institute of Global Health (ISGlobal), Barcelona, Spain, ¹³ University Pompeu Fabra, Barcelona, Spain, ¹⁴ CIBER Epidemiología y Salud Pública, Madrid, Spain

Background: The out-of-the-field absorbed dose affects the probability of primary second radiation-induced cancers. This is particularly relevant in the case of pediatric treatments. There are currently no methods employed in the clinical routine for the computation of dose distributions from stray radiation in radiotherapy. To overcome this limitation in the framework of conventional teletherapy with photon beams, two computational tools have been developed—one based on an analytical approach and another depending on a fast Monte Carlo algorithm. The purpose of this work is to evaluate the accuracy of these approaches by comparison with experimental data obtained from anthropomorphic phantom irradiations.

Materials and Methods: An anthropomorphic phantom representing a 5-year-old child (ATOM, CIRS) was irradiated considering a brain tumor using a Varian TrueBeam linac. Two treatments for the same planned target volume (PTV) were considered, namely, intensity-modulated radiotherapy (IMRT) and volumetric modulated arc therapy (VMAT). In all cases, the irradiation was conducted with a 6-MV energy beam using the flattening filter for a prescribed dose of 3.6 Gy to the PTV. The phantom had natLiF : Mg, Cu, P (MCP-N) thermoluminescent dosimeters (TLDs) in its 180 holes. The uncertainty of the experimental data was around 20%, which was mostly attributed to the MCP-N energy dependence. To calculate the out-of-field dose, an analytical algorithm was implemented to be run from a Varian Eclipse TPS. This algorithm considers that all anatomical structures are filled with

water, with the exception of the lungs which are made of air. The fast Monte Carlo code dose planning method was also used for computing the out-of-field dose. It was executed from the dose verification system PRIMO using a phase-space file containing 3×10^9 histories, reaching an average standard statistical uncertainty of less than 0.2% (coverage factor $k = 1$) on all voxels scoring more than 50% of the maximum dose. The standard statistical uncertainty of out-of-field voxels in the Monte Carlo simulation did not exceed 5%. For the Monte Carlo simulation the actual chemical composition of the materials used in ATOM, as provided by the manufacturer, was employed.

Results: In the out-of-the-field region, the absorbed dose was on average four orders of magnitude lower than the dose at the PTV. For the two modalities employed, the discrepancy between the central values of the TLDs located in the out-of-the-field region and the corresponding positions in the analytic model were in general less than 40%. The discrepancy in the lung doses was more pronounced for IMRT. The same comparison between the experimental and the Monte Carlo data yielded differences which are, in general, smaller than 20%. It was observed that the VMAT irradiation produces the smallest out-of-the-field dose when compared to IMRT.

Conclusions: The proposed computational methods for the routine calculation of the out-of-the-field dose produce results that are similar, in most cases, with the experimental data. It has been experimentally found that the VMAT irradiation produces the smallest out-of-the-field dose when compared to IMRT for a given PTV.

Keywords: teletherapy, photon, anthropomorphic, pediatric, Monte Carlo, PRIMO, TLD, analytical model

1 INTRODUCTION

Therapeutic advances in pediatric oncology have made it possible to increase the survival rates of children with cancer (1). Especially when treating pediatric patients, the protection of surrounding tissue and far-from-the-field tissue is important to prevent the development of radiation-induced second primary cancer (2, 3). Even though second primary malignancies are more likely to appear in high-dose areas, the risk of radiation-induced secondary cancer in lower-dose areas is not negligible (4, 5). Particular attention should be paid in pediatrics since organs are growing with massive cell proliferation (4, 6). Proliferating cells respond sensitively to radiation exposure during cell division (6). Additionally, anatomical structures in pediatric patients are closer in proximity to the treated target, which leads to an increased radiation dose in the same tissue compared to adult patients (4). The cumulative incidence of second primary malignancies is up to 20% of patients treated by radiotherapy (7). The cumulative prevalence rate of long-term sequelae is estimated between 40 and 84% (8, 9). Late effects and late morbidity of cancer treatments become more important, and an improved local tumor control does not have to compromise the protection of patients against long-term effects (4). Studies have shown that pediatric cancer patients have a three- to six-fold increased risk of developing a second primary cancer compared to the general population (5).

It is well known that clinical treatment planning systems (TPS) do not provide an adequate estimation of the out-of-field dose (3, 10–12). Planning computerized tomographies (CT)

only include the target volume and organs-at-risk (OARs) in proximity to the treatment field since, for radiation protection purposes and other considerations, they do not cover the full body. Even more important is the fact that algorithms in TPSs are, in general, not conceived for the simulation of the stray radiation far from the irradiated field, and dose measurements in these distant regions are challenging. Consequently, out-of-field dose estimations are limited to regions within the CT volume. Furthermore, the introduction of advanced radiotherapy techniques, such as intensity-modulated radiotherapy (IMRT) and volumetric modulated arc therapy (VMAT), allows a more homogeneous dose delivery to the tumor and potential sparing of the surrounding healthy tissue through spreading of the dose. Nevertheless, for healthy organs further away from the field, only a limited amount of out-of-field dose data evaluating the long-term side effects of these advanced techniques are available. A recent publication has shown that the use of VMAT during craniospinal irradiation (CSI) indicates a reduction of out-of-field doses in most organs (13). Another experimental study from pediatric CSI revealed that the conventional radiotherapy technique, three-dimensional conformal radiotherapy (3D-CRT), resulted in very high doses to a limited number of organs while it was able to spare organs such as the lungs and breast when compared to IMRT and helical tomotherapy (HT). Both IMRT and HT spread the dose over more organs and were able to spare the heart, thyroid, bladder, uterus, and testes when compared to 3D-CRT (14). Finally, another experimental study

performed for clinically relevant IMRT and 3D-CRT treatments of the same brain tumor has shown a better reduction of eye and non-target brain doses with 3D-CRT. Moreover, out-of-field doses were comparable for 3D-CRT and IMRT, except for the 3D-CRT irradiation using a mechanical wedge (12). An important limitation of the experimental assessment of out-of-field doses is that the comparison of different techniques that may not be generalized as out-of-field doses will depend on the current practice from the participating centers, applying different objectives and constraints in their dose optimization algorithms. Therefore, the development of methods for the routine calculation of out-of-field doses is a key step in the evaluation and optimization of radiation-induced secondary malignancies in pediatric patients.

Out-of-field dose estimations can be performed by other methods, such as Monte Carlo simulations, analytical methods (15, 16), or direct measurements (11). The purpose of this article is the experimental validation of two algorithms for calculating out-of-the-field absorbed doses. The ultimate goal is to routinely implement these computation techniques in the HARMONIC Consortium, a European project in which 24 clinical and research institutions collaborate in the investigation of radiation-induced primary second malignancies in pediatric patients.

2 MATERIALS AND METHODS

2.1 Experimental Setup

Aiming to simulate a realistic photon treatment plan of a brain tumor, a clinically applied treatment plan was transferred to the conditions of the experiment. The corresponding patient should feature a cranial size and shape, which has a reasonable resemblance with the corresponding features of the anthropomorphic phantom. To this end, a 7-year-old female patient with a diffuse midline glioma (WHO grade IV) was selected. The concerned patient was enrolled in the prospective registry study “KiProReg” (German Clinical Trials Register:

DRKS-ID: DRKS00005363) after consent was obtained from her legal guardians. This study was approved by the local ethics committee. The patient received a combined radiotherapy and chemotherapy after R3 resection. A dose of 50.4 Gy with 1.8 Gy per fraction was prescribed to the initial PTV, which was located in the cerebellum and had a volume of 195.2 cm³.

The experiment was performed using an anthropomorphic phantom ([ATOM, Computerized Imaging Reference Systems (CIRS), Inc, Norfolk, VA, USA] representing a 5-year-old child (type 705D). The phantom consists of tissue equivalent (TE) materials and is predrilled at 180 positions for organ dosimetry. The drilled holes are each filled with TE plugs that keep in position a thermoluminescent detector (TLD).

All irradiations for this article were done with a Varian TrueBeam STx linac operating with flattening filter at a nominal energy of 6 MV. The linac is equipped with a Varian Millennium 120 multileaf collimator.

2.1.1 Treatment Planning

For treatment planning, the Eclipse External Beam Planning system version 15.6 (Varian Oncology Systems, Palo Alto, CA, USA), using the AAA-algorithm (version 13.6), was employed. Treatment planning was performed using the planning CT of the ATOM phantom. The IMRT plan was calculated with 6-MV photons and consisted of five coplanar and isocentric fields with beam angles of 70°, 120°, 180°, 235°, and 280°, respectively (see **Figure 1**). In addition, VMAT was planned using two 360° isocentric rotations (see **Figure 1**). The plans were optimized with the photon optimization algorithm PO (Varian Medical Systems, version 13.6). The plans were iteratively optimized over several steps using the constraint V7Gy = 4% for the eyes and V40Gy = 5% and V25Gy = 5% for the left and right cochlea, respectively. A highly weighted general normal tissue objective was used. For comparison purposes of the different treatment plans, it was attempted to reach the predefined goals without further optimization, as it would have been done in a clinical setting. The planning target volume (PTV) was optimized using the prescribed dose as an upper and lower

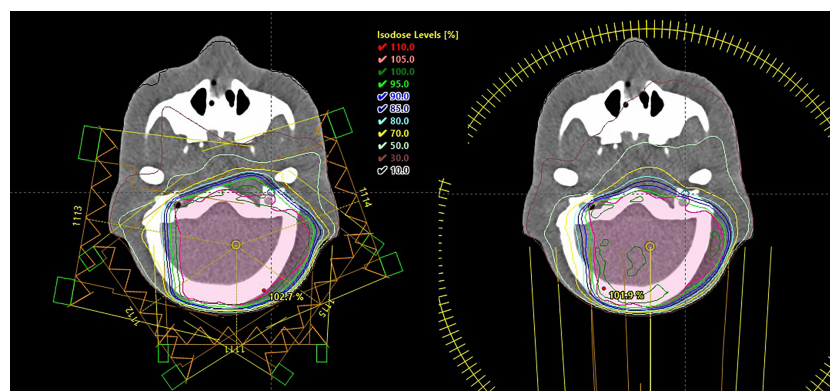


FIGURE 1 | Intensity-modulated radiotherapy (left) and volumetric modulated arc therapy (right) plans showing the isodose lines in the treated volume as computed by the treatment planning system Eclipse.

TABLE 1 | Sources of thermoluminescent dosimeter uncertainties ($k = 1$).

Sources of uncertainty	All positions
Dosimeter reproducibility	1.8%
Batch reproducibility	1.9%
Calibration uncertainty	2.4%
Background uncertainty	<1.0%
Angular response	1.0%
Energy response	15.0%
TLD positioning uncertainty	see Table 2
Linac uncertainty	2.0%

constraint to 0 and 100% of the volume, respectively. The treatment plans were normalized such that at least 95% of the PTV received at least 98% of the prescribed dose. The final plans resulted in 682 and 421 monitor units (MUs) per 1.8 Gy for IMRT and VMAT, respectively.

2.2 Dosimetric Measurements

2.2.1 Thermoluminescent Detectors

TLDs were produced by IFJ-PAN (Krakow Poland), namely, natural LiF : Mg, Cu, P (MCP-N) detectors were inserted in 150 out-of-field positions. The delivered dose in the experiments was 3.6 Gy to the PTV as adjusted to the sensitivity of the TLDs. The chosen dose corresponds to 2 fractions of 1.8 Gy of an actual treatment. One set of MCP-N detectors was irradiated with the IMRT plan and another set with the VMAT plan.

Before each exposure, the standard annealing protocol was applied: 10 min at 240°C followed by fast cooling at -10°C inside a temperature-controlled freezer. Following exposure, TLD detectors were read in Thermo Scientific Harshaw 5500 reader following a preheat for 30 min at 120°C to avoid signal fading and low temperature anomalies in the glow curves (17). A heating rate of 10°C/s was used to heat up TLDs up to 255°C. TLDs were calibrated with Co-60 source in terms of kerma “free in air”, K_{air} . K_{air} was then converted to absorbed dose to water (D_w) using the conversion factor $D_w/K_{\text{air}} = 1.12$ as determined by the ratio of mass energy absorption coefficient for water to air for the energy of Co-60 (18). Following normalization to the target dose delivered during treatment of the phantom (3.6 Gy), data were expressed as absorbed dose in water per target dose in units of mGy/Gy.

The distances from the isocenter to the center of each measurement point were calculated using the CT scan of the ATOM phantom. These distances were used for plotting purposes.

2.2.2 TLD Uncertainties

Uncertainties with TLD measurements (coverage factor $k = 1$) were assessed. **Table 1** shows an overview of the uncertainties

considered. The included uncertainty sources were dosimeter reproducibility (1.8%), batch reproducibility (1.9%), Co-60 calibration uncertainty (2.4%) as well as background uncertainties which were dependent on the measured dose but remained below 1% (19). From the angular response of MCP-N, previously published by (20), and assuming a uniform angular distribution of radiation, the angular uncertainty of 1% was also included. The uncertainty related to MCP-N photon energy response (17) due to beam softening out-of-field, as described in the study from (21), was also included. Far from the treatment field (at 50 cm off-axis), this study showed a reduced photon energy with an average photon energy of 200 keV. In the present study, a maximum energy dependence of 18% was considered for MCP-N detectors, and following a uniform distribution of the error, we estimated 15% uncertainty on the energy response ($k = 1$).

An investigation on the uncertainty due to the detector positioning within the plug-filled hole was performed for both VMAT and IMRT. Using the Monte Carlo computed (PRIMO) dose distributions, the variation of the dose within 2 mm in the longitudinal axis around each TLD position was assessed. Three regions in the phantom were defined according to their distance to the isocenter, namely, the penumbra (6 to 12 cm), the out-of-field (12 to 40 cm), and the far out-of-field (> 40 cm). The Monte Carlo computed dose for each TLD was classified according to these regions. Afterwards, the computed dose found at each position was compared to the corresponding computed dose 2 mm closer and 2 mm farther from the isocenter along the longitudinal axis of the phantom. The largest relative difference found in this comparison for each region and each treatment modality is reported in **Table 2**. Although the boundaries chosen for the definition of each region are arbitrary, they are related to dose gradient.

Finally, the uncertainty on the linac dose delivery was estimated to be smaller than 2%. This is the maximum variation allowed by the Swiss authorities. This uncertainty is verified by daily and weekly measurements and eventual adjustments of the linac output if necessary. This 2% value is a very conservative estimate of the uncertainty as, in reality, the linac output is more precise. The treatment plans were delivered for the measurements at the same day to keep the linac output variations minimal.

The combined uncertainty was calculated as the square-root of the linear sum of squared standard uncertainties from **Tables 1, 3**. The final results of TLD detectors' uncertainties for both IMRT and VMAT are shown in **Table 4**.

2.3 Analytical Model

A general model to analytically predict the stray dose of radiotherapy plans was applied (15) to the computation of the

TABLE 2 | Positioning uncertainties ($k = 1$) for different TLD positions in intensity-modulated radiotherapy (IMRT) and volumetric modulated arc therapy (VMAT) irradiations.

Positioning uncertainty	Penumbra 6 < d ≤ 12	Out-of-field 12 < d ≤ 40	Far out-of-field d > 40
IMRT	6.0%	2.0%	<0.1%
VMAT	8.0%	2.5%	<0.1%

Distance d to isocenter is expressed in centimeters.

TABLE 3 | Total estimated uncertainties ($k = 1$) for different thermoluminescent dosimeter positions in intensity-modulated radiotherapy (IMRT) and volumetric modulated arc therapy (VMAT) irradiations.

Total uncertainty	Penumbra $6 < d \leq 12$	Out-of-field $12 < d \leq 40$	Far out-of-field $d > 40$
IMRT	17%	16%	16%
VMAT	18%	16%	16%

Distance d to isocenter is expressed in centimeters.

out-of-field dose in the IMRT and VMAT irradiations of the ATOM phantom. The model concentrates on the three major components of stray dose: patient scatter, collimator scatter, and head leakage. The estimation of the out-of-field dose is based on a mechanistic model for patient scatter, whereas collimator scatter and head leakage were developed using an empirical approach. The parameters of the model were adjusted using measurements of total absorbed dose in simple geometries. The patient scatter contribution requires knowledge about the isocenter dose, the field width, and the field length. The collimator scatter calculation is based on information about the number of MU, the jaw width and length, and the mean multileaf collimator (MLC) length opening. To calculate head leakage, the number of monitor units must be known. The analytical model has been coded to run in the Eclipse (v. 15.6) TPS using the Varian Eclipse Scripting API (16). For this, the CT of the ATOM phantom and the treatment plan is transferred *via* the API into an external software package. Then, the peripheral three-dimensional dose distribution is calculated according to Hauri et al. (15). After that, the TPS dose distribution is fused with the calculated out-of-field dose distribution by determining in the cranial–caudal direction the 5% isodose and replacing the TPS dose with the out-of-field dose for doses smaller than 5% of the TPS dose.

The employed analytical model has a similar conception to that published by (22), with the advantage that the former has been coded as a plugging of the software Eclipse, thus allowing users of this TPS to perform the computation of the peripheral dose during planning. Both models are a substantial evolution of Peridose, published by (23).

The CT of the ATOM phantom consists of $256 \times 350 \times 256$ voxels of size equal to $0.130 \times 0.200 \times 0.130 \text{ cm}^3$. The analytical method considers all anatomical structures made of water, with the exception of the lungs which are made of air. For computing

the dose to each TLD, each detector was contoured in the CT of the ATOM. Each contoured TLD was considered to be filled of water, independently of its location in the ATOM's anatomy. In this way, the density and the material composition (water) contained inside each TLD contour are more similar to that of the actual detector which is water equivalent. The algorithm reports all absorbed doses as dose to water.

2.4 Monte Carlo Simulation

PRIMO (version 1.0.64.1814) is a Monte Carlo dose verification system that simulates medical linacs and the subsequent absorbed dose computation. The software employs two Monte Carlo engines: the general-purpose radiation transport code PENELOPE 2011 with a modified version of the steering program penEasy and a parallelized version of the fast Monte Carlo code for the simulation of electron–photon showers under radiotherapy conditions called dose planning method (DPM) (24–28).

The dose verification system contains a catalogue of predefined linac geometry files. For the simulations discussed in this article, the Varian C-series (e.g., Varian Clinac 2100), operating in photon mode with the Varian Millennium 120 MLC, is used. According to the disclosed information from Varian and as it has been experimentally shown (see next paragraph), the geometrical description of the Varian C-series can reproduce the dose distributions produced by the Varian TrueBeam linac operating with flattening filter at a nominal energy of 6 MV, which are the linac and energy employed in all the experiments conducted for this paper. The geometrical description of the Varian C-series contained in PRIMO uses the information provided in the Varian Monte Carlo Package document and the modifications proposed by (29). These documents do not give details about the shielding elements of the linac, which are part of the company's trade secrets. The

TABLE 4 | Average relative discrepancies between the computed and experimental dose in the three regions defined for both intensity-modulated radiotherapy (IMRT) and volumetric modulated arc therapy (VMAT) irradiations.

Modality, Comparison	Penumbra $6 < d \leq 12$	Out-of-field $12 < d \leq 40$	Far out-of-field $d > 40$
IMRT, PRIMO–experiment	–27%	–13%	–18%
IMRT, analytical–experiment	14%	–14%	–38%
IMRT, analytical–PRIMO	56%	3%	–24%
VMAT, PRIMO–experiment	–27%	–20%	42%
VMAT, analytical–experiment	–44%	–48%	10%
VMAT, analytical–PRIMO	–24%	–35%	–23%

For comparisons with experimental data, the measurements are taken as the reference data set. In the comparisons between the analytical method and PRIMO, the latter is taken as reference.

geometrical description of the Millennium 120 MLC is done according to the blueprints of the collimator. By following this approach and conducting an accurate transport of radiation through all the collimating and beam-modifying elements of the gantry, it is possible to reproduce the dose distributions conformed by the linac without resorting to non-physical parameters such as the dynamic leaf gap (26, 30, 31). The geometrical description of the MLC is a faithful model of the actual collimator.

PRIMO requires the user to define the characteristics of the pencil electron beam impinging in the bremsstrahlung target through four initial beam parameters, namely, the average energy of the electron beam ($\langle E \rangle$), the energy full-width at half-maximum (E_{FWHM}), the beam divergence (α), and the FWHM of the circular spot size (r_{FWHM}). These values are found through a trial-and-error process in which the experimental depth dose and lateral profiles for a 40×40 -cm² field irradiating a water phantom are compared with the simulated results for a given set of parameters. The initial beam parameters finally chosen for all IMRT and VMAT simulations were $\langle E \rangle = 6.180$ MeV, $E_{FWHM} = 0.125$ MeV, $\alpha = 0.000^\circ$, and $r_{FWHM} = 0.175$ cm. With these parameters, simulations of the linac irradiating fields of 40×40 cm², 20×20 cm², 10×10 cm², and 2×2 cm² were conducted. The simulated dose profiles in a water phantom were compared to the corresponding experimental profiles *via* the gamma index. The gamma criteria for the evaluations were set to 1%/1 mm. The obtained gamma pass rates were, in all cases, better than 98 and 93% for depth doses and lateral profiles, respectively. When the gamma criteria were relaxed to 2%/2 mm, the gamma pass rates were 100% for all profiles and fields.

PENELOPE and, hence, PRIMO require the user to define a set of radiation transport parameters. The transport parameters C_1 and C_2 were set to 0.02. C_1 determines the mean free path for hard elastic collisions and the cutoff angle to classify elastic events into hard and soft categories. The maximum fractional energy loss allowed within a single step is regulated by the parameter C_2 . The cutoff energies W_{cc} and W_{cr} define the cutoff value for energy losses in inelastic collisions and the cutoff value for bremsstrahlung emission, respectively. For W_{cc} and W_{cr} , the PRIMO default values were kept (both set to 0.2 MeV) (25, 32, 33).

PRIMO allows to tally phase-space files (PSF) at the downstream end of the patient-independent part of the linac, that is, just above the movable jaws. The simulation of the patient-independent part is done with the PENELOPE engine. A sufficiently rich PSF, containing W_{cc} and W_{cr} histories, was tallied using the chosen initial beam parameters and subsequently employed for all other simulations. The variance-reduction technique of splitting roulette was applied for tallying the PSF (34). The variance-reduction technique of movable skins was applied to all beam-facing surfaces of the linac (35).

DPM was used for the simulation of the radiation transport in the CT of the ATOM phantom. The same CT that was employed for the analytical method was used for the Monte Carlo simulation. The same contoured anatomical structures and contoured TLD positions were also used. For the simulation, the actual chemical composition of the materials used in ATOM,

as provided by the manufacturer, was employed. The calibration curve of the CT scanner employed for obtaining the CT image of ATOM was used in PRIMO for converting Hounsfield units to mass density values. It was checked that the yielded density values corresponded to the nominal mass densities reported by the manufacturer of ATOM for each material. Each TLD contour was filled with water in the same way as it was done for the analytical algorithm. PRIMO reports the absorbed dose as dose to medium, which, in the case of the TLDs, was dose to water because the contoured structure enclosing each TLD was filled with water.

The variance-reduction technique of splitting was applied in all simulations starting from the tallied PSF, with a splitting factor of 1,024. This value was chosen by means of a series of preliminary simulations in which the splitting factor was varied, and the simulation efficiency was studied. It was found adequate for not reaching the latent variance of the PSF (36). An Intel(R) Xeon(R) CPU E5-1670 v3 @2.30 GHz (2 processors) with 64-GB RAM was used. All simulations were executed employing 24 logical threads each.

3 RESULTS

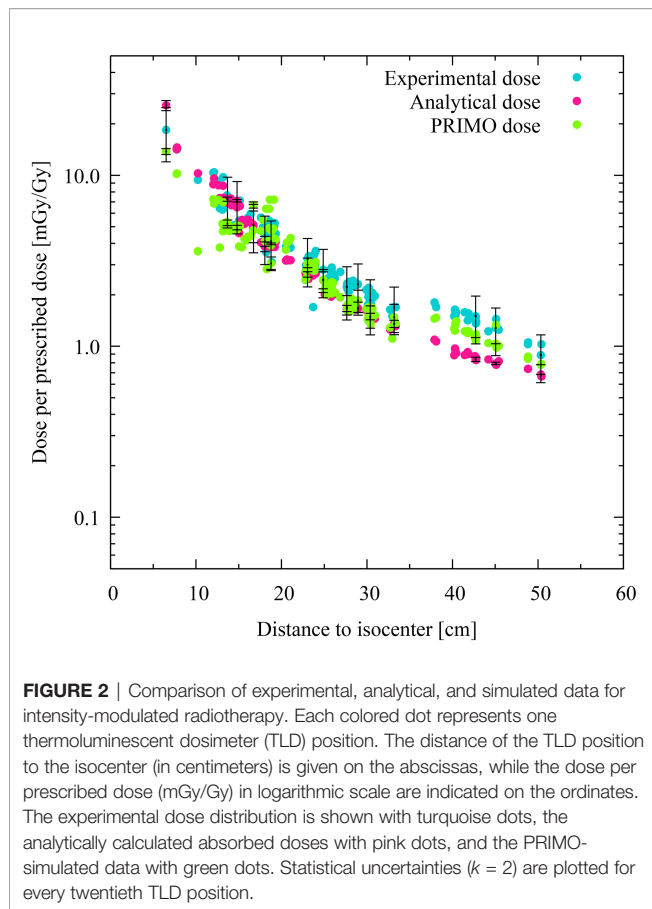
3.1 Comparison of the Computational Methods With the Experiment

The Monte Carlo simulation results reached an average standard statistical uncertainty of less than 0.2% ($k = 1$) on all voxels scoring more than 50% of the maximum dose. The absolute standard statistical uncertainty of out-of-field voxels did not exceed 5%. The simulations of the patient-dependent part of the linac and the CT for IMRT and VMAT took about 7 and 9 days, respectively. These exceedingly long simulation times were required in order to reach the low statistical uncertainty in the voxels located far from the PTV.

The doses computed at each TLD position of the phantom using the analytical model and the PRIMO simulation are plotted, together with the corresponding experimental data, for the IMRT and VMAT irradiations in **Figures 2, 3**, respectively. The absorbed doses are presented as a function of the distance to the isocenter.

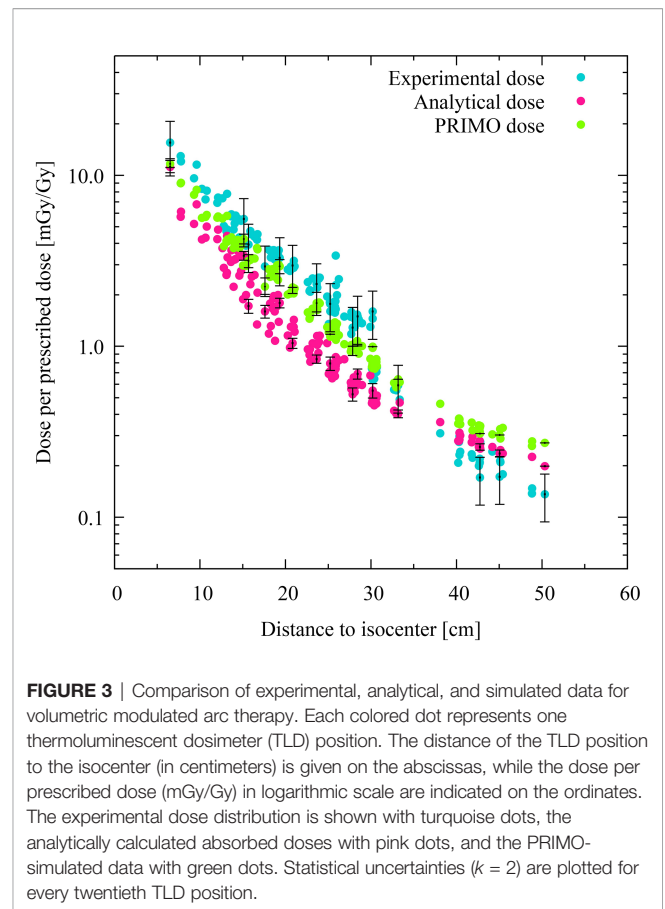
For the IMRT case, the experimental, analytical, and PRIMO results are compatible within the uncertainty ($k = 2$) in the penumbra and out-of-field regions. In the far out-of-field region, the PRIMO results are compatible with the experimental ones, but the analytical results show a statistically significant deviation from the other two sets of data. The average deviation of the analytical data from the experimental values in the far out-of-field region is of -38% (see **Table 3**).

The discrepancies between the analytical results and the experimental dose are more noticeable in the case of the VMAT irradiation, in which most of the TLD measurements produce results that are not compatible with the analytical data. The average discrepancies between these two data sets are -44% and -48% in the penumbra and the out-of-field region, respectively. The average discrepancy reduces to 10% in the far



out-of-field region, although the results are still not compatible. The PRIMO computed results and measurements are compatible within the uncertainty ($k = 2$) for most of the TLD positions in the penumbra and out-of-field region, with average discrepancies of -27% and -20% . However, in the far out-of-field region, the average discrepancies between PRIMO data and experimental data (42%) are larger than those found between the analytical data and the experimental data (10%). In all comparisons with the experimental data, the experiment has been taken as the reference data set. In the comparisons between the analytical results and the PRIMO data, the latter is the reference data set (see **Table 3**).

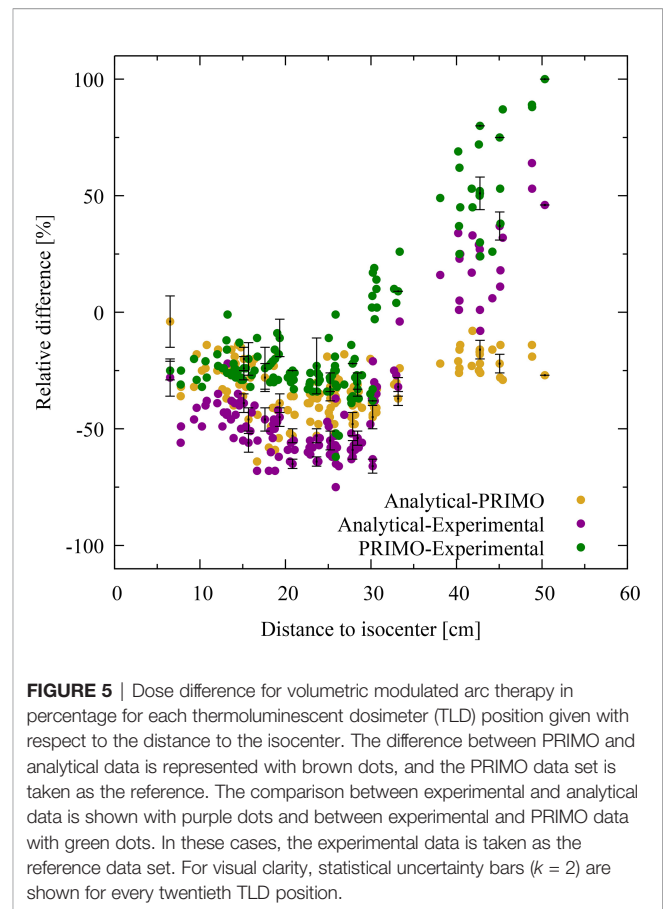
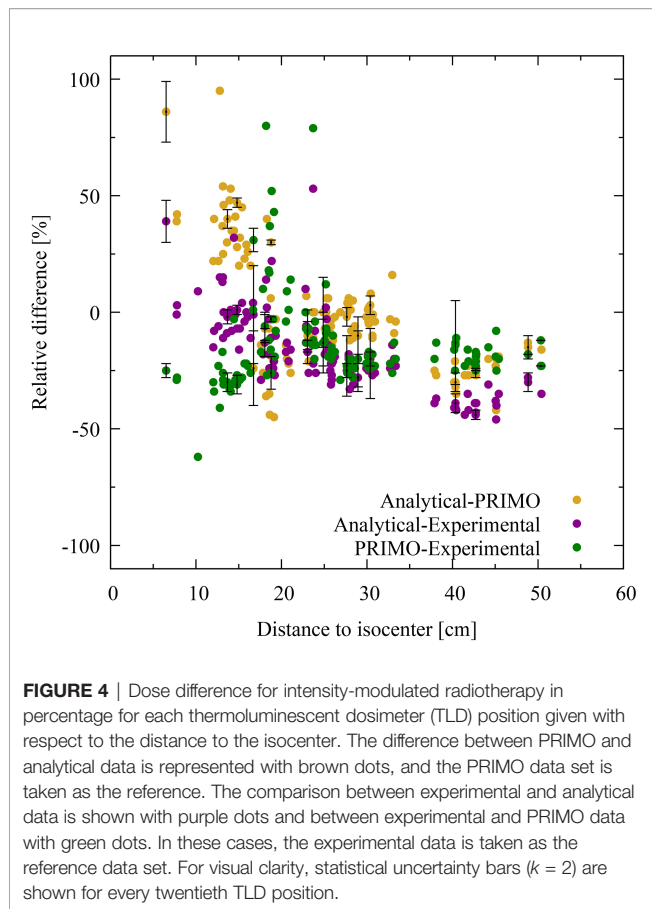
Figures 4, 5 show the relative dose difference between the distributions in percentage for each TLD position, with respect to the distance to the isocenter, for the IMRT and VMAT irradiations, respectively. The distance of the TLD position to the isocenter in centimeters is given on the abscissas and the dose difference in percentage is given on the ordinates. **Figure 4**, for the IMRT irradiation, shows that the highest discrepancies appear in the lung region at distances of about 20 cm, with the PRIMO dose being higher than the analytical and the experimental dose. In **Figure 5**, for the VMAT treatment, the largest differences between the three data sets (experimental, analytical, and Monte Carlo) can be observed for TLD locations most far from the treated volume at a distance of 40 to 50 cm.



3.2 Comparison Between IMRT and VMAT

The IMRT and VMAT modalities can be compared for the given PTV and treatment plan objectives (see Section 2.1.1). **Figure 6** shows the organ dose comparison of IMRT and VMAT for the experimental data. The comparison of the two modalities is presented only through the experimental data since the comparisons obtained through the Monte Carlo or the analytical data yield similar results and the same conclusions. The statistical uncertainties in **Figure 6** are plotted with a coverage factor of $k = 2$. The experimental uncertainties include the positional uncertainty of 2 mm within the hole, which was taken into account by means of the PRIMO computed dose. Each dot in the plot corresponds to a TLD position. The dose per prescribed dose at the PTV is given in mGy/Gy. The thyroid shows the larger dose, with values of around 15 mGy/Gy.

For all organs, both techniques yield dose values that are similar. However, a clearer picture can be seen if the dose values are plotted as a function to the distance to the isocenter. This is done in **Figure 7**, where the absorbed doses of each TLD position for IMRT and VMAT are plotted in logarithmic scale. It becomes evident that, for positions in the far out-of-field region, IMRT yields an absorbed dose which is about one order of magnitude higher than that from VMAT. The experimental data from both modalities are only compatible in parts of the penumbra and the out-of-field region. The IMRT modality produces an absorbed dose systematically higher than VMAT.



4 DISCUSSION

Overall, the two computed distributions feature an acceptable level of agreement with the experimental data for out-of-field considerations and epidemiological concerns considering the limitations of the dose comparison.

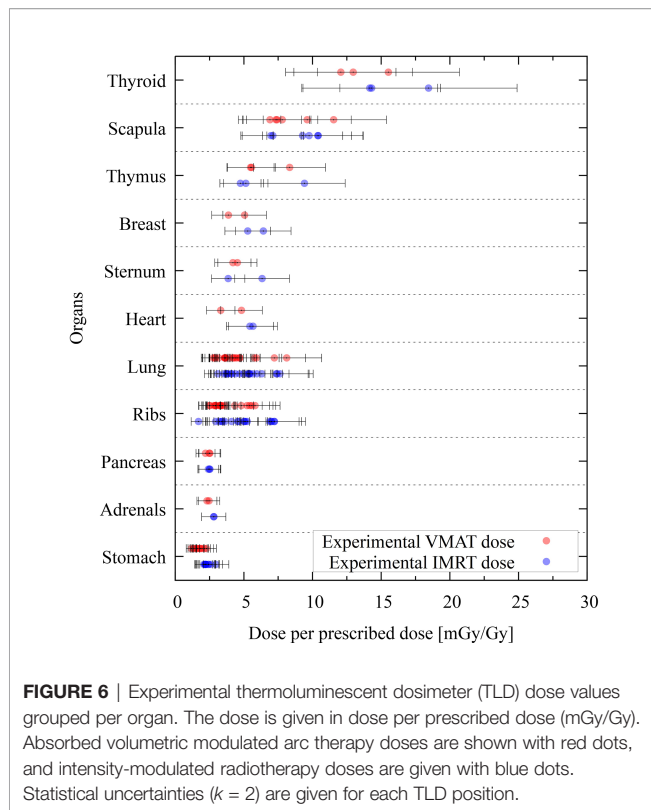
4.1 Evaluation of PRIMO for Out-of-Field Doses

In general, PRIMO simulations revealed the best agreement to experimental data. It is important to bear in mind that the Monte Carlo Package produced by Varian has the scope of providing researchers with the minimum necessary information for conducting Monte Carlo simulations aimed at reproducing the in-field dose distribution. Concurrently, PRIMO was designed as a dose verification system for radiotherapy, and therefore no specific methods for trying to circumvent the lack of geometrical information on the shielding of the linac have been devised. Still this is the first time PRIMO is used for modeling out-of-field doses, and the results are very promising given the limitations on the geometrical information related to those parts of the linac that have a significant contribution to the stray dose. In general, the agreement reached with the experimental dataset is acceptable and promising for the intended epidemiological studies on second primary cancer. Nevertheless, some discrepancies are observed—for example, during IMRT, the

lung dose was higher in PRIMO. Even though PRIMO modeled the lung tissue according to ATOM lung material, the discrepancy could come from TLDs being filled with water (as TLD dose is reported in dose-to-water) instead of LiF. During VMAT, PRIMO doses were compatible except in far out-of-field positions where both analytical and PRIMO doses were significantly higher. This could be explained by the fact that models are not fully correct for far out-of-field positions. In the case of PRIMO, the geometrical description of the linac only includes the parts provided by the manufacturer in the Monte Carlo documentation. The description of the shielding is not provided by the manufacturer, and therefore it is not simulated. The lack of these parts in the Monte Carlo simulation geometry certainly has an influence on the computed stray dose. Moreover, PRIMO does not model all the rooms, and the presence of additional equipment during the experiment is not included in the modeling.

4.2 Analytical Model for Out-of-Field Doses

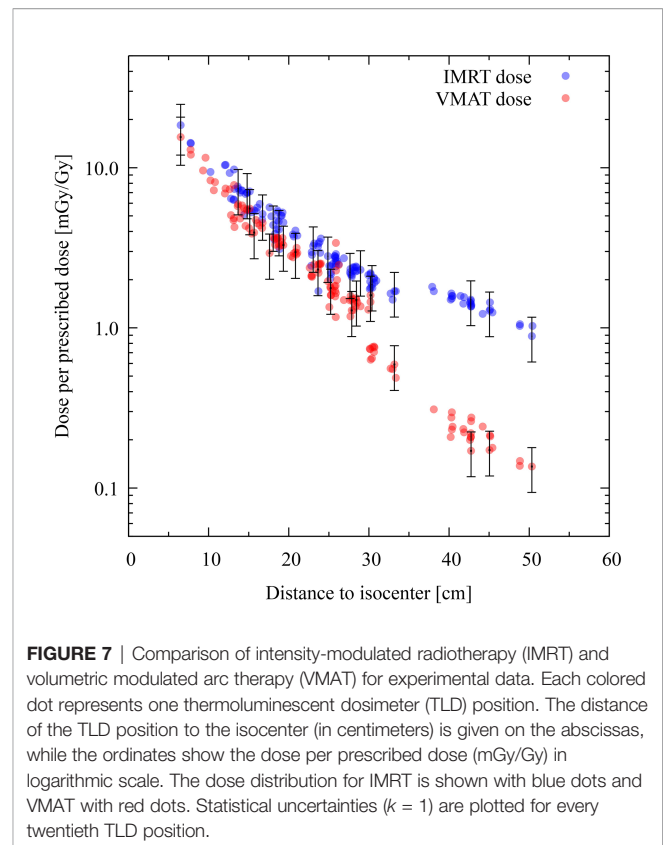
In general, analytical doses underestimate the dose when compared to the experimental and PRIMO doses. This is observed for both IMRT and VMAT. One explanation could come from the fact that the analytical model does not model ATOM materials, but uses water in all tissues, except air in lungs. Therefore, no bone which could explain the lower doses measured in and around bony



structures (1.52 g/cm^3) is modeled. Furthermore, in the case of lung tissue, air is used, which has a lower density than ATOM lung material (0.21 g/cm^3). The ATOM materials in soft tissue and brain also have slightly higher densities than water at 1.05 and 1.07 g/cm^3 , respectively. Moreover, the analytical method uses, as input for setting up its parameters, dose measurements obtained for specific gantry angles far from the field. It is therefore logical that the lowest average discrepancy observed in the far out-of-field region, with respect to the experimental data, was accountable to the analytical method in the VMAT modality, in which the influence of specific gantry angles is averaged out.

4.3 Uncertainties Related to TLD Experimental Data

Positioning uncertainties in the experiment can originate either from the phantom alignment for the irradiation or from filling the TLDs in the organ hole locations of the phantom. The phantom is only aligned by laser marks and not with X-ray control to avoid additional radiation exposure contributing to the TLD dose. The disclaimer of X-ray control is necessary to provide a reasonable comparison between experimental data and analytical or PRIMO data, but the accuracy of the phantom alignment is limited. The impact of positioning uncertainties is larger for in-field and penumbra TLD positions surrounded by larger dose gradients than for TLD positions located far from the treated volume. Another limitation is the uncertainty related to the energy dependence of TLD detectors. The MCP-N type demonstrates a decrease in the relative air kerma response with the decrease of the photon energy down to a local minimum of



approximately 0.8 for a photon energy of around 100 keV (17). It has been described in the study from (21) that the beam is softening out-of-field. This study shows a reduced average photon energy of around 200 keV far from the treatment field (at 50 cm off-axis). The mean photon energy, described for open fields and IMRT fields, was dependent on the out-of-field position and also dependent on the field size and tissue heterogeneity. For this reason, it was not possible to use these literature data to correct for the energy dependence of MCP-N detectors, but a calculated uncertainty on the energy dependence based on these literature data, which was on average 15% , was employed instead. The input from simulations to correct experimental data should be handled with caution as experimental data will not be independent from the simulations.

4.4 IMRT Versus VMAT and Comparison to Published Data

The current study revealed that VMAT irradiation produces results in the smallest out-of-the-field doses when compared to IMRT. Nevertheless, the comparison of different techniques in this study is based on the current practice from the hospital, which makes it difficult to generalize. Indeed results are not only technique dependent but also center dependent, as data might be different if different objectives and constraints are used in the dose optimization algorithms. Previously published experimental data, performed in the same anthropomorphic phantom, also reported on reduced out-of-field doses for VMAT when compared to 3D-CRT (13) for CSI. During brain treatment, the difference between

3D-CRT and IMRT has been shown to be small when not using a mechanical wedge (12). This latter paper reports on out-of-field doses during brain radiotherapy, where the brain tumor was represented by a sphere of diameter 5 cm (planning target volume diameter = 6 cm) located on the left-anterior side of the head (total volume, 113 cm³). In the current study, the PTV, which was located in the cerebellum, had a volume of 195.2 cm³, so it was slightly larger when compared to the previous study (12). The thyroid doses reported for the 5-year-old phantom was 8.2 mGy/Gy for 3D-CRT, while IMRT resulted in 3.4 mGy/Gy. In our study, the thyroid dose in both modalities is about 15 mGy/Gy (see **Figure 6**). When looking into breast dose, published data showed 3 and 2.6 mGy/Gy for 3D-CRT and IMRT, respectively, while our study revealed doses of 7 and 5 mGy/Gy for IMRT and VMAT, respectively. This comparison reveals an elevated dose in the current study, which can be expected from the increased size of the tumor as well as the different position in the brain. In the published study, the location of the tumor was more cranial (isocenter in slice 3) when compared to our study (isocenter is slice 6). As a result, the organs were closer to the isocenter in our study when compared to (12)—for example, the distance from the isocenter to the thyroid was 7.1 cm in this study *versus* 13.5 cm in (12). When looking into the dose as a function of distance, we can compare our study to the one previously published describing a descriptive and broadly applicable model for stray absorbed dose calculations (37). The model was validated with experimental data using 3D-CRT and for a field size of 10 × 10 cm² at various locations. The modeled doses ranged between 15 mGy/Gy (12 cm) and 0.75 mGy/Gy at 50 cm. The modeled data was underestimated, thus matching nicely the experimental data. These data are comparable to our data (see **Figure 7**). Furthermore, out-of-field doses for different treatment techniques were modeled and, in general, revealed highest doses for Cyberknife, followed by IMRT techniques, while VMAT and Tomotherapy techniques revealed lower doses (37). This is also in line with our study.

4.5 Impact on Risk and Epidemiological Studies

Tubiana et al. and Xu et al. have shown that pediatric second primary thyroid cancers are observed following doses as low as 100 mGy (4, 7). Thyroid cancer is the second most frequent second cancer in children associated with a decreasing risk for increasing age at irradiation date and with an increased tendency for female survivors (4, 5). Greater radiation effects for younger children originate from rapid cell proliferation during the development of the thyroid gland (4). Second primary thyroid cancer is recorded after radiation therapy for several primary cancers, including brain tumors (5). The thyroid is located in proximity to the brain, and the results show the thyroid being the organ with the highest absorbed dose outside the field edge. The presented absorbed dose of the thyroid in both modalities is about 15 mGy/Gy (see **Figure 6**). In clinical situations for the studied malignancy, it is common to prescribe 28 fractions of 1.8 Gy, for a total of 50.4 Gy. In a situation like this, the thyroid would receive a cumulative dose of about 750 mGy, widely exceeding the aforementioned 100-mGy value.

Besides an increased risk for thyroid cancer, subsequent secondary primary malignancies of breast, bone, soft tissue, and central nervous system following radiation treatment for childhood cancer have been reported (4, 5). A report from the childhood cancer survivor study relates radiation doses to the skin of more than 1 Gy with an increased risk for basal cell carcinomas (38). The childhood cancer survivor study is a multi-institutional retrospective study analyzing over 14,000 cases of childhood cancer (4). The study also found incidence for second primary neoplasms in survivors of childhood cancer for all primary diagnoses (39, 40). The highest risk for second neoplasms is within 10 years immediately after the first treatment (41). Olsen *et al.* reported that pediatric cancer survivors have a high risk for second malignant neoplasms in the central nervous system, thyroid, and bone (41). The risk to develop neoplasms in the liver, testes, pharynx, intestine, pancreas, and female breast is also higher than in the general population (41). For the lung, uterus, prostate, kidney, and bladder, the risk estimates are close to the risk for the general population (41). Bone sarcoma following childhood cancer are not as frequent as subsequent thyroid cancer but highly fatal (42).

Considerable excess relative risk for stomach cancer was found based on absorbed stomach doses greater than 1 Gy (4). Considering the total dose of 50.4 Gy in the studied treatment, the dose to the stomach would be, for both modalities, around 150 mGy, well below the cited threshold. This is not the case for breast cancer. In the present study, the dose to the breast was found to be about 250 mGy, a value close to 0.5 Gy as found by (4), in which an increased risk appears. Regarding lung cancer, the dose obtained herein is about 300 mGy, while according to (4), lung cancer might occur as a result of radiation therapy after the lungs received scattered doses of around 0.75 Gy. The absorbed doses to the out-of-field organs found in the present study range from 50 mGy (lowest dose in the stomach) to 1 Gy (largest dose in the thyroid). This range is in agreement with that stated by (43) between 10 mGy and 60 Gy for out-of-field organs.

5 CONCLUSION

The proposed computational methods for the calculation of the out-of-field and far out-of-field dose in IMRT and VMAT irradiations produce out-of-field absorbed dose distributions that are adequate for conducting epidemiological studies on radiation-induced second primary cancers. Although PRIMO has been extensively tested as a dose verification system, this is the first time in which the code has been benchmarked against experimental data for far out-of-field absorbed dose distributions. In the case of the analytic model, this is also the first benchmark in which experimental data obtained from measurements on an anthropomorphic phantom have been used. Although there is still room for improvement in both codes, they have shown that they are capable of computing the far out-of-field dose distribution with the accuracy required for epidemiological studies addressed to develop second primary

cancer models. Treatment plan optimization taking into account second primary cancer probabilities is an emerging area that is increasingly gaining importance.

The comparison of the out-of-field dose for a given set of planning objectives reveals that the VMAT irradiation produces an out-of-field absorbed dose distribution of up to one order of magnitude lower than IMRT. This phenomenon is known, and it is explained by the geometrical differences in dose delivery between the two techniques and the higher MUs associated to the IMRT treatments with a consequent increment of photon scattering in the MLC. This is a relevant fact when considering the thyroid, which has been identified as an organ with an elevated risk of radiation-induced second primary cancer in brain irradiation of young patients. It is therefore worthy to remark that, despite other elements that must be considered in making a decision, e.g., the irradiated volume, the lower out-of-field dose to proximal organs produced by VMAT strongly supports it as the modality of choice in cases when radiation-induced second primary cancer is a chief concern.

DATA AVAILABILITY STATEMENT

The raw data supporting the conclusions of this article will be made available by the authors without undue reservation.

AUTHOR CONTRIBUTIONS

MS-H: experimental design, experimental setup, data analysis, and writing of the manuscript. FSu Monte Carlo simulation

design, setup and execution, data analysis, and writing of the manuscript. FV: analytical simulation design, setup and execution, data analysis, and writing of the manuscript. FSt experimental setup, writing and review of the manuscript, and Monte Carlo data analysis. MR: Monte Carlo simulation setup, Monte Carlo and analytical data analysis, and writing and review of the manuscript. JD: experimental design and analysis. BT: clinical analysis, writing and review of the manuscript, and methodology. IT-C: epidemiological review, writing and review of the manuscript, and methodology. US: analytical simulation setup, analysis, writing and review of the manuscript, and methodology. LB: conceptualization, supervision, writing of the manuscript, data analysis, and review of the manuscript. All authors contributed to the article and approved the submitted version.

FUNDING

The presented research has been funded by the HARMONIC project. The HARMONIC project (Health effects of cArdiac fluoRoscopy and MODerN radIotherapy in paediatricCs) has received funding from the Euratom research and training programme 2014-2018 under grant agreement number 847707. MR acknowledges funding from the Sistema Nacional de Investigación de Panamá. ITC acknowledges support from the Spanish Ministry of Science and Innovation and State Research Agency through the “Centro de Excelencia Severo Ochoa 2019-2023” Program (CEX2018-000806-S) and support from the Generalitat de Catalunya through the CERCA Program.

REFERENCES

- Howell RM. Second Primary Cancers and Cardiovascular Disease After Radiation Therapy. *NCRP Report No 170 Med Phys* (2012) 39:7729–31. doi: 10.1118/1.4765651
- Taddei PJ, Jalbout W, Howell RM, Khater N, Geara F, Homann K, et al. Analytical Model for Out-of-Field Dose in Photon Craniospinal Irradiation. *Phys Med Biol* (2013) 58:7463. doi: 10.1088/0031-9155/58/21/7463
- Fry SF, Bednarz B, Howell RM, Dauer L, Followill D, Klein E, et al. AAPM TG 158: Measurement and Calculation of Doses Outside the Treated Volume From External-Beam Radiation Therapy. *Med Phys* (2017) 44:391–429. doi: 10.1002/mp.12462
- Xu GX, Bednarz B, Paganetti H. A Review of Dosimetry Studies on External-Beam Radiation Treatment With Respect to Second Cancer Induction. *Phys Med Biol* (2008) 54:1–58. doi: 10.1088/0031-9155/53/13/R01
- Bhatia S, Landier W. Evaluating Survivors of Pediatric Cancer. *Cancer J* (2005) 11:340–54. doi: 10.1097/00130404-200507000-00010
- National Academy of Science. *Health Risks From Exposure to Low Levels of Ionizing Radiation: BEIR VII PHASE 2*. Washington DC: The National Academies Press (2006).
- Tubiana M. Can We Reduce the Incidence of Second Primary Malignancies Occurring After Radiotherapy? *A Crit Review Radiother Oncol* (2009) 91:4–15. doi: 10.1016/j.radonc.2008.12.016
- Bhakta N, Liu Q, Ness KK, Baassiri M, Eissa H, Yeo F, et al. The Cumulative Burden of Surviving Childhood Cancer: An Initial Report From the St Jude Lifetime Cohort Study (SJLIFE). *Lancet* (2017) 390:2569–82. doi: 10.1016/S0140-6736(17)31610-0
- Norsker FN, Pedersen C, Armstrong GT, Robison LL, McBride ML, Hawkins M, et al. Late Effects in Childhood Cancer Survivors: Early Studies, Survivor Cohorts, and Significant Contributions to the Field of Late Effects. *Pediatr Clin* (2020) 67:1033–49. doi: 10.1016/j.pcl.2020.07.002
- Kang DJ, Shin YJ, Jeong S, Jung JY, Lee H, Lee B. Development of Clinical Application Program for Radiotherapy Induced Cancer Risk Calculation Using Monte Carlo Engine in Volumetric-Modulated Arc Therapy. *Radiat Oncol* (2021) 108:1–11. doi: 10.1186/s13014-020-01722-0
- Howell RM, Scarboro SB, Kry SF, Yaldo DZ. Accuracy of Out-of-Field Dose Calculations by a Commercial Treatment Planning System. *Phys Med Biol* (2010) 55:2–12. doi: 10.1088/0031-9155/55/23/S03
- Majer M, Stolarczyk L, De Saint-Hubert M, Kabat D, Knezevic Z, Miljanic S, et al. Out-Of-Field Dose Measurements for a 3D Conformal and Intensity Modulated Radiotherapy of a Pediatric Brain Tumor. *Radiat Prot Dosim* (2017) 176:331–40. doi: 10.1093/rpd/ncx015
- Majer M, Ambrožová I, Davidková M, De Saint-Hubert M, Kasabašić M, Knezevic Z, et al. Out-Of-Field Doses in Pediatric Craniospinal Irradiations With 3D-CRT, VMAT, and Scanning Proton Radiotherapy: A Phantom Study. *Med Phys* (2022) 49:2672–83. doi: 10.1002/mp.15493
- De Saint-Hubert M, Verellen D, Poels K, Crijns W, Magliona F, Depuydt T, et al. Out-Of-Field Doses From Pediatric Craniospinal Irradiations Using 3D-CRT, IMRT, Helical Tomotherapy and Electron-Based Therapy. *Phys Med Biol* (2017) 62:5293–311. doi: 10.1088/1361-6560/aa6c9e
- Hauri P, Hälgl RA, Besserer J, Schneider U. A General Model for Stray Dose Calculation of Static and Intensity-Modulated Photon Radiation. *Med Phys* (2016) 43:1955–68. doi: 10.1118/1.4944421

16. Hauri P, Radonic S, Vasi F, Ernst M, Sumila M, Mille MM, et al. Development of Whole-Body Representation and Dose Calculation in a Commercial Treatment Planning System. *Z Med Phys* (2022) 32:159–172. doi: 10.1016/j.zemedi.2021.05.001
17. Parisi A, Dabin J, Schoonjans W, Van Hoey O, Mégret P, Vanhavere F. Photon Energy Response of LiF : Mg,Ti (MTS) and LiF : Mg,Cu,P (MCP) Thermoluminescent Detectors: Experimental Measurements and Microdosimetric Modeling. *Radiat Phys Chem* (2019) 163:67–73. doi: 10.1016/j.radphyschem.2019.05.021
18. Hubbell JH, Seltzer SM. X-Ray Mass Attenuation Coefficients. *NIST Standard Reference Database 126*. Gaithersburg, MD, United States of America: National Institute of Standards and Technology (2004). doi: 10.18434/T4D01F.
19. De Saint-Hubert M, De Angelis C, Knezevic Z, Michalec B, Reniers B, Pyska E, et al. Characterization of Passive Dosimeters in Proton Pencil Beam Scanning—A EURADOS Intercomparison for Mailed Dosimetry Audits in Proton Therapy Centres. *Phys Med* (2021) 82:134–43. doi: 10.1016/j.ejmp.2021.01.073
20. Krzanovic N, Valentin B, Ciraj-Bjelac O, Johann P, Werner S, Zivanovic M, et al. Performance Testing of Dosimeters Used in Interventional Radiology: Results From the Veridic Project. *Radiat Meas* (2021) 141:106515. doi: 10.1016/j.radmeas.2021.106515
21. Scarboro SB, Followill DS, Howell RM, Kry SF. Variations in Photon Energy Spectra of a 6 MV Beam and Their Impact on TLD Response. *Med Phys* (2011) 38:2619–28. doi: 10.1118/1.3575419
22. Sánchez-Nieto B, El-far R, Irazola L, Romero-Expósito M, Lagares JI, Mateo JC, et al. Analytical Model for Photon Peripheral Dose Estimation in Radiotherapy Treatments. *Biomed Phys Eng Exp* (2015) 1:45205. doi: 10.1088/2057-1976/1/4/045205
23. van der Giessen PH. Peridose, a Software Program to Calculate the Dose Outside the Primary Beam in Radiation Therapy. *Radiother Oncol* (2001) 58:209–13. doi: 10.1016/S0167-8140(00)00326-1
24. Sempau J, Wilderman SJ, Bielajew AF. DPM, a Fast, Accurate Monte Carlo Code Optimized for Photon and Electron Radiotherapy Treatment Planning Dose Calculations. *Phys Med Biol* (2000) 45:2263–91. doi: 10.1088/0031-9155/45/8/315
25. Brualla L, Rodriguez M, Sempau J. *PRIMO User's Manual (PRIMO Project)*. (2019). Available at: <https://www.primoproject.net>.
26. Hermida-López M, Sánchez-Artuñedo D, Calvo-Ortega JF. PRIMO Monte Carlo Software Benchmark Against Reference Dosimetry Dataset for 6 MV Photon Beams From Varian Linacs. *Radiat Oncol* (2018) 144:1–10. doi: 10.1186/s13014-018-1076-0
27. Rodriguez M, Sempau J, Bäumer C, Timmermann B, Brualla L. DPM as a Radiation Transport Engine for PRIMO. *Radiat Oncol* (2018) 256:1–9. doi: 10.1186/s13014-018-1188-6
28. Rodriguez M, Brualla L. Many-Integrated Core (MIC) Technology for Accelerating Monte Carlo Simulation of Radiation Transport: A Study Based on the Code DPM. *Comput Phys Commun* (2018) 225:28–35. doi: 10.1016/j.cpc.2017.12.019
29. Chibani O, Ma CMC. On the Discrepancies Between Monte Carlo Dose Calculations and Measurements for the 18 MV Varian Photon Beam. *Med Phys* (2007) 34:1206–16. doi: 10.1118/1.2712414
30. Lloyd SA, Gagne IM, Bazalova-Carter M, Zavgorodni S. Validation of Varian TrueBeam Electron Phase-Spaces for Monte Carlo Simulation of MLC-Shaped Fields. *Med Phys* (2016) 43:2894–903. doi: 10.1118/1.4949000
31. Paganini L, Reggiori G, Stravato A, Palumbo V, Mancosu P, Lobefalo F, et al. MLC Parameters From Static Fields to VMAT Plans: An Evaluation in a RT-Dedicated MC Environment (PRIMO). *Radiat Oncol* (2019) 14:1–13. doi: 10.1186/s13014-019-1421-y
32. Salvat F. *PENELOPE, a Code System for Monte Carlo Simulation of Electron and Photon Transport*. Barcelona: Organisation for Economic Co-operation and Development (2019).
33. Rodriguez M, Sempau J, Brualla L. Technical Note: Study of the Electron Transport Parameters Used in PENELOPE for the Monte Carlo Simulation of Linac Targets. *Med Phys* (2015) 42:2877–81. doi: 10.1118/1.4916686
34. Rodriguez M, Sempau J, Brualla L. A Combined Approach of Variance-Reduction Techniques for the Efficient Monte Carlo Simulation of Linacs. *Phys Med Biol* (2012) 57:3013–24. doi: 10.1088/0031-9155/57/10/3013
35. Brualla L, Salvat F, Palanco-Zamora R. Efficient Monte Carlo Simulation of Multileaf Collimators Using Geometry-Related Variance-Reduction Techniques. *Phys Med Biol* (2009) 54:4131–49. doi: 10.1088/0031-9155/54/13/011
36. Sempau J, Sánchez-Reyes A, Salvat F, Ben Tahar HO, Jiang SB, Fernández-Varea JM. Monte Carlo Simulation of Electron Beams From an Accelerator Head Using PENELOPE. *Phys Med Biol* (2001) 46:1163–86. doi: 10.1088/0031-9155/46/4/318
37. Schneider CW, Newhauser W, Wilson LJ, Schneider U, Kadérka R, Miljanić S, et al. A Descriptive and Broadly Applicable Model of Therapeutic and Stray Absorbed Dose From 6 to 25 MV Photon Beams. *Med Phys* (2017) 44:3805–14. doi: 10.1002/mp.12286
38. Watt TC, Inskip PD, Stratton K, Smith SA, Kry SF, Sigurdson AJ, et al. Radiation-Related Risk of Basal Cell Carcinoma: A Report From the Childhood Cancer Survivor Study. *J Nat Cancer Inst* (2012) 104:1240–50. doi: 10.1093/jnci/djs298
39. Neglia JP, Robison LL, Stovall M, Liu Y, Packer RJ, Hammond S, et al. New Primary Neoplasms of the Central Nervous System in Survivors of Childhood Cancer: A Report From the Childhood Cancer Survivor Study. *J Nat Cancer Inst* (2006) 98:1528–37. doi: 10.1093/jnci/djj411
40. Friedman DL, Whitton J, Leisenring W, Mertens AC, Hammond S, Stovall M, et al. Subsequent Neoplasms in 5-Year Survivors of Childhood Cancer: The Childhood Cancer Survivor Study. *J Nat Cancer Inst* (2010) 102:1083–95. doi: 10.1093/jnci/djq238
41. Olsen JH, Garwicz S, Hertz H, Jonmundsson G, Langmark F, Lanning M, et al. Second Malignant Neoplasms After Cancer in Childhood or Adolescence. *Br Med J* (1993) 307:1030–6. doi: 10.1136/bmj.307.6911.1030
42. Schwartz B, Benadjaoud MA, Cléro E, Haddy N, El-Fayech C, Guibout C, et al. Risk of Second Bone Sarcoma Following Childhood Cancer: Role of Radiation Therapy Treatment. *Radiat Environ Biophys* (2014) 53:381–90. doi: 10.1007/s00411-013-0510-9
43. Harrison R. Out-Of-Field Doses in Radiotherapy: Input to Epidemiological Studies and Dose-Risk Models. *Phys Med* (2017) 42:239–46. doi: 10.1016/j.ejmp.2017.02.001

Conflict of Interest: The authors declare that the research was conducted in the absence of any commercial or financial relationships that could be construed as a potential conflict of interest.

Publisher's Note: All claims expressed in this article are solely those of the authors and do not necessarily represent those of their affiliated organizations, or those of the publisher, the editors and the reviewers. Any product that may be evaluated in this article, or claim that may be made by its manufacturer, is not guaranteed or endorsed by the publisher.

Copyright © 2022 De Saint-Hubert, Suesselbeck, Vasi, Stuckmann, Rodriguez, Dabin, Timmermann, Thierry-Chef, Schneider and Brualla. This is an open-access article distributed under the terms of the Creative Commons Attribution License (CC BY). The use, distribution or reproduction in other forums is permitted, provided the original author(s) and the copyright owner(s) are credited and that the original publication in this journal is cited, in accordance with accepted academic practice. No use, distribution or reproduction is permitted which does not comply with these terms.



Neutron Radiation Dose Measurements in a Scanning Proton Therapy Room: Can Parents Remain Near Their Children During Treatment?

Vladimir Mares^{1*}, Jad Farah², Marijke De Saint-Hubert³, Szymon Domański⁴, Carles Domingo⁵, Martin Dommert¹, Magdalena Kłodowska⁶, Katarzyna Krzempek⁷, Michał Kuć⁴, Immaculada Martínez-Rovira⁵, Edyta Michaś⁴, Natalia Mojżeszek⁷, Łukasz Murawski⁴, Ondrej Ploc⁸, Maite Romero-Expósito⁹, Marco Tisi¹, François Trompier², Olivier Van Hoey³, Laurent Van Ryckeghem², Marek Wielunski¹, Roger M. Harrison¹⁰, Liliana Stolarczyk^{7,11} and Paweł Olko⁷

OPEN ACCESS

Edited by:

James Chow,
University of Toronto, Canada

Reviewed by:

Konrad P. Nesteruk,
Harvard Medical School, United States
Roberto Sakuraba,
Albert Einstein Israelite Hospital, Brazil

*Correspondence:

Vladimir Mares
mares@helmholtz-muenchen.de

Specialty section:

This article was submitted to
Radiation Oncology,
a section of the journal
Frontiers in Oncology

Received: 24 March 2022

Accepted: 16 May 2022

Published: 14 July 2022

Citation:

Mares V, Farah J, De Saint-Hubert M, Domański S, Domingo C, Dommert M, Kłodowska M, Krzempek K, Kuć M, Martínez-Rovira I, Michaś E, Mojżeszek N, Murawski Ł, Ploc O, Romero-Expósito M, Tisi M, Trompier F, Van Hoey O, Van Ryckeghem L, Wielunski M, Harrison RM, Stolarczyk L and Olko P (2022) Neutron Radiation Dose Measurements in a Scanning Proton Therapy Room: Can Parents Remain Near Their Children During Treatment? *Front. Oncol.* 12:903706. doi: 10.3389/fonc.2022.903706

¹ Helmholtz Zentrum München, Institute of Radiation Medicine, Neuherberg, Germany, ² Institut de Radioprotection et de Sûreté Nucléaire (IRSN), PSE-Santé, Fontenay-aux-Roses, France, ³ Belgian Nuclear Research Center, (SCK CEN), Institute for Environment, Health and Safety (EHS), Mol, Belgium, ⁴ National Centre for Nuclear Research, Radiological Metrology and Biomedical Physics Division, Otwock-Świerk, Poland, ⁵ Departament de Física, Universitat Autònoma de Barcelona, Bellaterra, Spain, ⁶ Cambridge University Hospital National Health Service (NHS) Trust, Medical Physics, Cambridge, United Kingdom, ⁷ Institute of Nuclear Physics, Polish Academy of Sciences, (IFJ PAN), Krakow, Poland, ⁸ Department of Radiation Dosimetry, Nuclear Physics Institute of the Czech Academy of Sciences (CAS), Prague, Czechia, ⁹ The Skandion Clinic, Uppsala, Sweden, ¹⁰ Faculty of Medical Sciences, University of Newcastle upon Tyne, Newcastle upon Tyne, United Kingdom, ¹¹ Danish Centre for Particle Therapy, Aarhus University Hospital (AUH), Aarhus, Denmark

Purpose: This study aims to characterize the neutron radiation field inside a scanning proton therapy treatment room including the impact of different pediatric patient sizes.

Materials and Methods: Working Group 9 of the European Radiation Dosimetry Group (EURADOS) has performed a comprehensive measurement campaign to measure neutron ambient dose equivalent, $H^*(10)$, at eight different positions around 1-, 5-, and 10-year-old pediatric anthropomorphic phantoms irradiated with a simulated brain tumor treatment. Several active detector systems were used.

Results: The neutron dose mapping within the gantry room showed that $H^*(10)$ values significantly decreased with distance and angular deviation with respect to the beam axis. A maximum value of about 19.5 $\mu\text{Sv/Gy}$ was measured along the beam axis at 1 m from the isocenter for a 10-year-old pediatric phantom at 270° gantry angle. A minimum value of 0.1 $\mu\text{Sv/Gy}$ was measured at a distance of 2.25 m perpendicular to the beam axis for a 1-year-old pediatric phantom at 140° gantry angle. The $H^*(10)$ dependence on the size of the pediatric patient was observed. At 270° gantry position, the measured neutron $H^*(10)$ values for the 10-year-old pediatric phantom were up to 20% higher than those measured for the 5-year-old and up to 410% higher than for the 1-year-old phantom, respectively.

Conclusions: Using active neutron detectors, secondary neutron mapping was performed to characterize the neutron field generated during proton therapy of pediatric

patients. It is shown that the neutron ambient dose equivalent $H^*(10)$ significantly decreases with distance and angle with respect to the beam axis. It is reported that the total neutron exposure of a person staying at a position perpendicular to the beam axis at a distance greater than 2 m from the isocenter remains well below the dose limit of 1 mSv per year for the general public (recommended by the International Commission on Radiological Protection) during the entire treatment course with a target dose of up to 60 Gy. This comprehensive analysis is key for general neutron shielding issues, for example, the safe operation of anesthetic equipment. However, it also enables the evaluation of whether it is safe for parents to remain near their children during treatment to bring them comfort. Currently, radiation protection protocols prohibit the occupancy of the treatment room during beam delivery.

Keywords: scanning proton therapy, anthropomorphic pediatric phantom, secondary neutrons, active neutron monitors, ambient dose equivalent, clinical conditions

INTRODUCTION

In recent years, tremendous technical progress has enabled proton therapy facilities to become more compact and cost-effective. Their clinical applications have expanded beyond brain and eye tumors, and this has drastically increased the number of patients receiving such treatment worldwide (1). Stray neutron radiation inherent to proton therapy remains, however, a topic of concern for the protection of both patients, especially pediatric patients (higher sensitivity and longer life expectancy), and healthcare professionals (shielding design) (2–6).

Dose limits recommended by the International Commission on Radiological Protection (7) are specified in terms of the protection quantity effective dose, E . These limits ensure that individuals are not exposed to unnecessarily high doses and so are a fundamental component of radiation protection in most countries. This protection quantity—effective dose—is not measurable. This means that an operational quantity—ambient dose equivalent, $H^*(10)$ —is used instead as a conservative estimate of effective dose, E . Such an approach also applies for estimating stray radiation exposures in radiotherapy including proton and ion therapy. The limits are split into two groups, public and occupationally exposed workers. Within Europe for the public, the effective dose limit is 1 mSv/year (higher values are allowed in a single year if the average over 5 years is not above 1 mSv/year), while for the occupationally exposed workers, it is 20 mSv/year, averaged over defined periods of 5 years with no single year exceeding 50 mSv. In the U.S., the Nuclear Regulatory Commission (NRC) requires to limit the occupational exposure to 50 mSv per year. Dose limits do not apply to medical exposures; however, the concept of radiation protection is still relevant.

Many authors have used Monte Carlo (MC) simulations and/or experimental tools to determine and model stray neutrons in scattering and scanning proton therapy (8–12). In a continuous effort to assess neutron exposure in proton therapy, Working Group 9 of the European Radiation

Dosimetry Group (EURADOS WG9—Radiation dosimetry in radiotherapy) has performed a comprehensive intercomparison exercise to estimate neutron spectra and ambient dose equivalent around children treated using a spot scanning technique. At first, the work focused on determining neutron variability around a water phantom for a $10 \times 10 \times 10 \text{ cm}^3$ target (13). Next, neutron variability with beam parameters (energy, field size, modulation width) was measured and a simplistic parametric model describing neutron doses around the phantom was suggested (14). For these measurements, extended-range Bonner sphere spectrometry systems, neutron rem counters, and tissue-equivalent proportional counters were used and benchmarked to help in selecting the optimal detector for proton therapy neutron spectra (15). In addition to environmental measurements, EURADOS WG9 also measured neutron doses in both water and anthropomorphic phantoms, using bubble, etched track, thermoluminescent, and radiophotoluminescent detectors (16–20).

Knezevic and colleagues have measured secondary neutron dose equivalent in pediatric phantoms during a simulated brain tumor treatment in the pencil beam scanning (PBS) proton facility at the Cyclotron Centre Bronowice, IFJ PAN Kraków (21). They observed a slightly higher neutron dose in a 10-year-old phantom compared to a 5-year-old phantom in all organs at distances from 20 cm to 30 cm from the isocenter. Nevertheless, the ambient dose equivalent dependence on patient size measured around the pediatric phantoms in the treatment room has not been yet systematically studied.

In this work, a brain tumor treatment, without a range shifter, was simulated using a set of pediatric anthropomorphic phantoms representing a 1-, 5-, and 10-year-old pediatric patient. Two different beam angles were considered to achieve clinically acceptable tumor coverage while optimizing the sparing of healthy organs at risks. Neutron stray radiation measurements were hence performed around the phantoms at eight different locations using the same set of active neutron monitors as previously benchmarked.

MATERIALS AND METHODS

Pediatric Anthropomorphic Phantoms

For this study, three CIRS ATOM[®] anthropomorphic phantoms representing 1-, 5-, and 10-year-old children were used (CIRS—Computerized Imaging Reference Systems, Inc., Norfolk, VA, USA). CIRS ATOM[®] phantoms comprise 25-mm-thick sections with minimal interfaces between the slabs. The 1-year-old phantom is provided with arms and legs as a standard configuration, while arms and legs for 5-year and 10-year models can be fitted separately. The size and weight of each model is based on ICRP 23 (22), ICRU 48 (23), and available anatomical references (see **Table 1**). CIRS ATOM[®] phantoms are constructed from materials simulating average soft tissue, average bone tissue, cartilage, spinal cord, spinal disks, lung, brain, and sinus. Simulated bone tissue for pediatric models matches age-related density.

Proton Beam Specification, Irradiation Technique, and Irradiation Plans

The experiment was carried out at the Cyclotron Center Bronowice (CCB), which is a part of the Henryk Niewodniczański Institute of Nuclear Physics of Polish Academy of Sciences (IFJ PAN) in Kraków, Poland. The center is equipped with the Proteus C-235 cyclotron (IBA, Ion Beam Applications S.A., Belgium) able to accelerate protons for clinical use up to 226 MeV. Three treatment rooms have been available at CCB since 2016 for proton radiotherapy of cancer patients. These are two IBA 360° gantries with dedicated Pencil Beam Scanning (PBS) nozzles and a horizontal 70-MeV eye line. Computed tomography (CT) scans of CIRS phantoms representing 1-, 5-, and 10-year-old children were performed with the Siemens Somatom Definition AS Open scanner with a slice thickness of 0.2 cm, and then used in an Eclipse 13.6 Treatment Planning System (Varian Medical Systems) for preparation of irradiation plans calculated with the Proton Convolution Superposition (PCS) algorithm. The distance of the gantry nozzle to the isocenter inside the tumor was 46 cm. The spot size varied depending on the beam energy and depth inside the phantom. In the air at a distance of 46 cm from the gantry nozzle, 100-MeV and 140-MeV proton beams led to spot sizes of 5.3 mm and 4.4 mm, respectively. Two fields (proton beam directions) were applied to uniformly irradiate the 6-cm-diameter spherical target (5 cm tumor diameter plus 1 cm margin) situated inside the left hemisphere of the head

(intracranial tumor) (see **Figure 1**). The isocenter was located in the middle of slice #3 of the CIRS phantom. The detailed position of the isocenter is shown in **Figure 1**.

For each pediatric phantom, a specific irradiation plan was prepared. In the case of the 5-year-old phantom for the first field, 2,231 individual proton beams (spots) in 27 layers were deposited at a gantry position of 270° with a maximal and minimal energy of 137.7 MeV and 84.0 MeV, respectively. The second field was irradiated at a gantry angle of 140° using 2,168 spots in 30 layers, with a maximal and minimal energy of 127.5 MeV and 71.6 MeV, respectively. Proton beam specifications for all irradiation plans are given in **Table 2**. A high proton dose was required to create neutrons measurable with acceptable precision. Thus, a total physical dose of ~100 Gy was delivered to the target volume for the 5-year and 10-year phantoms and ~40 Gy for the 1-year phantom. The dose was delivered from two beam directions with 60% of the dose with gantry position at 270° and 40% of the dose with gantry position at 140°. For reference dosimetry, a Semiflex-type ionization chamber (PTW 31010, Freiburg, Germany) with a Unidos Webline electrometer (PTW-Freiburg, Germany) was used together with an RW3 slab phantom.

Experimental Setup Within the CCB Kraków Gantry Room

The experiment was carried out at CCB, focused on the creation of stray neutrons in conditions close to realistic treatment scenarios. Pediatric phantoms were placed on the therapeutic table perpendicular to the beam axis at an isocenter height of 1.25 m above the floor. The treatment was simulated using two fields (i.e., two gantry positions) at 140° and 270° angles (see **Figures 2, 3**).

Neutron dose rates were mapped in the treatment room using different active neutron monitors. The ambient dose equivalents, $H^*(10)$, were measured at several distances and angular positions with respect to the beam axis around the 1-, 5-, and 10-year-old phantoms (see **Figure 2**), namely, along the beam direction (positions B and H), around the head (positions A, F, and G), and around the body (positions C, D, and E). The distances to the isocenter and angles with respect to the beam axis for all measurement positions are given in **Table 3**.

Instruments

Neutron ambient dose equivalent, $H^*(10)$, around the pediatric phantoms was measured using several active neutron monitors: Hawk TEPC environmental monitors (Far West Technology, Inc.) from the Polish Institute of Nuclear Physics (IFJ), the French Institute for Radiological Protection and Nuclear Safety (IRSN), and the Czech Nuclear Physics Institute (NPI), and a TEPC chamber (Far West Technology, Inc.) from the Belgian Nuclear Research Centre (SCK CEN), as supplementary for the recombination chamber REM-2 type (POLON Bydgoszcz) with the GW2 ionization chamber from the National Centre for Nuclear Research (NCBJ). Various neutron rem counters were also used including the Berthold LB 6411 from Universitat Autònoma de Barcelona (UAB), Skandion Clinic, and the

TABLE 1 | Anatomical references of CIRS ATOM[®] 1-, 5-, and 10-year-old pediatric anthropomorphic phantoms used in this study, based on ICRP 23 (22), ICRU 48 (23) and available anatomical reference data.

Pediatric phantom	Height (cm)	Weight (kg)	Thorax dimension (cm × cm)
1 year	75	10.0	12 × 14
5 years	65*	13.1*	14 × 17
10 years	80*	21.5*	17 × 20

(©2015 Computerized Imaging Reference Systems, Inc.). *Without legs and arms.

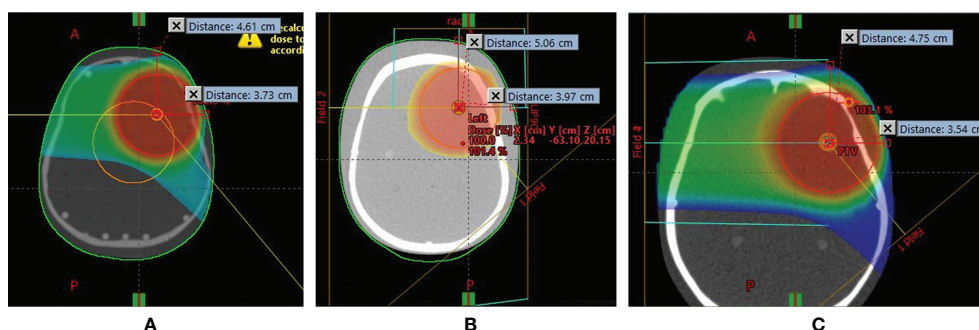


FIGURE 1 | Position of intracranial tumor inside the left hemisphere of (A) 1-year-old, (B) 5-year-old, and (C) 10-year-old pediatric anthropomorphic phantoms.

Belgian Nuclear Research Centre (SCK CEN), the Thermo Scientific™ WENDI-II from IFJ and IRSN, a conventional NM2B-458, and an extended-range NM2B-495Pb (NE Technology Ltd.) from Helmholtz Zentrum München (HMGU). Additionally, the Thermo Scientific™ RadEye™ NL from IRSN was applied. Further details are given in the Appendix.

The most important neutron monitor criterion for the successful measurements in neutron fields with a wide energy range, typically from thermal up to several hundred MeV, is its fluence response as a function of neutron energy. In the most favorable case, it should follow the shape of the $H^*(10)/\Phi$ energy dependence. In **Figure 4**, the neutron fluence response functions of the monitors used are plotted together with the $H^*(10)/\Phi$ fluence-to-dose conversion coefficients as recommended by the International Commission on Radiological Protection 74 (31) and extended to high energies with data from Pelliccioni (32). According to the fluence response functions shown in **Figure 4**, it could be concluded that conventional neutron rem counters such as Berthold LB 6411 and NM2B-458 are not well suited for high-energy neutron fields as encountered in a proton therapy treatment room. Since high-energy neutrons contribute significantly to $H^*(10)$, conventional neutron rem counters (LB-6411 and NM2B-458) with decreased response to neutrons above 10 MeV and calibrated in Am-Be or Cf-252 fields considerably underestimate neutron $H^*(10)$ (13). The drop in the response of the RadEye™ NL pager for neutrons above about 1 MeV is also evident in **Figure 4**.

Spectral Index

The same shape of the fluence response function of NM2B-495Pb and NM2B-458 rem counters from thermal neutrons up

to about 10 MeV (see **Figure 4**) provides the unique possibility to swiftly estimate the contribution of high-energy neutrons to the total $H^*(10)$ without time-consuming neutron spectrometry. The so-called spectral index (SI) is here defined as a ratio of $H^*(10)$ measured with a high-energy extended rem counter NM2B-495Pb and conventional NM2B-458. In situations where neutron spectrometry could not be carried out because of time constraints for example, the SI value can provide a reliable first guess estimation of the spectrum shape and the corresponding contribution of high-energy neutrons to ambient dose equivalent, $H^*(10)$.

Working group WG9 of EURADOS reported the results of a measurement campaign in the Trento proton therapy center (PTC) (13) where secondary neutron spectra were generated by a scanning proton beam targeting a cuboidal water tank phantom with dimensions of $30 \times 30 \times 60 \text{ cm}^3$. Neutron spectra were recorded by extended-range Bonner sphere spectrometer (ERBSS) systems, and $H^*(10)$ values were assessed by the same NM2B rem counters, as used in this study, at four positions around the phantom (0° , 45° , 90° , and 135°). The Trento study showed that high-energy neutrons ($>20 \text{ MeV}$) largely dominate the measured spectra along the beam axis (up to 60%) and drop with respect to the direction of the incident beam reaching 25% at 45° , 5% at 90° , and only 2% at 135° (see **Figure 5**). The spectral index in the Trento PTC was estimated to be equal to 2.25 along the beam axis (i.e., at 0°), 1.4 at 45° , 1.05 at 90° , and 1.0 at 135° .

Experimental conditions in the Trento and Kraków PTC are very similar and only differ by the beam size ($10 \times 10 \text{ cm}^2$ square field in Trento versus 6 cm diameter in Kraków) and maximum proton energy (172 MeV in Trento versus 144 MeV in Kraków). Positions 1, 2, 3, and 4 in Farah et al. (13) correspond to positions B, C, D, and E in this study for gantry position at 270° .

TABLE 2 | Proton beam specification.

Pediatric phantom	1 year		5 years		10 years	
	140°	270°	140°	270°	140°	270°
E_{\min} (MeV)	71.9	76.8	71.6	84.0	70.4	99.28
E_{\max} (MeV)	124.7	128.8	127.5	137.7	128.1	144.6
R80 (cm)	9.54	10.64	10.26	11.92	10.11	13.27

RESULTS

Spectral Index Values

The SI values assessed during the experiment in Kraków PTC are shown in **Figure 6**. The highest value of 1.55 was estimated for position H at the beam direction for the 5-year-old child in a

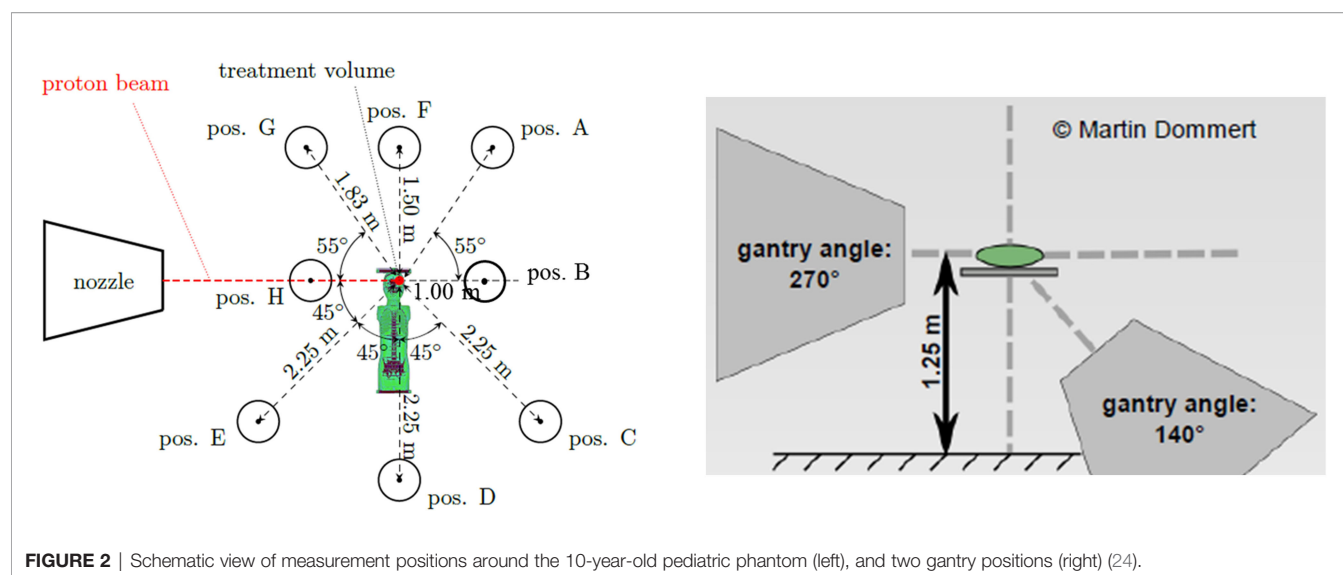


FIGURE 2 | Schematic view of measurement positions around the 10-year-old pediatric phantom (left), and two gantry positions (right) (24).

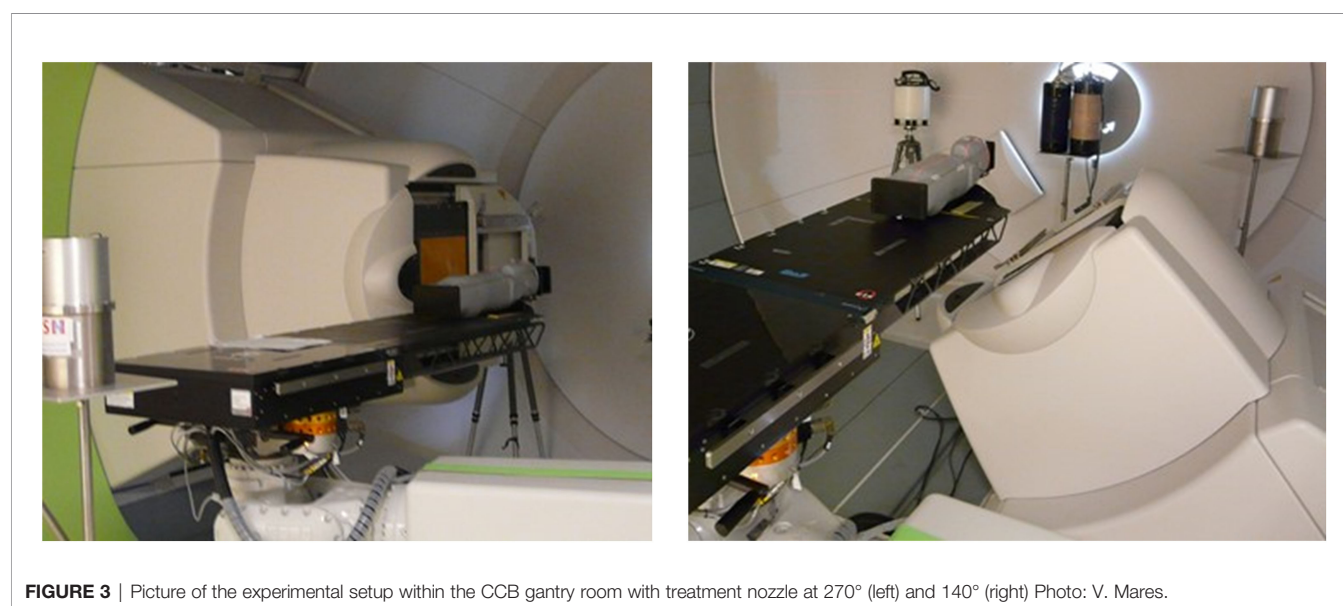


FIGURE 3 | Picture of the experimental setup within the CCB gantry room with treatment nozzle at 270° (left) and 140° (right) Photo: V. Mares.

TABLE 3 | Eight measurement positions around the 1-, 5-, and 10-year-old pediatric phantoms.

Position	Angle with respect to beam axis (°)	Distance to isocenter (m)
A	305	1.83
B	0	1.00
C	45	2.25
D	90	2.25
E	135	2.25
F	270	1.50
G	235	1.83
H	180	1.00

gantry position of 140°. At position to 1.36, while C at 45° (with 10-year-old child), the SI value was equal to 1.36, while at positions at larger angles with respect to beam direction, the SI values drop down to 1.10 (90°, position D, 5-year-old child) and 1.03 (135°, position E, 5-year-old child), respectively. It is noted that spectral index data for the 10-year-old child at position H and for the 5- and 10-year-old child at position B were not available, as well as all the data for the 1-year-old child.

The knowledge of the SI values has enabled data cleansing in the following way: at positions where SI was greater than or equal to 1.05, the $H^*(10)$ values measured with conventional detectors (i.e., applicable for neutrons below 10 MeV) were omitted from the dataset because of their underestimated values.

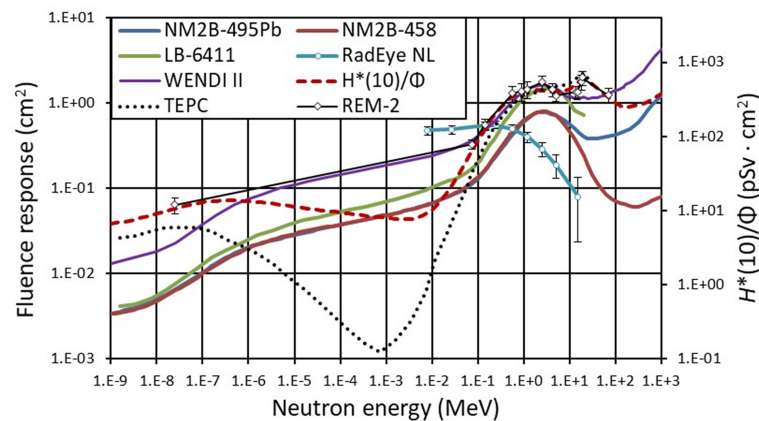


FIGURE 4 | Neutron fluence response functions of rem counters NM2B-495Pb and NM2B-458 (25), Berthold LB-6411 (26), Wendi II (27), RadEye NL (28), TEPC (29), and REM-2 (30). Dashed line (red) represents $H^*(10)$ conversion coefficients for neutrons radiation versus neutron energy following ICRP74 recommendation (31) extended to high-energy neutrons according to Pelliccioni (32). The lines connect the points as a guide to the eye.

Neutron Ambient Dose Equivalent Measured at Different Positions

The aforementioned active detectors measured neutron $H^*(10)$ at each position under the same experimental conditions. It should be noted that at positions where $SI \geq 1.05$, the $H^*(10)$ values measured with conventional rem counters (LB-6411 and NM2B-458) and RadEyeTM NL pager were omitted by data cleansing. For each specific position, the average value of all measured $H^*(10)$ was calculated and is shown in **Figure 7** per treatment Gy for the gantry position of 270° and in **Figure 8** for the gantry position of 140° for three pediatric phantoms used.

The $H^*(10)$ values show a significant decrease with both distance and angular position with respect to the beam axis. The highest neutron $H^*(10)$ value of 19.5 $\mu\text{Sv/Gy}$ was measured along the beam axis at a distance of 1.0 m from the isocenter (position B) for the 10-year-old child at 270° gantry position. The minimum $H^*(10)$ value of 0.1 $\mu\text{Sv/Gy}$ was measured at a distance of 2.25 m perpendicular to the beam axis (position D) for the 1-year-old child and for a 140° gantry angle.

The differences between $H^*(10)$ values in **Figures 7, 8** clearly show the influence of specific proton beam parameters such as beam direction, maximal proton energy, and range of protons (see **Table 2**). It should be noted that the energy of protons determines both the maximum energy of produced neutrons and also the range of protons. However, the range of each spot also depends on the density of the material on the proton path. To characterize the range of the proton field, R80 of the depth dose profile along the main axis of the beam was measured in the treatment planning system (TPS). For example, in the 1-year-old phantom, R80 for the field with energies 77–129 MeV is about 10.6 cm, while for the 10-year-old phantom, R80 for the field with energies 99–145 MeV increases to about 13.3 cm, which means that for a higher proton energy, a higher amount of secondary neutrons is generated along the longer proton path and a higher $H^*(10)$ is observed.

At 270° gantry position, measured $H^*(10)$ values are below 2.1 $\mu\text{Sv/Gy}$ at all positions except along the beam direction (position B). In contrast, at 140° gantry position, $H^*(10)$ values are below 1.1 $\mu\text{Sv/Gy}$ except at position H (i.e., in beam direction). It should be noted that measurements at positions H and B were not possible at gantry angles 270° and 140°, respectively, because of spatial limitations (see **Figure 3**).

Total Neutron Ambient Dose Equivalent

The sum of $H^*(10)$ values for two proton beam directions at 140° and 270° gantry positions is shown in **Figure 9**. The $H^*(10)$ sum value at positions B and H cannot be shown as, because of spatial limitations (see **Figure 3**), it was not possible to measure $H^*(10)$ at both positions for both beam directions. It could be seen that during treatment with two fields, the total $H^*(10)$ did not exceed 1.0 $\mu\text{Sv/Gy}$ at positions perpendicular to the beam axis at a distance of 2.25 m.

Impact of the Pediatric Patient Size

The $H^*(10)$ dependence on the size of the pediatric patient could be observed in **Figures 7–9**. At 270° gantry position, $H^*(10)$ values for the 10-year-old child were up to 20% and up to 410% higher than those measured for the 5- and 1-year-old child, respectively. At 140°, the patient size dependence of $H^*(10)$ for the 10- and 5-year-old child was markedly less prominent except at the position along the beam axis at 1-m distance from the isocenter (position H) where for the 10-year-old child increase of about 60% above $H^*(10)$ for the 5-year-old child was measured. The $H^*(10)$ values for the 10-year-old child were up to a factor of 5.5 higher than that for the 1-year-old child.

DISCUSSION

The measured ambient dose equivalent, $H^*(10)$, at positions along the beam axis, i.e., positions H and B, does not exceed

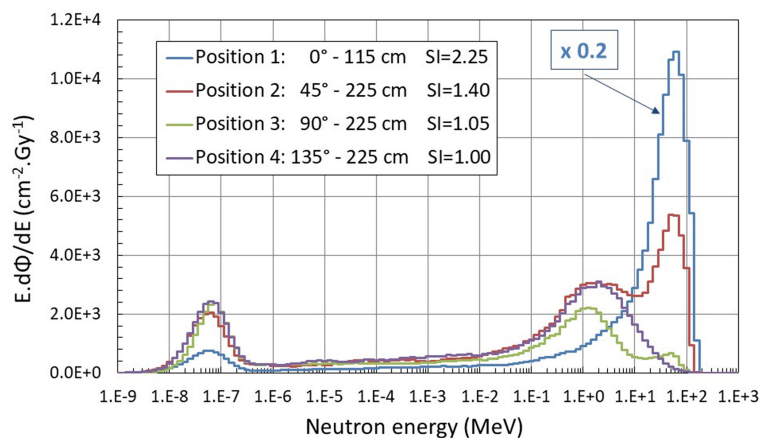


FIGURE 5 | Neutron spectra measured around the water phantom in Trento PTC using the extended-range Bonner sphere spectrometer (13). Additionally, spectral index (SI) values calculated as ratio of $H^*(10)$ measured with a high-energy extended rem counter NM2B-495Pb and a conventional NM2B-458 are indicated.

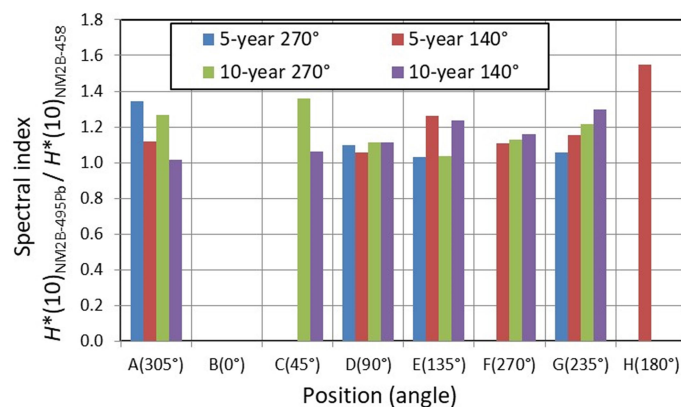


FIGURE 6 | Neutron spectral index expressed as a ratio of $H^*(10)$ values measured with NM2B-495Pb and NM2B-458 rem counters at different positions (and different angles with respect to the beam direction) around 5- and 10-year-old pediatric phantoms.

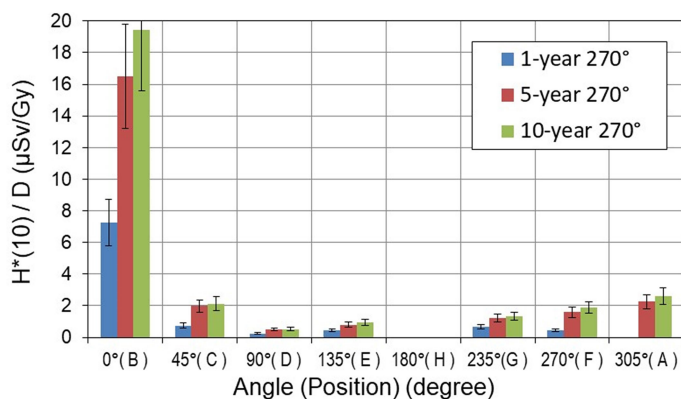


FIGURE 7 | Neutron ambient dose equivalent $H^*(10)$ per treatment Gy [$\mu\text{Sv/Gy}$] measured around pediatric phantoms at 270° gantry position. The error bars represent the standard deviation.

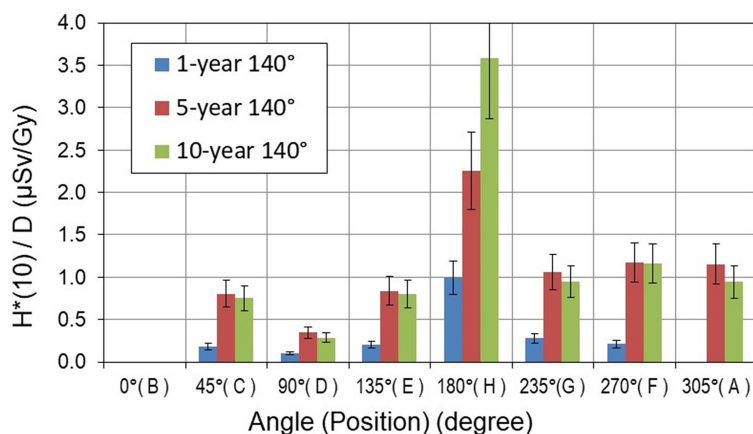


FIGURE 8 | Neutron ambient dose equivalent $H^*(10)$ per treatment Gy [$\mu\text{Sv/Gy}$] measured around pediatric phantoms at 140° gantry position. The error bars represent the standard deviation.

20 $\mu\text{Sv/Gy}$, and drops significantly to about 1 $\mu\text{Sv/Gy}$ and 3 $\mu\text{Sv/Gy}$ for positions perpendicular to the beam axis (i.e., positions D and F), respectively. It means that the total neutron exposure of a person located at a position perpendicular to the beam axis at a distance greater than 2 m from the isocenter (e.g., at position D) does not exceed 60 μSv during the whole treatment course for a total target dose of 60 Gy (in 30 fractions). This dose remains well below the annual dose limit of 1 mSv for the general public (recommended by the International Commission on Radiological Protection). It should be noted that the $H^*(10)$ of 60 μSv is comparable with a calculated effective dose of 52 μSv received by passengers from galactic cosmic rays on a single flight from Munich to New York (~9 h flight duration) in the time period of solar minimum (33) using fluence-to-dose conversion coefficients as recommended in ICRP Publication

103 (7). In other words, for the investigated treatment plan, the unwanted exposure, due to a presence in the room 2 m from the isocenter during an entire spot scanning proton radiotherapy treatment (30 fractions), is by at least an order of magnitude lower than the annual dose limit for the public.

This comprehensive analysis of variability of $H^*(10)$ is of key importance for neutron shielding and, for example, for safe operation of anesthetic equipment. Moreover, it also enables the evaluation of whether it is safe for parents to remain near their children during treatment to bring them comfort, which could even avoid anesthesia during treatment and/or reduce movement during treatment.

Nevertheless, current work does not yet allow the generalization of such practices, as neutron $H^*(10)$ depends on treatment plan parameters such as size of the target, patient

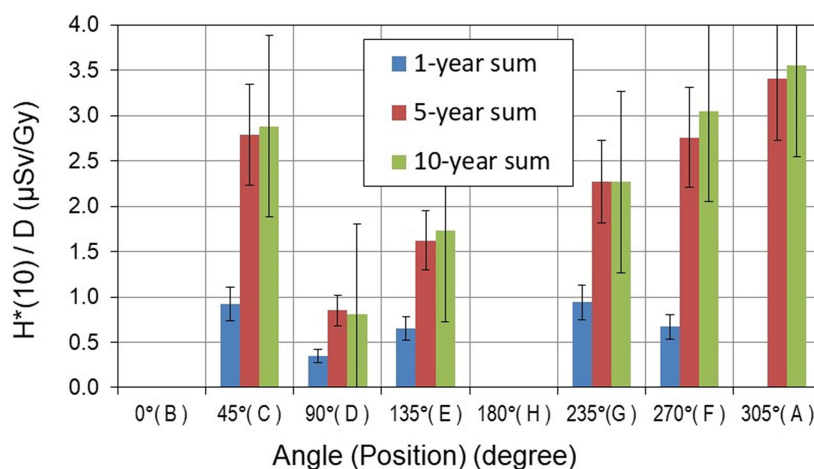


FIGURE 9 | Total neutron ambient dose equivalent $H^*(10)$ per treatment Gy [$\mu\text{Sv/Gy}$] measured around pediatric phantoms. The error bars represent the standard deviation.

position, number of beams, beam incidence, and proton energies (14). Future work will be needed to extensively study the impact of such parameters in order to generalize findings to ensure appropriate shielding, the safe operation of anesthesia, and the safe presence of parents during treatment of their children.

Another limitation is that, even though the experiment was conducted under conditions close to realistic treatment scenarios, no range shifter was used, as during the experiment, the range shifter was not fully commissioned. Therefore, for one of the treatment fields, a range shifter could not be used, and the tumor, located in the left hemisphere of the brain, was irradiated from the right side (270° angle) instead of the choice for a left-sided beam orientation. As such, the proton energy was slightly increased to reach the appropriate depth in brain and the clinical translatability is challenged. Even though this can be considered a limitation of the study, we believe that the corresponding neutron $H^*(10)$ can be considered as a conservative estimation of the $H^*(10)$, as it is increasing with increasing proton energy (14), and general findings of the paper are consistent.

CONCLUSIONS

The measurements performed to investigate the secondary neutron dose around 1-, 5-, and 10-year-old children in clinical PBS proton therapy showed that the size of the pediatric patient influences the magnitude of the neutron ambient dose equivalent at various positions in the treatment room. The clear dependence of $H^*(10)$ values on the size and age of the pediatric patient was observed mainly for the 270° proton beam direction (gantry position at 270°). In this case, $H^*(10)$ values for the 10-year-old child were up to 20% higher than those measured for the 5-year-old child and up to 290% higher than for the 1-year-old child.

This study also showed that the neutron ambient dose equivalent $H^*(10)$ decreases with distance from the isocenter and strongly depends on the position angle with respect to the beam axis. The highest $H^*(10)$ values were always measured along the beam axis, while the lowest $H^*(10)$ values were measured at positions located perpendicularly to the beam axis. The highest neutron ambient dose equivalent of about 19.5 $\mu\text{Sv/Gy}$ was measured at a distance of 1.0 m from the isocenter along the beam axis (i.e., at closest point during experiment) at a gantry position of 270° for the 10-year-old pediatric phantom. $H^*(10)$ values significantly decreased to 0.1 $\mu\text{Sv/Gy}$ at a distance of 2.25 m perpendicular to the beam axis for a 1-year-old pediatric phantom at a gantry position of 140°.

It was also demonstrated that during the whole treatment course with a target dose ≤ 60 Gy, the total neutron exposure of a person at a position perpendicular to the beam axis at a distance of 2.25 m remains well below the annual dose limit for the public. For the specific conditions of this study, it may be concluded that parents could remain 2 m away from their children to bring them comfort and possibly limit risks of patient motion during therapy, which could jeopardize treatment quality. Currently, the radiation protection protocols prohibit the occupancy of the

treatment room during beam delivery. The very low doses demonstrated here suggest that for proton therapy under the conditions described in this paper, the procedures and practices could be re-assessed. However, further work is required before definitive guidance on parental occupancy of the treatment room could be given.

DATA AVAILABILITY STATEMENT

The raw data supporting the conclusions of this article will be made available by the authors, without undue reservation.

AUTHOR CONTRIBUTIONS

VM: participation in measurement campaign, data evaluation, experiment management, data analysis, drafting and editing manuscript. JF: participation in measurement campaign, data evaluation, experiment management, data analysis, drafting and editing manuscript. MS-H: participation in measurement campaign, data evaluation, data analysis, drafting and editing manuscript. SD: participation in measurement campaign, data evaluation, drafting and editing manuscript. CD: participation in measurement campaign. MD: participation in measurement campaign. MaK: participation in measurement campaign, data evaluation, drafting and editing manuscript. KK: data evaluation. MiK: data evaluation. IM-R, participation in measurement campaign, drafting and editing manuscript. EM: data evaluation. NM, participation in measurement campaign, irradiation plan, drafting manuscript. LM: participation in measurement campaign. OP: participation in measurement campaign, data evaluation. MR-E: participation in measurement campaign, data evaluation, drafting and editing manuscript. MT: participation in measurement campaign. FT: data evaluation, data analysis, drafting and editing manuscript. OH: participation in measurement campaign, data evaluation, data analysis, drafting and editing manuscript. LR: participation in measurement campaign. MW: participation in measurement campaign. RH: participation in measurement campaign, data analysis, drafting and editing manuscript. LS: participation in measurement campaign, irradiation plan, experiment management, data analysis, drafting and editing manuscript. PO: participation in measurement campaign, experiment management, data analysis, editing manuscript. All authors contributed to the article and approved the submitted version.

FUNDING

I.M.-R. acknowledges the financial support from the Spanish Ministry of Science, Innovation and Universities (fellowship RYC2018-024043-I). The work of Ondrej Ploc on the paper was funded by EU Operational Program Research, Development, and Education, call 02_15_003 in project CRREAT, number CZ.02.1.01/0.0/0.0/15_003/0000481. The study was partially supported by the EU Project POWR.03.02.00-00-I004/16 and the Horizon 2020 project INSPIRE Grant Agreement 730983.

ACKNOWLEDGMENTS

This work was carried out within the European Radiation Dosimetry Group (EURADOS, WG9 Radiation Dosimetry in

Radiotherapy). The authors gratefully acknowledge the contribution and help from the staff of the Cyclotron Centre Bronowice, Krakow, Poland.

REFERENCES

- PTCOG. *Particle Therapy Co-Operative Group* (2022). Available at: <https://www.ptcog.ch/index.php/patient-statistics> (Accessed February 14, 2022).
- Zacharatou Jarlskog C, Paganetti H. Risk of Developing Second Cancer From Neutron Dose in Proton Therapy as Function of Field Characteristics, Organ, and Patient Age. *Int J Radiat Oncol Biol Phys* (2008) 72:228–35. doi: 10.1016/j.ijrobp.2008.04.069
- Newhauser WD, Durante M. Assessing the Risk of Second Malignancies After Modern Radiotherapy. *Nat Rev Cancer* (2011) 11(6):438–48. doi: 10.1038/nrc3069
- NCRP. National Council on Radiation Protection and Measurements. In: *Uncertainties in the Estimation of Radiation Risks and Probability of Disease Causation*. NCRP; Bethesda, MD: Report No. 171 (2012).
- Durante M, Loeffler JS. Charged Particles in Radiation Oncology. *Nat Rev Clin Oncol* (2009) 7(1):37–43. doi: 10.1038/nrclinonc.2009.183
- Jariskog CZ. Sensitivity of Different Dose Scoring Methods on Organ-Specific Neutron Dose Calculations in Proton Therapy. *Phys Med Biol* (2008) 53(17):4523–32. doi: 10.1088/0031-9155/53/17/004
- ICRP. *The 2007 Recommendations of the International Commission on Radiological Protection* Vol. 37. ICRP Publication 103, Ann. ICRP, Ann. ICRP (2007).
- Polf JC, Newhauser WD. Calculations of Neutron Dose Equivalent Exposures From Range-Modulated Proton Therapy Beams. *Phys Med Biol* (2005) 50(16):3859–73. doi: 10.1088/0031-9155/50/16/014
- Taddei PJ, Mirkovic D, Fontenot JD, Giebler A, Zheng YS, Kornguth D, et al. Stray Radiation Dose and Second Cancer Risk for a Pediatric Patient Receiving Craniospinal Irradiation With Proton Beams. *Phys Med Biol* (2009) 54(8):2259–75. doi: 10.1088/0031-9155/54/8/001
- Stolarczyk L, Cywicka-Jakiel T, Horwacik T, Olko P, Swakon J, Waligorski MPR. Evaluation of Risk of Secondary Cancer Occurrence After Proton Radiotherapy of Ocular Tumours. *Radiat. Meas* (2011) 46(12):1944–7. doi: 10.1016/j.radmeas.2011.05.046
- Farah J, Martinetti F, Sayah R, Lacoste V, Donadille L, Tromprier F, et al. Monte Carlo Modeling of Proton Therapy Installations: A Global Experimental Method to Validate Secondary Neutron Dose Calculations. *Phys Med Biol* (2014) 59:2747. doi: 10.1088/0031-9155/59/11/2747
- Hälg RA, Schneider U. Neutron Dose and its Measurement in Proton Therapy—Current State of Knowledge. *Br J Radiol* (2020) 93:20190412. doi: 10.1259/bjr.20190412
- Farah J, Mares V, Romero-Expósito M, Trinkl S, Domingo C, Dufek V, et al. Measurement of Stray Radiation Within a Scanning Proton Therapy Facility: EURADOS WG9 Intercomparison Exercise of Active Dosimetry Systems: Characterization of Stray Neutrons in Proton Therapy. *Med. Phys* (2015) 42(5):2572–84. doi: 10.1118/1.4916667
- Mojżeszek N, Farah J, Kłodowska M, Ploc O, Stolarczyk L, Waligorski MPR, et al. Measurement of Stray Neutron Doses Inside the Treatment Room From a Proton Pencil Beam Scanning System. *Phys Med* (2017) 34:80–4. doi: 10.1016/j.ejmp.2017.01.013
- Mares V, Romero-Expósito M, Farah J, Trinkl S, Domingo C, Dommert M, et al. A Comprehensive Spectrometry Study of a Stray Neutron Radiation Field in Scanning Proton Therapy. *Phys Med Biol* (2016) 61(11):4127–40. doi: 10.1088/0031-9155/61/11/4127
- Stolarczyk L, Trinkl S, Romero-Expósito M, Mojżeszek N, Ambrozova I, Domingo C, et al. Dose Distribution of Secondary Radiation in a Water Phantom for a Proton Pencil Beam—EURADOS WG9 Intercomparison Exercise. *Phys Med Biol* (2018) 63(8):085017. doi: 10.1088/1361-6560/aab469
- Knežević Ž, Ambrozova I, Domingo C, De Saint-Hubert M, Majer M, Martínez-Rovira I, et al. Comparison of Response of Passive Dosimetry Systems in Scanning Proton Radiotherapy – A Study Using Pediatric Anthropomorphic Phantoms. *Radiat Prot Dosimet* (2018) 180:1–4256–60. doi: 10.1093/rpd/ncx254
- De Saint-Hubert M, Majer M, Hršak H, Heinrich Z, Knežević Ž, Miljanić S, et al. Out-Of-Field Doses in Children Treated for Large Arteriovenous Malformations Using Hypofractionated Gamma Knife Radiosurgery and Intensity-Modulated Radiation Therapy. *Radiat Prot Dosimet* (2018) 181:100–10. doi: 10.1093/rpd/ncx301
- Wochnik A, Stolarczyk L, Ambrozova I, Davidková M, De Saint-Hubert M, Domański S, et al. Out-of-Field Doses for Scanning Proton Radiotherapy of Shallowly Located Paediatric Tumours—A Comparison of Range Shifter and 3D Printed Compensator. *Phys Med Biol* (2021) 66:035012. doi: 10.1088/1361-6560/abcb1f
- Majer M, Ambrozova I, Davidková M, De Saint-Hubert M, Kasabašić M, Knežević Ž, et al. Out-Of-Field Doses in Pediatric Craniospinal Irradiations With 3D-CRT, VMAT, and Scanning Proton Radiotherapy: A Phantom Study. *Med Phys* (2022) 49(4):2672–83. doi: 10.1002/mp.15493
- Knežević Ž, Ambrozova I, Domingo C, De Saint-Hubert M, Majer M, Martínez-Rovira I, et al. Comparison of Response of Passive Dosimetry Systems in Scanning Proton Radiotherapy—A Study Using Paediatric Anthropomorphic Phantoms. *Radiat Prot Dosimet* (2018) 180(1–4):256–60. doi: 10.1093/rpd/ncx254
- ICRP. *Report of the Task Group on Reference Man*. Oxford: ICRP Publication 23. Pergamon Press (1975).
- ICRU. Report 48, Phantoms and Computational Models in Therapy, Diagnosis and Protection. *J Int Commission Radiat Units Measurements* (1992) os25(1). doi: 10.1093/jicru/os25.1.Report48
- Dommert M. Secondary Neutrons in Hadron Therapy. [Master Thesis]. Munich, Germany: Technical University of Munich (TUM) (2015).
- Mares V, Sannikov AV, Schraube H. Response Functions of the Andersson-Braun and Extended Range Rem Counters for Neutron Energies From Thermal to 10 GeV. *Nucl Instrum Meth A* (2002) 476(1–2):341–6. doi: 10.1016/S0168-9002(01)01459-0
- Burghardt B, Fieg G, Klett A, Plewnia A, Siebert BRL. The Neutron Fluence and H*(10) Response of the New LB 6411 REM Counter. *Radiat Prot Dosim* (1997) 70:361–4. doi: 10.1093/oxfordjournals.rpd.a031977
- De Smet V, Stichelbaut F, Vanaudenhove T, Mathot G, De Lentdecker G, Dubus A, et al. Neutron H*(10) Inside a Proton Therapy Facility: Comparison Between Monte Carlo Simulations and WENDI-2 Measurements. *Radiat Prot Dosimet* (2014) 161(1–4):417–21. doi: 10.1093/rpd/nct289
- Tromprier F, Gressier V, B. Asselineau B, Martin A, Pelcot G, Pepino M. Investigation of the Neutron Energy Response of a New Commercial Neutron Survey-Meter. In: *Proceedings of the 12th Neutron and Ion Dosimetry Symposium, Aix-En-Provence*. France: Radiation Protection Dosimetry; ISSN 0144-8420; Worldcat (2013).
- Thomas DJ. The System of Radiation Protection for Neutrons: Does it Fit the Purpose? *Radiat Prot Dosim*. (2013) 161(1–4):3–10. doi: 10.1093/ppd/nct303
- Golnik N. Recombination Chambers—do the Old Ideas Remain Useful? *Radiat Prot Dosimet* (2017) 180:3–9. doi: 10.1093/rpd/ncx279
- ICRP. *International Commission on Radiological Protection Conversion Coefficients for Use in Radiological Protection Against External Radiation (Publication 74)* (Oxford: Pergamon). (1997).
- Pelliccioni M. Overview of Fluence-to-Effective Dose and Fluence-to-Ambient Dose Equivalent Conversion Coefficients for High Energy Radiation Calculated Using the FLUKA Code Radiat. *Prot Dosim*. (2000) 88:279–97. doi: 10.1093/oxfordjournals.rpd.a033046
- Mares V, Maczka T, Leuthold G, Ruehm W. Air Crew Dosimetry With a New Version of EPCARD. *Radiat Prot Dosimet* (2009) 136(4):262–6. doi: 10.1093/rpd/ncp129
- Briesmeister JF. (1993).
- Prael RE, Lichtenstein H. *User Guide to LCS: The LAHET Code System*. LA-UR-89-3014 (1989).
- Savitskaya EN, Sannikov AV. High Energy Neutron and Proton Kerma Factors for Different Elements. *Radiat. Prot Dosim*. (1995) 60(2):135–46. doi: 10.1093/oxfordjournals.rpd.a082710
- L Waters ed. *MCNPX User's Manual Version 2.4.0*, Los Alamos National Laboratory Document. Los Alamos, NM, USA: LA-UR-99-4999 (1999).

38. Bergmeier F. *Measurement of Doses of Secondary Neutrons From Cosmic Radiation by Means of Various REM Counters*. [Bachelor Thesis]. Munich, Germany: Ludwig Maximilian University of Munich (LMU). (2011).
39. Schinner K. *Bestimmung Der Empfindlichkeit Von REM-Counter Und Bonner-Kugeln Auf Gammastrahlung*. [Diploma Thesis]. Ilmenau, Germany: Ilmenau University of Technology (TU Ilmenau). (2014).
40. International Standard. *ISI/DIS 8529-1, Reference Neutron Radiations – Part 1: Characteristics and Methods of Production*. (2001).
41. Mares V, Trinkl S, Iwamoto Y, Masuda A, Matsumoto T, Hagiwara M, et al. Neutron Spectrometry and Dosimetry in 100 and 300 MeV Quasimono-Energetic Neutron Field at Osaka University, Japan. *EPJ Web Conf* (2017) 153:08020. doi: 10.1051/epjconf/201715308020
42. Olsher RH, Hsu HH, Beverding A, Kleck JH, Casson WH, Vasilik DG, et al. WENDI: An Improved Neutron Rem Meter. *Health Phys* (2000) 79(2):170–81. doi: 10.1097/00004032-200008000-00010
43. De Smet V, De Saint-Hubert M, Dinar N, Manessi GP, Aza E, Cassell C, et al. Secondary Neutrons Inside a Proton Therapy Facility: MCNPX Simulations Compared to Measurements Performed With a Bonner Sphere Spectrometer and Neutron H*(10) Monitors. *Radiat Measurements*. (2017) 99:25–40. doi: 10.1016/j.radmeas.2017.03.005
44. Conroy T. *Environmental Radiation Monitor with 500 Tissue Equivalent Proportional Counter (TEPC), HAWK Version 2. Operations and Repair Manual*. Goleta, CA, USA: Far West Technology Inc. (FWT) (2004).
45. ICRP. *1990 Recommendations of the International Commission on Radiological Protection*. ICRP Publication 60, Ann. ICRP 21 (1991).
46. Farah J, De Saint-Hubert M, Mojżeszek N, Chiriotti S, Gryzinski M, Ploc O, et al. Performance Tests and Comparison of Microdosimetric Measurements With Four Tissue-Equivalent Proportional Counters in Scanning Proton Therapy. *Radiat Measurements* (2017) 96:42–52. doi: 10.1016/j.radmeas.2016.12.005
47. Trompier F, Delacroix S, Vabre I, Joussard F, Proust J. Secondary Exposure for 73 and 200 MeV Proton Therapy. *Radiat Protect Dosim* (2007) 125(1–4):349–54.
48. Gressier V, Asselineau B, Guerre-Chaley JF, Martin A, Muller H. AMANDE Accelerator Energy Performances. In: *Proceedings of the International Workshop on Fast Neutron Detectors and Applications*. Cape Town, South Africa: University of Cape Town (2006).
49. Zielczyński M, Golnik N. Recombination Index of Radiation Quality - Measuring and Applications. *Radiat Prot Dosimet* (1994) 52(1–4):419–22. doi: 10.1093/oxfordjournals.rpd.a082226
50. Golnik N, Mayer S, Zielczyński M. Recombination Index of Radiation Quality of Low-LET Radiation. *Nucl Instruments Methods Phys Res Section B: Beam Interact Mater Atoms* (2004) 213:650–3. doi: 10.1016/S0168-583X(03)01679-3
51. AAPM. *American Association of Physicists in Medicine, Protocol for Neutron Beam Dosimetry*. AAPM Report No. 7. New York: American Institute of Physics (1980).
52. Tulik P, Tulik M, Maciak M, Golnik N, Kabat D, Byrski T, et al. Investigation of Secondary Mixed Radiation Field Around a Medical Linear Accelerator. *Radiat Prot Dosimet* (2018) 180(1–4):252–5. doi: 10.1093/rpd/ncx199

Conflict of Interest: The authors declare that the research was conducted in the absence of any commercial or financial relationships that could be construed as a potential conflict of interest.

Publisher's Note: All claims expressed in this article are solely those of the authors and do not necessarily represent those of their affiliated organizations, or those of the publisher, the editors and the reviewers. Any product that may be evaluated in this article, or claim that may be made by its manufacturer, is not guaranteed or endorsed by the publisher.

Copyright © 2022 Mares, Farah, De Saint-Hubert, Domański, Domingo, Dommert, Kłodowska, Krzempek, Kuć, Martínez-Rovira, Michaś, Mojżeszek, Murawski, Ploc, Romero-Expósito, Tisi, Trompier, Van Hoey, Van Ryckeghem, Wielunski, Harrison, Stolarczyk and Olko. This is an open-access article distributed under the terms of the Creative Commons Attribution License (CC BY). The use, distribution or reproduction in other forums is permitted, provided the original author(s) and the copyright owner(s) are credited and that the original publication in this journal is cited, in accordance with accepted academic practice. No use, distribution or reproduction is permitted which does not comply with these terms.

APPENDIX

A. Instruments

A-1: NM2B-495Pb and NM2B-458 rem counter

NM2B-458 and NM2B-495Pb (NE Technology Ltd., commercially available as an instrument pair NM500 and NM500X from Münchener Apparatebau für elektronische Geräte, GmbH) are cylindrical Andersson-Braun rem counters measuring neutron ambient dose equivalent, $H^*(10)$. Both rem counters are based on cylindrical BF_3 proportional counters of 3.1 cm outer diameter and 7.2 cm active length surrounded by an inner polyethylene moderator (1.7 cm thick), a 0.6-cm-thick boron-doped synthetic rubber absorber, and an outer polyethylene moderator (6.9 cm thick). In the case of the NM2B-495Pb model, a 1-cm-thick lead shell surrounding the boron rubber is added to extend the detection range to high-energy neutrons.

The fluence response functions from thermal to 10 GeV were calculated by means of different Monte Carlo codes, i.e., MCNP (34) for energy below 20 MeV, and LAHET (35), HADRON (36), and MCNPX (37) above 20 MeV. Details are described in Mares et al. (25). All calibrations were performed in HMGU using 185 GBq (5 Ci) $^{241}\text{Am-Be}$ (α, n) neutron source with an average neutron energy of 4.4 MeV (38–40). Both rem counters were also calibrated in 100 and 300 MeV quasi-monoenergetic neutron fields at RCNP in Osaka, Japan (41) and at CERF (<https://tis-div-rp-cerf.web.cern.ch/>). The measurement uncertainties were estimated to be $\pm 20\%$ for the NM2B-495Pb extended-range rem counter, and $\pm 30\%$ for the NM2B-458 conventional one.

In the present experiment in CCB Kraków, pulse height spectra were registered to control the photon background, to correct for pile-ups, and to properly set the region of interest (ROI) to evaluate appropriate number of counts. Applying the calibration factors estimated in HMGU, the ROI counts can be converted to corresponding ambient dose equivalent, $H^*(10)$.

A-2: LB 6411 Berthold

The LB 6411 probe (Berthold Technologies) consists of a polyethylene moderator sphere with a diameter of 25 cm and a cylindrical ^3He proportional counter at its center. This monitor is designed to measure neutron ambient dose equivalent $H^*(10)$ in the neutron energy range from thermal to 20 MeV. It is known to have a strongly decreasing sensitivity to neutrons above 20 MeV. The relative dose response function of the LB 6411 over the whole energy range was calculated with MCNP Monte Carlo code by Burgkhardt et al. (26). The calculated response was benchmarked with measurements in monoenergetic neutron reference fields.

The ^{252}Cf neutron source has been used for calibration. The calibration factor of 0.353 nSv/count is used to display the data as $H^*(10)$. The response to gamma radiation is about 10^{-3} counts per nSv. The overall measurement uncertainty of about 30% mainly include the uncertainties in detector calibration, dose delivery, detector positioning, and the energy response of the detectors.

A-3: WENDI-II

The WENDI-II (manufacturer: Thermo Scientific) is an extended-range rem counter built by Olsher et al. (42). It has an outer diameter of 22.86 cm and consists of a ^3He proportional counter surrounded by a cylindrical polyethylene assembly with an inner tungsten shell. Compared to a conventional rem counter, such as, e.g., the Berthold LB 6411, the sensitivity to high energy neutrons ($E > 20$ MeV) is significantly higher thanks to inelastic (n, xn) reactions occurring in the tungsten layer.

The ^{252}Cf calibration constant of the WENDI-II used for these measurements is 0.317 nSv/count. The relative dose response function, calculated as the absolute response function multiplied by this calibration constant and divided by the fluence-to- $H^*(10)$ conversion coefficients is shown in De Smet et al. (27, 43). The overall measurement uncertainty mainly including the uncertainties in detector calibration and the energy response of the detectors was estimated to be of about 20%.

A-4: “HAWK” Tissue-equivalent proportional counter monitor

The HAWK environmental Monitoring System FW-AD type 1 is a tissue-equivalent proportional counter from Far West Technology Inc. (Goleta, California, USA), composed of a spherical chamber (127 mm diameter) with a wall from A-150 tissue-equivalent plastic (2 mm thick) and filled with pure propane gas at low pressure (about 9.33 hPa) simulating a 2- μm site size (44). The outer container is made of 6.35-mm-thick stainless steel. The dose equivalent is calculated from a spectrum of single energy deposition events and a radiation quality factor Q , determined by the $Q(L)$ relation given in ICRP 60 (45), where L denotes the unrestricted linear energy transfer (LET) in the exposed material (7).

HAWK type 1 systems use two linear multichannel analyzers working in parallel with low and high gains. The low-gain analog-to-digital converter (ADC) measures LET spectra up to $1024 \text{ keV}\cdot\mu\text{m}^{-1}$ with $1 \text{ keV}\cdot\mu\text{m}^{-1}$ resolution. The high-gain channel uses an ADC measuring up to a lineal energy of $25.6 \text{ keV}\cdot\mu\text{m}^{-1}$ with a resolution of $0.1 \text{ keV}\cdot\mu\text{m}^{-1}$. The energy deposition of the low-LET and high-LET components and the associated quality factor are stored in an output file once per minute. The separation between the low-LET and the high-LET component is set at $10 \text{ keV}\cdot\mu\text{m}^{-1}$ according to the $Q(L)$ relationship (7). Events encountering significant electronic noise below the so-called low energy threshold ($0.3 \text{ keV}\cdot\mu\text{m}^{-1}$ for the HAWK used here) are not recorded. For data analysis, a simple coefficient (the average of correction factor determined for ^{60}Co and ^{137}Cs gamma-rays) was applied (46). No compensation of the counting loss due to dead time is included in the analysis software.

Correction factors, N_{low} and N_{high} , to ambient dose equivalent for the low-LET and high-LET components of the dose equivalent are used. N_{low} was determined in photon radiation fields with ^{60}Co and ^{137}Cs sources. N_{high} was defined using the neutron reference sources of $^{241}\text{Am-Be}$ or ^{252}Cf neutron sources. The values of N_{low} are 1.11 ± 0.02 and 1.34 ± 0.03 , and the values of N_{high} are 0.80 ± 0.09 and 0.84 ± 0.10 for IRSN and SL, respectively. Correction coefficients for neutrons

were also evaluated for neutron energies between 0.5 and 19 MeV and were found similar to Am–Be or ^{252}Cf neutron sources (47).

A-5: Tissue-equivalent proportional counter TEPC

The TEPC (Model LET-SW5, Far West Technology) used for these measurements is spherical, with an internal diameter of 12.55 cm and a 2-mm-thick shell of A-150 tissue-equivalent plastic. The TEPC was filled with propane tissue-equivalent gas at a pressure of 8.8 mbar to simulate a biological site size of 2 μm . The relative dose response function of this type of detector was calculated up to 20 MeV by Thomas (29). The ambient dose equivalent $H^*(10)$ was calculated as explained in Farah et al. (46). $H^*(10)$ value uncertainties are in the order of 15% when adding statistical (10%), alpha calibration (10%), extrapolation (2%), proton beam delivery (5%), and detector positioning (1%) uncertainties.

A-6: RadEye NL

The RadEyeTM NL pager (Thermo ScientificTM) is a small, lightweight, and highly sensitive radiation detection device that incorporates a ^3He counter filled at 2.5 bars to detect very low radiation levels of neutron radiation from any source. A polyethylene shell moderator, provided by Thermo ScientificTM to improve the detection sensitivity, was used for these measurements. This moderator has a non-standard geometry (parallelepiped shape), which cannot ensure an isotropic response and limit its use as a neutron rem counter.

The response function of this detector was previously (28) studied using various types of reference sources (^{241}Am -Be, bare and heavy water moderated ^{252}Cf) as well as with several monoenergetic neutron fields available at the AMANDE facility (48). Hence, the variation of the response with neutron energy was determined at 8 keV, 27 keV, 144 keV, 250 keV, 565 keV, 1.2 MeV, 2.5 MeV, 5 MeV, and 15 MeV. The fluence reference values in the monoenergetic fields are established with an IRSN long counter traceable to national standards. The response of the RadEyeTM NL pager was found to be similar to leak design counters, overestimating the $H^*(10)$ values at the lowest energies and underestimating it at the highest energies. In this particular calibration, the response of the detector was set to unity for the ^{252}Cf source while a 30% under-response is noticed for the ^{241}Am -Be. It should be noticed, however, that the main limitation of this counter is the non-isotropic moderator geometry that induces a large angular dependence depending on neutron energy; namely, a factor of ~ 2 under-response was observed at 144 keV when comparing a 0° front exposure of the moderator and a 90° side exposure of the moderator; this under-response drops to $\sim 10\%$ at 15 MeV.

A-7: GW2 and REM-2 ionization chamber

A research group from the National Centre for Nuclear Research, during the experiment, used unique gas detectors.

The recombination chambers are ionization chambers designed in such a way that, at a certain range of gas pressure and dose rates, the initial recombination of ions dominates over the volume recombination, when the chamber operates at polarizing voltages below saturation. In the aspect of scientific research, they are excellent devices for comparing methods and results with popular, commercially available neutron detectors.

The REM-2 type detector is a large recombination chamber filled with a gas mixture consisting of 95% methane and 5% nitrogen up to a pressure of 10 atm. The gas volume is 1800 cm^3 . The detector is a cylinder with outer dimensions of about 30 cm height and 15 cm diameter. Inside the detector, there are 25 parallel-plate tissue-equivalent 3-mm-thick electrodes with 7 mm space between. The total mass of the detector is about 6.5 kg with an effective wall thickness of about 2 g/cm^2 . Because of the large volume, the detector is very sensitive ($\sim 2.63 \times 10^6$ Gy/C for Air Kerma Rate in the ^{137}Cs isotopic radiation field). The device is a radiation sensor that allows one to determine radiation quality using the microdosimetric relationship between the initial recombination efficiency and local ion density. It has been proved (49, 50) that the recombination index of the radiation quality Q_4 parameter is a good approximation of the $Q(L)$ relation given in ICRP 60 (45). The main advantage of the chamber is the high compliance of the ambient dose equivalent at a depth of 10 mm $H^*(10)$ for ICRU spheres on a wide range neutron field energy spectrum from thermal up to 20 MeV and even further (30).

The tissue-equivalent REM-2 type detector and the non-hydrogen GW2-type gamma detector used in the experiment were placed side by side. The combination of hydrogen-free and tissue-equivalent detectors allows, independently from determining the radiation quality factor, the separation of the gamma and neutron components of mixed radiation (51, 52).

The GW2-type detector is an ionization chamber with aluminum electrodes and is filled with CO_2 up to 26 atm pressure. Dimensions and number of electrodes are similar to the REM-2-type detector. Due to its construction, GW2 is almost insensitive to neutron radiation. In this experiment, the chamber had been used as a monitor for the gamma radiation component of the radiation field. The sensitivity of the detector is about $\sim 9.58 \times 10^6$ Gy/C for Air Kerma Rate in the ^{137}Cs isotopic radiation field.

Before the experiment, both detectors were calibrated with the ^{137}Cs reference photon source and REM-2 was additionally checked against the radiation quality of the isotopic Am–Be neutron field. The ambient dose equivalent $H^*(10)$ calculation was adopted following Tulik et al. (52). Determined uncertainties of $H^*(10)$ values are in the order of 25%.



Out-of-Field Doses Produced by a Proton Scanning Beam Inside Pediatric Anthropomorphic Phantoms and Their Comparison With Different Photon Modalities

Željka Knežević^{1*}, Liliana Stolarczyk^{2,3}, Iva Ambrožová⁴, Miguel Á. Caballero-Pacheco⁵, Marie Davidková⁴, Marijke De Saint-Hubert⁶, Carles Domingo⁵, Kinga Jeleń^{3,7}, Renata Kopeć³, Dawid Krzempek³, Marija Majer¹, Saveta Miljanić¹, Natalia Mojżeszczek³, Maite Romero-Expósito^{5,8}, Immaculada Martínez-Rovira⁵, Roger M. Harrison⁹ and Paweł Olko³

OPEN ACCESS

Edited by:

Francesca Ballarín,
University of Pavia, Italy

Reviewed by:

Silva Bortolussi,
University of Pavia, Italy
Luca Silvi,

ENEA - INMRI (National Institute of
Ionizing Radiation Metrology), Italy

*Correspondence:

Željka Knežević
zknez@irb.hr

Specialty section:

This article was submitted to
Radiation Oncology,
a section of the journal
Frontiers in Oncology

Received: 25 March 2022

Accepted: 15 June 2022

Published: 22 July 2022

Citation:

Knežević Ž, Stolarczyk L, Ambrožová I, Caballero-Pacheco MÁ, Davidková M, De Saint-Hubert M, Domingo C, Jeleń K, Kopeć R, Krzempek D, Majer M, Miljanić S, Mojżeszczek N, Romero-Expósito M, Martínez-Rovira I, Harrison RM and Olko P (2022) Out-of-Field Doses Produced by a Proton Scanning Beam Inside Pediatric Anthropomorphic Phantoms and Their Comparison With Different Photon Modalities. *Front. Oncol.* 12:904563. doi: 10.3389/fonc.2022.904563

¹ Ruder Bošković Institute, Zagreb, Croatia, ² Danish Centre for Particle Therapy, Aarhus, Denmark, ³ Institute of Nuclear Physics, PAN, Krakow, Poland, ⁴ Nuclear Physics Institute of the Czech Academy of Sciences, CAS, Řež, Czechia, ⁵ Universitat Autònoma de Barcelona, Bellaterra, Spain, ⁶ Belgium Nuclear Research Centre, Mol, Belgium, ⁷ Tadeusz Kosciuszko Cracow University of Technology, Cracow, Poland, ⁸ Skandion Clinic, Uppsala, Sweden, ⁹ University of Newcastle upon Tyne, Newcastle upon Tyne, United Kingdom

Since 2010, EURADOS Working Group 9 (Radiation Dosimetry in Radiotherapy) has been involved in the investigation of secondary and scattered radiation doses in X-ray and proton therapy, especially in the case of pediatric patients. The main goal of this paper is to analyze and compare out-of-field neutron and non-neutron organ doses inside 5- and 10-year-old pediatric anthropomorphic phantoms for the treatment of a 5-cm-diameter brain tumor. Proton irradiations were carried out at the Cyclotron Centre Bronowice in IFJ PAN Krakow Poland using a pencil beam scanning technique (PBS) at a gantry with a dedicated scanning nozzle (IBA Proton Therapy System, Proteus 235). Thermoluminescent and radiophotoluminescent dosimeters were used for non-neutron dose measurements while secondary neutrons were measured with track-etched detectors. Out-of-field doses measured using intensity-modulated proton therapy (IMPT) were compared with previous measurements performed within a WG9 for three different photon radiotherapy techniques: 1) intensity-modulated radiation therapy (IMRT), 2) three-dimensional conformal radiation therapy (3D CDRT) performed on a Varian Clinac 2300 linear accelerator (LINAC) in the Centre of Oncology, Krakow, Poland, and 3) Gamma Knife surgery performed on the Leksell Gamma Knife (GK) at the University Hospital Centre Zagreb, Croatia. Phantoms and detectors used in experiments as well as the target location were the same for both photon and proton modalities. The total organ dose equivalent expressed as the sum of neutron and non-neutron components in IMPT was found to be significantly lower (two to three orders of magnitude) in comparison with the different photon radiotherapy techniques for the same delivered tumor dose. For

IMPT, neutron doses are lower than non-neutron doses close to the target but become larger than non-neutron doses further away from the target. Results of WG9 studies have provided out-of-field dose levels required for an extensive set of radiotherapy techniques, including proton therapy, and involving a complete description of organ doses of pediatric patients. Such studies are needed for validating mathematical models and Monte Carlo simulation tools for out-of-field dosimetry which is essential for dedicated epidemiological studies which evaluate the risk of second cancers and other late effects for pediatric patients treated with radiotherapy.

Keywords: scanning proton therapy, out-of-field doses, anthropomorphic phantoms, track detectors, RPL detectors, TL detectors, brain tumor irradiations

1 INTRODUCTION

Proton beam therapy offers a reduced entrance dose and a negligible exit dose when compared with photon irradiation techniques. The presence of the Bragg peak in proton therapy allows for better conformation of dose to the target and results in sparing of surrounding normal tissues and consequently can reduce the acute and late side effects of the treatment. Reducing the probability of short- and long-term complications of radiotherapy is of special importance when tumors are located next to the critical organs and while treating pediatric patients. In the past decades owing to new diagnostic procedures and continuous improvement and introduction of new treatment modalities, the probability of cancer cure and survival rate has risen considerably. In general, around 80% of children with malignant diseases are successfully treated with survival rates greater than 5 years (1). Central nervous system tumors such as gliomas, medulloblastoma, and ependymal tumors are the most common solid malignancies in childhood (30% of all pediatric tumors). Radiation therapy is an integral component of therapy for pediatric brain tumors. In recent years, the number of children, especially with brain tumors, treated using proton therapy has increased significantly (2–6). Improvement in the treatment outcome and the increase in the number of long-term survivors of child malignancies emphasize the importance of late radiation-induced effects. Due to a long-life expectancy after treatment, approximately 70% of children will develop some kind of short- or long-term treatment-related complications (7, 8). A multitude of radiation epidemiology studies have revealed the high prevalence of radiation-induced late effects including radiogenic secondary cancers (9, 10). The risk of developing secondary cancer following radiotherapy (years or decades after the treatment) is by a factor of 10 higher in children in comparison to adults and can be as high as 12% (7, 11–15). It depends upon multiple factors including patient age, size, biological and genetic predisposition of the individual, type of therapy received (chemotherapy and/or radiotherapy), the organ and tissue sites receiving radiation, and also the dose delivered during the treatment. Most existing risk models are designed for low-dose and low-dose-rate exposures and cannot be easily translated to radiotherapy, where dose is fractionated and organ doses may be heterogeneous (16). Therefore, dedicated

epidemiology studies are required for pediatric exposures during radiotherapy. Such studies need accurate dosimetry input from experiments in combination with validated analytical models or Monte Carlo simulations. In the recent years, the continued technological expansion of radiotherapy has resulted in the use of advanced treatment modalities, such as proton radiotherapy, intensity-modulated radiation therapy (IMRT), volumetric-modulated arc therapy (VMAT), image-guided radiotherapy (IGRT), and magnetic resonance linear accelerators (MR-LINAC). These new techniques provide better dose distributions and are more conformal in comparison to the conventional ones. Nevertheless, they still produce scattered or secondary radiation in the interactions of a primary beam with treatment unit and patient body. Doses outside the treatment fields are much lower in comparison to the doses within the primary field, but they are of radiobiological interest as they are received by healthy organs and may lead to secondary cancer (17, 18). Treatment planning systems (TPS) commonly used to estimate dose distributions inside a patient body calculate doses to the target and organs in the proximity of the target with high accuracy. Outside the treatment field, in the region of out-of-field doses, TPS calculations become inaccurate and may even underestimate the dose by up to 40% (18–21). Moreover, dose calculations in remote organs are often restricted by the limited anatomical coverage of the computed tomography (CT) used for treatment planning. In proton therapy, the situation is even more complicated due to a complex spectrum of secondary neutrons as well as secondary gammas and scattered charged particles contributing to out-of-field doses (22). Neutrons are of particular concern due to their high relative biological effectiveness (RBE) and cannot be neglected in the evaluation of the potential risks (23, 24). The limitations in tracking of secondary radiation in most clinical treatment planning systems make measurements essential for out-of-field dose estimation. As doses in the out-of-field region vary with delivery technique, treatment site, field characteristics, and energy spectrum, measurements in this region are challenging. In proton radiotherapy, out-of-field doses are mostly evaluated based on measurements with track-etched detectors, bubble detectors, ionization chambers, and thermoluminescent detectors supported by in-room measurements with active detectors or Bonner Spheres and Monte Carlo simulations. It is worth

pointing out that both energy and spatial distributions of secondary radiation can differ among different proton facilities. Therefore, it is important to model the specific beam and room geometries for Monte Carlo simulations of out-of-field doses. Such models should be validated against measurements. Most of the experiments described in the literature are aimed at measuring dose as a function of distance to the field (17, 18, 22, 25–27), and although such data are helpful for relative comparisons, information about organ doses is still missing in the literature. Moreover, in the published studies, experimental data for active scanning techniques are scarce as the majority of papers describe passive scattering techniques (14, 23, 26, 27). In the paper by Athar et al., out-of-field doses are simulated for an 8-year phantom and for different 6-MV IMRT plans and compared with passive and active proton therapy techniques (17). The results showed that at larger distances (25 cm and more) from the field edge, out-of-field organ doses are higher in IMRT than those in passive scattered proton therapy. For scanning proton beams, organ doses were lower (up to two orders of magnitude) in comparison to IMRT and also a proton passive scattering technique. In the paper by Ardenfors et al., organ doses from secondary radiation were calculated using MC simulations for an adult female patient and a 6-year pediatric patient for a proton spot scanning technique with different beam setups (25). The results showed that neutron equivalent doses for brain tumors treated with proton PBS are relatively low, of the order of mSv. In the publication by Gudowska et al., a literature review of the secondary doses to healthy tissues is given for different modern radiation therapy techniques (28). The review summarizes different methods of assessing secondary doses (MC simulations, TPS, measurements with different types of detectors). Doses were evaluated for organs in real patients or in different anthropomorphic and water phantoms. The data showed a large variation of secondary absorbed doses to healthy organs, ranging from ~0.007 mGy to 2.4 Gy per prescribed dose depending on the type and energy of the primary beam, irradiation technique, patient geometry, distance from the primary field tumor, and organ size.

In the literature, terminology on expressing secondary doses differs and it is not always clear how they are calculated and normalized and what radiation components are taken into account. In some studies, out-of-field doses are presented as absorbed doses, organ doses, or equivalent doses and one should be careful when comparing results within different studies. In addition, there is a variation with the target size and location but also type of phantom used, type of detector used, and their respective response in the secondary radiation field. Moreover, many studies focus only on one component of the secondary radiation field, namely, secondary neutrons, ignoring doses coming from secondary particles and secondary gamma radiation.

Since 2010, EURADOS Working Group 9 (Radiation Dosimetry in Radiotherapy) has been involved in the investigation of out-of-field radiation doses in photon and proton therapy especially in case of pediatric patients. Firstly, WG9 performed detailed characterization of the out-of-field

doses, associated with proton PBS in a water phantom with both measurements and MC simulation, which clearly showed complexity associated with the secondary radiation field produced in proton PBS (22, 29–31). The next step included measurement campaigns organized by WG9 in the Centre of Oncology, Krakow University Hospital Centre Zagreb, and University Hospital Osijek to study secondary radiation for different photon radiotherapy techniques (32–34). Those experiments were followed by a measurement campaign which is presented in this paper dedicated to proton radiotherapy with pencil beam scanning technique (PBS) carried out at the Cyclotron Centre Bronowice IFJ PAN (Krakow, Poland) (29). In all experiments performed by WG9 for pediatric patients, in both photon and proton therapy, out-of-field organ doses were measured inside 5- and 10-year-old anthropomorphic phantoms for the same target size and location. This experimental consistency allows a direct comparison of out-of-field organ doses for different modalities of photon radiotherapy and proton PBS radiotherapy. Our studies were performed for a realistic clinical treatment of a pediatric brain lesion, to give a fair comparison between different treatment methods in a clinical scenario.

The main goal of this paper is to present out-of-field organ dose measurement results for 5- and 10-year-old anthropomorphic phantoms for the brain target irradiated with proton pencil beam scanning (PBS) technique. Both neutron and non-neutrons components of the secondary radiation field were taken into account. Results are compared with previously published data for the same clinical condition but for different photon radiotherapy techniques. Such comparison allows the potency of intensity-modulated proton therapy (IMPT) to reduce late radiation-induced effects to be evaluated.

2. MATERIALS AND METHODS

2.1. Intensity-Modulated Proton Therapy

2.1.1 Experimental Setup

The irradiations were carried out at the Bronowice Cyclotron Centre (Krakow, Poland) with a pencil beam technique (PBS) at a dedicated scanning gantry (IBA Proton Therapy System - Proteus 235). Measurements of secondary gamma and neutron radiation were performed inside two anthropomorphic phantoms which represents 5- and 10-year-old children (CIRS phantom type 705D and type 706D ATOM, Computerized Imaging Reference Systems (CIRS), Inc., Norfolk, VA). Phantoms are made of tissue equivalent material and consist of 26 and 32 slices (each slice is 25 mm thick) with 180 and 213 detector holes for 5- and 10-year-old phantoms, respectively. Each slab contains holes of diameter 5 mm located within different organs. In this work, distance from the center of the dosimeter to the selected point within the phantom was used to characterize the out-of-field dose distribution for a given irradiation. These distances were calculated from CT images of the phantoms.

2.1.2. IMPT Irradiation Plan

Prior to irradiation, a CT (Siemens Somatom Definition AS Open) of each phantom was performed (2-mm slices, head first supine, FOV 500 mm). Radiotherapy plans were created using an IMPT treatment planning technique with an Eclipse v13.6 Treatment Planning System (TPS) (Varian). For both pediatric phantoms, treatment of a brain tumor was simulated. The planning target volume (PTV) comprises a 6-cm-diameter sphere (113 cm^3) with the center on the left anterior side of the head (located in slice 3 as shown in **Figure 1**). In each case, the target was irradiated using two coplanar fields with gantry positioned at 140° and at 270° (**Table 1**). Phantoms were aligned at the treatment table in the supine position. The energy layers ranged from 70 to 140 MeV. No range shifter was used.

For both phantoms, the planned physical dose to the target was $D_T = 100 \text{ Gy}$ for irradiation of luminescent dosimeters, $D_T = 40 \text{ Gy}$ for track-etched detectors. The applied dose was higher than usually used for actual treatments and was adapted to the sensitivity of the detectors in order to produce a signal above the detection threshold for detectors distant from the isocenter. The dose values for the two prescriptions and applying a proton RBI of 1.1 correspond to $D = 110 \text{ Gy}$ (RBE) and $D = 44 \text{ Gy}$ (RBE), respectively. Proton beam dosimetry was performed in a solid water RW3 phantom (PTW) with a Markus-type chamber (PTW) connected to the Unidos Weblin electrometer (PTW). The ionization chamber was positioned at the isocenter of the plan.

2.1.3. Dose Prescription for IMPT Brain Irradiations

Brain tumors and CNS tumors are, besides leukemia and lymphoma, the most common cancers in children, and proton radiotherapy is an important radiation modality for treating them. In clinical practice, proton therapy is performed in multiple fractions depending on the tumor location and patient age with doses in the range of 40–65 Gy and 1–2 Gy/fraction (3, 4, 6). Different field arrangements are used with lateral fields, vertex fields or a multi-field combination of these orientations. PT is also a recognized method of cerebral

arteriovenous malformation (AVM) treatment (usually treated with GK and LINAC stereotactic irradiation) with the advantage of minimal dose delivered behind the distal edge of the proton beam (35). Medium-size AVMs (diameter 3–6 cm) and large AVMs (diameter $> 6 \text{ cm}$) are typically treated with a total dose of 21–25 Gy (RBE) (36), 12–28 Gy (RBE) (37), or 36–46.2 Gy (RBE) (38).

2.2. Comparison of Proton and Photon Radiotherapy

Out-of-field doses following (IMPT) were compared with previous measurements carried out within EURADOS WG9 for different photon radiotherapy techniques: IMRT, 3D-CRT, and GK treatment. Photon measurements were performed on a Varian Clinac 2300 linear accelerator (LINAC) in the Centre of Oncology, Krakow, Poland, and on a Leksell Gamma Knife (GK) (Model 4 C, Elekta Instruments, Stockholm, Sweden) at University Hospital Centre Zagreb, Croatia (33, 34). It is important to note that phantoms and detectors which were used in previous experiments as well as target location were the same as for proton irradiations. Treatment plans for both photon (3DCRT, IMRT, and GK) and proton modalities (IMPT) simulated a realistic clinical situation and the typical planning protocols used in the participating radiotherapy centers. The irradiation conditions for different radiotherapy techniques are shown in **Table 2**.

2.3 Dosimetry Systems and Dose Calculations for Out-of-Field Dose Estimation

In conventional radiotherapy with high-energy X-rays, out-of-field doses are usually expressed in terms of neutron dose equivalent or equivalent dose in organ and gamma-ray-absorbed dose. In proton therapy, an additional contribution to out-of-field dose comes from scattered protons and from charged particles produced from nuclear reactions. Luminescence detectors, as thermoluminescent (TLDs) or radiophotoluminescent detectors (RPLs), are used for

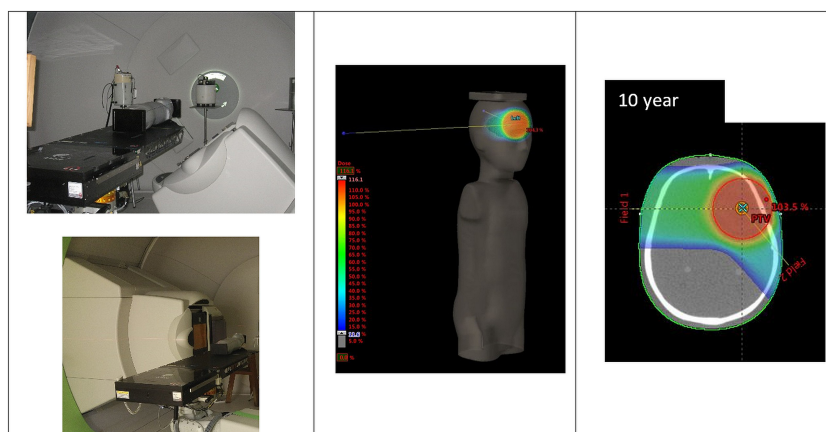


FIGURE 1 | Irradiation setup and tumor location for the IMPT-simulated treatment.


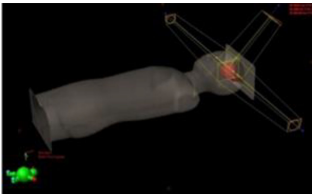
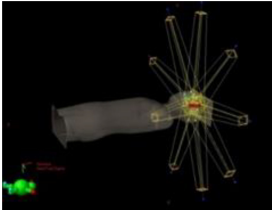

TABLE 1 | IMPT plans parameters for 5- and 10-year-old phantoms.

Phantom	Field	Min. energy (MeV)	Max. energy (MeV)
5-year	F1 (270°)	71.6	127.5
	F2 (140°)	84.0	137.8
10-year	F1 (270°)	70.5	128.2
	F2 (140°)	99.2	144.6

measurements of the gamma radiation component; however, they are sensitive to all types of ionizing particles. Their sensitivity differs depending on the detector type and isotopic composition. For example, for LiF-based TLDs the sensitivity to neutrons depends on the relative concentrations of Li-6 and Li-7 and on the neutron energy. Li-6-enriched TLDs are very sensitive to thermal neutrons due to their high ${}^6\text{Li}(n,\alpha){}^3\text{H}$ cross section for thermal neutron while Li-7-enriched TLDs, such as MTS-7, have a very low sensitivity to neutrons. The response of RPL dosimeters to neutrons is even lower than for TLDs enriched with Li-7.

Track detectors are used for measurements of the neutron component of out-of-field doses. The advantage of PADC detectors is their practical insensitivity to photons, but they may register not only secondaries from nuclear reactions with neutrons but also slowed-down protons. The neutron dose is expressed in terms of dose equivalent, to reflect their biological effect and allow a comparison among results. For the current application of dosimetry in proton therapy, the equivalent dose in organ can be assessed by the average of dose equivalent in representative points of the organ. As shown in the publication

TABLE 2 | Details of irradiation set-up for different RT techniques investigated by Eurados WG9.

Technique	Machine/Site	Irradiation plan	
IMPT	IBA Proton Therapy System - Proteus 235, Krakow, Poland	2 coplanar beams (140° and 270°) $D_T = 100$ Gy (luminescent detectors) $D_T = 40$ Gy (track detectors)	
3D-CRT(33)	Varian Clinac 2300, Centre of Oncology Krakow, Poland	3 non-coplanar beams (6MV) 336 MU Dynamic and mechanical wedge $D_T = 2$ Gy	
IMRT(33)	Varian Clinac 2300, Centre of Oncology Krakow, Poland	9 coplanar beams (6MV) 443 MU $D_T = 2$ Gy	
GammaKnife (34)	Leksell GK (model 4C), University Hospital Zagreb, Croatia	Collimated beams from array of Co-60 sources; 18 mm collimator $D_T = 4.1$ Gy	

by Romero-Expósito et al., the use of quality factor Q or radiation weighting factor w_R in the calculation of the dose equivalent in a point led to similar results and neutron doses evaluated using both factors are comparable with differences below 12% (39).

The response of different types of detectors used in this study was characterized for mixed radiation fields induced by proton pencil beams in previous papers published by EURADOS WG9 (22, 29). Here we summarize the most relevant aspects of the dosimetry systems used.

2.3.1 Luminescence Detectors Used for Non-Neutron Out-of-Field Dose Measurements

The basic principles of the RPL and TL dosimetry methods and their characteristics, applicability, and calibration procedures were described in the paper previously published by EURADOS WG9 (40). In the current study, we used data from TL MTS-7 detectors (manufactured by IFJ PAN, Poland) and RPL detectors (GD-352M, manufactured by AGC Techno Glass (41).

TL and RPL dosimeters were calibrated with a 60-Co source in terms of kerma “free in air”, K_{air} (K_{air} was then converted to absorbed dose to water, D_w), or directly in terms of D_w as described in Knežević et al. (40). Relative standard uncertainties (1 SD in %) of the determined dose for RPLs (GD-352M) and TLDs (MTS-7) were 2.1% (for 1 mGy–2 Gy) and 2.7% (below 1 mGy) and 2.9% (for 2 mGy–5 Gy) and 4.2% (below 12 mGy), respectively (28, 39).

The out-of-field doses in proton therapy in the proximity of the target are dominated by secondary protons. Further from the target, the contribution from protons decreases, and the contribution from secondary neutrons and photons produced through inelastic and non-elastic nuclear interactions becomes dominant (42). Results presented in this paper are measured outside the primary proton radiation field (minimal distance from the field edge is approximately 5 cm), in the mixed field of secondary protons, neutrons, and gamma radiation. For measurements in a mixed radiation field, the sensitivity to different radiation components is an important issue and should be considered. MTS-7 detectors (LiF : Mg, Ti) contain almost pure (99.9%) ^7Li and have a greatly reduced response to thermal neutrons (43). RPL dosimeters of type GD-352M contain a filter for compensation of energy dependence and have negligible response to neutrons (44). In this study, RPL dosimeters were chosen for organ dose measurements based on their lower sensitivity to neutrons in comparison to MTS-7. It should be noted that both TLDs and RPLs also measure the contribution from scattered and secondary protons (22, 29, 45). Moreover, it is not possible to distinguish the signal from protons from the signal from photons. For this reason, for doses measured with RPL detectors we use the term “non-neutron dose” to express the fact that RPL detectors register not only gamma rays but also to a limited extent neutrons and some charged particles. Measured non-neutron doses were normalized to the physical target dose D_T .

2.3.2 Track-Etched Detectors Used for Out-of-Field Neutron Dosimetry

Measurements of secondary neutrons were performed with two types of poly-allyl-diglycol carbonate (PADC) track-etched detectors, which relied on a different method for the calculation of the neutron dose equivalent, H_n (mSv). Type I track detectors (type HARZLAS TD-1, Nagase Landauer Ltd., Japan) use the relationship between the parameters of etched tracks and LET (46). Type II track detectors (Intercast Europe S.R.L., Parma, Italy) include a set of converters (polyethylene, Makrofol, and nylon) specifically designed to make the detector sensitive to neutrons from thermal to high energy range (47, 48). A weighted average of the fluence response factor can be evaluated from the specific response factor and the fraction of neutrons arriving to the point in each energy range (thermal, epithermal, evaporation, and high energy) (39). The assessment of neutron dose equivalent is then performed from neutron fluence following the procedure described in Romero-Expósito et al. (2016) (39). The overall uncertainties for both detector types are at the level of ~ 20%. More details about the detectors and their calibration can be found in the previously published papers (26, 46, 49). Type II track detectors were used only in the 5-year-old phantom with specially designed PMMA slices, which allowed the insertion of detectors inside the phantom at positions corresponding to 11 organs (thyroid, lungs, sternum, heart, liver, kidneys, stomach, intestines, bladder, ovaries, and testes) covering distances from the tumor in the range from approximately 6 to 40 cm from the isocenter.

The neutron contribution determined with PADC detectors is expressed as neutron dose equivalent, and the results are normalized per target dose (mSv or $\mu\text{Sv/Gy}$). The measurements with track detectors were limited to selected positions and distances (up to approximately 40 cm from the isocenter). In order to compare with the non-neutron component and with out-of-field doses for other radiotherapy modalities, results were extrapolated basing on the curve fitted to the experimental data. Neutron dose equivalents presented in this paper for distances from approximately 30 to 65 cm were calculated from the abovementioned fit.

2.4 Calculation of Total Out-of-Field Dose

Out-of-field doses following intensity-modulated proton therapy (IMPT) obtained in this study were compared with doses for different photon radiotherapy techniques (IMRT, 3D-CRT, GK) previously measured by EURADOSWG9 (33, 34). For comparison purposes for IMRT, 3D-CRT, and GK, the photon dose equivalent was calculated by multiplying measured photon dose, D (mGy), by the quality factor $Q = 1$. In the part of the paper where a comparison of measured doses for all irradiation techniques is shown, a total dose equivalent term was used for IMPT results. Total dose equivalent is the sum of the neutron component extrapolated from track detector measurements and the non-neutron component measured with RPL detectors.

3. RESULTS

3.1 Out-of-Field Dose in Proton Spot Scanning Radiotherapy

3.1.1. Out-of-Field Doses as a Function of Distance From the Isocenter

In this section, results are presented as function of distance from the isocenter. For each dosimeter, the distance was calculated from the middle of the detector to the center of the spherical tumor. Results are normalized to the target dose deposited at the isocenter, i.e., the center of the target volume.

Figure 2 shows the non-neutron doses (obtained with RPL detectors) as a function of distance for 5- and 10-year-old phantoms. The results indicate that non-neutron doses as a function of the distance from the isocenter are comparable for 5- and 10-year-old phantoms and that the size of the phantom does not have a significant influence on the attenuation of non-neutron radiation. For both phantoms, non-neutron doses increase significantly in the proximity of the target, due to the presence of secondary and scattered protons, which can reach up to 15 to 20 cm from the isocenter and contribute to the detector signal (**Figure 2**).

Results for the neutron component measured with track detectors as function of distance are presented in **Figure 3**. A comparison of neutron doses for the 5- and 10-year-old phantom shows slightly higher neutron doses measured in the 10-year-old phantom. The comparison was performed for a selected number of positions due to the large dimensions of type II PADC detectors and the need for dedicated holders.

The comparison of neutron doses and non-neutron doses for the 5-year-old phantom is shown in **Figure 4**. The neutron dose equivalent for the 5-year-old phantom was measured with two types of track detectors placed in different positions in the phantom. The agreement between them, taking into account the difference in calibration, calculation methodology, size, and location, is acceptable. As explained in Section 2.3.2 data,

Figure 4 presents extrapolated values of neutron dose equivalent based on the curve fitted to the measurements with two types of track detectors. As shown in **Figure 4**, close to the target, neutron doses are lower than secondary non-neutron doses. This again may be explained by the increase in signal measured by RPL detectors due to a contribution from secondary and scattered protons. It is expected that this contribution decreases strongly with distance. It was shown that at about 150 mm from the isocenter, protons contribute much less to the signal than gamma radiation (22). Further away from the target, outside the range of scattered protons the secondary neutron dose becomes larger than doses measured with RPL detectors. Both neutron and non-neutron doses decrease with distance from the target as, for PBS, secondary radiation is produced mainly by the interaction of protons with the patient body and lesser extent with the beam delivery system.

3.1.2. Out-of-Field Non-Neutron and Neutron Organ Doses

In **Figures 5** and **6**, the neutron and non-neutron organ doses, obtained with track and RPL detectors, respectively, are shown for 5- and 10-year-old phantoms. The results are normalized to the target dose deposited at the isocenter. Organ doses are calculated as average values of all detectors placed in the specific organ. **Figure 5** shows that non-neutron organ doses are on average three times higher in the 5-year-old phantom when compared to the 10-year-old phantom. The reason is that distances between organs and target in the 5- and 10-year-old phantom are different. In the smaller (5-year) phantom, organs are closer to the target and consequently to the main source of secondary radiation. For both phantoms, as non-neutron doses are increasing rapidly in the proximity of the target, doses for organs located close to the target are higher when compared with organs located distantly. The secondary non-neutron doses for the 5-year phantom ranged from about 0.47 mGy/Gy closer to the field edge (13 cm from the isocenter) to 1.5 μ Gy/Gy (50 cm

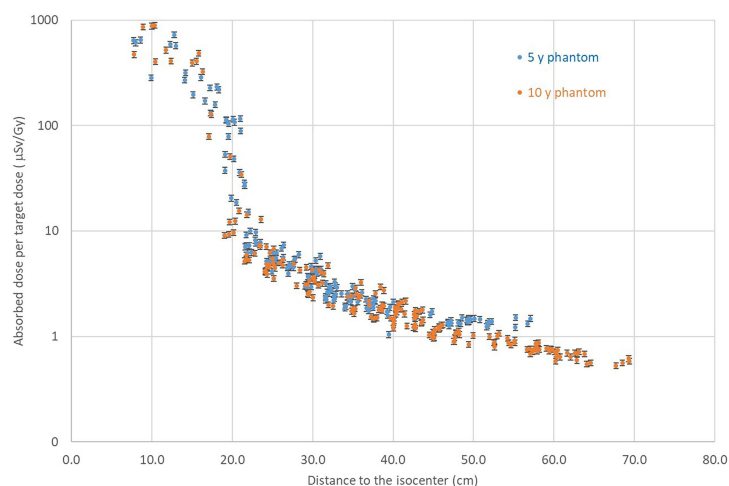


FIGURE 2 | Comparison of non-neutron doses measured with RPL detectors for the 5- and 10-year-old phantom as a function of the distance from the isocenter.

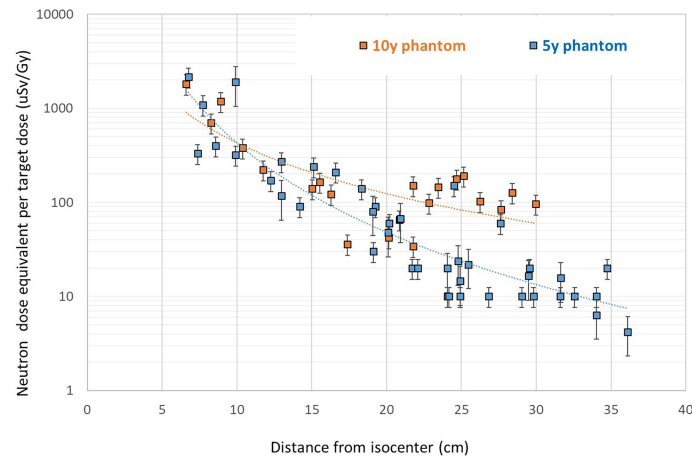


FIGURE 3 | Neutron dose equivalent for the 5- and 10-year-old phantoms measured with PADC detectors. Error bar represents overall uncertainty of the track detectors.

from the isocenter) for thyroid and testes, respectively. For the 10-year-old phantom, secondary non-neutron doses ranged from 0.25 mGy/Gy (15 cm from the isocenter) to 0.6 μ Gy/Gy (70 cm from the isocenter) for the thyroid and testes, respectively. For the full treatment course delivering 54 Gy (RBE) to the target volume, this would correspond to approximately 14 mGy and 32 mGy for thyroid and testes, respectively.

Organ neutron dose equivalents measured and fitted for different organs are shown in **Figure 6**. Organ neutron dose equivalents measured in the 10-year-old phantom are higher in comparison to the 5-year-old phantom. The difference increases with the distance from the isocenter varying by a factor of 1.5 in breasts, 3 in the liver to the largest difference observed for bladder, ovaries, and testes (an average factor of 7). The neutron dose equivalent in the 5-year-old phantom was 172

μ Sv/Gy, 59 μ Sv/Gy, 39.6 μ Sv/Gy, and 2.5 μ Sv/Gy for the thyroid, thymus, sternum, and bladder, respectively, and that in the 10-year-old phantom for the same organs was 173 μ Sv/Gy, 54 μ Sv/Gy, 50 μ Sv/Gy, and 17 μ Sv/Gy. H_n ranged from 1 mSv/Gy close to the field edge to the 0.01-mSv/Gy 30-cm distance from the isocenter. There are several possible explanations for the difference in neutron organ doses in 5- and 10-year-old phantoms. Bone density varies significantly with age, especially for children. Pediatric models of CIRS phantoms use bone equivalent materials, which mimic bone tissue composition and density related to age. Neutron interactions with tissues of higher density can enhance detector signals in the 10-year-old phantom. Also, the dimensions of the phantom are different, and the size influences both proton beam energy and neutron interactions. For the 10-year-old phantom, a slightly higher contribution of more energetic protons was needed to cover

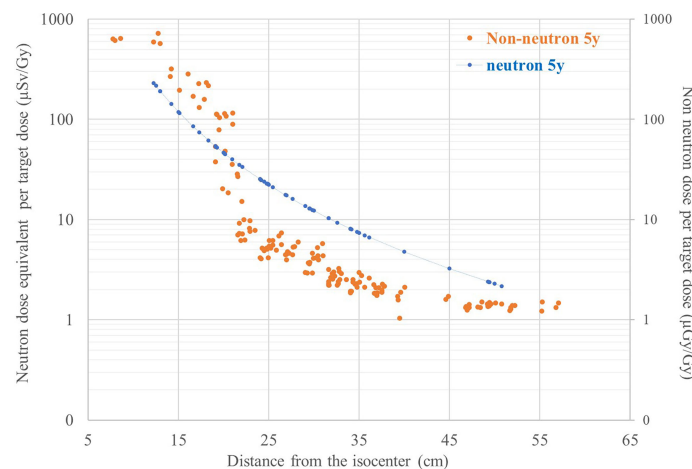


FIGURE 4 | Comparison of neutron and non-neutron dose per target dose as function of the distance from the isocenter for the 5-year-old phantom.

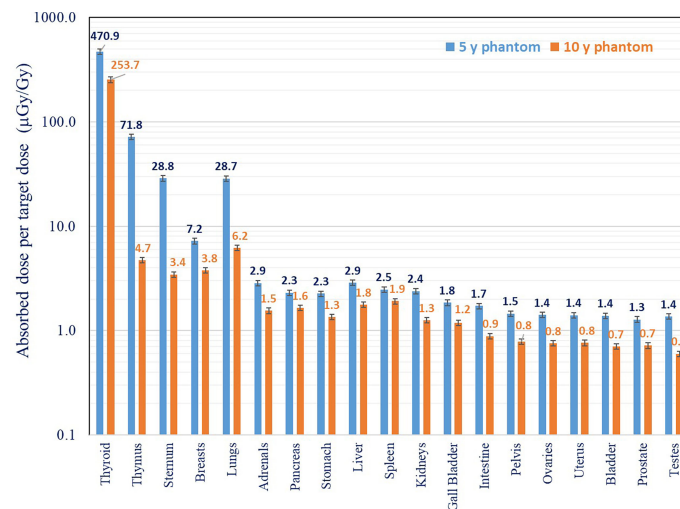


FIGURE 5 | Comparison of non-neutron out-of-field organ doses for 5- and 10-year-old phantom. Measurements were performed with RPL detectors.

the target, and then more neutrons are produced. On the other side, high-energy neutrons have less probability of interaction in a smaller volume, and if they are not slowed down enough, they can escape from the phantom without interaction. Conversely, in a larger phantom, the probability of interactions is higher and then the dose can be higher.

3.1.3. Out-of-Field Total Organ Dose

The comparison of neutron doses, non-neutron doses, and total organ doses (expressed as the sum of neutron and non-neutron doses) is shown in **Figures 7A, B** for both phantoms. As explained in Section 2.3.2, the neutron organ doses are calculated from fitting measurement results obtained with two types of track detectors. Due to the contribution from scattered protons in the organs close to the target, neutron

doses are lower in comparison to the secondary non-neutron doses. For organs further from the target, the neutron dose increases in comparison to the non-neutron dose and dominates in total dose (as explained in Section 3.1.1). Non-neutron doses measured in the thyroid at 13.5 and 16.6 cm from the isocenter are by factors of 3 and 1.5 higher in comparison to neutron doses for 5- and 10-year-old phantoms, respectively. For the organs further away from the field (intestine, bladder, ovaries, testes) in the 10-year-old phantom, the non-neutron doses are below 1 mGy and are not visible, as shown in **Figure 7B**. In the proton scanning beam, mean out-of-field total doses including neutron and non-neutron components range from 0.6 mSv/Gy (5-year), 0.4 mSv/Gy (10-year) in the thyroid to <0.01 mSv/Gy for both phantoms in the intestines, ovaries, bladder, and testes.

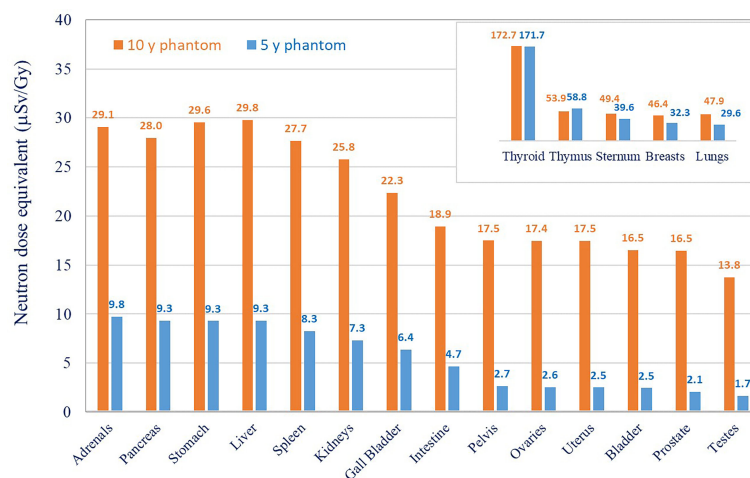


FIGURE 6 | Neutron dose equivalent in different organs for 5- and 10-year-old phantom. Results were extrapolated from data the measured with track detectors.

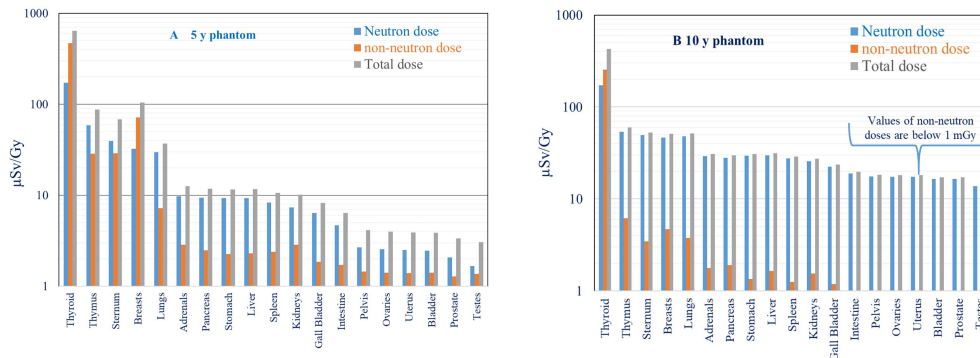


FIGURE 7 | (A, B) Comparison of neutron, non-neutron, and total equivalent organ doses ($\mu\text{Sv/Gy}$) for 5- (A) and 10-year-old (B) phantoms.

3.2 Comparison of Out-of-Field Doses for Different Radiation Therapy Modalities

Results obtained in this study were compared with out-of-field doses measured for different photon therapy modalities (Figures 8 and 9). In the previous experiments performed by EURADOS WG9, measurements of out-of-field doses in 5- and 10-year-old phantoms were performed for 3D CRT, IMRT, and GK radiotherapy (33, 43). In all experiments, the 5-cm-diameter brain tumor (PTV was 6 cm) was situated inside the left hemisphere of the head (intracranial tumor). Details of the irradiations for each technique are shown in Table 2. As shown in Figures 8A, B, a comparison of total dose equivalents measured as a function of distance from the isocenter is shown for 3D-CRT, GK, IMRT, and IMPT for 5- and 10-year-old phantoms. As the measurements with track detectors were performed only on limited positions, the results for distances from approximately 30 to 65 cm were calculated as described in Chapter 2.3.2.

A higher ratio of measured doses from 3D-CRT in comparison to measured doses with IMRT in the 5-year-old phantom compared to the 10-year-old phantom is shown in Figures 8A, B. This is explained in detail in a previously published paper by the

use of a mechanical wedge for 5-year-old phantom 3DCRT treatment which increases out-of-field doses (33). Except for the eyes which were better spared during the GK treatment in comparison to 3DCRT and IMRT, out-of-field doses for more distant organs were higher up to factors of 2.8 and 4 times for GK compared to IMRT in 5- and 10-year-old phantoms, respectively. Results for IMPT show significantly lower out-of-field doses for both phantoms (Figures 8A, B) when compared to all three photon therapy techniques. The difference close to the target is at the level of one order of magnitude and more than two orders of magnitude further away from the target. The difference between three photon techniques and IMPT is more pronounced for 5-year-old phantoms. The ratio of different photon techniques in comparison to IMPT is as follows: 3DCRT/IMPT, GK/IMPT, and IMRT/IMPT are 120, 185, and 62 for the 5-year-old phantom and 14, 61, and 14 for the 10-year-old phantom, respectively.

The comparison of total out-of-field organ doses in 5- and 10-year-old phantoms for IMPT and 3D-CRT, GK, and IMRT is shown in Figures 9A, B and Table 3. For photon techniques (3D-CRT, GK, and IMRT), beam energies are below 10 MeV and the contribution of secondary neutrons can be neglected. Consequently, the total out-of-field dose is considered to be

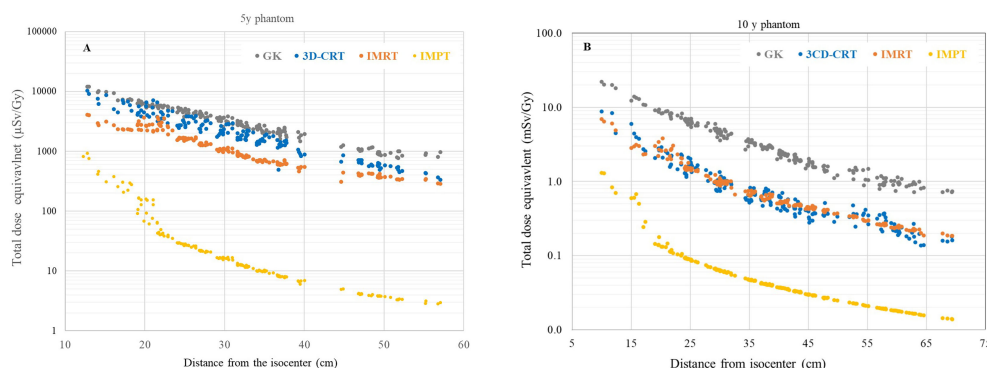


FIGURE 8 | (A, B) Comparison of total dose equivalent organ doses for all irradiation techniques as function of distance from the isocenter for 5- (A) and 10-year-old (B) phantoms.

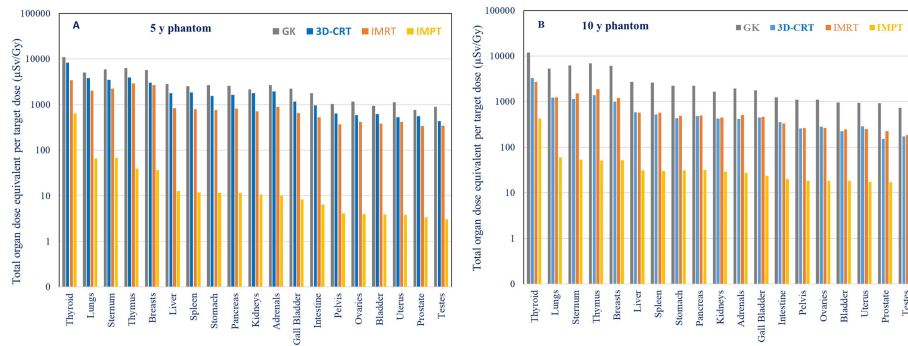


FIGURE 9 | (A, B) Comparison of total doses in a 5-year-old phantom and a 10-year-old phantom for IMRT, 3D-CRT, GK and IMPT. For IMPT, the total dose equivalent is taken as the sum of neutron and non-neutron contributions, and for the photon techniques, the total dose equivalent is simply the photon component.

the out-of-field photon dose. For IMPT, the total dose equivalent includes both contributions from neutron doses based on measurements and calculations based on track detector data and non-neutron doses measured with RPL detectors.

In all cases, for both photon and proton radiotherapy, higher organ doses were measured for the 5-year-old phantom in comparison to the 10-year-old phantom, as expected due to the smaller distance from healthy organs to the irradiated target. As shown in the previous study, organ dose equivalents were on average 1.1, 1.6, and 3.0 times higher for the 5-year-old than for the 10-year-old phantom for GK, IMRT, and 3D CRT, respectively (32, 33). Non-neutron organ dose comparisons performed in this study for IMPT show on average 1.8 times higher doses for the 5-year-old phantom than for the 10-year-old phantom.

4. DISCUSSION

Out-of-field organ dose measurements under realistic clinical conditions are important for validation and benchmarking of dose calculation methods and are also an important input for secondary cancer risk modeling. In the literature, there is little data on organ doses for child brain tumors irradiated with PBS.

Moreover, for PBS, there are no studies with measurements of secondary radiation doses to specific organs under realistic clinical conditions inside pediatric anthropomorphic phantoms containing materials with realistic tissue densities.

The available data are mostly for passive scattering techniques which are associated with higher doses from secondary radiation in comparison to active technique due to the contributions to secondary radiation from beam formation elements (14, 27, 50, 51). In the paper by Gudowska et al., a review of secondary doses in ion therapy is shown but mostly for adult patients, or passive scattering. The paper showed large variations of secondary absorbed doses to healthy organs from 7 μGy to up to 2.4 Gy (per prescribed dose) (28). In the paper by Ardenfors et al., the out-of-field absorbed and equivalent doses in different organs calculated by MC simulations for a whole-body phantom (age 25) ranged from 60.36 $\mu\text{Gy/Gy}$ to 0.22 $\mu\text{Gy/Gy}$ and from 151 $\mu\text{Sv/Gy}$ to 0.63 $\mu\text{Sv/Gy}$ for thyroid and ovaries, respectively (25). These values are lower than doses measured in the current study due to a larger phantom size and consequently larger distances from the target in the published study. Moreover, Ardenfors et al. used one lateral proton field with energies between 60 and 97 MeV to cover the 133- cm^3 target volume (25). In the current study, for both phantoms the PTV was 113 cm^3 and two proton

TABLE 3 | Comparison of measured total organ dose equivalent in selected organs for different techniques for the same brain tumor treatment in 5- and 10-year-old phantom.

5-year phantom						
Techniques	Total organ dose equivalent per target dose (mSv/Gy)					
	Thyroid	Thymus	Lungs	Liver	Bladder	Testes
GK	10.96	6.34	5.06	2.82	0.94	0.90
3D-CRT	8.28	3.93	3.80	1.78	0.62	0.43
IMRT	3.44	2.93	2.00	0.83	0.38	0.34
IMPT	0.64	0.04	0.06	0.01	0.004	0.003
10-year phantom						
GK	12.0	6.91	5.57	2.73	0.95	0.73
3D-CRT	3.26	1.38	1.22	0.58	0.22	0.17
IMRT	2.70	1.85	1.24	0.58	0.25	0.19
IMPT	0.42	0.05	0.06	0.03	0.02	0.01

fields with energies between 70 and 140 MeV were used. Higher proton energies correspond to higher out-of-field doses (31). In the other study by Ardenfors et al., the organ absorbed doses calculated for a 6-year-old male patient for brain proton radiotherapy with a pencil beam scanning technique were 23 $\mu\text{Gy}/\text{Gy}$ and 0.8 $\mu\text{Gy}/\text{Gy}$ for the thyroid and bladder, respectively. The treatment plans were created with one lateral and one vertex field with energies 80–110 MeV and 92–124 MeV, and the planned target volume (PTV) was 24 cm^3 (51). Out-of-field doses are increasing with proton energy, and primary field size (51 the difference in the PTV (24 cm^3 vs 113 cm^3) and maximum energy (124 MeV vs 140 MeV) may explain the differences between doses simulated by Ardenfors et al. and doses measured in the current study. Sayah et al. performed detailed simulations of secondary radiation doses for proton radiotherapy of pediatric patients treated for intracranial tumors using a passive scattering technique and reported averaged neutron equivalent doses for a 5-year-old patient of 1.79 mSv/Gy and 0.41 mSv/Gy for the thyroid and bladder, respectively (27). On the other hand, in the paper of Geng et al., neutron equivalent doses simulated for a proton pencil beam scanning technique for 14-year-old brain tumor patients were in the range of 100 $\mu\text{Sv}/\text{Gy}$ and 1 $\mu\text{Sv}/\text{Gy}$ for the thyroid and bladder, respectively (52). In turn, neutron equivalent doses simulated by Ardenfors et al. for a 6-year-old male patient for a brain proton PBS radiotherapy was 62 $\mu\text{Sv}/\text{Gy}$ and 2 $\mu\text{Sv}/\text{Gy}$ for the thyroid and bladder, respectively (51). Results obtained by both Geng et al. and Ardenfors et al. are similar to the data presented in this study, taking into consideration different field setups, size of PTV, and energies used in different studies. Organ dose equivalents for the 5-year-old phantom (with PTV 113 cm^3) from this study ranged from 176 to 1.8 $\mu\text{Sv}/\text{Gy}$ and are in a good agreement with MC simulations performed by Ardenfors et al. (51), where neutron equivalent doses to organs ranged between 141 and 0.5 $\mu\text{Sv}/\text{Gy}$ for the 6-year-old male patient (with PTV 24 cm^3).

When comparing different radiotherapy modalities presented in this paper, it can be seen that for IMPT with a typical treatment dose up to 2 (RBE) Gy in 27 fractions, the total absorbed doses (non-neutron + neutron component) are 32 mGy (5-year phantom) and 21 mGy (10-year phantom) in the thyroid, 1.77 mGy (5-year phantom) and 2.5 mGy (10-year phantom) in the breasts, and, on average for both phantoms, 0.4 mGy in the testes. This is significantly lower in comparison to the IMRT technique where for the full treatment the doses would be 169 mGy (5-year) and 133 mGy (10-year) for the thyroid, 131 mGy (5-year) and 59 mGy (10-year) for the breasts, and 17 mGy (5-year) and 9 mGy (10-year) for the testes. An additional comparison of total equivalent doses in selected organs for different techniques is shown in **Table 3**. The highest out-of-field organ doses (total dose equivalent) were measured for the GK technique (12 mSv/Gy in thyroid to 0.90 mSv/Gy in testes) while for IMPT the total dose equivalents were 0.42 mSv/Gy (10-year) and 0.65 mSv/Gy (5-year) in the thyroid and 0.003 mSv/Gy (5-year) and 0.01 mSv/Gy (10-year) in the testes. In the real clinical situation, the GK radiotherapy of a 5-cm-diameter target is performed for a large cerebral arteriovenous malformation

AVM, where a dose of 30 Gy is delivered in five fractions (53). In this case, organ doses to the entire treatment are from 344 mGy in the thyroid, 177 mGy in the breasts, and 24 mGy in the testes on average for both phantoms. Based on literature findings, proton radiotherapy can be successfully used in treating intermediate- and large-sized AVMs (35). For the large-sized AVMs typically treated with protons, the prescribed dose is approximately 21–25 Gy (36). Consequently, total organ doses (averaged over both phantoms) based on measurements from this study would be 12, 1, and 0.20 mGy for the thyroid, breasts, and testes, respectively. However, it should be noted that in a standard clinical treatment, GK is used to treat much smaller target volumes than presented here.

There is no similar comparison of out-of-field doses between photon and proton radiotherapy available in the literature. Previous studies are mostly performed by MC simulations or using TPS calculations. Even if the same phantoms and similar PTV are used, there are always differences in the configuration of the radiation fields between different techniques and also between different facilities, leading to difficulties in explaining differences between out-of-field doses. Also, clinically used treatment planning systems are not aimed at an accurate calculation of out-of-field doses originating from secondary radiation (54, 55).

Measurements of out-of-field doses in realistic conditions presented in this study provide appropriate methodology and are important for second cancer risk calculations as well as input to analytical models for eventual clinical implementation.

Even though for the same brain tumor treatment, the tissues and organs received much lower total dose equivalents during IMPT in comparison to different photon techniques as shown in this study, it is nevertheless important to consider the second cancer risk estimations in order to make risk–benefit judgements. It is therefore essential to develop databases of assessed doses from secondary radiation to healthy organs outside the primary fields in order to accurately evaluate the long-term outcomes associated with proton therapy.

5. CONCLUSIONS

In this study, out-of-field organ doses were measured inside 5- and 10-year-old pediatric anthropomorphic phantoms for the treatment of a 5-cm-diameter brain tumor using intensity-modulated proton therapy (IMPT) and compared with previous measurements for three different photon radiotherapy techniques: IMRT, 3D CDRT, and GK. The results showed that non-neutron doses are higher in the 5-year-old phantom compared to the 10-year-old phantom due to increased proximity of organs to the target. Neutron doses are lower than non-neutron doses close to the target (factor of 4 in thyroid). At the same time, neutron doses become larger than non-neutron doses further away from the target (factor of 3–4). The total dose equivalent in proton therapy ranges from 0.6 mSv/Gy in the thyroid to <0.01 mSv/Gy in the gonad region, while for photon techniques the total organ dose equivalent ranges from 12 mSv/Gy in the thyroid to 0.22 mSv/Gy in the gonad region. Proton therapy results in lower out-of-field doses compared to 3D-CRT, GK, and IMRT techniques by one

order of magnitude close to the brain and more than two orders of magnitude further away from the brain.

DATA AVAILABILITY STATEMENT

The raw data supporting the conclusions of this article will be made available by the authors, without undue reservation.

AUTHOR CONTRIBUTIONS

ŽK, LS, RH, and PO contributed to the conception and design of the study. The measurement data analysis and interpretation of neutron dose measurements were performed by IA, MD, MS-H, MÁC-P, CD, MR-E, IMR. The measurements with TLDs and RPLs, data analysis, and interpretation of the results were performed by ŽK, LS, MM, SM, NM, and MS-H. The design of the irradiation setup and preparation of radiotherapy treatment plans were performed by NM, LS, DK, KJ, and RK. ŽK wrote the first draft of the manuscript.

LS and MS-H wrote sections of the manuscript. All authors contributed to manuscript revision, discussion, and approval of the submitted version.

FUNDING

KJ acknowledges the support of InterDokMed project No. POWR.03.02.00-00-I013/ 16. The work was partly supported by the POIR.04.04.00-00-15E5/18 project carried out within the TEAM-NET program of the Foundation for Polish Science cofinanced by the European Union under the European Regional Development Fund. IMR acknowledges the financial support from the Spanish Ministry of Science, Innovation and Universities (RYC2018-024043-I).

ACKNOWLEDGMENTS

This study was carried out within, and partly supported by, the European Radiation Dosimetry Group (EURADOS, WG9 Radiation Dosimetry in Radiotherapy).

REFERENCES

- Howlader N, Noone AM, Krapcho M, Miller D, Brest A, Yu M, et al. *SEER Cancer Statistics Review, 1975-2017*. Bethesda, MD: National Cancer Institute (2020). Available at: https://seer.cancer.gov/csr/1975_2017/.
- Merchant TE, Hua C, Shukla H, Ying X, Nill S, Oelfke U. Proton Versus Photon Radiotherapy for Common Pediatric Brain Tumors: Comparison of Models of Dose Characteristics and Their Relationship to Cognitive Function. *Pediatr Blood Cancer* (2008) 51:110–17. doi: 10.1002/pbc.21530
- Mizumoto M, Oshiro Y, Yamamoto T, Kohzaki H, Sakurai H. Proton Beam Therapy for Pediatric Brain Tumor. *Neurol Med Chir* (2017) 57:343–55. doi: 10.2176/nmc.ra.2017-0003
- Rombi B, Vennarini S, Vinante L, Ravanelli D, Amichetti M. Proton Radiotherapy for Pediatric Tumors: Review of First Clinical Results. *Ital J Pediatr* (2014) 40:2640–74. doi: 10.1186/s13052-014-0074-6
- Leroy R, Benahmed N, Hulstaert F, Van Damme N, De Ruysscher D. Proton Therapy in Children: A Systematic Review of Clinical Effectiveness in 15 Pediatric Cancers. *Int J Radiat Oncol Biol Phys* (2016) 95:267–78. doi: 10.1016/j.ijrobp.2015.10.025
- Thomas H, Timmermann B. Paediatric Proton Therapy. *Br J Radiol* (2020) 93:20190601. doi: 10.1259/bjr.20190601
- Newhauser WD, Durante M. Assessing the Risk of Second Malignancies After Modern Radiotherapy. *Nat Rev Cancer* (2011) 11(6):438–48. doi: 10.1038/nrc3069
- Moteabbed M, Yock TI, Paganetti H. The Risk of Radiation-Induced Second Cancers in the High to Medium Dose Region: A Comparison Between Passive and Scanned Proton Therapy, IMRT and VMAT for Pediatric Patients With Brain Tumors. *Phys Med Biol* (2014) 59:2883–99. doi: 10.1088/0031-9155/59/12/2883
- Hall EJ. Intensity Modulated Radiation Therapy Proton, and the Risk of Second Cancers. *Int J Radiat Oncol Biol Phys* (2006) 65(1):1–7. doi: 10.1016/j.ijrobp.2006.01.027
- NCRP. *Second Primary Cancers and Cardiovascular Disease After Radiation Therapy: NCRP 390 Report No. 151*. Bethesda, 23 Maryland: National Council on Radiation Protection and Measurements (2011).
- National Research Council. *Health Risks From Exposure to Low Levels of Ionizing Radiation: BEIR VII – Phase 2*. Washington, DC: The National Academies Press (2006).
- Bassal M, Mertens AC, Taylor L, Neglia JP, Greffe BS, Hammond S, et al. Risk of Selected Subsequent Carcinomas in Survivors of Childhood Cancer. A Report From the Childhood Cancer Survivor Study. *Clin Oncol* (2006) 24:3 476–83. doi: 10.1200/JCO.2005.02.7235
- Neglia JP, Friedman DL, Yasui Y, Maetens AC, Hammond S, Stovall M, et al. Second Malignant Neoplasms in Five-Year Survivors of Childhood Cancer: Childhood Cancer Survivor Study. *Natl Cancer Inst* (2001) 93(8):618–29. doi: 10.1093/jnci/93.8.618
- Zacharatou Jarlskog C, Paganetti H. Risk of Developing Second Cancer From Neutron Dose in Proton Therapy as Function of Field Characteristics, Organ, and Patient Age. *Int J Radiat Oncol Biol Phys* (2008) 72:228–35. doi: 10.1016/j.ijrobp.2008.04.069
- Paganetti H, Blakely E, Carabe-Fernandez A, Carlson DJ, Das IJ, Dong L, et al. Report of the AAPM TG-256 on the Relative Biological Effectiveness of Proton Beams in Radiation Therapy. *Med Phys* (2019) 46:3 53–78. doi: 10.1002/mp.13390
- Dasu A, Toma-Asu I. Models for the Risk of Secondary Cancers From Radiation Therapy. *Phys Med* (2017) 41:232–38. doi: 10.1016/j.ejmp.2017.02.015
- Athar BS, Bednarz B, Seco J, Hancox C, Paganetti H. Comparison of Out-of-Field Photon Doses in 6 MV IMRT and Neutron Doses in Proton Therapy for Adult and Pediatric Patients. *Phys Med Biol* (2010) 55:2879–91. doi: 10.1088/0031-9155/55/10/006
- Sá AC, Barateiro A, Bednarz B, Borges C, Pareira J, Baptista M, et al. Assessment of Out-of-Field Doses in Radiotherapy Treatments of Paediatric Patients Using Monte Carlo Methods and Measurements. *Phys Med* (2020) 71:53–61. doi: 10.1016/j.ejmp.2020.02.008
- Howell RM, Scarboro SB, Kry SF, Yaldo DZ. Accuracy of Out-of-Field Dose Calculations by a Commercial Treatment Planning System. *Phys Med Biol* (2010) 55:26999–7008. doi: 10.1088/0031-9155/55/23/S03
- Miljanić S, Bessieres I, Bordy J-M, d'Errico F, Di Fulvio A, Kabat D, et al. Clinical Simulations of Prostate Radiotherapy Using BOMAB-Like Phantoms. *Results Photons Radiat Meas* (2013) 57:35–47. doi: 10.1016/j.radmeas.2012.12.012
- Sanchez-Nieto B, Medina-Ascanio KN, Rodriguez-Mongua JL, Doerner E, Espinoza I. Study of Out-of-Field Dose in Photon Radiotherapy: A Commercial Treatment Planning System Versus Measurements and Monte Carlo Simulations. *Med Phys* (2020) 47:4616–25. doi: 10.1002/mp.14356
- Stolarczyk L, Trinkl S, Romero-Exposito M, Mojzeszek N, Ambrozova I, Dominog C, et al. Dose Distribution of Secondary Radiation in a Water Phantom for a Proton Pencil Beam—EURADOS WG9 Intercomparison Exercise. *Phys Med Biol* (2018) 63:085017. doi: 10.1088/1361-6560/aab469

23. ICRP Publication 92. Relative Biological Effectiveness (RBE), Quality Factor (Q) and Radiation Weighting Factor (W_r). *Ann ICRP* (2003) 33:1–121. doi: 10.1016/S0146-6453(03)00024-1
24. Paganetti H, van Luijk P. Biological Considerations When Comparing Proton Therapy With Photon Therapy. *Semin Radiat Oncol* (2013) 23:77–87. doi: 10.1016/j.semradonc.2012.11.002
25. Ardenfors O, Dasu A, Lillhök J, Persson L, Gudowska I. Out-Of-Field Doses From Secondary Radiation Produced in Proton Therapy and the Associated Risk of Radiation-Induced Cancer From a Brain Tumor Treatment. *Phys Med* (2018) 53:129–36. doi: 10.1016/j.ejmp.2018.08.020
26. Clasié B, Wroe A, Kooy H, Depauw N, Flanz J, Paganetti H. Assessment of Out-of-Field Absorbed Dose and Equivalent Dose in Proton Fields. *Med Phys* (2010) 37:311–21. doi: 10.1118/1.3271390
27. Sayah R, Farah J, Donadille L, Hérault J, Delacroix S, De Marzi L, et al. Secondary Neutron Doses Received by Paediatric Patients During Intracranial Proton Therapy Treatments. *J Radiol Prot* (2014) 34:279–96. doi: 10.1088/0952-4746/34/2/279
28. Gudowska I, Ardenfors O, Toma-Dasu I, Dasu A. Radiation Burden From Secondary Doses to Patients Undergoing Radiation Therapy With Photons and Light Ions and Radiation Doses From Imaging Modalities. *Radiat Prot Dosim* (2014) 161:357–62. doi: 10.1093/rpd/nct335
29. Knežević Ž, Ambrožová I, Domingo C, De Saint-Hubert M, Majer M, Martínez-Rovira I, et al. Comparison of Response of Passive Dosimetry in Scanning Proton Radiotherapy—A Study Using Paediatric Anthropomorphic Phantoms. *Radiat Prot Dosim* (2018) 180:256–60. doi: 10.1093/rpd/ncx254
30. Farah J, Mares V, Romero-Exposito M, Trinkl S, Domingo C, Dufek V. Measurement of Stray Radiation Within a Scanning Proton Therapy Facility: EURADOS WG9 Intercomparison Exercise of Active Dosimetry Systems. *Med Phys* (2015) 42:2572–84. doi: 10.1118/1.4916667
31. Mojżeszek N, Farah J, Kłodowska M, Ploc O, Stolarczyk L, Waligórski, et al. Measurement of Stray Neutron Doses Inside the Treatment Room From a Proton Pencil Beam Scanning System. *Phys Med* (2017) 34:80–4. doi: 10.1016/j.ejmp.2017.01.013
32. Majer M, Ambrožová I, Davidková M, De Saint-Hubert M, Kasabašić M, Knežević Ž, et al. Out-Of-Field Doses in Pediatric Craniospinal Irradiations With 3D-CRT, VMAT and Scanning Proton. *Med Phys* (2022) 49:2672–83. doi: 10.1002/mp.15493
33. Majer M, Stolarczyk L, De Saint-Hubert M, Kabat D, Knežević Ž, Miljanić S, et al. Out-Of-Field Doses Measurements for 3D Conformal and Intensity Modulated Radiotherapy of a Paediatric Brain Tumour. *Radiat Prot Dosim* (2017) 176:331–40. doi: 10.1093/rpd/ncx015
34. De Saint-Hubert M, Majer M, Hršak H, Heinrich Z, Knežević Ž, Miljanić S, et al. Out-Of-Field Doses in Children Treated for Large Arteriovenous Malformations Using Hypofractionated Gamma Knife Radiosurgery and Intensity-Modulated Radiation Therapy. *Radiat Prot Dosim* (2018) 181:100–10. doi: 10.1093/rpd/ncx301
35. Lehrer EJ, Prabhu AV, Sindhu KK, Lazarev S, Ruiz-Garcia H, Peterson JL, et al. Proton and Heavy Particle Intracranial Radiosurgery. *Biomedicine* (2021) 9:1–27. doi: 10.3390/biomedicine9010031
36. Silander H, Pellettieri L, Enblad P, Montelius A, Grusell E, Vallhagen-Dahlgren C, et al. Fractionated, Stereotactic Proton Beam Treatment of Cerebral Arteriovenous Malformations. *Acta Neurol Scand* (2004) 109:85–90. doi: 10.1046/j.1600-0404.2003.00154.x
37. Hattangadi, Chapman PH, Bussière MR, Daartz J, Loeffler JS, Shih HA, et al. Planned Two-Fraction Proton Beam Stereotactic Radiosurgery for High-Risk Inoperable Cerebral Arteriovenous Malformations. *Int J Radiat Oncol Biol Phys* (2012) 83:533–41. doi: 10.1016/j.ijrobp.2011.08.003
38. Nakai Y, Ito Y, Sato M, Nakamura K, Shiigai M, Takigawa T, et al. Multimodality Treatment for Cerebral Arteriovenous Malformations – Complementary Role of Proton Beam Radiotherapy. *Neurol Med Chir (Tokyo)* (2012) 52:859–64. doi: 10.2176/nmc.52.859
39. Romero-Exposito M, Domingo C, Sanchez-Doblado F, Ortega-Galabert O, Gallego S. Experimental Evaluation of Neutron Dose in Radiotherapy Patients: Which Dose? *Med Phys* (2016) 43:360–67. doi: 10.1118/1.4938578
40. Knežević Ž, Stolarczyk L, Bessieres I, Bordy JM, Miljanić S and Olko P. Photon Dosimetry Methods Outside the Target Volume in Radiation Therapy: Optically Stimulated Luminescence (OSL), Thermoluminescence (TL) and Radiophotoluminescence (RPL) Dosimetry. *Radiat Meas* (2013) 57:9–18. doi: 10.1016/j.radmeas.2013.03.004
41. ATGC 2007. *Explanation Material of RPL Glass Dosimeter: Small Element System*. Tokyo, Japan: Asahi Techno Glass Corporation (2007).
42. Gottschalk B, Cascio EW, Daartz J, Wagner Miles S. On the Nuclear Halo of a Proton Pencil Beam Stopping in Water. *Phys Med Biol* (2015) 60:5627–54. doi: 10.1088/0031-9155/60/14/5627
43. Bilski P. Dosimetry of Densely Ionising Radiation With Three LiF Phosphors for Space Application. *Radiat Prot Dosim* (2006) 120:397–400. doi: 10.1093/rpd/nci674
44. Miljanić S, Ranogajec-Komor M, Blagus S, Pálfalvi JK, Pázmándi T, Deme S, et al. Response of Radiophotoluminescent Dosimeters to Neutrons. *Radiat Meas* (2008) 43:1068–71. doi: 10.1016/j.radmeas.2007.11.012
45. Silva EH, Struelens L, Covens P, Ueno S, Koguchi Y, Vanhavere F, et al. Optimization of Radiophotoluminescent Glass Dosimeter for Occupational Eye Lens Dosimetry in Interventional Radiology/Cardiology. *Radiat Prot Dosim* (2018) 182:177–83. doi: 10.1093/rpd/ncy046
46. Jadrničková I, Spurný F. To the Spectrometry of Linear Energy Transfer in Charged Particle Beams by Means of Track-Etch Detectors. *Radiat Meas* (2008) 43:S191–4. doi: 10.1016/j.radmeas.2008.04.010
47. Domingo C, de San Pedro M, García-Fusté MJ, Romero MT, Amgarou K. And Fernández F Estimation of the Response Function of a PADC Based Neutron Dosimeter in Terms of Fluence and Hp(10). *Radiat Meas* (2013) 50:82–6. doi: 10.1016/j.radmeas.2012.02.016
48. Romero-Exposito M, Martínez-Rovira I, Domingo C, Bedogni R, Pietropaolo A, Pola A, et al. Calibration of a Poly Allyl Diglycol Carbonate (PADC) Based Track-Etched Dosimeter in Thermal Neutron Fields. *Radiat Meas* (2018) 119:204–8. doi: 10.1016/j.radmeas.2018.11.007
49. Pachnerová Brabcová K, Ambrožová I, Kolísková Z, Malušek A. Uncertainties in Linear Energy Transfer Spectra Measured With Track-Etched Detectors in Space. *Nucl Instrum Meth A* (2013) 713:5–10. doi: 10.1016/j.nima.2013.03.012
50. Matsumoto S, Koba Y, Kohno R, Lee C, Bolch W, Kai M. Secondary Neutron Doses to Pediatric Patients During Intracranial Proton Therapy: Monte Carlo Simulation of the Neutron Energy Spectrum and its Organ Doses. *Health Phys* (2016) 110:380–86. doi: 10.1097/HP.0000000000000461
51. Ardenfors O, Gudowska I, Flejmer AM, Dasu A. Impact of Irradiation Setup in Proton Spot Scanning Brain Therapy on Orga Doses From Secondary Radiation. *Radiat Prot Dosim* (2018) 180:261–66. doi: 10.1093/rpd/ncy013
52. Geng C, Moteabbed M, Xie Y, Schuemann J, Yock T, Paganetti H. Assessing the Radiation-Induced Second Cancer Risk in Proton Therapy for Pediatric Brain Tumors: The Impact of Employing a Patient-Specific Aperture in Pencil Beam Scanning. *Phys Med Biol* (2016) 61:12–22. doi: 10.1088/0031-9155/61/1/12
53. Xiao F, Gorgulho AA, Lin CS, Chen CH, Agazaryan N, Vinuela F, et al. Treatment of Giant Cerebral Arteriovenous Malformation: Hypofractionated Stereotactic Radiation as the First Stage. *Neurosurgery* (2010) 67:1253–59. doi: 10.1227/NEU.0b013e3181efbaef
54. Kry SF, Bednarz B, Howell RM, Dauer L, Followill D, Klein D. AAPM TG 158: Measurements and Calculation of Doses Outside the Treated Volume From External-Beam Radiation Therapy Med. *Phys* (2017) 44:391–429. doi: 10.1002/mp.12462
55. Newhauser WD, Zhang R. The Physics of Proton Therapy. *Phys Med Biol* (2015) 60:155–209. doi: 10.1088/0031-9155/60/8/R155

Conflict of Interest: The authors declare that the research was conducted in the absence of any commercial or financial relationships that could be construed as a potential conflict of interest.

Publisher's Note: All claims expressed in this article are solely those of the authors and do not necessarily represent those of their affiliated organizations, or those of the publisher, the editors and the reviewers. Any product that may be evaluated in this article, or claim that may be made by its manufacturer, is not guaranteed or endorsed by the publisher.

Copyright © 2022 Knežević, Stolarczyk, Ambrožová, Caballero-Pacheco, Davidková, De Saint-Hubert, Domingo, Jeleni, Kopeć, Krzempek, Majer, Miljanić, Mojżeszek, Romero-Exposito, Martínez-Rovira, Harrison and Olko. This is an open-access article distributed under the terms of the Creative Commons Attribution License (CC BY). The use, distribution or reproduction in other forums is permitted, provided the original author(s) and the copyright owner(s) are credited and that the original publication in this journal is cited, in accordance with accepted academic practice. No use, distribution or reproduction is permitted which does not comply with these terms.



Comparison of Breast Cancer Radiotherapy Techniques Regarding Secondary Cancer Risk and Normal Tissue Complication Probability – Modelling and Measurements Using a 3D-Printed Phantom

OPEN ACCESS

Edited by:

Francisco Sanchez-Doblado,
Sevilla University, Spain

Reviewed by:

Khaled Elsayad,
University of Münster, Germany
Beatriz Sanchez-Nieto,
Pontifical Catholic University of Chile,
Chile

*Correspondence:

Marc Vogel
Marc.Vogel@uks.eu

[†]These authors share senior
authorship

Specialty section:

This article was submitted to
Radiation Oncology,
a section of the journal
Frontiers in Oncology

Received: 09 March 2022

Accepted: 15 June 2022

Published: 27 July 2022

Citation:

Vogel M, Gade J, Timm B,
Schürmann M, Auerbach H, Nüsken F,
Rübe C, Melchior P and Dzierma Y
(2022) Comparison of Breast Cancer
Radiotherapy Techniques Regarding
Secondary Cancer Risk and Normal
Tissue Complication Probability –
Modelling and Measurements
Using a 3D-Printed Phantom.
Front. Oncol. 12:892923.
doi: 10.3389/fonc.2022.892923

Marc Vogel^{1*}, Jonas Gade¹, Bernd Timm², Michaela Schürmann¹, Hendrik Auerbach¹,
Frank Nüsken¹, Christian Rübe¹, Patrick Melchior^{1†} and Yvonne Dzierma^{1†}

¹ Department of Radiotherapy and Radiation Oncology, Saarland University Medical Centre, Homburg, Germany,

² Siemens Healthcare GmbH, Technical Service, Erlangen, Germany

Background: Radiotherapy after breast-conserving therapy is a standard postoperative treatment of breast cancer, which can be carried out with a variety of irradiation techniques. The treatment planning must take into consideration detrimental effects on the neighbouring organs at risk—the lung, the heart, and the contralateral breast, which can include both short- and long-term effects represented by the normal tissue complication probability and secondary cancer risk.

Patients and Methods: In this planning study, we investigate intensity-modulated (IMRT) and three-dimensional conformal (3D-CRT) radiotherapy techniques including sequential or simultaneously integrated boosts as well as interstitial multicatheter brachytherapy boost techniques of 38 patients with breast-conserving surgery retrospectively. We furthermore develop a 3D-printed breast phantom add-on to allow for catheter placement and to measure the out-of-field dose using thermoluminescent dosimeters placed inside an anthropomorphic phantom. Finally, we estimate normal tissue complication probabilities using the Lyman–Kutcher–Burman model and secondary cancer risks using the linear non-threshold model (out-of-field) and the model by Schneider et al. (in-field).

Results: The results depend on the combination of primary whole-breast irradiation and boost technique. The normal tissue complication probabilities for various endpoints are of the following order: 1%–2% (symptomatic pneumonitis, ipsilateral lung), 2%–3% (symptomatic pneumonitis, whole lung), and 1%–2% (radiation pneumonitis grade ≥ 2 , whole lung). The additional relative risk of ischemic heart disease ranges from +25% to +35%. In-field secondary cancer risk of the ipsilateral lung in left-sided treatment is around 50 per 10,000 person-years for 20 years after exposure at age 55. Out-of-field

estimation of secondary cancer risk results in approximately 5 per 10,000 person-years each for the contralateral lung and breast.

Conclusions: In general, 3D-CRT shows the best risk reduction in contrast to IMRT. Regarding the boost concepts, brachytherapy is the most effective method in order to minimise normal tissue complication probability and secondary cancer risk compared to teletherapy boost concepts. Hence, the 3D-CRT technique in combination with an interstitial multicatheter brachytherapy boost is most suitable in terms of risk avoidance for treating breast cancer with techniques including boost concepts.

Keywords: radiation therapy, secondary cancer risk, normal tissue complication probability (NTCP), brachytherapy, breast cancer, 3D-printing

1 INTRODUCTION

Regarding the female sex, breast carcinoma was both the most frequent entity of all new cancer incidences and the most frequent cause of mortality of all cancer deaths in Europe in 2018 (1, 2). Due to this importance for society as a whole, screening programmes, targeted diagnostics, and a wide variety of therapy regimes are standard today and are subject to constant testing and further refinement. Adjuvant radiotherapy in the context of breast-conserving therapy (BCT) has been shown to be an indispensable component of the therapy regime. A meta-analysis of the Early Breast Cancer Trialists' Collaborative Group in 2011 found a significant reduction in the risk of recurrence within 10 years for adjuvant radiotherapy vs. no adjuvant radiotherapy (3). The German Society for Radiation Oncology (DEGRO) also clearly advocates adjuvant radiation in its guideline recommendation for the treatment of breast carcinoma, and at the same time, it emphasises the importance of additional dose saturation (boost) to the tumour bed in order to further reduce the risk of local recurrence (4).

For adjuvant breast irradiation (whole-breast irradiation, WBI), the procedures three-dimensional conformal radiotherapy (3D-CRT), intensity-modulated radiotherapy (IMRT), and volume-modulated arc therapy (VMAT) are currently mentioned in the S3 guidelines of the German Cancer Society, German Cancer Aid, and Association of the Scientific Medical Societies in Germany (AWMF) (5). 3D-CRT was the treatment standard until the 2010s but is increasingly being replaced by IMRT or VMAT, especially due to the higher computing power of the available computer hardware and improved planning software (6, 7). With regard to an additional dose saturation of the tumour bed, external irradiation procedures are available on the one hand, for example additive percutaneous irradiation sessions (sequential boost) following the total breast irradiation (WBI) or by means of a simultaneous integrated boost (SiB), in which the boost saturation is included in the percutaneous WBI (8–11). On the other hand, boost treatment can be applied by means of brachytherapy (12), e.g., using the afterloading technique with interstitial catheters, so that the additional desired dose can be deposited in the tumour bed over the course of several treatment sessions. The prognostic benefit of a boost is considered certain

and advocated for patients especially with an elevated risk for local relapse (age < 40–50 years) and for older patients with an elevated risk for local recurrence (G3, HER2+, triple negative, > T1). Bartelink et al. (13) were able to show that an additional dose escalation of the tumour bed with 16 Gy significantly reduces the 5-year local recurrence rate from 7.3% to 4.3% compared to a comparison group without boost irradiation. Kindts et al. (14) reached the same conclusion in a systematic review in 2017, which found a hazard ratio of 0.64 for local 5-year tumour control with boost irradiation. With regard to the superiority of a boost technique combined with percutaneous WBI for reducing the risk of local recurrence (percutaneous boost versus brachytherapy boost), technical subgroup analyses from the EORTC trial 22881/10882 by Portmans et al. (15) and retrospective studies from Bartelink and Hammer et al. (13, 16, 17) assumed a potential clinical advantage concerning local control and better cosmetic results in favour of integrated brachytherapy boost concepts.

While high-dose delivery to the planning target volume (PTV) are aimed for and desired, in return the requirement is to avoid or keep as low as possible the dose deposition in surrounding organs at risk (OAR) or normal tissue in order to avoid damage by ionising radiation. Even if the benefit of the adjuvant radiation regime in terms of tumour control, recurrence risk, and overall survival is significant, radiotherapeutic side effects in normal tissue must be taken into account as critical factors in treatment planning. This applies in particular to the OAR skin, heart, lungs, and the contralateral breast. Common or frequently described clinical findings are above all cosmetic damage, radiation dermatitis, and breast fibrosis as well as cardiac ischemic damage and radiation pneumonitis (18, 19). It must also be borne in mind that ionising radiation may induce second primary cancer (20–22), which is strongly dependent on the combination of the treatment concepts.

In this paper, we compare several standard breast treatment techniques with respect to dose, normal tissue complication probability, and secondary cancer risk. Given the fact that the different boost irradiation techniques have hitherto not been observed to differ in clinical benefit, we aim to address the question whether they do regarding treatment-related sequelae. To achieve this, both 3D-CRT and IMRT techniques with sequential and simultaneously integrated teletherapy boost and

afterloading multicatheter brachytherapy boost are considered for a collective of patients treated for left-sided breast cancer at our department. A dosimetric comparison includes the summation dose from the WBI and boost plans (corrected for different brachytherapy fractionation), which is used as input for the normal tissue complication probabilities (*NTCP*) and in-field (100% to 80% isodose area) to penumbra (80% to 20% isodose area, defined in ref. 24) secondary cancer risk models to account for the high-dose areas. In the low-dose regime outside the treatment beams (below 5% isodose area), the dose computations from the treatment planning systems are generally unreliable. Hence, for the out-of-field regions far from the primary beams, dose measurements are performed in an anthropomorphic phantom with realistic breast attachments created by 3D printing for afterloading catheter insertion. The measured average organ doses are then translated into secondary cancer risk using the linear non-threshold model. To our knowledge, this is the first study to include this comprehensive modelling and measuring approach for assessing the differences between these widespread breast treatment techniques in a realistic setting. Similar studies comparing late side effects with various techniques for different entities can be found in literature, e.g., the prostate (23).

2 MATERIALS AND METHODS

2.1 Study Design

Four different treatment scenarios are considered here:

scenario 1: 3D-CRT WBI treatment (25×2 Gy to a total dose of 50 Gy) planned using tangential beams with an additional sequential boost of 5×2 Gy using three beams.

scenario 2: 3D-CRT WBI treatment as above (25×2 Gy), followed by an interstitial multicatheter brachytherapy boost of 2×6 Gy.

scenario 3: IMRT treatment (fanned tangents, step-and-shoot technique) of 25×2 -Gy fractions applied with up to eight

beams, planned using direct machine parameter optimisation (DMPO), followed by an interstitial multicatheter brachytherapy boost of 2×6 Gy.

scenario 4: IMRT treatment with a SiB concept fractionated as 28×1.8 Gy to the whole breast and 28×2.14 Gy to the tumour bed.

The study design is shown schematically in **Figure 1**. In the in-field region, the investigation is performed retrospectively on the basis of the patients' CT data sets and calculated summation treatment plans. Since the treatment planning system (TPS, discussed in Section 2.3) is not intended to provide accuracy in the out-of-field region (24–27), we here perform thermoluminescent dosimeter (TLD) measurements in an anthropomorphic phantom. The respective plans are irradiated on the phantom, and dose measurements are carried out using the TLDs. After the TPS calculations, the *NTCP* for various endpoints, as well as the secondary cancer risk using the TLD measurements (out-of-field) and TPS calculations (in-field and penumbra), are determined. We investigate the exposure on all relevant OAR for breast cancer treatment—the heart, the contralateral breast, the ipsilateral and contralateral lung, and the whole lung. Based on this, the *NTCP* for various endpoints and the secondary cancer risk are determined.

2.2 Patient Cohort

Treatment plans for 38 patients with left-sided breast cancer treated at our institution after breast-conserving surgery between January 2011 and December 2019 were retrospectively included in our study. The selection of patients was based on the fact that in 2011, 3D-CRT with percutaneous or afterloading interstitial multicatheter brachytherapy boost was the standard treatment regime, and consecutive patients out of this collective were chosen. By 2019, most patients were treated either using IMRT + SiB or using IMRT + brachytherapy, so the last consecutive patients out of these ensembles were selected. It was tried to exclude patients from the transitional phase in which the new techniques were being established and hence still subjected to adjustments and improvements. January 2011 was

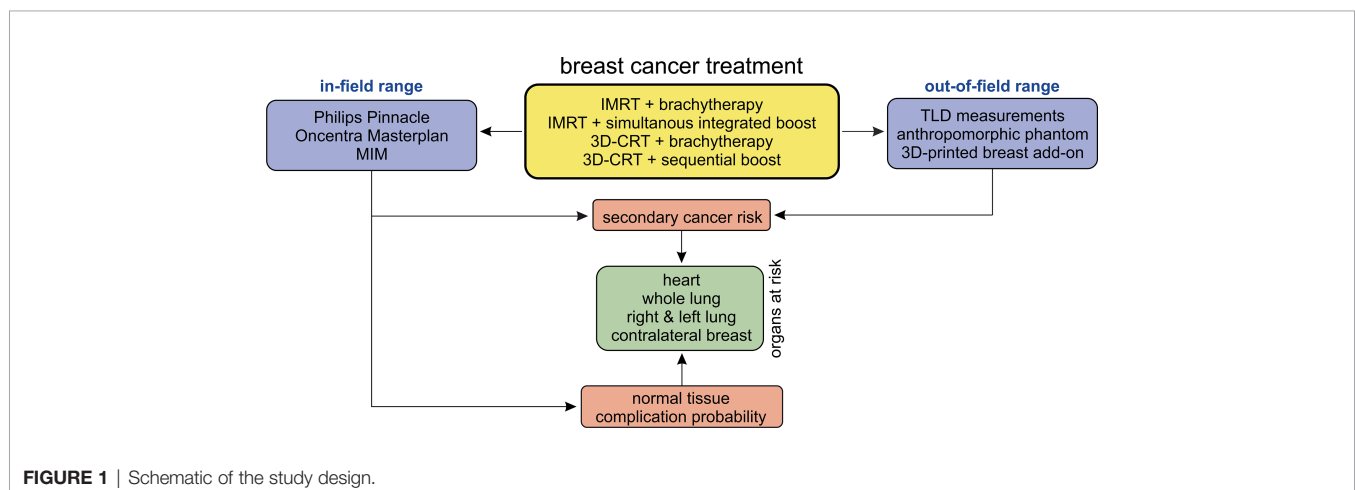


FIGURE 1 | Schematic of the study design.

taken as the starting time for study inclusion since this corresponds to the installation of a new set of three linear accelerators, afterloading unit, and CT scanner, all of which remained functional and in clinical use until the end of 2019, so that the same machines and treatment planning systems were used for all patients in this study. A target of 10 patients per scenario was set. For the cohort “3D-CRT + brachytherapy boost”, however, this resulted in only eight cases, as 3D-CRT was replaced by IMRT as standard in our clinic during the observation period.

Across the cohort of 38 patients, tumour gradings ranged from G1 to G3 and the tumour stages were pT1b/pT1c/pT2 pN0 cM0 L0 R0. In six cases, the diagnosis was pN1, in seven cases L1, and once an M1 diagnosis was made. The adjuvant or neoadjuvant systemic therapy was selected based on the usual guidelines regarding tumour stage and grade, patient age, hormone receptor expression (ER/PR) and menopausal status for endocrine therapy, and HER2-expression for targeted therapy (trastuzumab/pertuzumab). Chemotherapy was mainly applied using the EC regime (epirubicin, cyclophosphamide), often in combination with either paclitaxel/docetaxel, carboplatin, or 5-FU. Due to the relatively small collectives, no significant difference in systemic therapy regimes can be proven amongst the four scenarios. Overall, only two patients did not receive any systemic therapy at all. Eighteen patients (47%) received chemotherapy, four of whom in a neoadjuvant setting. Endocrine therapy was given in 28 cases (74%), targeted therapy in three patients (8%). The age of the patients varies between 35 and 76 years (median value: 52 years, mean value: 55 years). The cohort-related median/mean values are as follows: “IMRT + brachytherapy” (49/48 years), “IMRT + SiB” (59/59 years), “3D-CRT + brachytherapy” (46/46 years), and “3D-CRT + sequential boost” (64/61 years). A comparison of the two scenarios with brachytherapy boost shows no significant statistical difference in age (t-test: $p = 0.420$). The same applies for the scenarios using teletherapy boosts (t-test: $p = 0.610$). All other pairwise t-tests result in $p \leq 0.05$, i.e., patients receiving brachytherapy were significantly younger. Furthermore, comparing the breast and PTV volumes of the various cohorts show no significant statistical difference.

2.3 Treatment Planning and Treatment Machines

All percutaneous treatment plannings involved an in-house-acquired dedicated planning CT (Philips Brilliance Big Bore, 120 kV, Philips Healthcare, Amsterdam, Netherlands) dataset with the patients positioned supine with their arms raised above the head. The data were imported into the Philips Pinnacle treatment planning system (V. 9.0-9.8, 14.0, 16.0, and 16.2, Philips Medical Systems, Fitchburg, Wisconsin, USA), and treatment plans were created depending on the planning scenario (see below) for the three linacs available at our department. Dose calculation was performed using the collapsed cone convolution (CC) algorithm on a $2 \times 2 \times 2 \text{ mm}^3$ dose grid. The percutaneous radiotherapy of the patients was administered using a Siemens Oncor and two Siemens Artiste linear accelerators

(Siemens Healthcare, Erlangen, Germany) with identical 160 multi-leaf collimators. The beam energies for treatment were 6 and 18 MV, with beam matching amongst all machines for 6 MV and between one Artiste and the Oncor for 18 MV (28).

The 3D-CRT treatment plans for WBI used tangential beams with 6- and 18-MV mixed energies with dynamic wedges, with beam and couch angles adjusted to eliminate beam divergence in the lung. The 3D-CRT boost plan used three 6-MV beams in a field-in-field technique. IMRT plans (both for WBI and for SiB) involved up to eight beams with 6 MV and the step-and-shoot technique with direct machine parameter optimisation (DMPO) based on our in-house template of objectives, which is given in **Table 1**. The beams were distributed in a fan-like pattern depending on the patient anatomy, excluding beam angles through the back of the patient or the contralateral breast.

For the interstitial multicatheter brachytherapy boost, up to 16 catheters were implanted in the patient breast after the end of the percutaneous WBI series, based on the pre- and postoperative imaging information and positioning of titan clips on the localisation of the tumour bed. A planning CT was acquired using the same Philips Big Bore CT as for teletherapy planning, and the data were transferred to the Oncentra Masterplan TPS (version 4.6.0, Nucletron B.V., Veenendaal, Utrecht, Netherlands) for planning. The afterloader to apply the additional brachytherapy boost was a Flexitron (Elekta, Hamburg, Germany) using radioactive Iridium-192.

2.4 Plan Summation and Dosimetric Analysis

To compare all these scenarios with different fractionation schemes, the isoeffective total dose or biological effective dose (BED) must be considered (29):

$$BED = n \cdot d_T \cdot \left(1 + \frac{d_T}{\alpha/\beta} \right), \quad [1]$$

where α and β are the coefficients used in the linear-quadratic model, d_T is the single fraction dose, and n is the number of fractions. Since high-dose-rate (HDR) brachytherapy is considered here, the influence of protracted irradiation can be neglected as shown in Equation [1] (30). For late-responding tissue, we use the approximation $\alpha/\beta = 3$ (also used in the full model to calculate the secondary cancer risk; see Section 2.6.2).

The analysis software MIM (version 6.8.7, MIM Software Inc., Cleveland, OH, USA) was used to merge the planning CT images of teletherapy and brachytherapy treatment and thereby create summation plans. Deformable image registration from the percutaneous and brachytherapy planning CT datasets was performed by manually adjusting the automatically registered images so that the position of the left breast and the adjacent lungs showed best agreement. The registration result was independently verified by a senior radiation oncologist. The in-field dose distribution from Pinnacle and MIM was used to assess the dosimetric parameters of the plans, i.e., the mean heart dose, the mean dose to the ipsilateral and whole lung, $V_{20 \text{ Gy}}$ of the lung, $D_{1\%}$ of the contralateral breast (as an estimate of the maximum dose), and the mean dose to the contralateral breast.

TABLE 1 | Organs at risk TPS dose statistics versus planning objectives.

organ at risk	objectives	scenario 1 IMRT + brachytherapy	scenario 2 IMRT + SiB	scenario 3 3D-CRT + brachytherapy	scenario 4 3D-CRT + sequential boost
heart	$D_{\text{mean}} < 3 \text{ Gy}$	4.5 ± 1.3 (3.3 – 7.9)	4.4 ± 1.0 (2.8 – 6.1)	3.3 ± 1.6 (1.5 – 6.0)	4.8 ± 2.1 (2.4 – 7.6)
left lung (ipsilateral)	$D_{\text{mean}} < 12 \text{ Gy}$	9.9 ± 2.3 (7.5 – 14.9)	10.8 ± 1.8 (7.5 – 13.7)	7.9 ± 1.1 (6.6 – 9.9)	8.7 ± 2.2 (5.0 – 13.5)
whole lung	$D_{\text{mean}} < 10 \text{ Gy}$	5.3 ± 1.6 (4.0 – 9.5)	5.9 ± 1.3 (4.3 – 9.1)	3.9 ± 0.8 (3.0 – 5.3)	4.2 ± 1.1 (2.4 – 6.6)
	$V_{20 \text{ Gy}} < 10\%$	7.4 ± 1.6 (5.3 – 10.2)	8.6 ± 1.9 (4.9 – 11.9)	6.1 ± 1.3 (4.7 – 8.3)	6.3 ± 2.0 (3.1 – 10.2)
right breast (contralateral)	$D_{1\%} [\text{Gy}]$ minimised	9.6 ± 8.3 (3.0 – 24.7)	8.5 ± 12.2 (2.7 – 42.7)	3.4 ± 2.0 (1.2 – 8.0)	3.5 ± 1.3 (1.6 – 6.1)
	$D_{\text{mean}} [\text{Gy}]$ minimised	2.3 ± 2.2 (1.1 – 8.2)	2.5 ± 2.1 (1.2 – 8.4)	0.7 ± 0.7 (0.1 – 2.2)	0.8 ± 0.6 (0.3 – 2.1)

*marks a pairwise t-test with $p \leq 0.05$ including a Welch correction for different variances.

**marks a pairwise Mann-Whitney U test with $p \leq 0.05$.

The dose distributions were then used as an input to model the NTCP and secondary cancer risk as explained in Section 2.6.

2.5 Measurements of Out-of-Field Doses

In the out-of-field regions, commercially available TPSs commonly underestimate the real dose, with calculation accuracy decreasing with distance from the field edge (24–27). This is due to the dose calculation algorithm (collapsed cone convolution superposition in our case) which uses in-field kernel approximations to determine the dose distribution and can be circumvented by advanced algorithms such as grid-based

Boltzmann solvers or Monte Carlo calculations. Furthermore, the CCC algorithm does not realistically account for head leakage, collimator scatter, and patient scatter. Consequently, TLD-100H disks (Thermo Fisher Scientific, Waltham, MA, USA) were used to measure the dose out-of-field, using a Harshaw TLD 5500 reader (Thermo Fisher Scientific). The calibration and measurement settings for the TLDs have been described elsewhere (31). In short, the vendor-recommended time-temperature protocol was used, which presumes 5 s of preheating at 145°C, followed by acquisition at 10°C/s up to a maximum temperature of 260°C for 23 1/3 s, and finally

annealing at 260°C for 20 s. In all four scenarios, the out-of-field measurements were carried out inside an anthropomorphic phantom with breast attachments representing either a plausible large breast or small breast size (CIRS Atom Dosimetry Verification Phantom Model 701). Breast attachments with 350 and 1200 cc were selected, so that for each treatment scenario, the patient cohort was searched for two patients best matching the phantom anatomy and breast sizes—these patients were used for phantom measurements.

Using the MIM fusions, the teletherapy treatment plans could be mapped onto the phantom straight forward. For the experimentally more complex brachytherapy sub-cohorts, we developed 3D-printed phantom breast add-ons, since catheter insertion would not have been possible in the CIRS phantom breast attachments and also since the catheters result in deformation of the patient breast, which would not have been realistically reproduced by the phantom. Two representative breast models were reconstructed using CT data sets (one small and one large left breast) in order to allow for multicatheter placement. The manufacturing process is

depicted in **Figure 2**. We performed a DICOM export of the CT fusion from MIM towards Pinnacle, where regions of interest (ROIs) were contoured (see blue contours in **Figure 2A**, left and centre). To create the outer shape of the breast add-on, we used the skin contour of the patient brachytherapy CT and subtracted the co-registered body contour of the phantom CT for each CT layer. Afterwards, inner rings of 5 mm in diameter were created to realise a shell with 5-mm thickness, which was divided manually into front and backside part. All catheters were also contoured and subtracted from the ROI of the breast add-on in order to locate the catheter placement holes during the next step of the fabrication process. The final add-on contour for the small breast is shown in **Figure 2A** on the right side as a three-dimensional reconstruction. Now, the created structures were exported from Pinnacle to a DICOM node and manually imported into the Matlab software (version R2019b, MathWorks, Natick, MA, USA) to create a stereolithography point cloud. Afterwards, the software Fusion 360 (version 2.0.10148, Autodesk, San Rafael, CA, USA) was utilised to connect the points and to create a virtual computer-

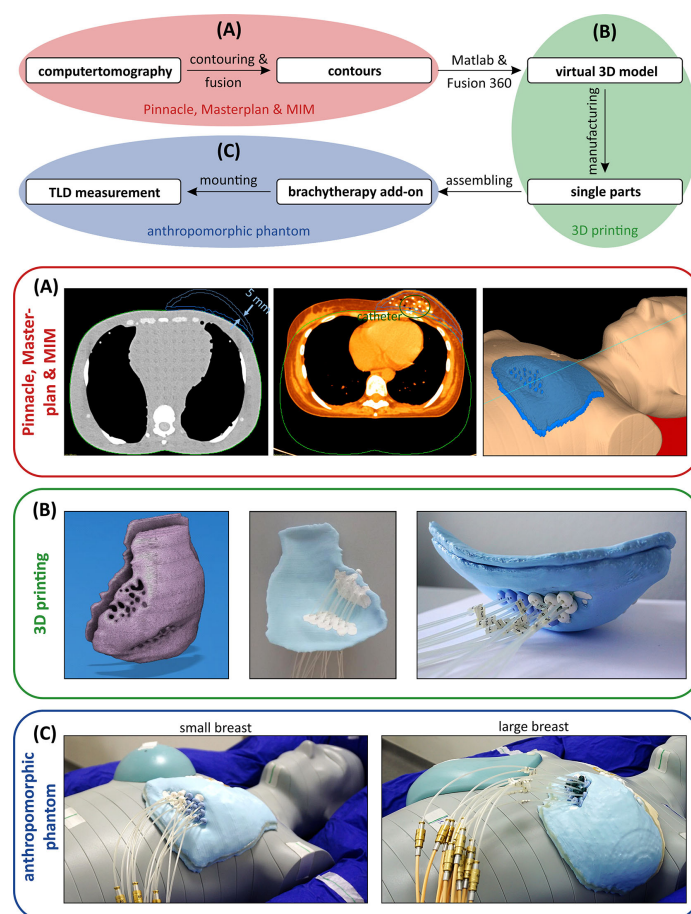


FIGURE 2 | Schematic process to fabricate a brachytherapy breast add-on for the anthropomorphic phantom to measure the dose in the out-of-field range using thermoluminescent dosimeters. **(A)** Fusing the brachytherapy planning and the anthropomorphic phantom CT to create contours as a starting point for the manufacturing. **(B)** From a virtual 3D model to a manufactured breast model. **(C)** Mounting the small (left) and large (right) breast models to the anthropomorphic phantom and the afterloader.

aided design (CAD) model (see **Figure 2B**, left). In the next fabrication step, we used the CAD to manufacture the single parts of the add-on using a commercially available 3D printer Prusa i3 MK3S+ (Prusa Research, Prague, Czech Republic). The printing layer thickness is 200 μm , the printing speed is 40 mm/s, and the filling factor is equal to 100%. We used 3DJAKE ecoPLA (niceshops GmbH, Paldau, Germany) as 3D-printing filament (mass density 1.24 g/cm³). Next, the catheters were placed in the predefined holes (see **Figure 2B**, centre), the front part was filled with white petroleum jelly (CAELO-PRIMA Vaseline, Caesar & Loretz GmbH, Hilden, Germany), and the printed backside part was used to assemble and seal the breast add-on (see **Figure 2B**, right). We use this filling material to model the breast in a most realistic way, since the jelly has a mass density of 0.9 g/cm³, which is very close to the density mean value of the representative breasts (0.89 ± 0.09 g/cm³). Both shells were fixated together using hot glue. In the third creation step of the brachytherapy add-on, we finally mounted the assembled parts to the anthropomorphic phantom and connected each catheter to the afterloader for irradiation. The overall result is shown in **Figure 2C** for the small (compare right inset of **Figure 2A**) and the large brachytherapy breast phantom. For all measurements (and prior to mounting the breast attachments), the TLDs were placed at representative places inside the phantom to determine the mean dose of each OAR. For this purpose, we used 20 TLDs—five per organ at risk (see **Figure 3**). Additionally, we included into the measurement three further TLDs which were placed outside the treatment room in order to measure the background radiation and subtract this from the measurement TLDs irradiated in the phantom. The localisation of the TLDs is also shown in **Figure 3**. The phantom was positioned inside a vacuum cushion with laser markings for better reproducibility of the measurements.

In total, we performed eight TLD measurements (one plan for a large and one for a small breast size for each of the four treatment scenarios) to determine the mean organ doses of the contralateral breast, the lung, and the heart. The data obtained are used for secondary cancer risk estimation only.

2.6 NTCP and Secondary Cancer Risk Modelling

Modelling secondary-cancer risk for low radiation doses usually relies on the linear non-threshold (LNT) assumption. In the high-dose regime, additional effects such as cell killing must be taken into account. A well-established secondary cancer risk model in the radiotherapeutic dose regime is the full (mechanistic) model by Schneider et al. (32–34). Schneider's approach is based on the linear-quadratic model of dose response which is fitted to combined empirical data including patients treated for Hodgkin's lymphoma and atomic bomb survivors to best adjust the available data in both the high- and low-dose ranges. In the low-dose limit, Schneider's model is equivalent to the LNT assumption. Both models are described in more detail in the following subsections. For secondary cancer risk estimation of the contralateral breast and lung, we use the TLD data. Here, the expected isodoses are below 20% and therefore out-of-field. On the other hand, the ventral part of the ipsilateral lung is exposed to isodoses up to 80% since the

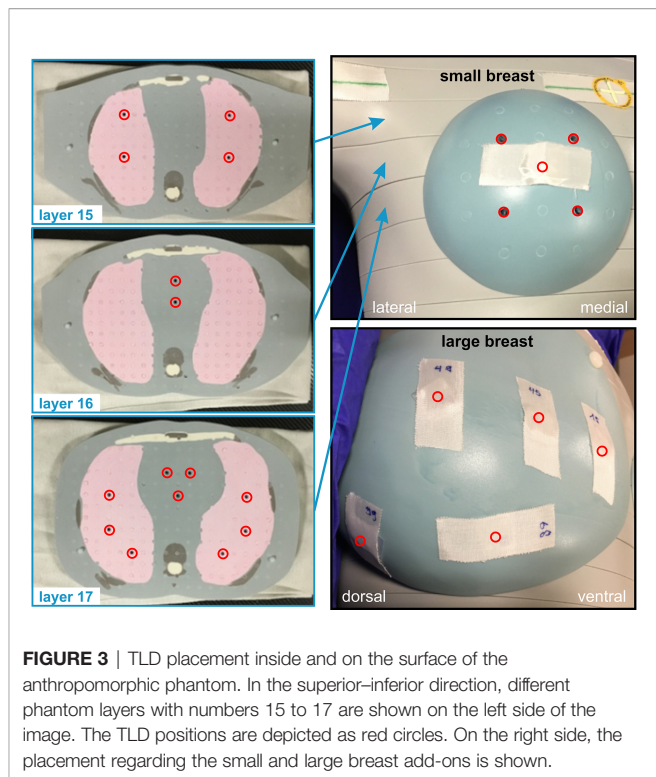


FIGURE 3 | TLD placement inside and on the surface of the anthropomorphic phantom. In the superior–inferior direction, different phantom layers with numbers 15 to 17 are shown on the left side of the image. The TLD positions are depicted as red circles. On the right side, the placement regarding the small and large breast add-ons is shown.

PTV is directly adjacent. Hence, the secondary cancer risk mainly originates from this high-dose exposure and the risk estimation relies on TPS data only.

Modelling of the normal tissue complication probability (NTCP) can be achieved via, e.g., the Lyman–Kutcher–Burman model (35–37). Here, a DVH is needed to calculate the NTCP, which results from the high-dose burden onto the organ. Thus, we only use the TPS data for risk estimation. From a clinical point of view, the paper of Emami et al. defined the first guidelines on NTCP in 1991 (38). Due to the technical improvement in the field of radiotherapy since then, the Quantitative Analysis of Normal Tissue Effects in the Clinic (QUANTEC) review summarises the currently available guidelines (39–41). Additionally, there are specific models for ischemic heart disease, which rely on a linear approach (42).

2.6.1 Linear Non-threshold Model—Out-of-field Secondary Cancer Risk

For low doses, the linear non-threshold model is generally accepted (43). We apply the parameterisation by Schneider for consistency with the high-dose regime (Section 2.6.2), where we also use the parameters proposed by the same authors (32–34).

$$EAR(D, age_x, age_a) = \delta \cdot D \cdot \mu(age_x, age_a), \quad [2]$$

where μ is an exponential function depending on the age of exposure (age_x) and the attained age (age_a) according to

$$\mu(age_x, age_a) = \exp\left(\gamma_e \cdot (age_x - 30) + \gamma_a \cdot \ln\left(\frac{age_a}{70}\right)\right). \quad [3]$$

TABLE 2 | *EAR* and *NTCP* calculation parameters.

model	organ at risk					
Schneider (32) <i>LNT and full model</i>		δ	γ_e	γ_a	α	R
		$[(10,000 \text{ PY Gy})^{-1}]$			$[\text{Gy}^{-1}]$	
	lung	8.0	0.002	4.23	0.042	0.83
	breast	8.2	-0.037	1.70	0.044	0.15
LKB		endpoint		n	m	$D_{50\%}$
						$[\text{Gy}]$
	lung	symptomatic pneumonitis (46) radiation pneumonitis (grade ≥ 2) (47)		1.000 0.990	0.35 0.37	37.6 30.8

γ_e and γ_a are organ-specific fit parameters. Furthermore, δ is the initial slope. In the out-of-field region, D is taken to be the mean organ dose. The average organ doses are determined from our TLD measurements in the contralateral breast and lungs (both ipsi- and contralateral).

2.6.2 Schneider's Full Model—in-field Secondary Cancer Risk

For the high-dose region inside the field and around the field edge, let us now discuss Schneider's full model (32). Equation [2] is modified to account for the in-field region and cell regeneration between two fractions as follows:

$$EAR(D, age_x, age_a) = \delta \cdot RED(D) \cdot \mu(age_x, age_a). \quad [4]$$

RED is the risk equivalent dose, which models the rate of cell regeneration:

$$RED(D) = \frac{\exp(-\alpha' \cdot D)}{\alpha' \cdot R} \cdot \left[1 - 2R + R^2 \cdot \exp(-\alpha' \cdot D) - (1 - R)^2 \cdot \exp\left(-\alpha' \cdot D \cdot \frac{R}{1 - R}\right) \right]. \quad [5]$$

α' is also a function of the total dose D . Moreover, the term $\alpha' \cdot D$ represents the linear-quadratic model of dose response including fractionation schemes, where

$$\alpha'(D) = \alpha + \beta \cdot \frac{d_T}{D_T} \cdot D. \quad [6]$$

The repopulation or repair capacity R of the tissue between two radiation fractions can take values between “0” (no regeneration) and “1” (complete regeneration). Both α' and R are organ- or tissue-specific parameters fit to the observations from the atomic bomb survivors data (low-dose exposure) and Hodgkin's lymphoma patients (high-dose radiotherapy). In **Table 2**, these parameters are listed exemplarily for the lung and the breast. Equation [4] is plotted in **Figure 4A** for $age_x = 55$ years (mean value of the overall cohort) and $age_a = 75$ years. The unit of EAR is per person years (PY^{-1}). The specific EAR of the OAR is finally computed in Matlab using the TLD measurements in the out-of-field regions and the in-field TPS dose distributions using an in-house Matlab script as described in a previous publication (44).

Please note that evidently only a small part of the ipsilateral lung and possibly a small medial portion of the contralateral breast may be included in the treatment field and therefore inside the “high-dose region”. Only for this region is the Schneider

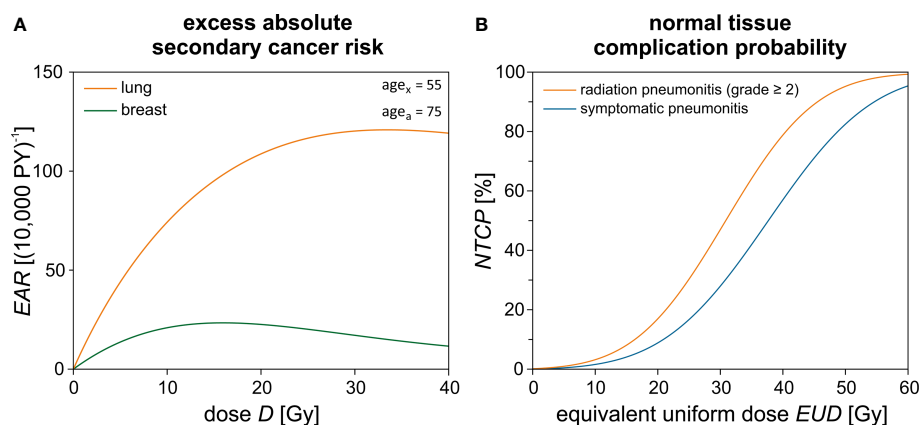


FIGURE 4 | Theoretical risk estimation using empirical models. **(A)** The excess absolute secondary cancer risk (EAR) is calculated for the lung and the breast dependent on the dose D using Schneider's model. The difference between the age exposed (age_x) and the attained age (age_a) is 20 years. **(B)** Normal tissue complication probability ($NTCP$) calculation for the lung and its respective endpoints dependent on the equivalent uniform dose (EUD).

model applied to assess the secondary cancer risk according to the isodose distribution from the TPS. For the major part of the volume of the lungs and breast, only out-of-field leakage and scattered radiation will contribute to the dose. In this low-dose region, the TLD measurements are used to assess the mean organ dose and calculate the secondary cancer risk using the LNT models for the organ dose. The two approaches are chosen with the intention to give a lower and upper estimate of the plausible secondary cancer risk in these organs located close to steep-dose gradients. An example dose–response relationship for Schneider’s model is shown in **Figure 4**.

2.6.3 Lyman–Kutcher–Burman Model for Normal Tissue Complication Probabilities

There are various mathematical models for estimating and modelling the risks of biological side effects. A common model, which is used in this work due to OAR parameter availability in literature, is the *NTCP* approach according to Lyman–Kutcher–Burman (35–37), which is expressed as follows:

$$NTCP(EUD) = \frac{1}{\sqrt{2\pi}} \int_{-\infty}^{u(EUD)} \exp\left(-\frac{t^2}{2}\right) dt. \quad [7]$$

The integrand describes a probability density function for the standard Gaussian distribution. The upper integral limit u is a function of the equivalent uniform dose *EUD* (45):

$$u(EUD) = \frac{EUD - D_{50\%}}{m \cdot D_{50\%}}, \quad [8]$$

where

$$EUD = \left(\sum_i v_i \cdot D_i^{1/n} \right)^n. \quad [9]$$

The *EUD* describes a uniform dose which leads to the same complication risk as caused by the given non-uniform dose distribution. m represents the slope of the *NTCP* curve, and $D_{50\%}$ is the uniform dose, which applied to the entire organ volume would result in 50% risk of complication. v_i is the i -th relative sub-volume receiving the dose D_i . Both values are determined by the dose–volume histogram (DVH) of the respective OAR. Furthermore, n is the volume exponent and determines whether the organ is of parallel ($n = 1$) or serial type ($n = 0$). If n equals 1, the *EUD* is simply given by the mean dose of the organ at risk. $D_{50\%}$, n , and m are empirical fit parameters and can be found in literature for the relevant OAR (46, 47). In **Table 2**, these parameters are listed for the endpoints symptomatic and radiation pneumonitis of the lung. The *NTCP* curves are plotted in **Figure 4B**. A sigmoidal shape of the *NTCP* curve is seen—as expected for a typical dose–response relationship. We use Matlab and the free software extension CERR (48) to determine the respective *NTCP* of each patient depending on the summation dose distributions and DVHs given by Pinnacle and MIM.

2.6.4 Linear Approach by Darby et al. for *NTCP* Calculation of the Heart

Darby et al. empirically investigated the risk of ischemic heart disease of women after breast cancer radiotherapy (42). They

conducted a population-based case–control study of major coronary events (MCE) and report on a correlation between the excess relative risk (*ERR*) for the endpoint MCE and the average dose D_{mean} :

$$ERR = D_{\text{mean}} \cdot 0.074 \text{ Gy}^{-1}, \quad [10]$$

where

$$\text{cumulative risk} = \text{baseline risk} \cdot (1 + ERR). \quad [11]$$

The rate for cardiovascular events increases linearly by +7.4% per Gy in dependency on the mean dose without threshold. The increase of *ERR* begins within a few years after exposure and continues for at least 20 years.

2.7 Data Analysis

Statistical analysis was performed using OriginPro 2019b (V. 9.6.5.169, OriginLab Corporation, Northampton, MA, USA). In all presented boxplots, the coloured area depicts the range from 25% to 75% of the data. The error bars correspond to the 1.5 interquartile range. The line dividing the box into an upper and lower part represents the median value. A black circle marks the mean value. All statistical outliers are shown as crosses. We first check if the given data are normally distributed. If true for both samples, we use a Student’s *t*-test including a Welch correction to assess for statistically significant differences between the cohorts. For non-gaussian data, Wilcoxon’s test was applied. Statistical significance was presumed for $p < 0.05$. In **Tables 2–5** the mean values and their respective standard deviation are shown. Furthermore, the range of values (min–max) is given inside the brackets.

3 RESULTS

3.1 Dosimetric Comparison of TPS Treatment Plans

Example dose distributions for the four planning scenarios are shown in **Figure 5** and the respective statistical analysis is depicted in **Figure 6**. The objective for the mean dose D_{mean} regarding the left and whole lungs is achieved in all cases. Moreover, the objective for the relative volume $V_{20 \text{ Gy}}$ which receives 20 Gy or more, is satisfied as well. The average dose to at least 1% of the contralateral breast ranges between 3.4 and 9.6 Gy. The maximal value in the scenario “3D-CRT + brachytherapy” (42.7 Gy) shows that it was not always possible to place the beam directions so as to completely exclude the contralateral breast for all patients (as is generally desired). However, only a small portion of the contralateral breast (if at all) is penetrated by the primary radiation, and the average mean dose ranges between 0.7 and 2.5 Gy as calculated by the TPS (compare TLD measurements below). However, regarding the ranges of the values, the high-dose outliers (maximum $D_{1\%}$ of 24.7 Gy for “IMRT + brachytherapy” and 42.7 Gy for “IMRT + SiB”) occur in the IMRT-based scenarios, while the 3D-CRT plans have values < 10 Gy for all patients included in the study (maximum $D_{1\%}$ 8.0 Gy for “3D-CRT + brachytherapy” and

TABLE 3 | Dose exposure for the complete radiotherapy regime as shown in **Figure 6**.

organ at risk	breast size	scenario 1 IMRT + brachytherapy	scenario 2 IMRT + SiB	scenario 3 3D-CRT + brachytherapy	scenario 4 3D-CRT + sequential boost
heart	small	1.1 ± 0.3 (0.9–1.6)	1.7 ± 0.4 (1.2–2.2)	0.6 ± 0.2 (0.6–0.9)	1.9 ± 0.7 (0.7–2.6)
	large	3.1 ± 2.8 (1.6–7.8)	1.2 ± 0.4 (0.8–1.9)	1.4 ± 0.5 (1.0–2.1)	1.3 ± 0.5 (0.9–2.0)
left lung (ipsilateral)	small	3.3 ± 2.4 (1.0–7.1)	2.3 ± 1.4 (0.7–3.6)	1.0 ± 0.7 (0.4–2.1)	1.5 ± 1.5 (0.4–4.0)
	large	18.8 ± 13.9 (7.8–38.3)	10.4 ± 18.3 (1.1–43.0)	12.8 ± 17.2 (1.0–41.5)	12.7 ± 17.1 (1.0–41.2)
right lung (contralateral)	small	0.4 ± 0.1 (0.3–0.5)	0.5 ± 0.2 (0.3–0.8)	0.2 ± 0.1 (0.2–0.3)	0.5 ± 0.4 (0.3–1.2)
	large	0.6 ± 0.1 (0.5–0.6)	0.4 ± 0.1 (0.3–0.4)	0.4 ± 0.1 (0.3–0.4)	0.4 ± 0.1 (0.3–0.4)
right breast (contralateral)	small	1.6 ± 0.6 (1.0–2.3)	1.7 ± 0.8 (0.9–2.7)	1.7 ± 0.6 (1.2–2.7)	2.4 ± 1.1 (1.3–3.8)
	large	1.2 ± 1.0 (0.2–2.8)	1.0 ± 0.7 (0.2–2.0)	1.0 ± 0.7 (0.1–2.0)	1.2 ± 1.1 (0.2–3.0)

All TLD measurement values are given for the small and large breasts [in (Gy)].

6.1Gy for “3D-CRT + sequential boost”). The mean heart dose falls outside the desired range below 3 Gy, while remaining below 5 Gy. In fact, at the time the patients were treated, a 5-Gy mean heart dose in left-sided breast cancer was considered the acceptable limit, while <3 Gy was aimed for if possible.

Therefore, the plans were accepted for clinical treatment despite this shortcoming. No statistical significance was found in the pairwise comparisons.

To summarise the scenarios and estimate the dose exposure on the relevant OARs, we calculated the respective mean DVHs

TABLE 4 | Secondary cancer risk for different organs at risk calculated using the TPS data and the TLD measurements.

organ at risk	age _x [years]	age _a [years]	scenario 1 IMRT + brachytherapy	scenario 2 IMRT + SiB	scenario 3 3D-CRT + brachytherapy	scenario 4 3D-CRT + sequential boost
left lung (ipsilateral) EAR [10,000 PY ⁻¹] full model TPS data	55	75	54 ± 13 (42 – 85)	56 ± 8 (45 – 70)	42 ± 7 (36 – 53)	44 ± 8 (30 – 62)
			<p>↑ ** p = 0.030</p> <p>↑ ** p = 0.038</p> <p>↑ * p < 0.001</p> <p>↑ * p = 0.003</p>			
	55	95	145 ± 35 (114 – 232)	153 ± 21 (122 – 189)	114 ± 18 (96 – 143)	121 ± 22 (81 – 169)
			<p>↑ ** p = 0.030</p> <p>↑ ** p = 0.038</p> <p>↑ * p < 0.001</p> <p>↑ * p = 0.003</p>			
right lung (contralateral) EAR [10,000 PY ⁻¹] linear model TLD data	55	75	5 ± 1 (4 – 6)	5 ± 1 (4 – 6)	3 ± 1 (2 – 4)	5 ± 1 (4 – 6)
		95	14 ± 3 (11 – 17)	13 ± 2 (11 – 15)	9 ± 3 (6 – 12)	14 ± 3 (11 – 17)
	55	75	5 ± 1 (4 – 6)	6 ± 2 (4 – 8)	5 ± 1 (4 – 6)	7 ± 2 (5 – 9)
		95	8 ± 1 (7 – 9)	9 ± 3 (6 – 12)	7 ± 2 (5 – 9)	10 ± 4 (6 – 14)

*marks a pairwise t-test with $p \leq 0.05$ including a Welch correction for different variances.

**marks a pairwise Mann-Whitney U test with $p \leq 0.05$.

TABLE 5 | Excess relative risk and normal tissue complication probabilities for different organs at risk calculated using the TPS data.

organ at risk	endpoint	scenario 1 IMRT + brachytherapy	scenario 2 IMRT + SiB	scenario 3 3D-CRT + brachytherapy	scenario 4 3D-CRT + sequential boost
left lung (ipsilateral) NTCP [%] LKB model TPS data	symptomatic pneumonitis	1.9 ± 1.0 (1.1 – 4.3)	2.2 ± 0.7 (1.1 – 3.5)	1.3 ± 0.3 (0.9 – 1.8)	1.5 ± 0.7 (0.7 – 3.3)
			↑ * p = 0.003	↑	
			↑ ** p = 0.017		↑
whole lung NTCP [%] LKB model TPS data	radiation pneumonitis (grade ≥ 2)	1.3 ± 0.7 (0.9 – 3.2)	1.5 ± 0.6 (1.0 – 3.0)	1.0 ± 0.2 (0.7 – 1.3)	1.0 ± 0.3 (0.6 – 1.7)
		↑ ** p = 0.037	↑	↑	
		↑ ** p = 0.035		↑	↑
	symptomatic pneumonitis	2.3 ± 1.0 (1.7 – 4.9)	2.6 ± 0.8 (1.8 – 4.6)	1.7 ± 0.3 (1.4 – 2.2)	1.8 ± 0.4 (1.2 – 2.9)
		↑ ** p = 0.037	↑	↑	
		↑ ** p = 0.031	↑ ** p = 0.003	↑ ** p = 0.005	↑
heart ERR [%] Darby model TPS data	ischemic heart disease	+33.4 ± 9.9 (24.3 – 58.7)	+32.8 ± 7.2 (20.6 – 44.8)	+24.5 ± 11.8 (11.4 – 44.6)	+35.2 ± 15.2 (18.1 – 55.9)

*marks a pairwise t-test with $p \leq 0.05$ including a Welch correction for different variances.

**marks a pairwise Mann-Whitney U test with $p \leq 0.05$.

(Figure 7). Each DVH shown has been averaged over the respective sub-cohort (see legend of Figure 7). In the following, we choose the points $D_{20\%}$ and $D_{10\%}$ as well as the regions $D < 5$ Gy and $D > 10$ Gy to characterise the DVH curve shape. Regarding the heart (Figure 7A), we find $D_{20\%} > 4.9$ Gy and $D_{10\%} > 8.2$ Gy for all curves. The highest-dose exposure of the heart in the region $D < 5$ Gy is exhibited by scenario “IMRT + SiB” in contrast to $D > 10$ Gy, where “3D-CRT + sequential boost” is highest. Overall, the heart DVH curve for “3D-CRT + brachytherapy” lies lowest.

For the contralateral breast (Figure 7B), we find $D_{20\%} > 2.7$ Gy and $D_{10\%} > 4.8$ Gy. In general, “IMRT + SiB” shows the highest values; “3D-CRT + brachytherapy” and “3D-CRT + sequential boost” are approximately identical and have the lowest-dose exposure in this range. In Figure 7C, the DVH of the ipsilateral lung is depicted. The parameters are $D_{20\%} > 19.0$ Gy and $D_{10\%} > 38.4$ Gy for all scenarios. Here, the DVH of scenario “IMRT + SiB” lies above all other scenarios. “3D-CRT + brachytherapy” and “3D-CRT + sequential boost” are approximately identical and lowest. The contralateral lung in Figure 7D indicates the DVH parameters $D_{20\%} > 2.2$ Gy and $D_{10\%} > 3.1$ Gy. For $D < 5$ Gy, “IMRT + SiB” and, for $D > 10$ Gy,

“3D-CRT + sequential boost” are the ones with the highest exposure. Figure 7E illustrates the average DVHs of the whole lung. Here, $D_{20\%} > 5.5$ Gy and $D_{10\%} > 15.4$ Gy. Furthermore, “IMRT + SiB” shows the highest curve while “3D-CRT + brachytherapy” and “3D-CRT + sequential boost” are almost identical and lowest.

3.2 TLD Measurement Results

The point dose measurements of each OAR were averaged to give the mean organ doses per fraction. Next, the values are multiplied by the number of fractions to obtain the dose exposure of the complete radiotherapy regime (see Table 3 and Figure 8). This allows for comparison to the high-dose in-field values given above. Amongst the four different scenarios, no statistically significant differences could be found. Subsequently, we compared the results for the small and large breast attachments.

The TLD measurements of the heart yield a 2.5 to 5.5 times smaller average dose exposure compared to the in-field TPS calculations. This is also caused by the given field orientation. The fields are touching the heart’s region of interest at its outer edge, and thus, the centrally located TLDs do not measure the in-field part of the primary treatment. Only the scattered out-of-

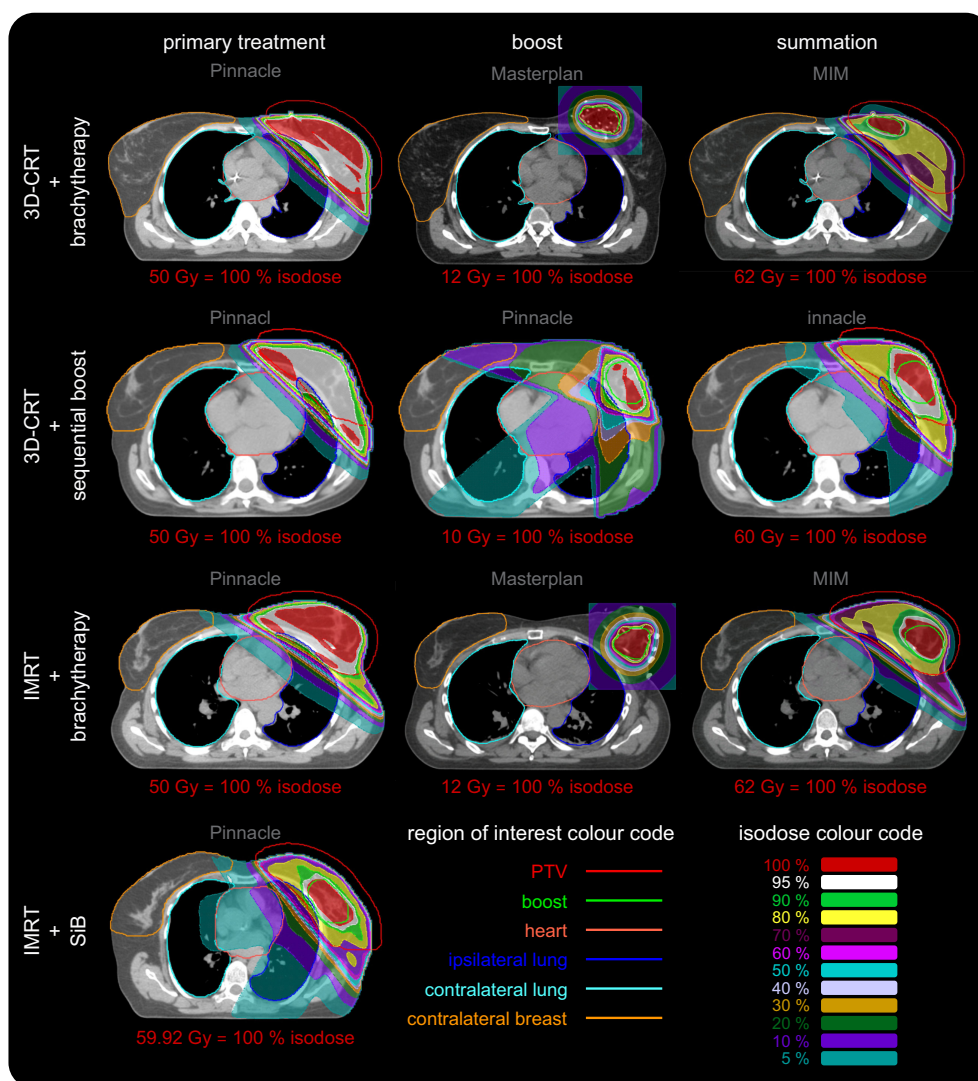


FIGURE 5 | Representative dose distributions of all four regarded scenarios for primary treatment, boost, and their summation. The dose distributions were calculated using Philips Pinnacle and Oncentra Masterplan. The screenshots were made in Pinnacle and MIM. The colour codes of the regions of interest and isodose curves are depicted in the lower right corner. The corresponding dose value of the red 100% isodose is given for each image separately. Each row depicts a different scenario. The columns represent the primary treatment (dose calculation in Pinnacle, left column), the additional boost (dose calculation in Pinnacle and Masterplan, centre column) and their summation (Pinnacle and MIM, right column). The scenario “IMRT + SiB” only has one column since this concept utilises an integrated boost. We use the software predefined windowing “breast” (Pinnacle) and “mediastinal” (MIM) to illustrate the local Hounsfield units or mass density distribution, respectively, as a grayscale. The brachytherapy CT image used to calculate the dose in Masterplan is presented after the deformed registration in MIM. The dose summation is shown without taking into account the BED in order to maintain visual comparability of all scenarios since “3D CRT + sequential boost” and “IMRT + SiB” do not show BED summation as well. In the latter case, direct comparability is not possible since the fractionation schemes are combined into one concept. The various OARs are highlighted as contours: the PTV (red line), the boost volume (green line), the heart (light red line), the left and the right lung (blue and teal line), and the contralateral breast (orange line). The dose distributions are depicted as coloured areas. See inset in the lower right corner for the colour code of the isodoses. The colour scale is normalised to the respective prescribed dose of each case and given below each image. The required minimum target volume coverage (PTV or boost) for clinical acceptance is at least 95 % (white areas), which is fulfilled for all primary WBI and boost treatments. Usually the lowest isodose scale is chosen to be 10 %. We also show the 5 % isodose area to visualise an approximation to the low-dose regime (additional scattering effects are not included) relevant for secondary cancer risk calculation and affected OARs in this respect: the heart, the ipsilateral and contralateral lung and the contralateral breast.

field radiation and the simultaneously integrated as well as the sequential boost are detected (see **Figure 5**). Comparing the achieved values of the small and large breasts, we find a statistical significant difference only in the case “3D-CRT + brachytherapy”

(small breast 1.1 ± 0.3 Gy vs. large breast 3.1 ± 2.8 Gy, $p = 0.016$). For the ipsilateral lung, the TLD measurements of the large breast show a large standard deviation due to an outlier, i.e., one TLD position located just barely in-field. In case the outlier is not

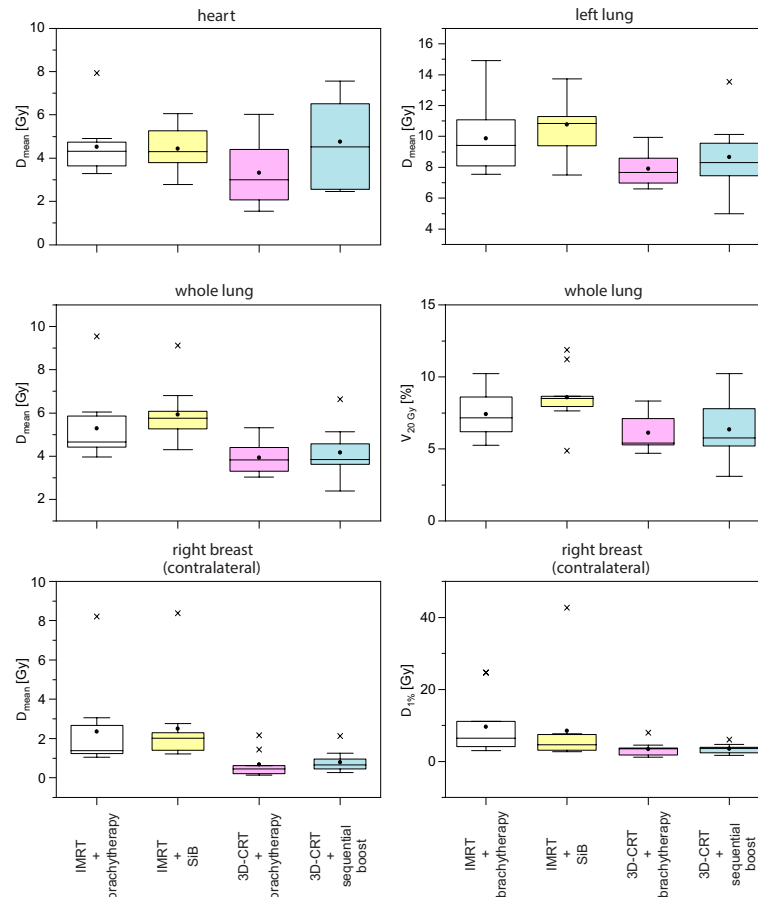


FIGURE 6 | Corresponding boxplots of the data and objectives given in **Table 1**.

considered, we obtain the following results for the large breast: 9.0 ± 1.3 Gy for “IMRT + brachytherapy”, 2.4 ± 2.0 Gy for “IMRT + SiB”, 2.0 ± 1.0 Gy for “3D-CRT + brachytherapy”, and 2.0 ± 0.9 Gy for “3D-CRT + sequential boost”. These values are more consistent with the TPS results. Regarding the small breast, the TLD results are smaller by a factor 3 to 8. This is mainly due to the shape of the tangent required to cover the WBI PTV: for a large breast extending more laterally and dorsally than a smaller breast, the beams are angled more towards the dorsolateral direction, thus including a larger portion of the ipsilateral lung. In general, the brachytherapy scenarios appear more favourable for the smaller breasts. However, the difference between the large and small breast only becomes statistically significant in the scenario “IMRT + brachytherapy” ($p = 0.040$). Comparing the TLD to the TPS data and including the standard deviations, the calculations and measurements match in all cases.

In summary, to model secondary cancer risk adequately only the OARs and their TLDs which are placed completely out-of-field are suitable. Thus, the heart and the ipsilateral lung are considered to be in-field and we use the TPS data for *EAR*, *ERR*, and *NTCP* calculation of these OARs as shown in Section 3.3.

Furthermore, the TLD measurements determine the secondary cancer and normal tissue complication risks of the contralateral lung and contralateral breast.

3.3 Secondary Cancer Risk and *NTCP*

In the in-field regions, the *EAR* for developing secondary cancer of the left lung are shown in **Figure 9**, calculated at 20 years (**Figure 9A**) and 40 years (**Figure 9B**) after radiation exposure at age 55 years. The results are listed in **Table 4**. In the first case, the magnitude of the *EAR* is around 50 per 10,000 PY. For a larger attained age after irradiation we obtain is scaled up by a factor of 2-3. We find statistically significant differences only for the cases “IMRT + brachytherapy” compared to “3D-CRT + brachytherapy”, as well as “IMRT + SiB” compared to “3D-CRT + sequential boost”. The *EAR* in the out-of-field regions (contralateral lung) calculated using the TLD measurements are of the order of 3–14 per 10,000 PY for all scenarios. The lowest *EAR* is associated with “3D-CRT + brachytherapy”. The highest secondary cancer risk for the right lung is given by “IMRT + brachytherapy” and “3D-CRT + sequential boost” (without statistical significance). Secondary cancer risk for the

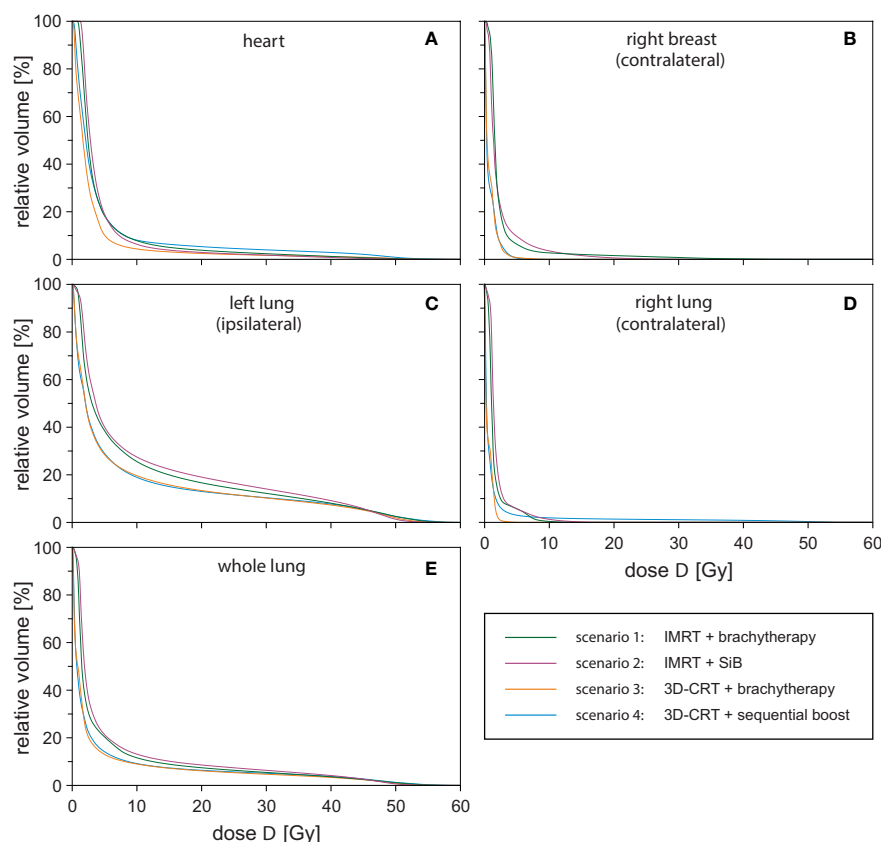


FIGURE 7 | Dose-volume-histograms for all investigated treatment techniques averaged over the respective sub-cohort and all regarded organs at risk: heart (A), contralateral breast (B), ipsilateral lung (C), contralateral lung (D), and whole lung (E).

contralateral breast ranges between 5 and 10 per 10,000 PY for all scenarios, with the lowest values calculated for “3D-CRT + brachytherapy” and highest for “3D-CRT + sequential boost”. However, statistical significance between the scenarios was not reached for any comparison in the out-of-field range.

The normal tissue complication probabilities for the OAR are shown in **Figure 9** and listed in **Table 5**. The calculated NTCP for symptomatic radiation pneumonitis of the left lung (**Figure 9D**) is of the order of 1%–2%, with significantly lower probability for the brachytherapy boost scenarios as compared with the “IMRT + SiB” technique. Statistical significance was reached for comparing “IMRT + brachytherapy” with “IMRT + SiB” and “IMRT + SiB” with “3D-CRT + sequential boost”. The complication risk regarding symptomatic pneumonitis of the whole lung (**Figure 9C**) ranges between 1.7% for “3D-CRT + brachytherapy” and 2.6% for “IMRT + SiB”. For the endpoint radiation pneumonitis grade ≥ 2 , we observe the same scenario ranking with a range from 1.0% to 1.5% (**Figure 9E**). Regarding the statistical significance, the pairwise Wilcoxon tests yield statistically significant differences for the comparisons “IMRT + brachytherapy” versus “3D-CRT + brachytherapy”, “IMRT + brachytherapy” versus “3D-CRT + sequential boost”, “IMRT + SiB” versus “3D-CRT + brachytherapy”, and “IMRT + SiB”

versus “3D-CRT + sequential boost”. In **Figure 9F**, the excess relative risk for a heart disease is depicted (also see **Table 5**). Regarding major coronary events, the average ERR ranges from approximately +25% to +35% for the different planning scenarios. No significances could be observed for the ERR comparisons.

3.4 IMRT Versus 3D-CRT Treatment Methods

To assess the contribution of the percutaneous radiotherapy technique, we now compare the 3D-CRT and the IMRT primary treatment methods in the in-field region independently of the boost technique. However, it must be kept in mind that averages are calculated by combining the “IMRT + brachytherapy” and “IMRT + SiB” scenarios on the one hand and combining the “3D-CRT + brachytherapy” and “3D-CRT + sequential boost” scenarios on the other hand, which means that very heterogeneous groupings are artificially created. Therefore, the absolute numbers are hardly representative; the emphasis here should be on the question of statistically significant differences. For calculation of the p-value, we use the Wilcoxon test.

Considering the secondary cancer risk for the left lung in the in-field region, IMRT shows a significantly higher EAR than the 3D-CRT treatment ($p < 0.001$), namely, 55 ± 10 versus 43 ± 7 per

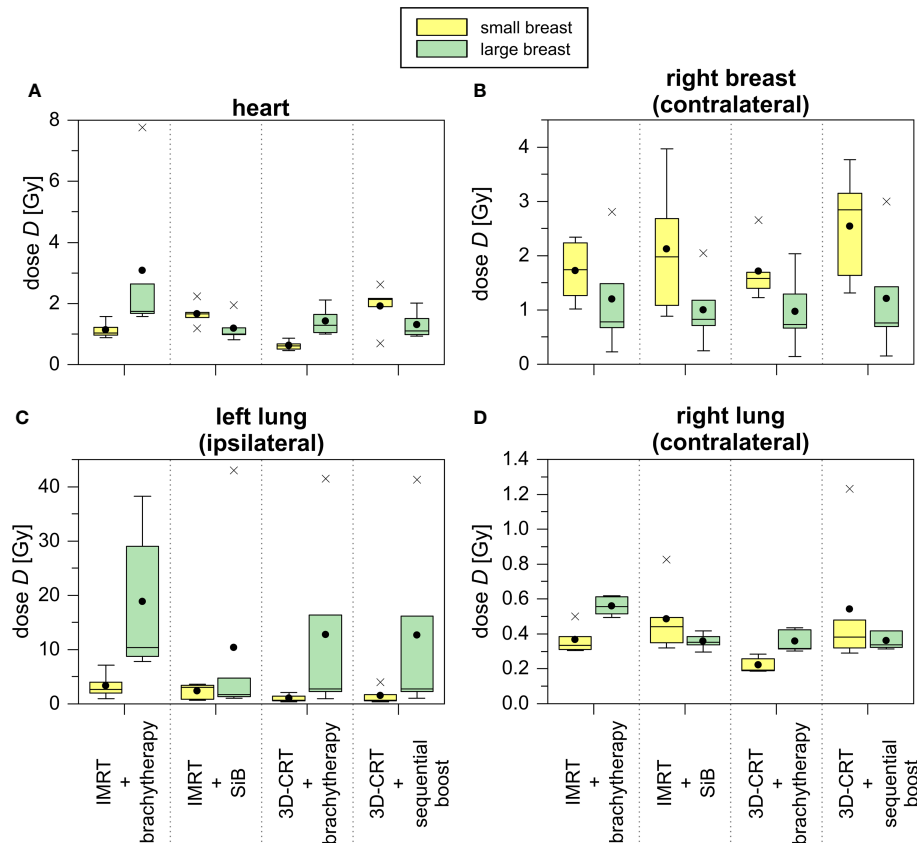


FIGURE 8 | TLD measurements of treatment plans concerning the representative small (yellow) and large (green) breast treatment plans for all scenarios depicted as boxplots. The TLDs were located in the heart (A), the contralateral breast (B), the ipsilateral (C) and contralateral (D) lung.

10,000 PY for 20 years difference in age and 149 ± 28 versus 118 ± 20 per 10,000 PY for an age difference of 40 years. In the out-of-field region, there are no statistically significant differences between the IMRT and 3D-CRT scenarios. Nevertheless, regarding only the mean values, 3D-CRT tends to have a lower *EAR* and *ERR* compared with IMRT.

The normal tissue complication risk of a symptomatic pneumonitis of the left lung is significantly lower for 3D-CRT ($1.4 \pm 0.6\%$) compared to IMRT ($2.0 \pm 0.8\%$) with $p = 0.003$. For the total lung and the endpoint symptomatic pneumonitis, we obtain the following results: IMRT $2.5 \pm 0.9\%$ versus 3D-CRT $1.8 \pm 0.4\%$ ($p < 0.001$). The risk of a radiation pneumonitis (grade ≥ 2) is $1.4 \pm 0.6\%$ for IMRT and $1.0 \pm 0.2\%$ for 3D-CRT. These results are statistically significant ($p < 0.001$). The excessive relative risk of an ischemic heart disease is $+33.1 \pm 8.4\%$ (IMRT) and $+30.4 \pm 14.5\%$ (3D-CRT) without a significant difference.

3.5 Brachytherapy Versus Teletherapy Boost Concepts

In parallel to the above section, we compare the teletherapy boost concepts against dose saturation of the tumour bed using

brachytherapy. Again, we place our main focus on the statistical comparison rather than the aggregated mean values.

The *EAR* calculation of the left lung results in a non-significant difference between both concepts: 48 ± 12 per 10,000 PY (brachytherapy) and 50 ± 10 per 10,000 PY (teletherapy) for $age_a = 75$ years (for an age difference of 40 years, 131 ± 32 per 10,000 PY for brachytherapy and 137 ± 27 per 10,000 PY for teletherapy). Regarding the out-of-field TLD measurements and *EAR* calculations for contralateral lung and breast cancer, again no statistical significance is found.

Next, the *NTCP* data are considered. The risk of symptomatic pneumonitis of the left lung is $1.6\% \pm 0.8\%$ for brachytherapy boosts and $1.8\% \pm 0.8\%$ for teletherapy boosts (no statistical significance). Symptomatic pneumonitis for the total lung is determined to be $2.1\% \pm 0.8\%$ for brachytherapy boosts and $2.2\% \pm 0.7\%$ for teletherapy boosts (no significant difference). Moreover, a radiation pneumonitis has a risk to appear in $1.2\% \pm 0.5\%$ (brachytherapy) and $1.3\% \pm 0.5\%$ (teletherapy) of all cases. Also, the risk for developing ischemic heart disease is not significantly different between the scenarios.

Irrespective of the non-given significances, a tendency regarding the average doses, normal tissue complication probabilities, and secondary cancer risks is recognisable (see

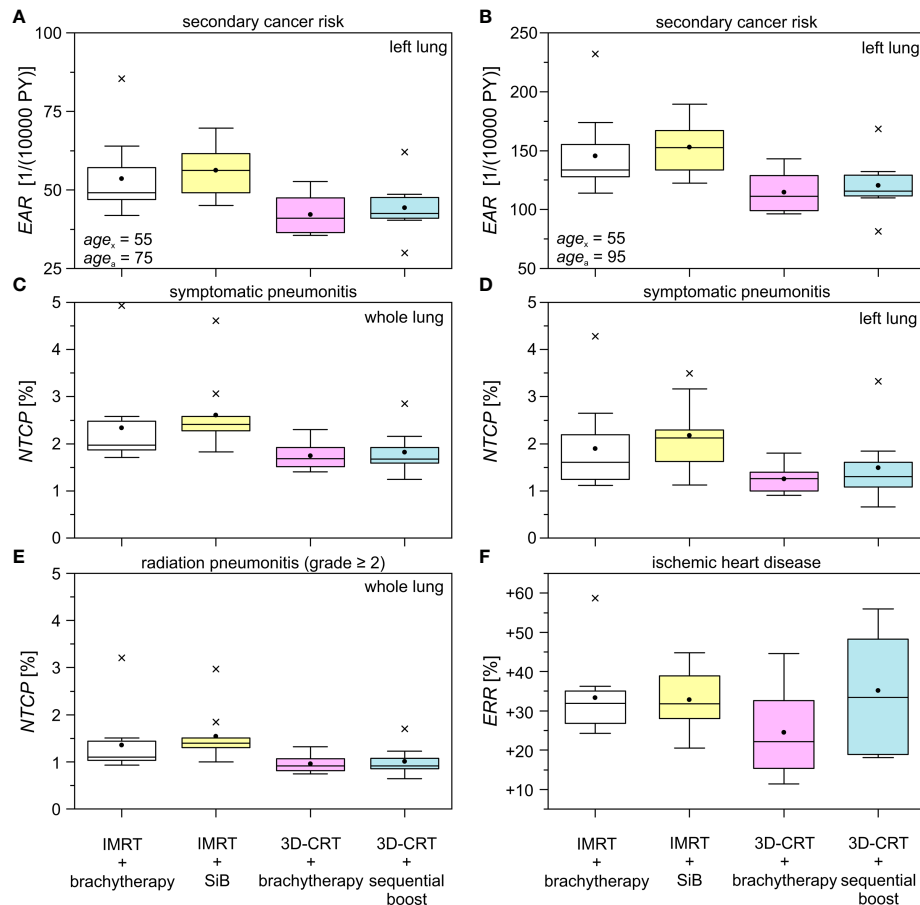


FIGURE 9 | Excess absolute risk (EAR), normal tissue complication probability (NTCP), and excess relative risk (ERR) for different treatment techniques and boost concepts as boxplots. The data is shown for the ipsilateral lung in the high dose range using the obtained dose distributions in Pinnacle & MIM. The difference in age between the mean exposed (age_x) and the hypothetically attained age (age_a) is 20 years (A) and 40 years (B), respectively. The investigated complications are symptomatic pneumonitis of the whole (C) and the left (D) lung, radiation pneumonitis (grade ≥ 2) of the whole lung (E), and the endpoint ischemic heart disease (F). See Tables 4, 5 for the respective statistical significances.

Figures 6, 9): the scenarios including a brachytherapy boost show smaller results/risks than the scenarios with the same primary WBI treatment and a teletherapy boost (“IMRT + brachytherapy” versus “IMRT + SiB” and “3D-CRT + brachytherapy” versus “3D-CRT + sequential boost”).

4 DISCUSSION

In this study, we have presented dose distributions of biologically accumulated BED2 doses for the complete adjuvant radiotherapy regime for patients with left-sided breast cancer, including WBI by either percutaneous tangential 3D-CRT or IMRT and a boost applied either sequentially by 3D-CRT, simultaneously with the IMRT, or as multicatheter interstitial brachytherapy afterloading technique. For the out-of-field region, TLD measurements were made inside an anthropomorphic phantom with breast attachment for two representative patient plans out of each group

—one with a large (1,200 cc) and one with a small (350 cc) breast. To take into account the considerable breast deformation which occurs on catheter insertion, 3D-printed phantoms were designed for the application of the brachytherapy dose distributions. To our knowledge, this is the first study to present such a detailed comparison of doses for the different scenarios, including the resulting NTCP, ERR, and EAR modelled by the most widespread approaches. In particular, only few studies have yet included boost doses in the comparison, and to our knowledge, SiB vs. brachytherapy boost scenarios have not been contrasted so far.

4.1 Strengths and Limitations of this Study

This study has several limitations: first of all, the relatively small number of 38 patients and the smaller sub-selection of plans for TLD measurements. Only one measurement per breast size and per scenario was performed; however, the patient anatomies for these plans were selected for optimum agreement amongst the patients and with the phantom breast attachments. An increased number in

TABLE 6 | Recent findings in literature compared to our results.

study	heart <i>D</i> _{mean} [Gy]	whole lung <i>D</i> _{mean} [Gy]	whole lung <i>V</i> _{20 Gy} [%]	ipsilateral lung <i>D</i> _{mean} [Gy]	comment
Xie 2020 (56)	<i>3D-CRT</i> 9.6 ± 3.7	<i>3D-CRT</i> 6.7 ± 1.0	<i>3D-CRT</i> 12.7 ± 2.0		
	<i>IMRT</i> 7.4 ± 1.3 (n.s.)	<i>IMRT</i> 5.9 ± 0.9 (p < 0.05)	<i>IMRT</i> 7.9 ± 2.6 (p < 0.05)		
Supakalin 2018 (58)				<i>3D-CRT</i> 9.5 ± 1.8 <i>IMRT</i> 7.7 ± 1.4 (p < 0.001)	Left- and right-sided breast cancer
Salvestrini 2022 (49)	1.3 - 7.2 without information on technique				Review of mean heart doses in free breathing
Vikström 2018 (54)	<i>3D-CRT</i> 6.2 ± 4.4			6.8 ± 1.2	
Saini 2019 (52)	1.88			6.1	
Sripathi 2017 (59)	<i>3D-CRT</i> 7.1 ± 3.0	<i>3D-CRT</i> 16.4 ± 4.4	<i>3D-CRT</i> 31.4 ± 10.8		
	<i>IMRT</i> 11.94 ± 1.73 6.5 ± 4.7	<i>IMRT</i> 20.2 ± 1.3	<i>IMRT</i> 35.3 ± 7.5		
Johansen 2011 (77)	2.5	5.4	9.1	13.7 ± 1.9	<i>3D-CRT</i>
Edvardsson 2015 (50)	3.5			7.6	<i>3D-CRT</i>
Tommasino 2017 (55)	3.42 ± 1.20			8.81 ± 1.33	<i>IMRT</i>
Kuo 2021 (51)	2.54 ± 1.40	3.6 ± 0.8			Tangential <i>IMRT</i> , medium expiration
Corradini 2018 (62)	<i>3D-CRT</i> 4.41 ± 2.2			<i>3D-CRT</i> 7.24 ± 2.59	<i>3D-CRT</i>
Haciislamoglu 2019 (65)	<i>IMRT</i> 8.40 ± 2.54			<i>IMRT</i> 12.58 ± 1.75	<i>3D-CRT</i>
Stewart 2008 (78)	3.5	6.5	10		Systematic review
Taylor 2017 (57)	5.2	5.7		9.0	(2010–2015)
This study	<i>3D-CRT + boost</i> 4.8 ± 2.1	<i>3D-CRT + boost</i> 4.2 ± 1.1	<i>3D-CRT + boost</i> 6.3 ± 2.0	<i>3D-CRT + boost</i> 8.7 ± 2.2	Total dose including boost/SiB
	<i>3D-CRT + brachy</i> 3.3 ± 1.6	<i>3D-CRT + brachy</i> 3.9 ± 0.8	<i>3D-CRT + brachy</i> 6.1 ± 1.3	<i>3D-CRT + brachy</i> 7.9 ± 1.1	
	<i>IMRT + SiB</i> 4.4 ± 1.0	<i>IMRT + SiB</i> 5.9 ± 1.3	<i>IMRT + SiB</i> 8.6 ± 1.9	<i>IMRT + SiB</i> 10.8 ± 1.8	
	<i>IMRT + brachy</i> 4.5 ± 1.3	<i>IMRT + brachy</i> 5.3 ± 1.6	<i>IMRT + brachy</i> 7.4 ± 1.6	<i>IMRT + brachy</i> 9.9 ± 2.3	

n.s., not significant.

patients and measurements would increase the significance of this study. Moreover, the comparability between the patients and scenarios is not absolute, since we do not calculate and measure four treatment plans (one per scenario) for each patient but rather compare different cohorts. We explicitly decided against performing a planning study and decided to retrospectively review real patient treatment plans from a collective of 38 patients. For all these patients, the same technical equipment was available (planning CT, linear accelerators, afterloading brachytherapy unit, treatment planning systems). Admittedly, this approach introduces some heterogeneity between the cohorts and precludes a pairwise comparison with linked samples; plausibly, statistical significance will be more difficult to achieve since the variance of the dose distributions is larger. A planning study would allow to assess what can optimally be achieved by the different technical approaches in a

uniform hypothetical setting and hence identify the most beneficial treatment scenario for each patient—however, this would in any case not be possible before the individual clinical treatment decision, since a planning CT with multicatheter implant would be required for such a comparison. In contrast, the advantage of our approach is that it reflects the clinical reality; these are not treatment plans optimised for study purposed in direct comparison, rather, they represent the standard that was actually accepted by the radiation oncologists for each technique and thereby the true treatment of our patients over that time. The collectives are adequately matched without any significant difference in breast and PTV volume amongst the cohorts.

Some OARs extend from the in-field or penumbra region to the low-dose region beyond the field edge. For these, both the TLD measurements and the TPS calculations present only part of the

truth. However, as has been shown for these cases, the TPS and TLD results agree relatively well in these special cases. In clinical practice, the combination of these risk estimates will come closer to the truth than either one separately: the *NTCP* will be mostly influenced by the higher isodoses and can therefore realistically be approximated by the TPS calculations. The secondary cancer risk may be higher with higher isodoses in those parts of the lungs and heart exposed to in-field or penumbra doses, and this is where Schneider's model should be applied. However, the larger parts of these organs will receive small out-of-field doses, and in these regions, the linear model using TLD measurements should realistically reflect the secondary cancer risk. A more relevant limitation in the risk models arises from the fact that other patient-specific parameters are not included in the models, such as the influence of chemotherapy such as anthracyclines on cardiac toxicity or smoking status on lung cancer. The modelled values therefore reflect only the additional risk posed by radiotherapy, assuming all other factors to remain equal throughout the patient collectives.

A final issue is the neglect of neutrons, which emerge in 18-MV photon irradiation. To make a rough estimate of the neutron contribution, we assessed which percentage of the total prescribed dose was applied by 18-MV beams. Depending on the patient and scenario, this was between 0% and 17%. Using a conservative maximum of 20% of the plan dose delivered by 18-MV photons, this amounts to around 12 Gy. Vanhavere et al. (49) estimate the organ-equivalent doses in prostate treatment, finding a secondary neutron exposure for directly adjacent OAR (the bladder in their case) of approximately 8 mSv per 2 Gy (= 4 mSv/Gy) for 3D-CRT and a Varian Clinac 2100 C-D linear accelerator. In our case, this would result in 48 mSv for 3D-CRT. Secondary neutron generation also depends strongly on the treatment technique. IMRT usually requires more MUs compared with 3D-CRT, and thus, the fluence for IMRT is estimated approximately three times larger than for 3D-CRT (50). With the values above, we obtain 144 mSv for the IMRT treatments. In reality, this is a drastic overestimation since only a minority of plans in our collective used 18 MV for IMRT treatment at all. In principle, it is our institutional policy to avoid IMRT with photon energies higher than 6 MV, and exceptions are only rarely made when the patient's anatomy is very difficult and adequate plans cannot be achieved with 6-MV photons only. Still, we will carry out the conservative estimate, assuming a 144-mSv neutron dose for IMRT plans and 48 mSv for 3D-CRT. Neutron generation is also dependent on the linear accelerator used, e.g., a Varian 21EX machine with an 18-MV nominal photon beam energy emits approximately 2.5 times more neutrons than a Siemens ONCOR, which shows a relatively flat photoneutron spectrum (51). Including this, we end up with a maximum of 58-mSv total neutron dose for the worst-case scenario IMRT plans. Comparing this value to the prescribed dose of 60 Gy results in approximately 1%. Thus, secondary neutrons were neglected in our case. This approximation is in line with the conclusions by (49), who stated that secondary neutron influence on *NTCP* and secondary cancer risk are small when compared with gamma radiation.

4.2 Comparison with Previous Studies

Comparing the different plan scenarios, we find for the primary course of radiotherapy treatment without boost a reduced *EAR*

and *NTCP* for 3D-CRT as opposed to IMRT. The reason is that the incident angles of the tangential fields are chosen in such a way that the left lung, the heart, and the contralateral breast are maximally shielded. In comparison, the IMRT—even with a fan-shaped beam arrangement—uses more widespread angles to obtain a sufficient number of free parameters for the inverse optimisation. While optimising PTV coverage, this leads to an increase in organ and normal tissue risks in those areas which were formerly completely blocked out.

4.2.1 Dosimetric Comparison

A number of studies have presented a dosimetric comparison for tangential 3D-CRT and IMRT planning techniques, considering the primary course of treatment without additional boost: in **Table 6**, several recent literature dose values are summarised for free-breathing techniques and 50-Gy whole-breast irradiation. While not always achieving our aim of reducing the mean heart dose to below 3 Gy, our dose values for the summation plans remain within the range observed by other authors. In particular, it has been observed that the mean heart dose reported has steadily decreased over the past years (52, 53), which may reflect greater emphasis on the heart sparing in the light of the elevated risk of ischemic heart disease and better technical possibilities to achieve improved OAR sparing in adjuvant treatment of left-sided breast cancer, such as deep-inspiration breath hold (DIBH) (54, 55) or respiratory-gated treatment (56, 57), prone vs. supine patient immobilisation (58), VMAT (59, 60), or even proton treatment (61).

Regarding dose to the lungs, our results are also consistent with previous studies in terms of retrieved dose values. The determined doses can be compared with the report by Taylor et al. (62). They find typical modern whole-lung doses to be 5.7 Gy and whole-heart doses to be 5.2 Gy for left-sided breast cancer treatment. For the comparison of techniques, Xie et al. (63) observed a significantly reduced whole-lung dose for IMRT vs. 3D-CRT; a similar result was obtained by Supakalin et al. (64) for the ipsilateral lung. This is not reflected in our data: the lung dose metrics in our collective are higher for “IMRT + SiB” vs. “3D-CRT + teletherapy boost” ($p = 0.033$ for the ipsilateral lung, $p = 0.005$ for the whole lung) and for “IMRT + brachytherapy” vs. “3D-CRT + brachytherapy” ($p = 0.033$ for the ipsilateral lung, $p = 0.023$ for the whole lung), respectively. This is also paralleled by the toxicity and secondary cancer risk comparisons presented in the following. The underlying reason may be that even the tangential fanned beams in the IMRT scenarios and more specifically the more widespread beams in the “IMRT + SiB” plans traverse a larger portion of the contralateral lung and breast than the tangents that were specifically designed to block out these organs at risk in the 3D-CRT plans. However, we have not assessed whether this is counterbalanced by improved PTV and boost coverage or conformity, as has been suggested in a number of studies (60, 63, 65–67). We did not include this comparison owing to the different delineation of teletherapy and brachytherapy targets. Besides, the brachytherapy plans are usually created and accepted for clinical use without considering a biological summation dose including the preceding percutaneous WBI as would be done for percutaneous WBI + boost, so in clinical practice these plans are differently evaluated in terms of quality metrics.

For the contralateral breast, for the most part this is not comprised inside the treatment fields and will mainly receive scattered doses as measured with the TLDs (of the order of 1 Gy for the large and up to 2 Gy for the small breast attachment). However, for some treatment plans, a small medial wedge of the right breast may be traversed by a treatment beam making up the edge of the tangent. Here the calculated doses from the TPS yield a mean contralateral breast dose between 0.7 and 2.5 Gy (higher for IMRT vs. 3D-CRT [$p < 0.001$] and for teletherapy vs. brachytherapy boost [n.s., not significant]), which corresponds adequately with the TPS predictions, and dose maxima in the right breast of the order of 3.4 Gy (3D-CRT + brachytherapy) to 9.6 Gy (IMRT + brachytherapy). The maxima evidently correspond to the in-field part of the contralateral breast.

Only few studies have investigated out-of-field organ doses for breast radiotherapy using TLD measurements. For the 50-Gy total dose, Williams et al. (68) measured contralateral breast doses in the range of 13–60 cGy for 3D-CRT and 103–124% of this for IMRT, somewhat lower than reported by Vlachopoulou et al. (69) for 3D-CRT (1.0 ± 0.4 Gy). Similarly, Behmadi et al. (70) obtained doses of 17.7–213.2 cGy for the ipsilateral lung, 14.8–31.6 cGy for the contralateral lung, and 53.6–134.2 cGy for the heart (again, for 50-Gy WBI using 3D-CRT). When scaled to the higher total dose, these results are in good agreement with ours, allowing for some deviations by the inclusion of the boost and the combination of different treatment techniques.

4.2.2 NTCP Models

As most studies regarding treatment techniques and toxicity after breast cancer radiotherapy have concentrated on the whole-breast treatment series (25×2 Gy or 28×1.8 Gy), we will first compare NTCP and EAR results for these scenarios before moving on to the complete treatment series including boost which we considered in this manuscript.

Using a tangential 3D-CRT beam setup for 50 Gy WBI, Edvardsson et al. (57) modelled an excess cardiac mortality probability of 0.49% and a risk of developing radiation pneumonitis of 0.31%. For the same fractionation applied using IMRT, Tommasino et al. (61) estimated a risk for a major coronary event of 2.0%, assuming a baseline cardiac risk without radiotherapy of 1.6%. Calculating our way back from the EAR to the ERR with this baseline risk, this corresponds to an ERR of 25%, which is similar to our estimates. Correspondingly, Corradini et al. (71) observed cardiac ERR values of approximately 20% for free-breathing 3D-CRT treatment.

Regarding the risk for symptomatic pneumonitis of the ipsilateral lung, Kuo et al. (56) report an estimate of 10.95% for treatment during mid-lung expansion. The difference between these values and those reported by Edvardsson (0.31%, see ref. 61) is rather large, comprising our range of values (1.3–2.2%).

4.2.3 EAR Estimates

The estimates of secondary cancer risk rely on very different models due to the very different dose regimes. In this work, we decided to

include the EAR for the ipsilateral lung as based on the full model by Schneider et al. (32) applied to the dose distribution from the TPS. The rationale for this choice is that the major contribution to left lung secondary cancer induction can be presumed to arise from the small high-dose tangent through the lung, which is comprised inside the open treatment beams. There will also be large areas of the ipsilateral lung exposed to very-low out-of-field doses, which will not be accurately estimated by the TPS. For this area of the shielded ipsilateral lung, the scattered doses will be considerably lower than the in-field doses and probably still higher than the scattered dose to the contralateral lung, which is completely outside the treatment beams. Therefore, to some degree our estimates represent the two extremes: the calculated TPS-dose-based excess absolute risks (EARs) for the left lung based on the mechanistic model on the one hand and the contralateral out-of-field doses measured by TLDs and translated into EAR according to the linear model on the other hand. For the ipsilateral lung, the EARs calculated for an age of exposure of 55 years and an attained age of 75 years are between 42 and 56 per 10,000 PY, depending on the treatment plan. Contralaterally, the risk is lower by about an order of magnitude (3–5 per 10,000 PY), which is in concordance with our assumption that the ipsilateral risk will be mainly attributed to the high-dose region.

The influence of different radiotherapy techniques (tangential 3D-CRT, IMRT, VMAT) on secondary cancer risk was investigated by Corradini et al. (71), Karpf et al. (72), and Hacıislamoglu et al. (73) for 50-Gy percutaneous WBI. For an age of exposure of 30 years and attained age of 70 years, Hacıislamoglu et al. (73) estimate an EAR for the contralateral lung of 4.4 ± 0.7 , 19.9 ± 3.6 , and 19.6 ± 1.9 per 10,000 PY for 3D-CRT, IMRT, and VMAT, respectively. For the ipsilateral lung, they report an EAR of 28.3 ± 8.0 , 61.7 ± 7.1 , and 65.2 ± 5.4 per 10,000 PY and for the contralateral lung of 3.5 ± 0.6 , 27.2 ± 4.4 , and 21.6 ± 3.3 per 10,000 PY, respectively (3D-CRT, IMRT, VMAT). For all these scenarios, they find a significant advantage for the 3D-CRT plans in comparison with IMRT and VMAT, but no significant difference between the IMRT and VMAT plans. Similarly, Karpf et al. (72) considered an IMRT scenario and used the actual age of exposure of the patients and a hypothetical attained age of 70 years, finding EAR values of 27.07 ± 2.18 per 10,000 PY for the ipsilateral lung, 7.13 ± 1.11 per 10,000 PY for the contralateral lung, and 2.99 ± 2.15 per 10,000 PY for the contralateral breast, which agrees comparatively well with our results when allowing for the different fractionation and age at exposure. Corradini et al. (71), comparing 3D-CRT and VMAT for 50 Gy WBI, an age of exposure of 50 years, and an attained age of 70 years, distinguished high- and medium-baseline-risk patients, resulting in a larger variation of modelled EAR values for the lung (8–67 per 10,000 PY for 3D-CRT vs. 9–78 per 10,000 PY for VMAT). Allowing for the different assumed ages and the limitation to only WBI, these values are in agreement with our model results. Zhang et al. (65) observe considerably larger EAR values than the other studies, which cannot be explained merely by the different assumed ages; however, the relative comparison of treatment techniques (tangential 3D-CRT, tangential two-field IMRT, six-field IMRT, and VMAT) confirms our results and those of the other authors cited, in that tangential 3D-CRT entails lower EAR than six-field IMRT, both remaining below the EAR of VMAT.

4.2.4 Comparison of the Boost Concepts

Moving on to include the boost concepts, we expect that the normal tissue and OAR are less exposed to ionising radiation due to the given placement of the interstitial catheters inside the target volume and the rapid dose fall-off of the Iridium isotope dose in tissue. The comparison of all four scenarios in Section 3.3 yields a favourable combination: the 3D-CRT primary treatment method and an additional dose escalation using a brachytherapy boost reduces the *EAR*, *ERR* and *NTCP* the most.

To our knowledge, boost concepts have only been considered by a small number of authors so far. A 3D-CRT vs. IMRT planning study for WBI of 50.4 and 1.8 Gy with a sequential boost of 16 Gy was presented by Simonetto et al. (22). These authors report mean organ doses of 1–5 Gy for the contralateral breast, 8–10 Gy for the ipsilateral lung, and 0.3–1 Gy for the contralateral lung, well in line with our results. Hayden et al. (74) and Aly et al. (75), respectively, consider SiB scenarios with different fractionation regimes (50/60 Gy in 25 fractions and 50.5/64.4 Gy in 28 fractions). The former, using an IMRT technique, observe a mean dose to the left lung of 13.41 Gy (compared with 10.8 Gy in our study), a mean heart dose of 6.88 Gy (vs. 4.4 Gy in this work), and a mean contralateral breast dose of 0.63 Gy (calculated in their TPS, compared to 1.56 Gy from our TLD measurements). Aly et al. (75) report a mean ipsilateral lung dose of 8.4 ± 1.6 Gy for 3D-CRT and 9.1 ± 1.5 Gy for a combined IMRT-VMAT approach ($p < 0.05$), a mean heart dose of 3.0 ± 0.9 Gy (3D-CRT) vs. 3.5 ± 1.0 Gy (IMRT-VMAT, not significant), and a mean contralateral breast dose of 1.1 ± 0.3 Gy vs. 1.2 ± 0.3 Gy (significant). Our results fall well between these two studies. A comparison between a sequential boost (3D-CRT, 50 Gy + 16 Gy in fractions of 2 Gy) and SiB (50/60 Gy in 25 fractions, static fields, or TomoTherapy technique) by Van Parijs et al. (76) reported no significant advantage of either technique for the mean heart dose (3.04, 3.12, and 2.97 Gy, respectively) and ipsilateral mean lung dose (6.26, 6.72, and 6.13 Gy, respectively) but a significant difference in calculated contralateral breast dose (0.36, 0.44, and 1.17 Gy, respectively). These doses correspond to the values we observe in the “3D-CRT + sequential boost” and “IMRT + SiB” scenarios.

Interstitial brachytherapy concepts were presented in 32- to 34-Gy accelerated partial breast irradiation concepts by Novotná et al. (77) and Chatzikonstantinou et al. (78), showing good cardiac dose sparing. As a boost after external beam radiotherapy, only Fröhlich et al. (79) combined interstitial multicatheter brachytherapy (3×4.75 Gy) with tangential beam WBI (15×2.67 -Gy accelerated fractionation), showing that brachytherapy achieved a higher dose to the target with equal sparing of OARs in comparison to percutaneous treatment of both series, which is consistent with our observations, albeit for a normally fractionated dose concept.

4.2.5 Comparison With Clinical Observations

Finally, how do our secondary cancer risk estimates compare with clinical observations? Second solid cancers observed in the SEER cancer registry for >5 year survivors presented by Berrington et al. (80) gave an *EAR* for contralateral breast cancer of 5 per 10,000 PY (and an increased incidence of lung cancer of 0.4% vs. 0.3% for non-irradiated patients, which translates into an *EAR* of 10 per 10,000 PY—compared to Xie et al. (81)). Our model predictions give a plausible

approximation of these observational study results, although a precise comparison is difficult due to different evaluated time lags and baseline risks—compared to Pignol et al. (82).

5 CONCLUSION

In this work, we compare four different adjuvant treatment techniques of breast cancer in context of breast-conserving therapy regarding normal tissue complication probabilities and secondary cancer risks: “IMRT + brachytherapy”, “IMRT + SiB”, “3D-CRT + brachytherapy”, and “3D-CRT + sequential boost”. In general, 3D-CRT shows the best risk reduction in contrast to IMRT. Concerning the boost concepts, brachytherapy is the most effective method in order to minimise *EAR* and *NTCP* compared to teletherapy boost concepts. Hence, the 3D-CRT technique in combination with an interstitial multicatheter brachytherapy boost shows the lowest secondary cancer risks and normal tissue complication probabilities for treating breast cancer with techniques including boost concepts. However, these results reflect only the normal tissue effects and do not compare other important endpoints such as the PTV coverage or the tumour control probability.

DATA AVAILABILITY STATEMENT

The raw data supporting the conclusions of this article will be made available by the authors, without undue reservation.

AUTHOR CONTRIBUTIONS

PM and CR were responsible for patient treatment. YD and FN devised and planned the project. PM advised regarding the medical aspects of the project. MV and YD wrote the manuscript based on a first draft of the medical doctoral thesis of JG, which is based on this project. YD and MV supervised the doctoral work by JG, in which JG performed the patient retrieval and review in the database, import into the planning systems, image registration, dose calculations, and export. The dosimetric analysis was facilitated by code provided by MV. The secondary cancer risk model was carried out in a Matlab script by MV. MV created the virtual 3D model and implemented the breast add-on into the setup of phantom and afterloader. BT manufactured both the brachytherapy breast phantoms using his private 3D printer. HA and MS performed the TLD preparation and read-out. JG and MV performed the statistical data analysis. Figures were prepared by MV and JG. All authors read and approved the final manuscript.

ACKNOWLEDGMENTS

We would like to thank Prof. Dr. Claudia Rübe (Laboratory for Molecular Radiooncology, Saarland University Medical Centre, Homburg, Germany) for supporting us by providing the anthropomorphic phantom.

REFERENCES

- Dafni U, Tsourti Z, Alatsathianos I. Breast Cancer Statistics in the European Union: Incidence and Survival Across European Countries. *Breast Care (Basel)* (2019) 14(6):344–53. doi: 10.1159/000503219
- Jani C, Saliccioli I, Rupal A, Al Omari O, Goodall R, Saliccioli JD, et al. Trends in Breast Cancer Mortality Between 2001 and 2017: An Observational Study in the European Union and the United Kingdom. *JCO Glob Oncol* (2021) 7:1682–93. doi: 10.1200/GO.21.00288
- Early Breast Cancer Trialists' Collaborative Group (EBCTCG), Darby S, McGale P, Correa C, Taylor C, Arriagada R, et al. Effect of Radiotherapy After Breast-Conserving Surgery on 10-Year Recurrence and 15-Year Breast Cancer Death: Meta-Analysis of Individual Patient Data for 10,801 Women in 17 Randomised Trials. *Lancet* (2011) 378(9804):1707–16. doi: 10.1016/S0140-6736(11)61629-2
- Sedlmayer F, Sautter-Bühl ML, Budach W, Dunst J, Fastner G, Feyer P, et al. Breast Cancer Expert Panel of the German Society of Radiation Oncology (DEGRO). DEGRO Practical Guidelines: Radiotherapy of Breast Cancer I: Radiotherapy Following Breast Conserving Therapy for Invasive Breast Cancer. *Strahlenther Onkol.* (2013) 189(10):825–33. doi: 10.1007/s00066-013-0437-8
- German Cancer Society, German Cancer Aid, and Association of the Scientific Medical Societies in Germany. *Guidelines Program Oncology: S3-Leitlinie Für Die Früherkennung, Diagnostik, Therapie Und Nachsorge Des Mammarkarzinoms. Version 4.4*. Available at: <https://www.awmf.org/leitlinien/detail/ll/032-045OL.html>.
- Kneschaurek P, Nüsslin F Entwicklung Von Bestrahlungsmethoden Und Geräten. *Strahlenther Onkol.* (2012) 188:245–52. doi: 10.1007/s00066-012-0188-y
- Duma MN, Brambs C, Wittig A. Neue Entwicklungen in Der Strahlentherapie. *Best Pract Onkologie.* (2020) 15:24–30. doi: 10.1007/s11654-020-00199-3
- Wortman BG, Post CCB, Powell ME, Khaw P, Fyles A, D'Amico R, et al. Radiation Therapy Techniques and Treatment-Related Toxicity in the PORTEC-3 Trial: Comparison of 3-Dimensional Conformal Radiation Therapy Versus Intensity-Modulated Radiation Therapy. *Int J Radiat Oncol Biol Phys* (2022) 112(2):390–9. doi: 10.1016/j.ijrobp.2021.09.042
- M Wannemacher, F Wenz and J Debus eds. *Strahlentherapie. 2nd edition.* Berlin: Springer (2013).
- McDonald MW, Godette KD, Whitaker DJ, Davis LW, Johnstone PA. Three-Year Outcomes of Breast Intensity-Modulated Radiation Therapy With Simultaneous Integrated Boost. *Int J Radiat Oncol Biol Phys* (2010) 77(2):523–30. doi: 10.1016/j.ijrobp.2009.05.042
- Meng J, Huang W, Mei X, Yu X, Pan Z, Ma J, et al. Adjuvant Breast Inversely Planned Intensity-Modulated Radiotherapy With Simultaneous Integrated Boost for Early Stage Breast Cancer: Results From a Phase II Trial. *Strahlenther Onkol.* (2020) 196(9):764–70. doi: 10.1007/s00066-020-016111
- Deng X, Wu H, Gao F, Su Y, Li Q, Liu S, et al. Brachytherapy in the Treatment of Breast Cancer. *Int J Clin Oncol* (2017) 22(4):641–50. doi: 10.1007/s10147-017-1155-5
- Bartelink H, Horiot JC, Poortmans P, Struikmans H, Van den Bogaert W, Barillot I, et al. Recurrence Rates After Treatment of Breast Cancer With Standard Radiotherapy With or Without Additional Radiation. *N Engl J Med* (2001) 345(19):1378–87. doi: 10.1056/NEJMoa010874
- Kindts I, Laenen A, Depuydt T, Weltens C. Tumour Bed Boost Radiotherapy for Women After Breast-Conserving Surgery. *Cochrane Database Syst Rev* (2017) 11(11):CD011987. doi: 10.1002/14651858.CD011987.pub2
- Poortmans P, Bartelink H, Horiot JC, Struikmans H, Van den Bogaert W, Fourquet A, et al. The Influence of the Boost Technique on Local Control in Breast Conserving Treatment in the EORTC 'Boost Versus No Boost' Randomised Trial. *Radiother Oncol* (2004) 72(1):25–33. doi: 10.1016/j.radonc.2004.03.007
- Hammer J, Track C, Seewald DH, Zoidl JP, Labeck W, Putz E, et al. Breast Cancer: External Beam Radiotherapy and Interstitial Iridium Implantation–10-Year Clinical Results. *EJC* (1998) 34(Suppl 1):32. doi: 10.1016/S0959-8049(97)89284-2
- Hammer J, Seewald DH, Track C. Breast Cancer: Primary Treatment With External-Beam Radiation Therapy and High-Dose-Rate Iridium Implantation. *Radiology* (1994) 193(2):573–7. doi: 10.1148/radiology.193.2.7972782
- Keller LM, Sopka DM, Li T, Klayton T, Li J, Anderson PR, et al. Five-Year Results of Whole Breast Intensity Modulated Radiation Therapy for the Treatment of Early Stage Breast Cancer: The Fox Chase Cancer Center Experience. *Int J Radiat Oncol Biol Phys* (2012) 84(4):881–7. doi: 10.1016/j.ijrobp.2012.01.069
- Allali S, Kirova Y. Radiodermatitis and Fibrosis in the Context of Breast Radiation Therapy: A Critical Review. *Cancers (Basel).* (2021) 13(23):5928. doi: 10.3390/cancers13235928
- Yang JF, Lee MS, Lin CS, Chao HL, Chen CM, Lo CH, et al. Long-Term Breast Cancer Patient Outcomes After Adjuvant Radiotherapy Using Intensity-Modulated Radiotherapy or Conventional Tangential Radiotherapy. *Med (Baltimore).* (2016) 95(11):e3113. doi: 10.1097/MD.00000000000003113
- Hoekstra N, Fleury E, Merino Lara TR, van der Baan P, Bahnerth A, Struik G, et al. Long-Term Risks of Secondary Cancer for Various Whole and Partial Breast Irradiation Techniques. *Radiother Oncol* (2018) 128(3):428–33. doi: 10.1016/j.radonc.2018.05.032
- Simonetto C, Rennau H, Remmele J, Sebb S, Kundrát P, Eidemüller M, et al. Exposure of Remote Organs and Associated Cancer Risks From Tangential and Multi-Field Breast Cancer Radiotherapy. *Strahlenther Onkol.* (2019) 195(1):32–42. doi: 10.1007/s00066-018-1384-1
- Sánchez-Nieto B, Romero-Expósito M, Terrón JA, Irazola L, García Hernández MT, Mateos JC, et al. External Photon Radiation Treatment for Prostate Cancer: Uncomplicated and Cancer-Free Control Probability Assessment of 36 Plans. *Phys Med* (2019) 66:88–96. doi: 10.1016/j.ejmp.2019.09.076
- Sánchez-Nieto B, Medina-Ascanio KN, Rodríguez-Mongua JL, Doerner E, Espinoza I. Study of Out-of-Field Dose in Photon Radiotherapy: A Commercial Treatment Planning System Versus Measurements and Monte Carlo Simulations. *Med Phys* (2020) 47(9):4616–25. doi: 10.1002/mp.14356
- Huang JY, Followill DS, Wang XA, Kry SF. Accuracy and Sources of Error of Out-of-Field Dose Calculations by a Commercial Treatment Planning System for Intensity-Modulated Radiation Therapy Treatments. *J Appl Clin Med Phys* (2013) 14(2):4139. doi: 10.1120/jacmp.v14i2.4139
- Howell RM, Scarboro SB, Kry SF, Yaldo DZ. Accuracy of Out-of-Field Dose Calculations by a Commercial Treatment Planning System. *Phys Med Biol* (2010) 55(23):6999–7008. doi: 10.1088/0031-9155/55/23/S03
- Joosten A, Matzinger O, Jeanneret-Sozzi W, Bochud F, Moeckli R. Evaluation of Organ-Specific Peripheral Doses After 2-Dimensional, 3-Dimensional and Hybrid Intensity Modulated Radiation Therapy for Breast Cancer Based on Monte Carlo and Convolution/Superposition Algorithms: Implications for Secondary Cancer Risk Assessment. *Radiother Oncol* (2013) 106(1):33–41. doi: 10.1016/j.radonc.2012.11.012
- Sadrollahi A, Nuesken F, Licht N, Rübe C, Dzierma Y. Monte-Carlo Simulation of the Siemens Artiste Linear Accelerator Flat 6 MV and Flattening-Filter-Free 7 MV Beam Line. *PLoS One* (2019) 14:e0210069. doi: 10.1371/journal.pone.0210069
- Withers HR, Thames HD Jr, Peters LJ. A New Isoeffect Curve for Change in Dose Per Fraction. *Radiother Oncol* (1983) 1(2):187–91. doi: 10.1016/s0167-8140(83)80021-8
- Albuquerque K, Hryckushko BA, Harkenrider MM, Mayadev J, Klopp A, Beriwal S, et al. Compendium of Fractionation Choices for Gynecologic HDR Brachytherapy-An American Brachytherapy Society Task Group Report. *Brachytherapy* (2019) 18(4):429–36. doi: 10.1016/j.brachy.2019.02.008
- Dzierma Y, Nuesken F. *Recent Advancements and Applications in Dosimetry. 1st ed.* MF Chan, editor. New York: Nova Science Publishers Inc (2018), ISBN:9781536137606
- Schneider U, Sumila M, Robotka J. Site-Specific Dose-Response Relationships for Cancer Induction From the Combined Japanese A-Bomb and Hodgkin Cohorts for Doses Relevant to Radiotherapy. *Theor Biol Med Model* (2011) 8:27. doi: 10.1186/1742-4682-8-27
- Schneider U. Mechanistic Model of Radiation-Induced Cancer After Fractionated Radiotherapy Using the Linear-Quadratic Formula. *Med Phys* (2009) 36:1138–43. doi: 10.1118/1.3089792
- Schneider U, Walsh L. Cancer Risk Estimates From the Combined Japanese A-Bomb and Hodgkin Cohorts for Doses Relevant to Radiotherapy. *Radiat Environ Biophys* (2008) 47:253–63. doi: 10.1007/s00411-007-0151-y
- Lyman JT. Complication Probability as Assessed From Dose-Volume Histograms. *Radiat Res Suppl.* (1985) 8:13–9. doi: 10.2307/3583506

36. Kutcher GJ, Burman C. Calculation of Complication Probability Factors for non-Uniform Normal Tissue Irradiation: The Effective Volume Method. *Int J Radiat Oncol Biol Phys* (1989) 16(6):1623–30. doi: 10.1016/0360-3016(89)90972-3
37. Deasy JO. Comments on the Use of the Lyman-Kutcher-Burman Model to Describe Tissue Response to Nonuniform Irradiation. *Int J Radiat Oncol Biol Phys* (2000) 47(5):1458–60. doi: 10.1016/s0360-3016(00)00500-9
38. Emami B, Lyman J, Brown A, Cola L, Goitein M, Munzenrider JE, et al. Tolerance of Normal Tissue to Therapeutic Irradiation. *Int J Radiat Oncol Biol Phys* (1991) 21(1):109–22. doi: 10.1016/0360-3016(91)90171-y
39. Bentzen SM, Constine LS, Deasy JO, Eisbruch A, Jackson A, Marks LB, et al. Quantitative Analyses of Normal Tissue Effects in the Clinic (QUANTEC): An Introduction to the Scientific Issues. *Int J Radiat Oncol Biol Phys* (2010) 76(3):3–9. doi: 10.1016/j.ijrobp.2009.09.040
40. Brodin NP, Kabarriti R, Garg MK, Guha C, Tomé WA. Systematic Review of Normal Tissue Complication Models Relevant to Standard Fractionation Radiation Therapy of the Head and Neck Region Published After the QUANTEC Reports. *Int J Radiat Oncol Biol Phys* (2018) 100(2):391–407. doi: 10.1016/j.ijrobp.2017.09.041
41. Marks LB, Yorke ED, Jackson A, Ten Haken RK, Constine LS, Eisbruch A, et al. Use of Normal Tissue Complication Probability Models in the Clinic. *Int J Radiat Oncol Biol Phys* (2010) 76(3 Suppl):10–9. doi: 10.1016/j.ijrobp.2009.07.1754
42. Darby SC, Ewertz M, McGale P, Bennet AM, Blom-Goldman U, Brønnum D, et al. Risk of Ischemic Heart Disease in Women After Radiotherapy for Breast Cancer. *N Engl J Med* (2013) 368(11):987–98. doi: 10.1056/NEJMoa1209825
43. Alaei P, Ding G, Guan H. Inclusion of the Dose From Kilovoltage Cone Beam CT in the Radiation Therapy Treatment Plans. *Med Phys* (2010) 37:244–8. doi: 10.1118/1.3271582
44. Dzierma Y, Mikulla K, Richter P, Bell K, Melchior P, Nuesken F, et al. Imaging Dose and Secondary Cancer Risk in Image-Guided Radiotherapy of Pediatric Patients. *Radiat Oncol* (2018) 13(1):168. doi: 10.1186/s13014-018-1109-8
45. Mohan R, Mageras GS, Baldwin B, Brewster LJ, Kutcher GJ, Leibel S, et al. Clinically Relevant Optimization of 3-D Conformal Treatments. *Med Phys* (1992) 19(4):933–44. doi: 10.1118/1.596781
46. Semenenko VA, Li XA. Lyman-Kutcher-Burman NTCP Model Parameters for Radiation Pneumonitis and Xerostomia Based on Combined Analysis of Published Clinical Data. *Phys Med Biol* (2008) 53(3):737–55. doi: 10.1088/0031-9155/53/3/014
47. Seppenwoolde Y, Lebesque JV, de Jaeger K, Belderbos JS, Boersma LJ, Schilstra C, et al. Comparing Different NTCP Models That Predict the Incidence of Radiation Pneumonitis. Normal Tissue Complication Probability. *Int J Radiat Oncol Biol Phys* (2003) 55(3):724–35. doi: 10.1016/s0360-3016(02)03986-x
48. Deasy JO, Blanco AI, Clark VH. CERR: A Computational Environment for Radiotherapy Research. *Med Phys* (2003) 30(5):979–85. doi: 10.1118/1.1568978
49. Vanhavere F, Huyskens D, Struelens L. Peripheral Neutron and Gamma Doses in Radiotherapy With an 18 MV Linear Accelerator. *Radiat Prot Dosimetry*. (2004) 110(1-4):607–12. doi: 10.1093/rpd/nch135
50. Howell RM, Ferenci MS, Hertel NE, Fullerton GD. Investigation of Secondary Neutron Dose for 18 MV Dynamic MLC IMRT Delivery. *Med Phys* (2005) 32(3):786–93. doi: 10.1118/1.1861162
51. Howell RM, Kry SF, Burgett E, Hertel NE, Followill DS. Secondary Neutron Spectra From Modern Varian, Siemens, and Elekta Linacs With Multileaf Collimators. *Med Phys* (2009) 36(9):4027–38. doi: 10.1118/1.3159300
52. Drost L, Yee C, Lam H, Zhang L, Wronski M, McCann C, et al. A Systematic Review of Heart Dose in Breast Radiotherapy. *Clin. Breast Cancer*. (2018) 18(5):e819–24. doi: 10.1016/j.clbc.2018.05.010
53. Desai MY, Windecker S, Lancellotti P, Bax JJ, Griffin BP, Cahlon O, et al. Prevention, Diagnosis, and Management of Radiation-Associated Cardiac Disease. *J Am Coll Cardiol* (2019) 74(7):905–27. doi: 10.1016/j.jacc.2019.07.006
54. Zurl B, Stranzl H, Winkler P, Kapp KS. Quantification of Contralateral Breast Dose and Risk Estimate of Radiation-Induced Contralateral Breast Cancer Among Young Women Using Tangential Fields and Different Modes of Breathing. *Int J Radiat Oncol Biol Phys* (2013) 85(2):500–5. doi: 10.1016/j.ijrobp.2012.04.016
55. Salvatrini V, Iorio GC, Borghetti P, De Felice F, Greco C, Nardone V, et al. The Impact of Modern Radiotherapy on Long-Term Cardiac Sequelae in Breast Cancer Survivor: A Focus on Deep Inspiration Breath-Hold (DIBH) Technique. *J Cancer Res Clin Oncol* (2022) 148(2):409–17. doi: 10.1007/s00432-021-03875-1
56. Kuo CC, Chang CC, Cheng HW, Lin JC, Tsai JT. Impact of Respiratory Motion in Dosimetric and Clinical Advantages for Adjuvant Left-Sided Breast Radiotherapy. *J Radiat Res* (2021) 62(6):1105–13. doi: 10.1093/jrr/rwab087
57. Edvardsson A, Nilsson MP, Amptoulach S, Ceberg S. Comparison of Doses and NTCP to Risk Organs With Enhanced Inspiration Gating and Free Breathing for Left-Sided Breast Cancer Radiotherapy Using the AAA Algorithm. *Radiat Oncol* (2015) 10:84. doi: 10.1186/s13014-015-0375-y
58. Saini AS, Das JJ, Hwang CS, Biagioli MC, Lee WE. Biological Indices Evaluation of Various Treatment Techniques for Left-Sided Breast Treatment. *Pract Radiat Oncol* (2019) 9(6):e579–90. doi: 10.1016/j.prro.2019.06.020
59. Ashby O, Bridge P. Late Effects Arising From Volumetric Modulated Arc Therapy to the Breast: A Systematic Review. *Radiography* (2021) 27(2):650–3. doi: 10.1016/j.radi.2020.08.003
60. Vikström J, Hjelstuen MH, Wasbø E, Mjaaland I, Dybvik KI. A Comparison of Conventional and Dynamic Radiotherapy Planning Techniques for Early-Stage Breast Cancer Utilizing Deep Inspiration Breath-Hold. *Acta Oncol* (2018) 57(10):1325–30. doi: 10.1080/0284186X.2018.1497294
61. Tommasino F, Durante M, D'Avino V, Liuzzi R, Conson M, Farace P, et al. Model-Based Approach for Quantitative Estimates of Skin, Heart, and Lung Toxicity Risk for Left-Side Photon and Proton Irradiation After Breast-Conserving Surgery. *Acta Oncol* (2017) 56(5):730–6. doi: 10.1080/0284186X.2017.1299218
62. Taylor C, Correa C, Duane FK, Aznar MC, Anderson SJ, Bergh J, et al. Estimating the Risks of Breast Cancer Radiotherapy: Evidence From Modern Radiation Doses to the Lungs and Heart and From Previous Randomized Trials. *J Clin Oncol* (2017) 35(15):1641–9. doi: 10.1200/JCO.2016.72.0722
63. Xie Y, Bourgeois D, Guo B, Zhang R. Comparison of Conventional and Advanced Radiotherapy Techniques for Left-Sided Breast Cancer After Breast Conserving Surgery. *Med Dosim*. (2020) 45(4):e9–e16. doi: 10.1016/j.meddos.2020.05.004
64. Supakalin N, Pesee M, Thamronganantakul K, Promsensa K, Supaadirek C, Krusun S. Comparison of Different Radiotherapy Planning Techniques for Breast Cancer After Breast Conserving Surgery. *Asian Pac J Cancer Prev* (2018) 19(10):2929–34. doi: 10.22034/APJCP.2018.19.10.2929
65. Zhang Q, Liu J, Ao N, Yu H, Peng Y, Ou L, et al. Secondary Cancer Risk After Radiation Therapy for Breast Cancer With Different Radiotherapy Techniques. *Sci Rep* (2020) 10:1220. doi: 10.1038/s41598-020-58134-z
66. Sripathi LK, Ahlawat P, Simson DK, Khadanga CR, Kamarsu L, Surana SK, et al. Cardiac Dose Reduction With Deep-Inspiratory Breath Hold Technique of Radiotherapy for Left-Sided Breast Cancer. *J Med Phys* (2017) 42(3):123–7. doi: 10.4103/jmp.JMP_139_16
67. Han EY, Paudel N, Sung J, Yoon M, Chung WK, Kim DW. Estimation of the Risk of Secondary Malignancy Arising From Whole-Breast Irradiation: Comparison of Five Radiotherapy Modalities, Including TomoHDA. *Oncotarget* (2016) 7(16):22960–9. doi: 10.18632/oncotarget.8392
68. Williams TM, Moran JM, Hsu SH, Marsh R, Yanke B, Fraass BA, et al. Contralateral Breast Dose After Whole-Breast Irradiation: An Analysis by Treatment Technique. *Int J Radiat. Oncol Biol Phys* (2012) 82(5):2079–85. doi: 10.1016/j.ijrobp.2011.01.049
69. Vlachopoulou V, Malatara G, Delis H, Kardamakis D, Panayiotakis G. Estimation of the Risk of Secondary Cancer in the Thyroid Gland and the Breast Outside the Treated Volume in Patients Undergoing Brain, Mediastinum and Breast Radiotherapy. *Radiat Prot Dosimetry*. (2013) 154(1):121–6. doi: 10.1093/rpd/ncs134
70. Behmadi M, Gholamhosseinian H, Mohammadi M, Naseri S, Momennezhad M, Bayani Sh, et al. Evaluation of Breast Cancer Radiation Therapy Techniques in Outfield Organs of Rando Phantom With Thermoluminescence Dosimeter. *J Biomed Phys Eng* (2019) 9:179–188. doi: 10.31661/jbpe.v0i0.1067
71. Corradini S, Ballhausen H, Weingandt H, Freislederer P, Schönecker S, Niyazi M, et al. Left-Sided Breast Cancer and Risks of Secondary Lung Cancer and Ischemic Heart Disease : Effects of Modern Radiotherapy Techniques. *Strahlenther Onkol*. (2018) 194(3):196–205. doi: 10.1007/s00066-017-1213-y
72. Karpf D, Sakka M, Metzger M, Grabenbauer GG. Left Breast Irradiation With Tangential Intensity Modulated Radiotherapy (T-IMRT) Versus Tangential Volumetric Modulated Arc Therapy (T-VMAT): Trade-Offs Between

- Secondary Cancer Induction Risk and Optimal Target Coverage. *Radiat Oncol* (2019) 14:156. doi: 10.1186/s13014-019-1363-4
73. Hacıslamoglu E, Cinar Y, Gurcan F, Canyilmaz E, Gungor G, Yoney A. Secondary Cancer Risk After Whole-Breast Radiation Therapy: Field-in-Field Versus Intensity Modulated Radiation Therapy Versus Volumetric Modulated Arc Therapy. *Br J Radiol* (2019) 92:20190317. doi: 10.1259/bjr.20190317
 74. Hayden AJ, Rains M, Tiver K. Deep Inspiration Breath Hold Technique Reduces Heart Dose From Radiotherapy for Left-Sided Breast Cancer. *J Med Imaging Radiat Oncol* (2012) 56(4):464–72. doi: 10.1111/j.1754-9485.2012.02405.x
 75. Aly MM, Glatting G, Jahnke L, Wenz F, Abo-Madyan Y. Comparison of Breast Simultaneous Integrated Boost (SIB) Radiotherapy Techniques. *Radiat Oncol* (2015) 10:139. doi: 10.1186/s13014-015-0452-2
 76. Van Parijs H, Reynders T, Heuninckx K, Verellen D, Storme G, De Ridder M. Breast Conserving Treatment for Breast Cancer: Dosimetric Comparison of Sequential Versus Simultaneous Integrated Photon Boost. *BioMed Res Int* (2014) 827475:1–8. doi: 10.1155/2014/827475
 77. Novotná V, Širáč I, Pohanková D, Jandík P, Kašáková L, Grepl J, et al. Cardiac Doses of Accelerated Partial Breast Irradiation With Perioperative Multicatheter Interstitial Brachytherapy. *Strahlenther Onkol* (2021) 197:288–95. doi: 10.1007/s00066-020-01699-5
 78. Chatzikonstantinou G, Scherf C, Köhn J, Ackermann H, Ramm U, Tselis N. Matched-Pair Dosimetric Comparison of Cardiac Radiation Exposure Between Deep-Inspiration Breath-Hold Whole-Breast Radiation Therapy With Active Breathing Coordinator and Interstitial Multicatheter High-Dose-Rate Brachytherapy as Accelerated Partial Breast Irradiation in Adjuvant Treatment of Left-Sided Breast Cancer After Breast-Conserving Surgery. *Strahlenther Onkol* (2021) 197:308–16. doi: 10.1007/s00066-020-01702-z
 79. Fröhlich G, Mészáros N, Smánykó V, Polgár C, Major T. Biological Dose Summation of External Beam Radiotherapy for the Whole Breast and Image-Guided High-Dose-Rate Interstitial Brachytherapy Boost in Early-Stage Breast Cancer. *J Contemp. Brachyther* (2020) 12(5):462–9. doi: 10.5114/jcb.2020.100379
 80. Berrington de Gonzalez A, Curtis RE, Gilbert E, Berg CD, Smith SA, Stovall M, et al. Second Solid Cancers After Radiotherapy for Breast Cancer in SEER Cancer Registries. *Br J Cancer*. (2010) 102(1):220–6. doi: 10.1038/sj.bjc.6605435
 81. Xie L, Lin C, Zhang H, Bao X. Second Malignancy in Young Early-Stage Breast Cancer Patients With Modern Radiotherapy: A Long-Term Population-Based Study (A STROBE-Compliant Study). *Medicine* (2018) 97(17):e0593. doi: 10.1097/MD.00000000000010593
 82. Pignol JP, Hoekstra N, Wilke D, Dahn H, Nolan M, Vicini F. Estimation of Annual Secondary Lung Cancer Deaths Using Various Adjuvant Breast Radiotherapy Techniques for Early-Stage Cancers. *Front Oncol* (2021) 11:713328. doi: 10.3389/fonc.2021.713328

Conflict of Interest: Author BT was employed by Siemens Healthcare GmbH.

The remaining authors declare that the research was conducted in the absence of any commercial or financial relationships that could be construed as a potential conflict of interest.

Publisher's Note: All claims expressed in this article are solely those of the authors and do not necessarily represent those of their affiliated organisations, or those of the publisher, the editors and the reviewers. Any product that may be evaluated in this article, or claim that may be made by its manufacturer, is not guaranteed or endorsed by the publisher.

Copyright © 2022 Vogel, Gade, Timm, Schürmann, Auerbach, Nüsken, Rübe, Melchior and Dzierma. This is an open-access article distributed under the terms of the Creative Commons Attribution License (CC BY). The use, distribution or reproduction in other forums is permitted, provided the original author(s) and the copyright owner(s) are credited and that the original publication in this journal is cited, in accordance with accepted academic practice. No use, distribution or reproduction is permitted which does not comply with these terms.



OPEN ACCESS

EDITED BY

Thomas FitzGerald,
University of Massachusetts Boston,
United States

REVIEWED BY

A Nasser Khalifeh,
University of Massachusetts Medical
School, United States
Fenghong Liu,
UMass Memorial Medical Center,
United States

*CORRESPONDENCE

Linda Eliasson
lindaeli@kth.se

SPECIALTY SECTION

This article was submitted to
Radiation Oncology,
a section of the journal
Frontiers in Oncology

RECEIVED 23 February 2022

ACCEPTED 05 July 2022

PUBLISHED 02 August 2022

CITATION

Eliasson L, Lillhök J, Bäck T, Billnert-
Maróti R, Dasu A and Liszka M (2022)
Range-shifter effects on the stray field
in proton therapy measured with the
variance-covariance method.
Front. Oncol. 12:882230.
doi: 10.3389/fonc.2022.882230

COPYRIGHT

© 2022 Eliasson, Lillhök, Bäck, Billnert-
Maróti, Dasu and Liszka. This is an
open-access article distributed under
the terms of the [Creative Commons
Attribution License \(CC BY\)](#). The use,
distribution or reproduction in other
forums is permitted, provided the
original author(s) and the copyright
owner(s) are credited and that the
original publication in this journal is
cited, in accordance with accepted
academic practice. No use,
distribution or reproduction is
permitted which does not comply with
these terms.

Range-shifter effects on the stray field in proton therapy measured with the variance-covariance method

Linda Eliasson^{1*}, Jan Lillhök², Torbjörn Bäck¹,
Robert Billnert-Maróti², Alexandru Dasu³
and Malgorzata Liszka⁴

¹Department of Physics, KTH, Stockholm, Sweden, ²The Swedish Radiation Safety Authority, Solna, Sweden, ³Medical Radiation Sciences, Department of Immunology, Genetics and Pathology, Uppsala University, Uppsala, Sweden, ⁴The Skandion Clinic, Uppsala, Sweden

Measurements in the stray radiation field from a proton therapy pencil beam at energies 70 and 146 MeV were performed using microdosimetric tissue-equivalent proportional counters (TEPCs). The detector volumes were filled with a propane-based tissue-equivalent gas at low pressure simulating a mean chord length of 2 μm in tissue. Investigations were performed with and without a beam range shifter, and with different air gaps between the range shifter and a solid water phantom. The absorbed dose, the dose-mean lineal energy, and the dose equivalent were determined for different detector positions using the variance-covariance method. The influence from beam energy, detector- and range-shifter positions on absorbed dose, LET, and dose equivalent were investigated. Monte Carlo simulations of the fluence, detector response, and absorbed dose contribution from different particles were performed with MCNP 6.2. The simulated dose response for protons, neutrons, and photons were compared with, and showed good agreement with, previously published experimental data. The simulations also showed that the TEPC absorbed dose agrees well with the ambient absorbed dose for neutron energies above 20 MeV. The results illustrate that changes in both dose and LET variations in the stray radiation field can be identified from TEPC measurements using the variance-covariance method. The results are in line with the changes seen in the simulated relative dose contributions from different particles associated with different proton energies and range-shifter settings. It is shown that the proton contribution scattered directly from the range shifter dominates in some situations, and although the LET of the radiation is decreased, the ambient dose equivalent is increased up to a factor of 3.

KEYWORDS

LET, TEPC, variance-covariance method, dose-mean lineal energy, out-of-field dose, dose equivalent, proton therapy, pencil beam

1 Introduction

Compared to conventional photon therapy, proton therapy has the potential of reducing exposure and radiation risks outside the target volume (1). Nevertheless, there is still a concern that stray radiation can increase secondary cancer risks. In an ongoing task within EURADOS working group 9, the relation between the most critical treatment parameters and the out-of-field neutron doses is therefore investigated. The outcome will hopefully be a first step toward a tool for medical physicists to estimate the neutron doses directly from the treatment parameters. Simulations and results from experimental campaigns are further described in Van Hoey et al. (2).

In the EURADOS WG9 campaign, the quantity used for comparison was the neutron ambient dose equivalent, $H_n^*(10)$ (3). During the measurement campaign at the Skandion Clinic in 2019, the Swedish Radiation Safety Authority contributed with three instruments, a Berthold LB6411 neutron monitor and two tissue-equivalent proportional counters (TEPCs), further called the Sievert detectors. TEPCs can detect and separate both high- and low-LET components, which makes them suitable for mixed radiation fields.

With varying different treatment settings in the experiment described by Van Hoey et al. (2), $H_n^*(10)$ was measured with different detectors in various positions around a solid water phantom. In one position, a significant increase in absorbed dose was measured with the Sievert detector when the range shifter was inserted. This increase was not supported by simulations or measurements performed by neutron monitors in the vicinity of the same position. A hypothesis was that scattered protons from the range shifter contributed to the absorbed dose in positions that were less shielded by the phantom.

Prior to the campaign described by Van Hoey et al. (2), several measurements as well as simulation comparisons of out-of-field doses have been conducted. It is, e.g., well known that the stray neutron fields are characterised by a thermal and high-energy component (4, 5). Range shifters and their effect on the stray neutron field have also been studied, and alternative methods to scan shallow tumours have been reported to decrease the high-LET contribution to the dose (6). However, proton scattering from the range shifter is rarely considered.

The ambient dose equivalent, $H^*(10)$, is defined in terms of the dose equivalent $H = D \cdot Q(L)$ at 10-mm depth in the ICRU sphere in an expanded and aligned radiation field (7, 8). Here D is the absorbed dose in tissue and $Q(L)$ is a quality factor that depends on the unrestricted linear energy transfer (LET) of charged particles in water. The linear energy transfer can be estimated by the lineal energy, y , measured with TEPCs simulating a tissue volume in the micrometre range (9). The distribution of y -values hence corresponds to the LET distribution of the radiation field. A change in this

distribution, or, e.g., the dose-mean lineal energy \bar{y}_D , reflects a change in the LET of the radiation field.

In addition to microdosimetric single-event measurements, the variance-covariance method (10) has been used for radiation protection applications in mixed fields. Lillhök et al. measured differences in the stray radiation fields between photon and proton therapy (11). Several cosmic radiation measurements have been performed, where the variance and variance-covariance methods have been compared with other methods (12, 13) and with several instruments (14). The method has also successfully been used in mixed workplace fields with photons and neutrons and strongly pulsed stray radiation fields from accelerators (15, 16). Single-event measurements are limited in high-intensity fields due to pile-up which can be the case, e.g., in a therapeutic beam. As described in Lillhök et al. (13), TEPCs used for both single- and multi-event measurements showed good agreement in the mixed field onboard an aircraft and showed that it can be used as a complementary method in mixed fields.

In the investigation presented in this article, measurements complementary to the EURADOS 2019 campaign (2) were performed at the Skandion Clinic, aiming to study the dose contribution and LET of the stray radiation component from the range shifter using two Sievert detectors, which as previously described are multi-event TEPCs. The absorbed dose and dose-mean lineal energy were measured using the variance-covariance method. A phantom was placed in the same position as in the 2019 campaign and irradiated with two different proton beam energies for a variety of different range-shifter settings. Measurements were also performed without a phantom to quantify the range-shifter component directly. The detector absorbed dose responses for neutrons, protons, photons, and electrons were simulated using MCNP 6.2. These response functions were used together with simulated fluence distributions at the detector positions to evaluate the relative absorbed dose contributions from different radiation field components.

2 Method

2.1 Experimental method and equipment

The Sievert detectors are made of A-150 plastic, contained in a 2-mm-thick aluminum container and filled with propane-based tissue-equivalent gas (17) to a pressure of 1.37 kPa, corresponding to a simulated tissue volume with a mean chord length of 1.88 μm . The instruments are cylindrical with diameters and heights equal to 11.54 cm and with an A150-plastic wall of thickness 5 mm. The electric charge generated in each detector is measured using a 1-nF feedback capacitor, where the voltage over the capacitor is measured 10 times per second with a 24-bit analogue-to-digital converter (ADS

1210U). One bit is used for polarity and the other 23 bits for dividing the maximum capacitor voltage of 5 V into steps of 0.6 μ V. The electronic noise is dominated by the 0.6- μ V (rms) contribution from the analogue-to-digital-converter (18). The absorbed dose to the detector gas during the integrated time is determined by

$$D_{det} = \frac{qW}{Mm_{det}}, \quad (1)$$

where q is the electric charge collected during the integration time, W is the mean energy expended to create an ion pair (in energy per charge), M is the gas multiplication factor, and m_{det} is the detector gas mass. The dose-mean lineal energy is calculated using the variance-covariance method,

$$\bar{y}_D = \frac{m_{det}(V_{rel} - C_{rel})}{\bar{l}_\mu} \bar{D}_{det}, \quad (2)$$

where V_{rel} is the relative variance in the absorbed dose during the repeated charge, C_{rel} is the relative covariance between two detectors experiencing the same field, \bar{l}_μ is the mean chord length for the simulated tissue, and \bar{D}_{det} is the average dose over repeated integration times (10). In a time-varying radiation field, a covariance correction is usually determined using a second detector. However, in some situations the radiation field variations at the two detector positions are not necessarily synchronised in time. In such cases, a covariance correction can be obtained from the consecutive charge integrations. This method is further described in Eliasson et al. (article in progress) and was used in the measurements presented here.

In a mixed field, where several components contribute, the measured total \bar{y}_D value is given by a combination of the relative dose contributions and their dose-mean lineal energies. As an example, the case with three components can be written as

$$\bar{y}_D = d_\gamma \bar{y}_{D,\gamma} + d_n \bar{y}_{D,n} + d_p \bar{y}_{D,p}, \quad (3)$$

where d_i is the relative dose contribution for photons, neutrons, and protons, respectively. From the equation, it is clear that a change in any of the component contributions will be reflected as a change in the measured \bar{y}_D value. As previously mentioned, the dose-mean lineal energies for the radiation components are energy dependent and can be estimated by using their simulated fluence distributions for the stray field and a known response function determined in monoenergetic beams (18, 19). The simulated response function and comparisons with measurements are described in the following sections. While the $\bar{y}_{D,\gamma}$ value depends strongly on the neutron energy, it is in stray fields from proton therapy dominated by high-energy neutrons, giving a $\bar{y}_{D,n}$ value typically around 100 keV/ μ m (1, 2), while the $\bar{y}_{D,\gamma}$ value is typically around 1.5 keV/ μ m (2, 11). For the proton component, the $\bar{y}_{D,p}$ value for a 1- μ m-diameter spherical object in water is approximately in the range 2–6 keV/ μ m for proton energies between 10 and 100 MeV but increases

with decreasing energies. At 1 MeV, the $\bar{y}_{D,p}$ value is approximately 40 keV/ μ m (20). Moreover, Kyllönen et al. measured dose-mean lineal energies in proton beams between 68 and 174 MeV with the Sievert detectors and reported \bar{y}_D values between 6.2 and 7.3 keV/ μ m (21).

Just as for the resulting \bar{y}_D value, the W value depends on the radiation components. However, the W values of photons, neutrons, and protons [26.8, 31, and 28.2 eV (22)] do not differ as dramatically from each other as the dose-mean lineal energies. Previous simulations of the stray field from a proton beam reported that the relative dose distribution from neutrons varied from approximately 54% to 95%, giving a W value that varied between 28.9 and 30.7 eV (11). The addition of a proton component does not change the mean value significantly, so the same mean value as reported by Lillhök et al. (11) was used for all irradiations in this article as well, and the variations were handled in the uncertainty estimation.

The $H^*(10)$ values were estimated from a measured dose equivalent, H^* , using a first-order approximation for the quality factor,

$$H^* = DQ_D = D(a + b\bar{y}_D), \quad (4)$$

where $a = 0.73$ and $b = 0.17 \mu\text{m/keV}$. (19). For this article, only total H^* values were determined, but it is possible to estimate the H^* values for the high- and low-LET components by using the relative dose contribution for each radiation component and the respective \bar{y}_D value in Equation 3.

No calibration factors relating the detector readings to D^* (10) or $H^*(10)$ directly are used. The absorbed dose (Equation 1) and dose-mean lineal energy (Equation 2) in the tissue-equivalent detector material are derived from traceable measures of air pressure and electric charge, where the physical detector volume with uncertainties is assumed to be representative of the true charge collecting volume. For the dose-equivalent measurements based on Equation 4, the constants a and b have been optimised for a neutron beam with a broad energy spectrum (19).

2.2 Experimental setup

The experiment was conducted at the Skandion clinic, which has been in operation since 2015 and is the first centre for proton beam therapy in the Nordic countries and the only centre situated in Sweden. By optimising the dose delivery to the target volume, the clinic can treat patients with tumours close to vital organs, reducing both the risk for secondary cancer and long-term side effects¹.

The proton beam at the facility is an IBA pencil beam and delivers protons with energies between 60 and 226 MeV (23–25).

¹ <https://skandionkliniken.se/en/>

A schematic illustration to scale and a photo of the setup are seen in Figures 1, 2. To better investigate the differences between range-shifter settings, only single-spot measurements were conducted, using a pristine beam. The detector positions A1 and C1 were similar to positions A and C in the 2019 campaign (2), while A3 and C3 were 10 cm further down the beam line. During the measurements, two detectors were used, where one detector was placed in any of the positions on the A side (A1 or A3) and the other was placed in the corresponding position on the C side (C1 or C3). The proton current was set to the same value, 0.6 nA, for all irradiations. A solid water (polystyrene) phantom of density 1.03 g/cm^3 , height and width equal to 30 cm, and length 60 cm was placed with its centre shifted 15 cm from the beam line. The range shifter is made of Lexan (polycarbonate) with a thickness of 3.11 cm and density of 1.20 g/cm^3 . Measurements were performed without the range shifter and with the range shifter at different air gaps (AG) from the phantom wall. For irradiations performed without the phantom, a proton beam dump was positioned at the far wall. The beam dump is made of PMMA with density 1.18 g/cm^3 , height 32 cm, thickness 6.5 cm, and length 40 cm. A total of 32 irradiations were performed with two different detector positions, two different proton beam energies, and a number of different range-shifter settings.

2.3 Simulations

The absorbed dose response of the detector and the particle fluence distributions in the different measurement positions were simulated with MCNP version 6.2 (26) in order to support and extend the analysis of the measurement results.

The response function for protons, neutrons, photons, and electrons were combined with the respective fluence distributions to calculate the relative absorbed dose contribution from each particle type.

2.3.1 Absorbed dose response of the Sievert detector

The absorbed dose response was simulated using a detector model in vacuum as shown in Figure 3, exposed to a parallel beam of monoenergetic particles with a beam diameter of 40 cm. The detector was filled with propane-based tissue-equivalent gas to a density of $26.12 \text{ } \mu\text{g/cm}^3$, corresponding to a mean chord length of $2 \text{ } \mu\text{m}$ tissue. The detector geometry was modelled as described in Section 2.1.

Simulations were carried out for 10^{-10} – 10^4 -MeV neutrons, 1 – 10^4 -MeV protons, 10^{-2} – 10^4 -MeV photons, and 10^{-2} – 10^4 -MeV electrons, using LA150 data libraries. Primary and secondary particles (photons, electrons, neutrons, protons, alpha-particles, deuterium, tritium ^3He , and heavy ions) were transported in all volumes. The absorbed dose in the cylindrical detector gas volume was scored using the +F6 tally for total heating. The +F6 tally scores energy depositions from all particles and not only a specific particle type. A linear energy binning was used for all particles with 10 bins per decade for neutrons and 20 bins per decade for protons, photons, and electrons. The total heating, i.e., absorbed dose, was normalised to the particle fluence.

2.3.2 Fluence distribution at the measurement positions

The fluence simulations were performed for a simple geometry only including a range shifter, a phantom, and a beam dump. The range shifter was modelled with dimensions $3.11 \text{ cm} \times$

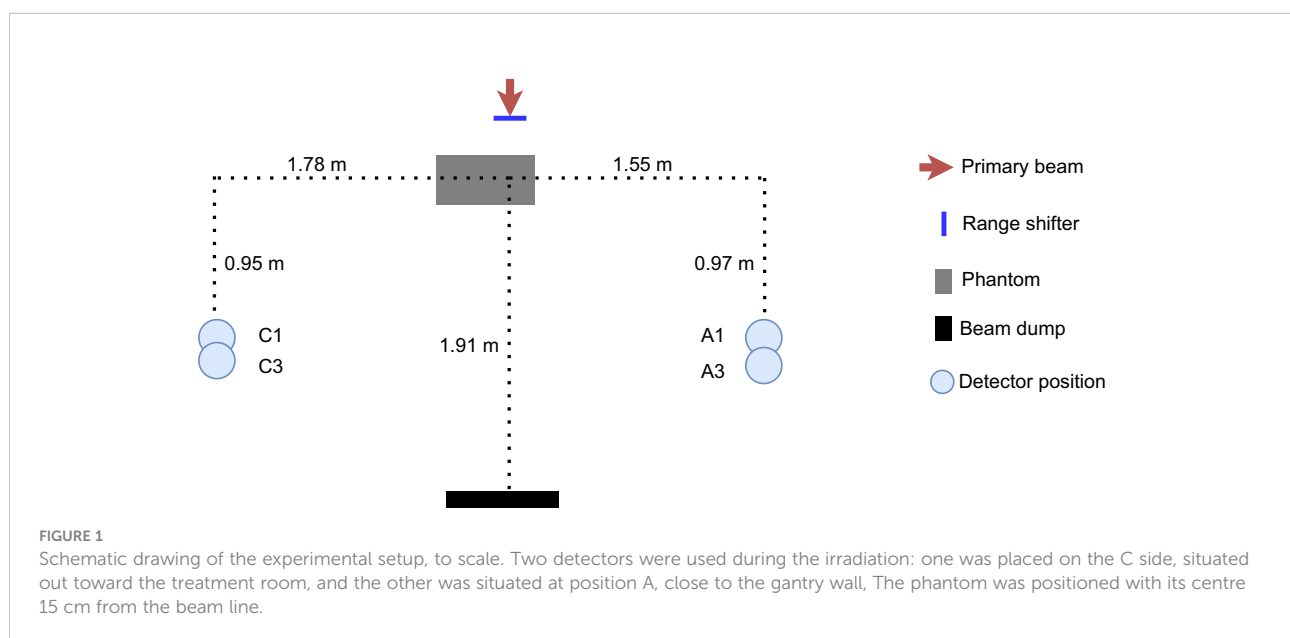




FIGURE 2

The experimental setup, with the two TEPCs in positions A and C. The C position is situated close to the gantry wall, while the A position in the foreground is facing the open treatment room.

15 cm × 15 cm, and the solid water phantom with dimensions as described in Section 2.2. Monoenergetic protons of energies 70 and 146 MeV in a circular and parallel beam of diameter 1 cm was transported through air to the range shifter positioned with different air gaps to the phantom. In order to quantify the effect of the range shifter, simulations were also performed with only the range shifter and no phantom, as well as only phantom with no range shifter. To further test the robustness of the relatively simple geometry, additional simulations were performed using a more comprehensive model with walls, floors, and the surrounding gantry structure (27).

The fluence distributions of neutrons, protons, photons, and electrons were first scored with tally F4 in spherical air volumes located in the same positions as the detectors in the measurements. Standard MCNP libraries were used, and photons, electrons, neutrons, protons, and alpha-particles were

transported in all volumes. A linear energy binning was used for all particles with 10 bins per decade for neutrons and 20 bins per decade for protons, photons, and electrons. The fluence was normalised to the number of initial protons.

2.3.3 The simulated absorbed dose

The fluence distributions and the detector response functions described above were used to estimate the relative dose contribution from neutrons, protons, photons, and electrons. The absorbed dose in the detector for particle type i is given by

$$D_{i,TEPC} = \sum_k d_{i,TEPC}(E_k) \Phi_i(E_k) \Delta E_k, \quad (5)$$

where $d_{i,TEPC}$ is the absorbed dose response per fluence of particle type i with energy E_k per energy bin, $\Phi(E_k)$ is the fluence

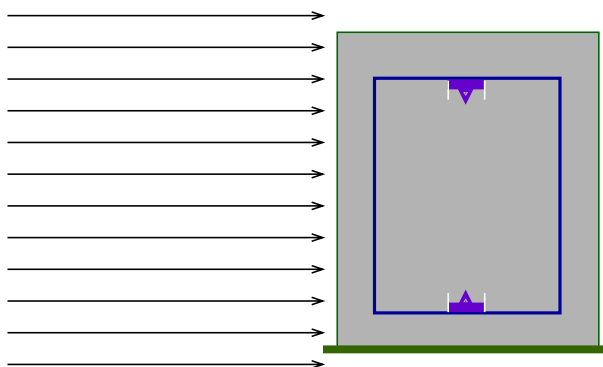


FIGURE 3

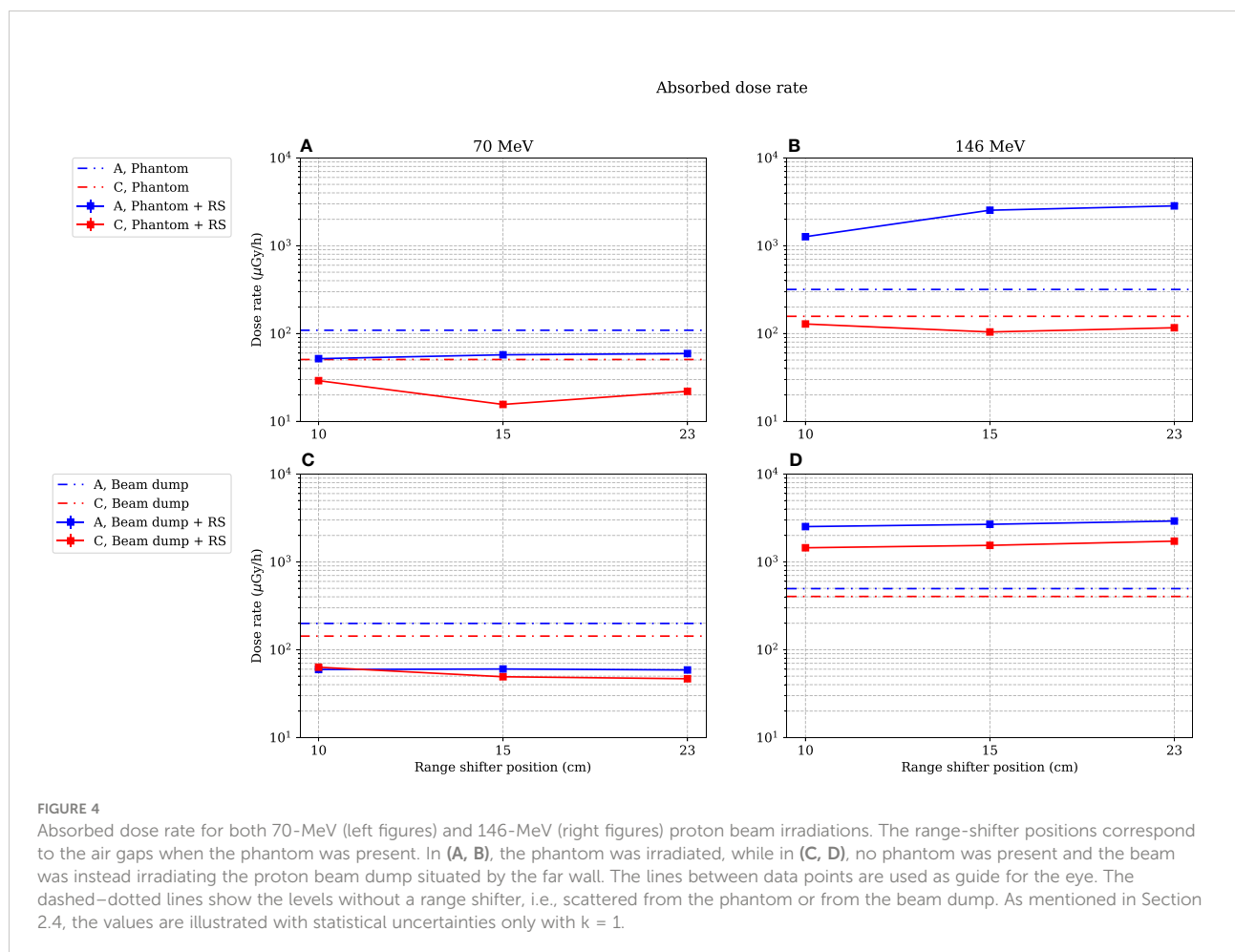
An illustration of the simulation geometry for the detector dose response simulations in MCNP 6.2. The cylindrical detector is confined in an aluminium container and exposed to monoenergetic beams.

of particle type i with energy E_k per energy bin, and ΔE_k is the bin width with the average energy E_k in the fluence distribution. D_{bTEPC} is therefore summed over all energy bins and gives the total absorbed dose for one particle type i .

2.4 Uncertainties

The statistical uncertainties were estimated for the absorbed dose rate and for the dose equivalent using conventional error propagation. For the dose-mean lineal energy, the statistical uncertainty was obtained by splitting each data set into smaller subsets and calculating the standard deviation of the mean. In the results presented in Figures 4, 5 and 9, 10, and both tables below, only the statistical uncertainties are included, with coverage factor $k = 1$. The coverage factor was chosen to harmonise with the uncertainties presented in Van Hoey et al. (2). In addition, uncertainties of the gas pressure, detector volume and diameter, electric charge, W-value, gas multiplication, $H^*(10)$ response, and accelerator reference data need to be accounted for. The gas pressure has an uncertainty of

0.17%, estimated from calibrations of the pressure gauge at the Swedish National Metrology Laboratory for Pressure and Vacuum (RISE). The uncertainty in the generated electric charge is estimated to be 0.5% from cross-calibrations with a reference electrometer at the Swedish National Metrology Laboratory for Ionising Radiation. The uncertainties in the detector diameter and height are estimated to be 0.25% and 1.5%, respectively. Uncertainties in the effective charge collecting volume of the detector have not been taken into account, and the uncertainty in the volume was calculated directly from the dimensions. For the W value, the uncertainty was estimated to be 4%, which is the reported uncertainty for W_p (22). The other W values (W_n and W_j) are reported with smaller uncertainties (22). The gas multiplication uncertainty (0.8%) was estimated from measurements in a calibrated ^{137}Cs field prior to and after the Skandion measurements. These above uncertainties give approximately 4% uncertainty contribution to add to the absorbed doses, the dose-mean lineal energies, and the dose equivalents. Since the Sievert instrument measures the absolute dose and variance between a series of 0.1-s charge collections, it is important that the proton current for each energy setting is



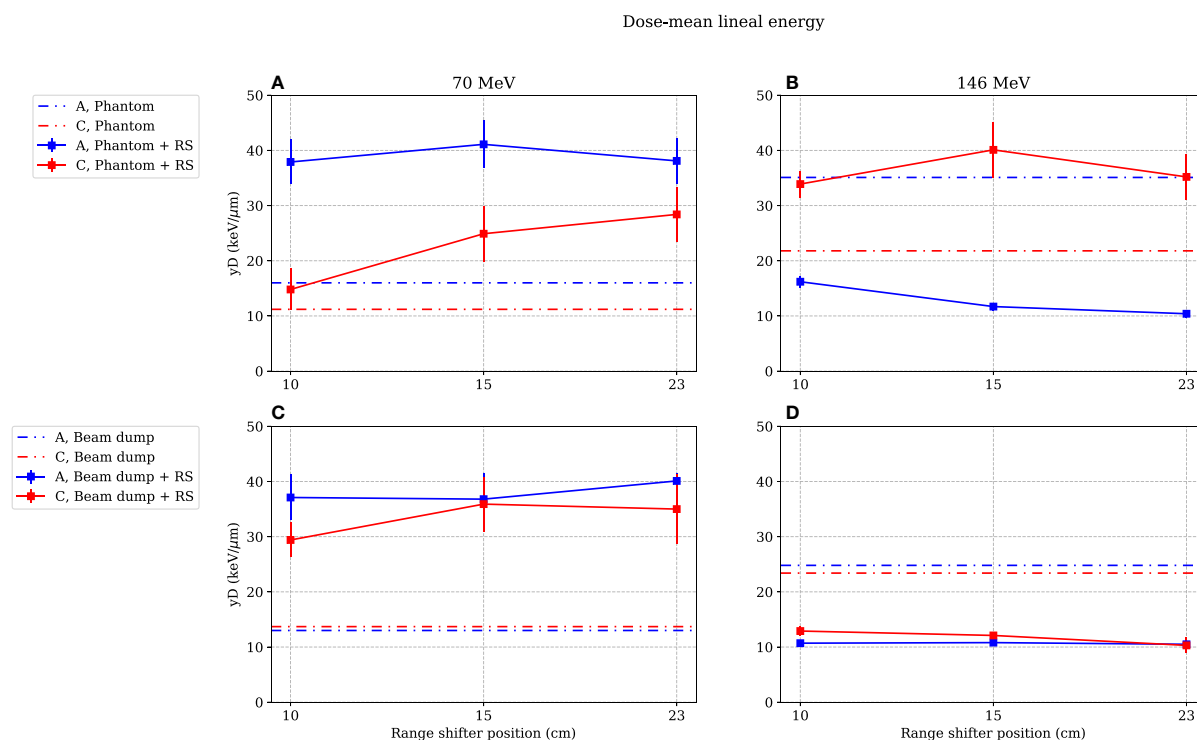


FIGURE 5

Dose-mean lineal energies as functions of range-shifter positions when irradiating the phantom (A, B) and the proton beam dump (C, D). The range-shifter positions correspond to the air gaps when the phantom was present. Irradiating with 70-MeV protons, the range shifter leads to a higher \bar{y}_D value at both positions A and C, while with 146 MeV, the \bar{y}_D value measured at position A is lower and decreases with increased range-shifter position with the presence of a phantom (B). When irradiating the beam dump with 146-MeV protons, the \bar{y}_D values decrease both at position A and position C (D). The lines between data points are used as guide for the eye. The dashed–dotted lines show the levels without range shifter, i.e., scattered from the phantom or from the beam dump. As mentioned in Section 3.4, the values are illustrated with statistical uncertainties only with $k = 1$.

stable, while the absolute value of the proton current is less relevant. The dosimetry uncertainty budget from the Skandion Clinic ensures that the relative dose variation is within 2% (11). This was confirmed by the clinic's monitoring ionisation chambers.

The uncertainty in the $H^*(10)$ response of the detectors has not been included. This contribution varies with the relative contributions of the radiation components and has been reported to be about 15%–25% in typical mixed field applications (18).

The simulations are reported with statistical uncertainties with the coverage factor $k = 1$. Uncertainty contributions from, e.g., interaction cross sections and deviations between the simulated and real geometry, have not been taken into account.

3 Results

The differences in measured absorbed doses and dose-mean lineal energies between positions 1 and 3 were small, so only the

results from positions A1 and C1 are reported here. The positions are onward referred to as position A and position C. The absorbed dose, D , the dose-mean lineal energy, \bar{y}_D , and the dose equivalent, H^* , as functions of different range-shifter positions are presented for 70- and 146-MeV primary proton beams. The range-shifter settings 10, 15, and 23 cm correspond to air gaps of 10, 15, and 23 cm when the phantom is present and are in the figures referred to as AG. The experimental results are also presented in Tables 1, 2.

3.1 Measured absorbed dose as function of range-shifter position

Figure 4 shows the absorbed dose rate in positions A and C as a function of range-shifter position, both when irradiating a phantom (Figures 4A, B) and when irradiating the proton beam dump by the far wall (Figures 4C, D). The dotted lines indicate the absorbed dose rate without a range shifter.

TABLE 1 Measured absorbed dose rates and \bar{y}_D values for different irradiation settings.

Proton energy (MeV)	Irradiated target	AG (cm)	Position	Dose rate ($\mu\text{Gy/h}$)	\bar{y}_D ($\mu\text{Gy/h}$)
70	Phantom	NoRS	A	109.1 \pm 0.2	16.0 \pm 2.3
70	Phantom	10	A	51.8 \pm 0.2	37.9 \pm 4.0
70	Phantom	15	A	57.3 \pm 0.2	41.1 \pm 4.3
70	Phantom	23	A	59.1 \pm 0.2	38.1 \pm 4.1
70	Beam dump	NoRS	A	199.1 \pm 0.3	13.0 \pm 1.0
70	Beam dump	10	A	59.5 \pm 0.2	37.1 \pm 4.1
70	Beam dump	15	A	60.3 \pm 0.2	36.8 \pm 4.8
70	Beam dump	23	A	58.8 \pm 0.2	40.1 \pm 1.4
70	Phantom	NoRS	C	50.7 \pm 0.9	11.2 \pm 2.2
70	Phantom	10	C	29.1 \pm 0.8	14.8 \pm 3.8
70	Phantom	15	C	15.6 \pm 0.7	24.9 \pm 5.0
70	Phantom	23	C	22.0 \pm 0.7	28.4 \pm 4.9
70	Beam dump	NoRS	C	142.9 \pm 1.6	13.7 \pm 1.0
70	Beam dump	10	C	63.2 \pm 0.2	29.4 \pm 3.1
70	Beam dump	15	C	49.2 \pm 0.2	35.9 \pm 4.9
70	Beam dump	23	C	46.7 \pm 0.2	35.0 \pm 6.3
146	Phantom	NoRS	A	318.2 \pm 0.5	35.1 \pm 2.7
146	Phantom	10	A	1268 \pm 2.0	16.2 \pm 1.0
146	Phantom	15	A	2539 \pm 4.0	11.7 \pm 0.7
146	Phantom	23	A	2844 \pm 4.0	10.4 \pm 0.7
146	Beam dump	NoRS	A	496.0 \pm 0.7	24.8 \pm 1.5
146	Beam dump	10	A	2524.0 \pm 3.7	10.7 \pm 0.6
146	Beam dump	15	A	2678.3 \pm 3.9	10.8 \pm 0.6
146	Beam dump	23	A	2920.8 \pm 4.3	10.5 \pm 0.5
146	Phantom	NoRS	C	157.2 \pm 1.8	21.8 \pm 2.9
146	Phantom	10	C	128.6 \pm 1.5	33.9 \pm 2.4
146	Phantom	15	C	104.3 \pm 1.3	40.1 \pm 5.0
143	Phantom	23	C	116.5 \pm 1.4	35.2 \pm 4.1
146	Beam dump	NoRS	C	404.1 \pm 4.3	23.4 \pm 1.6
146	Beam dump	10	C	1448 \pm 15	12.9 \pm 0.9
146	Beam dump	15	C	1543 \pm 16	12.1 \pm 0.6
146	Beam dump	23	C	1723 \pm 18	10.3 \pm 0.8

Either the phantom or a proton beam dump was irradiated, and irradiations were made either with a range shifter at a certain range-shifter position (AG) or without the range shifter (NoRS). The values are given with two significant figures, and as mentioned in Section 2.4, the values are illustrated with statistical uncertainties only with $k = 1$. Effects from, e.g., uncertainties in gas pressure, detector dimensions, and the W value, give an additional contribution of 4%.

In the stray radiation field from the 70-MeV proton beam (Figures 4A, C), the absorbed dose decreased when applying a range shifter in both positions A and C, both with and without the presence of the phantom.

It is apparent that when the phantom was irradiated with a 146-MeV proton field (Figure 4B), the absorbed dose rate was dramatically increased in the A position when the range shifter was applied. The absorbed dose rate increased with the air gap. It is also notable that the dose rate when irradiated with a 146-MeV proton beam seemed to be independent of the presence of a phantom (Figure 4B vs. 4D) at 15- and 23-cm range-shifter positions, which is an indication that the majority of the dose contribution came from the range shifter. In the C position, which was shadowed by the phantom when it was present, the

dose rate decreased when the range shifter was applied. When irradiating without a range shifter and phantom, directly on the proton beam dump, it is noteworthy that the scattering from the range shifter was still higher than scattering from the beam dump.

3.2 Measured dose-mean lineal energy as a function of the range-shifter position

The covariance corrections in all measurements were small, confirming the stability of both the beam and the measurement system. This stability makes comparisons between \bar{y}_D values at the different range-shifter positions more reliable.

TABLE 2 Estimated H^* values for different irradiation settings.

Proton energy (MeV)	Irradiated target	AG (cm)	Position	H^* ($\mu\text{Sv/h}$)
70	Phantom	NoRS	A	377 ± 43
70	Phantom	10	A	372 ± 36
70	Phantom	15	A	442 ± 42
70	Phantom	23	A	426 ± 41
70	Beam dump	NoRS	A	586 ± 33
70	Beam dump	10	A	418 ± 42
70	Beam dump	15	A	421 ± 50
70	Beam dump	23	A	452 ± 44
146	Phantom	NoRS	A	2130 ± 140
146	Phantom	10	A	4420 ± 210
146	Phantom	15	A	6880 ± 310
146	Phantom	23	A	7120 ± 320
146	Beam dump	NoRS	A	2550 ± 130
146	Beam dump	10	A	6430 ± 240
146	Beam dump	15	A	6870 ± 270
146	Beam dump	23	A	7350 ± 250

Either the phantom or a proton beam dump was irradiated, and irradiations were made either with a range shifter at a certain range-shifter position (AG), or without the range shifter (NoRS). The values are given with two significant figures and as mentioned in Section 2.4, the values are illustrated with statistical uncertainties only with $k = 1$. Effects from, e.g., uncertainties in gas pressure, detector dimensions, and the W value give an additional contribution of 4%.

Figure 5 illustrates the \bar{y}_D values for different range-shifter settings, when both the phantom (Figures 5A, B) and the proton beam dump (Figures 5C, D) were irradiated. When the phantom was irradiated with 70-MeV protons, the \bar{y}_D values increased in both positions when a range shifter was inserted. In the A position, the \bar{y}_D value seemed to be independent of the range-shifter position, while there was an increasing trend in the C position. The increasing \bar{y}_D value indicates an increasing dose contribution from a high-LET component.

The most prominent results are seen in the right figures. When irradiating the phantom with a 146-MeV proton beam (Figure 5B), the \bar{y}_D value measured in the A position decreased from approximately 35 to 15 keV/ μm when applying the range shifter at a 10-cm air gap and then continued to decrease slightly with the increased air gap. The C side, being more shielded by the phantom, experienced the opposite—the \bar{y}_D value increased, but there was no significant air gap dependence. Compared to the 70-MeV proton irradiation (Figure 5A), the \bar{y}_D value at the C position increased, which can be explained by production of neutrons that were more highly energetic when irradiating with a 146-MeV proton beam than with a 70-MeV proton beam.

Figure 5D shows that when there was no phantom present, the \bar{y}_D value in both positions decreased, indicating a larger contribution of a low-LET component from the range shifter when irradiating with a 146-MeV proton beam.

3.3 Simulated relative dose distributions

The simulated detector absorbed dose responses for neutrons, protons, photons, and electrons are presented in

Figure 6. Included are also measured values, using the same detectors, for neutrons, photons, and protons from Lillhök (18), Kyllönen et al. (19, 21), and Kyllönen and Mayer (28), as well as conversion coefficients to ambient absorbed doses from Ferrari and Pelliccioni (29) and Leuthold et al. (30). The conversion coefficients from Ferrari and Pelliccioni were calculated as the ratio of the reported H^* conversion coefficient and the effective quality factor at 10-mm depth in the ICRU sphere. A good agreement is seen between the simulated absorbed dose response and previously published experimental values for proton, neutrons, and photons. It can also be noted that the simulated detector absorbed dose and the ambient absorbed dose agree well for high neutron energies above 20 MeV where no experimental data were available. The energy-weighted fluence distributions at position A when the phantom is irradiated with a 146-MeV proton beam and the range shifter is applied at a 23-cm air gap are illustrated in Figure 7. The dose energy distribution for the same irradiation settings and position in Figure 8 shows that the dose deposited in the detector is mainly from > 10-MeV protons.

In Figure 9, the simulated relative dose distributions from photons, neutrons, and protons are shown for the A position. When irradiating with a 70-MeV proton beam and using a range shifter, the majority of the dose is due to neutrons, as indicated by the increase in \bar{y}_D value seen in Figure 5A. During 146-MeV proton beam irradiations, the neutron contribution in position A decreases with increasing range-shifter position while the proton contribution increases sharply. At 15 and 23 cm, the relative contributions from the radiation components does not change significantly. We note here that also the \bar{y}_D value was relatively

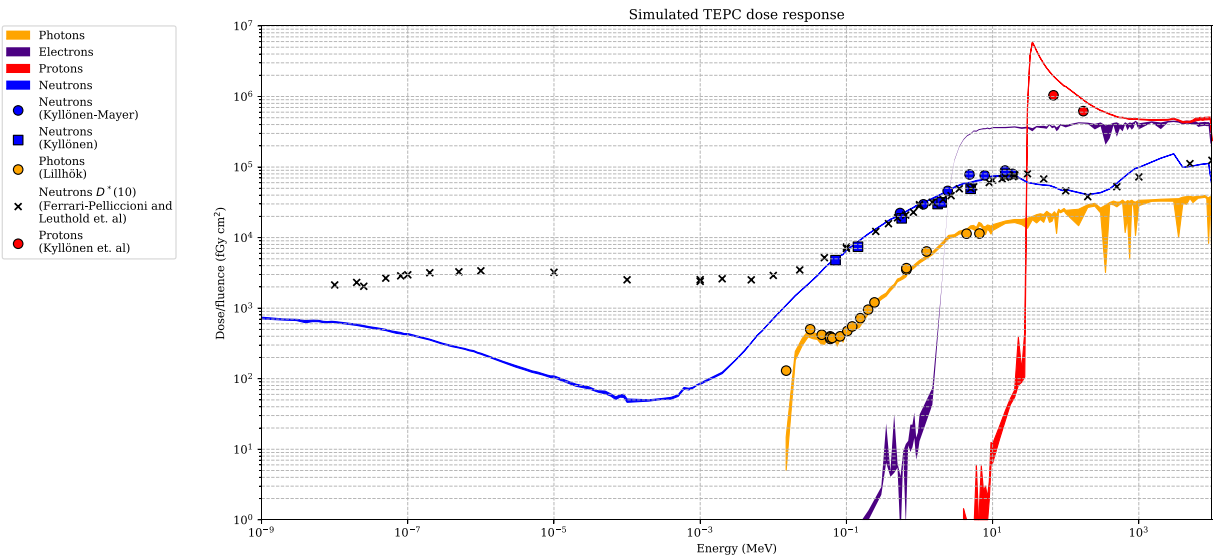


FIGURE 6
The dose-simulated response for the Sievert detectors, with associated uncertainties ($k = 1$) represented as colour bands. The simulated response is compared with experimental data from Kyllönen and Mayer (28), Kyllönen et al. (19), Lillhök (18), and Kyllönen et al. (21). Simulated conversion coefficients to ambient absorbed dose from Ferrari and Pelliccioni (29) and Leuthold et al. (30) are also included.

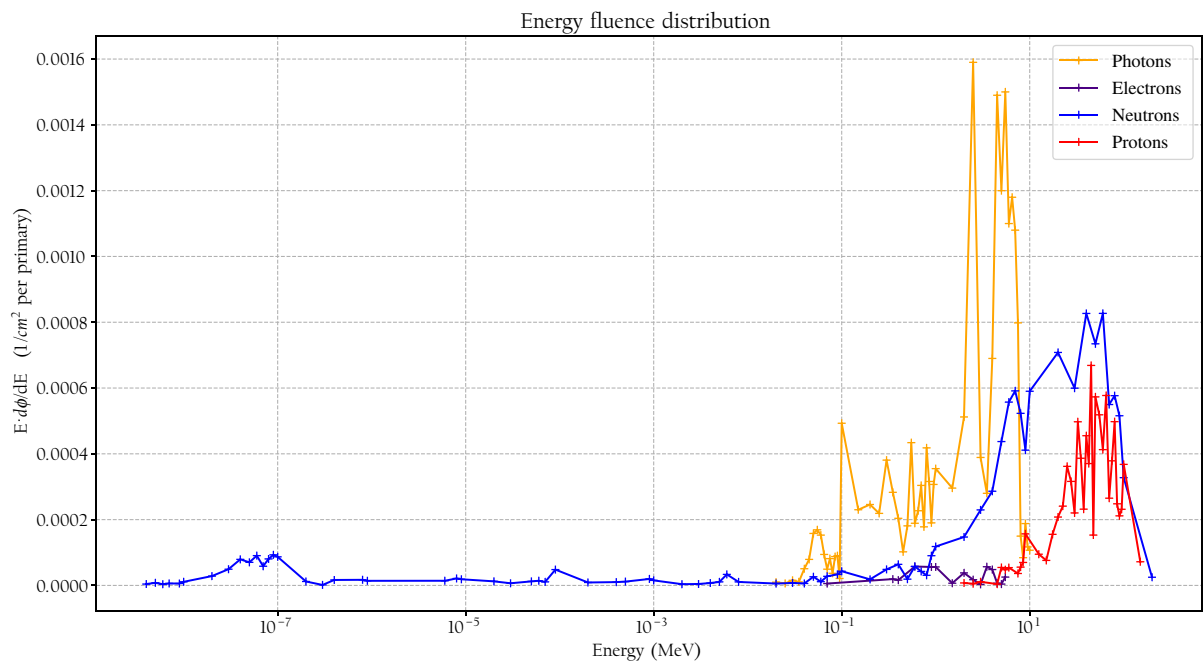


FIGURE 7
The simulated fluence distribution at position A when the phantom is irradiated with 146-MeV protons and a range shifter is applied with a 23-cm air gap.

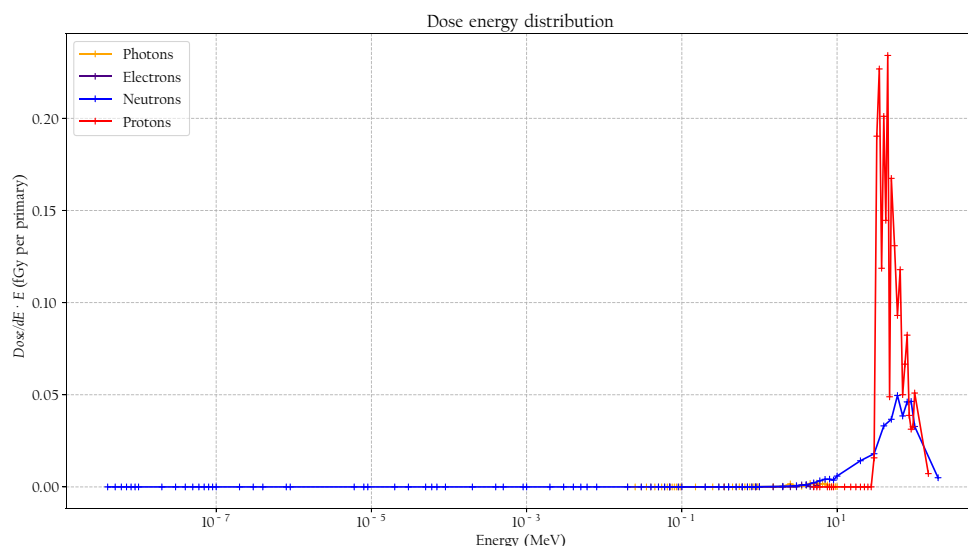


FIGURE 8

The simulated dose distribution at position A when the phantom is irradiated with 146-MeV protons and a range shifter is applied with a 23-cm air gap.

constant when comparing the 15- and 23-cm range-shifter positions (see Figure 5B).

The simulations were performed with a simple geometry, only including the detector, range shifter, phantom, and proton beam dump. To investigate the scattering effect of the surrounding structure, more thorough and hence time-consuming simulations were performed for a few cases, using a more comprehensive geometry modelled by Ardenfors et al. (27). These simulations showed that the surrounding walls were

important when relatively lowly absorbed doses were measured, particularly in position C, where the range shifter was shielded by the phantom. These complementary simulations did not change the conclusion that the primary beam was scattered in the range shifter. In position A, the increased absorbed dose was still completely dominated by the relative contribution of the scattered protons deposited in the detector.

From the simulated dose distribution, it is also evident that the contribution from photons is very low (see Figure 9), so any

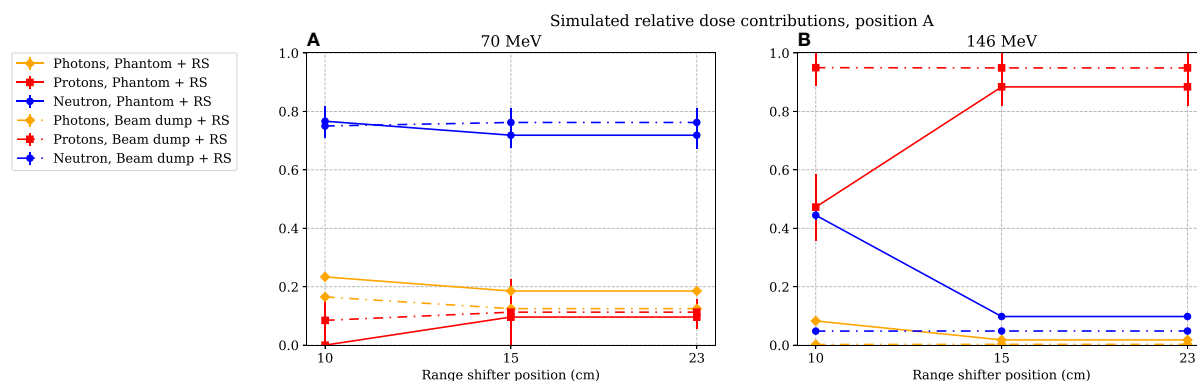


FIGURE 9

The simulated relative dose contribution at position A when the phantom or proton beam dump was irradiated with 70- and 146-MeV protons (A) and (B) respectively. The range-shifter positions correspond to the air gaps when the phantom was present. The lines between data points are used as guide for the eye. The dashed-dotted lines show the simulated relative dose contribution when no phantom was present, while the solid lines show the contributions when the phantom was irradiated. The values are illustrated with one standard uncertainty.

low-LET components leading to a decrease in the resulting \bar{y}_D value at 146 MeV were likely to come from protons.

3.4 Estimated dose equivalent as a function of the range-shifter position

As for the simulated dose contributions, only the investigation of position A is presented here. The dose equivalents as functions of different range-shifter settings were estimated during irradiations of both the phantom and the proton beam dump (see Figure 10). In Figure 10A, for the 70-MeV proton beam, it is seen that the H^* values were relatively constant even after applying a range shifter. The absorbed dose rate was lower, and the increase of high-LET neutrons was not high enough to give a higher H^* value. During irradiation with a 146-MeV proton beam, two noteworthy results can be pointed out. First, the H^* value without a range shifter was higher than when irradiating with a 70-MeV proton beam, indicating that the stray field from the phantom alone led to an increase with an increased proton beam energy. This increase is expected since the proton energy was more than double. Second, when applying the range shifter, the H^* values increased by almost a factor of 2 (for the smallest range-shifter position when irradiating the phantom), up to a factor more than 3 (23-cm air gap). At the 10-cm air gap, position A was partly shadowed by the phantom, which explains the air gap dependence. The increase in the H^* value here reflects the significantly higher absorbed doses by the scattered protons.

4 Discussion

When irradiating the phantom with 70-MeV protons, the absorbed dose rate at both positions A and C decreased and the

\bar{y}_D value increased when applying the range shifter, indicating a larger contribution from a high-LET component. In position C, an air gap dependency which was not seen in position A was noticed. The detected neutrons in position A were less moderated by the phantom even at small air gaps, while the neutrons that reached position C had a larger moderation due to more phantom material to penetrate. At larger air gaps, the exposed phantom material was reduced and the neutrons deposited were therefore more energetic. This is visualised in Figure 11, where the blue cones indicate the line of sight from the centre of the range shifter to the detectors at positions A and C. At larger air gaps, a particle travelling in a straight line from the range shifter to a detector passes through less phantom material than at smaller air gaps.

When the phantom was irradiated with 146-MeV protons, the absorbed dose rate in position A was significantly increased, which can be explained by protons scattering at a large enough angle from the range shifter to miss the phantom. A clear dependency on the air gap was observed. When the air gap was small, the phantom shadowed the detector, while at larger air gaps, the detector saw almost no effect from the phantom. The hypothesis that high-energy (>10-MeV) protons represent the main part of the dose contribution in the detector at position A is supported by the measured decrease in the \bar{y}_D value when the range shifter is applied, indicating a large contribution from a low-LET component. The simulated dose contributions agreed with the measurements and also indicated that contribution from photons was low, which further supports the hypothesis that the majority of the low-LET component comes from protons.

The H^* value is an approximation of the ambient dose equivalent, $H^*(10)$, and was calculated using a linear approximation. The differences between the ICRP Q value and

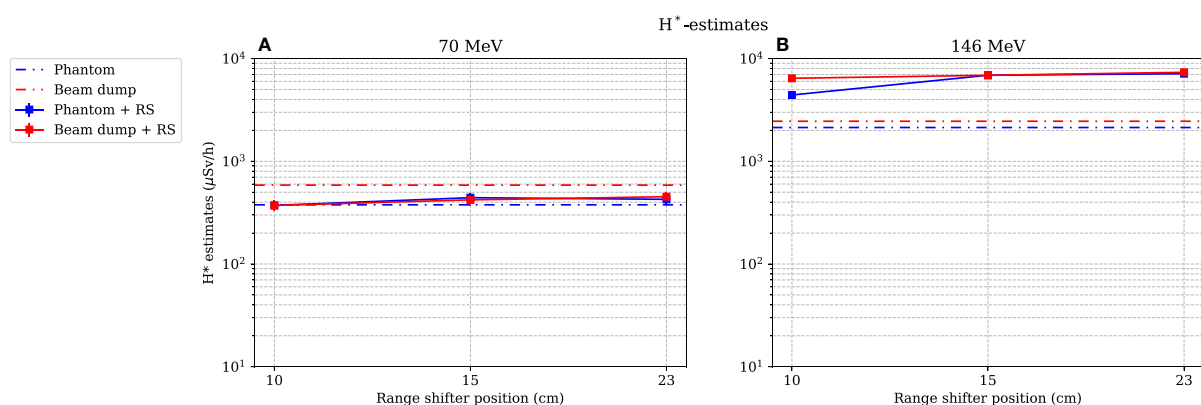


FIGURE 10
Estimation of the dose equivalent at position A, when both the phantom and the proton beam dump are irradiated with 70- and 146-MeV protons (A) and (B) respectively. The lines between data points are used as guide for the eye. The dashed-dotted lines show the levels without a range shifter, i.e., scattered from the phantom or from the beam dump. As mentioned in Section 2.4, the values are illustrated with statistical uncertainties with $k = 1$.

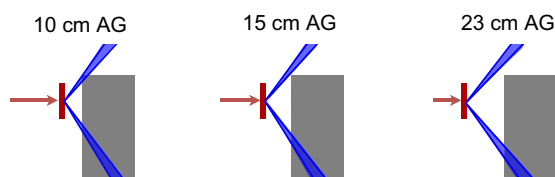


FIGURE 11

The blue cones indicate the path from the centre of the range shifter (red) to the borders of the detectors at positions A (top) and C (bottom). When the air gap is small, a particle that travels in a straight line needs to travel through more phantom material (grey) than when the air gap is large. This can be one reason to the air gap dependency that is seen for position C in Figure 5A.

this approximation is a source of uncertainty. In addition, e.g., back-scattering from the tissue material in the ICRU sphere was not detected in gas-filled TEPCs such as the Sievert detectors. Therefore, the absorbed dose from neutrons at intermediate energies is underestimated. An uncertainty of around 15%–25% has been estimated due to the abovementioned effects by Lillhök (18). The estimated H^* value during irradiations with 146-MeV protons was however several times larger with a range shifter than without and clearly exceeded the uncertainties in the ambient dose equivalent estimation even if the neutron energy distribution would change.

It is well established that the stray field in proton therapy contains both thermal and high-energy *neutron* components and that the magnitude of the contributions depends strongly on positions and proton beam energies (2, 4, 5). However, when applying a range shifter, the contributions at some positions that are less shielded by the phantom are not necessarily dominated by neutrons, and the thermal neutron contribution can be suppressed, as illustrated in Figures 7, 8. The range shifter can dramatically affect the stray radiation field. The potential presence of protons needs to be considered and included in simulations and measurements.

5 Conclusion

In a previous campaign, measuring the out-of-field neutron doses in a proton pencil beam facility, a significant increase in absorbed dose measured by a TEPC was detected at one position when a range shifter was applied. The measurements in the present study reproduced this increase, and measurements of the dose-mean lineal energy confirmed that the increased dose rate during irradiation with a 146-MeV proton beam consisted of low-LET radiation. The results were supported by Monte Carlo simulations showing that the low-LET component consisted of high-energy (>10-MeV) protons. The greatly enhanced dose rate when using the range shifter resulted in an up to three times higher dose equivalent compared to when no range shifter was applied. The results illustrate the importance of considering the potential dose contribution from protons in out-of-field

simulations as well as using instruments sensitive also to proton radiation during measurement campaigns.

Data availability statement

The raw data supporting the conclusions of this article will be made available by the authors, without undue reservation.

Author contributions

LE, JL, and TB planned the experimental measurements. RB-M performed the simulations. AD and ML planned and performed the irradiations at the Skandion Clinic. LE and JL performed pre-calibrations and preparations of the instruments. LE, JL, AD, and ML performed the measurements. LE performed the data analysis. LE did the main part of the writing and made the figures. All authors contributed to the article and approved the submitted version.

Funding

This project was funded by the Swedish Radiation Safety Authority, grant agreement no. 7030265-00. In addition, funding was received from Euratom's research and innovation programme 2019-20 under grant agreement no. 945196.

Acknowledgments

The authors would like to thank Oscar Ardenfors for providing a simulation geometry model for the Skandion treatment room. The Swedish National Metrology Laboratory for Ionising Radiation provided radioactive sources and equipment for control measurements and are gratefully acknowledged.

Conflict of interest

The authors declare that the research was conducted in the absence of any commercial or financial relationships that could be construed as a potential conflict of interest.

Publisher's note

All claims expressed in this article are solely those of the authors and do not necessarily represent those of their affiliated

organizations, or those of the publisher, the editors and the reviewers. Any product that may be evaluated in this article, or claim that may be made by its manufacturer, is not guaranteed or endorsed by the publisher.

References

- Smith AR. Vision 20/20 : Proton therapy. *Med Phys (Lancaster)* (2009) 36:556–68. doi: 10.1118/1.3058485
- Van Hoey O, Stolarczyk L, Lillhök J, Eliasson L, Mojzeszek N, Liszka M, et al. Simulation and experimental verification of ambient neutron doses in a pencil beam scanning proton therapy room as a function of treatment plan parameters. *Front Oncol* (2022) Submitted.
- ICRP. The 2007 recommendations of the international commission on radiological protection. *ICRP Publication 103. Ann. ICRP* (2007) 37:(2–4). doi: 10.1016/j.icrp.2007.10.003
- Farah J, Mares V, Romero-Expósito M, Trinkl S, Domingo D, Dufek V, et al. Measurement of stray radiation within a scanning proton therapy facility: EURADOS WG9 intercomparison exercise of active dosimetry systems. *Med Phys (Lancaster)* (2015) 42:2572–84. doi: 10.1118/1.4916667
- Trinkl S, Mares V, Englbrecht FS, Wilkens JJ, Wielunski M, Parodi K, et al. Systematic out-of-field secondary neutron spectrometry and dosimetry in pencil beam scanning proton therapy. *Med Phys (Lancaster)* (2017) 44:1912–20. doi: 10.1002/mp.12206
- Wochnik A, Stolarczyk L, Ambrozová, Davidkova M, De Saint-Hubert M, Dománski S, et al. Out-of-field doses for scanning proton radiotherapy of shallowly located paediatric tumours—a comparison. *Med Biol* (2021) 66(3):350123. doi: 10.1088/1361-6560/abcb1f
- ICRU. International Commission on Radiation Units and Measurements, Quantities and units in radiation protection dosimetry. *ICRU Report*. (1993) (ICRU, 7910 Woodmont Avenue, Suite 800: Bethesda, MD 208141) 51. doi: 10.1093/jicru_os26.2.15
- ICRU. International Commission on Radiation Units and Measurements, Determination of operational dose equivalent quantities for neutrons. *ICRU Report* (2001) (ICRU, 7910 Woodmont Avenue, Suite 800: Bethesda, MD 208141) 66. doi: 10.1093/jicru_1.3.3
- ICRU. International Commission on Radiation Units and Measurements, Microdosimetry. *ICRU Report 36* (1983) 36 (ICRU, 7910 Woodmont Avenue, Suite 800: Bethesda, MD 208141). doi: 10.1093/jicru_os19.1.80
- Kellerer AM, Rossi HH. On the determination of microdosimetric parameters in time-varying radiation fields: the variance-covariance method. *Radiat Res* (1984) 97:237–45. doi: 10.2307/3576275
- Lillhök J, Persson L, Andersen CE, Dasu A, Ardenfors O. Radiation protection measurements with the variance-covariance method in the stray radiation fields from photon and proton therapy facilities. *Radiat Prot Dosimetry* (2018) 180:338–41. doi: 10.1093/rpd/ncx194
- Kyllönen JE, Lindborg L, Samuelson G. Cosmic radiation measurements on-board aircraft with the variance method. *Radiat Prot Dosimetry* (2001) 93:197–205. doi: 10.1093/oxfordjournals.rpd.a006430
- Lillhök J, Beck P, Bottollier-Depois JF, Latocha M, Lindborg L, Roos H, et al. A comparison of ambient dose equivalent meters and dose calculations at constant flight conditions. *Radiat Meas* (2007) 42:323–33. doi: 10.1016/j.radmeas.2006.12.011
- Ambrozová I, Beck P, Benton ER, Billnert R, Bottollier-Depois JF, Caresana M, et al. REFLECT – research flight of EURADOS and CRREAT: Intercomparison of various radiation dosimeters onboard aircraft. *Radiat Meas* (2020) 137:106433. doi: 10.1016/j.radmeas.2020.106433
- Bolognese-Milstajn T, Bartlett D, Boschung M, Coeck M, Curzio G, d'Errico F, et al. Individual neutron monitoring in workplaces with mixed neutron/photon radiation. *Radiat Prot Dosimetry* (2004) 110:753–8. doi: 10.1093/rpd/nch220
- Mayer S, Golnik N, Kyllönen JE, Menzel HG, Otto T. Dose equivalent measurements in a strongly pulsed high-energy radiation field. *Radiat Prot Dosimetry* (2004) 110:759–62. doi: 10.1093/rpd/nch177
- McConn R, Gesh CJ, Pagh RT, Rucker RA, Williams RGIII. *Compendium of material composition data for radiation transport modeling. PNNL-15870, rev. 1. tech. rep.* Richland, Washington: Pacific Northwest National Laboratory (2011).
- Lillhök JE. *The microdosimetric variance-covariance method used for beam quality characterization in radiation protection and radiation therapy.* (2007) Ph.D. thesis, Stockholm University, Medical Radiation Physics, Stockholm University, Karolinska Institutet.
- Kyllönen JE, Lindborg L, Samuelson G. The response of the sievert instrument in neutron beams up to 180 MeV. *Radiat Prot Dosimetry* (2001) 94:227–32. doi: 10.1093/oxfordjournals.rpd.a006494
- Vassiliev ON, Peterson CB, Cao W, Grosshans DR, Mohan R. Systematic microdosimetric data for protons of therapeutic energies calculated with Geant4-DNA. *Phys Med Biol* (2019) 64:215018–8. doi: 10.1088/1361-6560/ab47cc
- Kyllönen JE, Grindborg JE, Lindborg L. Response investigations of a TEPC in high energy proton and neutron beams using the variance method. *Radiat Prot Dosimetry* (2002) 99:373–4. doi: 10.1093/oxfordjournals.rpd.a006807
- ICRU. International Commission on Radiation Units and Measurements, Average energy required to produce an ion pair. *ICRU Report* (1979) 31 (ICRU, 7910 Woodmont Avenue, Suite 800: Bethesda, MD 208141). doi: 10.1093/jicru_os16.2.50
- Ardenfors O, Dasu A, Kopeć M, Gudowska I. Modelling of a proton spot scanning system using MCNP6. *J Phys Conf Ser* (2017) 860:12025. doi: 10.1088/1742-6596/860/1/012025
- Almhagen E, Boersma DJ, Nyström H, Ahnesjö A. A beam model for focused proton pencil beams. *Phys Med* (2018) 52:27–32. doi: 10.1016/j.ejmp.2018.06.007
- Christensen JB, Almhagen E, Stolarczyk L, Liszka M, Hernandez GG, Bassler N, et al. Mapping initial and general recombination in scanning proton pencil beams. *Phys Med Biol* (2020) 65:115003–3. doi: 10.1088/1361-6560/ab8579
- Werner CJ, Bull JS, Solomon CJ, Brown FB, McKinney GW, Rising ME, et al. *MCNP version 6.2 release notes. tech. rep.* United States: Los Alamos National Lab (2018). doi: 10.2172/1419730
- Ardenfors O, Dasu A, Lillhök J, Persson J, Gudowska I. Out-of-field doses from secondary radiation produced in proton therapy and the associated risk of radiation-induced cancer from a brain tumor treatment. *Phys Med* (2018) 53:129–36. doi: 10.1016/j.ejmp.2018.08.020
- Kyllönen JE, Mayer S. *Response investigations of the sievert instrument in neutron beams between 0.5 and 19 MeV at PTB.* Tech. rep.
- Ferrari A, Pelliccioni M. Fluence to dose equivalent conversion data and effective quality factors for high energy neutrons. *Radiat Prot Dosimetry* (1998) 76:215–224. doi: 10.1093/oxfordjournals.rpd.a032267
- Leuthild G, Mares V, Schraube H. Calculation of the neutron ambient dose equivalent on the basis of the ICRP revised quality factors. *Radiat Prot Dosimetry* (1992) 40:77–84. doi: 10.1093/oxfordjournals.rpd.a081194



OPEN ACCESS

EDITED BY

Liliana Stolarczyk,
Aarhus University Hospital, Denmark

REVIEWED BY

Marija Majer,
Rudjer Boskovic Institute, Croatia
James Chow,
University of Toronto, Canada
Hrvoje Brkić,
Josip Juraj Strossmayer University of
Osijek, Croatia

*CORRESPONDENCE

Ana Cravo Sá,
anacravosa@ctn.tecnico.ulisboa.pt

SPECIALTY SECTION

This article was submitted to
Radiation Oncology,
a section of the journal
Frontiers in Oncology

RECEIVED 18 February 2022

ACCEPTED 04 July 2022

PUBLISHED 05 August 2022

CITATION

Sá AC, Barateiro A, Bednarz BP,
Almeida P, Vaz P and Madaleno T
(2022) Comparison of 3DCRT and
IMRT out-of-field doses in pediatric
patients using Monte Carlo simulations
with treatment planning system
calculations and measurements.
Front. Oncol. 12:879167.
doi: 10.3389/fonc.2022.879167

COPYRIGHT

© 2022 Sá, Barateiro, Bednarz, Almeida,
Vaz and Madaleno. This is an open-
access article distributed under the
terms of the [Creative Commons
Attribution License \(CC BY\)](https://creativecommons.org/licenses/by/4.0/). The use,
distribution or reproduction in other
forums is permitted, provided the
original author(s) and the copyright
owner(s) are credited and that the
original publication in this journal is
cited, in accordance with accepted
academic practice. No use,
distribution or reproduction is
permitted which does not comply with
these terms.

Comparison of 3DCRT and IMRT out-of-field doses in pediatric patients using Monte Carlo simulations with treatment planning system calculations and measurements

Ana Cravo Sá^{1,2,3*}, Andreia Barateiro⁴, Bryan P. Bednarz⁵,
Pedro Almeida³, Pedro Vaz¹ and Tiago Madaleno⁴

¹Radiation Protection and Safety Group, Centro de Ciências e Tecnologias Nucleares (C2TN), Bobadela, Portugal, ²Diagnostic, Therapeutic and Public Health Sciences Department, Escola Superior de Tecnologia da Saúde de Lisboa (ESTeSL), Lisbon, Portugal, ³Instituto de Biofísica e Engenharia Biomédica, Faculdade de Ciências, Universidade de Lisboa, Lisbon, Portugal,

⁴Radiotherapy Department, Portuguese Institute of Oncology Francisco Gentil, Lisbon, Portugal,

⁵Department of Medical Physics, Wisconsin Institutes for Medical Research, University of Wisconsin Hospital and Clinics, Madison, WI, United States

3DCRT and IMRT out-of-field doses in pediatric patients were compared using Monte Carlo simulations with treatment planning system calculations and measurements.

Purpose: Out-of-field doses are given to healthy tissues, which may allow the development of second tumors. The use of IMRT in pediatric patients has been discussed, as it leads to a “bath” of low doses to large volumes of out-of-field organs and tissues. This study aims to compare out-of-field doses in pediatric patients comparing IMRT and 3DCRT techniques using measurements, Monte Carlo (MC) simulations, and treatment planning system (TPS) calculations.

Materials and methods: A total dose of 54 Gy was prescribed to a PTV in the brain of a pediatric anthropomorphic phantom, for both techniques. To assess the out-of-field organ doses for both techniques, two treatment plans were performed with the 3DCRT and IMRT techniques in TPS. Measurements were carried out in a LINAC using a pediatric anthropomorphic phantom and thermoluminescent dosimeters to recreate the treatment plans, previously performed in the TPS. A computational model of a LINAC, the associated multileaf collimators, and a voxelized pediatric phantom implemented in the Monte Carlo N-Particle 6.1 computer program were also used to perform MC simulations of the out-of-field organ doses, for both techniques.

Results: The results obtained by measurements and MC simulations indicate a significant increase in dose using the IMRT technique when compared to the 3DCRT technique. More specifically, measurements show higher doses with IMRT, namely, in right eye (13,041 vs. 593 mGy), left eye (6,525 vs. 475 mGy),

thyroid (79 vs. 70 mGy), right lung (37 vs. 28 mGy), left lung (27 vs. 20 mGy), and heart (31 vs. 25 mGy). The obtained results indicate that out-of-field doses can be seriously underestimated by TPS.

Discussion: This study presents, for the first time, out-of-field dose measurements in a realistic scenario and calculations for IMRT, centered on a voxelized pediatric phantom and an MC model of a medical LINAC, including MLC with log file-based simulations. The results pinpoint significant discrepancies in out-of-field doses for the two techniques and are a cause of concern because TPS calculations cannot accurately predict such doses. The obtained doses may presumably increase the risk of development of second tumors.

KEYWORDS

radiotherapy planning, out-of-field dose, pediatric tumors, Monte Carlo simulations, computational voxel phantoms, IMRT, 3DCRT

Introduction

In photon radiotherapy, out-of-field doses are mainly caused by radiation scattered in the collimators, radiation leakage from the linear accelerator head, and radiation scattered inside the patient's body (1–10). Out-of-field doses are non-target doses that are outside of the planning target volume (PTV) and also outside the primary field edge (4). These doses are often disregarded in radiotherapy treatment planning, because they are considered “low doses” (4). The purpose of radiotherapy is to irradiate a tumor volume with high doses. Doses below 5% of the total dose prescribed or doses below 3 Gy are considered low doses (4) which are important because they can increase the probability of development of a second cancer (2, 11). The development of a second cancer probability increases when high doses are outside the treatment field, even in the tissues closest to the PTV; however, low doses further from the PTV cannot be ignored. This is particularly important in pediatric patients (2, 12), because children are considered to be a factor of 10 times more sensitive to radiation (12), when compared to adults. The higher radiosensitivity found in children can be attributed to several factors, such as higher cell proliferation in pediatric ages, higher susceptibility of normal tissues to the mutagenic effects of ionizing radiation in children, and genetic susceptibility related to some primary tumors (13). In addition, radiation-induced tumors may develop in organs contained within the treatment fields, e.g., in high-dose regions, or even in organs distant from the treatment fields exposed to lower radiation doses (12).

According to the National Council on Radiation Protection and Measurements (NCRP) report 116 (14), the intestine, lung, and stomach are the most common sites for the development of second tumors after exposure to radiation (12, 14). However, the

thyroid is also known to have a low tolerance to radiation, especially in children (12, 15). An increased incidence of thyroid cancer has been reported after exposure to an average dose of 0.05 Gy in children and young adults (12).

The increasing use of intensity-modulated radiotherapy (IMRT) techniques, such as volumetric-modulated arc therapy (VMAT), will lead to a higher risk of developing second tumors, given the administration of low doses to large volumes outside the treatment fields (10). Using IMRT, the total number of monitor units (MU) is usually higher for the treatment of similar cases when compared to 3D conformal radiotherapy (3DCRT) (7, 16, 17). Furthermore, the importance of knowing the variation of the doses as a function of the distance from the field edge was highlighted in a very recent study (18), where the authors provide a model for determining the out-of-field doses as a function of the distance from the field edge. In addition, the need to study and understand how the treatment planning system (TPS) accuracy impacts out-of-field doses in pediatric radiotherapy was emphasized in (19).

In our previous study (20), out-of-field doses for the 3DCRT technique were evaluated by measurements, MC simulations, and TPS calculations. To assess the out-of-field doses with the 3DCRT technique, we initially validated an MC model of a Varian 2100 linear accelerator and then we performed dose measurements with thermoluminescent dosimeters (TLDs) on a pediatric anthropomorphic phantom, based on the treatment planning performed in the TPS. In the present study, these previously obtained results only provide a comparison with the new results obtained for the IMRT technique.

Ruben et al., in 2011, compared 3DCRT with IMRT, concluding that the out-of-field doses with IMRT increases for i) smaller field dimensions, ii) higher MU, and iii) higher distance from the field edge (16). The same authors concluded

that IMRT yields a higher total dose of scattered radiation in the patient than 3DCRT (16). Additionally, in another study, other authors found that the IMRT increases the dose inside the patient's body, when compared with 3DCRT, and may presumably double the incidence of solid tumors in long-term survivors (3).

The aim of this study was to compare out-of-field doses in 3DCRT and IMRT treatments of pediatric patients, using the MC model of a linear accelerator (LINAC) head and associated multileaf collimators (MLCs), coupled to a computational pediatric voxel phantom developed and validated (20) from a physical phantom. To the best of our knowledge, no comparison between out-of-field doses in 3DCRT and IMRT using thermoluminescent dosimeter (TLD) measurements, MC simulations, and TPS calculations was yet undertaken prior to our study.

Our study accurately mimics a treatment with the IMRT technique applied to a pediatric case. To reproduce the dynamic movement of each leaf of the MLC during irradiation, we implemented an MC model of a LINAC. Several cutting-edge features of this work must be emphasized: i) a computational pediatric anthropomorphic phantom created from the original computed tomography (CT) images combined with an MC model of a LINAC head and MLC was used to calculate the organ doses by MC log file-based simulations for the IMRT technique; ii) the CT images of the pediatric phantom were used to calculate the organ doses with the treatment planning system (TPS) for the IMRT technique; and iii) TLD measurements in the physical pediatric anthropomorphic phantom were used to obtain the organ doses with the IMRT technique, creating a realistic scenario for treatment delivery. The combination of the listed features and methods allowed for an accurate comparison between 3DCRT and IMRT out-of-field doses using MC simulations, TPS calculations, and TLD measurements performed in a clinical environment, highlighting the innovation of this study, compared to those described in the literature.

Materials and methods

Treatment planning

An Atom[®] 5-year-old physical pediatric phantom from CIRS, named George, with 110 cm of height and 19 kg of weight was the anthropomorphic pediatric used in this work. Considering that the phantom lacks a tumor volume, an elliptically shaped PTV was defined with 9.8 cm (3) in the right hemisphere of the brain. The volume and shape of the tumor were based on the analysis of 47 pediatric clinical cases, aged between 4 and 7 years. The organs at risk (OARs) segmented were the lungs, thyroid, heart, C-spine, and eyes. These OARs were chosen essentially for two reasons: i) low dose-

induced biological effects to the OARs could affect function/growth; ii) OARs are well defined in the anthropomorphic phantom used in this study. In the TPS, the distance between the PTV and the different OARs evaluated was calculated by selecting the geometric center of each volume and then obtaining the distance between each of them.

A treatment planning was performed using the 3DCRT and IMRT techniques, for a 6-MV photon beam and with a total prescribed dose to the PTV of 54 Gy, with a dose per fraction of 1.8 Gy in both cases, as shown in Figure 1. The treatment plans were executed by the Eclipse TPS from Varian (Varian Medical Systems, Palo Alto, CA) Version 13.0 and using version 13.6.23 of the analytical anisotropic algorithm (AAA) dose calculation algorithm. The AAA was used to calculate organ mean doses. The 3DCRT treatment plan was created using six non-coplanar brain fields. The treatment field details are displayed in Table 1. For the OARs of this study, the QUANTEC tables were used (21–25), for both techniques. The IMRT treatment plan was created using seven coplanar brain fields. The treatment field details are displayed in Table 2. For MLC, the dynamic mode was used, and the progressive resolution optimizer performed the optimization of the dose calculation. Considering a brain irradiation and the previously segmented volumes, the dose objectives were defined for the eyes, since the eyes are the volumes of risk closest to PTV. In addition, in clinical environment, only the eyes would be considered as OARs, as shown in Table 3. The phantom was irradiated in the same LINAC under the conditions previously described, for the two techniques.

TLD measurements using a pediatric phantom

In this study, Harshaw Ext-Rad (LiF : Mg,Cu,P) TLDs were placed in the eyes, lungs, heart, thyroid, and C-spine of the pediatric phantom. A total of 76 dosimeters, divided into two groups of 38 dosimeters, were used. The first group of dosimeters was irradiated with the 3DCRT technique, and the second group of dosimeters was irradiated with the IMRT technique. Each dosimeter has a sensitive diameter of 0.5 cm, a length of 5.1 cm, a height of 1.34 cm, and a thickness of 0.1 cm. For each group, one dosimeter was placed in the right eye, one for the left eye, two for the c-spine, four for the thyroid, two for the heart, 12 for the right lung, and 16 for the left lung.

The TLDs were previously calibrated using air kerma with a Cs-137 source in a reference metrology laboratory. The day before irradiation, the TLDs were reset. The day after irradiation, readings were performed using a Harshaw 6600 reader with a previously defined temperature and time profile in order to avoid contributions from non-dosimetric peaks (26), and a preheating was performed. Transit dosimeters were used, but

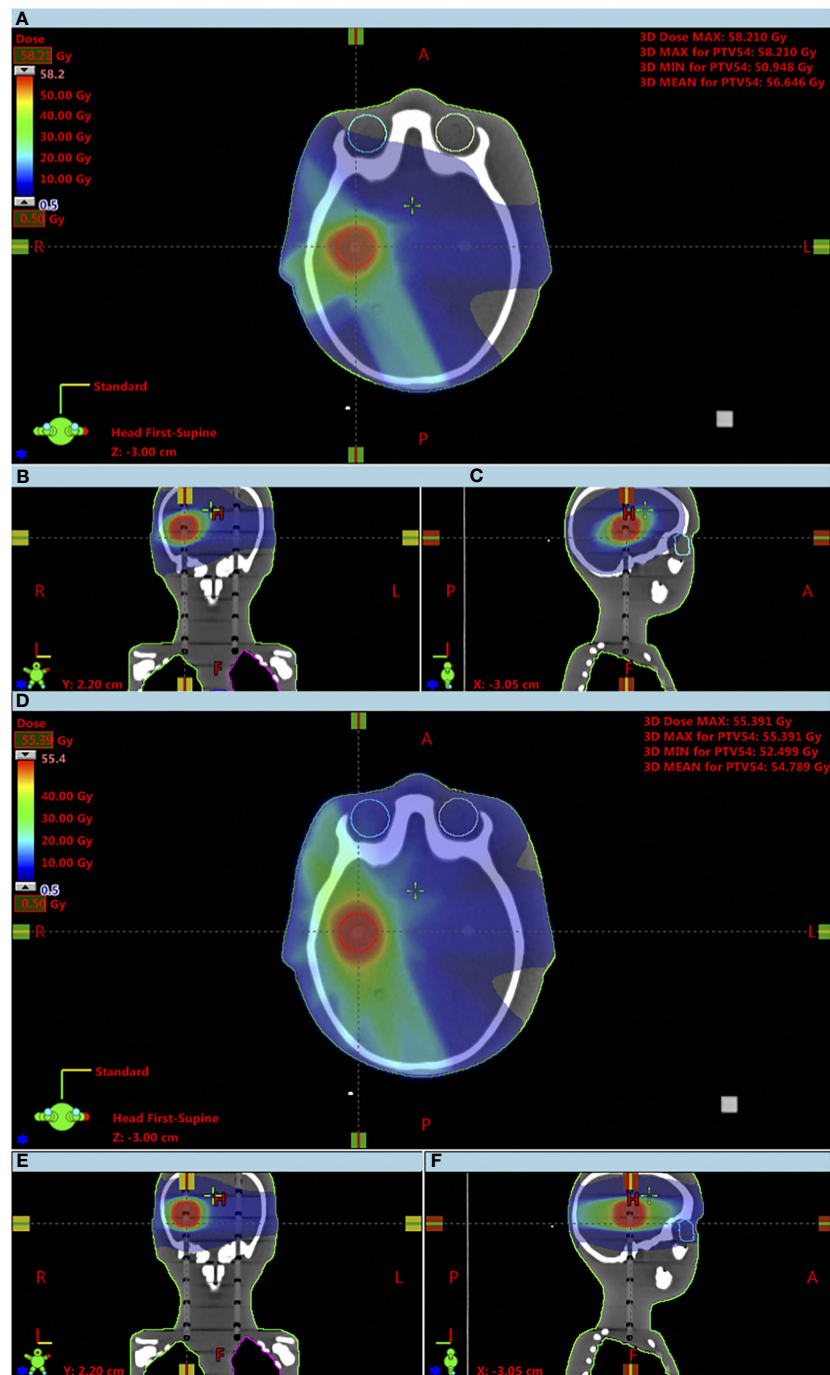


FIGURE 1

Comparison of obtained dose distributions between the 3DCRT and IMRT techniques up to a minimum dose of 500 mGy. (A) 3DCRT axial view; (B) 3DCRT coronal view; (C) 3DCRT sagittal view; (D) IMRT axial view; (E) IMRT coronal view; (F) IMRT sagittal view.

since their value was negligible, background subtraction was not performed.

The kerma in air (K_{air}) was calculated using the following equation (27):

$$K_{air} = \frac{RD \times Ecc}{RCF} \times f(Q) \times f(fad) \times f(E) \times f(\alpha) \quad (1)$$

For each TLD, the raw data (RD) is multiplied by the element correction coefficient (Ecc), the correction factors of

TABLE 1 3DCRT planning dose parameters.

Field ID	Gantry (deg)	Collimator (deg)	Couch (deg)	Field X (cm)	X1 (cm)	X2 (cm)	Field Y (cm)	Y1 (cm)	Y2 (cm)	Field weight	SSD (cm)	MU
1	320.0	0.0	0.0	3.2	+1.6	+1.6	3.2	+1.6	+1.6	0.70	95.1	32
2	270.0	0.0	0.0	3.2	+1.6	+1.6	3.2	+1.6	+1.6	0.70	96.5	30
3	235.0	0.0	15.0	3.4	+1.7	+1.7	3.4	+1.7	+1.7	0.70	95.9	31
4	40.0	0.0	50.0	3.4	+1.7	+1.7	3.4	+1.7	+1.7	1.10	90.1	63
5	155.0	0.0	345.0	3.4	+1.7	+1.7	3.4	+1.7	+1.7	1.00	91.5	53
6	60.0	309.0	30.0	3.4	+1.7	+1.7	3.5	+1.7	+1.8	1.00	89.3	60

reader stability ($f(Q)$), fading effect ($f(fad)$), energy dependency ($f(E)$), and angular dependency ($f(\alpha)$) and divided by the reader calibration factor (RCF).

The interval between the reset and the readout was negligible, and for this reason the correction due to the fading effect was not considered. The angular dependence correction factor was considered equal to 1, since TLDs have no angular dependence for the energy threshold (28).

The final dose value assessed at each position of the TLDs in the pediatric phantom was obtained based on the following equation (27), assuming that the electronic equilibrium condition is observed:

$$D_{tissue} = K_{air} \times \frac{(\mu_{en}/\rho)_{tissue}}{(\mu_{en}/\rho)_{air}} \quad (2)$$

where K_{air} was previously defined, $(\mu_{en}/\rho)_{tissue}$ is the mass energy-absorption coefficient for each tissue, and $(\mu_{en}/\rho)_{air}$ is the mass energy-absorption coefficient for air at an average energy of the photon spectrum of 6 MeV. The mass energy-absorption coefficients for air and tissues were obtained through a web-based National Institute of Standards and Technology (NIST) (29), as is seen in Table 4.

To calculate the final dose for each tissue, whenever there is more than one TLD per organ, the average of the dose readings of the TLDs for a given organ was performed.

The final relative uncertainty of the measurements was $\approx 16\%$ ($k = 1$), calculated using the law of propagation of uncertainties, as the square root of the sum of the uncertainties squared (30) from the following contributions:

(a) element correction coefficient (3.0%), (b) correction factors of reader stability (3.8%), (c) reader calibration factor (15.0%), and (d) energy dependency (1.4%) (26). The uncertainty value associated with each parameter was calculated using the maximum and minimum values of the variation interval obtained in each one of them during the time of uncertainty assessment.

Different probability distribution functions were used, depending on the expected distribution of the results. For a), the contribution of the element correction coefficient to the final uncertainty was obtained considering the stability of this factor along time. The stability of this factor was evaluated for 10 irradiation cycles, and the difference, for each detector, between the value obtained in each cycle and the previously dosimeter efficiency determined value was evaluated, assuming that the results present a Gaussian distribution; for b), the contribution from correction factors of reader stability was taken into consideration as well as the range of values obtained in quality control dosimeters during the period of 1 year, assuming a normal distribution of the results obtained; for c), the uncertainty was associated with the reader calibration factor results from the experimental history of the reader calibration factor over time and the uncertainty of the irradiance was reported by the Ionizing Radiation Metrology Laboratory of the Instituto Superior Técnico – Lisbon University; and for d), the energy dependence, it was considered that a dosimeter in normal routine conditions may be exposed to different radiation beams, and a rectangular distribution ($\alpha/\sqrt{3}$) was assumed since all the

TABLE 2 IMRT planning dose parameters.

Field ID	Gantry (deg)	Collimator (deg)	Couch (deg)	Field X (cm)	X1 (cm)	X2 (cm)	Field Y (cm)	Y1 (cm)	Y2 (cm)	Field weight	SSD (cm)	MU
1	340.0	0.0	0.0	5.0	+2.5	+2.5	3.6	+1.8	+1.8	1.0	93.5	51.0
2	314.0	0.0	0.0	5.0	+2.5	+2.5	3.6	+1.8	+1.8	1.0	95.4	47.0
3	266.0	0.0	0.0	5.0	+2.5	+2.5	3.6	+1.8	+1.8	1.0	96.5	43.0
4	228.0	0.0	0.0	5.0	+2.5	+2.5	3.6	+1.8	+1.8	1.0	95.8	43.0
5	197.0	0.0	0.0	5.0	+2.5	+2.5	3.6	+1.8	+1.8	1.0	94.2	47.0
6	173.0	0.0	0.0	5.0	+2.5	+2.5	3.6	+1.8	+1.8	1.0	92.7	50.0
7	154.0	0.0	0.0	5.0	+2.5	+2.5	3.6	+1.8	+1.8	1.0	91.5	53.0

TABLE 3 Optimization objectives for inverse planning.

Structure	Limit	Volume (%)	Dose (Gy)	Priority
Left eye	Upper	0.0	5.0	60
	Upper	5.0	3.0	60
Right eye	Upper	0.0	8.0	70
	Upper	5.0	6.0	70
PTV	Upper	0.0	55.1	220
	Lower	99.0	54.3	280
	Lower	100.0	54.00	280

Limit: constraints expressed as lower or upper dose limits for organs. Priority: priority in the optimization goal.

energies studied for the effect have equal probability of occurrence.

The energy dependence of TLDs is often assumed to be small across the range of photon energies of relevance for this study, since TLDs are nearly energy independent for treatment energies (31). Although there is a dependence on energy at greater distances, energy dependence was considered to be low, because we evaluated doses up to a distance of 20 cm. Its accurate assessment is difficult due to the sizable uncertainties on the spectra of the photon field and its effective energy in organs located outside the main radiation field in external radiotherapy. Detailed information about the energy dependence of TLDs and other dosimeters can be found in (32).

The reader calibration factor considers the results of the last years for the calibration factors as well as the uncertainty mentioned by the metrology laboratory.

MCNP6 Monte Carlo out-of-field dose simulations

For the IMRT technique, the MC simulations of the out-of-field doses in the organs were performed using the state-of-the-art computational program Monte Carlo N-Particle, version 6 (MCNP6) (33), using the developed pediatric voxel phantom developed in a previous study (20) and the implemented and validated LINAC head model (20). The pediatric voxel phantom was created from the CT images of a 5-year-old physical ATOM phantomTM. The ImageJ softwareTM was used

to build the phantom, considering structures such as the heart, lungs, eyes, soft tissues, thyroid, PTV, brain, whole body, bones, skin, spinal canal, and c-spine. In the end, a pediatric computational phantom was obtained with about 47 million voxels, each with a dimension of $x = 0.09766$ cm, $y = 0.09766$ cm, and $z = 0.3$ cm.

The IMRT MC simulations were performed in parallel processing mode with 10×10 (9) photons produced in the target. To model the 6-MV energy photon beam, a fine-tuning process was performed, in order to adjust the parameters previously described in other studies (34–39), such as the primary electron energy and the full width half maximum (FWHM) of the Gaussian beam intensity distribution. MC simulations were performed for different values of the primary electron energy and different values of FWHM. By comparing the measured and calculated depth dose profiles and beam profiles (40–43), the electron beam's energy of 6.2 MeV and the FWHM of 1.2 mm were selected. The source definition card (SDEF) was used to specify a single-beam source of photons from the target (option available in MCNP), as a source distribution function traveling along the z-axis. The electron and photon energy cutoffs were set to 0.1 and 0.01 MeV, respectively. The data libraries available from ENDF/B-VII were used for particle transport simulation. As for the implemented variance reduction techniques, "Russian roulette" together with splitting was used for all MC simulations. The tally *F8 was used for scoring the results, and a statistical relative uncertainty of the computational results of less than 5% for 1σ was obtained.

TABLE 4 Organ characteristics assessed in phantom.

Organ	μ_{en}/ρ (cm ² /g) @ 6 MeV	Nr. of phantom sections	Nr. of TLDs
Right eye	0.0179	1	1
Left eye	0.0179	1	1
C-spine	0.0179	2	2
Thyroid	0.0194	2	4
Heart	0.0179	2	2
Right lung	0.0179	5	12
Left lung	0.0179	5	16

For the 3DCRT technique, MC simulations were made for the six fields with the MLC positions described in Table 2. For IMRT, the positions of the MLCs were obtained through the MLC log file of each field. These log files were extracted from the Varian TPS Eclipse system, and each log file contains information for about 100 MLC positions for each field. There are about 700 positions of the MLC for the seven treatment fields of the IMRT plan. In order to minimize the computational effort, 20 MLC positions were selected for each field, totaling 140 simulations.

As in 3DCRT (Table 2), the movement of the leaves in IMRT appears only between the pair 27 and 34. Based on the log files and for each IMRT field, the indexes 5, 10, 15, 20, 25, 30, 35, 40, 45, 50, 55, 60, 65, 70, 75, 80, 85, 90, 95, and 100 were selected. In order to change the position of the leaves in MCNP6, it was necessary to use the cell coordinate transformation (*TRCL) card together with the surface coordinate transformation (*TR) card, to create the rotation of the leaves and, therefore, obtain different MLC positions based on the different secondary collimators (33).

In addition, as discussed by Frank Verhaegen (44), for each beam energy created by a LINAC a conversion factor (CF) can be obtained. Considering that the results in the MCNP6 are normalized per source particle, we used the previously calculated CF to achieve the absolute dose in mGy (20). These values were measured and calculated considering the SSD of 100 cm between the source and the water phantom in the central axis of the beam, under the reference conditions, i.e., 10 × 10 cm² field size with the MLC retracted. It is possible to use the same CF, since the MC model is the same and only the setup of the simulations varies, because the position of the MLCs in each simulation varies. All values obtained with the tally *F8 in MCNP6 for organs were multiplied by the CF.

In order to compare the three different approaches, it was defined that the relative differences are calculated as,

$$\text{Relative Differences} = \frac{|\text{Calculations} - \text{Measurements}|}{\text{Measurements}} \times 100 \quad (3),$$

where *Calculations* is related both to MCNP6 and TPS calculations.

Results

All results are given per prescribed dose of 54 Gy.

Measurements are considered the gold standard. The mean dose measured by TLDs for the 3DCRT and IMRT techniques is found in Table 5. Figures 2, 3 show the out-of-field doses in different OARs, obtained by the TPS calculations, the TLD measurements, and the MC simulations, for both techniques.

The comparison between the dose calculations performed by the TPS and the doses measured with TLDs shows that the out-

TABLE 5 Mean dose measured by TLDs in out-of-field organs.

Mean dose measured by TLDs (mGy) and corresponding standard deviation (SD, in mGy)

Out-of-field organ	3DCRT	± SD	IMRT	± SD
Right eye (6.2 cm from PTV center)	593.0	93.7	13040.6	2060.4
Left eye (8.4 cm from PTV center)	475.2	75.1	6525.3	1031.0
C-spine (11.1 cm from PTV center)	180.9	28.6	182.3	28.8
Thyroid (13.1 cm from PTV center)	69.7	11.0	79.4	12.5
Right lung (21.7 cm from PTV center)	28.0	4.4	37.4	5.9
Heart (22.2 cm from PTV center)	25.2	4.0	30.6	4.8
Left lung (23.3 cm from PTV center)	19.8	3.1	27.1	4.3

of-field dose values are always higher for the measurements with TLDs. In addition, the out-of-field measured doses with the IMRT technique are, on average, seven times higher than with the 3DCRT technique. Figures 2, 3 show that the difference between the dose calculation using the TPS and the dose measured by the TLDs increases in out-of-field organs at higher distances from the center of PTV.

Comparing the MC dose simulations with the TLD dose measurements (Figures 2, 3), a better agreement (i.e., lower differences) between the out-of-field doses can be observed, with respect to the comparison between TPS calculations and TLD measurements. For both TLD measurements and MC simulations, there is an increase in dose, namely, dose is, on average, 6.5 times higher using the IMRT technique, when compared to the 3DCRT technique (Figures 2, 3). For TPS calculations, there is also an increase in dose, namely, dose is, on average, 3.0 times higher using the IMRT technique, when compared to the 3DCRT technique.

Figure 2 compares the out-of-field doses with the TPS calculations and the measured doses with the TLDs for the 3DCRT technique, showing that the TPS has lower dose values for all organs. The dose values with the TLDs are approximately 1.5, 1.7, 1.8, 1.6, 14, 13, and 6.7 times higher for the right eye, left eye, C-spine, thyroid, right lung, heart, and left lung, respectively, when compared to TPS calculations. Figure 2 also relates the out-of-field doses with the MC and the measured doses with the TLDs for the 3DCRT technique. The dose values calculated with MC are about 1.1, 1.1, 1.2, and 1.2 times higher compared to TLD measurements, for the right eye, right lung, heart, and left lung, respectively. The doses measured with the TLDs are about 1.1, 1.2, and 1.2 times for the left eye, C-spine, and thyroid respectively, when compared to MC simulations.

Figure 3 shows the out-of-field doses calculated with the TPS and the doses measured with the TLDs for the IMRT technique. The TPS yields lower dose values for all organs. The doses measured with the TLDs are approximately 3.7, 3.0, 2.0, 2.1, 18.5, 15.5, and 9.0 times higher for the right eye, left eye, C-spine, thyroid, right lung, heart, and left lung, respectively, when compared to TPS calculations. Figure 3 also compares the out-

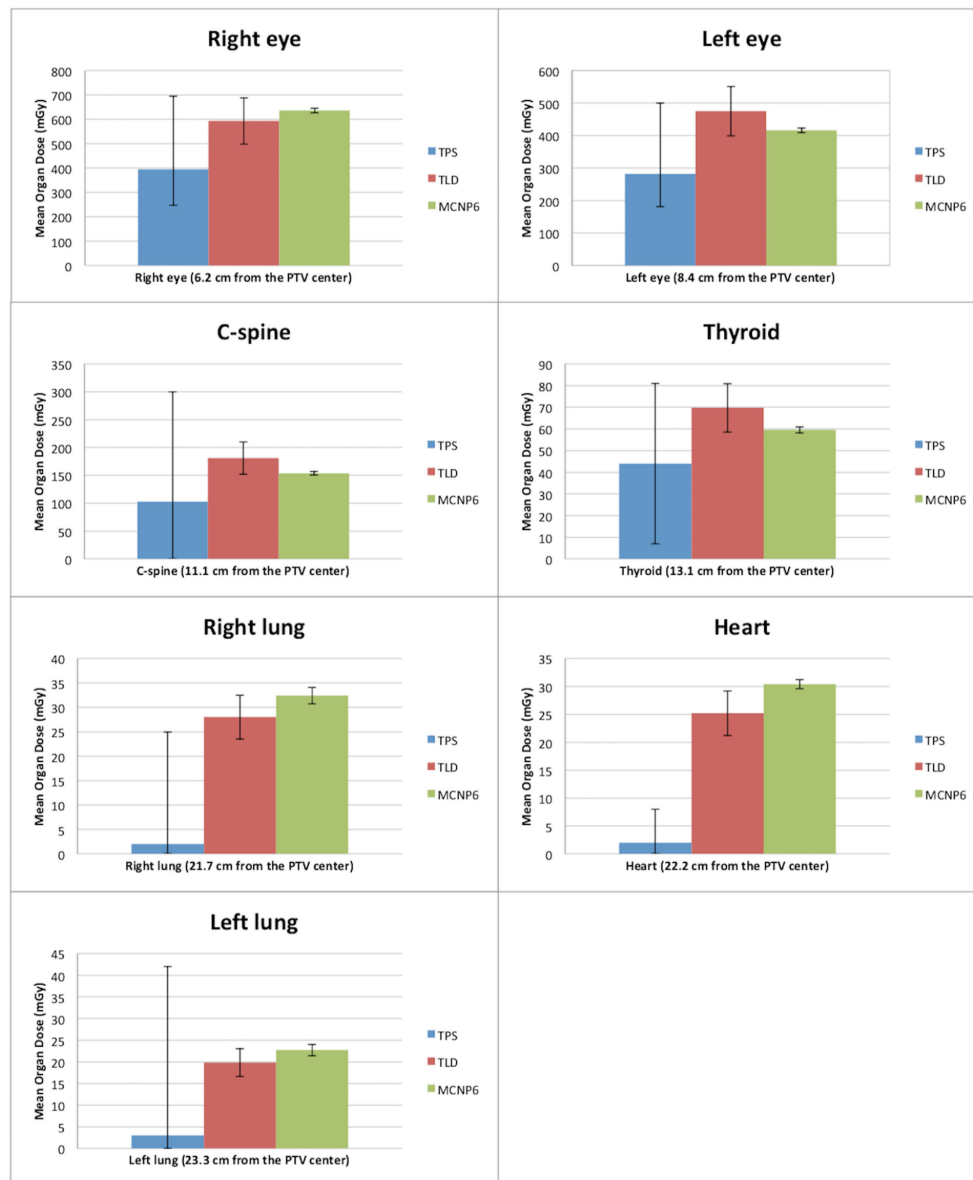


FIGURE 2

Comparison between doses outside the treatment fields obtained by TPS, TLDs, and MC for the 3DCRT technique. The error bars of the TPS dose calculations define the interval between the minimum and maximum calculated doses. The error bars of the measurements with the TLDs correspond to measurements of standard deviations. The error bars of the MC simulations correspond to the calculated uncertainty for each organ.

of-field doses with simulations in MC and measured doses with TLDs for the IMRT technique. It is observed that doses are about 1.1, 1.2, 1.1, 1.2, 1.1, and 1.1 higher with MC simulations, compared to TLD measurements, for the left eye, C-spine, thyroid, right lung, heart, and left lung, respectively. For the right eye, a higher dose was found with the TLDs in about 1.1 times, when compared to MC simulations.

In short, for the 3DCRT technique, the average relative dose difference between MC simulations and TLD

measurements is lower (14%) than the average relative dose difference between TPS-calculated dose values and TLD measurements (61%). For the IMRT technique, the average relative dose difference between MC simulations and TLD measurements is also lower (13%) than the average relative dose difference between TPS-calculated dose values and TLD measurements (74%). The agreement between TPS calculations and measurements is better for 3DCRT when compared with the IMRT technique, presumably due to a lower performance

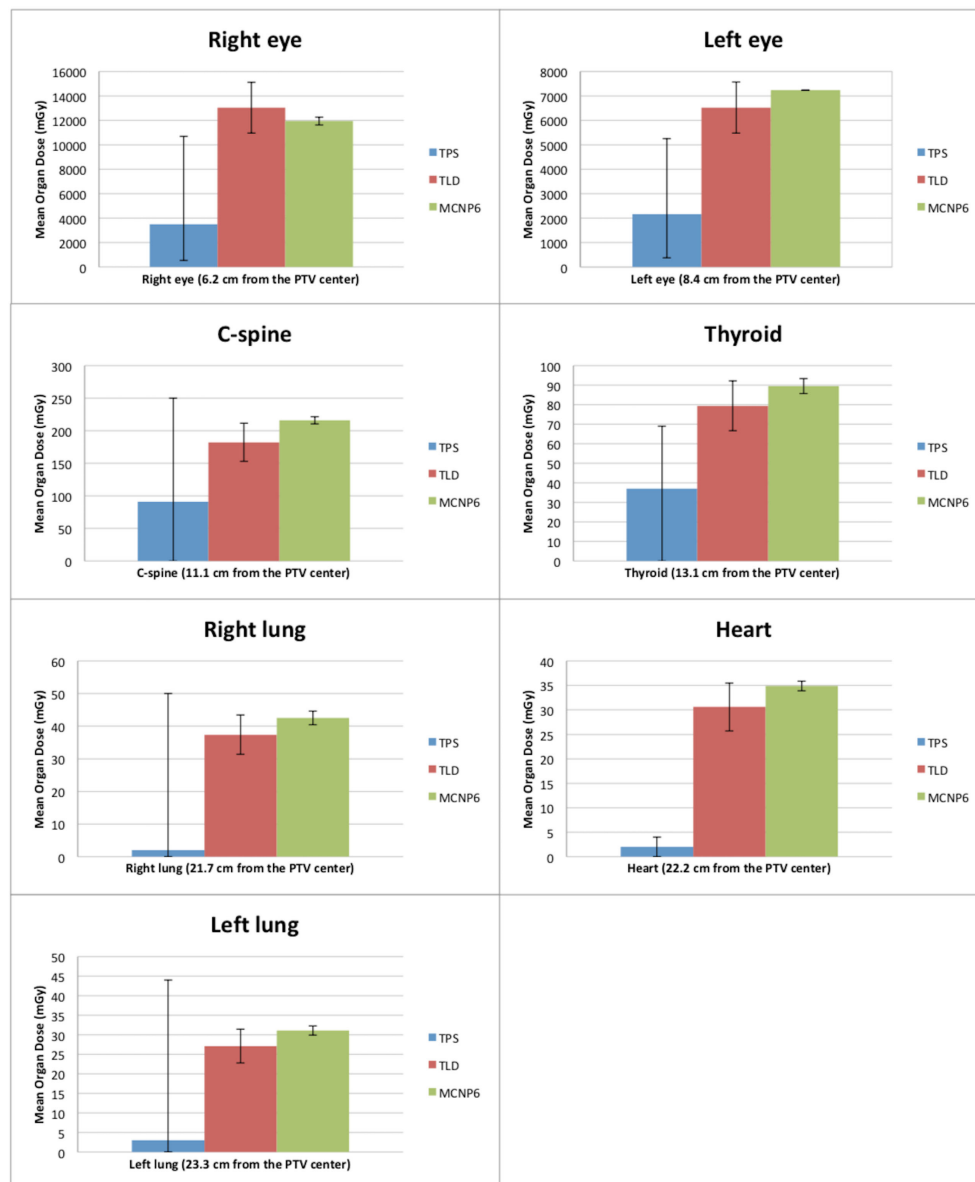


FIGURE 3

Comparison between doses outside the treatment fields obtained by TPS, TLDs, and MC for the IMRT technique. The error bars of the TPS dose calculations define the interval between the minimum and maximum calculated dose. The error bars of the measurements with the TLDs correspond to measurements of standard deviations. The error bars of the MC simulations correspond to the calculated uncertainty for each organ.

of the TPS calculation dose with the MLC movement in out-of-field regions.

Additionally, for organs at a distance up to 13 cm from the PTV, such as eyes, thyroid, and c-spine, a lower difference for MC vs. TLDs in comparison to a difference of TPS vs. TLDs was observed in all points. These dose differences are generally more pronounced for the organs further away (up to 23.3 cm) from the center of PTV, such as lungs and heart.

Discussion

Although there are other publications on this topic, our study presents several innovative points that differentiate it from others, such as the following: (i) This work is based on an MC-detailed model of a LINAC head and specifically an MLC, previously validated, rather than relying on a built-in LINAC library present in other MC calculation programs, as in a large

part of the studies presented in the literature. (ii) The movements of the different MLC leaves (in dynamic mode) were manually adjusted to each position of the treatment plan parameters in order to recreate a scenario closer to reality. (iii) The IMRT technique required a complex and new methodology to adjust all the parameters of the treatment plan to the computational pediatric phantom, namely, the different movements of the phantom in order to create the real movements of the treatment couch for each field. (iv) This study evaluates out-of-field doses with the IMRT technique by using measurements with TLDs, calculations with TPS, and calculations with MC methods for pediatric patients, and currently few studies in the literature combine these three approaches. In short, our study mimics an accurate and detailed MC model of a LINAC/MLC, a dose plan of a pediatric case using the IMRT technique with dynamic movement of the MLCs during irradiation, exhibiting a high degree of innovation and applied to a real scenario of clinical practice.

TPS dose calculations

The literature pinpoints that commercial TPSs are not suitable for correctly assessing and characterizing the doses in out-of-field locations, which receive low doses, i.e., doses below 5% of the total delivery dose (7, 9, 45–47). The results of this study are in agreement with previous studies, in which the out-of-field doses calculated by the TPS are systematically underestimated, when compared with MC simulations and TLD measurements (46, 48–50). Huang *et al.* were the first to evaluate the accuracy of the out-of-field doses using the Pinnacle (3) TPS for the IMRT technique (7). Huang *et al.* found that the TPS calculation significantly underestimated the out-of-field doses for both dynamic IMRT and step-and-shoot IMRT (7). In step-and-shoot IMRT, they obtained an underestimation by an average of 50%. Nonetheless, we should bear in mind the different dynamic IMRT treatment, TPS, and calculation algorithm used.

Our results report that the doses calculated by the TPS in the organs more distant from PTV (lungs and heart) are approximately the same for both 3DCRT and IMRT. Furthermore, in out-of-field organs closest to the PTV center, such as the eyes, the doses calculated by the TPS show higher values for the IMRT, when compared to the 3DCRT technique.

The lack of accuracy of the TPS calculation in organs outside and farther away from the treatment fields may be related to the dose discrepancies reported by TPS, which is probably due to the simplification of the AAA algorithm, which makes it faster and feasible in routine radiotherapy treatments. The dose in the eyes is higher, considering that these structures are closer to the field edge, when comparing to organs further away from PTV, such as the lungs and the heart. Howel *et al.* (46) also reported that as the

distance to the field boundary increases, the underestimation of the dose by the TPS also increases.

TLD measurements

Roger Harrison (51) points out that, in general, the out-of-field doses in radiotherapy vary in an extended range, between 10.0 and 60.0 Gy. For the 3DCRT technique, our study yielded out-of-field doses from 19.8 mGy to 593.0 mGy for measurements with TLDs. For the IMRT technique, out-of-field doses ranged from 27.0 to 13,041.0 mGy, for a total prescribed dose of 54.0 Gy in both techniques. These results should be considered with particular attention, as these are doses that could be delivered to pediatric patients and may increase the risk of development of a secondary cancer. The out-of-field measurements obtained in this study have a relative uncertainty of around 16% ($k = 1$) and were performed using an anthropomorphic physical pediatric phantom using TLDs. The work performed by Knežević *et al.* (32), reports a TLD uncertainty of $\approx 2.9\%$ for doses below 2 mGy and $\approx 4.2\%$ for doses below 2 mGy. This difference could be explained by the different approaches related to the calibration of the TLDs between the two studies, namely, in the reader calibration factor.

MC simulations

The MC simulations were extremely demanding, as well as innovative, since the movements of the MLCs were manually modified in the MLC/LINAC model script. Given the dynamic movement of the MLC, about 140 simulations of different leaf positions were performed. Therefore, part of the innovation of this study is related to the differentiation of manual adjustments in the beam geometry in order to represent more realistically and accurately all the geometry concerning the MLC movement that is required by the IMRT technique.

In this study, differences between dose simulation with MC and measurements with TLDs were obtained at up to 21.2% and 18.5% for the 3DCRT and IMRT techniques, respectively. In a recent study by Sánchez-Nieto *et al.* (52), dose differences outside treatment fields of up to about 20% were obtained between MC simulations and measurements with ionization chambers. These differences are also similar to those reported by Joosten *et al.* (47), Kry *et al.* (53), and Bednarz and Xu (34). On the one hand, in our study the differences between the 3DCRT and IMRT techniques could be explained by the MLC positioning approximations in order to mimic the dynamic IMRT treatment. In other words, in our MC model it was not possible to recreate a full IMRT treatment, as was possible with the 3DCRT treatment, due to the difficulty of not being able to move the leaves during the simulated irradiation. On the other hand, we have obtained discrepancies between measurements

and MC simulation between 13% and 14% that could be explained by the 15.8% uncertainty of the TLD measurements.

Comparison between TLD measurements, TPS, and MC simulations

The results of this study report the novel comparison between measurements and calculations in TPS and simulations of out-of-field doses, in a detailed MC model, mimicking the IMRT dose distributions in a computational phantom. The out-of-field doses for the IMRT technique were calculated for the first time, using MCNP6 and the pediatric computational voxel phantom combined with the Varian Clinac 2100 CD model, and also measured using TLDs placed in the pediatric physical phantom. For both TLD measurements and MC simulations, the IMRT technique yielded higher doses with respect to the IMRT technique. Although it is well known that TPSs are not commissioned to evaluate the out-of-field doses and our work verified an underestimation of these doses, an increasing underestimation with increasing distance from the treatment field edge was also verified. In our study, the organs located nearest to the PTV show lower relative differences with respect to TLD measurements or MC simulations, compared to organs located further away from the PTV. In organs nearest to the PTV such as the eyes, the TPS calculated the dose with the IMRT technique which is an order of magnitude higher than with the 3DCRT technique.

Some studies available in the literature report on measurements of out-of-field doses and compared them with doses calculated by TPS. Other researchers also used MC simulations to evaluate the out-of-field doses provided by the TPS software (2, 9). The findings of these studies vary and depend on the treatment modality and on the anatomical location of the target volumes (9). Joosten *et al.* found that in the first 10 cm outside the treatment fields, MC dose simulations are more accurate than those the dose calculations of commercial TPS (47). Our work reports that up to approximately 23 cm from the center of the target volume, the MC-based dose simulations produce more accurate results than the doses calculated by commercially available TPSs. The highest differences between phantom measurements and dose calculations were 20% for MC simulations and 179% for TPS calculations (47). Although our results report a large discrepancy between the dose calculation with the TPS and the dose measurement with the TLD, small discrepancies are found between dose simulation with MC and dose measurement with the TLDs.

Furthermore, in contrast to our results, Majer *et al.* show higher doses in the C-spine and thyroid for the 3DCRT technique when compared to the IMRT technique, both for measurements with TLDs and for dose calculations with TPS (54). We suggest that the differences between the results obtained in this study and the results

obtained by Majer *et al.* are due to the following. i) Differences in PTV locations and volumes: in Majer *et al.*'s (54) study, the PTV was spherical and located in the left-anterior side, and in our study the PTV was elliptical and located in the right-frontal side of the brain. ii) Different treatment plans: Majer *et al.* (54) performed an IMRT plan with nine coplanar fields and for 3DCRT three non-coplanar fields. We have performed an IMRT plan with seven coplanar fields and six non-coplanar fields for the 3DCRT technique. (iii) Different versions of the TPS: Majer *et al.* (54) performed the dose plans with Eclipse TPS version 8.6, and our study was performed with 13.0 version of the same TPS.

Beierholm *et al.* (48) conducted a study in which they measured the out-of-field doses in brain tumors in a pediatric phantom with TLDs, considering a prescribed dose of 54 Gy in 30 fractions. Beierholm *et al.* obtained for the thyroid a dose of 103.4 mGy with VMAT for a PTV smaller than 2 cm. Our results show that the thyroid was exposed to 69.7 and 79 mGy with 3DCRT and with IMRT, respectively. Although our work does not evaluate dose plans with VMAT, the MC model developed could be applied to VMAT treatments.

According to the literature, the out-of-field doses are higher using IMRT (8, 55), when compared to the 3DCRT technique. The doses obtained from our study support the literature because the doses for 3DCRT ranged from 20 to 590 mGy and the doses for IMRT ranged from 27 to 13,040 mGy.

According to Paganetti (11), about 50% of all second tumors seem to develop with doses delivered in tissues receiving less than 2,500 mGy (11). For the right eye, the obtained results by measurements of our study show that the IMRT technique yields doses about 13,040 mGy, for the left eye doses about 6,525 mGy, corroborating the concern about the out-of-field doses. These results may raise some concerns, as the dose tolerance tables for OARs only mention that the eyes should have a Dmax below 45–50 Gy (24, 25). Although our phantom has no eye lens, the findings of a recent study (56) showed a significantly higher cataract incidence in eyes that had received a maximum dose of 5 Gy in the eye lens. Additionally, the dose tolerance tables are created on the basis of retrospective results, always considering that the aim of radiotherapy treatment is to deliver the highest dose to the PTV and the lowest dose in the OARs. Tolerance doses in radiotherapy are not defined with special attention to the effects of low doses in the different organs and the individual risk analysis of developing secondary tumors after irradiation. Moreover, the authors of this study consider that for radiotherapy planning, there are organs/tissues further away and also close from the field edge that should be outlined, as OARs in order to consider possible side effects, especially relevant in pediatric patients.

In the present study, a specific and simplified clinical case of a tumor volume, defined in a phantom, was analyzed. However, the results in this study can be used by clinicians for better understanding of the possible risks that out-of-field doses carry, especially in pediatric patients.

Pediatric radiotherapy, second cancers—the way forward

In conclusion, despite the limitations of this study, namely, the simulation of a single scenario/tumor volume, the obtained results seem to indicate that out-of-field doses are higher with IMRT, compared to 3DCRT.

The obtained results indicate that out-of-field organs and tissue doses assessed in this work are of concern as they may presumably increase the risk of development of second tumors. It must, however, be emphasized that the decision on the type of radiotherapy treatment and modality should always be taken by the radiation oncologists, considering all the clinically relevant information about the patient.

Prospectively, on the basis of the methodology used, as well as the results obtained in this and other future studies, it will be possible to create an out-of-field dose database, which may have information from adult and pediatric patients. Such a database may improve radiotherapy treatment planning, as it allows the identification of dosimetric characteristics that may lead to higher out-of-field doses.

The methodology followed in this study, namely, the MC simulations combined with a Varian LINAC and pediatric phantom computational models, will allow the development of applications and tools that may benefit from individualized information, such as individualized dose assessment methodologies, retrospective dosimetric calculations for epidemiological studies, and radiological risk estimation models, to estimate the development of secondary cancers.

Summary

As widely described in the literature, dose measurements in a clinical environment lead to more realistic and detailed data on organ doses (54) in radiotherapy treatments and allow validation and benchmarking of doses calculated by TPS and simulated with MC methods. The results obtained in this study contribute to a better understanding of doses outside of treatment fields in pediatric patients, and these types of studies are scarce in the literature. Additionally, the present work combines, in a unique way, MC simulations, TPS calculations, and TLD measurements, using a pediatric voxel phantom segmented from CT images, the original pediatric physical phantom and a developed model of

the LINAC, which includes the MLC when IMRT is considered. Although in radiotherapy planning, doses outside the treatment fields in the order of cGy up to 2–3 Gy are often neglected, from the point of view of radiological protection and radiosensitivity, these doses cannot be ignored (2), especially for pediatric patients, because they can cause radiation-induced tumors in healthy organs and tissues.

Data availability statement

The datasets presented in this article are not readily available because we have a confidentiality agreement with Varian Medical Systems. Requests to access the datasets should be directed to AS, anacravosa@ctn.tecnico.ulisboa.pt.

Author contributions

AS, PA, and PV contributed to conception and design of the study. AS, AB, and TM performed the treatment plans and phantom irradiation. AS and BB perform the LINAC Monte Carlo model. AS wrote the first draft of the manuscript. PA, PV, AB, TM, and BB wrote sections of the manuscript. All authors contributed to manuscript revision, read, and approved the submitted version.

Conflict of interest

The authors declare that the research was conducted in the absence of any commercial or financial relationships that could be construed as a potential conflict of interest.

Publisher's note

All claims expressed in this article are solely those of the authors and do not necessarily represent those of their affiliated organizations, or those of the publisher, the editors and the reviewers. Any product that may be evaluated in this article, or claim that may be made by its manufacturer, is not guaranteed or endorsed by the publisher.

References

1. Schneider U. Modeling the risk of secondary malignancies after radiotherapy. *Genes (Basel)* (2011) 2(4):1033–49. doi: 10.3390/genes2041033
2. Taylor M, Kron T. Consideration of the radiation dose delivered away from the treatment field to patients in radiotherapy. *J Med Phys* (2011) 36(2):59. doi: 10.4103/0971-6203.79686
3. Cashmore J, Ramtohul M, Ford D. Lowering whole-body radiation doses in pediatric intensity-modulated radiotherapy through the use of unflattened photon beams. *Int J Radiat Oncol Biol Phys* (2011) 80(4):1220–7. doi: 10.1016/j.ijrobp.2010.10.002
4. Kry SF, Berdnarz B, Howell RM, Followill D, Klein E, Klein E, et al. AAPM TG 158: Measurement and Calculation of Doses Outside the Treated Volume from

External-Beam Radiation Therapy. *Med Phys* (2017) 44(10):e391–e429. doi: 10.1002/mp.12462

5. White P, Chan KC, Cheng KW, Chan KY, Chau MC. Volumetric intensity-modulated arc therapy vs conventional intensity-modulated radiation therapy in nasopharyngeal carcinoma: a dosimetric study. *J Radiat Res* (2013) 54(3):532–45. doi: 10.1093/jrr/rrs111
6. Mazonakis M, Berris T, Varveris C, Lyraraki E, Damilakis J. Out-of-field organ doses and associated radiogenic risks from para-aortic radiotherapy for testicular seminoma. *Med Phys* (2014) 41(5):051702. doi: 10.1118/1.4870376
7. Huang JY, Followill DS, Wang XA, Kry SF. Accuracy and sources of error of out-of-field dose calculations by a commercial treatment planning system for intensity-modulated radiation therapy treatments. *J Appl Clin Med Phys* (2013) 14(2):186–97. doi: 10.1120/jacmp.v14i2.4139
8. Harrison RM. Introduction to dosimetry and risk estimation of second cancer induction following radiotherapy. *Radiat Meas* (2013) 57:1–8. doi: 10.1016/j.radmeas.2013.01.018
9. Wang L, Ding GX. The accuracy of the out-of-field dose calculations using a model based algorithm in a commercial treatment planning system. *Phys Med Biol* (2014) 59(13):N113–28. doi: 10.1088/0031-9155/59/13/N113
10. Athar BS, Bednarz B, Seco J, Hancox C, Paganetti H. Comparison of out-of-field photon doses in 6 MV IMRT and neutron doses in proton therapy for adult and pediatric patients. *Phys Med Biol* (2010) 55(10):2879–91. doi: 10.1088/0031-9155/55/10/006
11. Paganetti H, Athar BS, Moteabbed M, A Adams J, Schneider U, Yock TI. Assessment of radiation-induced second cancer risks in proton therapy and IMRT for organs inside the primary radiation field. *Phys Med Biol* (2012) 57(19):6047–61. doi: 10.1088/0031-9155/57/19/6047
12. Kumar S. Second malignant neoplasms following radiotherapy. *Int J Environ Res Public Health* (2012) 9(12):4744–59. doi: 10.3390/ijerph9124744
13. Olch AJ. *Pediatric radiotherapy: Planning and treatment*. Boca Raton, FL: Taylor and Francis (2013).
14. National Council on Radiation Protection and Measurements. *Limitation of exposure to ionizing Radiation: Recommendations of the national council on radiation protection and measurements*. NCRP (1993).
15. Paganetti H. Applications to secondary radiation dosimetry in external beam radiation therapy. In: XG Xu, KF Eckerman, editors. *Handbook of anatomical models for radiation dosimetry*. Boca Raton, FL: Taylor and Francis (2010). p. 567–89.
16. Ruben JD, Lancaster CM, Jones P, Smith RL. A comparison of out-of-field dose and its constituent components for intensity-modulated radiation therapy versus conformal radiation therapy: Implications for carcinogenesis. *Int J Radiat Oncol Biol Phys* (2011) 81(5):1458–64. doi: 10.1016/j.ijrobp.2010.08.008
17. Kinkhikar R, Gamre P, Kadam S, Tambe C, Biju G, Suryaprakash, et al. Peripheral dose measurements with diode and thermoluminescence dosimeters for intensity modulated radiotherapy delivered with conventional and un-conventional linear accelerator. *J Med Phys* (2013) 38(1):4. doi: 10.4103/0971-6203.106599
18. Majer M, Ambrožová I, Davidková M, De Saint-Hubert M, Kasabašić M, Knežević Z, et al. Out-of-field doses in pediatric craniospinal irradiations with 3D-CRT, VMAT, and scanning proton radiotherapy: A phantom study. *Med Phys* (2022) 49(4):2672–83. doi: 10.1002/mp.15493
19. Colnot J, Zefkili S, Gschwind R, Huet C. Out-of-field doses from radiotherapy using photon beams: A comparative study for a pediatric renal treatment. *J Appl Clin Med Phys* (2021) 22(3):94–106. doi: 10.1002/acm2.13182
20. Cravo Sá A, Barateiro A, Bednarz B, Borges C, Pereira J, Baptista M, et al. Assessment of out-of-field doses in radiotherapy treatments of paediatric patients using Monte Carlo methods and measurements. *Phys Med* (2020) 71:53–61. doi: 10.1016/j.ejmp.2020.02.008
21. Emami B. Tolerance of normal tissue to therapeutic radiation. *Rep Radiother Oncol* (2013) 1(1):35–48.
22. Marks LB, Yorke ED, Jackson A, Haken RKT, Constine LS, Eisbruch A, et al. Use of normal tissue complication probability models in the clinic. *Int J Radiat Oncol* (2010) 76(3):S10–9. doi: 10.1016/j.ijrobp.2009.07.1754
23. Brodin NP, Tomé WA. Revisiting the dose constraints for head and neck OARs in the current era of IMRT. *Oral Oncol* (2018) 86:8–18. doi: 10.1016/j.oraloncology.2018.08.018
24. Yamazaki H, Shiomi H, Tsubokura T, Kodani N, Nishimura T, Aibe N, et al. Quantitative assessment of inter-observer variability in target volume delineation on stereotactic radiotherapy treatment for pituitary adenoma and meningioma near optic tract. *Radiat Oncol* (2011) 6(1):10. doi: 10.1186/1748-717X-6-10
25. Shaffer R, Nichol AM, Vollans E, Fong M, Nakano S, Moiseenko V, et al. A comparison of volumetric modulated arc therapy and conventional intensity-modulated radiotherapy for frontal and temporal high-grade gliomas. *Int J Radiat Oncol* (2010) 76(4):1177–84. doi: 10.1016/j.ijrobp.2009.03.013
26. Pereira J, Pereira MF, Rangel S, Saraiva M, Santos LM, Cardoso JV, et al. Fading effect of LiF:Mg,Ti and LiF:Mg,Cu,P ext-rad and whole-body detectors. *Radiat Prot Dosimetry* (2016) 170(1–4):177–80. doi: 10.1093/rpd/ncv445
27. Baptista M, Di Maria S, Vieira S, Pereira J, Pereira M, Vaz P. Organ dose measurements using an adult anthropomorphic phantom and risk estimation of cancer incidence from CBCT exposures. *Radiat Phys Chem* (2020) 171:108715. doi: 10.1016/j.radphyschem.2020.108715
28. Kry SF, Alvarez P, Cygler JE, DeWerd LA, Howell RM, Meeks S, et al. AAPM TG 191: Clinical use of luminescent dosimeters: TLDs and OSLDs. *Med Phys* (2020) 47(2):19–51. doi: 10.1002/mp.13839
29. Hubbell J, Seltzer S. *X-Ray mass attenuation coefficients*. NIST. Gaithersburg, MD (2004).
30. JCGM. *Evaluation of measurement data - guide to expression of uncertainty in measurement*. Sèvres, France: Sevres (2008).
31. A Darafsheh ed. *Radiation therapy dosimetry - a practical handbook. first*. Boca Raton: CRC Press - Taylor and Francis Group (2021).
32. K Ž, Stolarczyk L, Bessieres I, Bordy JM, Miljanić S, Olko P. Photon dosimetry methods outside the target volume in radiation therapy: Optically stimulated luminescence (OSL), thermoluminescence (TL) and radiophotoluminescence (RPL) dosimetry. *Radiat Meas* (2013) 57:9–18. doi: 10.1016/j.radmeas.2013.03.004
33. Pelowitz DB, Goorley JT, James MR, Booth TE, Brown FB, Bull JS, et al. *Mcn6 user [[A s manual*. Los Alamos, NM: Los Alamos National Laboratory (2013).
34. Bednarz B, Xu XG. Monte Carlo Modeling of a 6 and 18 MV Varian clinac medical accelerator for in-field and out-of-field dose calculations: development and validation. *Phys Med Biol* (2009) 54(4):N43–57. doi: 10.1088/0031-9155/54/4/N01
35. Sawkey DL, Faddegon BA. Determination of electron energy, spectral width, and beam divergence at the exit window for clinical megavoltage x-ray beams. *Med Phys* (2009) 36(3):698–707. doi: 10.1118/1.3070547
36. Dössel O, Schlegel WC. Updated beam parameters for Monte Carlo simulation of five Varian megavoltage. *IFMBE Proc* (2009) 25:1067–70. doi: 10.1007/978-3-642-03474-9_300
37. Cho SH, Vassiliev ON, Lee S, Liu HH, Ibbott GS, Mohan R. Reference photon dosimetry data and reference phase space data for the 6MV photon beam from Varian clinac 2100 series linear accelerators. *Med Phys* (2004) 32(1):137–48. doi: 10.1118/1.1829172
38. Keall PJ, Siebers JV, Libby B, Mohan R. Determining the incident electron fluence for Monte Carlo-based photon treatment planning using a standard measured data set. *Med Phys* (2003) 30(4):574–82. doi: 10.1118/1.1561623
39. Sheikh-Bagheri D, Rogers DWO. Monte Carlo Calculation of nine megavoltage photon beam spectra using the BEAM code. *Med Phys* (2002) 29(3):391–402. doi: 10.1118/1.1445413
40. Borges C, Zarza-Moreno M, Heath E, Teixeira N, Vaz P. Monte Carlo Modeling and simulations of the high definition (HD120) micro MLC and validation against measurements for a 6 MV beam. *Med Phys* (2012) 39(1):415–23. doi: 10.1118/1.3671935
41. Rogers DWO. AAPM task group report no. 105: Issues associated with clinical implementation of Monte Carlo - based photon and electron external beam treatment planning. *Med Phys* (2006) 105(1):7. doi: 10.1118/1.2795842
42. Jaffray DA, Battista JJ, Fenster A, Munro P. X-Ray sources of medical linear accelerators: Focal and extra-focal radiation. *Med Phys* (1993) 20(5):1417–27. doi: 10.1118/1.597106
43. Bencheikh M, Maghnouj A, Tajmouati J. Validation of Monte Carlo simulation of 6 MV photon beam produced by Varian clinac 2100 linear accelerator using BEAMnrc code and DOSXYZnrc code 1. *Phys Part Nucl Lett* (2017) 14(5):780–7. doi: 10.1134/S154747711705003X
44. Verhaegen F. Monte Carlo Modeling of external photon beams in radiotherapy. In: *Monte Carlo Techniques in radiation therapy*. CRC Press, Taylor & Francis Group (2013). p. 63–86.
45. Yoon J, Heins D, Zhao X, Sanders M, Zhang R. Measurement and modeling of out-of-field doses from various advanced post-mastectomy radiotherapy techniques. *Phys Med Biol* (2017) 62(23):9039–53. doi: 10.1088/1361-6560/aa94b5
46. Howell RM, Scarboro SB, Kry SF, Yaldo DZ. Accuracy of out-of-field dose calculations by a commercial treatment planning system. *Phys Med Biol* (2010) 55(23):6999–7008. doi: 10.1088/0031-9155/55/23/S03
47. Bochud F, Baechler S, Levi F, Mirimanoff R-O, Moeckli R. Variability of a peripheral dose among various linac geometries for second cancer risk assessment. *Phys Med Biol* (2011) 56:5131–51. doi: 10.1088/0031-9155/56/16/004
48. Beierholm AR, Nygaard DE, Juhl EL, Hansen R, Hansen J. Evaluating out-of-field doses during radiotherapy of paediatric brain tumours using lead shielding and flattening-filter free beams. *Phys Med* (2019) 60:1–6. doi: 10.1016/j.ejmp.2019.03.008

49. Shine N, Paramu R, Gopinath M, Jaon Bos R, Jayadevan P. Out-of-field dose calculation by a commercial treatment planning system and comparison by monte carlo simulation for varian TrueBeam[®]. *J Med Phys* (2019) 44(3):156. doi: 10.4103/jmp.JMP_82_18
50. Wang L, Ding GX. Estimating the uncertainty of calculated out-of-field organ dose from a commercial treatment planning system. *J Appl Clin Med Phys* (2018) 19(4):319–24. doi: 10.1002/acm2.12367
51. Harrison R. Out-of-field doses in radiotherapy: Input to epidemiological studies and dose-risk models. *Phys Med* (2017) 42:239–46. doi: 10.1016/j.ejmp.2017.02.001
52. Sánchez-Nieto B, Medina-Ascanio KN, Rodríguez-Mongua JL, Doerner E, Espinoza I. Study of out-of-field dose in photon radiotherapy: A commercial treatment planning system versus measurements and Monte Carlo simulations. *Med Phys* (2020) 47(9):4616–25. doi: 10.1002/mp.14356
53. Kry SF, Titt U, Followill D, Vassiliev ON, White RA, Stovall M, et al. A Monte Carlo model for out-of-field dose calculation from high-energy photon therapy. *Med Phys* (2007) 34(9):3489–99. doi: 10.1118/1.2756940
54. Majer M, Stolarczyk L, De Saint-Hubert M, Kabat D, Knežević Ž, Miljanić S, et al. Out-of-field dose measurements for 3d conformal and intensity modulated radiotherapy of a paediatric brain tumour. *Radiat Prot Dosimetry* (2017) 176(3):331–40. doi: 10.1093/rpd/ncx015
55. Paganetti H. Assessment of the risk for developing a second malignancy from scattered and secondary radiation in radiation therapy. *Health Phys* (2012) 103(5):652–61. doi: 10.1097/HP.0b013e318261113d
56. Nuzzi R, Trossarelo M, Bartoncini S, Marolo P, Franco P, Mantovani C, et al. Ocular complications after radiation therapy: An observational study. *Clin Ophthalmol* (2020) 14:3153–66. doi: 10.2147/OPTH.S263291



OPEN ACCESS

EDITED BY

Valdir Carlos Colussi,
University Hospitals Cleveland Medical
Center, United States

REVIEWED BY

Chris Allgower,
United States Department of Veterans
Affairs, United States
Sunyoung Jang,
Princeton Radiation Oncology Center,
United States

*CORRESPONDENCE

Olivier Van Hoey
ovhoey@scckcen.be

SPECIALTY SECTION

This article was submitted to
Radiation Oncology,
a section of the journal
Frontiers in Oncology

RECEIVED 24 March 2022

ACCEPTED 07 July 2022

PUBLISHED 08 September 2022

CITATION

Van Hoey O, Stolarczyk L, Lillhök J,
Eliasson L, Mojzeszek N, Liszka M,
Alkhiat A, Mares V, Trompier F,
Trinkl S, Martínez-Rovira I,
Romero-Expósito M, Domingo C,
Ploc O, Harrison R and Olko P (2022)
Simulation and experimental
verification of ambient neutron doses
in a pencil beam scanning proton
therapy room as a function of
treatment plan parameters.
Front. Oncol. 12:903537.
doi: 10.3389/fonc.2022.903537

COPYRIGHT

© 2022 Van Hoey, Stolarczyk, Lillhök,
Eliasson, Mojzeszek, Liszka, Alkhiat,
Mares, Trompier, Trinkl, Martínez-Rovira,
Romero-Expósito, Domingo, Ploc,
Harrison and Olko. This is an open-
access article distributed under the
terms of the [Creative Commons
Attribution License \(CC BY\)](https://creativecommons.org/licenses/by/4.0/). The use,
distribution or reproduction in other
forums is permitted, provided the
original author(s) and the copyright
owner(s) are credited and that the
original publication in this journal is
cited, in accordance with accepted
academic practice. No use,
distribution or reproduction is
permitted which does not comply with
these terms.

Simulation and experimental verification of ambient neutron doses in a pencil beam scanning proton therapy room as a function of treatment plan parameters

Olivier Van Hoey^{1*}, Liliana Stolarczyk^{2,3,4}, Jan Lillhök⁵,
Linda Eliasson⁶, Natalia Mojzeszek³, Malgorzata Liszka^{3,4},
Ali Alkhiat^{4,7}, Vladimir Mares⁸, François Trompier⁹,
Sebastian Trinkl^{8,10}, Immaculada Martínez-Rovira¹¹,
Maite Romero-Expósito¹¹, Carles Domingo¹¹, Ondrej Ploc¹²,
Roger Harrison¹³ and Pawel Olko³

¹Belgian Nuclear Research Center (SCK CEN), Institute for Environment, Health and Safety (EHS), Mol, Belgium, ²Danish Centre for Particle Therapy, Aarhus University Hospital (AUH), Aarhus, Denmark, ³Institute of Nuclear Physics, Polish Academy of Sciences, (IFJ PAN), Krakow, Poland, ⁴The Skandion Clinic, Uppsala, Sweden, ⁵Swedish Radiation Safety Authority, Solna, Sweden, ⁶Department of Physics, Royal Institute of Technology (KTH), Stockholm, Sweden, ⁷Department of Medical Radiation Physics and Nuclear Medicine, Karolinska University Hospital, Stockholm, Sweden, ⁸Helmholtz Zentrum München, Institute of Radiation Medicine, Neuherberg, Germany, ⁹Institut de Radioprotection et de Sécurité Nucléaire (IRSN), PSE-Santé, Fontenay-aux-Roses, France, ¹⁰Federal Office for Radiation Protection, Neuherberg, Germany, ¹¹Departament de Física, Universitat Autònoma de Barcelona, Bellaterra, Spain, ¹²Department of Radiation Dosimetry, Nuclear Physics Institute of the Czech Academy of Sciences (CAS), Prague, Czechia, ¹³Faculty of Medical Sciences, University of Newcastle upon Tyne, Newcastle Upon Tyne, United Kingdom

Out-of-field patient doses in proton therapy are dominated by neutrons. Currently, they are not taken into account by treatment planning systems. There is an increasing need to include out-of-field doses in the dose calculation, especially when treating children, pregnant patients, and patients with implants. In response to this demand, this work presents the first steps towards a tool for the prediction of out-of-field neutron doses in pencil beam scanning proton therapy facilities. As a first step, a general Monte Carlo radiation transport model for simulation of out-of-field neutron doses was set up and successfully verified by comparison of simulated and measured ambient neutron dose equivalent and neutron fluence energy spectra around a solid water phantom irradiated with a variation of different treatment plan parameters. Simulations with the verified model enabled a detailed study of the variation of the neutron ambient dose equivalent with field size, range, modulation width, use of a range shifter, and position inside the treatment room. For future work, it is planned to use this verified model to simulate out-of-field neutron doses inside the phantom and to verify the simulation results by comparison with previous in-phantom measurement campaigns.

Eventually, these verified simulations will be used to build a library and a corresponding tool to allow assessment of out-of-field neutron doses at pencil beam scanning proton therapy facilities.

KEYWORDS

Proton therapy, Pencil beam scanned proton therapy, Neutron doses, Monte Carlo simulations, Out-of-field neutron doses in radiation therapy, Neutron measurements

1 Introduction

One of the biggest challenges in radiotherapy is to maximize tumor damage, while sparing healthy tissues in order to minimize detrimental effects in these healthy tissues. With proton therapy, the radiation energy can be deposited more locally in the tumor in comparison with photon therapy. This leads to improved healthy tissue sparing (1). Therefore, the use of proton therapy has been increasing rapidly over the last decades with now over 100 active proton therapy facilities and over 250,000 patients treated worldwide (2).

However, despite the improved healthy tissue sparing, there is still some dose deposited in healthy tissues due to secondary and scattered radiation. The out-of-field doses in proton therapy are dominated close to the target by secondary protons and further away from the target by secondary neutrons and gamma radiation created by interactions of protons with the beamline, the patient, and the room. These out-of-field doses can lead to detrimental effects in healthy tissues and should be considered and possibly minimized during the treatment planning.

Several studies have already characterized the out-of-field neutron doses in proton therapy for some specific cases using Monte Carlo (MC) radiation transport simulations, measurements, or analytical models (3, 4). However, it is not straightforward to compare neutron doses in the literature and to estimate the neutron dose for a specific patient based on these studies due to the strong dependence of the neutron dose on the treatment plan parameters. The typical normalization of the out-of-field neutron doses to the absorbed dose in the target or the product of absorbed dose in the target and the treatment volume is not sufficient to allow direct comparison of out-of-field doses from different studies. Moreover, current treatment planning systems (TPS) do not take into account out-of-field neutron doses. However, there is an increasing need to include out-of-field neutron doses in the TPS, especially when treating children, pregnant patients, and patients with implants such as pacemakers or hearing implants.

In response to this demand, within EURADOS WG9, a dedicated task was set up. This task has the final aim to provide an easy-to-use tool to quickly assess the out-of-field neutron

doses in proton therapy as a function of position with respect to the isocenter and the beam direction and the most critical treatment plan parameters such as field size, range, modulation width, use of a range shifter, and air gap between the range shifter and patient. This task focuses on active pencil beam scanning (PBS) proton therapy systems, as these systems are now becoming standard in proton therapy (2) and limit the out-of-field neutron doses by avoiding significant creation of secondary neutrons in the proton delivery system. This task will lead to a better understanding of the relation between the out-of-field neutron doses and the treatment plan parameters and allow medical physicists to evaluate and, if necessary, adapt the treatment plan also with respect to the out-of-field neutron doses and associated detrimental effects. In the end, this will contribute to improving the patient's life expectancy and life quality.

This work presents the first steps that were performed within this task. An MC radiation transport simulation model was set up to simulate secondary radiation production and transport during patient treatment in PBS proton therapy facilities. For verification of the MC model, the neutron doses simulated outside an irradiated phantom were compared with ambient neutron monitor measurements at different positions close to the phantom for varying treatment plan parameters at two PBS proton therapy facilities. The goals of this study were to verify the MC model and to investigate the variation of the ambient neutron doses as a function of position, field size, range, modulation width, use of a range shifter, and air gap between the range shifter and phantom.

2 Materials and methods

2.1 Measurements

2.1.1 Proton therapy facilities

For verification of the MC simulations, measurements were performed at two PBS proton therapy facilities. A first exploratory measurement campaign was performed at the Bronowice Cyclotron Center (CCB) Institute of Nuclear

Physics (IFJ PAN) in Krakow (Poland) in May 2017. Based on the experience from this measurement campaign, a second more extensive measurement campaign was performed at the Skandion Clinic in Uppsala (Sweden) in July 2019. Both facilities are equipped with gantries with a dedicated scanning nozzle (IBA Proton Therapy System – Proteus 235). The range shifter at CCB is fixed at the nozzle, whereas at Skandion, it can be moved on the snout toward the patient.

2.1.2 Experimental setup

During both measurement campaigns, rectangular target volumes were delivered from the side with the nozzle at 270° to a 30 cm × 30 cm × 60 cm solid water phantom placed on the treatment table. The isocenter was positioned at 15 cm depth in the phantom and at 15 cm from top, bottom, and the three closest side faces of the phantom. The setup was similar to that described in (5). Treatment plans were prepared using Varian Eclipse treatment planning systems (version 13.6 and 15.6 in CCB IFJ PAN and Skandion, respectively). Plan variables included field size, range, Spread Out Bragg Peak (SOBP) modulation width, use of a range shifter, and air gap between the range shifter and solid water phantom. The dose delivered to the center of the SOBP for each irradiation was 20 Gy in CCB IFJ PAN and 5 Gy in Skandion. An overview of the covered plans for both measurement campaigns is shown in Table 1. Data for irradiations with the range shifter are presented in this work only for the Skandion proton therapy facility. To obtain the prescribed range and modulation width, for each plan, a set of proton energies was used. Minimal and maximal proton energies are also given in Table 1.

Six ambient neutron monitors were positioned around the solid water phantom at six fixed positions labeled A–F. A schematic representation and pictures of the setup and the measurement positions at both facilities are shown in Figure 1.

2.1.3 Ambient neutron monitors

The MC simulations were verified by measurements with ambient neutron monitors during the measurement campaigns at Skandion and CCB. Ambient neutron monitors measure the neutron dose in terms of the quantity ambient dose equivalent $H^*(10)$. This quantity, as defined in (6), is a measurable operational quantity that provides a conservative estimate of the

radiation protection quantity effective dose. Due to limitations in experimental time and ambient neutron monitor availability, it was not possible to use the same type of ambient neutron monitor at all six positions. However, the specific aspects and uncertainties of each monitor were taken into account in the data analysis. Therefore, different types of ambient neutron monitors from the different institutes participating in the measurement campaigns were used. However, each ambient neutron monitor was kept at a fixed position throughout the whole measurement campaign. The institute and type of the ambient neutron monitors used at the six measurement positions in Skandion and CCB are listed in Table 2. On the second and third lines in Table 2, also the manufacturer and the calibration date and source are specified for each monitor. All calibrations were still valid at the time of the measurement campaigns according to the calibration procedures of the respective institutes.

A very important characteristic of ambient neutron monitors is their energy response in terms of $H^*(10)$. Ideally, the $H^*(10)$ energy response should be close to unity for all possible neutron energies. However, in practice, no existing ambient neutron monitor has a perfect energy response for the wide range of possible neutron energies. This has to be taken into account when analyzing the measurement results and comparing them with the MC simulations. The different ambient neutron monitors are described in detail below. The $H^*(10)$ energy response functions are compared in Figure 2. Where necessary, they were normalized taking into account the energy spectrum of ^{252}Cf or Am-Be neutrons used during the calibration. For HAWK, these response data are obtained from measurements, while for the other monitors, the response data are obtained from simulations.

Neutron energy spectra at proton therapy facilities typically exhibit peaks for thermal, evaporation, and high-energy neutrons (11). The energy spectra of ^{252}Cf or Am-Be neutrons fall in the same energy range as the evaporation neutrons. The energy ranges of these peaks are indicated in Figure 2.

Figure 2 shows that the energy response is close to unity for all monitors in the evaporation neutron energy range. This is expected because they are calibrated with ^{252}Cf or Am-Be neutrons in the same energy range. In the other energy ranges there are significant deviations from unity and also significant differences between the different monitors.

TABLE 1 Overview of covered treatment plans during the measurement campaigns at the CCB IFJ PAN and Skandion proton therapy facilities with PBS.

Center	Range shifter (RS)	Air gap RS-phantom [cm]	Field size [cm ²]	Proton energies [MeV]	Range [cm]	SOBP modulation width [cm]
CCB IFJ PAN (Krakow, Poland)	–	–	25–400	Min: 74–148 Max: 146–192	15–25	10–20
Skandion Clinic (Uppsala, Sweden)	3.1 cm WET Lexan on movable snout	5.5–23	9–625	Min: 65–103 Max: 103–212	8–25	3–25

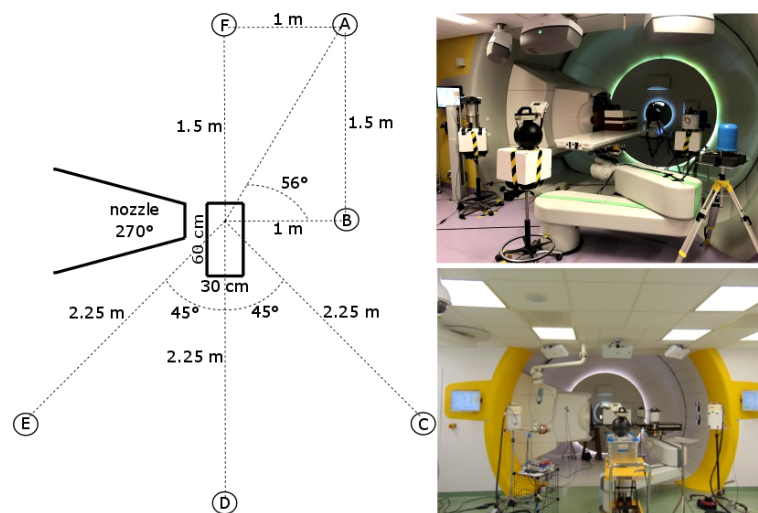


FIGURE 1

Schematic representation of the setup and the measurement positions (left), picture of the measurements at Skandion (right top), and picture of the measurements at CCB (right bottom).

One can see in Figure 2 that in the thermal energy range, the ambient neutron monitors exhibit an under-response between a factor of two and five. It can also be seen in Figure 2 that conventional ambient neutron monitors such as LB 6411, Wendi-II, NM2B-495Pb, and NM2B-458 exhibit a typical over-response in the epithermal energy range related to the very strong thermalization of epithermal neutrons in their moderator sphere. On the other hand, Tissue Equivalent Proportional Counters (TEPCs) such as Sievert have an under-response in the epithermal energy range due to lower backscattering in the gas volume in comparison with the ICRU sphere in the definition of $H^*(10)$. A similar under-response is expected for HAWK, but no response data are

available in the epithermal energy range. However, neutrons in the thermal and epithermal energy range are not expected to contribute more than a few percent to the neutron $H^*(10)$ in proton therapy treatment rooms (12). Therefore, the under-response in the thermal neutron range and the over-response and under-response of respectively conventional ambient neutron monitors and TEPCs in the epithermal neutron range are not expected to affect the measurements significantly.

Finally, one can observe in Figure 2 that the $H^*(10)$ energy response of LB 6411 and NM2B-458 drops to zero above 10–20 MeV due to their very limited sensitivity for high-energy neutrons. The sensitivity is increased for Wendi-II and NM2B-495Pb by an additional metallic shield embedded in the

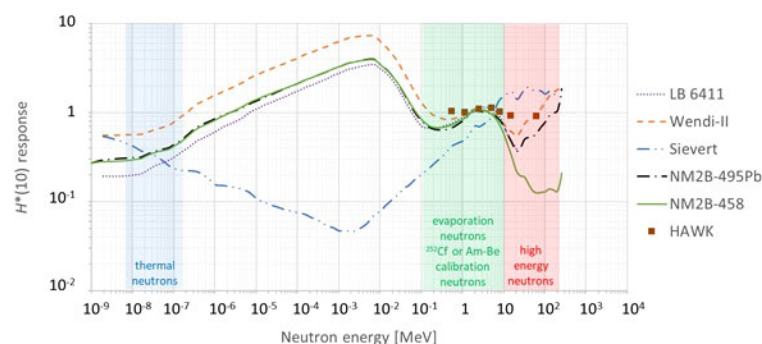


FIGURE 2

Plot with the simulated (lines) or measured (data points) $H^*(10)$ energy response functions of the different ambient neutron monitors used during the measurement campaigns at Skandion and CCB [LB 6411 (7), Wendi-II (8), Sievert [this work], NM2B-495Pb and NM2B-458 (9), HAWK (10)].

TABLE 2 Ambient neutron monitors used at the different positions at Skandion and CCB.

Position	Skandion July 2019	CCB May 2017
A	SSM Sievert SSM, Stockholm, Sweden Calibration: 09-2018, ²⁵² Cf and Am-Be	CCB Wendi-II Thermo Scientific, Waltham, USA Calibration: 06-2016, ²⁵² Cf and Pu-Be
B	SCK CEN Wendi-II Thermo Scientific, Waltham, USA Calibration: 05-2018, ²⁵² Cf	SCK CEN Wendi-II Thermo Scientific, Waltham, USA Calibration: 11-2015, ²⁵² Cf
C	SSM Sievert SSM, Stockholm, Sweden Calibration: 09-2018, ²⁵² Cf and Am-Be	HMGU NM2B-495Pb NE Technology Ltd., Benham, UK Calibration: 03-2017, Am-Be
D	Skandion LB 6411 Berthold, Bad Wildbad, Germany Calibration: 08-2013, Am-Be	UAB LB 6411 Berthold, Bad Wildbad, Germany Calibration: 06-2010, Am-Be
E	IRSN HAWK Far West Technologies, Puyallup, USA Calibration: 06-2019, Am-Be	HMGU NM2B-458 NE Technology Ltd., Benham, UK Calibration: 03-2017, Am-Be
F	SSM LB 6411 Berthold, Bad Wildbad, Germany Calibration: 09-2018, ²⁵² Cf and Am-Be	NPI LB 6411 Berthold, Bad Wildbad, Germany Calibration: 10-2014, Am-Be

SSM, Swedish Radiation Safety Authority, Stockholm, Sweden.

SCK CEN, Belgian Nuclear Research Center SCK CEN, Mol, Belgium.

Skandion, Skandionkliniken, Uppsala, Sweden.

IRSN, Institut de Radioprotection et de Sécurité Nucléaire, Fontenay-aux-Roses, France.

CCB, Bronowice Cyclotron Center IFJ PAN, Krakow Poland.

HMGU, Helmholtz Zentrum München, Munich, Germany.

UAB, Universitat Autònoma de Barcelona, Departament de Física, Cerdanyola del Vallès, Spain.

NPI, CAS, Nuclear Physics Institute, Prague, Czech Republic.

moderator. However, even for these monitors, there is still a limited under-response for high-energy neutrons. TEPCs such as Sievert and HAWK are intrinsically sensitive for high-energy neutrons. However, for Sievert, one can see that there is a limited over-response for high-energy neutrons. As high-energy neutrons can deliver a large fraction of the neutron dose in proton therapy rooms (12), the under-response and over-response of the ambient neutron monitors for high-energy neutrons is expected to affect the measurement results significantly. This will be discussed in detail in Sections 3.1.1.4 and 3.2.2.

2.1.3.1 Sievert

The two Sievert instruments used by SSM are TEPCs, made of A-150 plastic and filled with a propane-based tissue-equivalent gas held at 1.37 kPa pressure, simulating a tissue volume with a mean chord length of 1.88 μm . The sensitive volume is 1.207 dm³, with 11.5 cm for both height and diameter. The electric charge is measured using a capacitor feedback electrometer, where the voltage over a 1-nF capacitor is measured over a charge collection time of 0.1 s (13).

The average absorbed dose during a charge collection time is given by

$$\bar{D}_{det} = \frac{\bar{q}W/e}{M m_{det}}$$

where \bar{q} is the mean collected charge during the time interval, W/e is the average energy required to create an ion pair, M is the gas multiplication factor, and m_{det} the mass of the detector gas mass

The dose-mean lineal energy is calculated using the variance method

$$\bar{y}_D = \frac{m_{det}}{\bar{l}} \frac{V_{D,rel}}{\bar{D}_{det}}$$

where $V_{D,rel}$ is the relative variance in the absorbed dose during repeated charge integrations and \bar{l} is the mean chord length of the simulated tissue volume

The dose equivalent H^* is in turn determined by

$$H^* = \bar{D}_{det} (a + b\bar{y}_D)$$

where the constants $a = 0.88$ and $b = 0.09 \mu\text{m}/\text{keV}$ are chosen for the typical high-energy neutrons present in the proton therapy rooms (13). Thus, by measuring the dose-mean lineal energy using the TEPC, the dose equivalent in a mixed radiation field can be determined.

The absorbed dose fractions due to low and high LET radiation are calculated from the measured \bar{y}_D value and the dose-mean lineal energies of photon and neutron components, that is,

$$\bar{y}_D = \bar{y}_{D,\gamma}d_\gamma + \bar{y}_{D,n}d_n = \bar{y}_{D,\gamma}d_\gamma + \bar{y}_{D,n}(1 - d_\gamma)$$

The dose-mean lineal energies for photons $\bar{y}_{D,\gamma} = 1.4 \text{ keV}/\mu\text{m}$ and neutrons $\bar{y}_{D,n} = 96 \text{ keV}/\mu\text{m}$ are calculated from MC-simulated relative contribution in the mixed field. From the relative dose contributions, the dose equivalent for photons and neutrons, H_γ^* and H_n^* are estimated from

$$H_n^* = d_n D_{det} (a + b \bar{y}_{D,n}) \text{ and}$$

$$H_\gamma^* = (1 - d_n) D_{det} (a + b \bar{y}_{D,\gamma})$$

Using the relative dose fractions, a value of 28 eV was obtained for W/e.

In this work, single spot measurements at proton beam energies of 70, 146, and 212 MeV were performed to calculate \bar{y}_D values for different energies and positions. To determine the dose equivalent for the scanned irradiations, the maximum proton energy was used to choose which \bar{y}_D value to use. No \bar{y}_D measurements were performed with a range shifter. Therefore, no $H^*(10)$ measurements for the irradiations with the range shifter are presented for positions A and C at Skandion where the Sievert was used at those positions.

The Sievert $H^*(10)$ energy response plotted in Figure 2 was calculated by means of MC simulations. The response is fairly close to unity over the whole energy range, except for an under-response for epithermal neutrons and a slight over-response for high-energy neutrons.

2.1.3.2 HAWK

The HAWK environmental Monitoring System FW-AD1 from Far West Technology Inc. used by IRSN is a microdosimetric single-event TEPC-system. The detector is spherical with 127 mm diameter (Benjamin type) and filled with pure propane gas at 933 Pa to simulate an energy deposition in 2 μm biological site and a mean chord length of 1.33 μm (14). HAWK measures the energy deposition spectrum from particles correlated to a single initial particle event on a lineal energy scale calibrated using a proton edge calibration. The absorbed dose distribution in lineal energy $d(y)$ and the low- and high-LET components are defined as the contributions below and above 10 $\text{keV}/\mu\text{m}$ respectively. From this distribution, the dose equivalent is calculated according to

$$H^* = H_{low}^* + H_{high}^* \\ = N_{low} \int_{0.5}^{10} Q(y) d(y) dy + N_{high} \int_{10}^{1024} Q(y) d(y) dy$$

Here, N_{low} and N_{high} are the low-LET and high-LET $H^*(10)$ -correction calibration factors from ^{137}Cs and ^{60}Co photon and Am-Be neutron fields (10, 15). N_{low} aims to compensate for the relatively high value of the electronic threshold, making it impossible to measure events below 0.5 $\text{keV}/\mu\text{m}$. N_{high} aims to compensate for the uncorrected y value for the proton edge set by the manufacturer for the y scale calibration. N_{low} is equal to 1.1 ± 0.02 and N_{high} to 0.8 ± 0.09 . The high-LET component of

the dose equivalent H_{high}^* is used in this work as an approximation of the neutron $H^*(10)$.

For the $H^*(10)$ energy response of the HAWK, only a limited number of data points in the energy range from 0.5 to 60 MeV are available from (10). These are also shown in Figure 2. It can be seen that the response is very close to unity in this energy range. Similar to the Sievert and other TEPCs, also for the HAWK, an under-response for energies below 0.5 MeV can be expected. For high-energy neutrons, the response is expected to be close to unity as well.

2.1.3.3 LB 6411

The LB 6411 ambient neutron monitor from Berthold Technologies used by SSM, UAB, and NPI consists of a 25-cm-diameter polyethylene moderator sphere with internal Cd absorbers and perforations that surrounds a cylindrical ^3He proportional counter (7). The neutron sensitivity is around 3 counts per nSv of neutron $H^*(10)$. It has excellent photon rejection capabilities with less than 30 $\mu\text{Sv/h}$ of photon response in a 10 mSv/h photon radiation field.

This ambient neutron monitor is designed to measure thermal to 20 MeV neutrons and it is known to have a strongly decreasing sensitivity to neutrons above 20 MeV. This is clearly reflected in the $H^*(10)$ energy response plotted in Figure 2, as obtained from MC simulations (7). The response is fairly close to unity over the whole energy range, except for an over-response in the epithermal energy range and a strong under-response for neutrons with energies above about 20 MeV for which the LB 6411 is almost insensitive.

2.1.3.4 Wendi-II

The Wendi-II ambient neutron monitor from Thermo Scientific used by SCK CEN and CCB is an extended-range ambient neutron monitor designed by Olsher et al. (16). It consists of a cylindrical polyethylene moderator with an inner tungsten shell that surrounds a cylindrical ^3He proportional counter. The neutron sensitivity is around 3 counts per nSv of neutron $H^*(10)$. It has excellent photon rejection capabilities with less than 5 $\mu\text{Sv/h}$ of photon response in a 100 mSv/h photon radiation field.

The tungsten shell embedded in the polyethylene moderator greatly enhances the Wendi-II response to high-energy neutrons, extending the measurement range to about 5 GeV and thus well beyond the maximum neutron energy of about 200 MeV encountered in proton therapy facilities. This is clearly reflected in the $H^*(10)$ energy response plotted in Figure 2, as obtained from MCNPX 2.7 simulations (8). The response is fairly close to unity over the whole energy range, except for an over-response for epithermal neutrons.

2.1.3.5 NM2B-458 and NM2B-495Pb

A conventional NM2B-458 and an extended-range NM2B-495Pb ambient neutron monitor were used by HMGU. These

monitors are based on the Andersson-Braun (AB) model and manufactured by NE Technology Ltd. They consist of a cylindrical BF_3 proportional counters of 3.1 cm diameter and 7.2 cm active length surrounded by an inner 1.7-cm-thick moderating polyethylene layer, a 0.6-cm-thick boron-doped synthetic rubber absorber, and an outer 6.9-cm-thick polyethylene moderator. The NM2B-495Pb ambient neutron monitor additionally has a 1 cm thick lead shell surrounding the boron rubber to increase the response to high-energy neutrons.

The $H^*(10)$ energy responses of both ambient neutron monitors were calculated by means of MC simulations in the energy range from thermal to 10 GeV (9) and are shown in Figure 2. The response is fairly close to unity over the whole energy range up to about 10 MeV for both ambient neutron monitors, except for an over-response for epithermal neutrons. For higher-energy neutrons, only the NM2B-495Pb has a response fairly close to unity due to the additional lead shell. For the NM2B-458, the response for high-energy neutrons drops very rapidly above about 10 MeV.

2.2 Simulations

All the simulations in this work were performed with the MC radiation transport code MCNP6.2 (17).

The first important input in these simulations is the geometrical model. Two different geometrical models were implemented in this work. Firstly, a model was developed that does not take into account the specifics of the room. This model is shown on the left in Figure 3. It consists of

- * the 60-cm-long and 30 cm by 30 cm cross section solid water phantom made of white polystyrene type RW3 with 2% by weight TiO_2 and a density of 1.03 g/cm³ (green);

- * a mesh tally inside the phantom to tally the SOBP delivered by the proton beam (red);
- * the 3.11-cm-thick and 30 cm by 30 cm cross section range shifter made of Lexan with a density of 1.2 g/cm³ positioned with the appropriate air gap with respect to the phantom edge for the cases in which a range shifter was used (yellow); and
- * six 20-cm-diameter spherical air cells at the detector positions for tallying the neutron fluence energy spectrum and neutron $H^*(10)$ (blue).

The advantage of this model is that it is generally valid for any PBS proton therapy facility after adaptation of the range shifter dimensions. The disadvantage is that without inclusion of the walls, floor, ceiling, patient table, gantry cylinders, gantry cone, counterweight, and other components in the room, the neutrons created inside these components are not taken into account. The scattered thermal and epithermal neutrons are not expected to contribute more than a few percent to the total neutron $H^*(10)$ (12). However, evaporation neutrons that are partly created in iron-rich components such as the gantry cylinders, the gantry cone, and the counterweight (18) can contribute up to about 50% of the total neutron $H^*(10)$ (19).

As the goal of this work is to develop a tool to predict out-of-field neutron doses in any PBS proton therapy facility and to get a better understanding of the trends of the out-of-field neutron doses as a function of treatment plan parameters, development of detailed room models of the Skandion and CCB proton therapy facilities was beyond the scope of this work. However, in order to better understand the potential sources of deviations between simulations and measurements, it was decided to also develop a second geometrical model for the Skandion facility with a simplified representation of the room. This model is shown on the right in Figure 3. The top picture shows a view

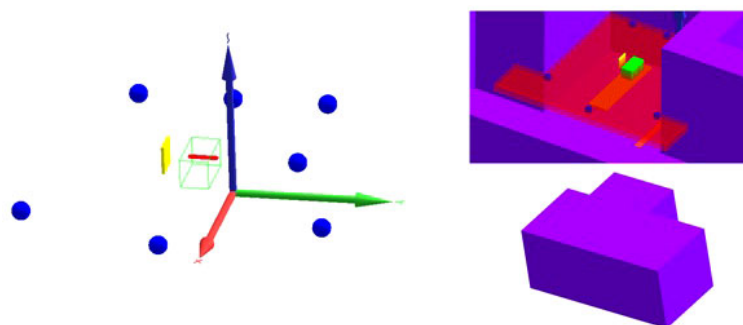


FIGURE 3
Geometrical models implemented in MCNP6.2. (Left) Model without room: solid water phantom (green), SOBP mesh tally (red), range shifter (yellow), and detectors (blue). (Right) Model with room with a view through the roof inside the room (top) and a view of the outside of the room (bottom): solid water phantom (green), positioning uncertainty mesh tally (red), range shifter (yellow), detectors (blue), table (orange), and walls, ceiling, and floor (purple).

inside the room through the roof, while the bottom picture shows an outside view of the room. In addition to the components implemented in the first model, this second model also contains

- * the 6-cm-thick and 220 cm by 52 cm table made of Kevlar with a density of 1.44 g/cm^3 (orange);
- * walls, ceiling, and floor made of 1-m-thick ordinary NIST concrete (20) with a density of 2.3 g/cm^3 (purple); and
- * a mesh tally for assessing the positioning uncertainty of the measurements (red).

The 1-m-thick concrete everywhere is an approximation and might lead to an overestimation of the scattered neutrons in the gantry area. Also, the iron-rich components of the gantry are not taken into account. This might lead to an underestimation of the evaporation neutrons that are, to a great extent, created in these components (18).

The second meaningful input in the simulations is the definition of the radiation source. The rectangular proton fields were modeled as a monodirectional collimated uniform square proton beam with size corresponding to the field size. The proton energy is sampled from the superposition of Gaussian energy distributions with $\sqrt{2}\sigma = 1.5\%$ and energies and weights obtained from the layer information in the *.pld file from the TPS.

The neutron reaction cross sections were taken from the ENDF/B-VIII.0 database (21) for a temperature of 0.02585 eV. Both protons and neutrons were tracked with a high-energy cutoff at 240 MeV, well above the maximum proton energy of 212 MeV. The Bertini Dresner intranuclear cascade and evaporation model was selected because it gave reliable results in previous simulations of neutron doses in proton therapy facilities (4, 22). Furthermore, a limited sensitivity study showed less than 10% difference in simulated neutron $H^*(10)$ values when using the default cross sections and physics models in MCNP6.2.

Finally, it is necessary to define the appropriate tallies in the simulations in order to obtain the desired quantities. A type 3 volumetric energy deposition mesh tally was defined in the target volume of the solid water phantom for assessing the SOBP absorbed dose profile. In this way, it could be checked whether the proton beam was modeled in a sufficiently realistic manner. F4 fluence energy spectrum and F4 $H^*(10)$ tallies were defined in the detector cells. The energy bin width in lethargy was fixed at $\ln(\frac{E_i}{E_{i-1}}) = 0.26$. This allowed direct comparison with the neutron $H^*(10)$ values measured by the ambient neutron monitors in this work and the neutron energy spectra measured with Bonner spheres during a previous measurement campaign at a similar PBS proton therapy facility in Trento (Italy) (11). A type 1 dose mesh tally with ICRP 74 fluence to $H^*(10)$ conversion coefficients using the TMESH DOSE keyword with option ic = 40 was defined in the horizontal plane at

the height of the detectors to obtain an estimation of the positioning uncertainty of the measurements. The simulation results are all expressed per simulation particle. However, as also the SOBP absorbed dose profile is simulated, all simulation results can be divided by the absorbed dose in the center of the SOBP per simulation particle in order to obtain the results expressed per unit of absorbed dose in the center of the SOBP. This allows direct quantitative comparison between the simulations and measurements.

3 Results and discussion

3.1 Uncertainties

For clarity of the plots presented here, uncertainty bars were not always added to the measurement and simulation results and their ratios. However, the order of magnitude of the uncertainties and the different contributions to the uncertainties are discussed in detail in this subsection. All uncertainties presented here are expressed at the $k = 1$ level.

3.1.1 Measurements

3.1.1.1 Positioning uncertainty

The positioning uncertainty is estimated by assuming that the positioning of the detectors was done with a precision of about 5 cm. The associated uncertainty on the measured $H^*(10)$ was estimated based on the simulated type 1 dose mesh tally with ICRP 74 fluence to $H^*(10)$ conversion coefficients in the horizontal plane at the height of the detectors. The simulated $H^*(10)$ on the mesh tally was averaged over the volume of a detector, shifting the detector positions 5 cm from the reference positions in the positive and negative direction along the x , y , and z axes. The positioning uncertainty was then assessed assuming a uniform distribution between the lowest and highest dose values obtained for each detector position. The obtained uncertainties averaged over all treatment plan parameters vary between 2.6% for position A and 5.0% for position B with a global average of 4%. As expected, a higher positioning uncertainty is found for the detector positions closer to the isocenter due to the higher dose gradient.

3.1.1.2 Calibration and instrument specific uncertainty

All ambient neutron monitors were calibrated using ^{252}Cf or Am-Be neutron sources. The calibration and instrument-specific uncertainty is estimated to be 5% for Sievert, 6% for HAWK, and about 2% for the other ambient neutron monitors.

3.1.1.3 Statistical uncertainty

The statistical uncertainty is the uncertainty on the measurement itself related to Poisson counting statistics. The relative statistical uncertainty was calculated as the inverse

square root of the number of counts obtained during the measurement. This uncertainty ranges between 6% and 18% with an average of 10% for Sievert at position A, between 9% and 25% with an average of 20% for Sievert at position C, between 1% and 3% for HAWK and well below 1% for the other ambient neutron monitors in most cases with exceptions up to 2% for very low doses.

3.1.1.4 Energy response uncertainty

The energy response uncertainty is related to the imperfect $H^*(10)$ energy response of the ambient neutron monitors. The expected responses of the different ambient neutron monitors at their measurement positions were estimated by convoluting the neutron $H^*(10)$ energy spectra simulated with the model without the room specifications at their measurement position with the monitor $H^*(10)$ energy response. The minimum, maximum, and average $H^*(10)$ responses for the different treatment plan parameters for each monitor are shown in Table 3.

No data are shown for HAWK because the $H^*(10)$ energy response was only available for a limited energy range. However, as discussed in Section 2.1.3.2, its response is expected to be close to unity for the measurements in this work. The NM2B-495Pb with extended energy range seems to perform worse than the NM2B-458 without extended energy range. However, it has to be taken into account that the NM2B-495Pb was used at position C, which is in the forward direction where high-energy neutrons are expected to contribute significantly to the dose, whereas the NM2B-458 was used at position E in the backward direction where virtually no high-energy neutrons are expected.

It can be seen that significant overestimations up to 47% and significant underestimations up to 67% are possible. Hence, the energy response will often be the biggest source of measurement uncertainty. Sievert shows a systematic overestimation, while all other ambient neutron monitors exhibit a systematic underestimation. This is well in line with the over-response and under-response for high-energy neutrons for respectively the Sievert and the other ambient neutron monitors as shown in Figure 2 and discussed in Section 2.1.3.

3.1.1.5 Target dose uncertainty

Finally, the uncertainty on the delivered absorbed dose in the target volume also contributes to the measurement uncertainty as both measurements and simulations are normalized to the absorbed dose in the target volume. This uncertainty is estimated to be about 2.5%. This uncertainty also includes the day-to-day variations of less than 0.5% based on the daily QA measurements.

3.1.1.6 Combined uncertainty

From the discussion above, it is clear that the measurement uncertainty varies significantly. It depends on the type of ambient neutron monitor, the measurement position, and the treatment plan parameters. Combining all the above uncertainties, it can be estimated that the combined measurement uncertainty is typically in the range between 15% and 30%.

3.1.2 Simulations

The number of particles in the MCNP6.2 simulations was taken sufficiently high to keep the statistical uncertainties on the simulated $H^*(10)$ values below 1% and on the simulated fluence energy spectra below 5% for all energy bins contributing significantly to the total fluence. However, the statistical uncertainties of MC simulations are only a minor component of the total uncertainty. The total uncertainty is dominated by uncertainties in the reaction cross sections, uncertainties in the physics models and simplifications or inaccuracies in the model geometry. Assessment of these uncertainties is not straightforward and was considered beyond the scope of this work. It just has to be kept in mind when comparing the measurements and simulations that the simulation results come with a significant uncertainty as well.

3.2 Verification of the simulations

3.2.1 SOBP depth profile

First, it was checked whether the proton beam was modeled in a sufficiently realistic way. For this, the simulated SOBP

TABLE 3 Minimum, maximum, and average $H^*(10)$ responses of the different ambient neutron monitors at the different positions A-F as estimated from the convolution of the neutron $H^*(10)$ energy spectra simulated with the model without room specifications and the simulated $H^*(10)$ energy responses.

Position	Skandion				CCB			
	Detector	Min	Max	Average	Detector	Min	Max	Average
A	SSM Sievert	1.34	1.42	1.38	IFJ Wendi-II	0.78	0.86	0.81
B	SCK CEN Wendi-II	0.72	0.97	0.85	SCK CEN Wendi-II	0.78	0.99	0.88
C	SSM Sievert	1.40	1.47	1.45	HMGU NM2B-495Pb	0.59	0.66	0.62
D	Skandion LB 6411	0.33	0.61	0.46	UAB LB 6411	0.35	0.53	0.44
E	IRSN HAWK	–	–	–	HMGU NM2B-458	0.81	0.90	0.86
F	SSM LB 6411	0.58	0.72	0.66	NPI LB 6411	0.63	0.73	0.69

profiles were plotted and compared with the range and modulation width of the corresponding treatment plan. The shape of the SOBP profiles agreed very well with the expected shape based on the range and modulation width for all cases. Three representative cases are shown in Figure 4. In this plot, the SOBP profiles are normalized to the average of the plateau of the SOBP. Hence, it could be concluded that the proton beam was modeled in a sufficiently realistic way.

3.2.2 Neutron ambient dose equivalent

Further verification of the simulation model was performed by comparison of the neutron ambient dose equivalent $H^*(10)$ from the simulations with the measured $H^*(10)$ from the ambient neutron monitors. The first measurement campaign was performed at CCB for a limited set of treatment plan parameters in May 2017. Later, in July 2019, a more extensive measurement campaign was performed at Skandion. The comparison between simulations and measurements will be made here in detail for the Skandion measurement campaign as it provides the most extensive data set. Furthermore, an approximate model of the Skandion treatment room was implemented in the simulations as explained in Section 2.2. In Section 3.3, the variation of the $H^*(10)$ with position and treatment plan parameters, and the measurements at Skandion and CCB are also compared with each other. An overview of all the irradiations and their treatment plan parameters for the measurement campaigns performed at Skandion and CCB is shown in Tables A.1 and A.2 in the appendix. Each of the listed irradiations was performed only once due to beam time limitations and expected stability of the irradiations.

The comparison between simulated and measured $H^*(10)$ is made for three different cases. In the first case, the measured H^*

(10) is compared with the simulated $H^*(10)$ from the simulations with the general geometrical model not taking into account the specifics of the room. In order to evaluate the uncertainty related to disregarding the specifics of the room, in the second case, the measured $H^*(10)$ is compared with the simulated $H^*(10)$ from the simulations with the simplified Skandion room model. For assessing the uncertainty related to the imperfect ambient neutron monitor $H^*(10)$ energy response, in the third case, the measured $H^*(10)$ is compared with the $H^*(10)$ obtained by convolution of the simulated neutron $H^*(10)$ energy spectra from the simulations without the specifics of the room with the $H^*(10)$ energy response of the appropriate ambient neutron monitor. For position E, the third case is not applicable, because the $H^*(10)$ energy response of the HAWK used at this position is only available for a limited energy range. Table 4 gives an overview of the average ratio of simulated over measured $H^*(10)$ per position and averaged over all positions for the three cases. The separate ratios of simulated over measured $H^*(10)$ for all irradiations separately are plotted in Figure 5 (position A, B, and C) and in Figure 6 (position D, E, and F) as a function of the irradiation number as specified in Table A.1 in the appendix. The ratios for the simulations without specifics of the room are shown as red crosses, the ratios for the simulations with specifics of the room are shown as blue circles, and the ratios for the simulations without specifics of the room and correction for the imperfect ambient neutron monitor $H^*(10)$ energy response are shown as green triangles. A green line indicating a ratio of one and two red lines indicating a factor of two over- or under-response are added to guide the eye. Error bars are not added here for clarity of the plots. However, a more detailed comparison with error bars is presented in Sections 3.3.2–3.3.5.

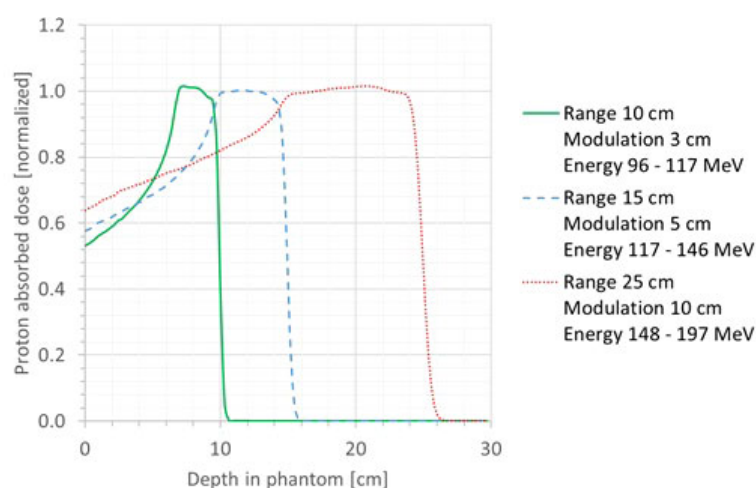


FIGURE 4

Plot of the simulated SOBP profiles for three different cases: range, 10 cm; modulation width, 3 cm (green full line); range, 15 cm; modulation width, 5 cm (blue dashed line); range, 25 cm; modulation width, 10 cm (red dotted line).

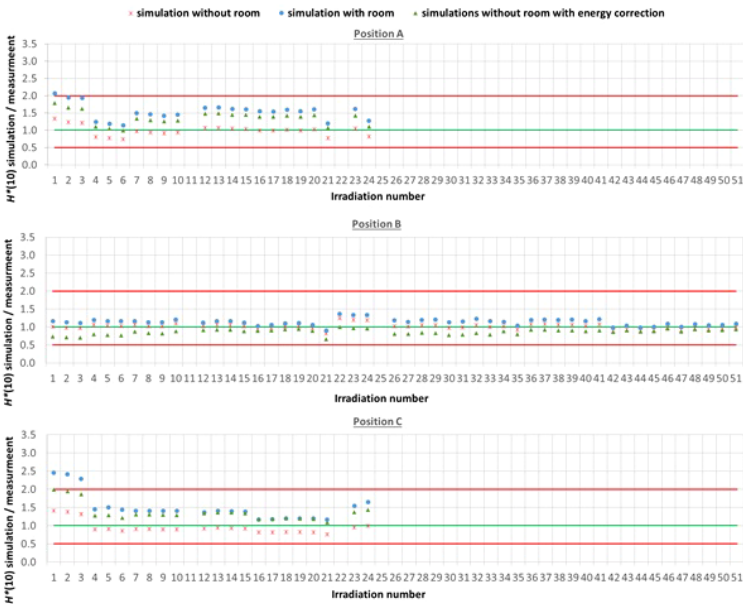


FIGURE 5
Plots with the ratio of simulated over measured $H^*(10)$ for positions (A–C) for the Skandion measurement campaign. Three cases are shown: simulations without room (red crosses), simulations with room (blue circles) and simulations without room and correction for the imperfect ambient neutron monitor $H^*(10)$ energy response (green triangles). A green line indicating a ratio of one and two red lines indicating a factor of two over- or under-response are added to guide the eye.

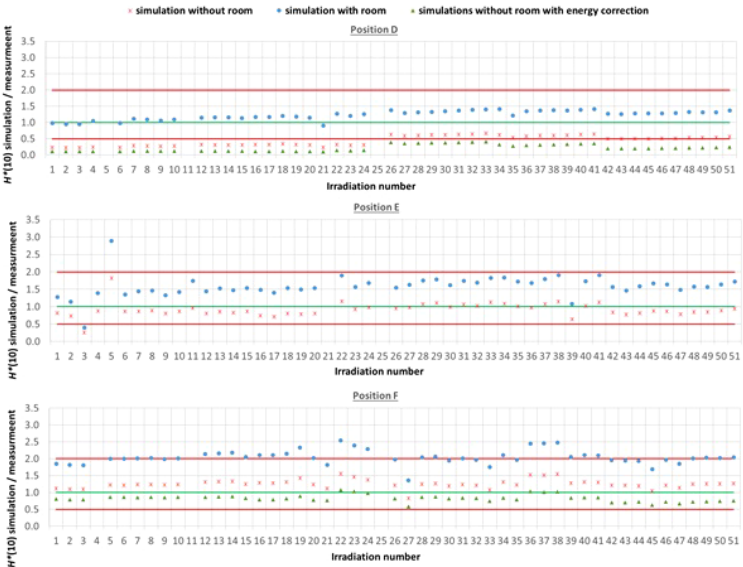


FIGURE 6
Plots with the ratio of simulated over measured $H^*(10)$ for positions (D–F) for the Skandion measurement campaign. Three cases are shown: simulations without room (red crosses), simulations with room (blue circles), and simulations without room and correction for the imperfect ambient neutron monitor $H^*(10)$ energy response (green triangles). A green line indicating a ratio of one and two red lines indicating a factor of two over- or under-response are added to guide the eye.

One can see in Figures 5, 6 that even without the room in the simulation model and without energy correction, most of the simulation data are already within a factor of two from the measurements. Only for position D and for one irradiation at position E are there stronger underestimations. From the results in Table 4 and Figures 5, 6, one can also see that introduction of the room in the simulation model significantly increases the simulated $H^*(10)$ values. This systematic increase for all irradiations is caused by the additional scattered neutrons from the room contributing to the neutron dose. For positions A, C, E, and F, the increase is about 60%. For position D, a much higher increase with almost a factor of three is observed. This is caused by the fact that position D is the most distant position from the gantry area perpendicular to the beam direction, where scattered neutrons are expected to contribute the most. There might also be an important dose contribution from neutrons created inside the bending magnet of the gantry, which are not taken into account in the simulations. These additional scattered neutrons are probably the reason for the underestimation of the neutron dose at position D in the simulations. On the other hand, for position B, the increase is limited to only 12%. This is also expected because position B is the position closest to the isocenter at only 1 m in the direction of the beam, where scattered neutrons are not expected to contribute significantly.

From the results in Table 4 and Figures 5 and 6, one can also see that when correcting for the imperfect energy response of the ambient neutron monitors, the ratio of simulations over measurements systematically increases with about 40% for the Sievert measurements at positions A and C, while it systematically decreases about 15%, 50%, and 35% for respectively Wendi-II at position B and LB 6411 at positions D and F. This is related to the imperfect energy response of the ambient monitors for high-energy neutrons as discussed in Sections 2.1.3 and 3.1.1.4.

For positions A, B, C, and E, the average agreement between the measurements and the simulations without the specifics of the room is within 8%. The agreement for individual irradiations is also well within 30% for most irradiations. Taking into account the measurement uncertainty in the range of 15% to 30% and the significant uncertainty on the simulations, this can already be considered as good agreement. The $H^*(10)$ values from the simulations with the specifics of the room in Table 4 show a significant overestimation with respect to the measurements. This overestimation is probably caused by an

overestimation of the scattered neutron dose contribution by using 1-m-thick concrete everywhere in the gantry area in the simulation model. Furthermore, there are also uncertainties in the concrete composition and concrete hydrogen content that can both strongly affect the scattered neutron contribution. Correction for the imperfect energy response of the ambient neutron monitors leads to a decrease of the measurements for positions A and C and an increase for position B as expected from the responses tabulated in Table 3. Correction for the imperfect energy response worsens the agreement between measurements and simulations. This can be caused by uncertainties in the neutron monitor energy response functions, uncertainties in the simulated neutron fluence energy spectra due to absence of the room and other important components influencing the energy spectra in the simulations, and the strong sensitivity of the neutron monitor response on the neutron energy. These observed effects of scattered neutrons from the room and the imperfect energy response of the ambient neutron monitor can also account for the limited deviations found between the measurements and the simulations.

For position D, one can observe a systematic underestimation of 56% for the simulations without the specifics of the room in comparison with the measurements. This underestimation could be expected because position D is 2.25 m away from the isocenter in a direction perpendicular to the proton beam. There, neutrons scattered by the room are expected to contribute significantly to the neutron dose. This is confirmed by the fact that the simulated $H^*(10)$ values for position D for the simulations with the specifics of the room are significantly higher and on average 23% above the measured $H^*(10)$ values. This overestimation can be related to uncertainties in the concrete composition and concrete hydrogen content, which can both strongly affect the scattered neutron contribution. Also, the systematic under-response of the LB 6411 ambient neutron monitor could explain this overestimation as can be seen in Table 3 and from the simulation results without the specifics of the room with energy correction in Table 4.

For position F, it can be seen that there is a systematic overestimation of 26% for the simulations without the specifics of the room in comparison with the measurements. Adding the specifics of the room in the simulations worsens the overestimation to about a factor of two. This is probably again

TABLE 4 Overview of the average ratio of simulated over measured $H^*(10)$ per position and averaged over all positions for the Skandion measurement campaign.

$H^*(10)$ Simulation/measurement	A	B	C	D	E	F	Average
Simulation without room	0.99	1.01	0.95	0.44	0.92	1.26	0.92
Simulation with room	1.54	1.13	1.50	1.23	1.58	2.04	1.50
Simulation without room with energy correction	1.36	0.86	1.37	0.21	–	0.82	1.36

due to an overestimation of the scattered neutron dose contribution because of the use of 1-m-thick concrete everywhere in the gantry area in the simulation model, especially since position F is completely at the back in the gantry area. The overestimation is probably caused by the underestimation of the LB 6411 ambient neutron monitor as can be seen from Table 3 and from the 30% decrease of the simulated $H^*(10)$ values when applying the energy correction in Table 4.

It can be concluded from this comparison that the simulation model without specifics of the room is sufficiently realistic. The deviations between the measured and simulated neutron $H^*(10)$ values were within the estimated combined uncertainty for all positions except for position D further away from the isocenter and perpendicular to the beam direction where scattered neutrons form an important dose contribution. Therefore, it is expected that also for the simulation of out-of-field neutron doses within the phantom, this simulation model will perform with sufficiently good accuracy.

3.2.3 Neutron fluence energy spectrum

The neutron fluence energy spectra are very important as both the neutron fluence to dose equivalent conversion coefficient and the ambient neutron monitor $H^*(10)$ energy responses depend strongly on the neutron energy. Therefore, verification of the simulated neutron fluence energy spectra was also performed by comparison with Bonner sphere measurements performed at a previous measurement campaign at a very similar proton therapy facility in Trento (11). The setup was very similar to the measurement campaigns at Skandion and CCB. The measurements in Trento were performed during an irradiation with 20 cm range, 10 cm modulation width, and 10 cm × 10 cm field size without a range shifter. The only difference was that position B in Trento was at a distance of 1.5 m from the isocenter instead of 1 m at Skandion and CCB.

Figure 7 compares the neutron fluence energy spectra at positions B, C, D, and E simulated in this work for Skandion with the simulation model with the specifics of the room (thick lines) and the neutron fluence energy spectra measured with Bonner spheres at the equivalent positions in Trento (thin lines). The treatment plan parameters were the same in both data sets: 20 cm range, 10 cm modulation width, and 10 cm × 10 cm field size without a range shifter. The fluence energy spectra are given per unit of absorbed dose in the target in Gy and plotted per unit lethargy. The neutron lethargy is defined as $\ln(\frac{E_i}{E_{i-1}}) = 0.26$ with E_i and E_{i-1} being the upper and lower energies of the energy bin, respectively. Neutron fluence energy spectra are commonly plotted per unit lethargy when the energy axis is logarithmic because, in this way, equal areas under the spectra represent equal amount of fluence. The top plot shows all positions, while the bottom plot zooms in on positions C, D, and E to have a more detailed view. The bottom plot additionally shows the

neutron fluence energy spectra at positions A and F simulated in this work for Skandion with the simulation model with the specifics of the room for comparison.

Very good agreement between simulations and measurements is observed for the high-energy neutron peak. Only for position B is a significantly higher peak observed in the simulations as expected because position B is 50 cm closer to the isocenter in the simulations in comparison with the measurements in Trento.

The evaporation neutron peaks for positions C and D are higher in the measurements in Trento than in the simulations. For position D, the shape is also different. This is probably caused by simplifications in the room model or differences in the rooms of Skandion and Trento. Evaporation neutrons are partly created in iron-rich components such as the gantry cylinders, the gantry cone, and the counterweight (18), and these components were not taken into account in the simplified room model of the simulations. However, the contribution of this peak to the total dose is less important closer to the phantom and inside the phantom as demonstrated by the good agreement between measured and simulated $H^*(10)$ values in Section 3.2.2.

The thermal neutron peaks in the simulations are systematically higher than those of the measurements in Trento. This is probably again caused by simplifications in the room model in the simulations or differences between the rooms in Skandion and Trento. As discussed already in Section 3.2.2, the 1-m-thick concrete everywhere probably overestimates the scattered neutron contribution and thus also the thermal neutron peak. Anyhow, thermal and even epithermal neutrons are expected to contribute only to the maximum, a few percent of the total out-of-field neutron dose in proton therapy (12).

In Section 3.2.2, it was shown that the use of the simulated neutron fluence energy spectra to correct for the imperfect energy response of the ambient neutron monitors can explain some of the deviations between the simulated and the measured $H^*(10)$ values. This gives further confidence that the simulated neutron fluence energy spectra are sufficiently realistic.

3.3 Variations of ambient dose equivalent

In Section 3.2, it was shown that the ambient neutron doses simulated with the MC model agree with the measurements within the uncertainties and thus that one can rely on the results of the simulations. In this subsection, the simulation results are used for analysis of the variation of the neutron ambient dose equivalent $H^*(10)$ as a function of position inside the room and treatment plan parameters. The simulations with the geometrical model without specifics of the room were used in order to make the results independent of the exact room geometry. The trends observed in the simulations are

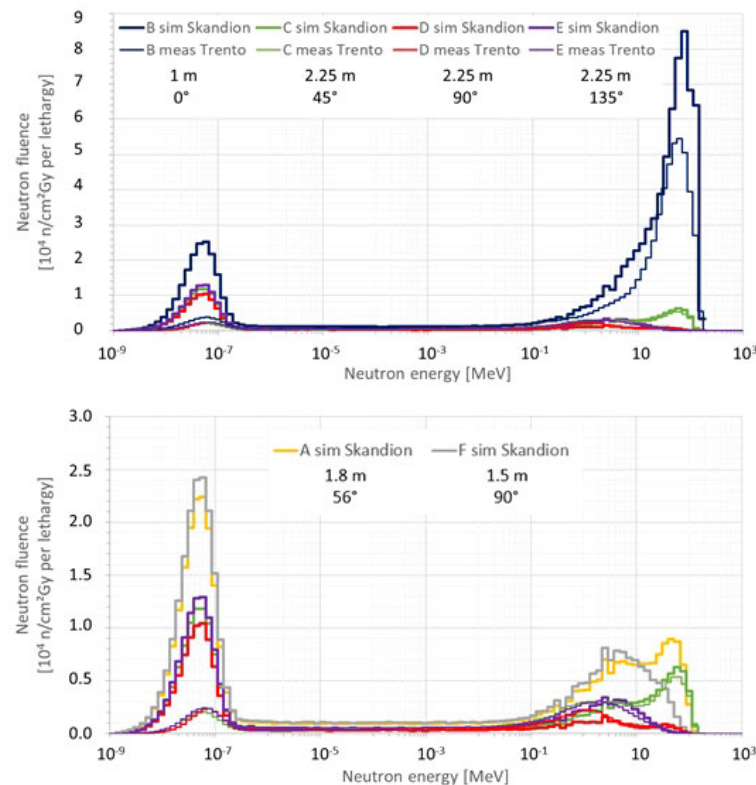


FIGURE 7

Plots comparing the neutron fluence energy spectra at positions (B–E) simulated in this work for Skandion (thick lines) and the neutron fluence energy spectra measured with Bonner spheres at the equivalent positions in Trento (thin lines). The treatment plan parameters were the same in both data sets: 20 cm range, 10 cm modulation width and 10 cm × 10 cm field size without a range shifter. The fluence energy spectra are given per unit of absorbed dose in the target in Gy and plotted per unit lethargy. The top plot shows all positions, while the bottom plot zooms in on the positions (C–E) to have a more detailed view. The bottom plot additionally shows the neutron fluence energy spectra at positions A and F simulated in this work for Skandion for comparison.

compared with those of the measurements performed at Skandion and, where available, also with the measurements performed at CCB IFJ PAN. All the results are presented in terms of ambient dose equivalent $H^*(10)$ per unit of absorbed dose in the center of the SOBP.

3.3.1 Position

The first important factor influencing neutron $H^*(10)$ is the position inside the room. Figure 8 shows the variation of the simulated $H^*(10)$ values (bars) and the measured $H^*(10)$ values (crosses) at Skandion as a function of the position. Average (green), minimum (blue), and maximum (red) values are shown. The positions are ordered from left to right according to increasing distance from the isocenter and for the same distances according to increasing angle with respect to the proton beam direction.

The observed trends for simulations and measurements are very similar. As expected, $H^*(10)$ decreases with

increasing distance from the isocenter and $H^*(10)$ is lower in backward direction than in forward direction of the proton beam. $H^*(10)$ values between 0.04 μSv and 292 μSv per Gy target dose were obtained in the simulations. The highest doses were found for position B with an average overall treatment plan parameters of about 66 μSv per Gy. This was expected as it is the closest position at only 1 m from the isocenter and located in the forward direction of the beam. Lowest doses were found for positions D and E with on average over all treatment plan parameters of about 1 and 3 μSv per Gy, respectively. Also, this was expected as these positions are furthest away at 2.25 m distance in directions perpendicular and backward with respect to the proton beam direction for positions D and E, respectively. Finally, it can be seen that the measurements at position D are significantly higher than the simulations. This is probably due to the missing scattered neutrons from the room in the simulations as discussed in Section 3.2.2.

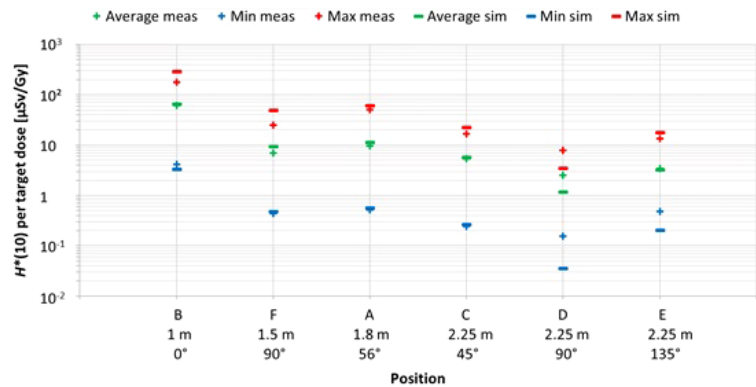


FIGURE 8
Plot of the variation of the simulated $H^*(10)$ values (bars) and the measured $H^*(10)$ values (crosses) at Skandion as a function of the position. Average (green), minimum (blue), and maximum (red) values are shown. The positions are ordered from left to right according to increasing distance from the isocenter and for same distances according to increasing angle with respect to the proton beam direction.

3.3.2 Field size

The second factor influencing neutron $H^*(10)$ is the field size. Figure 9 shows the variation of the simulated $H^*(10)$ (red bars connected with lines) and measured $H^*(10)$ (green and blue crosses) as a function of the field size for a range of 15 cm and a modulation width of 10 cm without a range shifter for the different positions inside the room. The error bars on the measurement data points represent the $k = 1$ measurement uncertainties. Figure 10 shows the same simulation data but

for all positions in one plot together with a linear fit through all data points. In this plot, the $H^*(10)$ is for each position normalized to the $H^*(10)$ for the lowest field size for that position. The fit has no physical meaning, but can be used as an approximate scaling law for modeling the dependence of the neutron $H^*(10)$ on the field size.

The observed trends in simulations and measurements at Skandion and CCB are very similar. Only for position D are the measurements significantly higher than the simulations. This is

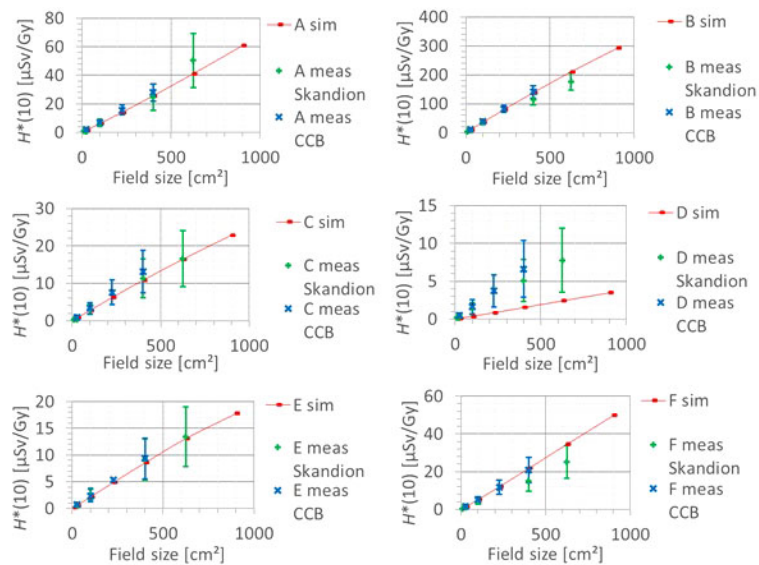


FIGURE 9
Plots of the variation of the simulated $H^*(10)$ (red bars) and measured $H^*(10)$ (green and blue crosses) as a function of the field size for a range of 15 cm and modulation width of 10 cm without a range shifter for the different positions.

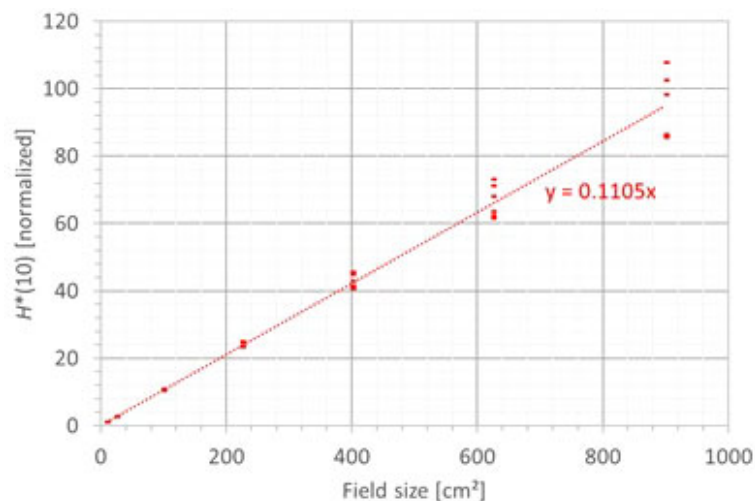


FIGURE 10

Plot of the variation of the simulated $H^*(10)$ as a function of the field size for all positions for a range of 15 cm and a modulation width of 10 cm without a range shifter with a linear fit through all the data points.

probably due to the missing scattered neutrons from the room in the simulations as discussed in Section 3.2.2. The neutron $H^*(10)$ increases linearly with field size area for all positions. The $H^*(10)$ increases with a factor of about 100 when changing from a field size of 3 cm × 3 cm to a field size of 30 cm × 30 cm. Inside the phantom, the treatment volume is closer and the neutron source deviates more strongly from a distant point source. Therefore, inside the phantom, there might be a deviation from this linearity with an additional position dependence.

The simulations also showed that the neutron energy spectrum does not vary significantly with changes in the field size area.

3.3.3 Range

The next factor influencing the neutron $H^*(10)$ is the proton range and the corresponding proton energy. Figure 11 shows the variation of the simulated $H^*(10)$ (red bars connected with lines) and measured $H^*(10)$ (green crosses) as a function of the range for a field size of 10 cm by 10 cm and a modulation width of 5 cm without a range shifter for the different positions. The error bars on the measurement data points represent the $k = 1$ measurement uncertainties. Figure 12 shows the same simulation data for all positions in one plot together with the data for the other modulation widths and a linear fit through all data points. In this plot, the $H^*(10)$ is for each position and modulation width normalized to the $H^*(10)$ for the lowest range for that position and modulation width. The fit has no physical meaning, but can be used as an approximate scaling law for modeling the dependence of the neutron $H^*(10)$ on the proton range.

The observed trends in the simulations and measurements at Skandion are very similar. Only for position D are the measurements significantly higher than the simulations. This is probably due to the missing scattered neutrons from the room in the simulations as discussed in Section 3.2.2. For the 10-cm modulation width, there are also measurements performed at CCB that are very well in line with the measurements at Skandion and the simulations. It can be seen that the $H^*(10)$ increases relatively linearly with the range. In this case, a general linear scaling law does not reproduce the trends for all modulation widths and positions properly. The increase in $H^*(10)$ as a function of the range depends significantly on the position. This is probably related to the difference in distance to the treatment volume as the main neutron source for different positions. When changing the range from 10 cm to 25 cm, the $H^*(10)$ increases with a factor of two to eight, depending on the position and modulation width.

The simulations also showed that the neutron fluence energy spectrum has a shift of the high-energy neutron peak towards higher energies and a decrease of the thermal neutron contribution with an increase in range. This is expected because an increased range means increased proton energy and thus also an increase of the energy of the high-energy neutrons and a decrease of the fraction of thermalized neutrons.

3.3.4 Modulation width

A fourth factor influencing the neutron $H^*(10)$ is the modulation width. Figure 13 shows the variation of the simulated $H^*(10)$ (red bars connected with lines) and

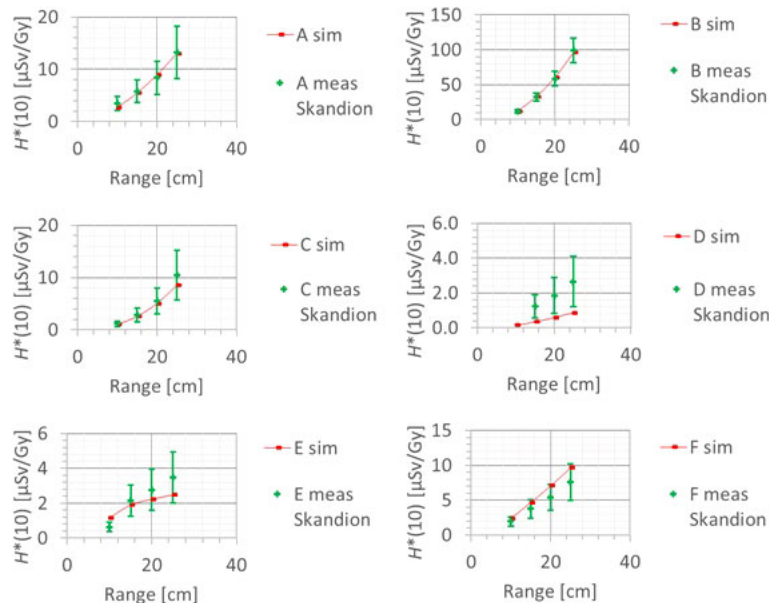


FIGURE 11
Plots of the variation of the simulated $H^*(10)$ (red bars) and measured $H^*(10)$ (green crosses) as a function of the range for a field size of 10 cm by 10 cm and a modulation width of 5 cm without a range shifter for the different positions.

measured $H^*(10)$ (green and blue crosses) as a function of the modulation width for a range of 20 cm and a field size of 10 cm by 10 cm without a range shifter for the different positions. The error bars on the measurement data points represent the $k = 1$ measurement uncertainties. Figure 14 shows the same simulation data for all positions in one plot together with the

data for the other ranges and a quadratic fit through all data points. In this plot, the $H^*(10)$ is for each position and range normalized to the $H^*(10)$ for the lowest modulation width for that position and range. The fit has no physical meaning, but can be used as an approximate scaling law for modeling the dependence of the neutron $H^*(10)$ on the modulation width.

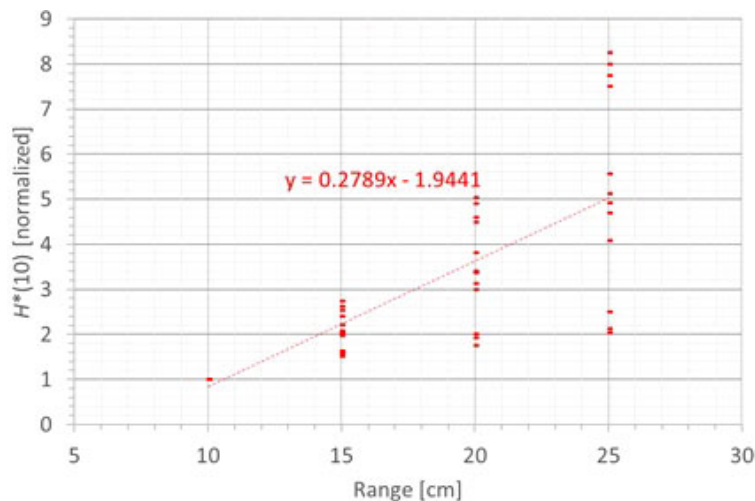


FIGURE 12
Plot of the variation of the simulated $H^*(10)$ as a function of the range for all modulation widths and positions for a field size of 10 cm by 10 cm without a range shifter with a linear fit through all the data points.

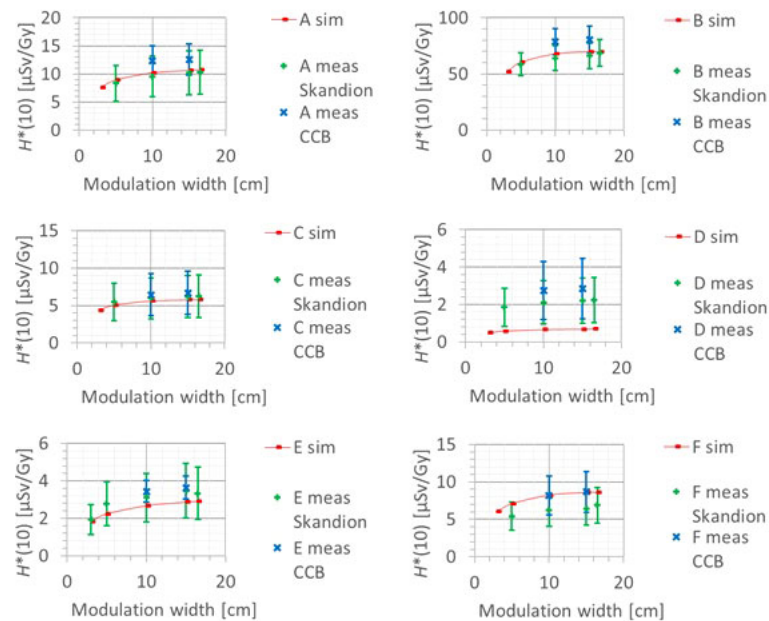


FIGURE 13
Plots of the variation of the simulated $H^*(10)$ (red bars) and measured $H^*(10)$ (green and blue crosses) as a function of the modulation width for a range of 20 cm and a field size of 10 cm by 10 cm without a range shifter for the different positions.

The observed trends in the simulations and measurements at Skandion and CCB are very similar. Only for position D are the measurements significantly higher than the simulations. This is probably due to the missing scattered neutrons from the room in

the simulations as discussed in Section 3.2.2. It can be seen that the $H^*(10)$ increases quadratically with the modulation width and that the increase becomes less steep for higher modulation widths. A quadratic fit reproduces the trends for different ranges

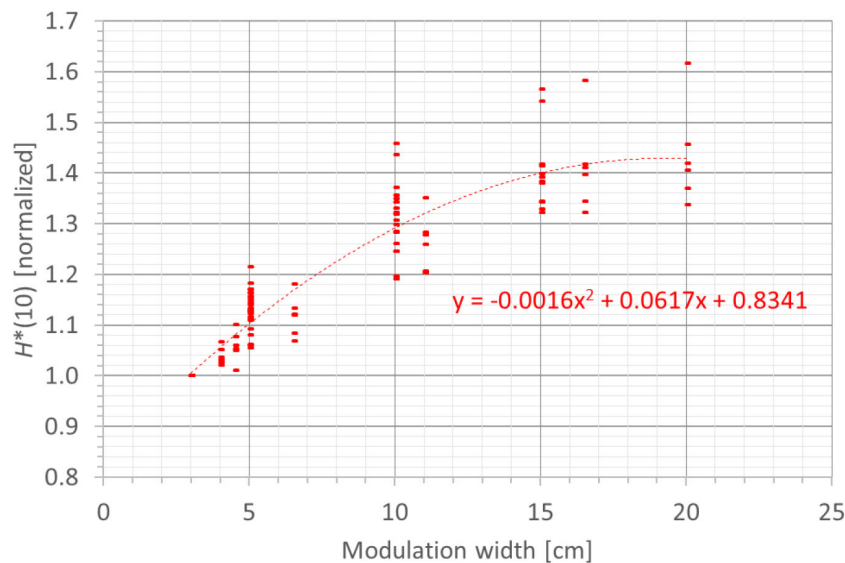


FIGURE 14
Plot of the variation of the simulated $H^*(10)$ as a function of the modulation width for all ranges and positions for a field size of 10 cm by 10 cm without a range shifter with a quadratic fit through all the data points.

and positions quite well, but there is a limited dependence on range and position. Similar to the range, this is probably related to the difference in distance to the treatment volume as the main neutron source for different positions. The $H^*(10)$ increases between 35% and 60% when increasing the modulation width from 3 cm to 20 cm, depending on the range and position.

The simulations also showed that the neutron energy spectrum does not change significantly when changing the modulation width.

3.3.5 Range shifter and air gap

The last investigated factor influencing the neutron $H^*(10)$ is the use of a range shifter. It was found both in the measurements and the simulations that the $H^*(10)$ increases on average by a factor of about two when introducing a range shifter for the same treatment. The increase was higher for lower ranges. For all positions except for position D, the increase is limited to a factor of 2.5, while for position D, an increase up to a factor of 6 was observed. This is probably due to the fact that the range shifter is positioned within line of sight from position D. The absorbed dose measured at position A with the Sievert was also shown to increase up to a factor of nine when introducing a range shifter. This increase is probably not due to neutrons but due to protons from the range shifter as discussed in detail in (23).

These observations are within expectations. When performing the same treatment, introducing a range shifter means increasing the proton energies as can be seen in Table A.1 in the appendix. This leads to an additional neutron creation in the range shifter. As a first approximation, one can consider that the range is increased by the solid water equivalent thickness of the range shifter. It can be seen indeed that the $H^*(10)$ values simulated with the range shifter are close to the $H^*(10)$ values

simulated without a range shifter for a range corresponding to the sum of the range with the range shifter and the solid water equivalent thickness of the range shifter.

The simulations also showed that, similar to an increase of the range, the use of a range shifter leads to a shift of the high-energy neutron peak towards higher energies and a decrease of the thermal neutron contribution.

Also, the dependence of the neutron $H^*(10)$ on the air gap between the range shifter and the phantom was studied, in both the simulations and the measurements. The error bars on the measurement data points represent the $k = 1$ measurement uncertainties. Figure 15 shows the variation of the simulated $H^*(10)$ (red bars connected with lines) and measured $H^*(10)$ (green crosses) as a function of the air gap between the range shifter and the phantom for a range of 10 cm, a modulation width of 5 cm, and a field size of 10 cm \times 10 cm for the different positions. Both the simulations and the measurements at Skandion showed no significant effect of the variation of the air gap on the neutron $H^*(10)$ for the investigated positions. Further research is necessary to evaluate the potential influence of the air gap at other positions such as inside the phantom, closer to the range shifter. The absorbed dose measured at position A with the Sievert was shown to increase with increasing air gap. This increase is probably not due to neutrons but due to protons from the range shifter as discussed in detail in (23).

4 Conclusions and outlook

A general MC radiation transport model was set up for simulation of neutron doses from scattered and secondary

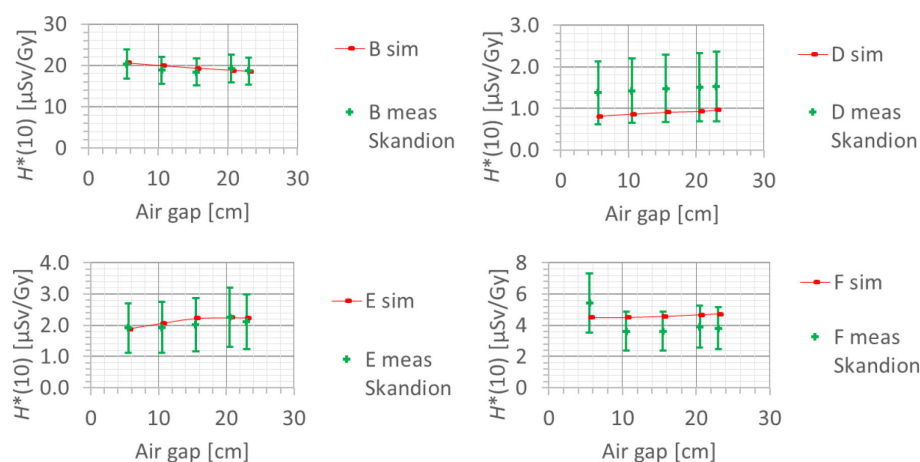


FIGURE 15

Plots of the variation of the simulated $H^*(10)$ (red bars) and measured $H^*(10)$ (green crosses) as a function of the air gap between the range shifter and the phantom for a range of 10 cm, a modulation width of 5 cm, and a field size of 10 cm by 10 cm for the different positions.

radiation at PBS proton therapy facilities. This model was successfully verified by comparison of simulated and measured ambient neutron doses for the irradiations of a solid water phantom at two different PBS proton therapy facilities using a variety of treatment plans. The simulated SOBP profile properly reflected the range and modulation width of the plans. Furthermore, the deviations between the simulated neutron $H^*(10)$ values and ambient neutron monitor measurements at six different positions around the solid water phantom were well within the expected uncertainties. Finally, the simulated neutron fluence energy spectra were in good agreement with Bonner sphere measurements performed during a previous measurement campaign with a similar setup. For the positions close to the phantom where scattered neutrons from the room do not contribute significantly to the dose, the agreement between simulated and measured neutron $H^*(10)$ was within 30%. Therefore, it is expected that with this general MC radiation transport model of PBS proton therapy facilities, it will also be possible to simulate out-of-field doses inside the phantom with a similarly good accuracy.

The MC simulations facilitated a detailed study of the variation of neutron $H^*(10)$ with position inside the room, field size, range, modulation width, use of a range shifter, and air gap between the range shifter and the phantom. The neutron $H^*(10)$ depends strongly on the position inside the room with a general decrease of the neutron $H^*(10)$ with increasing distance from the isocenter and higher neutron $H^*(10)$ in the forward direction of the proton beam in comparison with the backward direction. The linear increase with field size and the increase of up to a factor of eight with increasing range were found to be the strongest influences on the neutron $H^*(10)$. The neutron $H^*(10)$ was also found to increase by up to about 60% with increasing modulation width. The use of a range shifter on average increases the $H^*(10)$ by a factor of two. The air gap between the range shifter and the phantom did not have a significant influence on the neutron $H^*(10)$ at the investigated positions. Further research is needed to evaluate potential influence of the air gap inside the phantom, closer to the range shifter. Furthermore, it was found that the variations of the neutron $H^*(10)$ with the treatment plan parameters have interdependencies and also depend on the position inside the room. This inhibits the use of simple scaling factors to predict the $H^*(10)$ more precisely than within a factor of about three close to the phantom. More precise prediction of the neutron $H^*(10)$ requires simulations at the location of interest. Finally, this work demonstrates that, when reporting on out-of-field neutron doses in proton therapy, it is important not only to normalize the out-of-field neutron doses to the target dose or product of target dose with treatment volume, but also to provide the treatment plan parameters. This is crucial in order to be able to compare results from different studies.

The ambient neutron doses per unit of target dose in this study varied between 3 $\mu\text{Sv}/\text{Gy}$ and 300 $\mu\text{Sv}/\text{Gy}$ at 1 m from the isocenter in the beam direction and between 0.5 $\mu\text{Sv}/\text{Gy}$ and 50

$\mu\text{Sv}/\text{Gy}$ at 1.5 m from the isocenter perpendicular to the beam direction. The out-of-field neutron dose for a specific treatment in an organ at a certain distance from the isocenter can already be roughly estimated based on the dose data and scaling laws provided in this work in combination with the inverse square distance law to very roughly model the dependence on the distance from the isocenter. As a first test, this was done for the recently published extensive study of out-of-field neutron doses for a proton therapy brain treatment (24). The brain treatment in (24) can be approximated by an irradiation with 33 cm^2 field size, 5 cm modulation width, and 18 cm range. The irradiations in this treatment were performed under three different angles. The out-of-field neutron doses per unit of target dose assessed in (24) by means of measurements and MC radiation transport simulations ranged between 10 $\mu\text{Sv}/\text{Gy}$ at 50 cm from the isocenter and 1,000 $\mu\text{Sv}/\text{Gy}$ at 10 cm from the isocenter. The most comparable dose data from this work are the dose data for position B (in beam direction at 1 m from the isocenter) and position F (perpendicular to beam direction at 1.5 m from the isocenter) for the irradiation with 20 cm range, 5 cm modulation width, and 100 cm^2 field size. Based on the scaling laws obtained in this work, these dose data were divided by a factor of three to correct for the larger field size and multiplied with a factor of 0.84 to correct for the larger range. Then, they were recalculated to the distances of 10 cm and 50 cm by means of the inverse square distance law. This resulted in doses of 70 $\mu\text{Sv}/\text{Gy}$ (in beam direction) and 10 $\mu\text{Sv}/\text{Gy}$ (perpendicular to beam direction) at 50 cm and 1700 $\mu\text{Sv}/\text{Gy}$ (in beam direction) and 300 $\mu\text{Sv}/\text{Gy}$ (perpendicular to beam direction) at 10 cm. These doses are very well in line with the 10 $\mu\text{Sv}/\text{Gy}$ at 50 cm and 1000 $\mu\text{Sv}/\text{Gy}$ at 10 cm obtained in (24). This example demonstrates that rough estimates of out-of-field neutron doses can already be obtained easily based on the ambient neutron dose data and scaling laws provided in this work.

More accurate assessment of out-of-field neutron doses requires a more sophisticated approach that will be explored in future work. It is planned to use this verified MC radiation transport model for PBS proton therapy facilities to directly simulate out-of-field neutron doses inside the phantom instead of ambient neutron doses outside the phantom. The phantom will be filled with 2-mm-sized boxes to allow high spatial resolution close to the field where large dose gradients can be expected. Fluence energy spectra will be tallied in these boxes for neutrons, as well as for protons and photons that can also contribute significantly to the out-of-field doses. These fluence energy spectra will then be convoluted with fluence to dose equivalent conversion coefficients from literature to obtain the out-of-field doses per unit of target dose in terms of dose equivalent. The updated simulation model will first be verified again for a few specific sets of treatment parameters by comparison with a previous in-phantom measurement campaign performed within EURADOS WG9 at the Trento

proton therapy facility. After this verification, the simulations will be performed for a large series of relevant field sizes, ranges, modulation widths, and range shifters. The simulations will be performed both with beam direction along the long and the short axis of the phantom. The simulated out-of-field doses will then be used to build a library and a corresponding look-up tool to allow assessment of the out-of-field doses at PBS proton therapy facilities as a function of treatment plan parameters and position with respect to the isocenter and beam direction. The rectangular field treatment plans and the solid water phantom used in these simulations are of course simplified in comparison with the actual treatment of a real patient. However, actual treatment plans can be simplified as one or a combination of several rectangular treatment plans. In the first instance, different organs can be approximated as a series of boxes in the solid water phantom at a representative distance and angle with respect to the isocenter and beam direction. Later on, the simulations in the solid water phantom can be made more realistic by performing simulations in a series of representative anthropomorphic phantoms including the actual organs. In this way, the library and tool can be extended continuously and be made more realistic over time to allow, for instance, also taking into account differences between pediatric, adult, and pregnant patients. The tool that will be developed in this way will enable the optimization of treatment planning in terms of out-of-field doses and associated detrimental effects on healthy tissue.

Data availability statement

The original contributions presented in the study are included in the article/supplementary material. Further inquiries can be directed to the corresponding author.

Author contributions

OV: conceptualization, experimental setup, analysis of measurement data, Monte Carlo simulation design, setup, execution and analysis, manuscript writing, review and editing. LS: conceptualization, experimental design and setup, analysis of measurement data, manuscript writing, review and editing. JL: experimental setup, analysis of measurement data, manuscript writing, review and editing. LE: experimental setup, analysis of measurement data, manuscript review and editing. NM: conceptualization, experimental design and setup, analysis of measurement data. ML: experimental design and setup. AA: experimental design and setup, manuscript review. VM: conceptualization, experimental design and setup, analysis of measurement data, manuscript review and editing. FT: experimental setup, analysis of measurement data, manuscript review and editing. ST: experimental setup, analysis of measurement data. IM-R: experimental setup, analysis

of measurement data, manuscript review and editing. CD: experimental setup, analysis of measurement data. MR-E: experimental setup, analysis of measurement data. PO: experimental setup, analysis of measurement data. RH: conceptualization, experimental design, manuscript review and editing. PO: conceptualization, experimental design, experimental setup, manuscript review and editing. All authors contributed to the article and approved the submitted version.

Funding

This project has received funding from INSPIRE from the European Union's Horizon 2020 research and innovation programme under grant agreement No (730983) IM-R acknowledges the financial support from the Spanish Ministry of Science, Innovation and Universities (RYC2018-024043-I) The work of Ondrej Ploc on the paper was funded by EU Operational Program Research, Development, and Education, call 02_15_003 in project CRREAT, number CZ.02.1.01/0.0/0.0/15_003/0000481.

Acknowledgments

This work was carried out within the European Radiation Dosimetry Group (EURADOS, WG9 Radiation Dosimetry in Radiotherapy).

Conflict of interest

The authors declare that the research was conducted in the absence of any commercial or financial relationships that could be construed as a potential conflict of interest.

Publisher's note

All claims expressed in this article are solely those of the authors and do not necessarily represent those of their affiliated organizations, or those of the publisher, the editors and the reviewers. Any product that may be evaluated in this article, or claim that may be made by its manufacturer, is not guaranteed or endorsed by the publisher.

Supplementary material

The Supplementary Material for this article can be found online at: <https://www.frontiersin.org/articles/10.3389/fonc.2022.903537/full#supplementary-material>

References

- Loeffler J, Durante M. Charged particle therapy—optimization, challenges and future directions. *Nat Rev Clin Oncol* (2013) 107:10, 411–424. doi: 10.1038/nrclinonc.2013.79
- Aliyah F, Pinasti SG, Rahman AA. Proton therapy facilities: An overview of the development in recent years. *IOP Conf Ser: Earth Environ Sci* (2021) 927 (1):012042. doi: 10.1088/1755-1315/927/1/012042
- Hälg RA, Schneider U. Neutron dose and its measurement in proton therapy—current state of knowledge. *Br J Radiol* (2020) 93:20190412. doi: 10.1259/bjr.20190412
- De Saint-Hubert M, Farah J, Klodowska M, Romero-Expósito MT, Tyminska K, Mares V, et al. The influence of nuclear models and Monte Carlo radiation transport codes on stray neutron dose estimations in proton therapy. *Radiat Meas* (2022) 150:106693. doi: 10.1016/j.radmeas.2021.106693
- Mojżeszczek N, Farah J, Klodowska M, Ploc O, Stolarczyk L, Waligórski MPR, et al. Measurement of stray neutron doses inside the treatment room from a proton pencil beam scanning system. *Phys Med* (2017) 34:80–4. doi: 10.1016/j.ejmp.2017.01.013
- ICRP. The 2007 recommendations of the international commission on radiological protection. *Ann* (2007) 37(2–4). doi: 10.1016/j.icrp.2007.10.003
- Burgkhardt B, Fieg G, Klett A, Plewnia A, Siebert BRL. The neutron fluence and $H^*(10)$ response of the new LB 6411 remcounter. *Radiat Prot Dosim* (1997) 70:361–4. doi: 10.1093/oxfordjournals.rpd.a031977
- De Smet V. *Neutron measurements in a proton therapy facility and comparison with Monte Carlo shielding simulations*. PhD thesis. Université Libre de Bruxelles: Brussels (2016).
- Mares V, Sannikov AV, Schraube H. Response functions of the andersson-Braun and extended range rem counters for neutron energies from thermal to 10 GeV. *nucl. Instrum Meth* (2002) 476(1–2):341–6. doi: 10.1016/S0168-9002(01)01459-0
- Trompier F, Delacroix S, Vabre I, Joussard F, Proust J. Secondary exposure for 73 and 200 MeV proton therapy. *Radiat Prot Dosimetry* (2007) 125(1–4):349–54. doi: 10.1093/rpd/ncm154
- Farah J, Mares V, Romero-Expósito M, Trinkl S, Domingo C, Dufek V, et al. Measurement of stray radiation within a scanning proton therapy facility: EURADOS WG9 intercomparison exercise of active dosimetry systems. *Med Phys* (2015) 42(5):2572–2584. doi: 10.1118/1.4916667
- Mares V, Romero-Expósito M, Farah J, Trinkl S, Domingo C, Dommert M, et al. A comprehensive spectrometry study of a stray neutron radiation field in scanning proton therapy. *Phys Med Biol* (2016) 61:4127–40. doi: 10.1088/0031-9155/61/11/4127
- Kyllönen J-E, Lindborg L, Samuelson G. The response of the sievert instrument in neutron beams up to 180 MeV. *Radiat Prot Dosim* (2001) 94:227–32. doi: 10.1093/oxfordjournals.rpd.a006494
- Benjamin PW, Kemshall CD, Redfearn J. A high resolution spherical proportional counter. *Nucl Instr Meth* (1986) 59:77–85. doi: 10.1016/0029-554X(86)90347-9
- Farah J, De Saint-Hubert M, Mojżeszczek N, Chirioti S, Gryzinski M, Ploc O, et al. Performance tests and comparison of microdosimetric measurements with four tissue-equivalent proportional counters in scanning proton therapy. *Radiat Measurements* (2017) 96:42–52. doi: 10.1016/j.radmeas.2016.12.005
- Olsher RH, Hsu H, Beverding A, Kleck JH, Casson WH, Vasilik DG, et al. WENDI: an improved neutron rem meter. *Health Phys* (2000) 79:170–81. doi: 10.1097/00004032-200008000-00010
- Werner CJ, Bull JS, Solomon CJ, Brown FB, McKinney GW, Rising ME, et al. *MCNP version 6.2 release notes, Los alamos national laboratory report LA-UR-18-20808*. United States: Los Alamos National Lab (LANL) (2018).
- Englbrecht FS, Trinkl S, Mares V, Rühm W, Wielunski M, Wilkens JJ, et al. A comprehensive Monte Carlo study of out-of-field secondary neutron spectra in a scanned-beam proton therapy gantry room. *Z Med Phys* (2021) 31:215–28. doi: 10.1016/j.zemedi.2021.01.001
- Trinkl S, Mares V, Englbrecht FS, Wilkens JJ, Wielunski M, Parodi K, et al. Systematic out-of-field secondary neutron spectrometry and dosimetry in mp.12206
- McConn RJ Jr, Gesh CJ, Pagh RT, Rucker RA, Williams RG. *Compendium of material composition data for radiation transport modeling*. Pacific Northwest National Laboratory report: Richland, WA, USA (2011).
- Brown DA, Chadwick MB, Capote R, Kahler AC, Trkov A, Herman MW, et al. ENDF/B-VIII.0: The 8th major release of the nuclear reaction data library with CIELO-project cross sections, new standards and thermal scattering data. *Nucl Data Sheets* (2018) 148:1–142. doi: 10.1016/j.nds.2018.02.001
- De Smet V, De Saint-Hubert M, Dinar N, Manessi GP, Aza E, Cassell C, et al. Secondary neutrons inside a proton therapy facility: MCNPX simulations compared to measurements performed with a Bonner sphere spectrometer and neutron $H^*(10)$ monitors. *Radiat Measurements* (2017) 99:25–40. doi: 10.1016/j.radmeas.2017.03.005
- Eliasson L, Lillhök J, Bäck T, Billnert-Maróti R, Dasu A, Liszka M. Range-shifter effects on the stray field in proton therapy measured with the variance-covariance method. *Submitted to Front Oncol same special issue as this work* (2022) 12:882230. doi: 10.3389/fonc.2022.882230
- De Saint-Hubert M, Verbeek N, Bäumer C, Esser J, Wulff J, Nabha R, et al. Validation of a Monte Carlo framework for out-of-field dose calculations in proton therapy. *Front Oncol Volume* (2022) 12:882489. doi: 10.3389/fonc.2022.882489



OPEN ACCESS

EDITED BY

Loredana G. Marcu,
University of Oradea, Romania

REVIEWED BY

Raquel Bar-Deroma,
Rambam Health Care Campus, Israel
Phillip Taddei,
Mayo Clinic, United States

*CORRESPONDENCE

Beatriz Sánchez-Nieto
bsanchezn@uc.cl

SPECIALTY SECTION

This article was submitted to
Radiation Oncology,
a section of the journal
Frontiers in Oncology

RECEIVED 09 February 2022

ACCEPTED 09 September 2022

PUBLISHED 06 October 2022

CITATION

Sánchez-Nieto B, López-Martínez IN,
Rodríguez-Mongua JL and Espinoza I
(2022) A simple analytical model for a
fast 3D assessment of peripheral
photon dose during coplanar
isocentric photon radiotherapy.
Front. Oncol. 12:872752.
doi: 10.3389/fonc.2022.872752

COPYRIGHT

© 2022 Sánchez-Nieto,
López-Martínez, Rodríguez-Mongua
and Espinoza. This is an open-access
article distributed under the terms of
the [Creative Commons Attribution
License \(CC BY\)](#). The use, distribution
or reproduction in other forums is
permitted, provided the original
author(s) and the copyright owner(s)
are credited and that the original
publication in this journal is cited, in
accordance with accepted academic
practice. No use, distribution or
reproduction is permitted which
does not comply with these terms.

A simple analytical model for a fast 3D assessment of peripheral photon dose during coplanar isocentric photon radiotherapy

Beatriz Sánchez-Nieto^{1*}, Ignacio N. López-Martínez¹,
José Luis Rodríguez-Mongua² and Ignacio Espinoza¹

¹Instituto de Física, Pontificia Universidad Católica de Chile, Santiago, Chile, ²Departamento de Radiofísica, Fundación Arturo López Pérez, Santiago, Chile

Considering that cancer survival rates have been growing and that nearly two-thirds of those survivors were exposed to clinical radiation during its treatment, the study of long-term radiation effects, especially secondary cancer induction, has become increasingly important. To correctly assess this risk, knowing the dose to out-of-field organs is essential. As it has been reported, commercial treatment planning systems do not accurately calculate the dose far away from the border of the field; analytical dose estimation models may help this purpose. In this work, the development and validation of a new three-dimensional (3D) analytical model to assess the photon peripheral dose during radiotherapy is presented. It needs only two treatment-specific input parameter values, plus information about the linac-specific leakage, when available. It is easy to use and generates 3D whole-body dose distributions and, particularly, the dose to out-of-field organs (as dose-volume histograms) outside the 5% isodose for any isocentric treatment using coplanar beams [including intensity modulated radiotherapy and volumetric modulated arc therapy (VMAT)]. The model was configured with the corresponding Monte Carlo simulation of the peripheral absorbed dose for a 6 MV abdomen treatment on the International Commission on Radiological Protection (ICRP) 110 computational phantom. It was then validated with experimental measurements using thermoluminescent dosimeters in the male ATOM anthropomorphic phantom irradiated with a VMAT treatment for prostate cancer. Additionally, its performance was challenged by applying it to a lung radiotherapy treatment very different from the one used for training. The model agreed well with measurements and simulated dose values. A graphical user interface was developed as a first step to making this work more approachable to a daily clinical application.

KEYWORDS

radiotherapy, photon peripheral dose, photon out-of-field dose, secondary cancer, stochastic radiation risk, Monte Carlo, analytical model, periphocal

1 Introduction

Radiation therapy (RT) is an effective treatment for cancer. Considering that cancer survival rates have been growing (1) and nearly two-thirds of those survivors are exposed to clinical radiation during its treatment (2), the study of long-term radiation effects, especially secondary cancer induction, has become increasingly important. As many secondary cancers may appear far from the target volumes, the dose received by out-of-field (or peripheral) organs should always be considered for the theoretical secondary cancer risk assessment (3–6).

Unfortunately, up to now, commercial treatment planning systems (TPSs) are not designed for the precise calculation of this peripheral dose, and significant deviations, compared to measurements and/or Monte Carlo (MC) simulations, have been previously reported (7–9). There are several published mathematical models for estimating secondary cancer induction probability as a function of the radiation dose (10–12), which should count with an accurate out-of-field (peripheral) dose distribution received by the patient during RT.

Advanced RT techniques like intensity modulated radiotherapy (IMRT) or volumetric modulated arc therapy (VMAT) are highly effective for achieving tumor control and dose reduction in out-of-field volumes near the border of the field due to reduced internal scatter (13). However, these techniques usually need long beam-on times than conformal treatments, which increase machine scatter and leakage and, consequently, distant peripheral doses. How much the increase in machine scatter and leakage outweighs the internal scatter depends on specific IMRT plans (optimization on the number of monitor units (MUs), tumor size, patient size, etc.). Some studies have quantified the global peripheral dose increase as a 1.8 (14)–1.9 (15) factor. For volumes distant from the border of the field, where the MU-dependent leakage predominates, a factor of 3 with respect to conformal fields has been found (16).

The peripheral photon dose (PPD) has three sources: i) leakage through the head shielding and the collimation systems, ii) scattering from the head and secondary collimators, and iii) scattering inside the patient (17) (see Figure 1). The scattering in the patient is the dominant source of the peripheral dose in regions close to the irradiated volume. However, its relative contribution to the total PPD rapidly decreases for further distances from the treatment edge (considered as the 50% isodose), leaving collimator scattering and leakage as the predominant dose sources in those regions. At considerable distances, leakage is the only relevant dose source (14, 18).

The software Peridose (19) was probably the first attempt for scattered dose calculation outside the primary beam for individual treatments. However, it was only designed to be used for rectangular fields. Then, a simple and flexible analytical model for PPD estimation, also implemented into a computer program termed PERIPHOCAL, correctly predicted the peripheral dose inside a humanoid phantom irradiated with IMRT and VMAT techniques (13, 20). It presents, however, two main limitations: i) the model was trained using only a few measurements points placed inside a humanoid phantom, and ii) it is one dimensional, *i.e.*, it assumed that the organs were described only by the *z* coordinate of the organ and its length along the craniocaudal direction.

Hauri et al. (21) chose a different approach to model the peripheral dose using complex mathematical functions to represent the physics behind each process and calculate the three peripheral dose components separately. Other recently published models (22, 23) also considered calculating each contribution of the PPD separately. They did calculations in water cylinders with fast computation times but at the price of needing several fitting coefficients. Despite their high accuracy, the main disadvantage of those approaches is their complexity, which makes the clinical application very cumbersome.

In this work, a new analytical model to assess PPD associated with RT is proposed. The model has been trained and validated. It needs only two treatment-specific input variables plus information about the linac-specific leakage when available. As the absorbed dose is given in mGy/MU, the total number of MUs used for the whole treatment will be required for the estimation of the absolute total peripheral absorbed dose. It makes calculations on the whole-body virtual CT of specific patients, which can be generated using a home-made software developed by the authors (24), available upon request. The model has been coded in a piece of software and interacts with the user through a graphical user interface (GUI), making accurate photon peripheral organ dose estimation applicable to the clinical workflow.

2 Methods and materials

2.1 The analytical model

We propose the following expression to model the 3D distribution of PPD (in mGy/MU):

$$PPD(x, y, z) = \left\{ \begin{array}{ll} \frac{\varepsilon(MU) \cdot F(f) \cdot (A_1 - A_2 |z|) \cdot e^{-A_3 \cdot \sqrt{x^2 + y^2 + z^2}}}{x^2 + y^2 + z^2} + (L_u - L_r); & \forall (x, y, z) / \sqrt{x^2 + y^2 + z^2} \leq 40 \text{ cm} \\ L_u; & \forall (x, y, z) / \sqrt{x^2 + y^2 + z^2} > 40 \text{ cm} \end{array} \right\} \quad (\text{Eq.1})$$

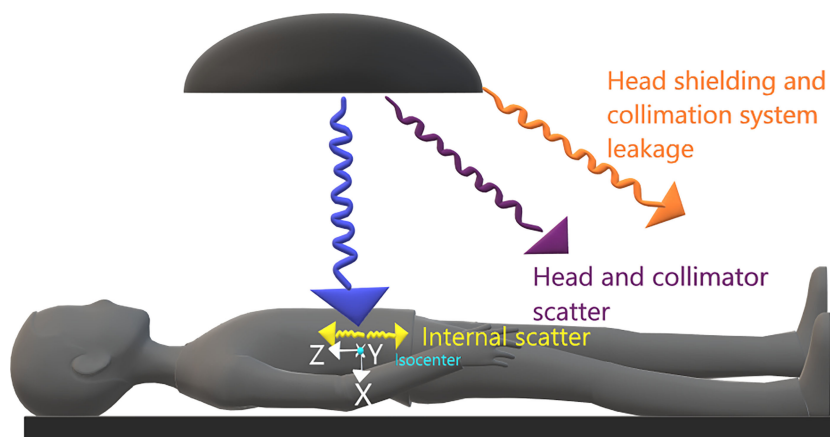


FIGURE 1
Representation of sources of peripheral dose and coordinate system at the present work.

where the coordinates x , y , and z (cm) indicate the position of each calculation point in a coordinate system with the origin at the treatment isocenter (whichever it is). x , y , and z go in the anterior–posterior, left–right, and caudal–cranial directions, respectively (see Figure 1). The model is intended to be used for dose estimation outside the 5% isodose surface from where TPSs are not accurate enough (3, 7). In agreement with other published works (14, 21, 25), our model assumes that for distances to the isocenter larger than 40 cm, the main contribution to PPD comes from the leakage (L_u), which is considered constant for the purposes of this work.

Equation 1 has some similarities with the model previously proposed by Sánchez-Nieto et al. (13). As in that work, the following correction factors considered here are

- $F(f)$: It corrects the field size when it is different from the one used in the reference treatment (see *Reference treatment on the ICRP 110 male phantom*). This correction is essential as the scattered radiation is field size dependent (25–27). In this work $F(f) = F_U(f)/F_R$, where F_U and F_R are the areas representing the field sizes used in the user and reference treatment plan, respectively. For field size calculation, we propose to take the average of the areas inside the 50% isodoses at the coronal and sagittal planes of the 3D dose distribution at the isocenter level. The estimated value for F_R was 149.2 cm².

- $\epsilon(MU)$: It corrects the number of monitor units (MUs) when they differ from the reference treatment plan (see *Reference treatment on the ICRP 110 male phantom*). This correction accounts that the PPD depends on the number of MUs corresponding to each treatment. In this work, $\epsilon(MU) = \frac{E_U(MU)}{E_R}$, where E_U represents the efficiency of the user treatment (in terms of the prescribed dose at the isocenter per MU) and, E_R is the treatment efficiency of the reference treatment plan. E_R was calculated, for the calibration conditions of the linac for which

the reference treatment was created (1cGy/MU at Source to Surface Distance (SSD), at d_{max}), as the MU that delivers 2 Gy to the isocenter of the ICRP 110 phantom as if it was made of water ($E_R = 2 \cdot \frac{10^3 \text{Gy}}{278 \text{ MU}} = 7.2 \frac{\text{mGy}}{\text{MU}}$)

- L_u : It corrects the leakage value whenever it is different from the one used in the reference treatment (L_r). This quantity should be measured (in mGy/MU) for every accelerator, but if this parameter is not available, we recommend using the value in this work as an approximation (see *Results*).

The values of the fitted coefficients $A_1(\text{mGy cm}^2 \text{ MU}^{-1})$, $A_2(\text{mGy cm MU}^{-1})$, and $A_3(\text{cm}^{-1})$ were obtained by fitting the model to the 3D PPD distribution simulated with MC for the reference treatment plan (see *Reference treatment on the ICRP 110 male phantom* for more details).

In summary, to use this model, the user requires for each calculation point (coordinates in cm), $E_U(MU)$ in $\frac{\text{mGy}}{\text{MU}}$, $F_U(f)$ in cm², and L_u (when available) in mGy/MU. If the absolute absorbed dose is needed, the total MU will be additionally required.

2.2 Reference treatment on the ICRP 110 male phantom

The reference treatment was an equally spaced eight-field isocentric plan centered at the mid-abdomen of the adult reference computational phantom ICRP 110 (28), with 10×10cm² open fields. The whole-body dose distribution was generated by an MC simulation (BEAMnrc code) of an Elekta Axesse with the Agility collimation system, up to 40 cm from the isocenter. The technical details of the MC simulation can be found in Sánchez-Nieto et al. (7). The MC simulation of the ICRP 110 considers the electronic density of each voxel. The

uncertainty of the MC dose to points is given directly by the BEAMnrc code within the dose output file (*.3ddose") as a relative error value array in row 6 of the file.

2.3 Model calibration

Parameters A_1 , A_2 , and A_3 were obtained by fitting Equation 1 to the 3D MC dose distribution corresponding to the reference treatment ($\epsilon = 1$ and $F = 1$) using the *fminsearch* function in MATLAB® (version R2021a). No information about the electronic density is considered by Equation 1 but the spatial position of the voxels. Only phantom voxels outside the 5% isodose surface were considered for the fitting, as the TPSs accurately estimate the dose distribution inside (7). Voxels representing the body contour were also excluded for the parameterization due to possible electron contamination, which is not considered by this model. As the geometry of the MC simulation did not include the gantry's shielding, MC data were only used up to 40 cm from the isocenter, and, farther than this point, our measurement of leakage was used instead ($L_r = L_u = 0.001 \frac{\text{mGy}}{\text{MU}}$). The fitting process gave the values of the constant coefficients. $A_1 (\text{mGy cm}^2 \text{ MU}^{-1})$, $A_2 (\text{mGy cm MU}^{-1})$, and $A_3 (\text{cm}^{-1})$.

2.4 Dose to organs

The model in Equation 1 depends on the three Cartesian coordinates; therefore, when the calculation is made on a whole-body CT, the model generates a 3D out-of-field dose cube from which the dose-volume histogram (DVH) of the contoured organs can also be extracted.

2.5 Experimental validation

2.5.1 Validation using TLD-100 in an anthropomorphic phantom

We first tested the model by applying it to a case of the pelvic irradiation of an anthropomorphic phantom and comparing the results with TLD-100 measurements. A 6 MV VMAT treatment for prostate cancer was planned (MONACO) and delivered to the male 701-D ATOM phantom (CIRS®) with an Elekta Synergy linac (different from the one used as reference). The phantom, which only consists of the head and torso, held 271 TLD-100 chips distributed in 20 predefined internal organs. The Thermoluminescent Dosimeter (TLDs) had been previously calibrated using one X-ray equipment with beam quality corresponding to an Half Value Layer (HVL) = 6.141 mm Al. Energy corrections according to the mean energy at each point (7) were applied following Duggan's model (29). The ATOM

phantom was previously scanned for planning. Then, on the planning station, the prostate gland and rectum outlines were drawn following the contours of a real plan of another prostate cancer patient with similar physical characteristics. Finally, a VMAT plan was created to deliver one fraction of 1.8 Gy at the isocenter, corresponding to a total of 498 MU (i.e., $E_U = 3.6 \text{ mGy/MU}$). F_U was equal to 53.2 cm^2 in this case (calculated as the average of the areas inside the 50% isodoses at the coronal and sagittal planes of the 3D dose distribution at the level of the isocenter). The absorbed dose to each point measured by the TLDs was compared to our model predictions using the following values of the model variables: $\epsilon = \frac{1.8 \times 10^3 / 498}{2.10^3 / 278} = \frac{3.6}{7.2} = 0.48$ and $F = \frac{53.2}{149.2} = 0.35$ and $L_u = 0.0032 \text{ mGy/MU}$ (measured with TLD-100 at 40 cm from the isocenter).

Uncertainty in the dose estimated by TLD measurements was calculated from the propagation of the variables' uncertainty involved in dose calculation (i.e., experimental TLD calibration, individual sensitivity, and energy correction factors).

2.5.2 Testing the model using a Monte Carlo simulation of a lung treatment on the ICRP phantom

The performance of the model was challenged by applying it to a case very different from the reference treatment: a three-field equally weighted lung irradiation plan ($5 \times 5 \text{ cm}^2$ open fields) with one AP (60°) and two posterior oblique (220° and 240°) fields. The plan was simulated with MC on the ICRP110 reference phantom (7). The treatment isocenter was located at the upper-right lung lobe receiving 2 Gy per fraction. The whole-body dose distribution was obtained and compared with the estimations of the model presented in this work. The ϵ and F values used for the model estimations were $\epsilon = \frac{2 \times 10^3 / 266}{2.10^3 / 278} = 1.04$, $F = \frac{53.41}{149.2} = 0.36$ and $L_u = L_r = 0.001 \frac{\text{mGy}}{\text{MU}}$.

The absorbed dose to organs calculated with the proposed model, the MC simulation, and the software PERIPHOCAL (13) were also compared, using the same leakage and field size for the modeling cases. The same organs considered by PERIPHOCAL were selected for comparison. The PERIPHOCAL model calculates dose uncertainty ranges (95% confidence interval) using the expression 7 of the publication (13). The contours for those organs were taken from the ICRP 110 phantom.

3 Results

3.1 Reference treatment and model calibration

Representative isodoses of the reference treatment plan on the ICRP 110 phantom are shown in Figure 2.

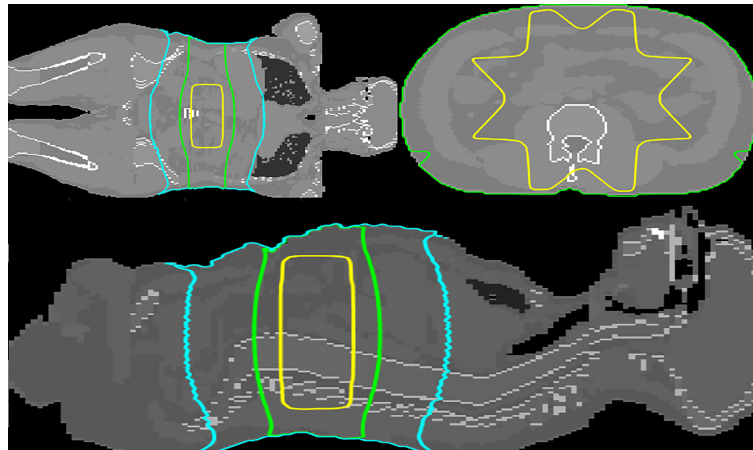


FIGURE 2

Transversal, coronal and sagittal views at the level of the isocenter (mid-abdomen). The 50%, 5%, and 1% isodoses are depicted in yellow, green, and cyan, respectively. The dose distribution was calculated by MC simulation.

The fitted constant coefficients are (*Model calibration*) $A_1 = 37.890 \pm 1.415 \left(\frac{\text{mGy cm}^2}{\text{MU}} \right)$, $A_2 = 0.679 \pm 0.074 \left(\frac{\text{mGy cm}}{\text{MU}} \right)$, $A_3 = 0.007 \pm 0.004 \left(\text{cm}^{-1} \right)$.

The final (calibrated) version of the model can therefore be written (for points outside the 5% isodose) as in Eq (2).

$$PPD(x, y, z) = \begin{cases} \frac{\frac{E_U(\text{MU})}{7.2 \text{ MU}} \cdot \frac{F_U(f)}{149.2 \text{ cm}^2} \cdot \left(37.890 \frac{\text{mGy cm}^2}{\text{MU}} - 0.679 \frac{\text{mGy cm}}{\text{MU}} * |z| \right) \cdot e^{-0.007 * \sqrt{x^2 + y^2 + z^2}}}{x^2 + y^2 + z^2} + \left(L_u - 0.001 \frac{\text{mGy}}{\text{MU}} \right); & \forall (x, y, z) / \sqrt{x^2 + y^2 + z^2} \leq 40 \text{ cm} \\ L_u; & \forall (x, y, z) / \sqrt{x^2 + y^2 + z^2} > 40 \text{ cm} \end{cases} \quad (\text{Eq.2})$$

The uncertainty of the model was calculated considering the absolute percentage differences between the doses given by the model and the ones given by MC, relative to MC. In total, 95% of all points (x, y, and z) presented an absolute percentage difference < 23.2% (the average percentual difference was 7.84%).

Hereafter, the model in Equation 2 will be named Periphocal 3D. Figure 3 depicts the peripheral dose to points relative to the isocentric dose, estimated by Periphocal 3D and MC used for calibration. Note that this model does not use any electronic density information.

3.2 Model validation and testing

3.2.1 Validations using TLD-100 inside the ATOM phantom

Measurements obtained with the TLDs and the dose estimated by Periphocal 3D for the same positions are

depicted in Figure 4. The average absolute difference between Periphocal 3D dose estimations and the TLD dose measurements, relative to the latter, is 16.8%, with a maximum difference on one point of 15.8 mGy/Gy (31.4 mGy/Gy predicted by the model, 47.2 mGy/Gy measured by

TLD). The model performance is in the low extreme of mean differences of 11%–44% mentioned in Mazonakis and Damilakis (3).

3.2.2 Testing in a more complex scenario

Representative isodoses calculated with MC on the ICRP 110 phantom, corresponding to the lung plan described in *Testing the model using a Monte Carlo simulation of a lung treatment on the ICRP phantom*, are shown in Figure 5. Figure 6 depicts the peripheral dose, relative to the isocentric dose, calculated by Periphocal 3D and MC for the same case.

The average of absolute differences relative to MC is 44.0%, with a maximum difference of 34.9 mGy/Gy on a point (14.1 mGy/Gy predicted by the model and 49.0 mGy/Gy simulated by MC).

The comparison of absorbed dose to a set of organs, given by PERIPHOCAL (13), Periphocal 3D, and the MC simulation, is shown in Figure 7.

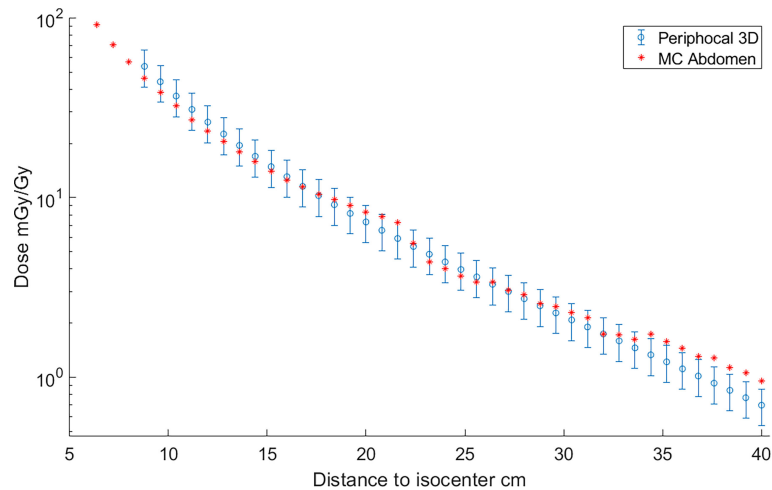


FIGURE 3

Absorbed dose, expressed as peripheral dose (mGy) given by bothPeriphocal 3D and the MC simulation for the reference plan on the ICRP 110 phantom, relative to the isocentric dose (Gy) vs. distance to isocenter. Displayed symbols correspond to points along the craniocaudal axis (towards the phantom's head) at the isocenter depth. The uncertainty associated withPeriphocal 3D is $\pm 23.2\%$. The uncertainties of the MC dose values are within the size of the symbols. Even though the model was parameterized using the dose distribution calculated by MC, which considers the electronic density of each voxel, and the analytical model assumes a uniform electronic density, there is an agreement for most of the points.

4 Discussion

Periphocal 3D gives the PPD in 3D as a function of the point's coordinates, and it requires only three input treatment parameters: the field size, total MU, and the MU per Gy to the

isocenter (L_u is the fourth parameter, which can be used when available). It has three empirically fitted coefficients A_1 , A_2 , and A_3 . Even though those coefficients do not have a direct physical meaning, A_3 may be seen as an 'effective' linear attenuation coefficient of photons scattered inside and outside the patient.

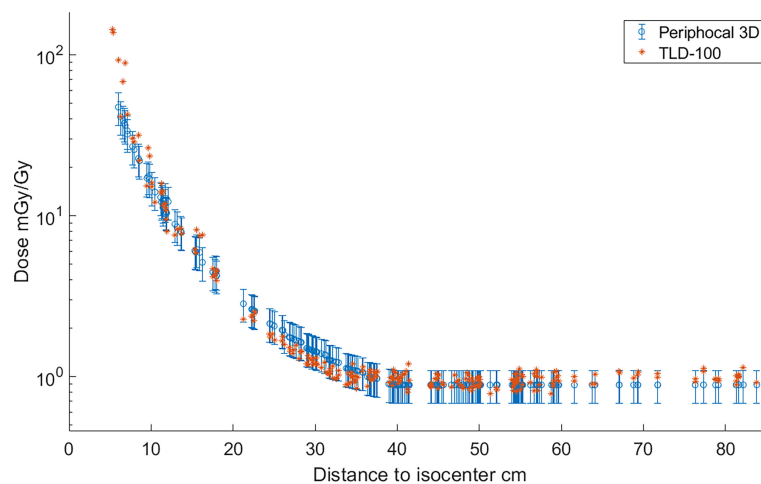


FIGURE 4

Absorbed dose, expressed as peripheral dose (mGy), calculated byPeriphocal 3D and measured with TLD-100, relative to the isocentric dose (Gy) for a VMAT irradiation of the prostate. As TLDs positions are scattered inside the ATOM phantom, the dose values were plotted versus Euclidean distance to the isocenter. TLDs uncertainties are within the size of the symbol.

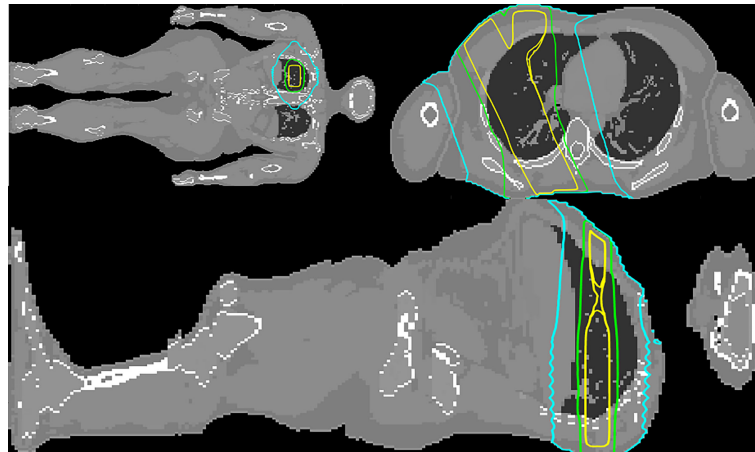


FIGURE 5

Coronal, transversal and sagittal views at the level of the isocenter of the MC simulated upper right lung irradiation with three square beams of . The 50%, 5%, and 1% isodoses are depicted in yellow, green, and cyan, respectively.

4.1 Limitations of the model

Although Periphocal 3D represents an improvement compared to its previous version, there are some limitations to take into account. Regarding geometry and X-ray attenuation, it is worth noting that Periphocal 3D was

calibrated with a nearly symmetrical eight-field treatment (see Figure 2) and Equation 1 has spherical symmetry. Thus, the model should become less accurate when non-symmetrical isodoses, usually associated with plans with fewer beams, as in Figure 5 (lung case), are generated. Luckily, VMAT and IMRT treatments usually consider several beam entries around the

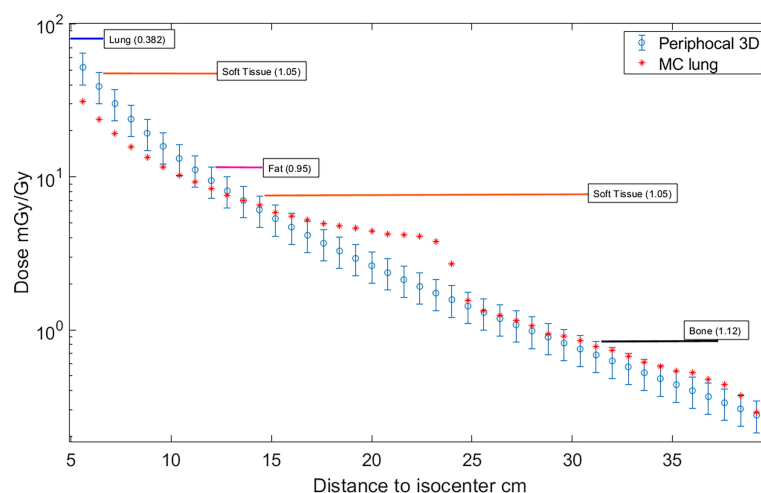


FIGURE 6

Absorbed dose, expressed as peripheral dose (mGy), calculated by Periphocal 3D and MC for the lung case, relative to the isocentric dose (Gy). Displayed symbols correspond to points along the craniocaudal axis (towards the phantom's feet) at the isocenter depth. The uncertainties of the MC dose values are within the size of the symbols. It has also been displayed the type of tissue together with the corresponding electronic density in which calculations were performed (e.g., from 7 cm to 12 cm far from the isocenter is soft tissue).

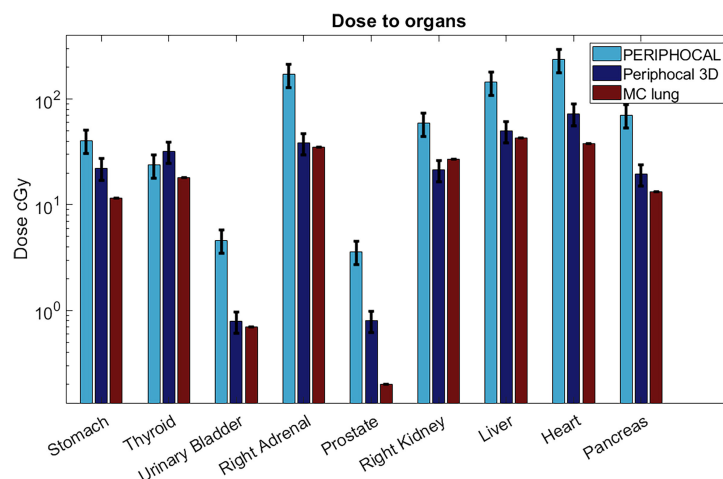


FIGURE 7

Absorbed dose to organs according to Periphocal 3D, PERIPHOCAL, and the MC simulation of the lung plan for the 60 Gy delivered to the isocenter. Error bars are presented as the uncertainty in each model (25% for PERIPHOCAL and 23.2% for Periphocal 3D).

isocenter. Another possible issue is the attenuation of X-rays inside the patients when significant tissue heterogeneities are present. Since Periphocal 3D was calibrated in the abdomen, which is mainly composed of soft tissue, its application to the treatments of tumors in tissues with different X-ray attenuation characteristics will necessarily imply worse accuracy. This can be observed in Figure 6, where calculations within the soft tissue after the lung shows an overestimation of the dose because it does not take into consideration the smaller backscatter contribution from the lung tissue. Additionally, in bone, as Periphocal 3D assumes that everything is water, the calculated absorbed dose underestimates the MC calculation.

It is worth noting that the large discrepancy between MC and Periphocal 3D calculations in the lung plan is mainly associated with the use of small fields ($5 \times 5 \text{ cm}^2$) for which a sharp drop at 21 or 22 cm approximately from the isocenter occurs in correspondence with the edges of the primary collimator that provides additional shielding. The same phenomenon has been described elsewhere (30, 31). This drop is much softer for larger beams, as seen in Figure 3 for the $10 \times 10 \text{ cm}^2$, in agreement with Kaderka et al. and Jagetic and Newhauser (30, 31). That is, the full MC simulation recreates a profile shape that the Periphocal 3D does not (see *Comparison with another analytical model* to verify how a more complex physics-based model also fails in fitting the decrease due to the additional shielding of the primary collimator).

The A_1 , A_2 , and A_3 coefficients were established by fitting the model to the dose distribution generated by the MC simulation of an Elekta Linac. Stoval et al. (18) showed in Appendix A how peripheral dose profiles depend on the design and construction of the machine head and collimators. However, our measurements—figure 1.a in Sánchez-Nieto et al. (13)—of peripheral doses for the same treatment delivered on the same phantom using different combinations of energy and linacs allowed us to conclude that the observed variability was within the model's uncertainty. Those who can generate a 3D dose distribution of their specific linac from a full MC model or thorough experimental measurements can obtain their specific A_1 , A_2 , and A_3 coefficients.

Periphocal 3D does not work for skin dose calculations. A peripheral skin dose can be separately estimated based on other previously published works (32).

4.2 Dose to organs

The availability of 3D dose distribution allows for the calculations of DVHs for peripheral organs (input for some models of secondary cancer risk), dose profiles along any axis or 2D dose distributions on any plane. The 3D dose distribution may also be helpful, for example, when the patient has a pacemaker, an intern defibrillator at positions where TPSs are not accurate, or for any of the harmful effects listed by Mazonakis and Damilakis (3).

Figure 7 shows the dose to organs for a lung treatment in comparison to PERIPHOCAL and MC. This is a case for which Periphocal 3D presents some limitations, as discussed in the previous section. Even so, the model offers an improvement compared to PERIPHOCAL for all organs but the thyroid. Both PERIPHOCAL and Periphocal 3D overestimate the dose, which can be explained by the highly non-symmetrical geometry of the dose distribution in this area. For the prostate, despite Periphocal 3D performing much better than PERIPHOCAL, a significant difference compared with MC is still present. As we already mentioned, the geometry of our MC did not include the gantry's shielding and, therefore, might not correctly account for leakage. Thus, the dose for the prostate (farther away than 40 cm from the isocenter) given by MC may be underestimated. A detailed study of the effect of linac's shielding on the leakage is being conducted. For the urinary bladder, close to the prostate but closer to the isocenter than 40 cm, Periphocal 3D and MC agree.

This model can be used retrospectively and prospectively (for example, using the virtual whole-body CT generated by our home-made software (24) to calculate in a systematic way dose to peripheral organs and, together with clinical follow-ups, detecting possible secondary cancers, creating a database for a more accurate parameterization of secondary cancer models (3–6).

Sánchez et al. (13) showed that PPD does not significantly change with energy (differences within the model's uncertainty), and thus, Periphocal 3D can be used even above 10 MV. However, neutron contamination might become relevant above this threshold. For those dealing with energies >10 MV,

the total peripheral dose to organs should include the peripheral neutron dose to organs. The model published by Irazola et al. (33) can be used to estimate the neutron dose to out-of-field organs.

4.3 Comparison with another analytical model

Schneider et al. (22) developed a nice physics-based analytical model of the total absorbed dose for the primary, scattered, and leakage radiation of square fields of 6 MV at any arbitrary point in a phantom. That work is one of the latest models published but tested only for square fields. They mention the validation of the model for arbitrary MLC aperture to determine the model applicability to IMRT treatments as a future step. Thus, to our knowledge, no other analytical model has been developed and tested for intensity-modulated treatments with which we can compare.

Figure 8 depicts the comparison between the dose as calculated by our model and Schneider's model for irradiation with a $10 \times 10 \text{ cm}^2$ field using a 6 MV beam. The parameter field size $F_U(f)$ at the isocenter was estimated from the width of the profile at 50% of the isocenter dose as $F_U(10) = 103.63 \text{ cm}^2$. It was also assumed that $\epsilon_U = \epsilon_R$.

Both models agree within our model's uncertainties. Curiously enough, both models fail to reproduce the additional shielding of the primary collimator as predicted by Schneider's MC model. Note that this effect is sharper for

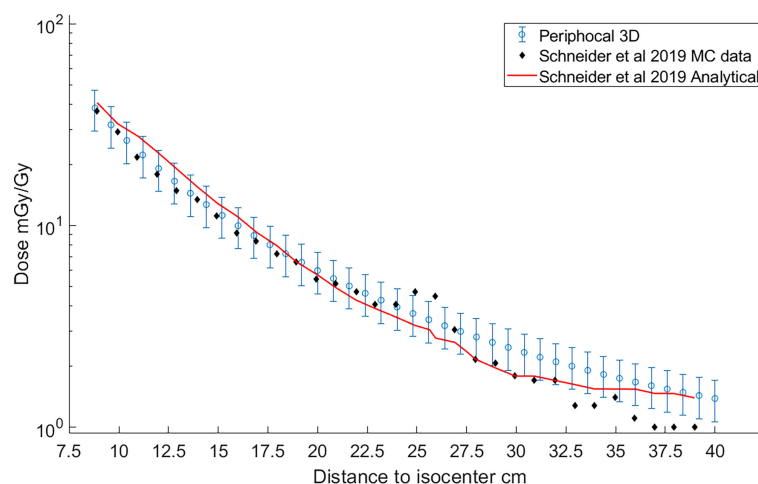


FIGURE 8

Comparison of the peripheral dose calculated with Periphocal 3D (light-blue open symbols with uncertainty bars) and Schneider et al. (22) model (solid line). Schneider model's data were recreated from figure 14.a of the publication (22). Additionally, the MC data used to fit the 30 parameters of the peripheral dose of Schneider's model—table 4 in Schneider et al. (22)—are also included as black diamonds.

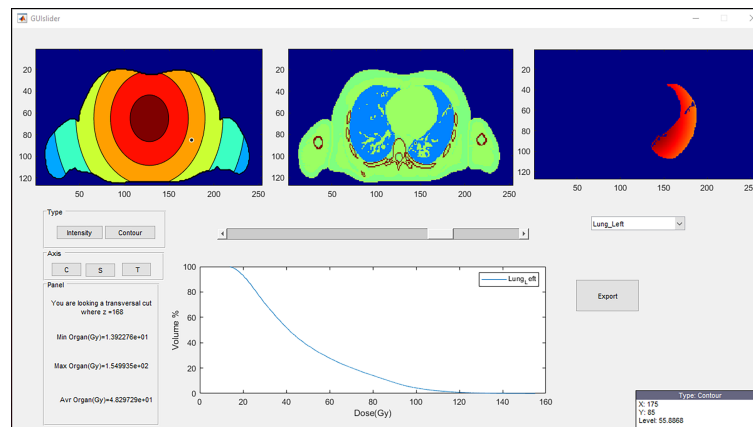


FIGURE 9

A representative visualization of the Periphocal 3D's GUI. The three upper boxes can be displayed as transversal (T), coronal (C), or sagittal (S) views. The upper-left box represents the peripheral dose normalized to the maximum (which is always displayed in red) (i.e., the red color might represent a different level of dose at each different slice), and the central box is the anatomical information. The upper-right box represents the dose distribution of the chosen organ (lung in this example) from the list of all contoured organs. Its corresponding cumulative DVH is displayed in the plot below. The DVH can be exported as an ASCII file. The lower-left box informs the value of the z coordinate, together with the maximum, minimum, and average dose of the chosen organ. The user can finally move around the upper-left and central boxes so that the coordinates and dose level (in mGy/Gy) of the cursor are displayed in the lower-right box. The GUI can be shared with those who request it.

smaller fields, as in the case of Figure 6, corresponding to a treatment plan of $5 \times 5 \text{ cm}^2$.

4.4 Whole-body CT

In this work, the ICRP 110 phantom and the CT of the ATOM phantom were used for the 3D calculations. However, for personalized clinical applications, a whole-body CT of each patient is needed. We have solved this problem without actually irradiating the patient (which would be unacceptable due to the unjustified additional dose), following a methodology presented in the companion article. This methodology uses the always-available planning CT to generate an approximate patient-specific whole-body CT based on a rigid 3D image registration algorithm. The input for calculating the 3D dose distribution is the whole-body CT ignoring the differences in electronic density between the voxels but with all organs' contours considered in the ICRP110.

4.5 Graphical user interface

A GUI was created in MATLAB[®] (version R2021a) to ease the use of Periphocal 3D (Figure 9). The output of our whole-

body CT software is a MATLAB array. Periphocal 3D's GUI takes less than 10 s to calculate the whole-body dose distribution after loading those MATLAB arrays. However, Periphocal 3D's GUI also accepts CT DICOM files. Additionally, for all organs segmented in the input CT, a DVH is created. Figure 8 depicts an example of the mentioned GUI.

5 Conclusions

A simple 3D analytical model was created for photon peripheral dose estimation outside the 5% isodose for isocentric coplanar treatments with any field sizes (with or without intensity modulation) and applicable to all linacs manufacturers. The model was successfully tested with experimental dose measurements on an anthropomorphic phantom irradiated with a VMAT treatment plan and compared with one physics-based analytical model. It only uses three (or four) input parameters to characterize each radiotherapy treatment. As a first step to making this work more approachable to a daily clinical application, a graphical interface was developed, making the calculation of DVHs in peripheral organs and the 3D visualization of the corresponding dose distributions possible.

Data availability statement

The standalone software Periphocal 3D and the ICRP 110 adult reference phantom, with the format required by Periphocal 3D, are available upon request to bsanchezn@uc.cl.

Author contributions

BS-N designed the project, got the funding, co-supervised the work of IL-M, and wrote the paper. IL-M worked in the development of the model under the guidance of BSN and IE. JR-M brought out the Monte Carlo Simulations and help IL-M to develop the model. IE co-supervised the work of IL-M and collaborated with the writing of the manuscript. All authors contributed to the article and approved the submitted version.

Funding

This work was funded by ANID (FONDECYT N1181133).

References

1. American Cancer Society. Cancer treatment and survivorship facts and figures 2019–2021. *Am Cancer Soc* (2019) 2019, 1–48. Available at: <https://www.cancer.org/research/cancer-facts-statistics/survivor-facts-figures.html>.
2. Smart DR. *Physician characteristics and distribution in the US*. Chicago, IL: American Medical Association, (2015).
3. Mazonakis M, Damilakis J. Out-of-field organ doses and associated risk of cancer development following radiation therapy with photons. *Phys Med* (2021) 90:73–82. doi: 10.1016/j.ejmp.2021.09.005
4. National Research Council. BEIR VII: health risks from exposure to low levels of ionizing radiation: report in brief. *Natl Acad* (2006) 93:93–6. doi: 10.17226/11340
5. De Gonzalez AB, Iulian Apostoaei A, Veiga LHS, Rajaraman P, Thomas BA, Owen Hoffman F, et al. RadRAT: A radiation risk assessment tool for lifetime cancer risk projection. *J Radiol Prot* (2012) 32(3):205–22. doi: 10.1088/0952-4746/32/3/205
6. Taddei PJ, Khater N, Zhang R, Geara FB, Mahajan A, Jalbout W, et al. Inter-institutional comparison of personalized risk assessments for second malignant neoplasms for a 13-year-old girl receiving proton versus photon craniospinal irradiation. *Cancers (Basel)* (2015) 7(1):407–26. doi: 10.3390/cancers7010407
7. Sánchez-Nieto B, Medina-Ascanio KN, Rodríguez-Mongua JL, Doerner E, Espinoza I. Study of out-of-field dose in photon radiotherapy: A commercial treatment planning system versus measurements and Monte Carlo simulations. *Med Phys* (2020) 47(9):4616–25. doi: 10.1002/mp.14356
8. Howell RM, Scarboro SB, Kry SF, Yaldo DZ. Accuracy of out-of-field dose calculations by a commercial treatment planning system. *Phys Med Biol* (2010) 55(23):6999–7008. doi: 10.1088/0031-9155/55/23/S03
9. Azab H, Moussa R, Kamaleldin M. Peripheral photon doses from different techniques delivered in prostate radiotherapy: Experimental measurements and TPS calculations. *Arab J Nucl Sci Appl* (2019) 0(0):0–0. doi: 10.21608/ajnsa.2019.13839.1222
10. Sánchez-Nieto B, Romero-Expósito M, Terrón JA, Sánchez-Doblado F. Uncomplicated and cancer-free control probability (UCFCP): A new integral approach to treatment plan optimization in photon radiation therapy. *Phys Medica* (2017) 42:277–84. doi: 10.1016/j.ejmp.2017.03.025
11. Schneider U. Modeling the risk of secondary malignancies after radiotherapy. *Genes (Basel)* (2011) 2(4):1033–49. doi: 10.3390/genes2041033
12. Hall EJ, Wu CS. Radiation-induced second cancers: The impact of 3D-CRT and IMRT. *Int J Radiat Oncol Biol Phys* (2003) 56(1):83–8. doi: 10.1016/S0360-3016(03)00073-7
13. Sánchez-Nieto B, Elfar R, Irazola L, Romero-Expósito M, Lagares JI, Mateo JC, et al. Analytical model for photon peripheral dose estimation in radiotherapy treatments. *BioMed Phys Eng Express* (2015) 1(4). doi: 10.1088/2057-1976/1/4/045205
14. Ruben JD, Lancaster CM, Jones P, Smith RL. A comparison of out-of-field dose and its constituent components for intensity-modulated radiation therapy versus conformal radiation therapy: Implications for carcinogenesis. *Int J Radiat Oncol Biol Phys* (2011) 81(5):1458–64. doi: 10.1016/j.ijrobp.2010.08.008
15. Chen MJ, da Silva Santos A, Sakuraba RK, Lopes CP, Gonçalves VD, Weltman E, et al. Intensity-modulated and 3D-conformal radiotherapy for whole-ventricular irradiation as compared with conventional whole-brain irradiation in the management of localized central nervous system germ cell tumors. *Int J Radiat Oncol Biol Phys* (2010) 76(2):608–14. doi: 10.1016/j.ijrobp.2009.06.028
16. Klein EE, Maserang B, Wood R, Mansur D. Peripheral doses from pediatric IMRT. *Med Phys* (2006) 33(7):2525–31. doi: 10.1118/1.2207252
17. Kase KR, Svensson GK, Wolbarst AB, Marks MA. Measurements of dose from secondary radiation outside a treatment field. *Int J Radiat Oncol Biol Phys* (1983) 9(8):1177–83. doi: 10.1016/0360-3016(83)90177-3
18. Stovall M, Blackwell CR, Cundiff J, Novack DH, Palta JR, Wagner LK, et al. Fetal dose from radiotherapy with photon beams: report of AAPM radiation therapy committee task group no. 36. *Med Phys* (1995) 22(1):63–82. doi: 10.1118/1.597525
19. Van Der Giessen PH. Peridose, a software program to calculate the dose outside the primary beam in radiation therapy. *Radiother Oncol* (2001) 58(2):209–13. doi: 10.1016/S0167-8140(00)00326-1
20. Sanchez-Nieto B, Irzola L, Romero-Expósito, Terrón-Leon JA S-DF. Validation of a clinical peripheral photon dose model: Prostate IMRT irradiation of alderson phantom. *Radiother Oncol* (2016) 119(S1):S385–6. doi: 10.1016/S0167-8140(16)32058-8
21. Hauri P, Hälgl RA, Besserer J, Schneider U. A general model for stray dose calculation of static and intensity-modulated photon radiation. *Med Phys* (2016) 43(4):1955–68. doi: 10.1118/1.4944421
22. Schneider CW, Newhauser WD, Wilson LJ, Kapsch RP. A physics-based analytical model of absorbed dose from primary, leakage, and scattered photons

Acknowledgments

We would like to acknowledge Jessica Hernández and Gabriel Zelada (Clínica Alemana-Universidad del Desarrollo, Santiago, Chile) for the data set of TLD-100 measurements.

Conflict of interest

The authors declare that the research was conducted in the absence of any commercial or financial relationships that could be construed as a potential conflict of interest.

Publisher's note

All claims expressed in this article are solely those of the authors and do not necessarily represent those of their affiliated organizations, or those of the publisher, the editors and the reviewers. Any product that may be evaluated in this article, or claim that may be made by its manufacturer, is not guaranteed or endorsed by the publisher.

from megavoltage radiotherapy with MLCs. *Phys Med Biol* (2019) 64(18):21. doi: 10.1088/1361-6560/ab303a

23. Wilson LJ, Newhauser WD, Schneider CW, Kamp F, Reiner M, Martins JC, et al. Method to quickly and accurately calculate absorbed dose from therapeutic and stray photon exposures throughout the entire body in individual patients. *Med Phys* (2020) 47(5):2254–66. doi: 10.1002/mp.14018
24. Muñoz I, Sánchez-Nieto B, Espinoza I. PO-1559 synthetic patient-specific whole-body CT for the calculation of peripheral dose during radiotherapy. *Radiother Oncol* (2022) 170:S1341–2. doi: 10.1016/S0167-8140(22)03523-X
25. Bordy JM, Bessieres I, D'Agostino E, Domingo C, D'Errico F, Di Fulvio A, et al. Radiotherapy out-of-field dosimetry: Experimental and computational results for photons in a water tank. *Radiat Meas* (2013) 57:29–34. doi: 10.1016/j.radmeas.2013.06.010
26. Balasubramanian R, Sellakumar P, Bilimappa RS, Supre SS, Sankar BN. Measurements of peripheral dose for multileaf collimator based linear accelerator. *Rep Pract Oncol Radiother [Internet]* (2006) 11(6):281–5. doi: 10.1016/S1507-1367(06)71073-2
27. Miljanić S, Bordy JM, D'Errico F, Harrison R, Olko P. Out-of-field dose measurements in radiotherapy - an overview of activity of EURADOS working group 9: Radiation protection in medicine. *Radiat Meas* (2014) 71:270–5. doi: 10.1016/j.radmeas.2014.04.026
28. ICRP. *Adult reference computational phantoms ICRP publication 110* Vol. 39. Oxford: Elsevier (2009).
29. Duggan L, Hood C, Warren-Forward H, Haque M, Kron T. Variations in dose response with x-ray energy of LiF:Mg,Cu,P thermoluminescence dosimeters: Implications for clinical dosimetry. *Phys Med Biol* (2004) 49(17):3831–45. doi: 10.1088/0031-9155/49/17/001
30. Kaderka R, Schardt D, Durante M, Berger T, Ramm U, Licher J, et al. Out-of-field dose measurements in a water phantom using different radiotherapy modalities. *Phys Med Biol* (2012) 57(16):5059–74. doi: 10.1088/0031-9155/57/16/5059
31. Jagetic LJ, Newhauser WD. A simple and fast physics-based analytical method to calculate therapeutic and stray doses from external beam, megavoltage x-ray therapy. *Phys Med Biol* (2015) 60(12):4753–75. doi: 10.1088/0031-9155/60/12/4753
32. García-Hernández T, Vicedo-González A, Sánchez-Nieto B, Romero-Expósito M, Roselló-Ferrando J. Peripheral surface dose from a linear accelerator: Radiochromic film experimental measurements of flattening filter free versus flattened beams. *Radiat Prot Dosimetry* (2020) 188(3):285–98. doi: 10.1093/rpd/ncz286
33. Irazola L, Terrón JA, Sánchez-Nieto B, Roberto B, Sánchez-Doblado F. Peripheral equivalent neutron dose model implementation for radiotherapy patients. *Phys Med [Internet]* (2017) 42:345–52. doi: 10.1016/j.ejmp.2017.03.018

Frontiers in Oncology

Advances knowledge of carcinogenesis and tumor progression for better treatment and management

The third most-cited oncology journal, which highlights research in carcinogenesis and tumor progression, bridging the gap between basic research and applications to improve diagnosis, therapeutics and management strategies.

Discover the latest Research Topics

[See more →](#)

Frontiers

Avenue du Tribunal-Fédéral 34
1005 Lausanne, Switzerland
frontiersin.org

Contact us

+41 (0)21 510 17 00
frontiersin.org/about/contact

